UNIVERSITÉ D'ORLÉANS

ÉCOLE DOCTORALE Energie, Matériaux, Sciences de la Terre et de l'Univers

ICARE-CNRS

THÈSE présentée par :

Alaa Hamadi

soutenue le : **09 Décembre 2021**

pour obtenir le grade de : **Docteur de l'Université d'Orléans**

Discipline/ Spécialité Energétique, génie des procédés

Experimental study on the formation of soot precursors by shock tube technique

THÈSE dirigée par :

M. COMANDINI Andrea	Chargé de recherche, ICARE-CNRS, Orleans, France

RAPPORTEURS :

Mme. BATTIN-LECLERC Frédérique	Directrice de recherche, LRGP-CNRS, Nancy, France
M. FRASSOLDATI Alessio	Professeur assistant, Politecnico di Milano, Italie

---

JURY :

M. CATOIRE Laurent	Professeur, Université Paris-Saclay, Président du Jury
M. COMANDINI Andrea	Chargé de recherche, ICARE-CNRS, Orleans, France
Mme. CHAUMEIX Nabiha	Directrice de recherche, ICARE-CNRS, Orleans, France
Mme. BATTIN-LECLERC Frédérique	Directrice de recherche, LRGP-CNRS, Nancy, France
M. FRASSOLDATI Alessio	Professeur assistant, Politecnico di Milano, Italie

Alaa HAMADI

Étude expérimentale sur la formation de précurseurs de suie par la technique des tubes à choc

Résumé : La thèse vise à développer un modèle cinétique complet, mettant l'accent sur la chimie de la formation des HAP, basé sur les profils des espèces obtenus dans un tube de choc couplé à des techniques de chromatographie / spectrométrie de masse. Cette configuration est conçue et développée afin de mesurer avec précision les espèces stables jusqu'à quatre cycles aromatiques. En particulier, la pyrolyse de différents combustibles et mélanges aromatiques est étudiée dans des conditions de combustion moteur, à des températures de 900 à 1800 K, à une pression d'environ 20 bars et un temps de réaction de 4 ms. Les combustibles étudiés comprennent le propylène, le propyne, le benzène et le toluène avec ou sans combustibles C_2/C_3 ajoutés, le phénylacétylène, le phénylacétylène + acétylène/éthylène, les alkylbenzènes en C_8-C_{10}.

Les résultats de mes travaux comprennent : i) l'obtention d'une vaste base de données expérimentales sur les profils d'espèces; ii) développement d'un modèle cinétique chimique détaillé et complet; iii) une compréhension avancée des schémas cinétiques et des mécanismes impliqués dans la décomposition thermique des combustibles et la formation de molécules précurseurs de suie. Ces résultats peuvent servir de développement de modèles futurs concernant des combustibles plus complexes ainsi que la base pour la construction de codes de suie pour la simulation de la formation de particules dans les applications de combustion.

Mots-clés : tube de choc, formation de suie, chromatographie en phase gazeuse / spectrométrie de masse, modélisation cinétique chimique, HAP, benzène, toluène, phénylacétylène, alkylbenzènes, acétylène, éthylène, propylène, propyne

Experimental study on the formation of soot precursors by shock tube techniques

Summary: Polycyclic aromatic hydrocarbons (PAHs) are considered important soot precursors. Exploring and understanding the PAH formation pathways are essential building-blocks toward developing reliable kinetic models that can accurately simulate soot formation. This work aims at developing a comprehensive kinetic model emphasizing on PAH formation chemistry based on the detailed species profiles obtained in a high-purity single-pulse shock tube coupled to gas chromatography / mass spectrometry techniques. In particular, the pyrolysis of different aromatic fuels and mixtures is studied under combustion-like conditions, over a wide temperature range (900-1800 K), pressures of around 20 bar, and reaction times of 4 ms. The fuels include propylene, propyne, benzene and toluene with and without addition of C2/C3 fuels, phenylacetylene, phenylacetylene + acetylene/ethylene, C_8-C_{10} alkylbenzenes.

The outputs of the present work include: i) an extensive experimental database of species profiles, including PAHs up to four-rings; ii) development of a detailed and comprehensive chemical kinetic model; iii) advanced understanding on the kinetic schemes and mechanisms involved in the fuels thermal decomposition and formation of soot precursor molecules. These results can serve for future model developments concerning more complex fuels and surrogates as well as the base for the construction of soot codes for simulation of particle formation in combustion applications.

Keywords: single-pulse shock tube, soot formation, gas chromatography / mass spectrometry, chemical kinetic modeling, PAHs, benzene, toluene, phenylacetylene, alkylbenzenes, acetylene, ethylene, propylene, propyne

ICARE-CNRS
1C, av de la Recherche Scientifique
CS 50060
45071 ORLEANS Cedex 2

Résumé

La thèse vise à développer un modèle cinétique complet, mettant l'accent sur la chimie de la formation des HAP, basé sur les profils détaillés des espèces obtenus dans un tube de choc à impulsion unique couplé à des techniques de chromatographie / spectrométrie de masse. Cette configuration est conçue et développée afin de mesurer avec précision les espèces stables jusqu'à quatre cycles aromatiques. En particulier, la pyrolyse de différents combustibles et mélanges aromatiques est étudiée dans des conditions de combustion motrice, sur une large plage de températures, de 900 à 1800 K, à une pression constante d'environ 20 bars et un temps de réaction de 4 ms.

Les mécanismes des réactions impliquées dans la décomposition thermique du propylène et du propyne et la croissance moléculaire subséquente jusqu'à des produits à quatre cycles sont d'abord ajoutés et mis à jour sur la base de la dernière version du modèle CRECK, car le propylène et le propyne sont des produits abondants résultant d'une consommation du combustible. La chimie du phényle et du benzyle est ensuite étudiée par pyrolyse du benzène et du toluène, respectivement. Les deux combustibles sont étudiés avec et sans ajout d'autres molécules généralement présentes dans tous les systèmes réactionnels, tels que l'acétylène (C_2H_2), l'éthylène (C_2H_4), le propène (C_3H_6) ou le propyne (C_3H_4-P). Pour traiter de l'influence des combustibles en C_2 ou C_3 ajoutés sur la spéciation des HAP du benzène et du toluène, différents mélanges binaires sont examinés. La spéciation des HAP à partir du phénylacétylène, intermédiaire de combustion, est investiguée. Étant donné que le phénylacétylène est également un intermédiaire important dans le mécanisme d'addition d'hydrogène-abstraction-acétylène (HACA) à partir du benzène, les mélanges phénylacétylène/C_2 sont étudiés afin de mettre en évidence les étapes HACA ultérieures entre le combustible et les hydrocarbures légers insaturés. Enfin, les voies de réaction du benzyle sont examinées plus en détail en considérant les alkylbenzènes linéaires en C_8-C_{10} comme combustibles initiaux, car la chimie correspondante de la formation de HAP est également contrôlée par des réactions impliquant le radical benzyle.

Les résultats de mes travaux comprennent : i) l'obtention d'une vaste base de données expérimentales sur les profils d'espèces, y compris les intermédiaires de HAP jusqu'à quatre anneaux, provenant de la pyrolyse de composants et de mélanges de combustibles clés; ii) développement d'un modèle cinétique chimique détaillé et complet validé par confrontation aux

résultats expérimentaux ; iii) une compréhension avancée des schémas cinétiques et des mécanismes impliqués dans la décomposition thermique des combustibles et la formation de molécules précurseurs de suie. Ces résultats peuvent servir de développement de modèles futurs concernant des combustibles plus complexes et des substituts ainsi que la base pour la construction de codes de suie pour la simulation de la formation de particules dans les applications de combustion.

Mots-clés : hydrocarbures aromatiques, benzène, toluène, phénylacétylène, alkylbenzènes, acétylène, éthylène, propylène, propyne, HAP, tube de choc à impulsion unique, formation de suie, chromatographie en phase gazeuse / spectrométrie de masse, modélisation cinétique chimique

Introduction

La forte dépendance à l'égard des combustibles fossiles conventionnels et non conventionnels réduit non seulement leur disponibilité, mais entraîne également des risques pour l'environnement et la santé en raison des polluants émis. Ces émissions polluantes comprennent le monoxyde de carbone (CO), les oxydes d'azote (NO_X), les oxydes de soufre (SO_X), les hydrocarbures aromatiques polycycliques (HAP) et les particules (PM_X). Parmi ces sous-produits de combustion, les particules de suie en suspension dans l'air constituent un polluant environnemental majeur dont les effets négatifs sont nombreux, allant de la mauvaise qualité de l'air au réchauffement de la planète, en passant par de graves dangers pour la santé humaine. Pour ces raisons, des efforts sont déployés pour limiter les émissions de particules en imposant des réglementations internationales de plus en plus strictes. Les stratégies visant à réduire la formation de particules comprennent l'optimisation de la conception des dispositifs de combustion et la reformulation des carburants à l'aide d'additifs. Le développement de telles stratégies repose souvent sur des calculs de dynamique des fluides computationnelle (CFD) où la description cinétique chimique détaillée de la formation des PM constitue une partie fondamentale. Pourtant, les mécanismes détaillés de la formation de la suie pendant la combustion incomplète des combustibles dans des conditions de pyrolyse ou de manque d'oxygène sont l'un des problèmes de combustion les moins bien résolus, principalement en raison que les mécanismes de formation de la suie sont très complexes et impliquent un grand nombre de processus chimiques et physiques [5]-[8]. Les processus physico-chimiques de

formation des particules de suie à partir de molécules de carburant hydrocarboné sont représentés dans la figure 1.1 [9]. Dans un premier temps, les molécules de carburant se décomposent en molécules d'hydrocarbures plus petites et en radicaux libres par des réactions de pyrolyse ou d'oxydation dans un environnement à haute température. Ces espèces contribuent aux réactions de croissance en formant des cycles aromatiques stables. Dans la complexité de ces processus menant à la suie, les étapes limitantes de la chaîne globale sont la formation ultérieure du premier cycle aromatique (benzène) et les voies menant aux HAP. La formation du premier cycle aromatique est aujourd'hui assez bien comprise [5]. En réalité, les HAP sont généralement considérés comme les principaux précurseurs des particules de suie et également comme des espèces importantes participant au processus de croissance de la suie. Ainsi, une meilleure compréhension des voies de réaction chimique menant à la formation des HAP est une question essentielle pour comprendre la croissance et la formation de la suie dans les environnements de combustion. Une fois que les précurseurs moléculaires de la suie sont disponibles dans l'environnement de combustion, la première particule est formée pendant la nucléation. La coagulation de la particule et la croissance de sa surface font que la particule gagne en masse et en taille, tandis que les phénomènes d'oxydation tendent à contrecarrer la croissance en éliminant le carbone sous forme de CO et de CO_2.

A partir de la brève description présentée ci-dessus, il est clair que des mécanismes cinétiques détaillés fiables qui décrivent précisément la formation des HAP sont nécessaires pour la modélisation de la formation des particules de suie. L'objectif de cette thèse est de fournir des bases de données expérimentales pour la chimie de la formation des HAP dans des conditions typiques rencontrées dans les dispositifs de combustion modernes et, à partir de ces résultats expérimentaux, de développer un modèle cinétique détaillé et complet décrivant la formation des HAP qui peut être utilisé comme base pour des modèles améliorés de prédiction des suies. Les expériences pyrolytiques ont été choisies pour permettre une simplification de la chimie et l'isolement des mécanismes de réaction qui conduisent à la croissance des structures multi-cycles. Un tube de choc à impulsion unique couplé à des diagnostics de chromatographie en phase gazeuse - spectrométrie de masse a été développé pour mesurer les intermédiaires stables, y compris les grands HAP jusqu'à quatre cycles, à haute pression, haute température et dans des conditions de forte dilution. Ces données ont été utilisées pour la validation du modèle cinétique chimique complet et détaillé.

Etude bibliographique

Ce chapitre est divisé en deux sections. La première section résume un certain nombre de mécanisme et de voies réactionnelles de formation des HAP. Les principaux mécanismes présentés dans cette partie sont mécanisme HACA (Abstraction d'hydrogène et addition d'acétylène) qui représente le processus de formation des composés aromatiques polycycliques par l'arrachage d'un atome d'hydrogène suivie de l'addition d'acétylène, mécanisme HAVA (Abstraction d'hydrogène et addition de vinyle) qui représente le processus de formation des composés aromatiques polycycliques par l'arrachage d'un atome d'hydrogène à la molécule aromatique puis l'addition de vinyle sur la radicale formé, mécanisme d'addition des phényles et de cyclisation (PAC) qui implique l'addition d'un radical phényle sur un site de fusion d'une espèce aromatique suivie d'une déhydrocyclisation, fragmentation par cycloaddition diradicalaire (CAF) qui constitue l'addition d'o-benzyne à une molécule aromatique et leur fragmentation ultérieure pour former des HAP plus grands et de l'acétylène, mécanisme d'addition de méthyle et de cyclisation (MAC) qui commence par l'addition d'un ou plusieurs radicaux méthyles avant la déshydrogénation et la cyclisation et conduit à la formation de HAP péricondensés, recombinaison des radicaux stabilisés par résonance, recombinaison radical-radical et réactions radical-molécule.

La deuxième partie contient une vue d'ensemble des recherches disponibles dans la littérature concernant la pyrolyse des hydrocarbures aromatiques, y compris le benzène, le toluène, le phénylacétylène, l'éthyl-, le propyl- et le n-butyl-benzène, et les mélanges à base de benzène/toluène qui sont pertinents pour la présente étude.

Etude expérimentale

Ce chapitre décrit le principe du tube à choc à impulsion unique et le système analytique GC/GC-MS utilisé dans ce travail. Il démontre également les méthodes expérimentales utilisées pour obtenir les facteurs d'étalonnage qui sont à leur tour utilisés pour obtenir les profils de concentration. Enfin, la validation du montage expérimental en utilisant le carburant heptane largement étudié est également fournie. Une brève description est donnée ici.

L'appareil à tube de choc à impulsion unique se compose d'une section entraînée (longueur : 6 m ; diamètre intérieur : 78 mm) et d'une section pilote (longueur : 3,7 m ; diamètre intérieur : 120

mm), séparées par un double diaphragme. Un réservoir de 150 litres est placé à proximité du diaphragme du côté de la section motrice afin de faire fonctionner le tube à choc en une seule impulsion. La section basse pression est chauffée à 90°C pour éviter la condensation et l'absorption de combustibles et de produits de réaction lourds. Pour éviter les dépôts de carbone, la surface intérieure du tube de choc est nettoyée régulièrement.

Quatre capteurs de pression (CHIMIE METAL A25L05B) couplés à des oscilloscopes numériques rapides (Tektronix modèle TDS5034B et Keysight Technologies modèle DSOX2014A) sont montés à un intervalle de 150 mm le long de la partie terminale de la section entraînée, le dernier étant à 82 mm de la paroi terminale. Le temps mis par l'onde de choc pour passer chaque intervalle est utilisé pour déduire la vitesse de l'onde incidente. Cette valeur, ainsi que la pression, la température et la composition du mélange initial (gaz d'essai), permettent de déterminer la température et la pression derrière l'onde de choc incidente et l'onde de choc réfléchie (T_5 et p_5) en résolvant les équations de conservation. Cette méthode s'est avérée donner des conditions thermodynamiques précises derrière les ondes de choc réfléchies pour des vitesses d'ondes de choc et des conditions initiales définies. Pour chaque expérience, le profil de pression dans le temps est également fourni pour une simulation précise des résultats. Une autre méthode de calcul de T_5 dans les expériences de tubes à choc à impulsion unique, adoptée par divers groupes de recherche, consiste à utiliser des thermomètres chimiques pour calculer les températures moyennes tout au long du processus de réaction. Cette méthode compense les non-idéalités rencontrées dans la mesure expérimentale, mais elle est sujette à certaines incertitudes liées à : i) la mesure de la vitesse de l'onde de choc incidente ; ii) la définition des paramètres de la constante de vitesse de réaction unimoléculaire pour les espèces sélectionnées ; iii) l'extrapolation des courbes d'étalonnage en dehors de la plage de température des thermomètres chimiques (valable principalement pour les températures supérieures à 1350-1400K). En outre, des études antérieures ont montré que l'utilisation de thermomètres chimiques ou de conditions de pression constante ne peut pas rendre compte correctement des réactions impliquant les radicaux stabilisés par résonance. Considérant que le présent travail est effectué avec un tube de choc de grand alésage où les non-idéalités sont minimisées, la méthode actuelle basée sur le calcul théorique de T5 est préférée ici. L'incertitude maximale estimée de la T_5 calculée est de l'ordre de ±30 K. Cette estimation est basée sur des considérations liées aux dimensions physiques des capteurs (2 mm de diamètre, 1,2 mm de surface sensible) qui peuvent entraîner

une erreur dans la correspondance entre l'élévation du signal due au passage de l'onde et la position réelle sur la surface sensible. Il s'agit d'une estimation conservatrice qui inclut également les incertitudes dues à l'atténuation de l'onde. Un capteur de pression PCB Piezotronics, protégé par une couche de silicone vulcanisé à température ambiante (RTV), est monté sur la paroi d'extrémité de la section entraînée et est utilisé pour enregistrer l'historique de pression pour chaque choc à partir duquel le temps de réaction correspondant peut être défini. Le temps de réaction est l'intervalle de temps entre l'arrivée de l'onde de choc et le moment où la pression tombe à 80 % de p_5. Le temps de réaction nominal dans la configuration expérimentale actuelle est de 4 ms. Les mélanges post-chocs sont échantillonnés par une vanne actionnée par air, fournie par la High Pressure Equipment Company (HiP modèle 30-11HF4), fixée au centre de la paroi d'extrémité. La vanne d'échantillonnage est déclenchée par le capteur de pression de la paroi d'extrémité avec un délai de 4 ms qui est équivalent au temps de réaction nominal. L'ouverture et la fermeture de la vanne nécessitent des centaines de millisecondes, ce qui donne un volume d'échantillon relativement important qui permet de détecter de très petites concentrations de HAP (~ 10-2 ppm). En raison de ce grand volume d'échantillon, la vitesse moyenne est utilisée au lieu de la vitesse extrapolée pour la détermination de T_5 et p_5, car elle ressemble plus aux conditions réelles rencontrées par les mélanges de carburant. L'atténuation de la vitesse pour la plupart des expériences est inférieure à 2,5 %, de sorte que la différence entre les T_5 calculées avec la vitesse moyenne et celles extrapolées est généralement inférieure à 20 K, ce qui est dans les limites de l'incertitude mentionnée ci-dessus. Il est également à noter que le long temps d'échantillonnage n'affecte pas les concentrations des espèces en raison de la très basse température à la fin de la période de trempe.

Le gaz échantillonné est transféré au système d'analyse par des tubes SilcoTek, qui sont chauffés à 210 °C pour éviter la condensation. Le premier GC (Agilent 7890) est équipé d'un détecteur à ionisation de flamme (FID) relié à une colonne DB-17-ms pour les mesures des espèces lourdes. Un détecteur de conductivité thermique (TCD) est couplé à une colonne Molsieve 5A pour contrôler l'absence d'air. Une boîte à vanne externe qui peut réguler la température jusqu'à 320 °C est utilisée pour ce GC afin de minimiser la perte de composés lourds due à la condensation. Un FID couplé à une colonne HP Plot Q est installé dans le second GC (Thermo Trace GC Ultra), utilisé pour les mesures de petits hydrocarbures, et un spectromètre de masse DSQ™ (dual stage quadrupole) est également connecté pour aider à l'identification des espèces. Les

connexions du système analytique et les paramètres de fonctionnement ont été optimisés dans ce travail, apportant des avantages sous différents aspects, notamment une sensibilité accrue des espèces de HAP à l'état de traces et une meilleure séparation des espèces de HAP qui ont un temps de rétention similaire. Par exemple, les isomères $C_{14}H_{10}$, le phénanthrène et l'anthracène, qui apparaissent à 11.41 et 11.50 min, respectivement, peuvent être mieux séparés et quantifiés maintenant. Les expériences actuelles permettent de détecter des espèces de HAP comportant jusqu'à quatre cycles et dont la concentration maximale est supérieure à 10^{-2} ppm.

L'identification des espèces de HAP dépend principalement de leur temps de rétention connu grâce aux injections de standards. Pour les espèces sans standards disponibles, le spectromètre de masse fournit des informations sur les masses moléculaires, à partir desquelles il est possible de déduire la composition élémentaire, et il suggère également d'éventuels candidats isomères. La quantification des concentrations des espèces repose sur les calibrations de la réponse du FID. Les petits hydrocarbures, à l'exception du diacétylène (C_4H_2) et du triacétylène (C_6H_2), sont étalonnés à l'aide de mélanges standard de composition connue. L'étalonnage du C_4H_2 et du C_6H_2 est réalisé dans des expériences de pyrolyse à haute température de l'acétylène (C_2H_2), sur la base de la conservation de l'atome de carbone. Les principales espèces de HAP jusqu'à trois cycles, notamment l'indène, l'indane, le naphtalène, l'acénaphtalène, le bibenzyle, le biphénylméthane, le fluorène, le phénanthrène et l'anthracène, sont étalonnées en phase gazeuse selon les procédures suivantes : i) des quantités connues de composés spécifiques de HAP sont dissoutes dans du dichlorométhane pour préparer les solutions d'étalonnage ; ii) une petite quantité (1-5 µl) de la solution est injectée dans un récipient en verre (d'un volume de 500 ml) à l'aide d'une seringue GC ; la solution se vaporise immédiatement dans le récipient en verre, qui est préalablement mis sous vide et chauffé à 200 °C ; iii) le récipient est ensuite rempli d'argon à une pression d'environ 900 Torr, et le mélange gazeux résultant contenant les standards de HAP repose pendant environ 15-20 min pour garantir une bonne homogénéité ; iv) le mélange gazeux est injecté dans le système de chromatographie en phase gazeuse au moins trois fois pour en vérifier l'homogénéité et les surfaces de pic pour l'étalon de HAP correspondant sont normalisées par la pression d'injection ; v) la procédure est répétée pour plusieurs fractions molaires d'étalons qui couvrent la gamme nécessaire pour les expériences, et les facteurs d'étalonnage correspondants sont dérivés. Les HAP à quatre cycles (pyrène et fluoranthène) ne peuvent pas être vaporisés de façon régulière avec l'approche ci-dessus. Par conséquent, leurs facteurs d'étalonnage sont déterminés

par extrapolation à partir de ceux des HAP à deux et trois cycles, à savoir le naphtalène et le phénanthrène. L'incertitude des mesures de concentration devrait être de l'ordre de 5 % pour les petites espèces étalonnées directement, et de 10 à 15 % pour les espèces de HAP étalonnées en phase gazeuse, tandis que l'erreur dans les concentrations mesurées des espèces de HAP à quatre cycles peut atteindre 50 %.

En ce qui concerne les produits chimiques utilisés dans les expériences, les carburants et les étalons de HAP sont achetés chez Sigma-Aldrich, et les gaz, notamment l'acétylène (>99,5 %), l'éthylène (>99,5 %), le propylène (>99,5 %), l'argon (>99,9999 %) et l'hélium (>99,995 %), sont fournis par Air Liquide. Un purificateur de gaz 450B Matheson avec une cartouche 454 est connecté à la bouteille d'acétylène pour éliminer les éventuelles traces d'acétone, et l'acétone se trouve en dessous de la limite de détection du système GC dans toutes les expériences. Les mélanges expérimentaux sont préparés dans un cylindre en acier inoxydable électropoli de 136 L, préalablement évacué à des pressions inférieures à 10^{-5} mbar à l'aide d'une pompe turbo moléculaire. Pour préparer un mélange expérimental avec une composition requise, les composants du carburant sont introduits dans le cylindre et les pressions partielles sont mesurées avec un transducteur de pression MKS Baratron 0-10 Torr (modèle 122BA). De l'argon est ensuite ajouté jusqu'à une pression d'environ 10 bars, surveillée par un transducteur de pression MKS Baratron de 0-10 000 Torr (modèle 627D). Avant les expériences, le mélange gazeux repose pendant une nuit pour s'homogénéiser et la composition réelle est analysée avec le GC. La section entraînée est mise sous vide avec une pompe turbo moléculaire jusqu'à ce que la pression soit inférieure à 10^{-5} torr avant d'être remplie avec le mélange expérimental.

Des expériences d'essai pour la pyrolyse du n-heptane à la concentration initiale de combustible de 100 ppm ont été réalisées à la P_5 nominale de 10 bar avec T_5 allant de 900 à 1800 K. Les profils de concentration des espèces ont été comparés aux prédictions de différents modèles cinétiques largement validés, comme le montre dans la **figure 3.12**. Le bon accord entre les mesures et les simulations sur les formes et les tailles des profils confirme la fiabilité de l'installation actuelle.

Modélisation cinétique

Dans ce chapitre, un modèle cinétique détaillé mettant l'accent sur les mécanismes de formation des HAP à deux de quatre cycles est établi. Le modèle CRECK [144] est choisi comme base pour le développement du modèle cinétique actuel. Des études récentes [153], [154] ont suggéré que le processus de combustion peut être découplé en étapes séparées de pyrolyse et d'oxydation. Par conséquent, ce travail permettra de démêler le réseau complexe de réactions dans les systèmes de combustion dans des conditions de pyrolyse à haute pression afin de réduire la complexité cinétique. En conséquence, la pyrolyse de combustibles purs comprenant le benzène (C_6H_6), le toluène (C_7H_8), le propylène (C_3H_6), le propyne (C_3H_4-P), le phénylacétylène ($C_6H_5C_2H$) et l'alkyl benzène C_8-C_{10} ainsi que des mélanges de combustibles avec des hydrocarbures insaturés couvrant $C_6H_5C_2H + C_2H_x$, $C_6H_6 + C_2H_x/C_3H_y$, et des mélanges $C_7H_8 + C_2H_x/C_3H_y$ (x=2,4, y=4,6) sont réalisés. Les voies de réaction déterminées théoriquement et les coefficients de vitesse rapportés dans des études récentes sont utilisés par le modèle actuel. En outre, des voies de réaction possibles sont proposées sur la base des observations expérimentales.

Les simulations dans ce travail ont été réalisées avec le modèle de réacteur homogène du logiciel COSILAB, avec un temps de réaction nominal de 4.0 ms sous une pression constante de 20 bar. L'hypothèse de la pression constante est typiquement utilisée pour simuler les résultats de spéciation échantillonnés à partir d'expériences de tubes à chocs à impulsion unique, et elle est bien justifiée pour les tubes à chocs de grand diamètre comme le HPST, où les non-idéalités sont minimisées [137], [150]. Néanmoins, des réactions impliquant des radicaux stabilisés par résonance ou des radicaux méthyles peuvent potentiellement se produire pendant la trempe post-choc [151], [152]. Par conséquent, des simulations utilisant des profils de pression allant jusqu'à 10 ms sont également effectuées pour surveiller l'impact de telles réactions sur les fractions molaires finales observées des espèces.

Résultats et discussions

Ce chapitre fera la synthèse des principaux résultats expérimentaux et de simulations numériques obtenus pendant cette thèse. Ils seront commentés et discutés.

Pyrolyse du propylène et du propyne :

L'étude sur les carburants C_3 est menée avec environ 500 ppm de propylène et de propyne dans l'argon comme réactif initial. Le propylène et le propyne ont un profil de décomposition distinct

(**Figure 5.1**). Le propylène suit une courbe lisse, tandis que le propyne présente un profil de décomposition en deux étapes. Le propylène est principalement consommé par la réaction chimiquement activée $H+C_3H_6=CH_3+C_2H_4$ dans toute la gamme de températures. Dans la première étape, l'isomérisation en allène régit la consommation de propyne, tandis que dans la deuxième étape, la réaction $H+C_3H_4\text{-}P=CH_3+C_2H_2$ devient la voie de décomposition prédominante du propyne. Le propyne fait partie des produits de décomposition du propylène et, par conséquent, tous les produits de pyrolyse issus des expériences sur le propyne sont également présents dans le pool d'espèces du propylène. D'autre part, la pyrolyse du propylène donne lieu à une variété de petits hydrocarbures et à des teneurs plus faibles en aromatiques par rapport à la pyrolyse du propyne. Les teneurs en aromatiques dépendent fortement de la formation du premier cycle aromatique, le benzène, qui résulte en grande partie de la réaction d'auto-recombinaison du propargyle. La dissociation du propyne induit plus de radicaux propargyles et donc plus de benzène. Cependant, les analyses de modélisation montrent que les voies de réaction responsables de la formation des HAP sont similaires dans la pyrolyse du propylène et du propyne. L'indène (**Figure 5.8 a**) dépend principalement de la consommation de 1-phényl-propyne ($C_6H_5C_3H_3P\_1$) et phényl-allène ($C_6H_5C_3H_3A$), et le chemin benzyl+acétylène ($C_7H_7+C_2H_2$) a également une contribution mineure. $C_6H_5C_3H_3P\_1$ (**Figure 5.8 b**) est principalement formée par les réactions moléculaire+radicalaire de $C_3H_4\text{-}P+C_6H_5$ et $C_6H_5C_2H+CH_3$, et cette dernière voie est prédominante à température élevée. En ce qui concerne la formation de $C_6H_5C_3H_3A$ (**Figure 5.8 c**), la réaction radical+radical de $C_6H_5+C_3H_3$ est la source principale, et la réaction $C_3H_4\text{-}P+C_6H_5 = C_6H_5C_3H_3A+H$ a également des contributions dans la pyrolyse du propyne à des températures modérées. Les interactions ultérieures de l'indényle avec le méthyle et le propargyle conduisent à la formation des espèces de HAP les plus abondantes, respectivement le naphtalène (**Figure 5.9 a**) et l'acénaphtylène (**Figure 5.10 e**). Les radicaux naphtyle participent ensuite à la production d'aromatiques plus importants, notamment le méthyl naphtalène (**Figure 5.10 b**), l'éthynyl-naphtalène (**Figure 5.10 d**), le fluorène (**Figure 5.10 f**) et le phényl-naphtalène (**Figure 5.12 c**). En outre, quatre espèces différentes de $C_{14}H_{10}$ sont identifiées et quantifiées dans la pyrolyse du propylène et du propyne, y compris le phénanthrène dominant ($PC_{14}H_{10}$), et ses isomères, le 9-méthylène-fluorène ($C_{13}H_8CH_2$), l'anthracène ($AC_{14}H_{10}$) et le diphénylacétylène ($C_6H_5CCC_6H_5$). Les réactions d'addition-élimination de $C_6H_5+C_6H_5C_2H$ donnent $C_{13}H_8CH_2$ (**Figure 5.11 b**) et $C_6H_5CCC_6H_5$

(**Figure 5.11 a**), qui s'isomérisent ensuite en $PC_{14}H_{10}$ (**Figure 5.11 c**). L'isomérisation du $PC_{14}H_{10}$ conduit à la formation de l'$AC_{14}H_{10}$ (**Figure 5.11 d**). Des traces de fluoranthène ($FC_{16}H_{10}$) et de pyrène ($PC_{16}H_{10}$) sont présentes. Le $FC_{16}H_{10}$ (**Figure 5.12 a**) est principalement formé par la déshydrogénation de phényl-naphtalène ($C_{10}H_7C_6H_5$) suite à la réaction entre $C_{10}H_7$ et C_6H_6 ; tandis que la production de $C_{16}H_{10}$ (**Figure 5.12 b**) repose sur le mécanisme HACA du radical phénanthryle ($PC_{14}H_9$)+C_2H_2.

Pyrolyse du benzène et ajout de combustibles C_2/C_3 :

Le benzène est étudié en tant que le seul combustible (100 et 200 ppm dans l'argon) et avec l'ajout d'environ 500 ppm des hydrocarbures C_2/C_3 typiques disponibles dans tous les environnements de combustion. Le benzène est principalement consommé par la réaction $H+C_6H_6=H_2+C_6H_5$ dans tous les systèmes étudiés constituant le benzène dans le mélange initial. De fortes interactions sont notées entre le phényle et les combustibles C_2, en particulier l'acétylène, par des réactions $C_6H_5+ C_2H_x= C_6H_5C_2H_{x-1} +H$ (x=2, 4). Les preuves directes de ces interactions comprennent l'amélioration de la réactivité de décomposition des deux composants du combustible en raison de l'abondance des atomes d'hydrogène résultant des réactions $C_6H_5+C_2H_x$ (x=$_2$, $_4$), et la formation remarquable de mono-aromatique hydrocarbures en C_8 (phenylacetylene et styrene). Dans la co-pyrolyse benzène-C_3, les niveaux des espèces C_1-C_3 sont plus élevés par rapport à la pyrolyse du benzène pur. Cela provoque la formation de benzène par des réactions d'auto-recombinaison de propargyle dans la région de basse température, et le propyne a des effets plus prononcés (**Figure 5.31 a**). Parmi les petits hydrocarbures ajoutés au mélange initial, seul le profil de l'acétylène est significativement affecté par la présence du benzène (**Figure 5.25 b-c and Figure 5.31 b-c)**. En ce qui concerne les produits aromatiques à un seul cycle, la présence d'acétylène dans le mélange initial ou comme produit de la décomposition thermique de l'éthylène ou des combustibles en C_3 entraîne, à des degrés divers, la formation de fractions molaires importantes de phénylacétylène par rapport au cas du benzène pur, par la réaction $C_6H_5+C_2H_2$. Le phénylacétylène (**Figure 5.27 f and Figure 5.34 a)** joue un rôle central dans la formation des grands HAP. Pour des raisons similaires, les concentrations de diéthynylbenzène (**Figure 5.27 h and Figure 5.34 b)** sont plus élevées dans les mélanges binaires que dans le cas du benzène. Le styrène est l'un des principaux produits dans le cas benzène + éthylène et benzène + propylène, par les réactions $C_6H_5+C_2H_4$ et $C_6H_6+C_2H_3$, alors

qu'il est produit en plus petites quantités dans la copyrolyse benzène + propyne (**Figure 5.27 g and Figure 5.34 c)**. La présence de combustibles en C_3 favorise également la formation de toluène **(Figure 5.34 d)** et d'autres hydrocarbures aromatiques alkylés **(Figure 5.34 e-j)**. La chimie des produits HAP est fortement influencée par les réactions impliquant les hydrocarbures insaturés ajoutés. En particulier, le rôle central des réactions impliquant les intermédiaires C_3 et le cycle unique dans la formation de l'indène a été confirmé et validé expérimentalement pour la première fois. Dans la co-pyrolyse benzène + C_3, le radical indényle est également important pour la formation du méthylindène **(Figure 5.37 c)** et du benzofulvène **(Figure 5.37 a)**, qui sont des précurseurs fondamentaux du naphtalène et de l'acénaphtylène. Ces voies complètent les voies conventionnelles de l'HACA. En effet, la formation de naphtalène (**Figure 5.28 b and Figure 5.37 b)** et d'acénaphtylène (**Figure 5.28 d and Figure 5.37 h)** est fortement améliorée lorsque l'on considère les carburants en C_3 par rapport à la co-pyrolyse benzène + éthylène et à la co-pyrolyse benzène + acétylène. Dans les cas benzène + C_2, les voies HACA sont les principales sources de naphtalène bien que les faibles concentrations d'atomes H inhibent la réaction $C_{10}H_7$ + H. En ce qui concerne l'acénaphtylène, dans la co-pyrolyse benzène + acétylène, la voie HACA et la décomposition thermique / isomérisation du biphényle jouent un rôle majeur, tandis que pour la co-pyrolyse benzène + éthylène, une voie supplémentaire par la réaction $C_{10}H_7$ + C_2H_4 est accessible. L'abondance de C_2H_2 dans le système réactionnel des combustibles binaires donne lieu à de nombreux composés à branches éthynyles tels que l'éthynyl naphtalène (**Figure 5.28 c and Figure 5.37 g)**, le diéthynyl naphtalène (**Figure 5.28 h and Figure 5.37 j)**, l'éthynyl acénaphtylène (**Figure 5.28 i and Figure 5.37 k)** et l'éthynyl biphényle (**Figure 5.28 f and Figure 5.37 l)**. D'autre part, les réactions des radicaux $C_{10}H_7$ avec les espèces CH_3 et C_3 dans la co-pyrolyse benzène-C_3 conduisent à la formation de méthylnaphtalène **(Figure 5.37 d)** et favorisent la production de fluorène **(Figure 5.37 i)**, respectivement. Enfin, les voies de formation des produits $C_{14}H_{10}$ (**Figure 5.28 g, j-l and Figure 5.37 m-p)** sont similaires dans tous les cas, bien que significativement améliorées par la présence de concentrations plus élevées de phénylacétylène dans les cas de mélanges binaires.

Pyrolyse du toluène et ajout de combustibles C_2/C_3 :

Le toluène (C_7H_8) est étudié en tant que composant unique (100 et 200 ppm) et en addition avec des hydrocarbures C_2/C_3. Le toluène est principalement consommé par une réaction d'absorption

de l'hydrogène produisant un radical benzyle. Dans tous les mélanges binaires, la réactivité de décomposition du C_7H_8 est améliorée en raison de la grande quantité d'atomes d'hydrogène produits par les réactions $C_7H_7+C_2H_x$ et de l'abondance des radicaux CH_3 générés par la consommation de propylène et de propyne dans les co-pyrolyses toluène-C_2 et toluène-C_3, respectivement (**Figure 5.48 a and Figure 5.65 a)**. La présence de toluène augmente les taux de consommation de C_2H_x, ce qui démontre un effet synergique entre les composants du combustible (**Figure 5.48 b-c)**. En revanche, l'existence de C_7H_8 n'a aucun impact sur les taux de conversion des carburants C_3 **(Figure 5.65 b-c)**. L'ajout de carburants C_3 favorise la formation de benzène principalement par la réaction d'auto-recombinaison du propargyle, tandis que l'ajout de carburants C_2 n'a pratiquement aucun impact sur la concentration de benzène (**Figure 5.50 and Figure 5.68 a)**. Les aromatiques C_9 sont largement observés dans le pool d'espèces des mélanges binaires, et l'indène est l'espèce C_9 dominante. En effet, la réaction par l'intermédiaire de l'indényle + acétylène a été étudiée dans le passé comme une voie principale pour la formation de l'indène, et cette voie, y compris les paramètres cinétiques associés, a été confirmée et validée dans cette étude avec une investigation dépendant de la concentration du système toluène (100 ppm) + acétylène (~50 à ~500 ppm) **(Figure 5.53 a)**. La formation d'indène par la réaction $C_7H_7+C_2H_2$ est plus efficace que les réactions C_6+C_3 correspondantes. D'autre part, les traces d'indane **(Figure 5.54 b)** dans la co-pyrolyse toluène + éthylène indiquent que l'interaction entre le benzyle et l'éthylène est plus faible que celle du benzyle + acétylène. Il convient de mentionner que les voies de réaction responsables de la formation des HAP dans la pyrolyse du toluène pur et dans la co-pyrolyse toluène-C_2/C_3 sont les mêmes. Les HAP dont la formation dépend des réactions impliquant des espèces en C_1-C_3 et le radical indényle ont des fractions molaires plus élevées dans les systèmes binaires, et ces HAP comprennent le méthylène indène (**Figure 5.59 b and Figure 5.69 c)**, le méthyl indène (**Figure 5.59 c and Figure 5.69 f-g)**, le naphtalène (**Figure 5.59 a and Figure 5.69 d)**, l'acénaphtylène (**Figure 5.61 a and Figure 5.69 j)** et le vinyl naphtalène (**Figure 5.69 k)**. En particulier, le naphtalène et l'acénaphtylène sont les plus importants et ils seront brièvement analysés ici. L'ajout de carburants C_3 a des effets plus prononcés sur la formation de naphtalène que les carburants C_2. Le naphtalène est principalement formé par des réactions $C_7H_7+C_3H_3$ et $C_9H_7+CH_3$ dans tous les cas étudiés pour le toluène. La production abondante de tous les précurseurs mentionnés et la voie supplémentaire par $C_7H_7+C_3H_4$-P/C_3H_4-A dans la co-pyrolyse toluène-C_3 entraînent cette forte augmentation de la

formation de naphtalène, et notamment dans la co-pyrolyse toluène-propyne. La formation accrue des espèces C_{10} est une preuve directe de l'efficacité des interactions entre le toluène et les carburants C_3. La formation d'acénaphtylène par $C_9H_7+C_3H_3$ est facilitée dans tous les mélanges binaires et surtout dans la pyrolyse toluène-propyne en raison de la production accrue des deux précurseurs. Des tendances à la hausse sont également observées dans les pics de concentration des HAP qui comptent sur les radicaux naphtyles et les espèces C_1-C_2 comme précurseurs, y compris le méthylnaphtalène (**Figure 5.60 a and Figure 5.69 h)** et l'éthynylnaphtalène (**Figure 5.61 b and Figure 5.69 i)**. Le niveau des radicaux C_7 est réduit en raison de leurs réactions avec les espèces C_1-C_3. Par conséquent, les HAP qui dépendent largement des réactions en C_7, à savoir le bibenzyle (**Figure 5.56 and Figure 5.71 c)**, le diphénylméthane (**Figure 5.62 b and Figure 5.71 b)**, le fluorène (**Figure 5.62 a and Figure 5.71 a)** et les aromatiques à trois cycles que sont le phénanthrène (**Figure 5.64 a and Figure 5.71 g)** et l'anthracène (**Figure 5.64 b and Figure 5.71 h)**, présentent des fractions molaires de pointe plus faibles dans les mélanges binaires.

<u>Pyrolyse du phénylacétylène + réactions avec l'acétylène/éthylène:</u>

L'une des principales voies d'apparition et de croissance des HAP et des particules est le mécanisme HACA. Le phénylacétylène est le produit de la première addition d'acétylène à la structure monocyclique, il constitue donc la base pour l'apparition du second cycle. Le phénylacétylène est étudié en tant que composant unique (~100 ppm dans l'argon) et avec des intermédiaires C_2 ajoutés (environ 500 ppm) afin d'étudier les ajouts ultérieurs de C_2H_2 comme pour la voie HACA. La décomposition du phénylacétylène (**Figure 5.73 a)** commence par la fission des liaisons C-H du cycle aromatique. Ensuite, la réaction bimoléculaire $C_6H_5C_2H+H = C_6H_5+C_2H_2$ domine la consommation de $C_6H_5C_2H$ dans toute la gamme de température. Les réactions d'addition-élimination entre le phénylacétylène et le phényle maintiennent la réactivité de la désintégration du combustible en produisant des atomes de H et contribuent directement à la formation de plusieurs isomères de HAP $C_{14}H_{10}$, notamment le diphénylacétylène (**Figure 5.73 h)**, le 9-méthylène-fluorène (**Figure 5.73 i)** et le phénanthrène (**Figure 5.73 j)**. De même, la réaction combinée $C_6H_5C_2H+C_6H_4C_2H$ entretient la réactivité du combustible en produisant des espèces $C_{16}H_{10}$ ($C_2HC_6H_4C_6H_4C_2H$ (**Figure 5.73 k)** et pyrène (**Figure 5.73 l)**) et en libérant des atomes d'hydrogène. Le C_2H_2 supplémentaire influence à peine le taux de consommation de

$C_6H_5C_2H$, et sa consommation à haute température est compensée par sa production directe à partir de la décomposition de $C_6H_5C_2H$ (**Figure 5.75 a)**. Cependant, le C_2H_4 ajouté augmente légèrement la décomposition de $C_6H_5C_2H$ (**Figure 5.75 a)** en raison de l'augmentation du nombre d'atomes d'hydrogène. Bien que l'ajout de C_2H_2 et de C_2H_4 affecte de façon négligeable le taux de conversion de $C_6H_5C_2H$, ils modifient considérablement les comportements de spéciation des HAP. L'acétylène ajouté permet au mécanisme HACA partant du radical phénylacétylène de se produire à des températures relativement basses. Le noyau naphtyle obtenu ne se stabilise pas dans le naphtalène en raison du manque d'atomes H dans le système réactionnel, et il réagit ensuite avec une autre molécule d'acétylène, ce qui aboutit à des concentrations élevées d'acénaphtylène (**Figure 5.79 c)**. L'éthylène ajouté intensifie également les voies de l'HACA car sa consommation produit de l'acétylène. La présence de C_2H_4 dans le système réactionnel favorise la formation de $C_{10}H_8$ (**Figure 5.79 a)** par la réaction $C_6H_4C_2H+C_2H_4$ et fournit un atome d'hydrogène à $C_{10}H_7$ qui se transforme en $C_{10}H_8$ par la réaction $C_{10}H_7+C_2H_4 => C_{10}H_8+C_2H_3$. Le niveau des radicaux $C_6H_4C_2H$ est réduit en raison de leurs réactions avec les espèces C_2 dans les mélanges binaires, ce qui inhibe la formation de $C_6H_5CCC_6H_5$ (**Figure 5.79 d),** $C_{13}H_8CH_2$ (**Figure 5.79 e)**, et $C_2HC_6H_4C_6H_4C_2H$ (**Figure 5.79 g)**. Le $PC_{14}H_{10}$ (**Figure 5.79 f)** présente des fractions molaires maximales légèrement plus élevées dans les mélanges binaires en raison du niveau accru d'atomes H, qui facilitent les réactions d'isomérisation assistée par H à partir de $C_6H_5CCC_6H_5$ et de $C_{13}H_8CH_2$. Le $PC_{16}H_{10}$ (**Figure 5.79 h)** est principalement produit par la voie HACA à travers la réaction $C_{14}H_9+C_2H_2$ dans les systèmes de réaction binaires, contrairement au cas de la pyrolyse pure $C_6H_5C_2H$, ce qui justifie le déplacement de son profil vers des températures plus élevées.

Pyrolyse des alkylbenzènes :

Les alkylbenzènes sont des composants majeurs des mélanges de carburants. Une étude comparative est ici mise en œuvre pour comparer le comportement pyrolytique de trois alkylbenzènes, à savoir l'éthylbenzène, le n-propylbenzène et le n-butylbenzène. Pour tous les combustibles, la voie de consommation initiale passe par la fission C-C benzylique formant des radicaux benzyle et alkyle C_1-C_3, suivie par des réactions d'absorption de H et des ipso-additions. Les trois combustibles ont une réactivité de décomposition plus élevée que le toluène, l'alkylbenzène le plus simple. Le n-propylbenzène se décompose à des températures plus basses

que l'éthylbenzène et à des températures similaires à celles du n-butylbenzène (**Figure 5.83)**. La raison de cette différence réside dans la décomposition initiale du n-propylbenzène qui entraîne la formation de radicaux C_7H_7 et C_2H_5. La consommation de C_2H_5 conduit à une grande quantité d'atomes H qui stimulent la décomposition du n-propylbenzène et favorisent la formation de benzène (**Figure 5.87 a)** et de toluène (**Figure 5.87 b)** par rapport aux deux autres alkylbenzènes. Simultanément, les radicaux alkyle en C_1-C_3 formés ont un impact remarquable sur la formation de petits hydrocarbures (**Figure 5.84-5.86)** et de MAH, y compris l'éthylbenzène (**Figure 5.87 e)** et l'allylbenzène (**Figure 5.87 f)**. Par rapport à la pyrolyse du toluène pur, le styrène (**Figure 5.87 c)** a des concentrations beaucoup plus élevées dans la pyrolyse des alkylbenzènes et il est directement issu des voies liées au carburant. Les voies de formation des HAP sont simplement influencées par la chimie du combustible et sont similaires au cas de la pyrolyse du toluène, où les radicaux C_7H_7 et C_7H_5 jouent un rôle crucial dans la formation des HAP. La seule voie notable spécifique au combustible est la formation d'indène (**Figure 5.88 a)** à partir de 1-phényl-2-propényle dans la pyrolyse du n-propylbenzène et du n-butylbenzène à des températures relativement basses. Le styrène est un produit abondant et sa réaction avec le phényle joue un rôle clé dans la formation des produits en $PC_{14}H_{10}$ (**Figure 5.88 h)**.

Conclusion

Des expériences de pyrolyse de différents combustibles hydrocarbonés, dont le propylène, le propyne, le benzène, le toluène, le phénylacétylène, les alkylbenzènes linéaires en C_8-C_{10}, et des mélanges de combustibles avec des hydrocarbures insaturés en C_2/C_3 sont réalisées à l'aide d'un tube à chocs à une seule impulsion sur une plage de température de 950-1800 K pour une pression nominale de 20 bars et un temps de réaction d'environ 4 ms. Les compositions chimiques des mélanges post-chocs sont échantillonnées et analysées à l'aide des techniques GC-GC/MS. Les profils de fraction molaire des espèces en fonction de T_5 sont obtenus. Dans un premier temps, la méthode expérimentale est validée en utilisant un combustible bien connu comme le n-heptane, pour lequel des modèles de cinétique chimique ont été développés depuis des décennies. Des expériences de pyrolyse du n-heptane sont réalisées et le bon accord entre les mesures et les simulations prouve la fiabilité du dispositif expérimental actuel à employer pour l'objectif de cette thèse. Le dernier modèle CRECK est utilisé comme point de départ pour

développer un modèle cinétique complet mettant l'accent sur la formation des HAP. Un certain nombre de réactions sont mises à jour et ajoutées sur la base d'études théoriques récentes, et des voies de réaction possibles de formation et de décomposition sont proposées sur la base d'observations expérimentales. En général, le modèle cinétique peut reproduire de manière satisfaisante la décomposition du combustible et les mesures des espèces allant des petits hydrocarbures acycliques aux HAP dans tous les systèmes de réaction individuels. Les simulations sont effectuées en utilisant le module de réacteur homogène du logiciel COSILAB. Deux méthodes de simulation différentes sont utilisées : (i) une pression constante (P_5) de 20 bar et un temps de réaction nominal de 4 ms ; (ii) des profils de pression mesurés jusqu'à 10 ms ainsi que le T_5 et le temps de résidence mesurés. Cette dernière méthode est plus précise lorsque les réactions impliquent des radicaux stabilisés par résonance, car ces réactions peuvent se poursuivre pendant la période de quenching. En effectuant des analyses ROP et de sensibilité, les réseaux de réaction pour la consommation de carburant et la croissance aromatique sont mis en évidence pour les cas étudiés.

Abstract

Polycyclic aromatic hydrocarbons (PAHs), especially fused aromatics, are considered important soot precursors. Exploring and understanding the formation pathways of PAHs are essential building-blocks toward developing reliable kinetic models that can accurately simulate soot formation. This work aims at developing a comprehensive kinetic model emphasizing on PAH formation chemistry based on the detailed species profiles obtained in a high-purity single-pulse shock tube coupled to gas chromatography / mass spectrometry techniques. This set-up is designed and developed in order to accurately measure stable species up to four-rings. In particular, the pyrolysis of different aromatic fuels and mixtures is studied under combustion-like conditions, over a wide temperature range of 900-1800 K at a constant pressure of around 20 bar and a reaction time of 4 ms.

The reaction mechanisms involved in propylene and propyne thermal decomposition and the subsequent molecular growth up to four-ring products are first added and updated on the basis of the latest CRECK model version, as propylene and propyne are abundant products resulting from larger fuels' consumption. Phenyl and benzyl chemistry are then investigated through benzene and toluene pyrolysis, respectively. Both fuels are studied with and without the addition of other molecules typically present in the all reaction systems, such as acetylene (C_2H_2), ethylene (C_2H_4), propene (C_3H_6), or propyne (C_3H_4-P). To address the influence of added C_2 or C_3 fuels on benzene and toluene PAH speciation, different binary mixtures are carried out and examined. Later, the PAH speciation from phenylacetylene, important combustion intermediate, is inspected. Since phenylacetylene is also an important intermediate in the hydrogen-abstraction-acetylene-addition (HACA) mechanism starting from benzene, phenylacetylene/C_2 mixtures are studied in order to highlight the subsequent HACA steps between the fuel and small unsaturated hydrocarbons. Finally, benzyl reaction pathways are further examined considering C_8-C_{10} linear alkylbenzenes as initial fuels as the corresponding PAH formation chemistry is also controlled by reactions involving the benzyl radical.

The outputs of the present work include: i) an extensive experimental database of species profiles, including PAH intermediates up to four-rings, from the pyrolysis of key fuel components and mixtures; ii) development of a detailed and comprehensive chemical kinetic

model validated against the experimental results; iii) advanced understanding on the kinetic schemes and mechanisms involved in the fuels thermal decomposition and formation of soot precursor molecules. These results can serve for future model developments concerning more complex fuels and surrogates as well as the base for the construction of soot codes for simulation of particle formation in combustion applications.

Keywords: aromatic hydrocarbons, benzene, toluene, phenylacetylene, alkylbenzenes, acetylene, ethylene, propylene, propyne, PAHs, single-pulse shock tube, soot formation, gas chromatography / mass spectrometry, chemical kinetic modeling

Acknowledgements

Every gesture in life is important. When someone does something good, it becomes equally important to thank them for the effort and initiative they have taken.

On the very outset of this project, I am ineffably indebted to my director Dr. Andrea Comandini and Dr. Wenyu Sun for their enthusiasm, conscientious guidance, constant supervision, unrelenting support, valuable advices, constructive comments and suggestions, and encouragement to accomplish my PhD study and research. It is hard to conclude how positively they impact the execution of the project.

I would like to thank Dr. Nabiha Chaumeix and Dr. Said Abid for all their valuable suggestions, smart ideas, useful comments and constructive discussions throughout this research work.

I would like to extend my sincere and heartfelt obligation towards Eng. Benoît Grosselin for the constant scientific and technical support.

I would like to thank Dr. Maxence Lailliau who have helped in running shocks during the confinement period. Without his active help, I would not have been made headway in this project.

I would like to express my special thanks to Dr. Sharath Nagaraju for his endless help, kindness and understanding spirit.

Not everyone is privileged enough to have someone rooting them on even when they have lost all hope. Token of thanks and appreciation to all my friends who directly or indirectly helped me to complete this thesis, especially Leticia Carneiro Piton, Alka Karan, and Fabian Esneider Cano Ardila with whom I spent these two years overwhelmed with friendly, genuine, and agreeable atmosphere. With your consistent words of encouragement, immense support and willingness to help me, you have pushed me a lot in overcoming all the problems and achieving the goals I thought were farfetched at that stage in my life. Your support has been a big strength and boon for me. Thanks for the kind advices that I got from you in the time of need. Thank you for listening to me over the past three years, as getting through my dissertation required more than academic support.

Dr. Gustav Nyrenstedt- nothing I would say will ever convey the amount of gratitude. I extremely appreciate everything you taught me concerning research, integrity, leadership and communication skills. Thank you for all the beneficial talks as well as for your time.

I also acknowledge with deep sense of reverence my gratitude towards my parents for their unremitting boost, valuable assistance, unending inspiration, and their strong belief in me. Thank you for making me more than I am.

Most of all, to the Almighty GOD for the wisdom, strength and continuous blessings He gave.

Any omission in this brief acknowledgement does not mean lack of gratitude and respect.

Contents

1 Introduction 16
2 Literature Review 19
2.1 Main PAH formation pathways 19
2.1.1 HACA mechanism 20
2.1.2 HAVA (Hydrogen Abstraction and Vinyl Addition) mechanism 21
2.1.3 Phenyl Addition and Cyclization (PAC) mechanism: 21
2.1.4 Diradical Cycloaddition Fragmentation (CAF) 22
2.1.5 Methyl Addition/ Cyclization (MAC) 23
2.1.6 Resonantly stabilized radicals 24
2.1.7 Other radical-radical recombination and radical-molecule reactions 24
2.1.8 Ring-expansion via radical-radical reactions 25
2.2 Literature overview on relevant aromatic hydrocarbons 25
2.2.1 Benzene 25
2.2.2 Toluene 28
2.2.3 Styrene 29
2.2.4 Phenylacetylene 30
2.2.5 Ethylbenzene 30
2.2.6 Propylbenzene 31
2.2.7 Butylbenzene 32
2.2.8 Benzene and toluene based mixtures 33
3 Experimental Set-Up 34
3.1 Shock tube theory 34
3.1.1 Principle - Evaluation of the thermodynamic parameters 34
3.1.2 Observation time 39
3.1.3 Dump tank - Single pulse shock tube 40
3.2 High purity single-pulse shock tube at ICARE 41
3.3 Analytical instrumentation- GC/GC-MS 47
3.3.1 GC/GC-MS system description 47
3.3.2 Qualitative and Quantitative Analysis 51
3.4 Gas mixture preparation 55
3.4.1 Degassing liquid Samples 55
3.4.2 Gas-mixture preparation procedure 56

3.5 Validation of the experimental Set-Up 56
4 Kinetic Modeling 57
4.1 Structure 57
4.2 Simulation 58
4.3 Kinetic model development 61
4.3.1 C_0-C_4 core mechanism 62
4.3.2 Fuel mechanism 64
4.3.3 Secondary mechanism 75
5 Results and discussion 89
5.1 Propylene and propyne pyrolysis 89
5.1.1 Motivation 89
5.1.2 Fuels decomposition and the formation of small hydrocarbons 89
5.1.3 Formation of the first aromatic ring 95
5.1.4 PAH speciation 98
5.1.5 Model validation against experimental data of propylene pyrolysis in literature 107
5.1.6 Model validation against experimental data of propyne pyrolysis in literature 112
5.2 Benzene pyrolysis & addition of C_2/C_3 fuels 114
5.2.1 Motivation 114
5.2.2 Benzene thermal decomposition 115
5.2.3 Impacts of added acetylene and ethylene on benzene pyrolysis 117
5.2.4 Impacts of added propylene and propyne on benzene pyrolysis 125
5.3 Toluene pyrolysis and its reactions with C_2/C_3 hydrocarbons 138
5.3.1 Motivation 138
5.3.2 Toluene thermal decomposition 139
5.3.3 Impacts of added acetylene and ethylene on toluene pyrolysis 143
5.3.4 Influences of added propyne and propylene on toluene pyrolysis 169
5.4 Phenylacetylene pyrolysis + reactions with acetylene/ethylene 183
5.4.1 Motivation 183
5.4.2 Phenylacetylene thermal decomposition 184
5.4.3 Influences of added acetylene and ethylene 188
5.5 Alkylbenzenes pyrolysis 195
5.5.1 Motivation 195
5.5.2 Fuel decomposition and small hydrocarbon products 196
5.5.3 The formation of MAH species 201
5.5.4 The formation of PAH species 203

6 Conclusion 209
Annex 215

Table of Figures

Figure 1.1: Schematic of soot formation steps 18
Figure 2.1: Formation of naphthyl, acenaphthylene and phenanthryl by the HACA mechanism [8] 20
Figure 2.2: PAH growth process via vinyl radical addition from ethylene pyrolysis 21
Figure 2.3: Examples of phenyl addition-cyclisation [22]. 22
Figure 2.4: Formation of aromatics by the CAF mechanism. 23
Figure 2.5: Formation of aromatics by the MAC mechanism. 24
Figure 2.6 : Naphthalene formation through indenyl and methyl recombination. The dashed arrow resembles a multi-step reactions. 25
Figure 3.1: Schematic picture of a shock tube and (x, t) diagram showing the various regions associated with a shock wave at a time t after the bursting of the diaphragm at the origin O. 36
Figure 3.2: Real view of the heated shock tube, and a schematic diagram of the shock tube used in this work. 43
Figure 3.3: Schematic drawings of the dump tank. 43
Figure 3.4: Typical end wall pressure history with and without dump tank. 44
Figure 3.5: Typical end wall pressure history and the definition of reaction time [138]. 45
Figure 3.6: Experimental mole fractions for intermediates affected by presence of oxygen in 100 ppm benzene pyrolysis. 46
Figure 3.7: Detailed schematic of the online analytical device 48
Figure 3.8: Six-port valve operation in: (a) Agilent GC, (b) Thermo GC 49
Figure 3.9: Split/Splitless injector modes 50
Figure 3.10: TCD principle 51
Figure 3.11: The signals detected for C_4 species in propylene pyrolysis at T_5 = 1368 K, p_5 = 21.1 bar. The overlapping peaks are separated through multiple Gaussian fittings [140]. 52
Figure 3.12: GC signals recorded in neat toluene, toluene + propylene (C_3H_6) and toluene + propyne (C_3H_4-P) pyrolysis at T_5 around 1360 K [141]. 53
Figure 3.13: GC signals for PAH species detected in (a) 210 ppm benzene pyrolysis at T_5 = 1553 K, P_5= 21.8 bar and (b) 216 ppm toluene pyrolysis at T_5 =1435 K, P_5=21.1 bar [138]. 53
Figure 3.14: The calibrations for typical two- to three- ring PAH species. The slope k is the FID response factor for each shown PAH [143]. 55
Figure 3.15: Species concentrations as a function of T_5 from 100 ppm heptane pyrolysis experiments at the nominal P_5 of 20 bar. Symbols: measurements; Solid lines: simulations with LLNL model [144]; dotted lines: simulations with JetSurF2.0 model [145]; Dot-dashed lines: simulations with the latest version of CRECK model [146]. 57
Figure 4.1: Kinetic model predictions by LLNL model (solid lines), JetSurF2.0 (dashed lines) and CRECK model (dash-dotted lines) for fuels, C_2H_2 and C_2H_4 concentrations compared against experimental measurements (symbols) in (a) benzene and (b) toluene pyrolysis. 62
Figure 4.2: Rate coefficients reported in literature for (a) R8, $C_6H_5C_2H+H \Rightarrow C_6H_5+C_2H_2$ and (b) R-8, $C_6H_5+C_2H_2 \Rightarrow C_6H_5C_2H+H$. Measurements in [54], [190] and calculations in [183], [186], [191] were for R-8, while the measurement in [81] was for R8. The reverse rate coefficients were computed through

chemical equilibrium with the thermochemical data provided in [192]. The shadowed areas indicate three-fold uncertainties centered on the calculated rate coefficients for R-8 [191] and on the derived reverse rate coefficient for R8. 68
Figure 4.3: Thermal decomposition of benzene and phenylacetylene under similar experimental conditions. 69
Figure 5.1: Measured (symbols) and simulated (lines) fuel mole fraction profiles as a function of T_5 in (a) propylene pyrolysis and (b) propyne pyrolysis. Thick solid red lines: simulations using the current kinetic model with the constant p_5 of 20 bar and the nominal reaction time of 4 ms; thick dashed black lines: simulations using the current model with measured pressure profiles up to 10 ms; thin dashed blue lines: simulations using the NUIMech1.0 (for propylene [227] and for propyne [228]) with the constant p_5 of 20 bar and the nominal reaction time of 4 ms; thin dot dashed green lines: simulations using the LLNL PAH model [123] with constant p_5 of 20 bar and the nominal reaction time of 4 ms. 92
Figure 5.2: Measured (symbols) and simulated (lines) small intermediates mole fraction profiles as a function of T_5 in propylene pyrolysis. Thick solid red lines: simulations using the current kinetic model with the constant p_5 of 20 bar and the nominal reaction time of 4 ms; thick dashed black lines: simulations using the current model with measured pressure profiles up to 10 ms; thin dashed blue lines: simulations using the NUIMech1.0 [227] with the constant p_5 of 20 bar and the nominal reaction time of 4 ms; thin dot dashed green lines: simulations using the LLNL PAH model [123] with constant p_5 of 20 bar and the nominal reaction time of 4 ms. 93
Figure 5.3: Measured (symbols) and simulated (lines) small intermediates mole fraction profiles as a function of T_5 in propyne pyrolysis. Thick solid red lines: simulations using the current kinetic model with the constant p_5 of 20 bar and the nominal reaction time of 4 ms; thick dashed black lines: simulations using the current model with measured pressure profiles up to 10 ms; thin dashed blue lines: simulations using the NUIMech1.0 [228] with the constant p_5 of 20 bar and the nominal reaction time of 4 ms; thin dot dashed green lines: simulations using the LLNL PAH model [123] with constant p_5 of 20 bar and the nominal reaction time of 4 ms. 94
Figure 5.4: Major fuel consumption pathways at T_5 of 1300 K and 1400 K based on integrated ROP analyses results 95
Figure 5.5: Measured (symbols) and simulated (lines) benzene and fulvene mole fraction profiles as a function of T_5 in propylene pyrolysis and propyne pyrolysis. Thick solid red lines: simulations using the current kinetic model with the constant p_5 of 20 bar and the nominal reaction time of 4 ms; thick dashed black lines: simulations using the current model with measured pressure profiles up to 10 ms; thin dashed blue lines: simulations using the NUIMech1.0 (for propylene [227] and for propyne [228]) with the constant p_5 of 20 bar and the nominal reaction time of 4 ms; thin dot dashed green lines: simulations using the LLNL PAH model [123] with constant p_5 of 20 bar and the nominal reaction time of 4 ms. 97
Figure 5.6: Measured (symbols) and simulated (lines) MAHs mole fraction profiles as a function of T_5 in propylene pyrolysis and propyne pyrolysis. Thick solid red lines: simulations using the current kinetic model with the constant p_5 of 20 bar and the nominal reaction time of 4 ms; thick dashed black lines: simulations using the current model with measured pressure profiles up to 10 ms; thin dashed blue lines: simulations using the NUIMech1.0 (for propylene [227] and for propyne [228]) with the constant p_5 of 20 bar and the nominal reaction time of 4 ms; thin dot dashed green lines: simulations using the LLNL PAH model [123] with constant p_5 of 20 bar and the nominal reaction time of 4 ms. 98
Figure 5.7: Carbon recovery with and without considering the PAH species in the current experiments of (a) propylene pyrolysis and (b) propyne pyrolysis. 99
Figure 5.8: Measured (symbols) and simulated (lines) mole fraction profiles for C_9H_8 isomers as a function of T_5 in propylene and propyne pyrolysis. Thick solid red lines: simulations using the current kinetic model with the constant p_5 of 20 bar and the nominal reaction time of 4 ms; thick dashed

black lines: simulations using the current model with measured pressure profiles up to 10 ms; thin dot dashed green lines: simulations using the LLNL PAH model [123] with constant p_5 of 20 bar and the nominal reaction time of 4 ms..... 102
Figure 5.9: Measured (symbols) and simulated (lines) mole fraction profiles for $C_{10}H_8$ isomers as a function of T_5 in propylene and propyne pyrolysis. Thick solid red lines: simulations using the current kinetic model with the constant p_5 of 20 bar and the nominal reaction time of 4 ms; thick dashed black lines: simulations using the current model with measured pressure profiles up to 10 ms; thin dot dashed green lines: simulations using the LLNL PAH model [123] with constant p_5 of 20 bar and the nominal reaction time of 4 ms..... 103
Figure 5.10: Measured (symbols) and simulated (lines) mole fraction profiles for C_{10}–C_{13} PAH species as a function of T_5 in propylene and propyne pyrolysis. Thick solid red lines: simulations using the current kinetic model with the constant p_5 of 20 bar and the nominal reaction time of 4 ms; thick dashed black lines: simulations using the current model with measured pressure profiles up to 10 ms; thin dot dashed green lines: simulations using the LLNL PAH model [123] with constant p_5 of 20 bar and the nominal reaction time of 4 ms..... 105
Figure 5.11: Measured (symbols) and simulated (lines) mole fraction profiles for $C_{14}H_{10}$ isomers as a function of T_5 in propylene and propyne pyrolysis. Thick solid red lines: simulations using the current kinetic model with the constant p_5 of 20 bar and the nominal reaction time of 4 ms; thick dashed black lines: simulations using the current model with measured pressure profiles up to 10 ms; thin dot dashed green lines: simulations using the LLNL PAH model [123] with constant p_5 of 20 bar and the nominal reaction time of 4 ms..... 106
Figure 5.12: Measured (symbols) and simulated (lines) mole fraction profiles for C_{16} PAH species as a function of T_5 in propylene and propyne pyrolysis. Thick solid red lines: simulations using the current kinetic model with the constant p_5 of 20 bar and the nominal reaction time of 4 ms; thick dashed black lines: simulations using the current model with measured pressure profiles up to 10 ms; thin dot dashed green lines: simulations using the LLNL PAH model [123] with constant p_5 of 20 bar and the nominal reaction time of 4 ms..... 107
Figure 5.13: Predictions (lines) by the current model for the measured (symbols) species mole fractions in propylene pyrolysis experiments reported by Burcat et al. [225] (Shock tube, Set A: 0.4 % C_3H_6 diluted in Ar; post-shock pressure p_5 = 6.2–8.8 atm; reaction time τ = 700–900 μs)..... 108
Figure 5.14: Predictions (lines) by the current model for the measured (symbols) species mole fractions in propylene pyrolysis experiments reported by Burcat et al. [225] (Shock tube, Set B: 1.6 % C_3H_6 diluted in Ar; post-shock pressure p_5 = 5.5–8.6 atm; reaction time τ = 690–890 μs)..... 108
Figure 5.15: Predictions (lines) by the current model for the measured (symbols) species mole fractions in propylene pyrolysis experiments reported by Burcat et al. [225] (Shock tube, Set C: 1.6 % C_3H_6 diluted in Ar; post-shock pressure p_5 = 1.3–2.9 atm; reaction time τ = 700–910 μs)..... 109
Figure 5.16: Predictions (lines) by the current model for the measured (symbols) species mole fractions in propylene pyrolysis experiments reported by Hidaka et al. [169] (Shock tube, Set 1: 2.5 % C_3H_6 diluted in Ar; nominal post-shock pressure p_5 = 2 atm; reaction time τ = 860–1880 μs)..... 109
Figure 5.17: Predictions (lines) by the current model for the measured (symbols) species mole fractions in propylene pyrolysis experiments reported by Hidaka et al. [169] (Shock tube, Set 2: 5.0 % C_3H_6 diluted in Ar; nominal post-shock pressure p_5 = 2 atm; reaction time τ = 800–2500 μs)..... 110
Figure 5.18: Predictions (lines) by the current model for the measured (symbols) species mole fractions in propylene pyrolysis experiments reported by Davis et al. [223] (flow reactor, 0.288 % C_3H_6 diluted in N_2; T = 1210 K; p = 1 atm; reaction time τ shifted by 40 ms in the simulation)..... 110

Figure 5.19: Predictions (lines) by the current model for the measured (symbols) species mole fractions in propylene pyrolysis experiments reported by Wang et al. [173] (Flow reactor, 50% C_3H_6 diluted in N_2, p = ~0.8 atm; residence time τ = ~2.4, ~1.2 and ~0.5 s) 111
Figure 5.20: Predictions (lines) by the current model for the measured (symbols) species mole fractions in propylene pyrolysis experiments reported by Nagaraja et al. [227] (Shock tube, 2% C_3H_6 + 0.5% Kr diluted in Ar, post-shock pressure p_5 = ~2 bar; reaction time τ = 2.8–4.4 ms) 112
Figure 5.21: Predictions (lines) by the current model for the measured (symbols) species mole fractions in propyne pyrolysis experiments reported by Hidaka et al. [169] (Shock tube, 4% C_3H_4-P diluted in Ar, post-shock pressure p_5 = ~2 atm; reaction time τ = 1.8–2.4 ms) 113
Figure 5.22: Predictions (lines) by the current model for the measured (symbols) species mole fractions in propyne pyrolysis experiments reported by Davis et al. [222] (flow reactor, 0.297 % C_3H_6 diluted in N_2; T = 1210 K; p = 1 atm) 113
Figure 5.23: Predictions (lines) by the current model for the measured (symbols) species mole fractions in propyne pyrolysis experiments reported by Panigrahy *et al*. [228] (Shock tube, 2% C_3H_4-P + 0.5% Kr diluted in Ar, post-shock pressure p_5 = ~2 bar; reaction time τ = 2.8–4.1 ms) 114
Figure 5.24: Mole fraction profiles (symbols) of fuel and its major products are measured from 210 ppm benzene pyrolysis in a shock tube at 20 bar. Solid lines indicate the model predictions. 116
Figure 5.25: Experimental (symbols) and simulated (solid lines) mole fractions of (a) C_6H_6 in the three investigated cases, (b) C_2H_2 in the pyrolysis of 108 ppm C_6H_6 + 500 ppm C_2H_2 mixture and (c) C_2H_4 in the pyrolysis of 108 ppm C_6H_6 + 532 ppm C_2H_4 mixture. The dashed lines in (b) and (c) represent the simulated mole fractions of C_2H_2 and C_2H_4 when C_6H_6 is absent from the corresponding mixtures. 118
Figure 5.26: Sensitivity analyses for C_6H_6 consumption at T_5=1487 K, P_5=20 bar and reaction time=4 ms in the pyrolysis of neat C_6H_6, C_6H_6+C_2H_2 and C_6H_6+C_2H_4 118
Figure 5.27: Measured (symbols) and simulated (solid lines) mole fractions of small products as a function of T_5 in the pyrolysis of 109 ppm C_6H_6, 108 ppm C_6H_6 + 500 ppm C_2H_2 mixture and 108 ppm C_6H_6 + 532 ppm C_2H_4 mixture at the nominal P_5=20 bar. 119
Figure 5.28: Experimental (symbols) and modeling (solid lines) mole fractions of polyaromatic hydrocarbons (PAHs) as a function of the post shock temperature T_5 in neat benzene, benzene+C_2H_2 and benzene+C_2H_4 pyrolysis at a nominal pressure (P_5) of 20 bar. 120
Figure 5.29: Experimental (symbols) and modeling (solid lines) mole fraction of vinyl naphthalene as a function of the post shock temperature T_5 in benzene+C_2H_4 pyrolysis at a nominal P_5=20 bar. 122
Figure 5.30: Simulated species mole fractions as a function of time with the measured pressure profiles in (a) neat C_6H_6 pyrolysis at T_5=1569 K, P_5= 21.51 bar; (b) C_6H_6/C_2H_2 pyrolysis at T_5=1552 K, P_5=22 bar; (c) C_6H_6/C_2H_4 pyrolysis at T_5=1571 K, P_5= 21.45 bar. The dashed vertical lines indicate the start of quenching. 125
Figure 5.31: Experimental (symbols) and simulated (solid lines) mole fractions of (a) C_6H_6 in the three investigated cases, (b) C_3H_6 in the pyrolysis of 108 ppm C_6H_6 + 532 ppm C_3H_6 mixture and (c) C_3H_4-P in the pyrolysis of 108 ppm C_6H_6 + 500 ppm C_3H_4-P mixture. The dashed lines in (b) and (c) represent the simulated mole fractions of C_3H_6 and C_3H_4-P when C_6H_6 is absent from the corresponding mixtures. .. 126
Figure 5.32: Rate of production analyses at reaction time=4ms for benzene in (a) C_6H_6+C_3H_6 and C_6H_6+C_3H_4-P pyrolysis at T_5=1387 K and (b) in C_6H_6+C_3H_6 pyrolysis at T_5=1316 K. 126
Figure 5.33: Measured (symbols) and simulated (solid lines) mole fraction profiles of small hydrocarbon products as a function of T_5 during the pyrolysis of 109 ppm C_6H_6, 108 ppm C_6H_6+532ppm C_3H_6 and 108ppm C_6H_6+ 500ppm C_3H_4-P mixtures. 127
Figure 5.34: Measured (symbols) and simulated (solid lines) mole fractions for MAHs in neat benzene, benzene + C_3H_6 and benzene + C_3H_4-P pyrolysis. 129

Figure 5.35: Rate of production analysis at reaction time=4ms for toluene in C_6H_6+C_3H_6 and C_6H_6+C_3H_4-P pyrolysis at T_5=1400 K. 130
Figure 5.36: Experimental (symbols) and modeling (solid lines) mole fractions of indene (C_9H_8) as a function of the post shock temperature T_5 in neat benzene, benzene+C_3H_4-P and benzene+C_3H_6 pyrolysis 131
Figure 5.37: Measured (symbols) and simulated (solid lines) mole fractions of polyaromatic hydrocarbons (PAHs) as a function of the post shock temperature T_5 in neat benzene, benzene+C_3H_4-P and benzene+C_3H_6 pyrolysis 132
Figure 5.38: Carbon recovery with and without considering the PAH species in (a) benzene pyrolysis (b) benzene + acetylene pyrolysis and (c) benzene + ethylene pyrolysis. 132
Figure 5.39: Carbon recovery with and without considering the PAH species in (a) benzene + propyne pyrolysis and (b) benzene + propylene pyrolysis. 133
Figure 5.40: Simulated species mole fractions as a function of time with the measured pressure profiles in (a) C_6H_6/C_3H_4-P pyrolysis at T_5=1568 K, P_5=21.57 bar; (c) C_6H_6/C_3H_6 pyrolysis at T_5=1536 K, P_5= 21.4 bar. The dashed vertical lines indicate the start of quenching. 138
Figure 5.41: Experimental (symbols) and simulated (solid lines) mole fraction profiles of fuel, C_0-C_4 species and MAHs in 216 ppm toluene pyrolysis at P_5=20 bar. Dashed lines indicate the model predictions with the measured pressure-profiles. 140
Figure 5.42: Experimental (symbols) and simulated (solid lines) mole fraction profiles of PAHs in 216 ppm toluene pyrolysis at P_5=20 bar. Dashed lines indicate the model predictions with the measured pressure-profiles. 143
Figure 5.43: Species concentrations as a function of T_5 in neat toluene pyrolysis, including measurements (symbols), modeling results at constant pressure of 20 bar within a fixed reaction time of 4.0 ms (grey solid lines) and simulations with measured pressure profiles up to a time scale of 10 ms (black dashed lines). 144
Figure 5.44: Species concentrations as a function of T_5 in TA_50 pyrolysis, including measurements (symbols), modeling results at constant pressure of 20 bar within a fixed reaction time of 4.0 ms (red solid lines) and simulations with measured pressure profiles up to a time scale of 10 ms (black dashed lines). 145
Figure 5.45: Species concentrations as a function of T_5 in TA_216 pyrolysis, including measurements (symbols), modeling results at constant pressure of 20 bar within a fixed reaction time of 4.0 ms (solid lines) and simulations with measured pressure profiles up to a time scale of 10 ms (dashed lines). 146
Figure 5.46: Species concentrations as a function of T_5 in TA_459 pyrolysis, including measurements (symbols), modeling results at constant pressure of 20 bar within a fixed reaction time of 4.0 ms (solid lines) and simulations with measured pressure profiles up to a time scale of 10 ms (dashed lines). 147
Figure 5.47: Species concentrations as a function of T_5 in TE pyrolysis, including measurements (symbols), modeling results at constant pressure of 20 bar within a fixed reaction time of 4.0 ms (solid lines) and simulations with measured pressure profiles up to a time scale of 10 ms (dashed lines). 148
Figure 5.48: Measured (symbols) and simulated (lines) fuel mole fractions as a function of the post-shock temperature T_5 in toluene/acetylene (ethylene) pyrolysis. The dark dashed lines are simulated fuel decomposition profiles of (a) neat toluene (105 ppm in argon), (b) neat acetylene (50, 216 and 459 ppm in argon) and (c) neat ethylene (516 ppm in argon). The inset of (a) shows toluene concentrations over the temperature range of 1300−1400 K. 150
Figure 5.49: Measured (symbols) and simulated (lines) mole fraction profiles of (a) ethylene in toluene/acetylene pyrolysis and (b) acetylene in toluene/ethylene pyrolysis. Simulated and experimental mole fractions in neat toluene (105 ppm in argon) pyrolysis are also shown as a reference. The inset in (a) plots the measured (dark open square) and simulated (gray cross) C_2H_4 peak concentrations against the

initial C_2H_2 contents; linear regressions (the dashed lines) of the data points are shown as a visual guide. 151
Figure 5.50: Experimental (symbols) and modeling (solid lines) benzene (C_6H_6) mole fractions as a function of the post-shock temperature T_5 in (a) toluene/C_2H_2 pyrolysis and (b) toluene/C_2H_4 pyrolysis. The inset in (a) plots the measured (dark open square) and simulated (gray cross) C_6H_6 peak concentrations against the initial C_2H_2 contents; linear regressions (the dashed lines) of the data points are shown as a visual guide. Simulated and experimental C_6H_6 mole fractions in neat toluene (105 ppm in argon) pyrolysis are also shown as a reference. 152
Figure 5.51: Simulated H atom and benzyl radical (C_7H_7) concentrations in the pyrolysis of neat toluene (105 ppm in argon) and toluene/acetylene (ethylene) binary mixtures. 152
Figure 5.52: Experimental (symbols) and modeling (solid lines) mole fractions of C_8 MAH species as a function of the post-shock temperature T_5. The left panel: toluene/C_2H_2 pyrolysis; the upper left insets plot the measured (dark open square) and simulated (gray cross) peak concentrations of separate species against the initial C_2H_2 contents; linear regressions (the dashed lines) of the data points are shown as a visual guide. The right panel: toluene/C_2H_4 pyrolysis. The experimental and simulated species mole fraction profiles in neat toluene pyrolysis are shown as a reference. 154
Figure 5.53: Experimental (symbols) and modeling (solid lines) mole fractions of C_9H_8 species as a function of the post-shock temperature T_5 in toluene/acetylene pyrolysis. The upper right insets plot the measured (dark open square) and simulated (gray cross) peak concentrations of separate species against the initial C_2H_2 contents; linear regressions (the dashed lines) of the data points are shown as a visual guide. Simulated and experimental mole fraction profiles in neat toluene pyrolysis are shown as a reference 155
Figure 5.54: Experimental (symbols) and modeling (solid lines) mole fractions of C_9 species as a function of the post-shock temperature T_5 in neat toluene and toluene/ethylene pyrolysis. 156
Figure 5.55: ROP-analyzed percentage contributions of benzyl consumption in the pyrolysis of toluene/C_2 binary mixtures at 1400 K. The ROP-analyzed percentage contributions of benzyl consumption in neat toluene pyrolysis (the gray bars) are also shown as a reference. 157
Figure 5.56: Bibenzyl ($C_6H_5C_2H_4C_6H_5$) mole fraction profiles as a function of the post-shock temperature T_5 in (a) toluene/C_2H_2 pyrolysis and (b) toluene/C_2H_4 pyrolysis. Symbols: measurements; solid lines: simulations with a constant pressure of 20 bar within a reaction time of 4.0 ms; dashed lines: simulations with measured pressure histories up to 10 ms. The upper left inset in the left panel plot the measured (dark open square), simulated constant pressure assumption (gray cross) and measured pressure histories (red cross) peak $C_6H_5C_2H_4C_6H_5$ concentrations against the initial C_2H_2 contents; the linear regressions (the dashed lines) of the data points are shown as a visual guide. 158
Figure 5.57: Simulated species mole fractions as a function of time with the measured pressure profiles in (a) TA_459 pyrolysis at T_5 =1416 K; (b) TE pyrolysis at T_5 = 1427 K. The dashed vertical lines indicate the start of quenching. 158
Figure 5.58: Simulated species mole fractions as a function of time with the measured pressure profiles in (a) TA_50 pyrolysis at T_5 =1433 K; (b) TA_216 pyrolysis at T_5 = 1411 K. The dashed vertical lines indicate the start of quenching. 159
Figure 5.59: Experimental (symbols) and modeling (solid lines) mole fraction of C_{10} PAH species as a function of the post-shock temperature T_5. The left panel: toluene/C_2H_2 pyrolysis; the upper left insets plot the measured (dark open square) and simulated (gray cross) peak concentrations of separate species against the initial C_2H_2 contents; linear regressions (the dashed lines) of the data points are shown as a visual guide. The right panel: toluene/C_2H_4 pyrolysis. The simulated and experimental mole fraction profiles of C_{10} PAH species in neat toluene pyrolysis are shown as a reference. 160

Figure 5.60: Experimental (symbols) and modeling (solid lines) mole fraction of C_{11} PAH species as a function of the post-shock temperature T_5. The left panel: toluene/C_2H_2 pyrolysis; the upper left insets plot the measured (dark open square) and simulated (gray cross) peak concentrations of separate species against the initial C_2H_2 contents; linear regressions (the dashed lines) of the data points are shown as a visual guide. The right panel: toluene/C_2H_4 pyrolysis. The simulated and experimental mole fraction profiles of C_{11} PAH species in neat toluene pyrolysis are shown as a reference. 162
Figure 5.61: Experimental (symbols) and modeling (solid lines) mole fraction of C_{12} PAH species as a function of the post-shock temperature T_5. The left panel: toluene/C_2H_2 pyrolysis; the upper left insets plot the measured (dark open square) and simulated (gray cross) peak concentrations of separate species against the initial C_2H_2 contents; linear regressions (the dashed lines) of the data points are shown as a visual guide. The right panel: toluene/C_2H_4 pyrolysis. The simulated and experimental mole fraction profiles of C_{12} PAH species in neat toluene pyrolysis are shown as a reference. 164
Figure 5.62: Experimental (symbols) and modeling (solid lines) mole fraction of C_{13} PAH species as a function of the post-shock temperature T_5. The left panel: toluene/C_2H_2 pyrolysis; the upper left insets plot the measured (dark open square) and simulated (gray cross) peak concentrations of separate species against the initial C_2H_2 contents; linear regressions (the dashed lines) of the data points are shown as a visual guide. The right panel: toluene/C_2H_4 pyrolysis. The simulated and experimental mole fraction profiles of C_{13} PAH species in neat toluene pyrolysis are shown as a reference. 166
Figure 5.63: Simulated phenyl radical (C_6H_5) concentrations in the pyrolysis of neat toluene (105 ppm in argon) and toluene/C_2H_2 (C_2H_4) binary mixtures..... 167
Figure 5.64: Experimental (symbols) and modeling (solid lines) mole fraction of C_{14} PAH species as a function of the post-shock temperature T_5. The left panel: toluene/C_2H_2 pyrolysis; the upper left insets plot the measured (dark open square) and simulated (gray cross) peak concentrations of separate species against the initial C_2H_2 contents; linear regressions (the dashed lines) of the data points are shown as a visual guide. The right panel: toluene/C_2H_4 pyrolysis. The simulated and experimental mole fraction profiles of C_{14} PAH species in neat toluene pyrolysis are shown as a reference. 168
Figure 5.65: Fuel mole fraction profiles as a function of the post-shock temperature T_5 in (a) neat toluene and toluene/C_3 pyrolysis, (b) toluene/C_3H_6 pyrolysis and (c) toluene/C_3H_4-P pyrolysis. Symbols: measurements; solid lines: simulations with a constant pressure of 20 bar within a reaction time of 4.0 ms; dashed lines: simulations with measured pressure histories up to 10 ms. Simulated fuel mole fraction profiles in neat propylene and propyne pyrolysis are given as gray solid lines in (b) and (c). 170
Figure 5.66: Integrated ROP-analyzed percentage contributions of toluene consumption in the pyrolysis of neat toluene toluene/C_3 binary mixtures at 1400 K. 170
Figure 5.67: Small species mole fraction profiles as a function of the post-shock temperature T_5 in neat toluene, toluene + C_3H_6 and toluene + C_3H_4-P pyrolysis. Symbols: measurements; solid lines: simulations with a constant pressure of 20 bar within a reaction time of 4.0 ms; dashed lines: simulations with measured pressure histories up to 10 ms. 172
Figure 5.68: MAH mole fraction profiles as a function of the post-shock temperature T_5 in neat toluene, toluene + C_3H_6 and toluene + C_3H_4-P pyrolysis. Symbols: measurements; solid lines: simulations with a constant pressure of 20 bar within a reaction time of 4.0 ms; dashed lines: simulations with measured pressure histories up to 10 ms. 174
Figure 5.69: C_9-C_{12} PAH mole fraction profiles as a function of the post-shock temperature T_5 in neat toluene, toluene + C_3H_6 and toluene + C_3H_4-P pyrolysis. Symbols: measurements; solid lines: simulations with a constant pressure of 20 bar within a reaction time of 4.0 ms; dashed lines: simulations with measured pressure histories up to 10 ms. 177

Figure 5.70: Simulated mole fraction profiles of $C_{13}H_{10}$ isomers, which are potential products of $C_{10}H_7+C_3H_3/C_3H_4$ reactions, in toluene-propyne co-pyrolysis. The different colors of the molecules correspond to their relative profile. 179
Figure 5.71: C_{13}-C_{14} PAH mole fraction profiles as a function of the post-shock temperature T_5 in neat toluene, toluene + C_3H_6 and toluene + C_3H_4-P pyrolysis. Symbols: measurements; solid lines: simulations with a constant pressure of 20 bar within a reaction time of 4.0 ms; dashed lines: simulations with measured pressure histories up to 10 ms. 181
Figure 5.72: Carbon recovery with and without considering the PAH species in (a) toluene pyrolysis (b) toluene + propylene pyrolysis and (c) toluene + propyne pyrolysis. 182
Figure 5.73: Mole fraction profiles (symbols) of fuel and its major products are measured from 103 ppm phenylacetylene pyrolysis in a shock tube at 20 bar. Solid lines indicate the model predictions. 184
Figure 5.74: Sensitivity analyses for phenylacetylene at different post-shock temperatures (T_5s). 186
Figure 5.75: Experimental (symbols) and simulated (solid lines) mole fractions of (a) $C_6H_5C_2H$ in the three investigated cases, (b) C_2H_2 in the pyrolysis of 104 ppm $C_6H_5C_2H$ + 415 ppm C_2H_2 mixture and (c) C_2H_4 in the pyrolysis of 105 ppm $C_6H_5C_2H$ + 504 ppm C_2H_4 mixture. The dashed lines in (b) and (c) represent the simulated mole fractions of C_2H_2 and C_2H_4 when $C_6H_5C_2H$ is absent from the corresponding mixtures. 189
Figure 5.76: ROP-analysis for $C_6H_5C_2H$ consumption at T_5 = 1450 K and P_5 = 20 bar in the pyrolysis of neat $C_6H_5C_2H$, $C_6H_5C_2H+C_2H_2$ and $C_6H_5C_2H+C_2H_4$ mixtures. 190
Figure 5.77: Measured (symbols) and simulated (lines) mole fractions of small molecule products as a function of T_5 from the pyrolysis of 104 ppm $C_6H_5C_2H$, 104 ppm $C_6H_5C_2H$ + 415 ppm C_2H_2 and 105 ppm $C_6H_5C_2H$ + 504 ppm C_2H_4 mixtures at the nominal P_5 of 20 bar 191
Figure 5.78: ROP analysis for C_6H_6 production at T_5 = 1550 K, P_5 = 20 bar and reaction time = 4ms in the pyrolysis of neat $C_6H_5C_2H$, $C_6H_5C_2H+C_2H_2$ and $C_6H_5C_2H+C_2H_4$. 191
Figure 5.79: Measured (symbols) and simulated (lines) mole fractions of PAHs as a function of T_5 from the pyrolysis of 104 ppm $C_6H_5C_2H$, 104 ppm $C_6H_5C_2H$ + 415 ppm C_2H_2 and 105 ppm $C_6H_5C_2H$ + 504 ppm C_2H_4 mixtures at the nominal P_5 of 20 bar 192
Figure 5.80: ROP analysis for $C_{10}H_8$ production at T_5 = 1500 K, P_5 = 20 bar and reaction time = 4ms in the pyrolysis of neat $C_6H_5C_2H$, $C_6H_5C_2H+C_2H_2$ and $C_6H_5C_2H+C_2H_4$. 193
Figure 5.81: ROP analysis for $C_{12}H_8$ production at T_5 = 1500 K, P_5 = 20 bar and reaction time = 4ms in the pyrolysis of neat $C_6H_5C_2H$, $C_6H_5C_2H+C_2H_2$ and $C_6H_5C_2H+C_2H_4$. 194
Figure 5.82: ROP analysis for (a) $C_6H_5CCC_6H_5$ and (b) $C_{13}H_8CH_2$ production at T_5 = 1400 K, P_5 = 20 bar and reaction time = 4ms in the pyrolysis of neat $C_6H_5C_2H$, $C_6H_5C_2H+C_2H_2$ and $C_6H_5C_2H+C_2H_4$. 195
Figure 5.83: Experimental (symbols) and simulated (solid lines) fuel mole fractions as a function of T_5 in C_8–C_{10} linear alkylbenzenes pyrolysis. Simulated fuel conversion profile in 100 ppm toluene pyrolysis is shown as the dashed line for comparison purpose. 197
Figure 5.84: Experimental (symbols) and simulated (lines) mole fractions of small hydrocarbon products as a function of T_5 in ethylbenzene pyrolysis. 200
Figure 5.85: Experimental (symbols) and simulated (lines) mole fractions of small hydrocarbon products as a function of T_5 in n-propylbenzene pyrolysis. 201
Figure 5.86: Experimental (symbols) and simulated (lines) concentrations of small hydrocarbon products as a function of T_5 in n-butylbenzene pyrolysis. 201
Figure 5.87: Experimental (symbols) and simulated (lines) mole fractions of MAH products as a function of T_5 in C_8–C_{10} linear alkylbenzenes pyrolysis. Simulated speciation profiles in 100 ppm toluene pyrolysis are shown as dashed lines for comparison purpose. 203

Figure 5.88: Experimental (symbols) and simulated (lines) mole fractions of PAH products as a function of T_5 in C_8–C_{10} linear alkylbenzenes pyrolysis. Simulated speciation profiles in 100 ppm toluene pyrolysis are shown as dashed lines for comparison purpose. 205
Figure 5.89: Species mole fractions as a function of T_5 in ethylbenzene pyrolysis. Symbols: measurements; solid lines: modeling results at constant 20 bar within a fixed reaction time of 4.0 ms; dashed lines: simulations with measured pressure profiles up to a time scale of 10 ms. 206
Figure 5.90: Species mole fractions as a function of T_5 in n-propylbenzene pyrolysis. Symbols: measurements; solid lines: modeling results at constant 20 bar within a fixed reaction time of 4.0 ms; dashed lines: simulations with measured pressure profiles up to a time scale of 10 ms. 207
Figure 5.91: Species mole fractions as a function of T_5 in n-butylbenzene pyrolysis. Symbols: measurements; solid lines: modeling results at constant 20 bar within a fixed reaction time of 4.0 ms; dashed lines: simulations with measured pressure profiles up to a time scale of 10 ms. 208

List of Tables

Table 4.1: A list of the reactions representing the interactions between $CH_3C_6H_4$ and the C_3 radicals/molecules 79

Table 5.1: Compositions of the gas mixtures used for experiments. 115

1 Introduction

Since the construction of the first American well in 1859 by Colonel Drake, the use of oil fuels has experienced a dramatic expansion. The primary market for oil had begun to disappear when Thomas Edison invented the light bulb and revolutionized the electric generation industry. However, in the 20th century, oils started to play an important role in the world's primary energy production by the appearance of the gasoline and diesel fuels. These fuels provide the energy for many practical systems such as thermal power plants, residential and commercial heating/air conditioning systems, automobile and aeronautical engines or even incinerators.

Despite the unprecedented efforts towards diversification of renewable energy sources, there is no short-term solution for the world's dependence on conventional and unconventional fossil fuel technologies. The most recent report from the International Energy Agency [1] shows that in 2018 more than 80% of the worldwide energy production is derived from non-renewable fossil fuels (excluding biofuels) with 32% from oils only. Such strong dependence not only reduces the availability of the resources with risks related to the energy supply security, but it is also the cause of the production and release into the atmosphere a huge range of pollutants that pose environmental and health threats. Typically, these pollutant emissions include carbon monoxide (CO), nitrogen oxides (NO_X), sulfur oxides (SO_X), polycyclic aromatic hydrocarbons (PAH) and particulate matter (PM_X). Among these combustion by-products, airborne soot particles are a major environmental pollutant with numerous negative impacts ranging from the reduction of air quality to global warming [2], and a serious hazard for human health [3]. For all these reasons, considerable efforts have been made to limit emissions of particulate as required by more and more stringent international regulations. Strategies aimed at reducing PM formation in combustion devices include design optimization of combustion equipment and reformulation of fuels with and without the use of additives. The development of such strategies often relies on computational fluid dynamics (CFD) calculations where the detailed and accurate chemical kinetic description of PM formation constitutes a fundamental part. Based on the most recent regulations on car engine emissions [4], both the mass of particles and their number (and indirectly their size) need to be accurately modeled. In addition, complications arise from the fact that soot structure and composition strongly affect the consequences that the suspended particles may have on the environment and human health. All these characteristics need to be taken into consideration as function of numerous parameters like for example the chemical sources or the combustion regimes. Yet, the detailed mechanisms of soot formation during incomplete combustion of fuels under pyrolytic or oxygen-lean conditions are one of the least well-resolved combustion problems, mainly due to the fact that the mechanisms of soot formation are highly

complex and involve a large number of chemical and physical processes [5]–[8]. This is despite several decades of research in the field, especially during the last few years when research has been driven by the pressing constraints on the industrial systems based on combustion technologies (both economical (reduction of costs, increased energy efficiency, improved performance ...) and environmental (reduction of pollutant emissions, noise emissions ...)).

The physico-chemical processes for the formation of soot particles from hydrocarbon fuel molecules are represented in **Figure 1.1** [9]. Soot particles are formed in regions of the flame where there is not enough oxygen to oxidize the fuel. As a first step, the fuel molecules break down into smaller hydrocarbon molecules and free radicals either by pyrolysis or oxidation reactions in a high temperature environment. The relative contribution of these species in growth reactions (formation of stable aromatic rings) depend strongly on the fuel structure, i.e. aromatic or aliphatic, and the thermodynamic conditions. Within the complexity of these processes leading to soot, the limiting steps of the overall chain are the subsequent formation of the first aromatic ring (benzene) and the pathways leading to multi-ring compounds. Benzene constitutes the base for the formation of all molecular rings by reaction with small intermediates and other aromatic rings themselves. The formation of the first ring is nowadays quite well understood [5]. On the other hand, the knowledge on the chemistry involved in the appearance and growth of the typical PAH intermediates is still limited [10]. In reality, PAHs are generally considered the main precursors of soot particles and also important species participating in the soot growth process. Thus, a better understanding of chemical reaction pathways leading to the PAH formation is an essential issue in order to understand the growth and formation of soot in combustion environments. Once the soot molecular precursors are available in the combustion environment, nucleation process occurs during which the very first particles are formed. Particle coagulation and surface growth cause the particle to gain mass and increase in size, while oxidation phenomena tend to counteract the growth by removing carbon as CO and CO_2. Eventually, when the soot particles become large enough, agglomeration starts resulting in macroscopic chain-like aggregates called mature soot.

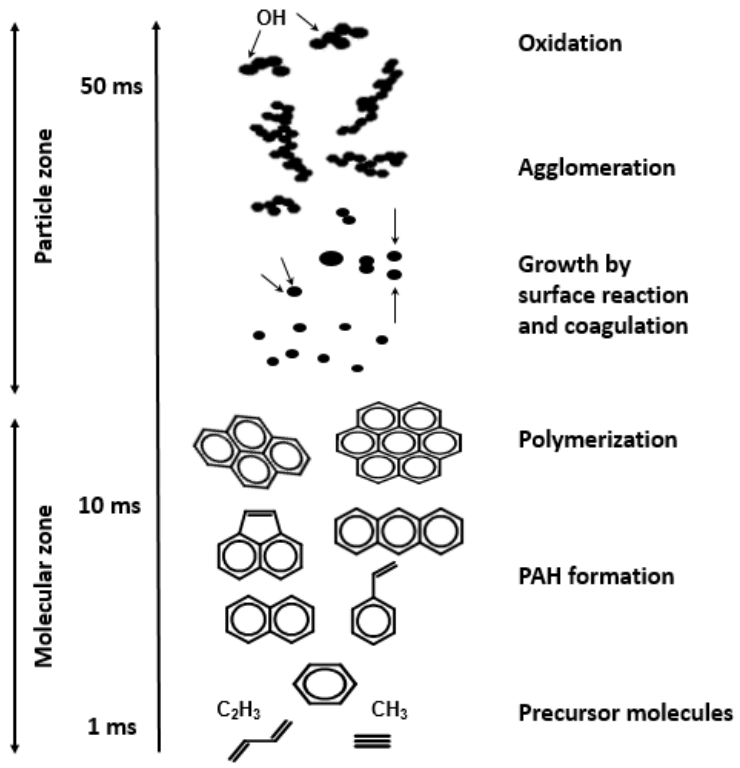

Figure 1.1: Schematic of soot formation steps

From the brief description presented above, it is clear how reliable detailed kinetic mechanisms that accurately describe PAH formation are required for soot particles formation modeling. Indeed, the gas-phase chemistry is a crucial part of the soot models and need to be carefully elaborated. If the routes leading to different PAH species can be established, the combustion conditions (such as the temperature, pressure, fuel/oxygen ratio, fuel composition) can be altered to shift the overall reaction sequence towards the formation of less problematic PAH structures. In general, the accuracy of the chemical kinetic model for PAH chemistry constitutes the fundamental base for the development of predictive models describing the heterogeneous and solid phase chemistry, for use towards less pollutant combustion devices and more efficient utilization of petroleum-based fuels and biofuels.

The aim of this thesis is to provide experimental databases for PAH formation chemistry at typical conditions encountered in modern combustion devices and, based on such experimental results, develop a detailed comprehensive kinetic model describing PAH formation that can be used as a base for improved soot prediction models. Since diesel and gasoline fuels contain, among the others, a mixture of saturated, unsaturated, branched and aromatic hydrocarbons, pyrolysis experimental data from different mono-aromatic hydrocarbons and mixtures with C_2 and C_3 species have been assessed in order to address the influence of fuel molecular structure and the addition of small species on the PAH formation. The

highlighted mechanistic pathways are common to all combustion systems, the relative importance will change based on the specific fuel molecule and thermodynamic conditions. Pyrolytic experiments have been chosen to allow a simplification of the chemistry and the isolation of the reaction mechanisms which lead to the growth of multi-ring structures. A single pulsed shock tube coupled with gas chromatography – mass spectrometry diagnostics was developed to measure stable intermediates, including large PAHs up to four rings, at high pressure, high temperature, and highly diluted conditions. These data were used for the validation of the comprehensive, detailed chemical kinetic model.

My specific contributions to this work mainly regard developing and conducting the shock tube experiments for all the fuel mixtures presented in this thesis. The kinetic modeling has been mainly performed by Dr. Wenyu Sun except for benzene+C_2/C_3 reaction systems for which I developed the model. It is important to underline the fact that the latter is the last version of the model, thus it has been built based on a comprehensive validation against all the experimental results with different fuels and mixtures.

The remainder of this dissertation is organized as follows. Chapter 2 summarizes the main PAH mechanisms necessary for the phenomenological understanding of PAH formation pathways and presents the state of art on the mono-aromatic fuels used in this study. Chapter 3 describes the experimental set-up and the analytic techniques used during this thesis. The development of the kinetic model emphasizing on PAH formation based on recent theoretical studies is demonstrated in Chapter 4, as well as the simulation methods used in the current study. Chapter 5 presents the predictive performance of the kinetic model against the experimental data. Analytic tools are used to provide insights into the chemistry of fuels' decomposition and the subsequent PAH growth (conventional or specific-fuel pathways). Discussions focusing on the impact of C_2/C_3 unsaturated hydrocarbons on fuel decomposition and PAH speciation in binary blends are also revealed. Conclusions and recommendations for future work are given in Chapter 6.

2 Literature Review

2.1 Main PAH formation pathways

Once the first aromatic ring is produced, the formation of polycyclic aromatic hydrocarbons (PAHs) will be able to take place. These aromatic species constitute the bridge between the gas phase and the particle chemistry. The PAH formation and growth involve a large number of pathways depending on the fuel structure and the thermodynamic conditions. The main mechanistic schemes proposed in the literature are briefly described below.

2.1.1 HACA mechanism

The hydrogen-abstraction-acetylene-addition (HACA) mechanism is a repetitive reaction scheme first introduced by Bockhorn et al. [11] and by Frenklach et al. [12] in the early eighties and then refined and expanded in numerous subsequent works (as for example, Frenklach and Wang [13], Appel et al [14], and Frenklach [8]) to describe PAH growth from the first aromatic ring. It involves H-abstraction from an aromatic ring by another H atom to create a radical site. This is followed by C_2H_2 addition to the radical site and then ring closure. An example of the HACA mechanism for the formation of two-and three-ring structures from benzene is shown in **Figure 2.1**.

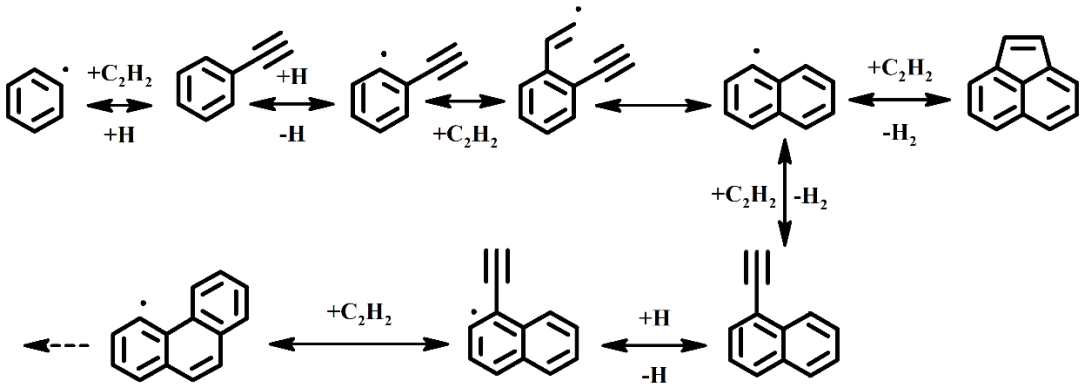

Figure 2.1: Formation of naphthyl, acenaphthylene and phenanthryl by the HACA mechanism *[8]*

The importance of this mechanism is based on its intrinsic features, such as low reaction barriers and high exothermicities for some of the steps involved. For example, for acetylene additions to PAH radicals beyond the second ring, the predicted barriers are usually within 2-6 kcal/mole and the exothermicities are ~30-40 kcal/mole, whereas the subsequent ring closure steps normally exhibit ~2-5 kcal/mole barriers and are ~30-50 kcal/mole exothermic[15]. On the other hand, the PAHs need to be activated by H abstraction reactions which involve relatively high barriers and a certain degree of reversibility. From this, the importance of the high temperature conditions encountered in flames. Another reason for HACA to be the prevalent PAH growth mechanism is the high abundance of acetylene in combustion environments and in various types of aliphatic and aromatic flames where high temperatures are reached.

A slightly different but related mechanism involves the formation of a ring-ethen-2-yl radical moiety followed by the migration of the radical site to the ring and subsequent acetylene addition and ring closure. The prototype of this mechanism was investigated by Moriarty et al. [16] concerning the reactions leading to the second ring starting from styrene ($C_6H_5C_2H_3$).

Despite its undeniable importance, several recent studies [17], [18] highlighted that HACA mechanism alone is too slow to account for the very fast processes of PAHs and soot formation and growth. The main competing mechanisms will be presented in the following sections.

2.1.2 HAVA (Hydrogen Abstraction and Vinyl Addition) mechanism

A novel route for PAH growth was proposed by Shukla et al. [19] in investigating acetylene and ethylene pyrolysis in a quartz reaction tube connected to a linear time-of-flight mass-spectrometer (TOFMS). The authors showed that PAH growth take place by addition of any C_2H_x species (radical or neutral) such as C_2H_2/C_2H (ethyne/ethynyl) for acetylene pyrolysis (HACA route) and C_2H_4/C_2H_3 (ethylene/ethenyl) for ethylene pyrolysis (HAVA route). These intermediates are produced in significant concentrations in the corresponding cases and they promote the formation of a wide range of products including PAHs. Therefore, the nature of species involved in the growth process depends considerably on fuel structure and operating conditions.

An example of HAVA pathway is shown in **Figure 2.2** for the case of ethylene pyrolysis:

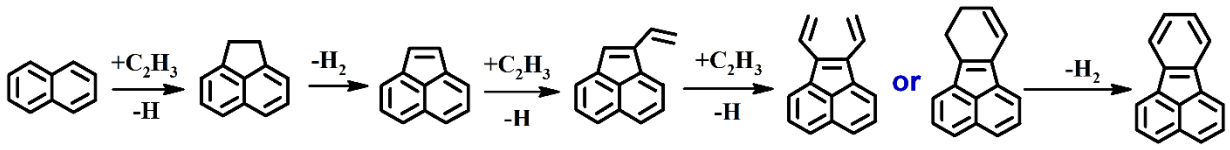

Figure 2.2: PAH growth process via vinyl radical addition from ethylene pyrolysis

2.1.3 Phenyl Addition and Cyclization (PAC) mechanism:

The idea of the importance of aromatic addition to aromatic molecules and radicals was first formulated by Howard [20] and by Richter et al.[21], and recently re-proposed by Shukla and Koshi under the name of Phenyl addition-cyclisation (PAC) mechanism. Shukla and Koshi [22], [23] have investigated the role of phenyl radical during benzene pyrolysis with or without addition of acetylene in a flow tube reactor with TOFMS diagnostics.

Phenyl addition-cyclisation (PAC) is an efficient alternative mechanism for HACA and it is particularly efficient for ring growth from any fusing site, i.e. sites where several aromatic rings are present. This mechanism is shown in **Figure 2.3** and involves the addition of a phenyl radical at a fusing site of an aromatic species followed by dehydrocyclization. Because this mechanism can generate two new active sites in each step, it can easily result in a chain mechanism with subsequent additions and cyclization

reactions. Addition of an acetylene molecule on the same site would lead to ethynyl derivatives without possibility of further growth unless the molecule is "activated" by an H abstraction. In fact, the single step of the HACA mechanism (addition of one acetylene) can lead to the formation of a new ring structure only if the addition takes place on a triple fusing site of a PAH to produce symmetrical PAHs. The two mechanisms, the HACA and the PAC, are complementary processes for fast PAH growth where the HACA can trap radicals effectively while PAC can provide efficient growth.

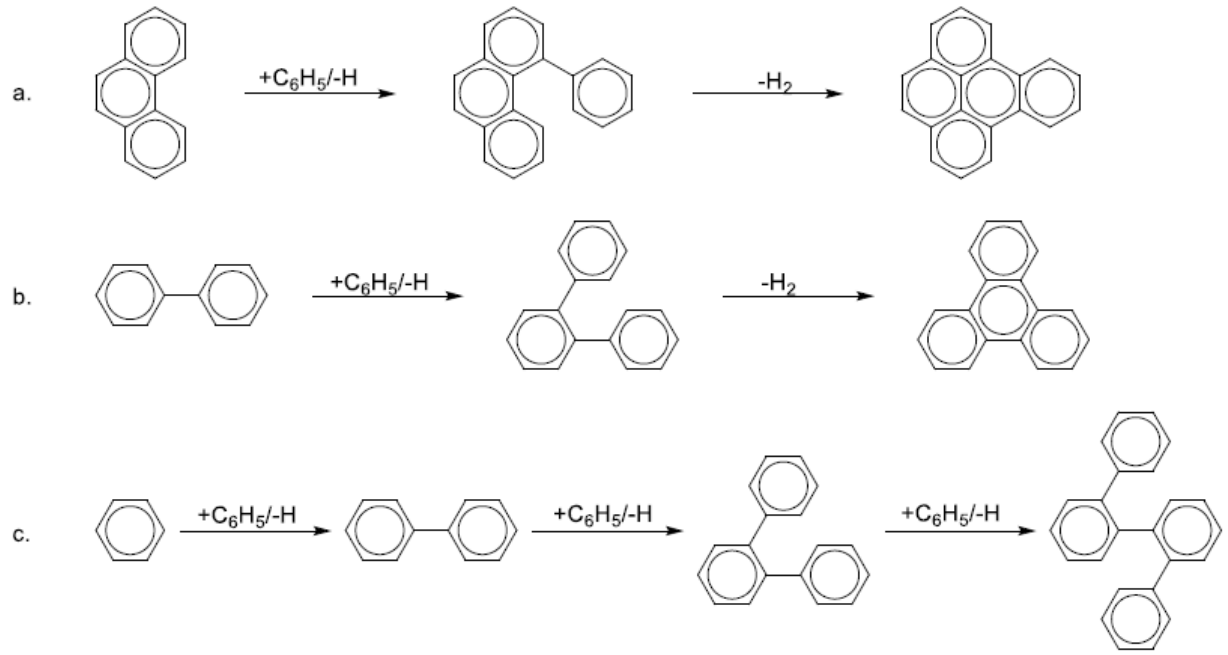

Figure 2.3: Examples of phenyl addition-cyclisation *[22]*.

2.1.4 Diradical Cycloaddition Fragmentation (CAF)

Comandini et al. [24] and Shukla et al. [25] were the first to highlight the importance of the 1,4-cycloaddition of o-benzyne to benzene and their subsequent fragmentation to form naphthalene and acetylene. Experimental evidences for the formation of naphthalene mainly through o-benzyne + benzene reaction is obtained by Comandini et al. [26] through their kinetic analysis of the pyrolytic gas-phase products of phenyl iodide and phenyl iodide/acetylene mixtures. Inspired by the results, Comandini and Brezinsky [27] extended their theoretical study on the radical/π-bond addition to investigate the reactions between o-benzyne and cyclic C_5 hydrocarbons. Recently, Comandini et al. [28] examined the CAF mechanism between o-benzyne and the typical two- to four- ring aromatics in order to determine the influence of the molecular size of the reactants on the entrance barriers. The analysis performed is based on relatively low-level theory, and it indicates that the entrance barrier decreases with the size in the case of linearly fused PAHs while it increases in case of non-linearly fused PAHs. The authors also studied the

CAF reactions between different multi-ring diradicals and benzene. Examples on this mechanism are shown in **Figure 2.4**.

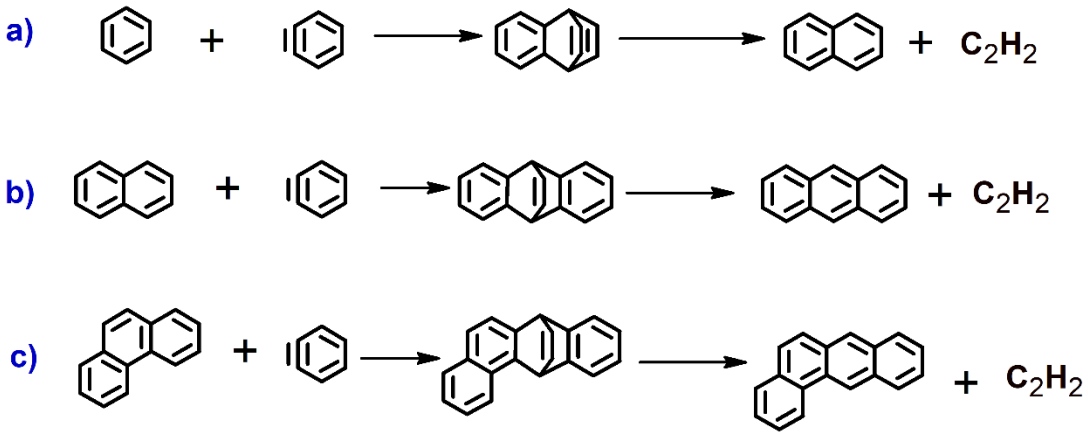

Figure 2.4: Formation of aromatics by the CAF mechanism.

2.1.5 Methyl Addition/ Cyclization (MAC)

Wellmann et al. [29] was the first one to suggest that methyl radicals might be significant in PAH growth and soot formation . Similar to acetylene, methyl radical is also produced in significant concentrations during the pyrolysis and oxidation of most aliphatic and alkyl aromatic hydrocarbons. Shukla et al. [30] explored the MAC mechanism through their kinetic analysis of the mass spectra products from the pyrolysis of toluene and toluene/acetone mixtures. This mechanism, shown in **Figure 2.5,** 124==. The ring expansion resulting from methyl radical addition followed by cyclization has also been reported by McEnally et al. [31], [32] and Lifshitz et al.[33]. However, the MAC mechanism is not as efficient as HACA and PAC in the PAH growth rate and this is due to the lower mass of CH_3 relative to C_2H_2 and C_6H_5.

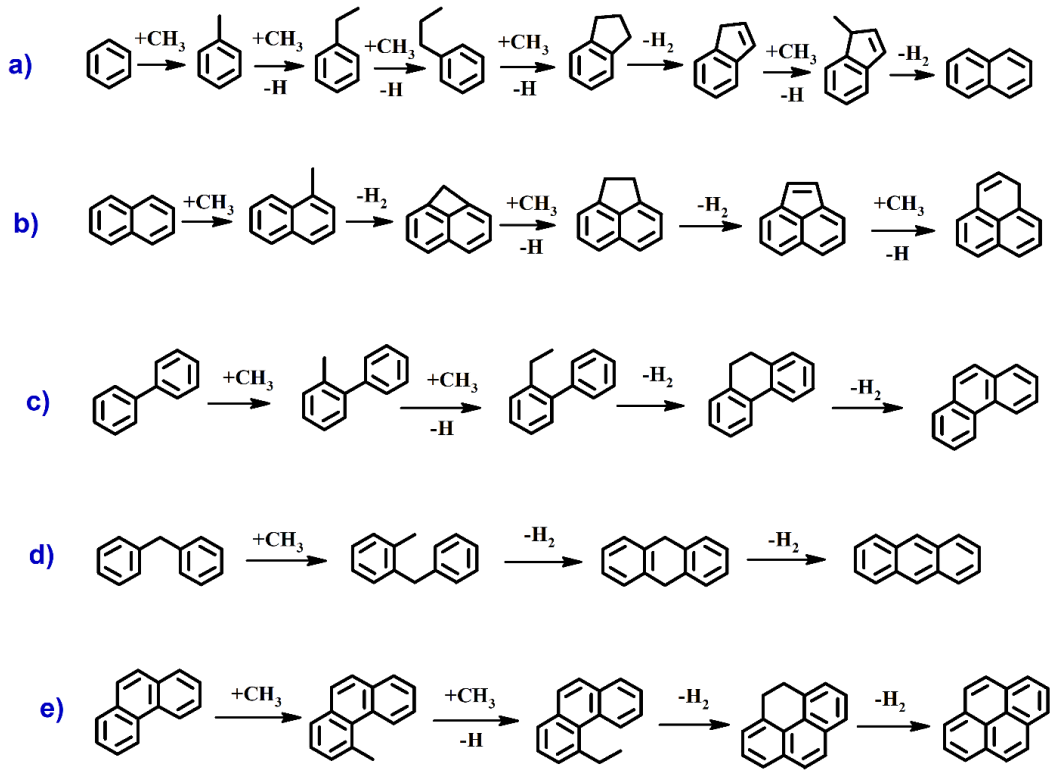

Figure 2.5: Formation of aromatics by the MAC mechanism.

2.1.6 Resonantly stabilized radicals

Resonantly stabilized radicals (RSRs) are present in abundance in combustion environments due to their high stability, and thus they play a crucial role in aromatics formation. Some common RSRs are propargyl (C_3H_3), allyl (C_3H_5), cyclopentadienyl (C_5H_5), benzyl ($C_6H_5CH_2$) and indenyl (C_9H_7). For instance, Castaldi et al. [34] reported that cyclopentadienyl combination play a key role for naphthalene formation. Similarly, Lu and Mulholland [35] studied the recombination of indenyl radical to form the three $C_{18}H_{12}$ isomers (chrysene, benzo-phenanthrene and benzo-anthracene). Colket et al. [36] and Marinov et al. [37] independently established the mechanism of naphthalene formation through recombination between benzyl and propargyl.

2.1.7 Other radical-radical recombination and radical-molecule reactions

Homann and Wagner [38] proposed the mechanism for the formation of soot precursors by aromatic radical-radical recombination and radical-molecule reactions, the base for the subsequent kinetic model developments by Richter et al.[21]. The reactions of phenyl radical with benzene and benzyl radical

produce biphenyl and biphenyl methane respectively. Based on this mechanism, Wang et al [39] also suggested the reaction between naphthyl radical and naphthalene to produce pyrene. Similarly, Unterreiner et al. [40] suggested the benzene addition to naphthyl radical to form fluoranthene.

2.1.8 Ring-expansion via radical-radical reactions

Mebel et al. [41] and Morozov and Mebel [42] elaborate the contribution of phenyl radicals with the propargyl radicals to the formation of indene**.**

Zhao et al. [43] also recommend an additional pathway for the PAH formation, shown schematically in **Figure 2.6**, by recombination of methyl radical (CH_3) with the 1-indenyl radical (C_9H_7) leading eventually to the formation of naphthalene ($C_{10}H_8$).

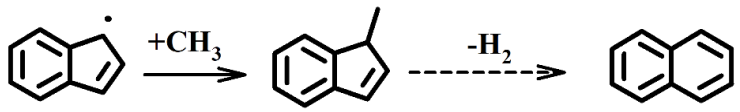

Figure 2.6 : Naphthalene formation through indenyl and methyl recombination. The dashed arrow resembles a multi-step reactions.

Despite the separate advantage of each route, the combination of all of them explain the fast growth of PAH and better predict their formation. As well, the dominancy of one pathway among the others depends strongly on the fuel structure and the operating conditions (temperature and pressure).

2.2 Literature overview on relevant aromatic hydrocarbons

Aromatic hydrocarbons are major components of petroleum-based transportation fuels and are widely used as major components of surrogate fuels for gasoline, diesel oil and kerosene. They play a crucial role as anti-knock additives to enhance the octane number of the fuels, as they have high resistance to auto-ignition [44]. They are also the key building blocks for the formation of the typical polycyclic aromatic hydrocarbons, the main soot precursors [45]. Consequently, understanding the pyrolytic combustion chemistry of aromatic hydrocarbons is crucial for the development of kinetic models describing not only the decomposition of these important fuel components but also the gas phase molecular growth process in the soot formation mechanisms. The following sections contain a brief summary of the investigations available in the literature concerning the pyrolysis of aromatic hydrocarbons relevant to the present thesis.

2.2.1 Benzene

Benzene, the simplest aromatic compound, is an essential component of conventional and surrogate fuels, a relevant intermediate of several combustion processes and a key precursor to soot formation. Several research investigations have suggested that the high temperature chemistry of benzene has significant

impact on the formation of heavier PAH and soot [46], but unfortunately its own pyrolysis mechanism has not been fully clarified yet. The identification of gas phase products of benzene pyrolysis is limited even though many studies have been carried out in shock tubes and flow reactors.

Regarding speciation information, Hou et al.[47] investigated pyrolysis of benzene using a tubular flow reactor for a temperature range 1173-1523 K at pressure ~735 torr and a residence time from 20 to 250 ms; the authors suggested that biphenyl is the dominant product under temperature conditions lower than 1300 K. Kern et al. [48] used shock tube techniques coupled to time-of-flight mass spectrometry (TOF) to investigate the thermal decomposition of benzene (C_6H_6) in dilute inert gas mixtures (21,000 ppm) over a wide range of total pressures (0.21-0.57 atm) and temperatures (1415-2190 K). Concentration profiles were obtained during typical observation times of 700-1000 µsec. The major products were C_2H_2 and C_4H_2 with minor amounts of C_6H_2 and C_8H_2 formed at higher temperatures, and no products with molecular weight higher than benzene were observed.

On the other hand, continuous efforts were made to explore the related PAH formation chemistry. Bohm et al. [49] modeled PAH growth before soot inception during C_6H_6 pyrolysis in a shock tube at temperatures between 1600 and 2400 K, P = 60 bar. The formation of high molecular PAHs was mainly affected by two different reaction pathways: (1) HACA and (2) a combinative ring-ring condensation of aromatics. The authors noted that ring-ring condensation is more efficient than the HACA route in producing high aromatics at short reaction times. The authors also mentioned the importance of cyclopentadienyl pathways leading to the formation of anthracene and phenanthrene. Laskin and Lifshit [50] investigated the thermal decomposition of benzene behind reflected shock waves in a single-pulse shock tube at the pressure of 5 atm, temperatures between 1400 and 2000 K and average reaction time of 2 ms. The major species detected by gas chromatography (GC) technique were acetylene (C_2H_2), diacetylene (C_4H_2), biphenyl ($C_{12}H_{10}$) and phenylacetylene (C_8H_6). Regarding their experimental results, the authors reported a detailed kinetic modeling study explaining the dominance of biphenyl at low temperatures and the ring opening of phenyl radical at high temperatures to produce small species passing through the linear -C_6H_5• radical. Sivaramakrishnan et al.[51] studied benzene pyrolysis under elevated pressures (30 - 50 bar) in the temperature range 1200-1800 K for reaction times in the order of 1.2-1.5 ms using a high pressure single pulse shock tube (HPST). The primary species detected using GC were acetylene and diacetylene. Because of the usage of highly diluted mixtures and the HPST being unheated, the authors failed to detect heavy molecules including biphenyl which usually have high concentrations in low temperature region. Nevertheless, the authors updated their model [52] so it could capture the benzene decay and acetylene profile. Shukla et al. [22] proposed a highly efficient PAH growth mechanism for the pyrolysis of benzene with and without addition of acetylene and for pure acetylene.

Pyrolytic reactions were performed in a flow tube reactor at five different temperatures in the range 1140–1473 K with constant pressure of 10.18 Torr and constant residence time of 0.61 s with and without addition of acetylene to benzene, and at temperatures 1136–1507 K with constant pressure of 10.12 Torr and constant residence time of 0.56 s for pure acetylene. The products, including large polycyclic aromatic hydrocarbons, were detected and qualitatively measured by an in situ direct sampling mass spectrometric technique using a vacuum ultraviolet (VUV) single photon ionization (SPI) time of flight mass spectrometry (TOFMS). The authors remarked the only difference between pure benzene and benzene + acetylene mixture is the higher production of phenylacetylene and phenanthrene at low temperatures, while no significant influence of acetylene addition to benzene was observed at high temperatures. The authors also highlighted the high efficiency of the PAC mechanism compared to the HACA mechanism on the formation and growth of PAHs and the importance of the synergy between the two mechanisms to account for the fast PAH growth.

Moreover, several shock tube pyrolysis experiments were conducted using nitroso benzene (C_6H_5NO) and phenyl iodide (C_6H_5I) as a precursors of phenyl (C_6H_5), the fuel radical of benzene. Horn et al. [53] and Heckmann et al. [54] thermally dissociated C_6H_5NO behind shock waves to study the self-recombination reaction of C_6H_5 around 1-2 atm over temperature range of 800-1000 k and 1050-1450 K, respectively. Later, Tranter et al. [55] performed C_6H_5I pyrolysis experiments using a diaphragmless shock tube (DFST) coupled to both a time-of-flight mass spectrometer (TOF-MS) and laser schlieren (LS) densitometry diagnostics for temperatures ranging from 1276 to 1853 K. The LS experiments were carried out at pressures of 22, 54, and 122 Torr, while the TOF-MS experiments were carried out at pressures in the range 500-700 Torr. The authors investigated theoretically and experimentally the self-reaction kinetics of phenyl radicals. Comandini et al. [26] developed a kinetic model for C_6H_5I and C_6H_5I + C_2H_2 pyrolysis focusing on the mechanism of PAH formation based on an experimental investigation carried out using HPST at nominal pressures of 25 and 50 atm for a temperature range between 900 and 1800 K.

Concerning the modeling efforts in a more recent work, Saggese et al. [56] analyzed in detail the benzene chemistry using a single refined kinetic model based on the originally developed CRECK model [57]. The predictions of the refined model were compared with a vast amount of experimental measurements focused on benzene pyrolysis and oxidation performed with different techniques and methods over wide ranges of temperature and pressure conditions.

2.2.2 Toluene

Toluene (C_7H_8) exists naturally in transportation fuels and it is considered as an important component in surrogate fuels. For example, jet fuels and gasoline contain 20-30% toluene by mole fraction due to its high energy density and anti-knocking capacity. Being an important combustion intermediate, it has been widely investigated also in relation to the formation and growth of polycyclic aromatic hydrocarbons (PAHs). Indeed, its major initial decomposition product, benzyl radical [58], is a resonantly stabilized radical and thus it is a key intermediate in combustion environments. Furthermore, the benzyl chemistry, and thus indirectly the toluene pyrolysis, is fundamental for the understanding of the decomposition of all alkylated aromatic hydrocarbons, for which the initial decomposition steps leads to the formation of the benzyl radical.

The pioneering work of toluene pyrolysis was performed by Smith [59] in both quartz and tungsten Knudsen cells at very low pressures (10^{-5} to 1 torr) and temperatures up to 1800°C using electron-impact ionization (EI) mass spectrometry (MS). The results for quartz and tungsten Knudsen cells were quite similar. At the lower pressures, only products with molecular weights lower than C_7H_8 were observed, including CH_3, C_2H_2, C_3H_3, C_4H_2, C_4H_3, C_4H_4, C_5H_5, C_6H_6 and C_7H_7, while at higher pressures, these products undergo bimolecular reactions to form heavier compounds up to at least $C_{20}H_{12}$. Subsequently, Pamidimukkala et al. [60], Colket and Seery [36] and Sivaramakrishnan et al. [61], [62] performed shock tube pyrolysis studies on toluene. Pamidimukkala et al. [60] investigated the pyrolysis of toluene at temperatures of 1550–2200 K and pressures from 0.2 to 0.5 atm using two independent shock tube, techniques time-of-flight (TOF) MS and laser-schlieren densitometry. The primary species observed in these experiments were C_2H_2, C_4H_2, CH_4 and C_7H_7. The proposed mechanism was initiated by two parallel dissociation channels (C-H and C-C bond fissions), and the authors were able to define the rate of only one of these channels, the irreversible C-C bond fission. Colket and Seery [36] studied the pyrolysis of 1% toluene in argon using a single-pulse shock tube at pressure of 10 atm, temperature range 1200–1850 K and reaction time of 600 μs. The observed stable products were analyzed using gas chromatography (GC), including some PAHs. Mole fraction profiles of many stable species from H_2 and CH_4 to pyrene were measured. A detailed chemical kinetic mechanism was constructed for describing the formation of aromatics and other species. The work of Sivaramakrishnan et al. [61], [62] was performed at 27 and 45 bar over a wide temperature range (1200–1900 K) with the average reaction time of 2 ms. Stable species were detected using GC combined with MS (GC–MS) only up to indene (C_9H_8). Their model was restricted to depict the formation of PAHs up to naphthalene ($C_{10}H_8$). The decay of indene and phenylacetylene observed at the highest experimental temperature conditions could not be captured by the model.

Afterwards, Shukla et al.[63] and Zhang et al. [64] performed toluene pyrolysis in a low-pressure flow reactor coupled to vacuum ultraviolet (VUV) photoionization. Shukla et al. [63] studied the pyrolysis of toluene and toluene/acetylene mixtures in a low-pressure flow reactor at pressures of 8.15-15.11 Torr and temperatures of 1136-1507 K with constant residence time 0.56 s. The product species including PAHs were detected using a vacuum ultraviolet (VUV) single photon ionization (SPI) time-of-flight mass spectrometer (TOFMS). Some species, especially the isomeric forms of the large multi-ring structures, were difficult to be distinguished with the fixed photon energy at 10.50 eV. Despite this, they examined from a qualitative point of view the effects of acetylene addition on the formation of PAHs and they suggested possible reaction mechanisms for the formation of PAHs. Zhang et al. [64], [65] also studied the pyrolysis of toluene (1.24 vol.% toluene in argon) in a flow reactor at 10 Torr in the temperature range of 1270–1870 K using the tunable synchrotron VUV photoionization and molecular-beam mass spectrometry (MBMS), and the results were investigated by a kinetic modeling study in which the roles of the radicals formed in the decomposition of toluene were examined. The high energy resolution and wide tunable range of synchrotron VUV light (photon energy from 7.80 to 24.00 eV) helped reduce fragmentation via near-threshold photoionization and distinguish most isomers.

Moreover, Matsugi et al.[66] constructed a detailed kinetic model for toluene pyrolysis focusing on the mechanism for the formation of two- and three-ring aromatic hydrocarbons based on their theoretical calculations [67], [68]. Their model was validated against the mass spectrometric studies on the low-pressure (10 Torr) pyrolysis of toluene and toluene/acetylene and toluene/benzene mixtures carried out by Shukla et al.[63], [69]. They also indicated the importance of the reactions of resonance stabilized radicals such as benzyl, fulvenallenyl and propargyl radicals for the PAHs formation processes. A more recent work on the pyrolysis of toluene was performed by Yuan et al.[70], [71] who studied the flow reactor pyrolysis of toluene from low to atmospheric pressures and temperatures from 1100 to 1730 K using synchrotron vacuum ultraviolet photoionization mass spectrometry. The authors discussed the formation pathways of measured small species, radicals and PAHs with a detailed kinetic model which was validated against their experimental results and experimental data from the literature for toluene pyrolysis.

2.2.3 Styrene

Styrene is a significant product with high concentration levels in combustion and pyrolysis of most aromatic fuels [72]–[75] and it plays an important part in the formation of PAHs. Despite its fundamental role, there have been very few investigations that focused on its chemistry. Müller-Markgraf and Troe [76] and by Grela et al. [77] performed kinetic experiments to derive the reaction rate constant of the styrene dissociation to benzene and vinylidene. Litzinger et al. [72] investigated the oxidation of styrene

in an atmospheric-pressure flow reactor at temperatures around 1060 K and equivalence ratio of 0.56. The authors provided species profiles for the main intermediates and products of styrene oxidation. Other studies on styrene include the work of Yuan et al. [78] who reported experimental data and a kinetic model on styrene combustion. In particular, low pressure laminar premixed flames of styrene and atmospheric pressure jet stirred reactor oxidation of styrene/benzene mixtures were investigated under lean, stoichiometric and rich conditions using synchrotron vacuum ultraviolet photoionization mass spectrometry and gas chromatography, respectively. The kinetic model was validated against the species profiles. The authors indicated the importance of 1-phenylvinyl radical, phenylacetylene, and phenyl radical regarding the aromatic growth (from naphthalene and stilbene to phenanthrene). In a more recent work, Comandini et al. [79] studied the laminar flame speeds and ignition delay times using a spherical bomb and a shock tube, respectively. A kinetic model was developed and validated against the experimental results based on the toluene oxidation model by Metcalfe et al. [80]. On the other hand, in the literature no experimental or kinetic speciation studies were performed on styrene pyrolysis especially in relation to the formation of PAH products.

2.2.4 Phenylacetylene

Although phenylacetylene ($C_6H_5C_2H$) is considered as a significant product in combustion and pyrolysis of most fuels and main PAH precursor, no theoretical or modeling work has been performed on the combustion and pyrolysis of phenylacetylene. The only available kinetic investigation centering on $C_6H_5C_2H$ consumption was performed by Herzler and Frank [81] through shock tube experiments, in which the rate coefficients for the major reactions accounting for its decomposition were derived at a pressure of 2 bar over the temperature range of 1600-1900 K. Another work [82] implementing theoretical calculations was done to assess the influence of phenylacetylene addition on PAH growth compared to the HACA mechanism. Although the reaction schemes for phenylacetylene pyrolysis and oxidation exist in all kinetic models which include the aromatic chemistry, the lack of experiments focused on the phenylacetylene chemistry leads to insufficient understanding of its decomposition and of the related PAH chemistry pathways.

2.2.5 Ethylbenzene

Ethylbenzene, the simplest alkyl-benzene after toluene, is receiving growing attention due to its increase usage in commercial fuels and to its significant role in PAH formation. Nevertheless, experimental and kinetic studies on ethylbenzene pyrolysis is limited, especially regarding PAH formation. Most of the existing literature is from last decade and focused on measuring the rate constant of the unimolecular

decomposition of ethylbenzene below 1000°K [83]–[90] and above 1200°K [91]–[93], [76] by a variety of methods.

Brooks et al. [94] investigated the pyrolysis of ethylbenzene using a static reactor operating at 778 K and 833 K temperatures with 2 min residence time. A satisfactory reaction mechanism was developed to account for all the major species observed (styrene, toluene, benzene, ethylene, methane and ethane). Afterwards, Mizerka and Kiefer [93] and Pamidimukkala and Kern [95] studied the high temperature thermal decomposition of ethylbenzene using shock tubes. Mizerka and Kiefer [93] used the laser schlieren (LS) technique for the reaction conditions 1300-1800 K, 70-550 Torr, while Pamidimukkala and Kern [95] used TOF mass spectrometry over the temperature and pressure ranges of 1350-2080 K and 0.25-0.5 atm. Both of them formulated a reaction mechanism capable of reproducing the experimental results observed in their experiments, in particular species up to C_8 in the TOF-MS measurements. Subsequently, Bruinsma and Moulijn [96] discussed the PAH formation from ethylbenzene pyrolysis in the temperature range of 900-1250 K for a residence time of 5 sec using a reactor coupled to GC. The authors pointed out the importance of dimerization reactions in the formation of PAHs at low temperatures.

In a more recent study, Yuan et al. [73] examined ethylbenzene pyrolysis using a flow reactor connected to synchrotron vacuum ultraviolet photoionization mass spectrometry (SVUV-PIMS) under the temperature range 850-1500 K for pressures of 0.04, 0.2, and 1.0 atm. A new kinetic model for ethylbenzene reproducing both small species and PAH profiles was developed and validated on a wide range of conditions, including their data and the experimental data from the literature. The authors indicated that PAH formation process in ethylbenzene pyrolysis is strongly influenced by the fuel structure. For instance, in toluene pyrolysis, benzyl radical plays a dominant role in PAH formation. However, in ethylbenzene, although benzyl radical is still important, several PAHs could be produced from C_8 mono-aromatic hydrocarbons (MAHs) such as phenylacetylene, 1-phenylvinyl radical, vinyl phenyl radical, and styrene.

2.2.6 Propylbenzene

For the reason of its widely utilization as a surrogate component for jet fuels [97], propylbenzene kinetics analyses in pyrolytic environments are important to predict the PAH formation in practical applications. The very early work on propylbenzene pyrolysis aimed to calculate its unimolecular decomposition [98], [85], [99]. Later, Chen and Froment [100] studied the thermal cracking of n-propylbenzene, carried out in a bench scale tubular reactor, for a temperature range 620-790°C and pressure 1.3 bar. The authors developed a kinetic model reproducing the reaction products up to the single ring aromatic hydrocarbons,

identified by means of retention times and a GC-MS. On the other hand, the only two existing detailed models for PAH formation for *n*-propylbenzene were done by Gudiyella and Brezinsky [101] and Yuan et al. [74]. Gudiyella and Brezinsky [101] investigated n-propylbenzene pyrolysis using a high pressure single pulse shock tube coupled to gas chromatographic techniques in the temperature range 1027-1678 K and a nominal pressure of 50 bar. The authors modified their existing model on n-propylbenzene oxidation [102] to better simulate the stable species profiles in pyrolytic conditions, including PAH products. Yuan et al. [74] reported the experimental results on n-propylbenzene pyrolysis obtained with a flow reactor connected to SVUV-PIMS at pressures of 0.04, 0.2 and 1 atm and temperature range 800-1500 K. The authors built a comprehensive kinetic model based on the experimental results capable to provide insights into the chemistry of n-propylbenzene consumption and PAH formation, with validation extended to the shock tube results [101]. On the basis of their kinetic model analyses, they found that indene (one of the main PAH products) is formed through an unconventional formation pathway strongly dependent on the specific fuel structure.

2.2.7 Butylbenzene

Butylbenzene is not only an aromatic representative component in jet-fuels and diesel fuels [103], [104] but also a model fuel for large alkylbenzenes, such as n-pentylbenzene, etc… [105]. Much research on the fundamental combustion parameters of n-butylbenzene was performed, including ignition delay [105]–[109], flame speeds [75], [110], [111], species concentrations [112]–[114]. Therefore, kinetic mechanisms were constructed based on these studies [105], [111], [75], [113]. Besides, other studies have focused on n-butylbenzene thermal decomposition under initial near-critical and supercritical-conditions [115] and the computational study on the $C_{10}H_{14}$ potential energy surface including its unimolecular decomposition [116]. However, two studies on n-butylbenzene pyrolysis were carried out [117], [118]. Freund and Olmstead [117] constructed a kinetic model to simulate Rebick's unpublished n-butylbenzene pyrolysis experiments for a narrow temperature range 600-100K. Only the work by Zhang and co-workers [118] contains a detailed modeling and experimental investigation on the n-butylbenzene pyrolysis. In particular, the authors developed a kinetic model based on the experimental results obtained with a flow reactor connected to SVUV-PIMS at pressures of 30, 150 and 760 Torr and temperature range 800-1300 K. This mechanism is an updated version of their kinetic model for the n-butylbenzene flames [75]. The authors emphasized that the benzylic C-C bond dissociation and H abstractions are the key reactions for n-butylbenzene consumption. On the basis of their kinetic model analyses, they found also that the formation and growth of PAHs (indene and naphthalene) are strongly influenced by the specific fuel structure where conventional pathways have negligible role. Their work revealed the strong influence of the side-chain length on the pyrolytic chemistry of alkylbenzenes.

2.2.8 Benzene and toluene based mixtures

'Real fuels' are mostly a mixture of various hydrocarbons ranging from paraffin to aromatics. Blended fuels containing at least two components can have enhanced combustion characteristics than each of them alone [119]–[123], including enhanced PAH formation and soot emissions, fuels' reactivity and so on. Few previous works studied the binary benzene and toluene mixtures through experimental and kinetic modeling approaches. Knorre et al. [124] studied the shock tube co-pyrolysis of benzene and acetylene in the temperature range 1560-2580 K at pressures of 6 and 60 bar. A remarkable increase in soot formation was observed compared to the pyrolysis of pure benzene and pure acetylene. Shukla et al. [22] investigated both pure benzene and benzene + acetylene mixture pyrolysis using flow reactor techniques. Acetylene addition to benzene induced the production of phenylacetylene and phenanthrene at low temperatures, while no significant influence was observed at high temperatures. Later, Comandini et al. [26] developed a kinetic model focusing on PAH formation based on the phenyl iodide and phenyl iodide + acetylene based on shock tube pyrolysis experiments.

Shukla et al. [63], [69] have studied the pyrolysis of toluene, toluene/acetylene and toluene/benzene mixtures in a low-pressure flow reactor by detecting product species including PAHs using a vacuum ultraviolet (VUV) single photon ionization (SPI) time-of-flight mass spectrometer (TOFMS). They investigated qualitatively the effect of acetylene and benzene addition on the formation of PAHs and suggested possible reaction mechanisms for the formation of PAHs. Later, a kinetic model was proposed by Matsugi and Miyoshi [66] to interpret the two- and three-ring PAH formation from the pyrolysis of toluene and toluene-C_2H_2 mixtures. The model satisfactorily predict the experimental observations in [63]. Very recently, Li et al. [125] investigated the pure toluene pyrolysis, pure acetylene pyrolysis and co-pyrolysis of toluene and C_2H_2 in a flow reactor at atmospheric pressure over temperature range 1057–1340 K. Mole fractions of fuels and key products were measured via a photoionization mass spectrometer. Through comparisons with the cases of neat toluene and neat C_2H_2 pyrolysis, Li et al. [125] pointed out that the decomposition of both fuels is greatly stimulated in toluene-C_2H_2 pyrolysis,. Such phenomenon is due to the reaction between benzyl radical and acetylene that converts toluene and acetylene to indene and H_2. Li et al. [125] work focused mainly on the synergistic effects of fuel decomposition, so only limited PAH speciation measurements were reported.

3 Experimental Set-Up

3.1 Shock tube theory

A shock tube is an ideal totally adiabatic reactor, where the experimental gas is brought almost instantaneously to a known and controlled temperature and pressure condition by means of the passage of a shock wave in the gas [126]. A shock wave is a disturbance that travels at a velocity higher than the characteristic speed of sound through the medium (in this case, gas). Unlike the sound waves which do not generate a substantial change in the properties of the gas, the shock waves cause an abrupt increase in temperature, pressure, and density of the tested-gas. The generation of shock waves inside a controlled volume, the shock tube, coupled with a variety of measurement and analytical instrumentation is a valuable tool for the study of physical and chemical processes [127].

Moreover, the instantaneous and homogeneous heat-up of the tested gas through gas-dynamic effects within a time of around 1μs enables the investigation of fast gas-phase kinetics without influences of transport processes. The abrupt increase of temperature is too fast for molecules to diffuse to the wall of the shock tube; thus, heterogeneous reactions are negligible. In addition, the uniform temperature distribution and the homogeneity of the mixtures permit a rigorous decoupling of the physical (ex: diffusion) and chemical (kinetics) processes within the timescale of the experiment. These properties have proven shock tubes as versatile tools to study chemical processes under combustion conditions [128].

The shock tubes offer the possibility to reach a wide range of temperature conditions from 600 to 4000 K and pressures from 0.1 to 1000 bar.

3.1.1 Principle - Evaluation of the thermodynamic parameters

In general, shock tubes are thick-walled tubes made of stainless steel with circular, square, or rectangular cross sections with a very smooth inner surface. They are made up of two parts (a high-pressure section, called driver section, and a low-pressure section, called driven section), separated by a single or double diaphragm system. The driven section is filled with the test-gas mixture at a temperature T_1 and a pressure P_1 while the driver section with the driver gas at a temperature T_4 and a pressure P_4 (Figure 3.1). The driver gas is always chosen to have low heat capacity ratio (γ) and low molecular weight (resulting in high speed of sound) in order to obtain increased shock strength, all the other initial parameters being the same. H_2 and He are the most frequently used driver gases.

The abrupt rupture of the diaphragm generates a series of compression waves. Each wave is stronger and possesses a higher velocity compared to the previous waves since it travels through a gas which has

already been heated and compressed. As a consequence, these waves rapidly coalescence to form a unique shock wave traveling in the low-pressure section. The interface between the driver gas and the test-gas is called “contact surface”. The incident shock wave travels at a constant and supersonic speed (W_S) with respect to the gas at rest (state 1, Figure 3.1), while the contact surface travels at a lower speed. The incident shock wave generates a sudden rise in temperature and pressure for the gas under investigation, now called shocked gas (state 2). The incident shock wave propagating inside the shock tube finally reaches the end wall of the driven section and then it gets reflected. The reflected shock wave causes a second increase in pressure and temperature of the shocked gases. The gas behind the reflected shock wave is at rest and in state 5 based on the nomenclature in Figure 3.1. The temperature and pressure behind the reflected shock wave (T_5 and P_5) remain relatively stable up to a few milliseconds. Simultaneously to the bursting of the diaphragm, a sequence of rarefaction waves traveling opposite side compared to the compression waves are formed in the high-pressure section. The expansion waves lead to a reduction in temperature ($T_3 < T_4$) and in pressure such that $P_3 = P_2$ ($P_3 < P_4$). The zone between the head and the tail of the rarefaction waves is called the expansion fan. After reaching the end flange, the reflected expansion waves propagate towards the reaction zone. The reflected expansion waves are usually utilized in shock tube experiments to quench the reactions as they generate a rapid decrease in the temperature and pressure once entering the reaction zone.

Figure 3.1 represents the evolution of the conditions inside the shock tube with respect to time as explained in the previous paragraph. And the indices 1, 2, 3, 4 and 5 respectively denote:

- The initial thermodynamic conditions in the low-pressure section.
- The conditions behind the incident shock wave (the pressure, density, and temperature have incident shock wave).
- The conditions behind the contact surface.
- The initial thermodynamic conditions in the high-pressure section.
- The conditions behind the reflected shock wave.

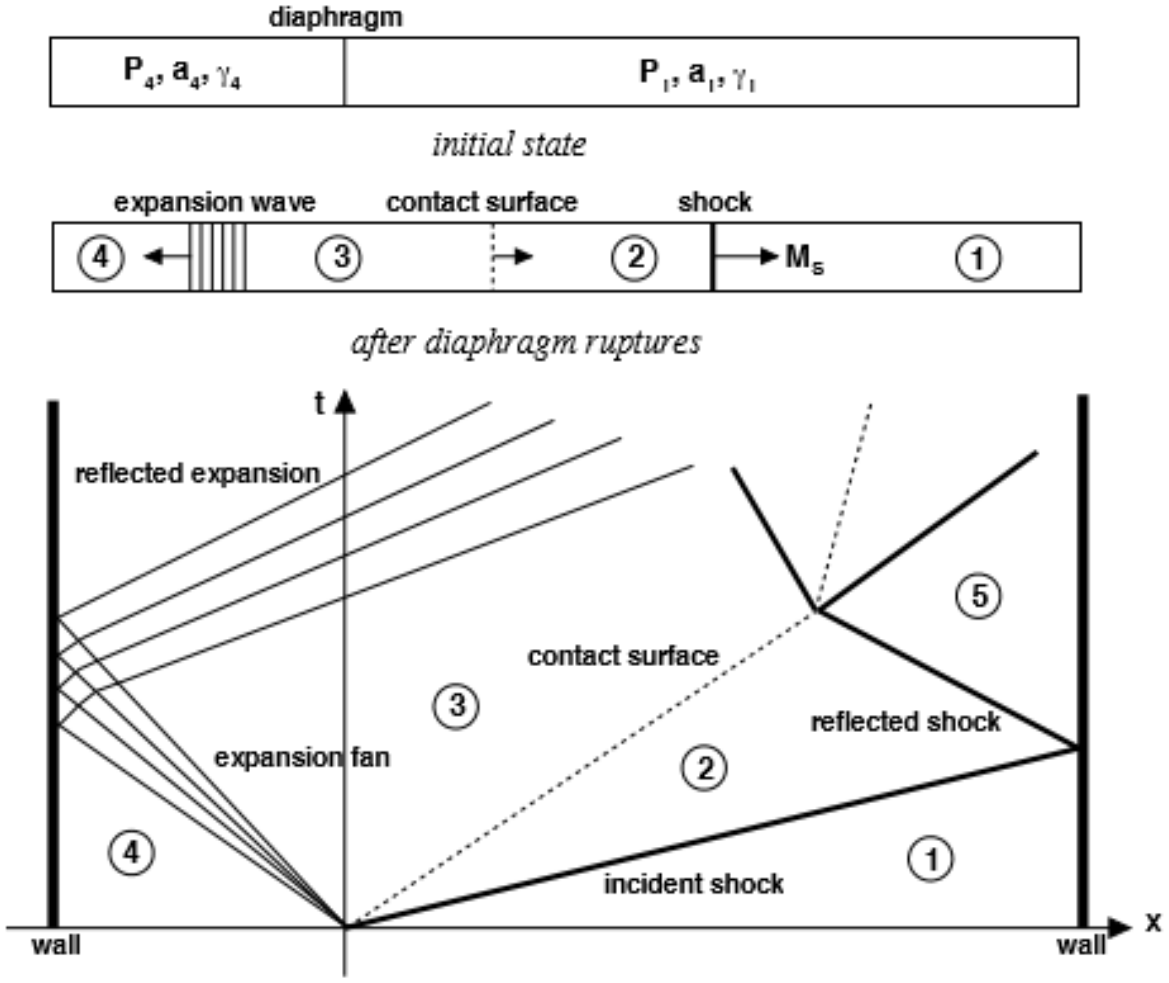

Figure 3.1: Schematic picture of a shock tube and *(x, t) diagram showing the various regions associated with a shock wave at a time t after the bursting* of the diaphragm at the origin O

In order to calculate the thermodynamic parameters: pressure (*p*), temperature (*T*) and density (ɻ) behind the incident and reflected shock waves, the following hypotheses are considered:

- ¶ The gases obey the ideal gas law

  = = —

- ¶ Negligible viscosity
- ¶ Heat losses by conduction through the walls of the shock tube and by radiation can be neglected (reaction times are small (few milliseconds) and gases have low emissivity)

These calculations use the conservation of mass, momentum, and energy equations. It's important to point out that the initial velocity v of the gas molecules in the driven gas relative to the shock tube is $v_1=0$, while the velocity of the shock front relative to the tube is referred to as W_S. Practically, it is more convenient to express the basic equations of the gas motion in relation to the shock front, considered at rest, which means considering a relative velocity u.

For the first step, the shock front propagates as a single entity through the driven section increasing the pressure, temperature, and density of the gas initially at condition 1. The final conditions after the passage of the wave front (zone 2 in Figure 3.1) can be determined by solving the undermentioned equations:

$$_1 \ _1 = \ _2 \tag{3.1}$$

$$_1 \ \frac{^2_1}{} + \ _1 = \ _2 \ \frac{^2_2}{} + \ _2 \tag{3.2}$$

$$\frac{1}{2} \ ^2_1 + \ _1 = \frac{1}{2} \ ^2_2 + \ _2 \tag{3.3}$$

Where *u* and *h* are the velocity and enthalpy, respectively.

This is a system with three equations and six unknowns. Treating the gas in the shock tube as an ideal gas with constant isentropic ratio (γ), allows using the following equations:

$$_2 = \ _2 \ \ _2 \tag{3.4}$$

$$_2 - \ _1 = \ (\ _2 - \ _1) = \frac{}{ - 1} \ (\ _2 - \ _1) \tag{3.5}$$

The combination of the three conservation equations with the assumption of constant isentropic ratio allow the application of Rankine-Hugoniot relations [129]–[131]. Substituting equations (3.4) and (3.5) in equations (3.1) to (3.3), we have three equations with four unknowns ($_1$, $_2$, $_2$, and $_2$). Because the velocity of shock front ($_1$) can be measured, the final conditions after the passage of the wave front (state 2) can be determined by the following equations:

$$\frac{2}{1} = \frac{2 \quad {}_1^2 - (\quad - 1)}{+ 1} \tag{3.6}$$

$$\frac{2}{1} = \frac{(\quad + 1) \quad {}_1^2}{(\quad - 1) \quad {}_1^2 + 2} \tag{3.7}$$

$$\frac{2}{1} = \frac{2 \quad 1}{1 \quad 2} = \frac{(\quad {}_1^2 - \frac{\quad - 1}{2})(\quad {}_1^2 \frac{\quad - 1}{2} + 1)}{\frac{(\quad - 1)^2}{4} \quad {}_1^2} \tag{3.8}$$

Where is the specific heat ratio and M_1 is the Mach number. The Mach number M_1 for an ideal gas can be determined from the velocity of incident shock wave using the following equation:

$$_1 = \frac{1}{1} = \frac{1}{\sqrt{\quad 1}} \tag{3.9}$$

Where the denominator is the speed of sound *a* and *MW* is the molar mass of the test gas.

On the other hand, it would be useful from a practical point of view to obtain a relation between the strength of the shock and only the initial conditions 1 and 4. Applying the assumptions mentioned above, the equation (3.10) can be obtained which relates the initial pressures in the driver and driven sections with M_I[126]. By varying the ratio of P_4 over P_1, we can obtain shock waves with different strength. Once M1 is known, the final conditions T_2 and P_2 can be subsequently calculated using the equations (3.6) to (3.8)

$$\frac{4}{1} = \frac{2 \quad 1 \quad {}_1^2 - (\quad 1 - 1)}{1 - 1} \quad \{1 - \frac{4 - 1}{4 + 1} \quad \frac{1}{4} \quad (\quad 1 - \frac{1}{1})\}^{-(\frac{2 \quad 4}{4 - 1})} \tag{3.10}$$

As for the reflected shock wave, it propagates in the gases previously heated and compressed by the incident shock wave. The reflected shock wave therefore has the effect of further raising the temperature and pressure of the gases. As mentioned before the thermodynamic parameters behind the shock wave are indexed as 5. The ratios P_5/P_1 and T_5/T_1 are obtained in the same manner described above which implies

to replace the indices in the previous equations by 5 instead of 2 and 2 instead of 1 and then expressing P_2 and T_2 as a function of P_1, T_1 and M_1.

$$\frac{5}{1} = \left[\frac{2 \quad {}_1^2 - (\quad - 1)}{+ 1}\right]\left[\frac{(3 \quad - 1) \quad {}_1^2 - 2(\quad - 1)}{(\quad - 1) \quad {}_1^2 + 2}\right] \tag{3.11}$$

$$\frac{5}{1} = \left[\frac{2(\quad - 1) \quad {}_1^2 - (3 - \quad)}{(\quad + 1)^2}\right]\left[\frac{(3 \quad - 1) \quad {}_1^2 - 2(\quad - 1)}{{}_1^2}\right] \tag{3.12}$$

During this study, the calculations are made by iterations considering the variation of the heat capacity of gases with temperature using the python software developed in the laboratory "ICARE-CNRS" by the 'Onde de Choc' team.

3.1.2 Observation time

The observation time in a shock tube experiment can be referred as the time available for the measurements in the uniform region behind the incident or the reflected shock wave, depending on the type of study. It is decided by the:

a) Length of observation station from diaphragm
b) Length of driver section (due to the influence of the reflected rarefaction fan)
c) Length of the end wall from diaphragm (influence of the reflected shock)
d) Growth of the boundary layer

The high purity single-pulse shock tube at ICARE is a device used for the study of chemical processes behind reflected shock wave as described in detail in the next sections. For this purpose, the estimation of the observation time behind reflected shock wave will be discussed.

Two events are responsible for the perturbation of the uniform conditions behind the reflected shock wave which consequently lead to an interruption of the observation time. The first one is the arrival of the reflected rarefaction head to the location where the observation occurs. This event that abruptly decreases the pressure and the temperature of the experimental gas can be manipulated by either increasing the driver section length or adding a portion of heavy gases into the usually light driver gases. Argon or

nitrogen is added to the piston mixture (originally composed of helium or hydrogen) to slow down the time taken for the reflected rarefaction head to meet the contact surface and thus increase the observation time. The second factor that limits the observation time depends on the nature and the subsequent wave pattern formed by the interaction between the reflected shock wave and the contact surface. In the usual situation when $_2 = _3$, the interaction between the reflected shock wave and the contact surface leads to varying results depending on the relative velocities of the gases in region 2 and 3. When $a_2 > a_3$, the reflected shock after passing through the contact surface enters a region of higher Mach number. The resultant properties in the region 3 would be greater than those in region 2. Since, across the contact surface equality of pressure is required, additional shock system is generated in region 5. Conversely, when $a_2 < a_3$, the Mach number will fall across the interface and an expansion wave is required to restore the pressure equality. Hence in both cases, the reflected shock region is disturbed by an additional waves generated, and the observation time can be obtained using the following expression derived in reference [126].

$$\Delta = \left[\frac{1}{1 \cdot 1}\right]\left[\frac{(- 1)}{2}\right] \tag{3.13}$$

Where $_1$ is the length of the driven section.

In order to have larger observation times behind the reflected shock a_2 is designed to be the same as a_3. When $a_2=a_3$, the pressure across the interface is automatically conserved and no reflected wave results. This is called ‘tailoring’ of the shock tube contact surface. In this case the uniform conditions would in theory persist until the arrival of the reflected rarefaction head.

3.1.3 Dump tank - Single pulse shock tube

The first dump tank was presented by Lifshitz et al. [132] in 1963. The function of the dump tank is to prevent multiple re-heating of the test gases by multiple shock wave reflections inside the tube [133]–[135]. Hence, the volume of the dump tank must be much larger compared to the volume of the shock tube in order to act as a reservoir (at least 5-6 times the volume of the driven section). The dump tank needs to be located as close as possible to the diaphragm section and connected to the shock tube through a tube of maximum internal diameter (maximum conductance) and optimally at an angle of 45° (to favor the flow into the tank). The presence of the dump tank permits the shock tube to operate in a single-pulsed fashion. Thus, single-pulse shock tubes (SPST) are composed of high- and low-pressure sections and a

dump tank. They are designed to heat a gas mixture for a constant period, the dwell or residence time, and then rapidly quench the hot gases stopping the reaction processes and “freezing” the gas composition.

Operation of a single pulse shock tube involves filling the low-pressure section and the dump tank to the same pressure, pressurizing the high-pressure section, and bursting the diaphragm. Sample gas can be withdrawn through an orifice located in the center of the end wall of the driven section and through a sampling port for subsequent analyses.

As mentioned, pressure remains constant for a certain time after the arrival of the reflected shock wave, and then it rapidly decreases due to the arrival of the quenching fan. From the equation of adiabatic expansion, the ratio of the pressure P at time t and the reflected shock pressure P_5 is related to the ratio of the reflected shock temperature T_5 and the temperature T during the cooling phase by the following equation:

$$\frac{}{5} = \left(\frac{}{5}\right)^{\overline{-1}} \tag{3.14}$$

Where P_5 and T_5 are calculated using the equations listed in the previous section. The rate of change of temperature with respect to time is described by:

$$\frac{}{} = \left(\frac{-1}{}\right)\left(\frac{5}{5}\right)\left(\frac{}{}\right) \tag{3.15}$$

Where γ is the heat capacity ratio for the gas in the reflected zone (zone 5).

Typical cooling rates of 105–106 K/s reported in ([132];[136]) are so large that the chemical reactions can be frozen very quickly. It is practice to define an effective reaction time as the time interval between incident shock wave arrival at the end wall and the time when the reflected shock pressure decreases to 80 % of its maximal value, when most reactions are terminated [137]. However, some reactions can persist during this cooling phase, especially the ones involving the resonantly stabilized radicals, and this needs to be taken-into-consideration during the data modeling.

3.2 High purity single-pulse shock tube at ICARE

The shock tube used in this study has been converted to operate in a single pulse-fashion for the purpose of performing measurements of stable species behind reflected shock wave. Considering the importance

of the reacting mixture to be rapidly quenched and for avoiding the reflected shock waves reenter the reaction zone modifying the well-defined reaction conditions, a dump tank was designed and constructed as presented below.

The shock tube, called high-purity shock tube (HPST) from its remarkable characteristics which allow detailed kinetic studies at highly-diluted conditions, is shown in **Figure 3.2**. It is an electro polished stainless-steel tube capable to sustain static pressures up to 60 bar and uniformly heated in order to be able to study the formation and growth of PAHs from hydrocarbons that have a low saturating vapor pressure at room temperature. The low-pressure section is 6 meters long with an internal diameter of 78 mm, while the high-pressure section is 3.7 meters and it has an internal diameter of 120 mm. A double membrane (or diaphragm) system separates the high-pressure from the low-pressure section. A dump tank of 150 L volume was added close to the diaphragm on the driven section side to operate the shock tube in the single-pulsed fashion. The schematic of the dump tank and the support structure is presented in **Figure 3.3**. The support structure allows the dump tank to slide at an angle of 45° compared to the shock tube. The dump tank is separated from the driven section by a ball valve with internal bore equal to 760 mm provided by Adler S.p.A. (FM2 model).

As an example of the effects induced by the presence of the dump tank, two pressure profiles are reported in **Figure 3.4**, obtained with same initial P_1 = 700 Torr and P_4 = 16.5 bar but with or without the dump tank open before the experiment. The blue profile (no dump tank) shows a strong shock wave arriving at the end-wall after around 20 ms from the incident shock wave. Multiple reflections at later times can be also observed. On the other hand, the use of the dump tank significantly reduces the wave at around 20 ms and it eliminates the subsequent ones. The equilibrium pressure attained in the shock tube is also lower with the dump tank in place, helping to maintain the temperature of the gases to low levels over longer.

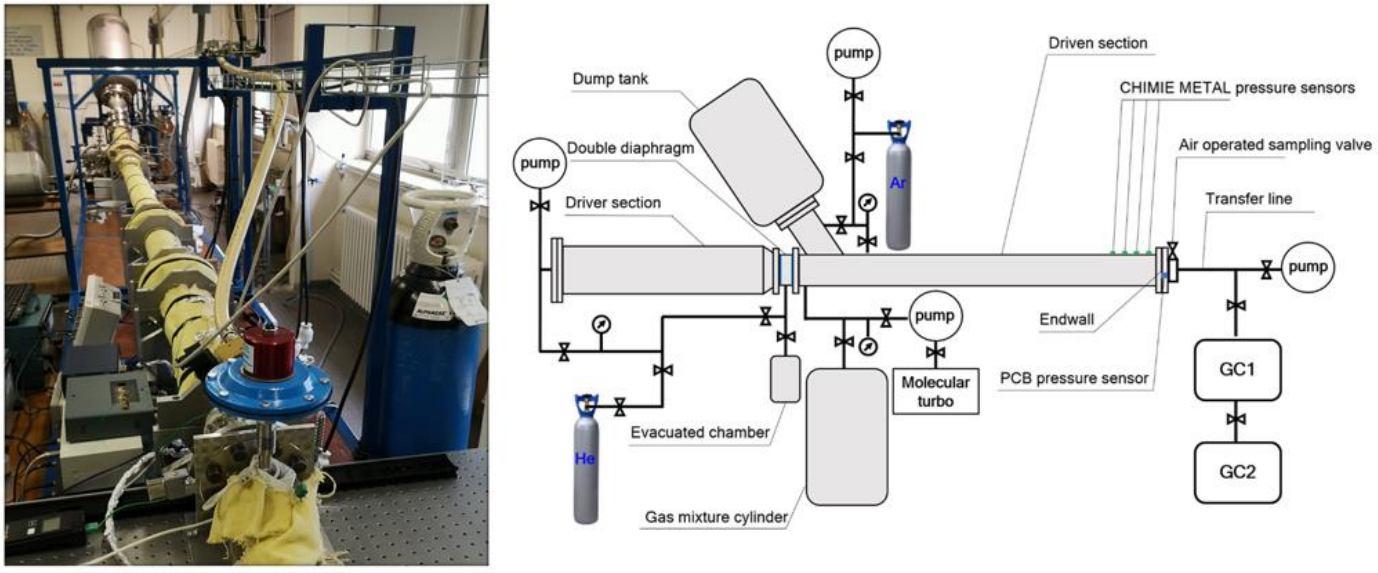

Figure 3.2: Real view of the heated shock tube, and a schematic diagram of the shock tube used in this work.

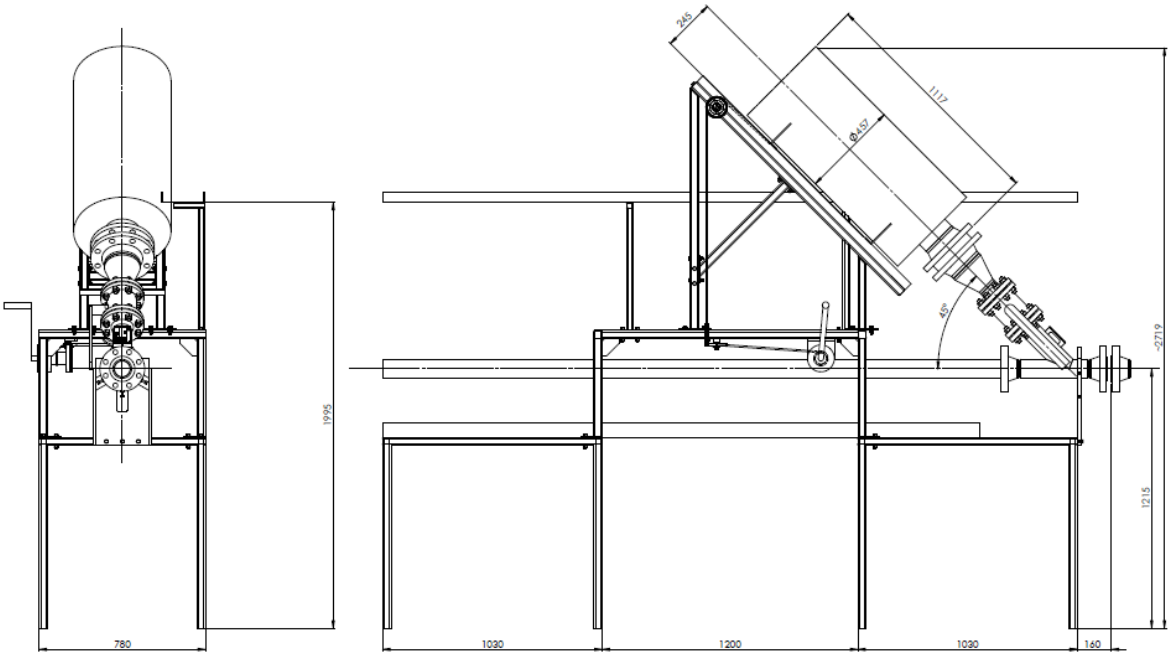

Figure 3.3: Schematic drawings of the dump tank

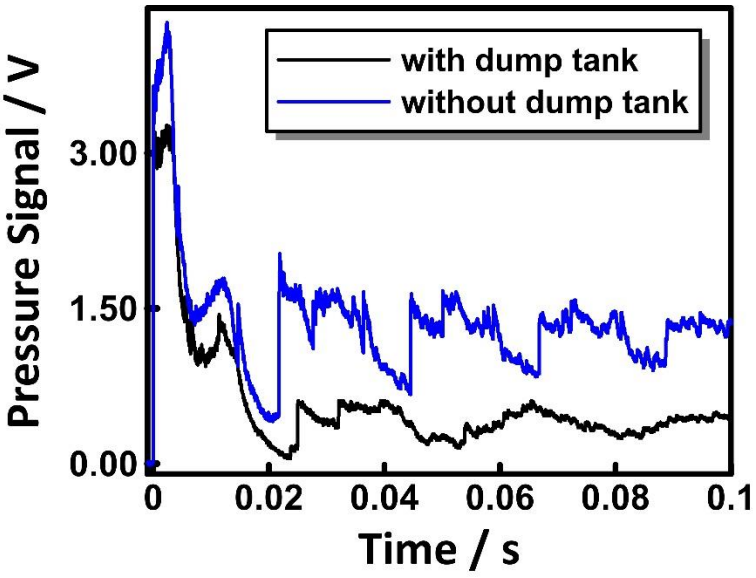

Figure 3.4: Typical end wall pressure history with and without dump tank.

A series of four pressure sensors (CHIMIE METAL A25L05B) coupled to fast digital oscilloscopes are mounted with a distance interval of 150 mm along the ending part of the driven section, with the last one being 82 mm away from the end wall. The times taken for the shock wave to pass at each sensor location are used to derive the velocity of the incident wave. This value together with the initial pressure and temperature conditions and mixture composition (test gas) allows the determination of the temperature and pressure behind the incident and the reflected shock waves as well as the Mach number by solving the conservation equations [129]–[131]. The physical dimension of the shock detectors introduces uncertainties in the correlation between the time when the pressure rise is observed and the corresponding location on the sensitive area of the sensors. The sensitive areas extend around ± 1 mm with respect to the center of the sensor, thus the maximum error in the distance between two adjacent sensors is 2 mm. The presence of shock wave attenuation (below 2.5% for most experiments) can affect the correct estimate of the temperature since the withdrawn sample has an average composition that spans a relatively large volume. Given all the mentioned factors, an uncertainty of ±30 K is estimated in the calculated T5. Also, a PCB pressure sensor shielded by a layer of RTV is located on the end-wall to record the end wall pressure time-history from which the reaction time could be defined as mentioned in the previous section [137]. A typical pressure profile with the reaction time is shown in **Figure 3.5**. In the present work, the reaction time with the current experimental set-up is 4ms.

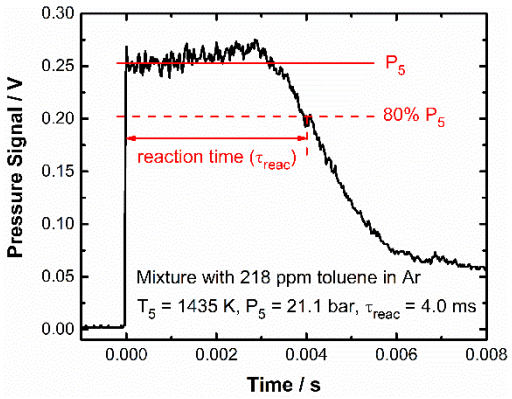

Figure 3.5: Typical end wall pressure history and the definition of reaction time *[138]*

The PCB pressure signal is also used to trigger the operation of an air actuated HIP valve (HIP 30-11HF4) mounted on the end wall to withdraw the post-shock gas mixture. The sampling process takes hundreds of milliseconds thus a long time compared to the dwell times. On the other hand, the necessity to increase the sensitivity of the experimental set-up to measure trace levels of PAH products (less than 0.1 ppm) did not allow the implementation of a fast sampling valve which would result in small sample amounts. Since the volume of the withdrawn gas is relatively large, the average velocity is used to calculate the conditions behind the reflected shock (T_5 and P_5) because it is more representative of the conditions encountered by the sampled gas compared to the extrapolated one.

The driven section of the shock tube is heated up to a temperature of 90°C to avoid the condensation of fuels and heavy products. The heating system includes heating collars at the flanges of the diaphragm section, the end-wall, and the ball valve connected to the dump tank, and heating tapes surrounding the entire length of the tube. Ten independent regulators (maximum power between 500 to 1250W) are used to control the temperature of the different zones. The system is isolated by a thick glass wool layer to ensure uniform temperatures along the tube. The low-pressure section is also connected to a turbo-molecular pump (LeyBold TURBOVAC 361) which permits to obtain a vacuum below 10^{-5} torr before each experiment. On the contrary, the high-pressure section with the diaphragm system (diaphragm-depressurized chamber) and the dump tank are connected to primary pumps. The double diaphragm system uses membranes made of terphane (glycol ethylene polyterephtalate) of different thickness, from 100 to 225 µm, depending on the load pressure ratio of the two sections (high-pressure and low-pressure). Furthermore, the inner surface of the shock tube is cleaned every day to remove eventual carbon deposits formed during the experiments. Reaching the vacuum levels mentioned above and assuring the purity of the entire apparatus is mandatory for the kind of experiments performed in this work (pyrolytic conditions with highly diluted mixtures) as even a very small amount of impurities or oxygen (from residual air in the tube or from a small leak) may strongly affect the accuracy of the experimental results. A clear

example is provided by the preliminary experiments performed on the pyrolysis of 100 ppm benzene at pressures of around 10 bar. Formation of certain intermediates including propylene, toluene and indene are estimated to come from 40 ppm of O_2 due to a small leak in the end port of the driven section as subsequently verified. The estimated O_2 concentrations are determined based on kinetic analyses. To reduce the leaks, experiments at P_5 of ~20 bar are carried out instead of 10 bar as P_1 is ≥ atmospheric pressure for these experimental conditions. A direct validation is presented in **Figure 3.6**, where the red data resembles the experiments at 10 bar and the blue ones at 20 bar for 100 ppm benzene pyrolysis. Thus, performing experiments at around 20 bar combined with filling fast the driven section eliminate the possibility of having oxygen as a reactant.

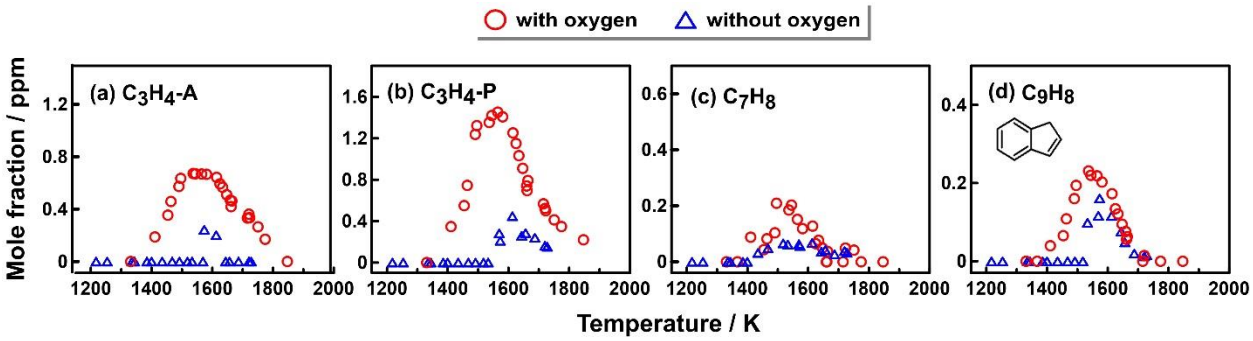

Figure 3.6: Experimental mole fractions for intermediates affected by presence of oxygen in 100 ppm benzene pyrolysis.

The procedure carried out for each shock run can be summarized as follows. After attaining the desired vacuum level in the whole shock tube, the insertion of gases into the driven and driver sections begin. At the beginning of the experiment, the ball valve connecting the shock tube with the dump tank is closed. The low-pressure is filled up to a given pressure with the gas under investigation (generally a mixture of fuel mixture diluted in argon). The dump tank is filled with argon (Ar) to the same pressure as the low-pressure section. At this point, the ball valve is opened and P1 registered. Then the driver gas (helium) is introduced both in the double diaphragm section (up to a pressure of $P_4/2$) and in driver tube (filled up to P4). The generation of the shock wave is obtained by the opening a valve that allows the helium inside the diaphragm section to flow into the depressurization cylinder (evacuated chamber in the figure 3.3), which is under vacuum. This results in a very fast increase of pressure difference across the diaphragms and, as a consequence, in their rupture. Each experiment generates one reaction condition (T_5, P_5). In order to obtain a complete set of species profiles, several shocks need to be run, varying the initial reaction temperature for similar pressure conditions. This is obtained by tuning the initial pressures in the driven and driver sections.

3.3 Analytical instrumentation- GC/GC-MS

The first experiments using gas chromatography for sampling behind a reflected shock wave dates back to 1985 when Bradley and Kistiakowsky [139] studied the thermal decomposition of nitrous oxide in shock tube. Since then, shock tube has been widely used for speciation studies by gas chromatography and mass spectrometry.

3.3.1 GC/GC-MS system description

The withdrawn pre-shock and post-shock samples from the driven section, transferred through a SilcoTek treated line heated to 200°C, are analyzed using two gas chromatographs (GC) and one mass spectrometer (MS). In particular, a 7890B Agilent GC is placed in series with a Thermo Trace GC Ultra coupled to a Thermo DSQ mass spectrometer.

The first GC, specifically designed to measure PAHs up to four rings, is equipped with a flame ionization detector (FID) coupled to a DB-17ms column for heavy species separation, and a thermal conductivity detector (TCD) coupled to a Molseive 5A column for monitoring the absence of air and the dilution coming from the helium driver gas. The second GC is equipped with an FID detector connected to an HP Plot Q column for measuring light species up to mono-aromatic species and TCD for detecting the internal standard neon, if any. A DSQ mass spectrometer can be connected to the second GC to aid the PAH species identification. For this, the column of the TCD is replaced by a DB-17ms column having similar dimensions and characteristics as that connected to the FID in order to have the similar retention times and an easier comparison. A schematic for the instruments used in this thesis is shown in **Figure 3.7**.

Both GCs are equipped with air-actuated valves as well as liquid injection ports. Particularly, the valves of Agilent GC as well as the 1/16” transfer lines are placed in an external oven which keeps the temperature to 250°C to effectively recover and store the heavy species before injection. It is also modified such that the gas sample is introduced directly into the DB-17ms column in order to avoid any cold spot that can cause a condensation or loss of some heavy species. For achieving this result, a metallic, separately-heated interface element was placed between the external oven and the GC oven; the connection between the 1/16” transfer line and the column is inserted inside such interface element.

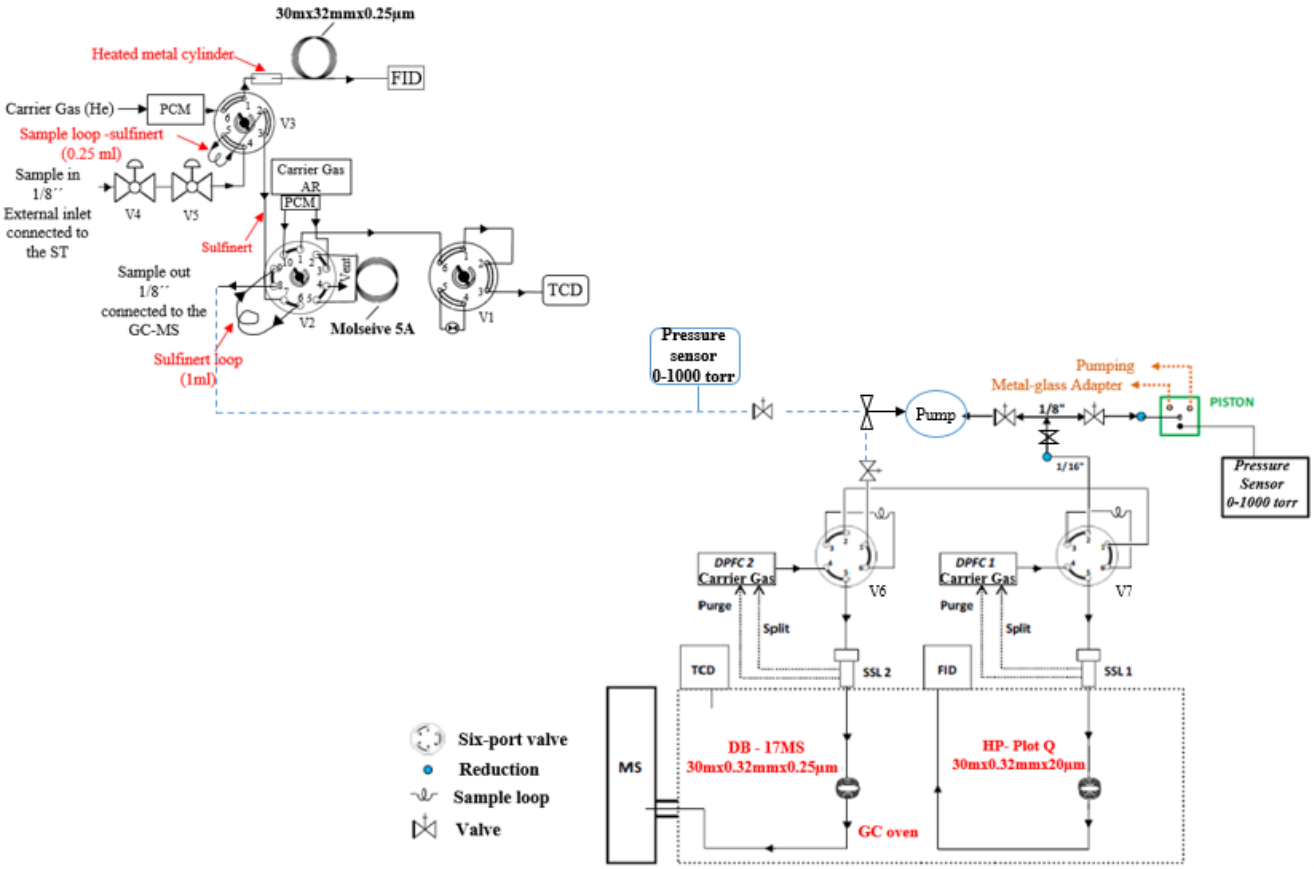

Figure 3.7: Detailed schematic of the online analytical device

To better understand the configuration of the analytical set-up and how it works, the main parts composing the GCs are explained briefly below:

- The Digital Pressure and Flow Control (DPFC) devices in the Thermo GC which control numerically the inlet pressure and the flow of the carrier gas (CG) flow. The carrier gas is helium (Air Liquide He alphagaz 2,> 99.9999%).
- The pressure control modules (PCMs) are general-purpose modules with two independent control channels, designated by 1 and 2. The two channels are not identical. Channel 1 is a simple forward-pressure regulated channel that maintains constant flow or pressure through a fixed restrictor, while channel 2 is used either as a forward-pressure regulator or as a back-pressure regulator, simply by reversing the input and output connections, and it can only control the pressure. The PCMs are used to control the pressure and flow of the carrier gas in the first GC, which is He for the FID (Air Liquide He alphagaz 2,> 99.9999%) and Ar for the TCD (Air Liquide Ar alphagaz 2,> 99.9999%).

¶ The injection loops (sample loops) that stores the sample before injection, of different size as needed for the specific applications (larger sample loops implicate higher sensitivities but worst peak shapes for most cases).

¶ V1, V2, V3, V4, V5, V6, and V7 are pneumatically driven valves controlled by solenoid valves that control the flow of air to the valve actuators. The characteristic of the valves in the Agilent GC (V1-V5) is that they can be heated up to 300°C. V4 and V5 are used to regulate the pressure of the gas sample if too high compared to the specification of valve V1. V1 and V3 are 6-port valves while V2 is a 10-port valve. The combination of these valves allows great flexibility in the use of the GC; for example, it is possible to back flush the column or perform a Deans Switching analysis. They have two positions controlled by the [On] and [Off] keys in the Agilent GC (**Figure 3.8 (a)**).

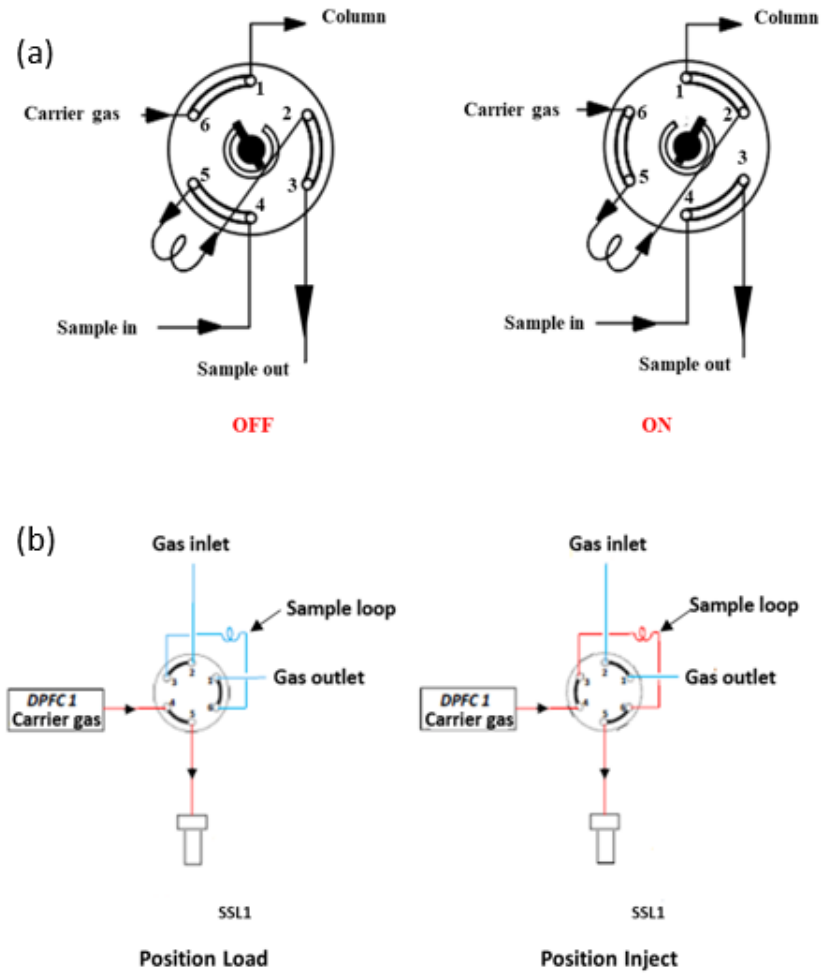

Figure 3.8: Six-port valve operation in: (a) Agilent GC, (b) Thermo GC

¶ "Split /splitless" injectors (SSL). This type of injector is placed in a heated injection chamber, traversed by the carrier gas and closed by a septum. The injector is lined with a glass tube called "inlet liner" whose configuration depends on the injection mode chosen (split or splitless). In the split mode, only a fraction of the sample is transferred onto the head of the column. The remainder of the sample is removed from the injection port via the split vent line. This mode is used to avoid column saturation when high concentrations are expected and to improve the peak shape. In splitless mode, the entire sample is injected into the column (**Figure 3.9**). The process of performing either split or splitless injection is controlled by changing the flow path and flow rate of the carrier gas through the injection port. Having this type of injector also allows to work with liquids by injecting directly using a syringe into the injector. In this case, the sample is instantaneously evaporated and then transferred into the column.

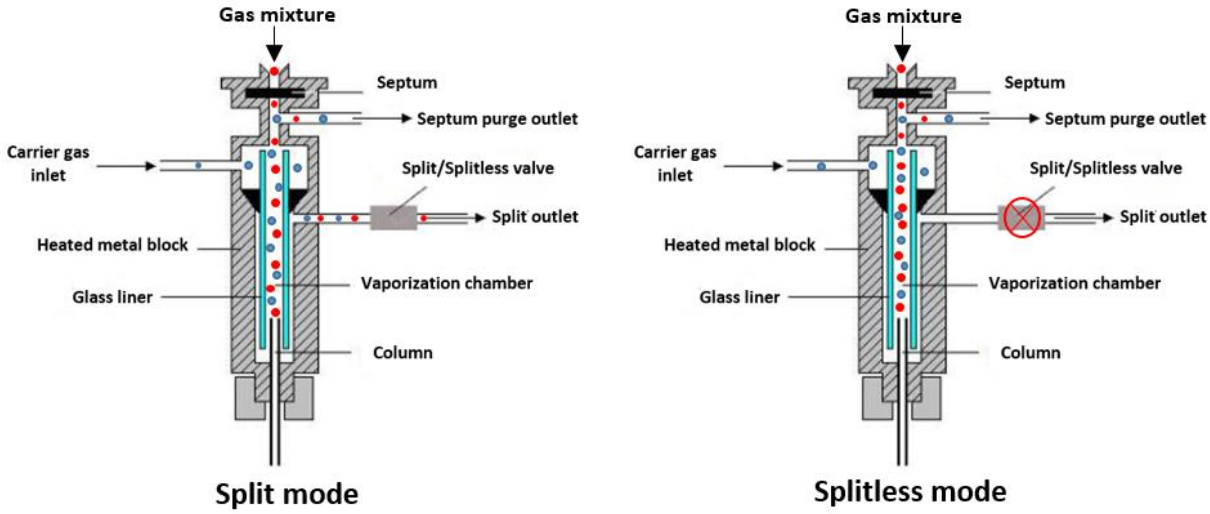

Figure 3.9: Split/Splitless injector modes

¶ Thermal conductivity detectors (TCDs). This detector measures differences in the thermal conductivity of the effluent gas from the column with the one of a reference flow of carrier gas. Since all compounds, organic and inorganic, have a thermal conductivity different from the carrier gas, virtually all compounds can be detected. That's why it is often defined as a universal detector. The TCD is not too sensitive and it is mostly used to analyze permanent gases such as argon, neon, oxygen, nitrogen, carbon monoxide, and carbon dioxide. **Figure 3.10** shows simply how a TCD detector works.

¶ Flame ionization detectors (FIDs). The FID is more sensitive than the TCD, but less universal, because it gives no response to inorganic compounds nor to permanent gases (for example: O2, N2, CO). The operation of the FID is based on the detection of ions formed during combustion of

organic compounds in a hydrogen flame. The generation of these ions is proportional to the concentration of organic species in the sample gas.

- All the lines (tubes and injection loops) in the chromatographic systems are made of SilcoTek treated stainless steel in order to limit adsorption on the walls.

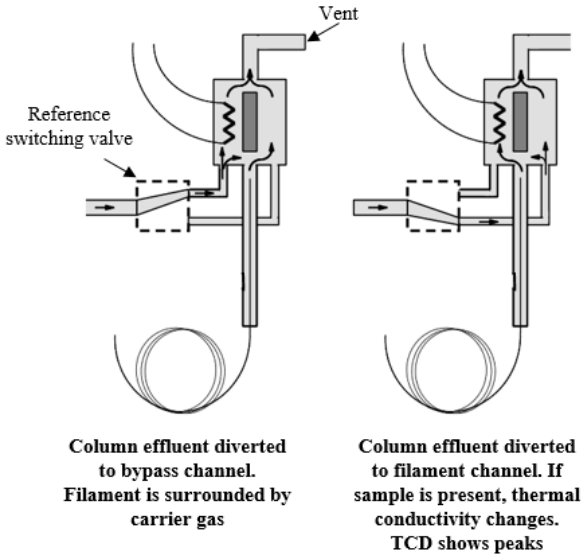

Figure 3.10: TCD principle

3.3.2 Qualitative and Quantitative Analysis

Qualitative Analysis:

Mono-aromatic fuels, light hydrocarbons and PAH species detected from the experiments are well separated. They are identified through a combination of retention times known from prior injections of standards and from the mass spectra. Concerning the FID measurements with the Thermo GC, separation between the different C_4 isomers was particularly challenging. **Figure 3.11** shows the signal recorded in propylene pyrolysis at T_5 of 1368 K and p_5 of 21.1 bar. All C_4 species are identified according to their retention times. The overlapping peaks of the C_4 species with close retention times are well separated through multiple Gaussian fittings, and that thanks to the good symmetrical Gaussian peak shapes obtained using a split injection mode (split ratio of 10). Examples of gas chromatogram for the PAH compounds are also reported here. **Figure 3.12** shows the GC signals in neat toluene pyrolysis, toluene-propylene and toluene-propyne co-pyrolysis at similar T_5s around 1360 K. For C_9 species, indene, indane, 1-phenyl-propyne ($C_6H_5C{\equiv}CCH_3$, $C_6H_5C_3H_3P\_1$), 3-phenyl-propyne ($C_6H_5CH_2C{\equiv}CH$, $C_6H_5C_3H_3P\_3$), phenyl-allene ($C_6H_5CH{=}C{=}CH_2$, $C_6H_5C_3H_3A$) and allylbenzene are identified according to their

retention time. For other small peaks, their formulas are known from mass spectrometry, but their structures cannot be unambiguously identified, because some possible isomers have similar fragmentation patterns and standard mass spectra for some candidates are not available in the library. As presented in **Figure 3.12**, these C_9 species are assigned as ethynyl-toluene and vinyl-toluene isomers. A collection of C_{10} species, which mostly correspond to the small peaks between indene and naphthalene (see **Figure 3.12**), are observed in the co-pyrolysis of toluene and propylene (or propyne). The dominant ones identified in this work include methyl indene isomers, dihydronaphthalene and benzofulvene. All other PAHs up to C_{18} with the structures shown in **Figures3.13** for benzene and toluene pyrolysis (temperature correspondent to around 50% fuel decay, ~200 ppm initial fuel, nominal pressure of 20 bar) are identified through prior injections of standard mixtures.

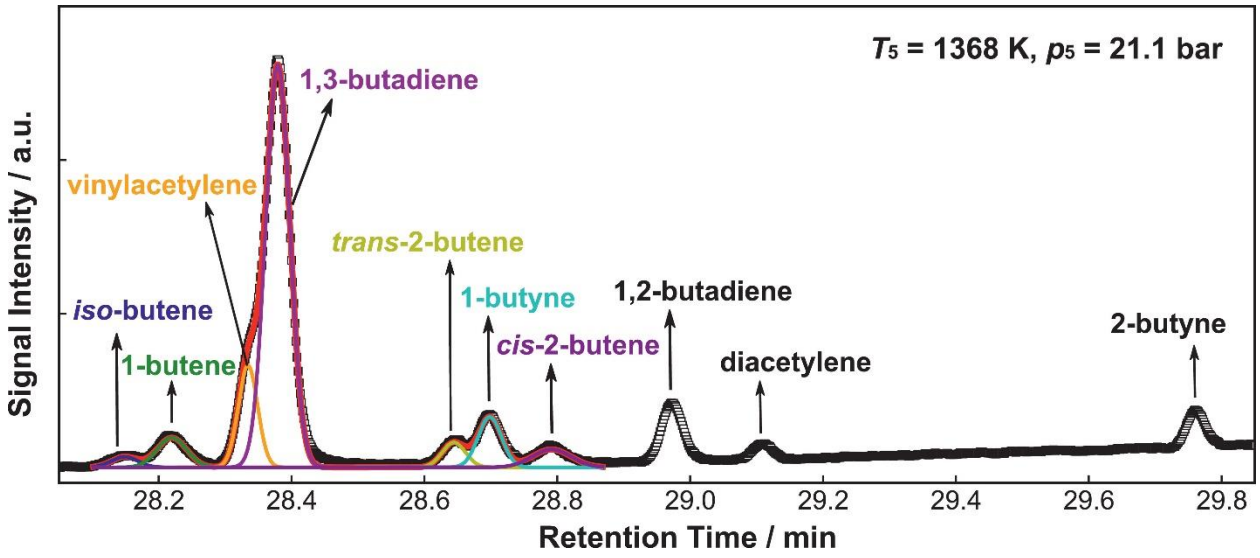

Figure 3.11: The signals detected for C_4 species in propylene pyrolysis at T_5 = 1368 K, p_5 = 21.1 bar. The overlapping peaks are separated through multiple Gaussian fittings [140].

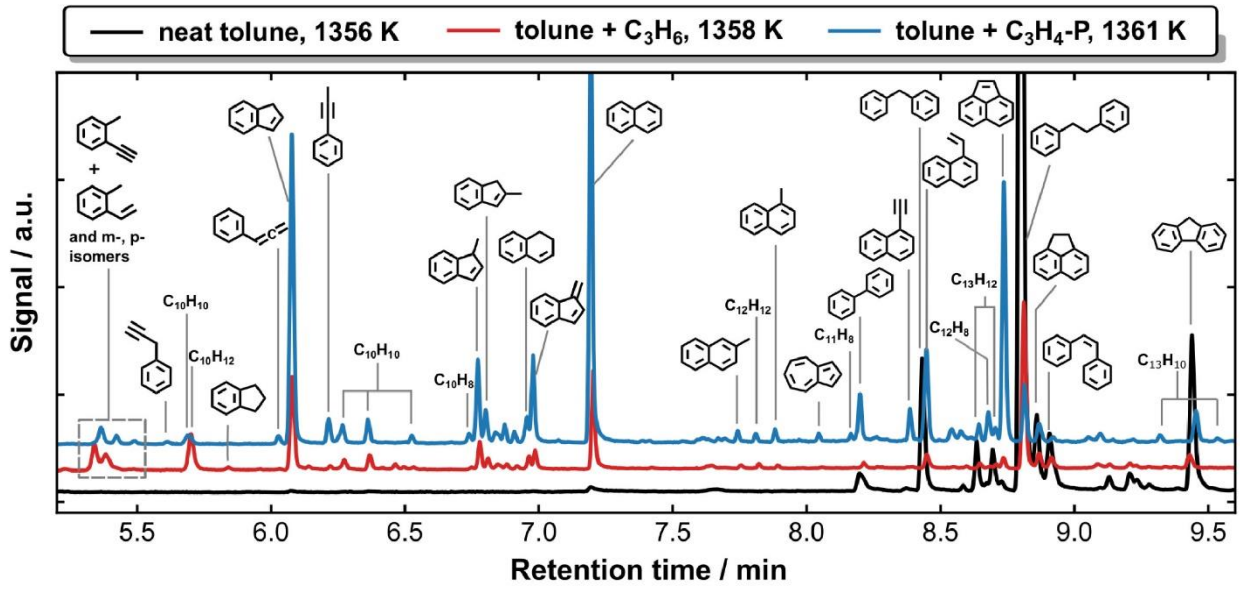

Figure 3.12: GC signals recorded in neat toluene, toluene + propylene (C_3H_6) and toluene + propyne (C_3H_4-P) pyrolysis at T_5 around 1360 K [141].

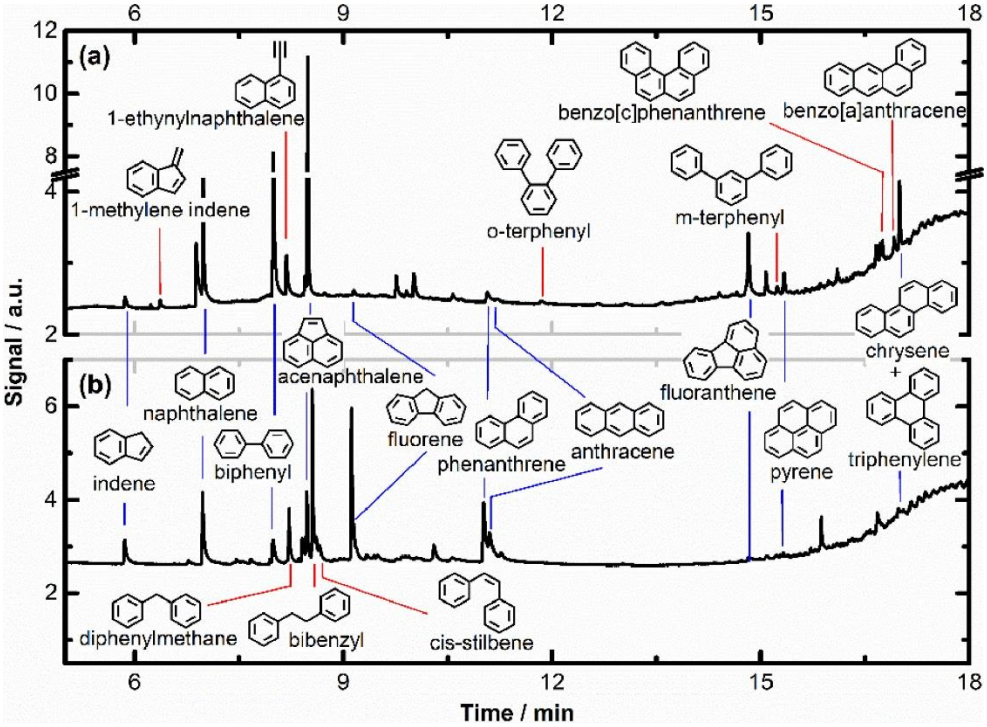

Figure 3.13: GC signals for PAH species detected in (a) 210 ppm benzene pyrolysis at T_5 = 1553 K, P_5= 21.8 bar and (b) 216 ppm toluene pyrolysis at T_5 =1435 K, P_5=21.1 bar [138].

Quantitative Analysis:

Before a species can be quantified, a calibration factor (relationship between peak area and mole fraction) must be determined. This detector calibration process is done using mixtures of known composition and relating the specific peak area with the corresponding mole fraction for each species. The specific peak area is obtained by dividing the peak area from the GC chromatogram by the injection pressure measured by a pressure gauge.

Standard gas mixtures are used for the calibration of light species representing C_1-C_5 hydrocarbons except for diacetylene (C_4H_2) and triacetylene (C_6H_2) where their calibration factor is obtained from acetylene (C_2H_2) decomposition experiments through carbon atom conservation. Likewise, SIGMA-ALDRICH liquid samples are used to calibrate fuels (including toluene, benzene, styrene, phenylacetylene, ethyl-/propyl-/butyl-benzene and ortho-/meta-/para- xylene). These liquid samples are degassed before use to eliminate air and reduce impurities. On the other hand, for small PAHs (comprising indene, naphthalene, biphenyl, ethynyl naphthalene, diphenylmethane, bibenzyl, biphenylene, acenaphthylene, fluorene, cis-/trans- stilbene, diphenylacetylene, dihydrophenanthrene, phenanthrene and anthracene), calibrations are performed with gas-phase mixtures prepared in a heated glass vessel up to 200°C to minimize the surface absorption [142]. Calibration solutions are composed of specific quantity of PAH standards dissolved in dichloromethane. A known volume (2-5 l) of the calibration solution is injected to the vacuumed heated glass vessel using a 5 l GC syringe. The solution evaporates immediately. The vessel is then filled with argon to around 850 Torr, and the resulting gas mixture stands for around 15-20 minutes to homogenize. Afterwards, the gas mixture is injected to the Agilent GC at least three times to ensure a good consistency of the normalized FID response. This procedure is conducted with three different mole fractions for each PAH species. The pressure-normalized peak areas are plotted against the mole fractions of the respective PAH species. The slope of the linear regression line resembles the desired calibration factor. Examples of the calibration curves for typical PAHs up to three rings are shown in **Figure 3.14**. Four ring PAHs (namely pyrene, fluoranthene and chrysene) cannot be steadily vaporized with the above-mentioned gas-phase calibration approach. Therefore, their calibration factors are determined through extrapolation of the one- to three- ring aromatics, i.e. benzene, naphthalene and phenanthrene.

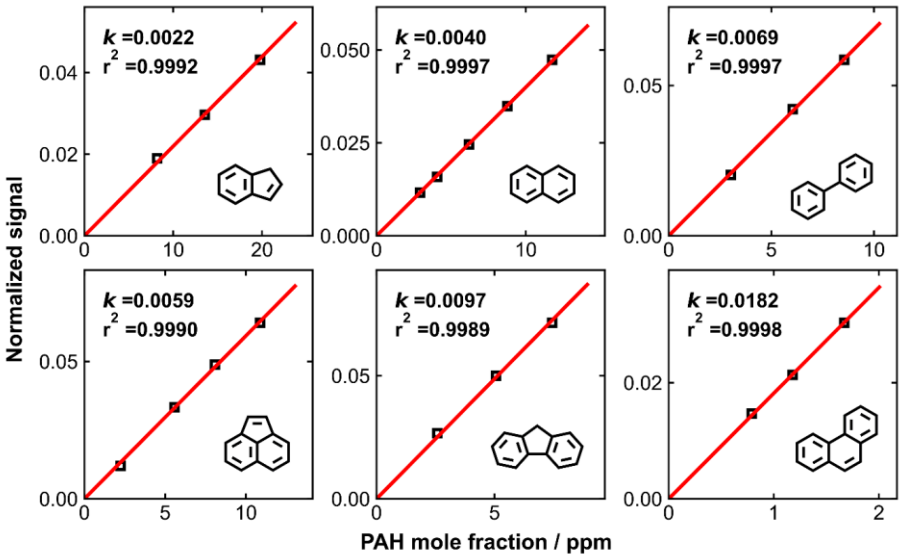

Figure 3.14: The calibrations for typical two- to three- ring PAH species. The slope k is the FID response factor for each shown PAH *[143]*.

The calibration and the FID response are the major uncertainty sources for concentration measurements. For species calibrated in gas-phase, an uncertainty less than 10% is expected. However, for large species who undergo indirect gas-phase calibrations, the uncertainty varies from 20% to a factor of 2 depending on the species molecular weight relative to naphthalene [142].

3.4 Gas mixture preparation

The preparation of gas mixtures is an important and delicate step. The mixture must be as precise as possible. The mixtures prepared in this study consist of hydrocarbon fuel mixtures diluted in argon. Since the goal behind this thesis is to study the PAH formation and growth in deficient-oxygen zones as relevant to soot formation in combustion devices, pyrolysis experiments are performed (absence of oxygen).

3.4.1 Degassing liquid Samples

Since the experiments in this work are very sensitive to the presence of oxygen and/or impurities, degassing the liquid samples is an important step before preparing a mixture. From its name, it consists in the removal of the dissolved gases from liquids.

The sample to be degassed is placed in a Schlenk tube and frozen using liquid nitrogen. The headspace above the sample is then evacuated using a vacuum pump. Afterward, the sample is sealed and thawed allowing the dissolved gases to migrate into the evacuated head space. This process is typically repeated three times in order to have a good degasification efficiency.

3.4.2 Gas-mixture preparation procedure

The mixture is prepared by the partial pressure method in a 136-liter tank with internal diameter equal to 406 mm specifically constructed for the experimental work presented in this thesis. It is a movable electro polished, stainless steel tank capable to sustain static pressures up to 16 bar. The tank is pumped down to 10^{-5} Torr using a turbo molecular pump before the beginning of the mixture preparation. A mixture of 10 bar is normally prepared to have a complete profile for the fuel decomposition and the species formation with respect to temperature. From this point, the partial pressure of the fuels is calculated according to the equation (3.16). After the fuel introduction into the mixing tank, the tank is filled with argon up to the total pressure.

$$[\quad] = \frac{\quad}{\quad} \tag{3.16}$$

The experimental mixing rig is made of glass and includes several connections for metallic lines (to the gas bottles), for glass bulbs (where liquid fuels are stored), and for pressure manometers with different pressure ranges for accurate mixture preparation (0-10 Torr MKS Baratron 122BA and 0-1000 Torr). The mixing rig is also connected to a turbo molecular pump (LeyBold TURBOVAC 361) and it can be pumped down to 10^{-6} Torr. Since glass tubes can't withstand high pressures, in the first moment argon is introduced into the tank at pressures slightly higher than the atmospheric one. A second stainless steel line connected to a 0–10000 Torr MKS Baratron pressure transducer (model 627D) is used to complete the tank filling. The mixture is then allowed to stand overnight before using it to well homogenize.

3.5 Validation of the experimental Set-Up

Heptane fuel was chosen to validate the experimental set-up because it has been extensively studied in the last decades and its chemistry is relatively well-known. Testing experiments for n-heptane pyrolysis at initial fuel concentration 100 ppm with a cold and a heated shock tube were carried out at a nominal pressure P_5 of 10 bar and a temperature T_5 range from 900 to 1900 K. The fuel decomposition and the yielded species concentration profiles are compared by different extensively-validated kinetic models as shown in **Figure 3.15**.

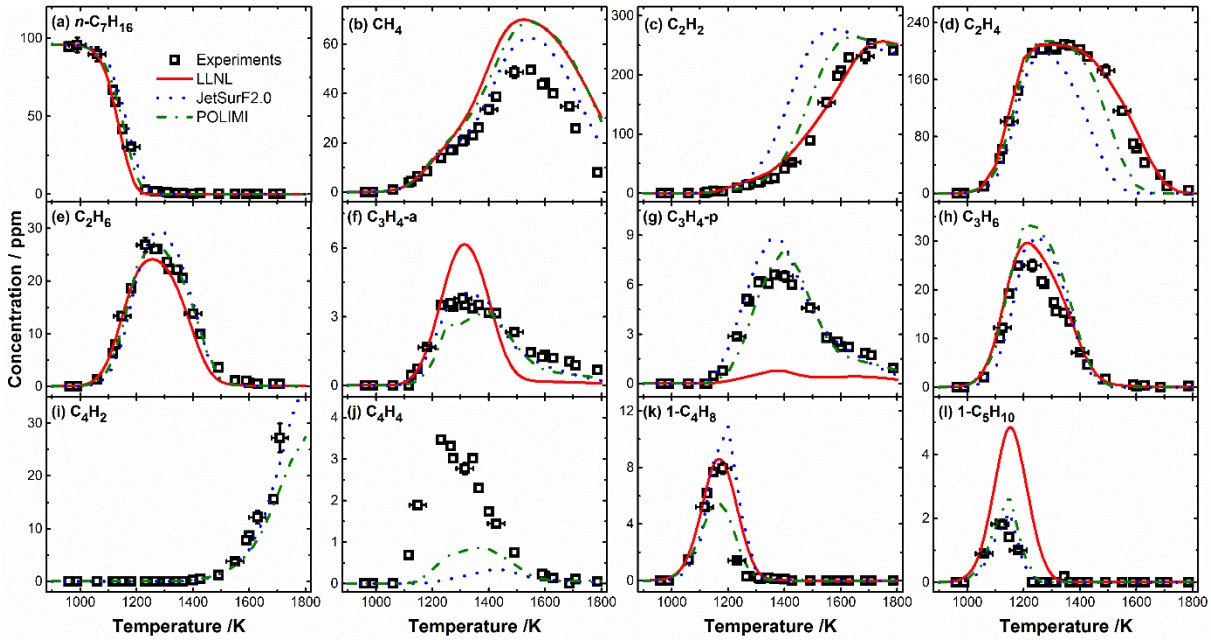

Figure 3.15: Species concentrations as a function of T_5 from 100 ppm heptane pyrolysis experiments at the nominal P_5 of 20 bar. Symbols: measurements; Solid lines: simulations with LLNL model *[144]*; dotted lines: simulations with JetSurF2.0 model *[145]*; Dot-dashed lines: simulations with the latest version of CRECK model *[146]*.

The good agreement between the experimental results and numerical simulations on both shapes and sizes of the profiles prove the reliability of the current set-up to be used for the goal of the thesis.

4 Kinetic Modeling

4.1 Structure

Every detailed kinetic mechanism is composed of the gas-phase kinetics (reaction mechanism) and the definition of the reacting species (thermodynamic data).

The reaction mechanism file is not just a set of elementary reactions and their formation and consumption rate coefficients, but also a collection of interacting sub-mechanisms. Structuring a large detailed mechanism as a sum of sub-mechanisms (primary mechanisms, secondary mechanisms and base mechanisms) helps in building the mechanism itself. The primary mechanism consists generally of the reactions that consume the fuel and the fuel radicals. The base mechanism is usually a well-validated detailed mechanism for C_0-C_4 small hydrocarbons, like AramcoMech, USCMech II … The secondary mechanism is a necessary link between the primary mechanism and the reaction base mechanism.

The reactions' parameters can be directly measured experimentally, calculated using quantum calculations, or estimated based on analogy. A particular issue in combustion is usually the broad

temperature and pressure range. It can easily cover several hundred Kelvins and one or two pressure decades. Accordingly, the temperature and pressure dependencies of the kinetic parameters are of crucial importance. The rate coefficients are often expressed by the modified empirical Arrhenius equation.

$$= \frac{-}{} \tag{4.1}$$

The reliability of the model predictions depends on the accuracy of the thermodynamic data of the species (stable molecules, radicals and individual atoms) present in the system. Thermodynamic data provide the species' thermochemical properties (enthalpy, entropy, and specific heat capacity). The thermochemical properties are used to derive the rate constant parameters of the reverse reaction starting from the parameters of the forward reaction given in the mechanism file. The forward and the reverse rate constants are related by the following equation:

$$= \frac{}{} \tag{4.2}$$

where the k_{eq} is the equilibrium constant of the reaction and is defined as:

$$= (\quad)^{-\Delta} \quad \frac{-\Delta\ ^{0}}{} \quad \frac{-\Delta\ ^{0}}{} \tag{4.3}$$

Δ is the change of number of moles of the reaction. $\Delta\ ^{0}$ and $\Delta\ ^{0}$ are the standard enthalpy and entropy, respectively. They are derived using the NASA polynomials as a function of temperature T [147].

Extensive databases for thermochemical data are available in literature, including the online NIST database [148] and Prof. Burcat's database [149]. When the reaction parameters come from a theoretical work, it is a common practice to use the thermo properties provided in the specific publication. Finally, group additivity is implemented to estimate the thermo properties of molecules and radicals when not available from other sources; in particular, the thermochemical data are computed with the program THERM [150].

4.2 Simulation

The chemical processes in the HPST occurs behind reflected shock waves. As mentioned in the previous section, shock waves instantaneously raise the test-gas mixture to the desired temperature and pressure, which last for a defined reaction time (around 4 ms in the current work) before the arrival of the

rarefaction wave fan quenching the reaction. The very short period of time makes the heat losses by conduction and radiation negligible (adiabatic system). The pressure is also nearly constant during the reaction time as observed experimentally (isobaric system). An additional feature of gases behind reflected shock waves is the absence of net flow along the direction of propagation, i.e. there are no inlets or outlets flow during the period of interest. Considering the mentioned features, the experimental data obtained using the HPST are simulated using the COSILAB software [151] developed by Rotexo with the closed homogeneous batch reactor. Therefore, the problem is solved by both constraining the pressure and giving it as a function of time *p(t)*, and solving the equations for mass and energy conservation (Q=0; adiabatic system):

$$\frac{(\quad)}{\quad} = \quad \cdot \tag{4.4}$$

$$\left(\sum_{=1} \quad \text{——}\right) = \frac{dp}{dt} - \left(\sum_{=1} \quad \cdot\right) + \text{—} \tag{4.5}$$

Where is the mass fraction of the ith species, is the molecular weight of the ith species, $\cdot$ is the molar rate of production of the ith species by gas-phase chemical reaction per unit volume, C_{pi} is the specific heat of the ith species, and the h_i is the enthalpy of the ith species.COSILAB is organized into different modules allowing the simulation of different combustion phenomena of combustion. Each module is composed of different segments that facilitate the representation of the chemical systems and their solution in terms of chemical kinetic processes:

- A "kinetic mechanism" file that incorporates all the species and the chemical reactions involved in the mechanism.
- A "thermodynamic data" file that contains the phase and thermodynamic data of each chemical species.
- A "transport" file that comprises the gas transport data of each species involved in the kinetic mechanism, and it is an optional file for the homogeneous reactor model. The present work does not make use of this optional data.
- A control file, where information such as: pressure, temperature, residence time, method of solving the equations, convergence criteria, etc. are defined.
- A fuel file, where the composition of the gas-mixture is described.

After running a module, COSILAB generates an output file that includes the calculated parameters of interest. Aiming at predicting the PAH formation from the pyrolysis of different fuels and fuel mixtures in

the current work, the COSILAB output file contains concentration profiles as a function of temperature T_5.

In particular, the speciation measurements are simulated via two methods:

1. Constant pressure (P_5) of 20 bar and a nominal reaction time of 4 ms.
2. Measured pressure profiles up to 10 ms together with the measured T_5.

The constant pressure assumption is typically used in simulating the speciation results sampled from single-pulse shock tube experiments, and it is well justified for large-bore shock tubes as the HPST, where the non-idealities are minimized [137], [150]. Nevertheless, reactions involving resonantly stabilized radicals or methyl radicals can potentially proceed during the post-shock quenching [153], [154]. Therefore, simulations using pressure profiles up to 10 ms are performed to monitor the impact of such reactions on the final observed species mole fractions.

Modeling analysis tools including the rate of production (ROP) analysis and the sensitivity analysis are used in order to provide insight into the chemistry of fuels' decomposition and aromatics growth.

Sensitivity analysis allows quantitative understanding of how the model will respond to changes in the rate parameters. Sensitivity can be calculated from species mass fractions to rate constants. Thus, a sensitivity coefficient for species *j* for a reaction *i* is expressed as follows:

$$, = \frac{}{} = \frac{}{} \tag{4.6}$$

Where k_i is the rate constant of reaction *i*, Y_j is the mass fraction of species *j*. As a result, a positive sensitivity coefficient means that the concentration of species *j* increases with the rate constant k_i. A negative sensitivity coefficient indicates that the concentration of species *j* decreases when the rate constant k_i increases.

The ROP analysis determines the contribution of each reaction to the net production or destruction rates for one particular species (at specific thermodynamic conditions as function of time) and helps constructing schemes which clarify how the various compounds are chemically related in the formation/consumption of a specific species. The total rate of production $r_{f,j}$ and total rate of consumption $r_{c,j}$ for species *j* from all the N reactions in the mechanism are expressed as follows:

$$, = \sum_{=1} , , \tag{4.7}$$

$$, = \sum_{=1} , , \quad (4.8)$$

The rate of production $ROP_{f,j}$ and the rate of consumption $ROP_{f,j}$ for a reaction i are defined as:

$$, = \frac{, ,}{,} \quad (4.9)$$

$$, = \frac{, ,}{,} \quad (45.0)$$

It is noteworthy to point out that $, ,$, $, ,$, $, ,$, and $,$ rates are integrated over time in this manuscript.

4.3 Kinetic model development

The target of this study is to establish a detailed kinetic model emphasizing on the formation mechanisms of two-to-four ring PAHs from the combustion of practical and surrogate fuels. Recent studies [155], [156] suggested that the combustion process can be decoupled into separate pyrolysis and oxidation steps. Therefore, this work will unravel the complicated reaction network in combustion systems under high-pressure pyrolytic conditions in order to reduce the kinetic complexity. Accordingly, pyrolysis of pure fuels including benzene, toluene, propylene (C_3H_6), propyne (C_3H_4-P), phenylacetylene and C_8-C_{10} alkyl benzene as well as mixtures of fuels with unsaturated hydrocarbons covering $C_6H_5C_2H$ + C_2H_x, C_6H_6+ C_2H_x/C_3H_y, and C_7H_8+ C_2H_x/C_3H_y blends are carried out.

Different literature kinetic models including CRECK model [146], LLNL model [144] and JetSurF2.0 model [145] were tested against benzene and toluene pyrolysis measurements as shown in **Figure 4.1**. The CRECK model [146] correctly captures the fuel decomposition reactivity and well predicts the formation of C_2H_2 and C_4H_2 at high temperatures which ensure a reasonable carbon balance. Hence, it is chosen as a basis for the current kinetic model development.

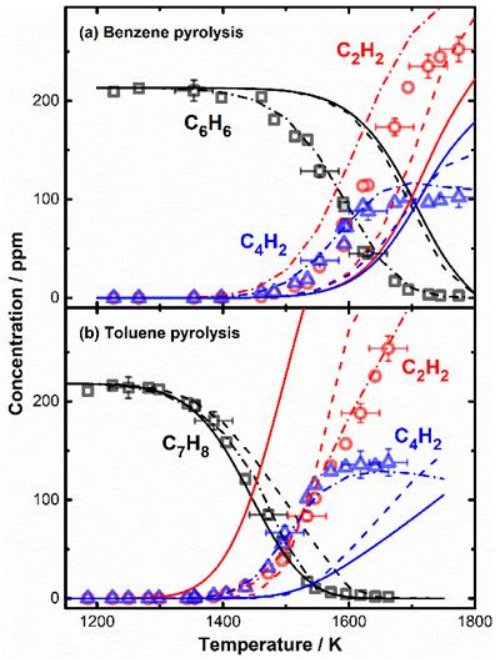

Figure 4.1: Kinetic model predictions by LLNL model (solid lines), JetSurF2.0 (dashed lines) and CRECK model (dash-dotted lines) for fuels, C_2H_2 and C_2H_4 concentrations compared against experimental measurements (symbols) in (a) benzene and (b) toluene pyrolysis.

Theoretically determined reaction pathways and rate coefficients reported in recent studies are used by the current model. Besides, possible reaction pathways are proposed based on the experimental observations. Modeling results with the CRECK model and the current kinetic model are shown in the figures A1-A19 in the appendix. The CRECK model gives decent predictions for most shown species, however, the current model improved the predictions for ethylene thermal decomposition, the formation of the different C_4 species, phenylacetylene decomposition and speciation (never thoroughly studied before though its sub-mechanism is included in CRECK aromatics' mechanisms), and both PAH concentrations and formation temperature windows, mainly due to the inclusion of some missing pathways, as will be detailed later in this section. In addition, the butylbenzene chemistry was added as not present in the original model. For clarity, the development of the kinetic model will be divided into three main parts where the reactions added and modified will be discussed in detail.

4.3.1 C_0-C_4 core mechanism

The C_0-C_4 core mechanism is usually a well-validated detailed mechanism for small species. It constitutes the base on which the chemistry of more complex fuels is coupled, and its accuracy affects the accuracy of the entire model. In other words, it is impossible to obtain a well-established kinetic model without an accurate and validated C_0-C_4 sub-mechanism. C_2H_2 and C_2H_4 sub-mechanisms already embedded in the CRECK model [146] over-estimate the decomposition rate of C_2H_4 compared to the current-

measurements. The unimolecular decomposition to $C_2H_2+H_2$ turns out to be the prominent channel responsible for C_2H_4 decay in CRECK model [146] according to the analysis performed at high - P, high – T conditions in the present work. Based on this observation, this reaction is removed and replaced with elementary steps from USC Mech [157], including C_2H_4 decomposing to H_2+vinylidene (H_2CC) (R1) and H_2CC isomerizing to C_2H_2 (R2 and R3) or participating in other reactions. Several theoretical studies [158], [159] rationalize ethylene decomposition in two stepwise processes involving 1,1-elimination of H_2 forming H_2CC which rapidly isomerizes to C_2H_2 over a small energy barrier ~0.9 Kcal/mol. Additionally, the hydrogen abstraction rate coefficient from C_2H_4 by H (R3) is updated by the value recommended by Baulch et al. [160]. The model validation for the mixtures containing C_2H_4 will be presented in sections 5.2, 5.3 and 5.4.

$C_2H_4(+M) = H_2+H_2CC(+M)$ (R1)

$C_2H_2 (+M) = H_2CC (+M)$ (R2)

$C_2H_2 +H = H_2CC +H$ (R3)

$H+C_2H_4 = H_2+C_2H_3$ (R4)

As C_2 hydrocarbons, the C_3 sub-mechanism is also included in the core mechanism of the CRECK model [146]. The rate coefficients of propylene (C_3H_6) and propyne (C_3H_4-P) unimolecular decomposition reactions and the C_3H_6/C_3H_4-P+H reactions are updated from the theoretical work of Klippenstein and coworkers [161]–[164] on the C_3H_{4-7} potential energy surfaces (PESs). The reaction between singlet methylene and acetylene ($^1CH_2 + C_2H_2 = C_3H_4$-P) [165] is added to the kinetic model, since its reverse reaction potentially contributes to propyne dissociation. The corresponding C_3H_6 and C_3H_4-P radicals, in particular, the resonantly-stabilized allyl (C_3H_5-A) and propargyl (C_3H_3), are important benzene precursors in the combustion of acyclic fuels. Rate coefficients for the C_3H_3 recombination reactions forming fulvene and benzene are from the theoretical work of Miller and Klippenstein [166]. The rate coefficient reported by Jasper and Hansen [167] is used for the hydrogen assisted isomerization of fulvene to benzene. The rate coefficient of the reaction $C_3H_3+C_3H_5$-A= fulvene + 2H is taken from Hansen et al. [168]. Theoretically determined rate coefficients for $C_3H_3+C_3H_4$-P/C_3H_4- A = C_6H_6+H reactions are not available in literature, and the ones used in [146] originate from an early study on propyne and allene (C_3H_4- A) pyrolysis by Hidaka et al. [169]. Future theoretical works are necessary to improve the accuracy of the kinetic parameters of such reactions due to their significant role in benzene formation. The C_3H_5-A self-recombination mainly leads to a straight-chained 1,5-hexadiene (CH_2=$CHCH_2CH_2CH$=CH_2, DIALLYL) unlike the C_3H_3 self-recombination that leads to a cyclic species. Rate coefficients for C_3H_5-A self-recombination leading to both DIALLYL and $C_3H_6+C_3H_4$-A come from

the shock tube studies by Lynch et al. [170] and Fridlyand et al. [171], respectively. The CH_2=$CHCH_2$ $\dot{H}CH$=CH_2 radical, formed through the H-abstraction of 1,5-hexadiene, appears on the C_6H_9 PES. This surface also includes the addition reactions of vinyl (C_2H_3)+1,3-butadiene (C_4H_6) and C_3H_5-A+C_3H_4-P/C_3H_4-A, and the formation/consumption of five-membered and six-membered cyclic species through reactions such as cyclopentadiene (CYC_5H_6)+CH_3, methyl-cyclopentadiene ($C_5H_5CH_3$)+H and cyclohexadiene (CYC_6H_8)+H. The corresponding rate coefficients of these relevant reactions, studied by Wang et al. [172], are incorporated in the current kinetic model. The rate coefficients for the reactions pathways between C_3H_6 and C_3H_5-A, found on the C_6H_{11} PES [173], are used in the current model. The reactions between C_3 fuels and the C_2 intermediates result in the formation of C_5 species. Reactions on the C_5H_9 PES, including C_3H_6+C_2H_3, C_3H_5-A+C_2H_4, C_3H_4-P/C_3H_4-A+C_2H_3, reported by Wang et al. [173] are integrated in the current model. The resonantly stabilized cyclopentadienyl (C_5H_5) radical react with CH_3 resulting in C_6 species that further lead to benzene and fulvene through dehydrogenation processes. Relevant reactions and the corresponding rate coefficients reported in [174], [175] are used in the current model. Similarly, C_5H_5 + C_2H_2 reaction can lead to benzyl (C_7H_7). The reaction rate of this channel is adopted from the theoretical work of da Silva et al. [176]. The model validation for the mixtures containing C_3 species will be presented in sections 5.1, 5.2 and 5.3.

Updates are also made for the C_4 sub-mechanisms. The rate coefficients for the decomposition and isomerization reactions of C_4H_6 isomers (2-butyne (C_4H_6–2), 1,2-butadiene ($C_4H_6$12) and 1,3-butadiene (C_4H_6)) are taken from the theoretical work done by Huang et al. [177]. Since the rate coefficients of 1-butyne (C_4H_6–1) decomposition reactions are not addressed in Huang et al. theoretical work [177], the ones reported by Lockhart et al. [178] are used. The C_3H_3+CH_3 recombination reactions leading to $C_4H_6$12/C_4H_6–1 are used to represent the reversible unimolecular decomposition processes, by employing the latest theoretical rate coefficients reported by Pham et al. [179]. Vinylacetylene (C_4H_4) decomposition reactions and relevant kinetic parameters are adopted from the recent theoretical work by Zador et al. [180]. The reactions between C_4H_4 and C_3H_3 result in the formation of C_7 species, in particular benzyl (C_7H_7). Involved reactions and corresponding rates reported in [181] are considered in the current work.

4.3.2 Fuel mechanism

The fuel mechanism is composed of the decomposition reactions of the fuel and the consumption reactions of the directly derived radicals. It needs to be coupled to the C_0-C_4 sub-mechanism. The choice of the reactions and the corresponding rate parameters is based on previous theoretical and experimental investigations as well as on analogy with similar reaction systems. Details about the single fuels studied in this thesis are presented below, with particular attention to the modifications made to the original CRECK model.

4.3.2.1 Benzene sub-mechanism

Unimolecular decomposition and H-abstraction reactions leading to the formation of C_6H_5 account for the benzene consumption. C_6H_5, the most significant product from the initial decomposition steps of benzene, lead to the formation of o-benzyne (o-C_6H_4) [26], [55] through self-recombination and dissociation reactions. Computed rate coefficients for o-C_6H_4 decomposition reported by Ghigo et al. [182] are adopted in the current model. A modification is made in the CRECK model regarding the decomposition of the linear C_6H_5 (LC_6H_5). Two reactions: $LC_6H_5 \rightarrow C_4H_3+C_2H_2$ and $LC_6H_5 \rightarrow 2C_2H_2+C_2H$ were included in the original CRECK model. The latter one is removed in the current model due to its redundancy, as the reaction $C_4H_3 \rightarrow C_2H_2+C_2H$ already existed. This modification does not significantly change the reactivity of the benzene, but slightly improves the predictions of C_2H_2 and C_4H_2.

4.3.2.2 Toluene sub-mechanism

The well-established competing channels leading to benzyl (C_7H_7) +H and C_6H_5+ methyl (CH_3) account for the unimolecular decomposition of toluene. The further decomposition of C_7H_7 produces various radicals including fulvenallenyl (C_7H_5), cyclopentadienyl (C_5H_5), and propargyl (C_3H_3). No modifications are done to the original CRECK model.

4.3.2.3 Styrene sub-mechanism

The unimolecular decomposition reactions and hydrogen ipso-substitution reactions, responsible for the consumption of styrene, are updated based on the kinetic models of Wang and Frenklach [183] and Yuan et al. [78], respectively. Another unimolecular decomposition reaction for styrene ($C_6H_4C_2H_3$+H (+M) = $C_6H_5C_2H_3$ (+M)) is suggested in analogy to the reaction C_6H_5+H (+M) = C_6H_6 (+M). The stable styrene radicals, 1-styryl ($C_6H_5CH\dot{C}H$) and o-vinylphenyl ($C_6H_4C_2H_3$), experience the Bittner-Howard route [184] and the modified Frenklach route [185] contributing to $C_{10}H_8$ formation [186] at high pressures. The adduct $C_6H_4(CHCH_2)(CH\dot{C}H)$ produced from the C_2H_2 addition to $C_6H_4C_2H_3$ can go through six-member ring closure giving $C_{10}H_8$+H [186].

The styrene and phenyl addition/elimination reactions contributing to the formation of stilbene ($C_6H_5C_2H_2C_6H_5$) are considered in the model construction [66]. Reaction sequences between styrene and phenyl leading to 9,10-dihydrophenanthrene ($C_{14}H_{12}$) are referred to similar reactions between phenylacetylene and phenyl contributing to phenanthrene ($C_{14}H_{10}$) [66]. The decomposition of $C_{14}H_{12}$ yielding to $C_{14}H_{10}$ is acquired from analogous reaction of dihydro-naphthalene consumption ($C_{10}H_{10}$) to naphthalene ($C_{10}H_8$) + H_2 [118].

4.3.2.4 Phenylacetylene sub-mechanism

The molecular structure of $C_6H_5C_2H$ and the bond dissociation energies (BDEs) calculated at the ROCBSQB3 level of theory [187] are provided in **Scheme 4.1**. The indicated RO methodology eliminates the empirical corrections used in standard CBS-QB3 [188] to compensate for spin contamination [187]. The C-H bond strengths in the phenyl and ethynyl moieties are close to those in benzene (112.9 kcal/mole [189]) and acetylene (132.8 kcal/mole [189]), respectively.

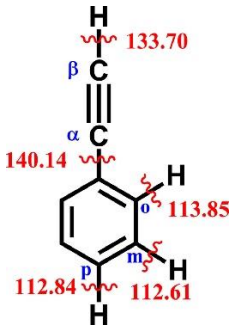

Scheme 4.1: The schematic of the phenylacetylene ($C_6H_5C_2H$) molecule and bond dissociation energies (BDEs) calculated at the ROCBS-QB3 level of theory *[187]*.

Apparently, the ring C-H bond fission reaction (R5) is expected to be the main bond fission reaction initiating the decomposition of $C_6H_5C_2H$ as the ring C-H bonds have lower energy compared to the C-H bond in ethynyl moiety (**Scheme 4.1**). The yielded o-, m- and p- radicals are lumped as $C_6H_4C_2H$ in the current model for the purpose of simplification. Herzler and Frank [81] are the only ones who evaluated the rate constant of (R5) according to the shock tube experiments performed at 2 bar over the temperature range of 1600-1900 K. This rate constant is increased by a factor of five to align with the current high-pressure conditions (20 bar). The adopted value of $k_5 = 2.50\times10^{17}\exp(-113000/RT)$ cm^3 $mole^{-1}$ s^{-1} is about 35%-50% of the C-H bond fission rate constant proposed by Sivaramakrishnan et al. [51] to fit the benzene decay profiles from their high-pressure high-temperature shock tube pyrolysis experiments. The model also includes the C-H bond fission (R6) in the ethynyl moiety with the rate coefficient assigned as that for C-H bond fission in acetylene in the latest version of CRECK model [146]. The unimolecular C-C bond fission (R7) recommended by Yuan et al. [71] is considered as well in the current model.

$C_6H_5C_2H = C_6H_4C_2H+H$ (R5)

$H+C_6H_5CC(+M) = C_6H_5C_2H(+M)$ (R6)

$C_6H_5C_2H(+M) = C_2H+C_6H_5(+M)$ (R7)

Bimolecular reactions between $C_6H_5C_2H$ and H atom occur after the production of H atoms. Various reactions leading to different possible products (R8-R12) are extensively taken into consideration in the current model construction. In the early work by Herzler and Frank [81], only the two channels (R8) and (R9) were proposed. The rate coefficient of (R8) producing $C_6H_5+C_2H_2$ was derived experimentally despite the fact of being considered the predominant pathway [81]. Nevertheless, $C_6H_5+C_2H_2$ => $C_6H_5C_2H+H$, reverse of (R8), is a fundamental step of the HACA route leading to naphthalene formation from benzene. It also represents a prototypical addition of C_2H_2 to an aromatic radical site. Due to its kinetic significance, (R-8) has been investigated experimentally [54], [190] and theoretically [183], [186], [191] so that the corresponding rate coefficients k_{-8} are extensively available in the literature. Rate coefficients for (R8) including the direct measurement [81] and those determined through chemical equilibrium from literature-reported k_{-8} [54], [183], [186], [190], [191] are compared in **Figure 4.2(b)**. Negative pressure dependence of k_{-8} is depicted by Wang and Frenklach [183] and Mebel et al. [186] theoretical works, while weak pressure effects are revealed in the calculated value by Tokmakov and Lin [191]. Owing to the compatibility of Tokmakov and Lin [191] k_{-8} with measurements [54], [81] over different temperature ranges, this rate constant is employed in the present model for R8. As shown in **Figure 4.2**, for the chosen rate expression, three-fold uncertainty centered on both forward and reverse rate coefficients can cover all available measurements and calculations at 1 atm in the temperature range of 1000-2000 K.

$C_6H_5C_2H+H = C_6H_5+C_2H_2$ (R8)

$C_6H_5C_2H+H = C_6H_4C_2H+H_2$ (R9)

$C_6H_5C_2H+H = C_6H_6+C_2H$ (R10)

$C_6H_5C_2H+H = C_6H_5CH\dot{C}H$ (R11)

$C_6H_5C_2H+H = C_6H_5\dot{C}CH_2$ (R12)

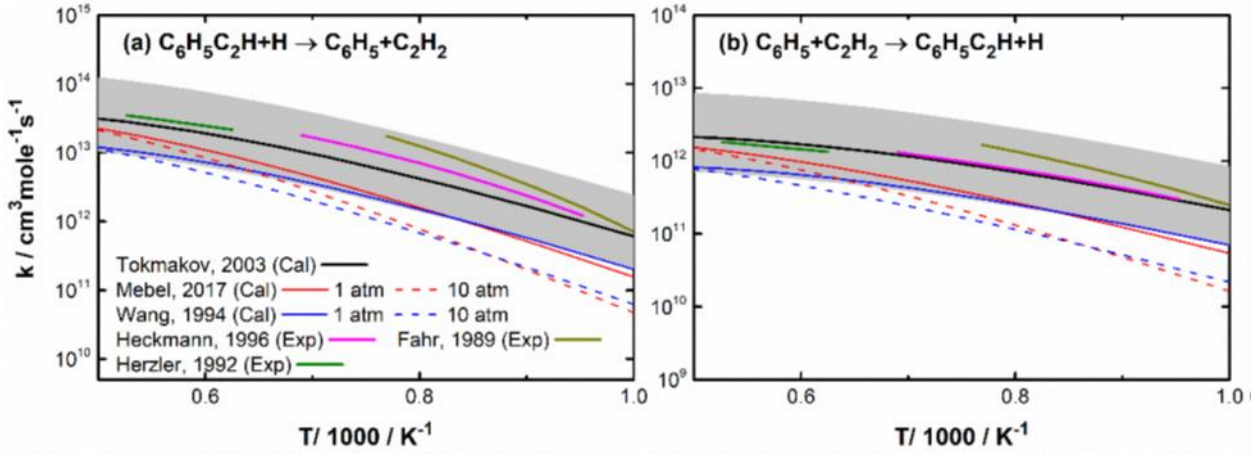

Figure 4.2: Rate coefficients reported in literature for (a) R8, $C_6H_5C_2H+H$ => $C_6H_5+C_2H_2$ and (b) R-8, $C_6H_5+C_2H_2$ =>$C_6H_5C_2H+H$. Measurements in *[54], [190]* and calculations in *[183], [186], [191]* were for R-8, while the measurement in *[81]* was for R8. The reverse rate coefficients were computed through chemical equilibrium with the thermochemical data provided in *[192]*. The shadowed areas indicate three-fold uncertainties centered on the calculated rate coefficients for R-8 *[191]* and on the derived reverse rate coefficient for R8.

The rate coefficient k_9 = 2.50×104 exp (-16000/RT) cm^3 mole^{-1} s^{-1} proposed in *[192]* is adopted for the hydrogen abstraction reaction (R9). With the current rate coefficients assignments, the branching ratio of the hydrogen abstraction channel (R9) is about 0.1 compared to (R8) over the entire investigated temperature range, which is consistent with the value recommended in *[81]* (<0.2). For the ipso-substitution reaction (R10), its reverse form with a rate coefficient of k_{-10}=5.0×1013 cm^3 mole^{-1} s^{-1} confiscated from the kinetic model describing the PAH formation and growth by Wang and Frenklach *[192]* is incorporated in the current model. H-addition reactions (R11 and R12) to the triple bond form C6H5CHĊH and C6H5ĊCH2 radicals. The rate coefficients of their forward and reverse reactions are included in the present model by the values reported in *[186]* and *[191]*, respectively. The consequent consumption of C6H5CHĊH and C6H5ĊCH2 through isomerization and decomposition steps was studied by Tokmakov and Lin *[191]*. Here, this part of their model is added.

The faster decomposition of phenylacetylene compared to benzene at the same pyrolytic conditions (**Figure 4.3**) and the minor reactivity of the radicals produced by the above-mentioned bimolecular reactions (R8-R12) indicate the existence of chain-branching processes enhancing the reactivity within the reaction system. In view of the abundant C_6H_5 from R8, reactions between $C_6H_5C_2H$ and C_6H_5 are added to the model. Besides abstracting a hydrogen atom from $C_6H_5C_2H$, C_6H_5 can either add to the triple carbon-to-carbon bond at the or site to form two types of $C_{14}H_{11}$ adducts: $C_6H_5C(\dot{C}H)C_6H_5$ and $C_6H_5\dot{C}CHC_6H_5$ (R13, R14), or undergo chemically-activated reactions (R15-R17) to produce diphenylacetylene ($C_6H_5CCC_6H_5$), phenanthrene ($PC_{14}H_{10}$) and 9-methylene-fluorene ($C_{13}H_8CH_2$). The

subsequent decomposition of $C_6H_5\dot{C}CHC_6H_5$ leads to $C_6H_5CCC_6H_5$ formation via direct -scission releasing a hydrogen atom (R18). On the other hand, $C_6H_5\dot{C}CHC_6H_5$ and $C_6H_5C(\dot{C}H)C_6H_5$ are likely to go through intramolecular hydrogen transfer and ring closure steps (R20-R22) contributing to phenanthrene and 9-methylene-fluorene formation, respectively. The above reaction sequences starting from C_6H_5 addition to the ethynyl branch of $C_6H_5C_2H$ are summarized schematically in **Scheme 4.2**.

$C_6H_5C_2H+C_6H_5 = C_6H_5C(\dot{C}H)C_6H_5$ (R13)

$C_6H_5C_2H+C_6H_5 = C_6H_5\dot{C}CHC_6H_5$ (R14)

$C_6H_5C_2H+C_6H_5 = C_6H_5CCC_6H_5+H$ (R15)

$C_6H_5C_2H+C_6H_5 = C_{14}H_{10}+H$ (R16)

$C_6H_5C_2H+C_6H_5 = C_{13}H_8CH_2+H$ (R17)

$C_6H_5\dot{C}CHC_6H_5 = C_6H_5CCC_6H_5+H$ (R18)

$C_6H_5CCC_6H_5+H = PC_{14}H_{10}+H$ (R19)

$C_6H_5\dot{C}CHC_6H_5 = PC_{14}H_{10}+H$ (R20)

$C_6H_5C(CH)C_6H_5 = C_6H_5C(CH_2)C_6H_4$ (R21)

$C_6H_5C(CH_2)C_6H_4 = C_{13}H_8CH_2+H$ (R22)

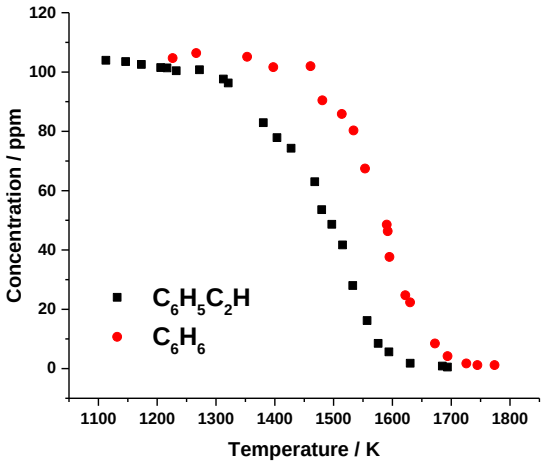

Figure 4.3: Thermal decomposition of benzene and phenylacetylene under similar experimental conditions.

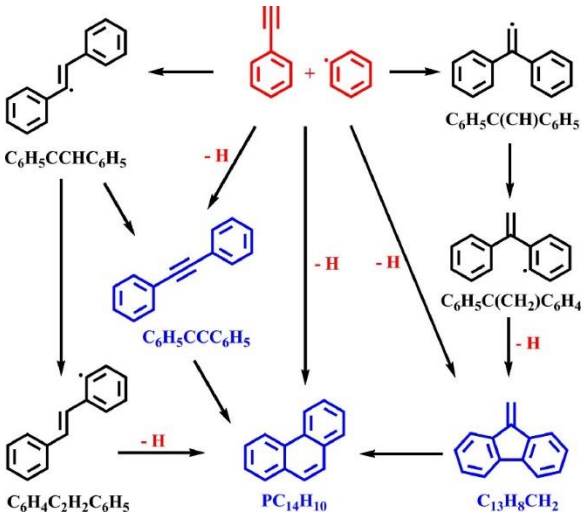

Scheme 4.2: Reaction sequences starting from C_6H_5 addition to the ethynyl branch of $C_6H_5C_2H$ *[193]*.

The fate of $C_6H_5\dot{C}CHC_6H_5$ was theoretically explored by Matsugi and Miyoshi [66]. Pressure-dependent rate coefficients reported in [66] are used for R14 and R18-R20. The rate coefficients of R15 and R16 calculated theoretically in a recent work by Tuli and Mebel [194] are used in the current model. The $C_6H_5C(\dot{C}H)C_6H_5$ formation (R13), its subsequent reactions (R21, R22) and the chemically activated reaction (R17) were not investigated previously to the best of our knowledge. The reaction sequence accounting for $C_{13}H_8CH_2$ formation through the stepwise conversion (R21, R22) and the chemically activated reaction (R17) are proposed analogously to the reaction sequence responsible for $PC_{14}H_{10}$ formation in the current model. Taking into consideration the kinetic similarities, the rate coefficients for the C_6H_5 addition step (R13) and the chemically activated step (R17) are equal to those of R14 and R16, respectively. The rate coefficient for the hydrogen transfer step (R21) is determined through an analogy to the isomerization between 2-phenyl-vinyl radical ($C_6H_5CH\dot{C}H$) and 2-vinylphenyl radical ($C_6H_4C_2H_3$) [191]. The rate coefficient assigned to the ring closure step (R22) is analogized to the fluorene ($C_{13}H_{10}$) formation from o-benzyl-phenyl radical ($C_6H_5CH_2C_6H_4$) [68].

The H-abstraction by C_6H_5 is also a dominant reaction in the consumption of phenylacetylene and results in the formation of benzene. The rate coefficient of this reaction is equivalent to the rate of the reaction $C_6H_5+C_6H_5CH_3 = C_6H_6+C_6H_4CH_3$

The addition/elimination reaction of $C_6H_5C_2H + C_6H_5$ and $C_6H_5C_2H + C_6H_4C_2H$ leads to the formation of ethyl-biphenyl ($C_6H_4(C_2H)C_6H_5$) and diethynyl-biphenyl ($C_2HC_6H_4C_6H_4C_2H$) compounds, respectively (R23, R24). Their rate constants are taken in analogy with the reaction between phenyl and benzene [195] with a three-fold increase. The original rate constant from [195], covering a temperature range of 298–1330 K, was obtained through a combination of cavity ring down spectrometry measurements at 40 Torr

and theoretical calculations at the B3LYP/6–311G(d,p) level. Uncertainties of a factor of three is common when it is used for analogous reactions under higher temperature and pressure conditions. Nevertheless, future theoretical calculations are highly necessary to derive the rate coefficients for reactions which influence the reactivity of phenylacetylene. The self-recombination of the $C_6H_4C_2H$ radical resulting in $C_2HC_6H_4C_6H_4C_2H$ (R25) is also considered, with same rate coefficient as phenyl self-recombination [55]. The isomers of $C_6H_4(C_2H)C_6H_5$ and $C_2HC_6H_4C_6H_4C_2H$ are lumped in the current model, since they have similar growth pathways and yield products of similar structures.

$C_6H_5C_2H+C_6H_5 = C_6H_4(C_2H)C_6H_5+H$ (R23)

$C_6H_5C_2H+C_6H_4C_2H = C_2HC_6H_4C_6H_4C_2H+H$ (R24)

$C_6H_4C_2H+C_6H_4C_2H = C_2HC_6H_4C_6H_4C_2H$ (R25)

Further reactions of both $C_6H_4(C_2H)C_6H_5$ and $C_2HC_6H_4C_6H_4C_2H$ species can form phenanthrene and pyrene, respectively (R26-R29) similar to the transformation of $C_{10}H_7C_2H$ to acenaphthalene [70].

$C_6H_4(C_2H)C_6H_5+H = C_{14}H_{10}+H$ (R26)

$C_2HC_6H_4C_6H_4C_2H+H = C_{14}H_9C_2H+H$ (R27)

$C_{14}H_9C_2H+H = PC_{16}H_{10}+H$ (R28)

$C_2HC_6H_4C_6H_4C_2H+H = PC_{16}H_{10}+H$ (R29)

Moreover, the H-addition to $C_6H_5\dot{C}CHC_6H_5$ gives stilbene ($C_6H_5C_2H_2C_6H_5$), which in turn undergoes H-abstraction reactions resulting in hydrogen, methane and benzene formation. This reaction sequence discussed by Matsugi and Miyoshi [66] is added to the current model. On the other hand, the fate of the H-addition to $C_6H_5C(\dot{C}H)C_6H_5$ (R30) and its subsequent decomposition (R31) are not previously examined. The rate constants of R30 and R31 are analogous to those of $H+C_2H$ (+M) = C_2H_2 (+M) and $C_6H_5CH_2C_6H_5 = C_{13}H_{10}+H_2$, respectively [146].

$C_6H_5C(CH)C_6H_5+H(+M) = C_6H_5C(CH_2)C_6H_5(+M)$ (R30)

$C_6H_5C(CH_2)C_6H_5 = C_{13}H_8CH_2+H_2$ (R31)

4.3.2.5 Ethylbenzene sub-mechanism

The unimolecular decomposition reactions of ethylbenzene include the homolysis reactions forming benzyl (C_7H_7) and methyl (CH_3) radicals (R32) and phenyl (C_6H_5) and ethyl (C_2H_5) radicals (R33) and the C-H bond fission on the ethyl side chain forming 1- phenylethyl ($C_6H_5CHCH_3$) (R34) and 2-phenylethyl

($C_6H_5C_2H_4$) (R35). The rate constants for the unimolecular decomposition reactions are the recommended theoretical rate coefficients reported by Matsugi and Miyoshi [66]. Rate constants for the ipso-substitution reactions and H-abstraction reactions by H, CH_3 and C_6H_5 are taken from the ethylbenzene kinetic model proposed by Yuan et al. [73]. The consumption of the two fuel radicals $C_6H_5CHCH_3$ and $C_6H_5C_2H_4$ lead to styrene production. Their corresponding rate constants are derived from the theoretical work of Tokmakov and Lin [196].

$C_7H_7+CH_3 = C_6H_5C_2H_5$ (R32)

$C_6H_5+C_2H_5 = C_6H_5C_2H_5$ (R33)

$C_6H_5CHCH +H = C_6H_5C_2H_5$ (R34)

$C_6H_5C_2H_4+H = C_6H_5C_2H_5$ (R35)

4.3.2.6 Propylbenzene sub-mechanism

The n-propylbenzene ($C_6H_5C_3H_7$) sub-mechanism, established in the CRECK model [146], is highly lumped. Thus, the following sub-mechanism is updated in the current work. The unimolecular decomposition reactions of $C_6H_5C_3H_7$ include C-C bond cleavage (R36-R38) and C-H bond cleavage (R39-R41) yielding to 3-phenyl-1-propyl ($C_6H_5C_3H_6$-A), 1-phenyl-2-propyl ($C_6H_5C_3H_6$-B) and 1-phenyl-1-propyl ($C_6H_5C_3H_6$-C). The corresponding rate coefficients are taken from the kinetic model proposed by Diévart and Dagaut [113]. Rate constants for the H-abstraction reactions and ipso-substitution reactions by H and CH_3 are taken from the theoretical work of Robinson and Linstedt [197] and from the n-propylbenzene kinetic model developed by Yuan et al.[74], respectively. Rate coefficients for H-abstraction reactions by other radicals including C_2H_5, C_6H_5 and C_7H_7 are from Diévart and Dagaut work [113]. The unimolecular decomposition of $C_6H_5C_3H_6$-A has two possible pathways which produce 3-phenyl-1-propene ($C_6H_5C_3H_5$-1) +H atom and $C_2H_4+C_7H_7$. The decomposition of $C_6H_5C_3H_6$-B radical has three possible pathways which produce 1-phenyl-1-propene ($C_6H_5C_3H_5$-2) +H atom, $C_6H_5C_3H_5$-1 +H and C_6H_5 + propylene (C_3H_6). The unimolecular decomposition of $C_6H_5C_3H_6$-C radical leads either to $C_6H_5C_3H_5$-2 +H or to styrene ($C_6H_5C_2H_3$) + CH_3 radical. The rate constants of the fuels radicals' unimolecular decomposition reactions and the isomerization reactions are from the work of Jin et al. [198]. The other isomerization reaction of $C_6H_5C_3H_6$-B to phenyl-iso-propene (C_6H_5-IC_3H_6) is taken from the work of Diévart and Dagaut [113]. The subsequent unimolecular decomposition of C_6H_5-IC_3H_6 to both $C_6H_5C_2H_3$ + CH_3 and C_6H_5 + C_3H_6 as well as the corresponding rate coefficients are adopted from the kinetic model by Yuan et al. [74].

$C_6H_5C_3H_7= C_7H_7 + C_2H_5$ (R36)

$C_6H_5C_3H_7 = C_6H_5 + NC_3H_7$ (R37)

$C_6H_5C_3H_7 = C_6H_5C_2H_4 + CH_3$ (R38)

$C_6H_5C_3H_7 = C_6H_5C_3H_6\text{-A} + H$ (R39)

$C_6H_5C_3H_7 = C_6H_5C_3H_6\text{-B} + H$ (R40)

$C_6H_5C_3H_7 = C_6H_5C_3H_6\text{-C} + H$ (R41)

Direct formation of indene (C_9H_8) through the ring-closure steps of 1-phenyl-2-propenyl ($CC_6H_5C_3H_4$-1) is addressed as a relevant pathway to the fuel structure (**Scheme 4.3**). The corresponding reaction rate as well as the $C_6H_5C_3H_5$-1 unimolecular decomposition and H-abstraction reactions' rates by H and CH_3 yielding to $CC_6H_5C_3H_4$-1 are adopted from the recent kinetic model proposed by Jin et al. [198].

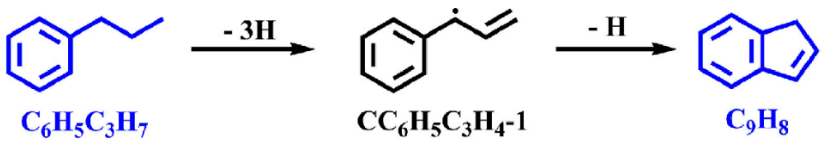

Scheme 4.3: Reaction pathway leading to indene formation starting from n-propylbenzene.

4.3.2.7 Butylbenzene sub-mechanism

The *n*-butylbenzene ($C_6H_5C_4H_9$) sub-mechanism is added in the current model as it is absent in the CRECK model [146], which is the basis of our current kinetic model. The rate constants of all the unimolecular initiations (R42-R49) involving the dissociation of the C-C and C-H bonds of the alkyl chain are taken from the kinetic model suggested by Diévart and Degaut [113]. The C-H bond cleavage leads to the following fuel radicals: 4-phenyl-1-butyl ($C_6H_5C_4H_8$-A), 3-phenyl-2-butyl ($C_6H_5C_4H_8$-B), 2-phenyl-3-butyl ($C_6H_5C_4H_8$-C) and 1-phenyl-1-butyl ($C_6H_5C_4H_8$-D). H-abstraction reactions between the radicals formed by the fuel thermal decomposition (H, CH_3, C_2H_5, C_6H_5 and C_7H_7) and butylbenzene lead to the formation of fuel radicals and stable products (H_2, CH_4, C_2H_6, C_6H_6 and C_7H_8). The rate constants for the corresponding reactions are taken from the model of Diévart and Degaut [113]. The "ipso" attack by H atoms and CH_3 radicals on butylbenzene results in butyl radical (PC_4H_9) + benzene and butyl radical + toluene, respectively. The kinetic parameters of these ipso-additions are taken from Zhang et al. [118]. The consumption reactions of *n*-butylbenzene fuel radicals are shown in **Scheme 4.4**. The rate coefficients from the work by Zhang et al. [118] are adopted. For isomerization reactions of phenylbutyl radicals, the recommended rate coefficients by Zhang et al. [118] are used.

$C_6H_5C_4H_9 = C_7H_7 + NC_3H_7$ (R42)

$C_6H_5C_4H_9 = C_6H_5 + PC_4H_9$ (R43)

$C_6H_5C_4H_9 = C_6H_5C_2H_4 + C_2H_5$ (R44)

$C_6H_5C_4H_9 = C_6H_5C_3H_6\text{-A} + CH_3$ (R45)

$C_6H_5C_4H_9 = C_6H_4C_4H_8\text{-A} + H$ (R46)

$C_6H_5C_4H_9 = C_6H_5C_4H_8\text{-B} + H$ (R47)

$C_6H_5C_4H_9 = C_6H_5C_4H_8\text{-C} + H$ (R48)

$C_6H_5C_4H_9 = C_6H_5C_4H_8\text{-D} + H$ (R49)

The unimolecular decomposition of *n*-butylbenzene fuel radicals leads to the formation of butenylbenzene products as shown in **Scheme 4.4** ($C_6H_5C_4H_7$-1, $C_6H_5C_4H_7$-2 and $C_6H_5C_4H_7$-3). H-atom abstraction reactions on butenylbenzene isomers by H/CH_3 to form phenyl-butenyl radicals ($C_6H_5C_4H_6$) radicals are incorporated. The consumption of $C_6H_5C_4H_6$ radicals lead either to dihydro-naphthalene ($C_{10}H_{10}$) through ring-closure steps or to 1,3-butadienyl-benzene ($C_6H_5C_4H_5$). $C_{10}H_{10}$ and $C_6H_5C_4H_5$ can further result in naphthalene ($C_{10}H_8$) formation through losing two hydrogen atoms or hydrogen molecule and in 1-methyleneindanyl radical ($C_9H_7CH_2$) which transforms into $C_{10}H_8$ through ring- arrangement, respectively. Rate coefficients for the involved reactions are adopted from recent kinetic model [118] while the schematic for reaction pathways leading to the fused PAH species ($C_{10}H_8$) is shown in **Scheme 4.5**.

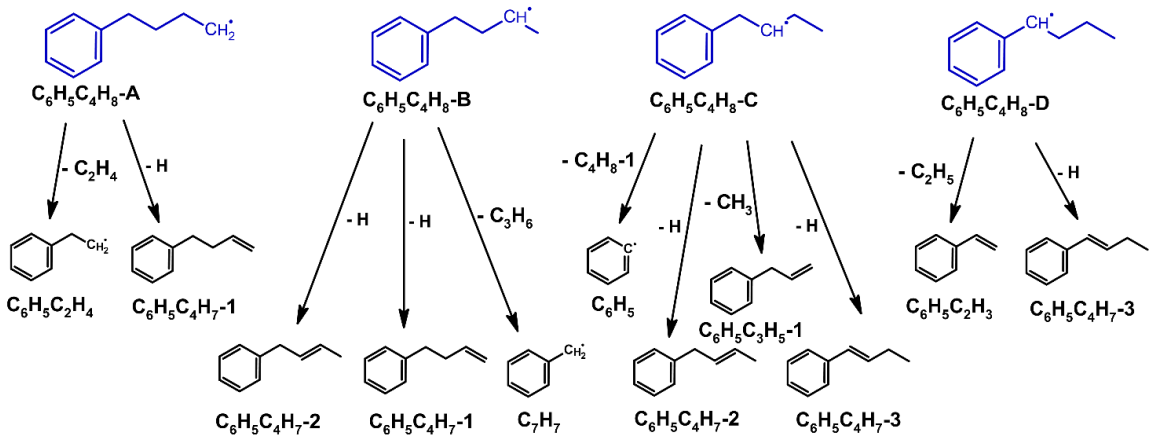

Scheme 4.4: Consumption scheme of *n*-butylbenzene radicals.

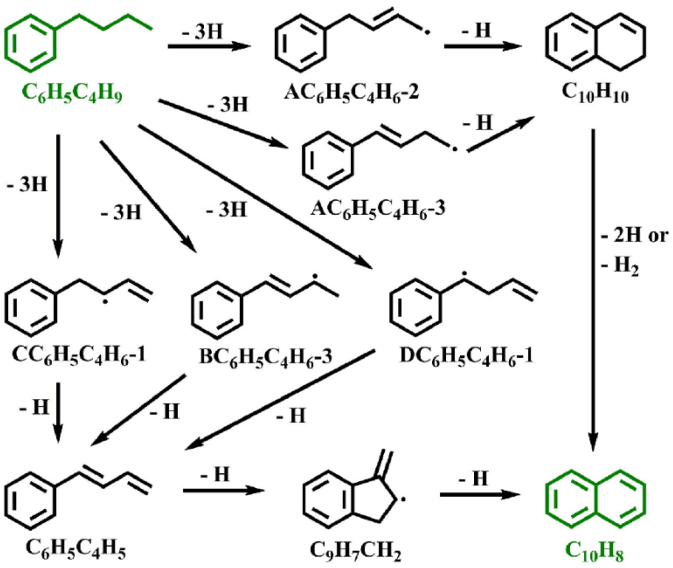

Scheme 4.5: Schematic for fuel-specific reactions pathways leading to naphthalene.

4.3.3 Secondary mechanism

It is a link between the primary mechanism and the reaction base mechanism. The secondary mechanism includes the reactions which involve the products of the primary fuel decomposition mechanism and the C_0-C_4 hydrocarbons. These reactions include, among the others, the elementary steps leading to PAH appearance and growth.

4.3.3.1 Aromatics + CH_3 reactions

The 1-, 2- and 3-methyl indene are formed from the reactions between methyl (CH_3) radical and indene. The rate constants of these reactions are taken from the theoretical work of Mebel et al. [41]. The consumption of methyl indene occurs mainly via H-atom abstraction leading to methyleneindanyl radical ($C_9H_7CH_2$). $C_9H_7CH_2$ contributes to $C_{10}H_8$ formation through dehydrogenation and ring-arrangement steps [66], which is considered in the present model.

The reaction system of CH_3+acenaphthyl radical ($C_{12}H_7$-4) have been investigated in a recent theoretical work by Porfiriev et al. [199]. The results indicate that the $C_{12}H_7$-4 + CH_3 reaction proceeds by a fast radical-radical recombination mechanism and most likely produces collisional stabilized 1-methylacenaphthalene ($C_{12}H_7CH_3$) or a $C_{13}H_9$ radical ($C_{12}H_7CH_2$) after H-loss from the CH_3 group. $C_{12}H_7CH_2$, obtained from $C_{12}H_7$-4 + CH_3 reaction or via H-abstraction of $C_{12}H_7CH_3$, can interconvert to phenalenyl radical ($PC_{13}H_9$) via an isomerization process involving formal insertion of the CH_2 group into a C–C bond of the five-member ring leading to expansion of this ring to a six-member ring. The H

addition reaction to phenalenyl radical forms phenalene ($PC_{13}H_{10}$). All the above-mentioned reactions and corresponding reaction rates are integrated in the current model.

4.3.3.2 Aromatics + C_2H_2/C_2H reactions

The presence of C_2H_2 in an initial mixture will further enhance the concentration of the PAH species with ethynyl branches ($C_mH_nC_2H$) in the species pool like diethynyl benzene, ethynyl-naphthalene, diethynyl-naphthalene, ethynyl acenaphthalene, ethynyl-biphenyl, diethynyl-biphenyl, ethynyl-phenanthrene and ethynyl-pyrene. This is due to the contribution of two types of reactions represented by $C_mH_n+C_2H_2 = C_mH_nC_2H+H$ and $C_mH_{n+1}+C_2H = C_mH_nC_2H+H$. The reaction sequence leading to the formation of 1,2-diethynyl benzene starting from phenylacetylene are updated from the theoretical work of Liu et al.[200]. Pressure-dependent reaction rates for the addition reactions of acenaphthyl ($C_{12}H_7$), 1-ethynylnaphthyl and 2-ethynylnaphyl radicals to C_2H_2 leading to the formation of ethynyl acenaphthylene and diethynyl naphthalene respectively are incorporated in the current model [201]. Rate coefficients for the unimolecular decomposition and hydrogen abstraction reactions by H of acenaphthylene, 1-ethynylnaphthylene and 2-ethynylnaphthylene are also introduced from the same publication. Ethynyl phenanthrene is formed via phenanthryl radical + C_2H_2 reaction, where the reaction rates are taken from [200]. Reactions yielding to all the other species mentioned-above are included in the model with rate coefficients taken from the corresponding R8 and R10 reactions.

The C_2H_2 addition extends the contribution of ethynyl-naphthyl radical ($C_{10}H_6C_2H$) in building bigger PAHs by following a supplementary pathway generating dehydrophenanthrene. This reaction sequence is translated in three reaction steps: R50, R51 and R52 which are analogous respectively to the following reactions: $C_6H_4C_2H+C_2H_2 => C_{10}H_7$ [186], $C_6H_4C_2H+C_2H_2 => C_{10}H_6+H$ [186] and $C_6H_5(+M) => H+o\text{-}C_6H_4(+M)$.

$C_{10}H_6C_2H+C_2H_2 => C_{14}H_9$ (R50)

$C_{10}H_6C_2H+C_2H_2 => C_{14}H_8+H$ (R51)

$C_{14}H_9(+M) => H+C_{14}H_8$ (R52)

C_2H_2 addition to $C_6H_4C_2H$ leads to the formation of $C_6H_4(C_2H)(C_2H_2)$, which either loses an H atom to form diethynyl benzene or undergoes a six- or five-member ring closure to form 1-naphthyl or a benzofulvenyl radical, respectively. The reaction pathway as well as the corresponding reaction rates leading to benzofulvenyl (C_9H_6CH) are taken from the theoretical work by Mebel et al. [186].

The addition reactions between C_2H_2 and toluene fuel radicals, namely benzyl (C_7H_7) and methyl phenyl ($CH_3C_6H_4$), result in a variety of products. The reaction of C_7H_7 with acetylene forms indene as one of the

main products. Vereecken et al. [202] concluded this from their RRKM/ME calculations based on a density functional PES. Later, Mebel et al. [41] investigated this reaction channel and noted the formation of two bimolecular products: indene (C_9H_8) + H and 3-phenylpropyne ($C_6H_5C_3H_3P\_3$) + H. The latter one converts to C_9H_8 through H-assisted isomerization. Temperature- and pressure-dependent rate expressions for the aforementioned reactions are integrated to the current kinetic model from the theoretical work of Mebel et al. [41]. C_9H_8 can also be formed from the reaction of C_7H_6 and C_2H_2 [198]. Indene is mainly decomposed to produce indenyl (C_9H_7) radical. The rate constant of H-abstraction reaction to produce C_9H_7 is mainly taken from the model of Jin et al. [198]. Addition-elimination reaction between $CH_3C_6H_4$ and C_2H_2 forming $CH_3C_6H_4C_2H_2$+H is considered in the current model, and its rate coefficients are analogous to phenyl + C_2H_2 reaction. The consumption of $CH_3C_6H_4C_2H_2$ through unimolecular decomposition and H-abstraction reactions is considered to proceed through a similar scheme to that of toluene.

The current model also includes reactions between indenyl (C_9H_7) and acetylene producing ethynyl-indene ($C_9H_7C_2H$) and methyl naphthalene radical ($C_{10}H_7CH_2$). The corresponding rate coefficients originate from a recent kinetic model for indene pyrolysis [198].

4.3.3.3 Aromatics + C_2H_4/C_2H_3 reactions

The reaction between C_6H_5 and C_2H_4 studied by Tokmakov and Lin [196] leads to the formation of styrene ($C_6H_5C_2H_3$) along with the ipso-substitution reaction (R53) analogous to $C_6H_5CH_3$+H = C_6H_6+CH_3.

$$C_6H_5C_2H+C_2H_3 = C_6H_5C_2H_3+C_2H \quad \text{(R53)}$$

Reactions between benzyl (C_7H_7) and ethylene (C_2H_4) are considered to proceed in a similar manner as C_7H_7 + C_2H_2 reactions, leading to the formation of the cyclic species indane (C_9H_{10}) the single-chain aromatic 3-phenyl-1-propene ($C_6H_5C_3H_5$-1). The rate coefficients of C_7H_7+ C_2H_4 = C_9H_{10}+H and C_7H_7+ C_2H_4 = $C_6H_5C_3H_5$-1+H are determined through an analogy to the reactions C_7H_7+ C_2H_8 = C_9H_8+H [202] and CH_3+C_2H_4 = C_3H_6+H [146], respectively. Nevertheless, future theoretical works are highly demanded to derive accurate kinetic parameters. C_9H_{10} is consumed through H_2 elimination forming indene (C_9H_8) and ring-opening processes leading to o-vinyl-toluene ($CH_3C_6H_4C_2H_3$) and 3-phenyl-1-propene ($C_6H_5C_3H_5$-1). Rate coefficients for H_2 elimination are determined through an analogy with $C_{10}H_{10}$=> $C_{10}H_8$ +H_2. Kinetic parameters for ring-opening reactions are evaluated through analogies with the isomerization of cyclopentene to 1,3-pentadiene ($CH_3CH=CHCH=CH_2$) and 1,4-pentadiene ($CH_2=CHCH_2CH=CH_2$), respectively [203]. Addition-elimination reaction between the minor fuel radical of toluene ($CH_3C_6H_4$) and C_2H_4 forming $CH_3C_6H_4C_2H_3$+H is also considered in the current model, and its

rate coefficients are analogous to phenyl + C_2H_4 reaction. The consumption of $CH_3C_6H_4C_2H_3$ through unimolecular decomposition and H-abstraction reactions is considered to proceed through a scheme similar to that of toluene.

Moreover, the combination reactions of C_2H_4/C_2H_3 with ethynyl-naphthyl ($C_{10}H_6C_2H$)/ ethynyl-naphthalene ($C_{10}H_7C_2H$) and $C_{12}H_7$/ $C_{12}H_8$ give rise to phenanthrene ($C_{14}H_{10}$). Finally, pyrene is the product of the addition of vinyl radical to diethenylnaphthalene ($C_{10}H_6(C_2H)_2$) and $C_{14}H_8$, respectively. The mentioned C_2H_4/C_2H_3 addition reactions to phenanthrene and pyrene are introduced into the present model.

4.3.3.4 Aromatics + C_3 reactions

Mebel and coworkers derived temperature- and pressure-dependent rate coefficients for the molecule + radical reaction channels including phenyl + propyne (C_6H_5+C_3H_4-P), phenyl + allene (C_6H_5+C_3H_4-A), benzene + propargyl (C_6H_6+C_3H_3), phenyl + propylene (C_6H_5+C_3H_6) and benzene + allyl (C_6H_6+C_3H_5-A) [41], and the radical + radical reactions of phenyl + propargyl (C_6H_5+C_3H_3) [42] and phenyl + allyl (C_6H_5+C_3H_5-A) [204] by employing ab initio RRKM theory for the reaction pathways involved on C_9H_x (x = 8-11) PESs. Indene (C_9H_8), 1-phenylpropyne ($C_6H_5C_3H_3$P_1), phenylallene ($C_6H_5C_3H_3$A), 3-phenylpropyne ($C_6H_5C_3H_3$P_3) and phenylacetylene ($C_6H_5C_2H$) are the main products of the interactions between benzene (or phenyl) and C_3H_3 radical (or C_3H_4 molecules). Likewise, indane (C_9H_{10}), 1-phenylpropene ($C_6H_5C_3H_5$-1), 2-phenylpropene ($C_6H_5C_3H_5$-2) and styrene ($C_6H_5C_2H_3$) are the major outputs of the interactions between benzene (or phenyl) and C_3H_5-A radical (or C_3H_6 molecule).The reaction pathways and the corresponding kinetic parameters, reported in [41], [42], [204], are included in the current model.

The interactions between C_3 molecule/radicals and toluene fuel radicals, namely benzyl (C_7H_7) and methyl phenyl ($CH_3C_6H_4$), may arise in a variety of products. The C_7H_7+C_3H_3 recombination reaction channels have been computationally investigated at the CASPT2/cc-pVTZ//B3LYP/6-311G(d,p) level of theory by Matsugi and Miyoshi [67], and the respective rate constants have been calculated using the transition state theory. The RSRs recombination produces two $C_{10}H_{10}$ MAH isomers: 3-butynylbenzene ($C_6H_5CH_2CH_2C{\equiv}CH$, C_6H_5CCCTC) and 2,3-butadienylbenzene ($C_6H_5CH_2CH{=}C{=}CH_2$, $C_6H_5CC_VC_VC$). 1-methylene-indanyl ($C_9H_7CH_2$) radicals are formed directly through the C_7H_7+C_3H_3 reaction or via the ring closure of $C_6H_5CCVCVC$. The consumption of $C_9H_7CH_2$ results in naphthalene ($C_{10}H_8$) and its isomer benzofulvene ($C_9H_6CH_2$) which also isomerize to naphthalene. The mentioned reaction mechanisms and the kinetics represented by Chebyshev [67] are included in the current kinetic model. Other C_7+C_3 reaction systems have not been investigated through theoretical approaches, so the resulting products and the corresponding rate coefficients are assessed through analogies to similar reactions. The addition of

C_7H_7 to the triple bond of propyne (C_3H_4-P) resemble the $C_7H_7+C_2H_2$ reactions, which have been theoretically studied by Mebel et al. [41]. $C_7H_7+C_3H_4$-P reactions resulting in the formation of a cyclopenta-ring structures, $C_9H_8+CH_3$, 2-methylindene ($C_9H_7CH_3$-2) +H and 3-methylindene ($C_9H_7CH_3$-3) +H are analogous to $C_7H_7+C_2H_2= C_9H_8+H$ reaction [41]. Alternative $C_7H_7+C_3H_4$-P reaction channel can lead to side chain lengthening forming 2-butynylbenzene ($C_6H_5CH_2C{\equiv}CCH_3$, C_6H_5CCTCC). The rate coefficients of this reaction are similar to $C_7H_7+C_2H_2= C_6H_5C_3H_3P\_3+H$ reaction [41]. Besides, the formation of 1,2-dihydronaphthalene ($C_{10}H_{10}$) through $C_7H_7+C_3H_4$-P is also possible. The corresponding rate parameters are analogous to the reaction C_3H_5-A+C_3H_4-P = 1,3-cyclohexadiene(CYC_6H_8)+H. $C_6H_5C_4H_7$-1 and $C_6H_5C_4H_7$-2 are probable products of the $C_7H_7+C_3H_5$-A reaction, and their rate coefficients are taken from the C_3H_5-A+CH_3 reactions forming 1-butene (C_4H_8-1) and 2-butene (C_4H_8-2), respectively [146]. The interaction between C_7H_7 and C_3H_6 produce C_4/C_2 substituted-benzene species including $C_6H_5CH_2CH_2\dot{C}HCH_3$ ($C_6H_5C_4H_8$B), $C_6H_5CH_2CH_2CH_2\dot{C}H_2$ ($C_6H_5C_4H_8$A), $C_6H_5C_4H_7$-1, $C_6H_5C_4H_7$-2 and $C_6H_5C_2H_4$, and the rate coefficients are determined through analogies to the $CH_3+C_3H_6$ reactions forming PC_4H_9, SC_4H_9 , C_4H_8-1+H, C_4H_8-2+H and $C_2H_5+C_2H_4$, respectively [146]. $C_7H_7+C_3H_6$ = C_9H_{10}+H is also taken into account, which is analogous to the five membered ring formation process C_3H_5-A+C_3H_6 = cyclopentene (CYC_5H_8) + H [173]. Reactions between C_3 species and $CH_3C_6H_4$ involve the radical site on the benzene ring. Thus, the reaction pathways and the corresponding rate coefficients are determined through analogies to the reactions between C_6H_5 and C_3 species based on the serial theoretical works done by Mebel and coworkers [41], [42], [204]. **Table 4.1** summarizes the nature of products resulting from the interaction between C_3 and $CH_3C_6H_4$.

Table 4.1: A list of the reactions representing the interactions between $CH_3C_6H_4$ and the C_3 radicals/molecules

Reactants	Products	Analogous Reactions
$CH_3C_6H_4$ + C_3H_3	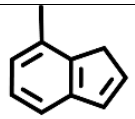 $CH_3C_9H_7$	$CH_3C_6H_4$ + C_3H_3= $CH_3C_9H_7$ Analogy to: C_6H_5 + C_3H_3= C_9H_8 [42]
	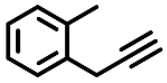 $CH_3C_6H_4C_3H_3P\_3$	$CH_3C_6H_4$ + C_3H_3= $CH_3C_6H_4C_3H_3P\_3$ Analogy to:

		$C_6H_5 + C_3H_3 = C_6H_5C_3H_3P\_3$ [42]
	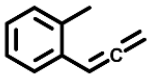 $CH_3C_6H_4C_3H_3A$	$CH_3C_6H_4 + C_3H_3 = CH_3C_6H_4C_3H_3A$ Analogy to: $C_6H_5 + C_3H_3 = C_6H_5C_3H_3A$ [42]
	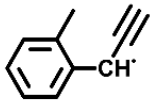 $CH_3C_6H_4C_3H_2$	$CH_3C_6H_4 + C_3H_3 = CH_3C_6H_4C_3H_2$ Analogy to: $C_6H_5 + C_3H_3 = C_6H_5C_3H_2$ [42]
$CH_3C_6H_4 + C_3H_4\text{-}P$	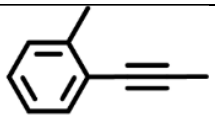 $CH_3C_6H_4C_3H_3P\_1$	$CH_3C_6H_4 + C_3H_4\text{-}P = CH_3C_6H_4C_3H_3P\_1 + H$ Analogy to: $C_6H_5 + C_3H_3\text{-}P = C_6H_5C_3H_3P\_1 + H$ [41]
	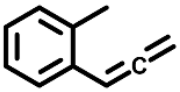 $CH_3C_6H_4C_3H_3A$	$CH_3C_6H_4 + C_3H_4\text{-}P = CH_3C_6H_4C_3H_3A + H$ Analogy to: $C_6H_5 + C_3H_3\text{-}P = C_6H_5C_3H_3A + H$ [41]
	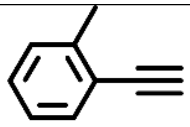 $CH_3C_6H_4C_2H$	$CH_3C_6H_4 + C_3H_4\text{-}P = CH_3C_6H_4C_2H + CH_3$ Analogy to: $C_6H_5 + C_3H_3\text{-}P = C_6H_5C_2H + CH_3$ [41]

	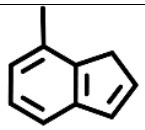 $CH_3C_9H_7$	$CH_3C_6H_4 + C_3H_4\text{-}P = CH_3C_9H_7 + H$ Analogy to: $C_6H_5 + C_3H_4\text{-}P = C_9H_8 + H$ [41]
$CH_3C_6H_4 + C_3H_4\text{-}A$	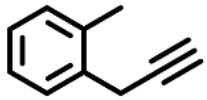 $CH_3C_6H_4C_3H_3P\_3$	$CH_3C_6H_4 + C_3H_4\text{-}A = CH_3C_6H_4C_3H_3P\_3 + H$ Analogy to: $C_6H_5 + C_3H_4\text{-}A = C_6H_5C_3H_3P\_3 + H$ [41]
	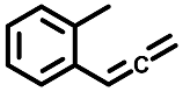 $CH_3C_6H_4C_3H_3A$	$CH_3C_6H_4 + C_3H_4\text{-}A = CH_3C_6H_4C_3H_3A + H$ Analogy to: $C_6H_5 + C_3H_4\text{-}A = C_6H_5C_3H_3A + H$ [41]
	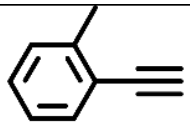 $CH_3C_6H_4C_2H$	$CH_3C_6H_4 + C_3H_4\text{-}A = CH_3C_6H_4C_2H + CH_3$ Analogy to: $C_6H_5 + C_3H_4\text{-}A = C_6H_5C_2H + CH_3$ [41]
	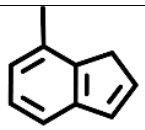 $CH_3C_9H_7$	$CH_3C_6H_4 + C_3H_4\text{-}A = CH_3C_9H_7 + H$ Analogy to: $C_6H_5 + C_3H_4\text{-}A = C_9H_8 + H$ [41]
$CH_3C_6H_4 + C_3H_5\text{-}A$	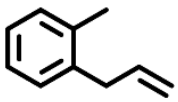 $CH_3C_6H_4C_3H_5\text{-}1$	$CH_3C_6H_4 + C_3H_5\text{-}A = CH_3C_6H_4C_3H_5\text{-}1$ Analogy to:

		$C_6H_5 + C_3H_5\text{-A} = C_6H_5C_3H_5\text{-1}$ [204]
	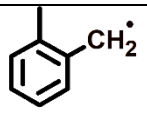 RXYLENE	$CH_3C_6H_4 + C_3H_5\text{-A} = \text{RXYLENE} + C_2H_3$ Analogy to: $C_7H_7 + C_2H_3 = \text{RXYLENE} + C_2H_3$ [204]
$CH_3C_6H_4 + C_3H_6$	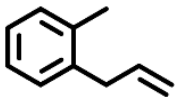 $CH_3C_6H_4C_3H_5\text{-1}$	$CH_3C_6H_4 + C_3H_6 = CH_3C_6H_4C_3H_5\text{-1} + H$ Analogy to: $C_6H_5 + C_3H_6 = C_6H_5C_3H_5\text{-1} + H$ [41]
	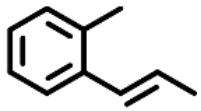 $CH_3C_6H_4C_3H_5\text{-2}$	$CH_3C_6H_4 + C_3H_6 = CH_3C_6H_4C_3H_5\text{-2} + H$ Analogy to: $C_6H_5 + C_3H_6 = C_6H_5C_3H_5\text{-2} + H$ [41]

The combination of indenyl and propargyl can eventually lead to the formation of acenaphthylene and vinylnaphthalene as proposed recently by Jin et al. [198]. The multi-step scheme for the addition of propargyl to indenyl that is employed in the present model is shown in **Scheme 4.6.**

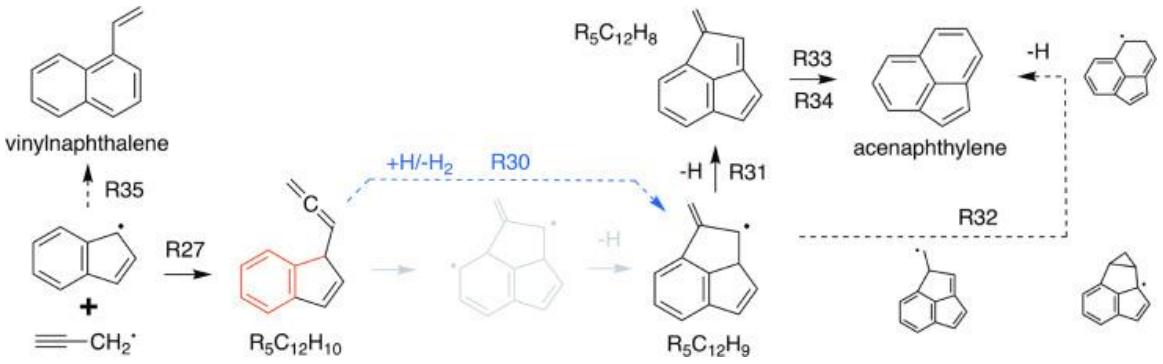

Scheme 4.6: Reaction scheme proposed for C_9H_7 + C_3H_3 *[198]*. Solid arrows represent elementary reaction steps, dashed-arrows represent multiple reaction steps. Blue dashed arrow highlights the key H-abstraction reaction step.

The interactions between naphthalene/naphthyl radicals ($C_{10}H_7$_1 and $C_{10}H_7$_2) and C_3 species result in various products. Raj et al. [17] mapped out the formation scheme of the $C_{13}H_{10}$ isomers, phenalene ($PC_{13}H_{10}$) and 1-methylene-1,2-dihydroacenaphthalene ($C_{12}H_8CH_2$), initiated by C_3H_3 addition to naphthalene and 1-naphthyl radical ($C_{10}H_7$_1). Zhao et al. [205] investigated the reaction pathways between $C_{10}H_7$_1 and C_3H_4-P/C_3H_4-A. The relevant reactions yield to the formation of ethynyl naphthalene, C_3 substituted naphthyl species, cyclopenta-ring-fused structures on the naphthyl core and $PC_{13}H_{10}$. Oleinikov et al. [206] also studied the growth mechanism of PAHs via reactions of $C_{10}H_7$_1 (or $C_{10}H_7$_2) with C_3H_4-P/C_3H_4-A. Similar reaction pathways are expected in the $C_{10}H_7$_2+C_3H_4-P/C_3H_4-A system as in the $C_{10}H_7$_1+C_3H_4-P/C_3H_4-A system, except that $PC_{13}H_{10}$ cannot be formed. Since both Zhao et al. [205] and Oleinikov et al. [206] didn't provide any reaction rate coefficients, the rate constants are adopted analogously to the reactions of phenyl radical with C_3H_4-P/C_3H_4-A from the theoretical studies by Mebel et al. [41]. Moreover, ring expansion by methylation can occur on the cyclopenta-ring fused species, $C_{10}H_7$CYC5 and $C_{10}H_7$CYC5_2, eventually forming phenanthrene ($PC_{14}H_{10}$) and anthracene ($AC_{14}H_{10}$), respectively. Such reaction pathways are estimated through analogies to the reactions of indenyl (C_9H_7) + methyl (CH_3) leading to naphthalene [41], [43]. All mentioned reaction pathways are integrated in the current kinetic model and are shown in **Scheme 4.7**.

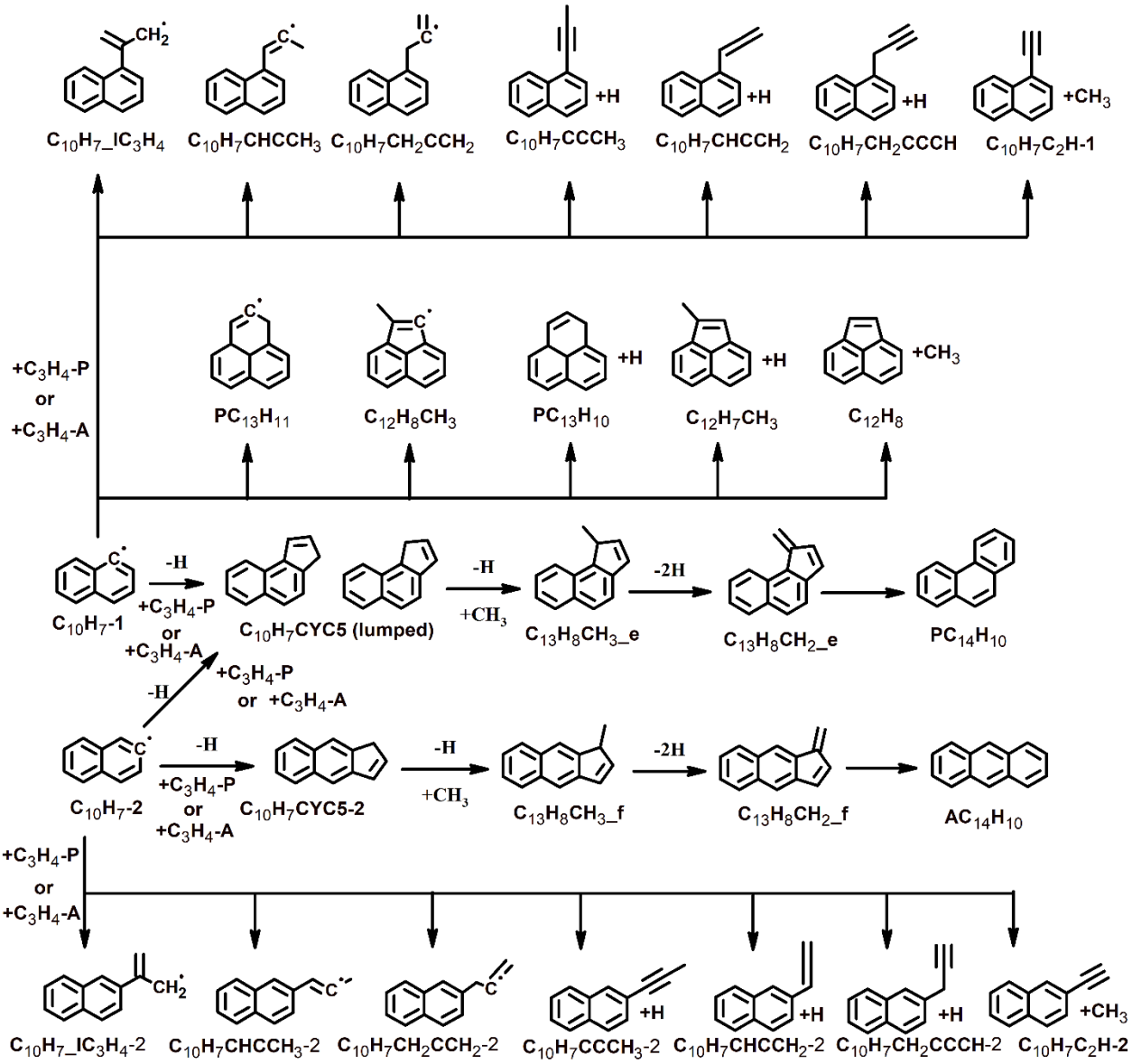

Scheme 4.7: Reactions between naphthyl radicals and propylene/allene that are incorporated in the kinetic model.

1- and 2-ethynyl naphthyl radicals may react with C_3H_4 isomers and their radical C_3H_3 forming diethynyl naphthalene and C_3 substituted ethynyl naphthyl species (**Scheme 4.8**). The corresponding rate coefficients are estimated through analogies with the reactions between C_6H_5+ C_3H_4-P/C_3H_4-A and C_6H_5+C_3H_3 [41], [42]. Acenaphthylene radicals having the radical site on the benzene ring also react with C_3H_4 isomers and their radical C_3H_3 forming ethynyl acenaphthylene, C_3 substituted ethynyl acenaphthylene species and cyclopenta-ring-fused structures on the naphthyl core (**Scheme 4.9**). Their rate coefficients are estimated through analogies to the reactions between C_6H_5+ C_3H_4-P/C_3H_4-A and C_6H_5+C_3H_3 [41], [42]. Only one of the ethynyl naphthyl radicals and acenaphthyl radicals' are considered in the **Schemes 4.8 and 4.9** for simplification purpose.

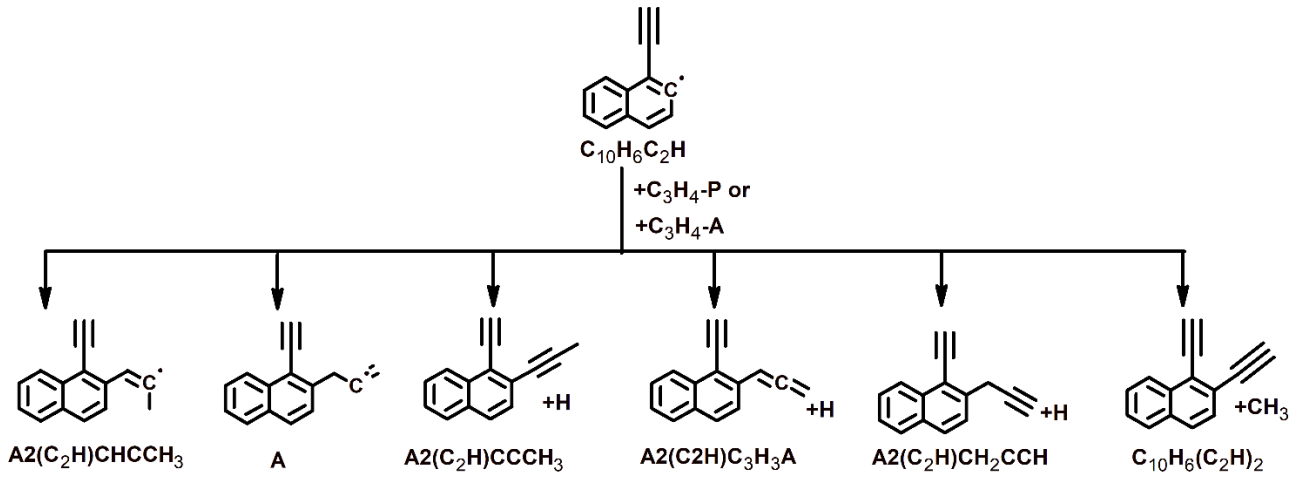

Scheme 4.8: Reactions between ethynyl naphthyl radicals and propylene/allene that are considered in the kinetic model.

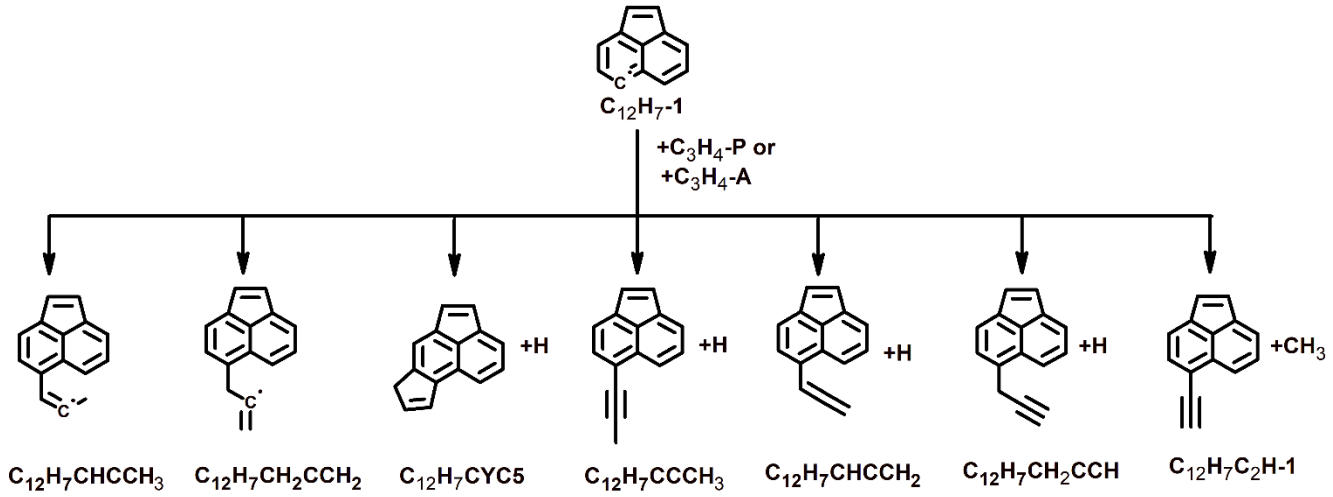

Scheme 4.9: Reactions between acenaphthyl radicals and propylene/allene that are considered in the kinetic model.

In a similar manner, the reactions of biphenyl radical ($C_{12}H_9$) and phenanthryl radical ($C_{14}H_9$) with C_3H_4-P/C_3H_4-A/C_3H_3 are added to the model. A variety of products are expected to be produced. **Scheme 4.10** shows all the reactions incorporated in the current model starting from $C_{12}H_9$/ $C_{14}H_9$ + C_3H_4-P/C_3H_4-A/C_3H_3.

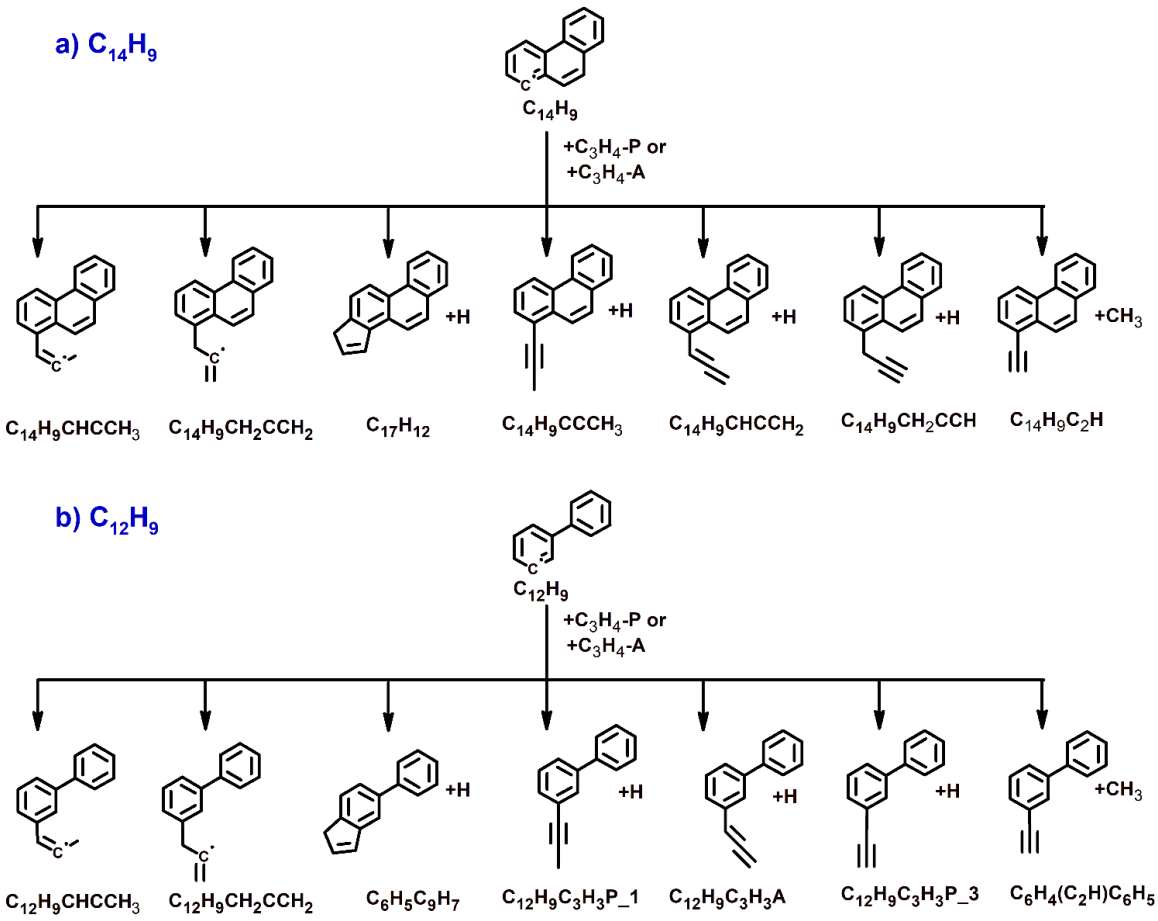

Scheme 4.10: Reactions between biphenyl radical ($C_{12}H_9$) and phenanthryl radical ($C_{14}H_9$) and propylene/allene that are considered in the kinetic model.

4.3.3.5 Aromatics + C_4H_4 reactions

The C_6H_5 + C_4H_4 reactions lead to the formation of naphthalene ($C_{10}H_8$) as well as the non-PAH $C_6H_5C_4H_3$ species. These reaction channels are considered in the current model, and their rate coefficients are taken from the theoretical work of Mebel et al. [207]. In a similar manner, the reaction between naphthyl ($C_{10}H_7$_1) radical and C_4H_4 results in phenanthrene, which is included in the current model through an analogy to C_6H_5+C_4H_4 = $C_{10}H_8$+H reaction [207].

4.3.3.6 Aromatics + C_4H_2 reactions

Reactions between C_6H_5, $C_{10}H_7$_1, $C_{10}H_7$_2 and acenaphthyl radicals and diacetylene (C_4H_2) are added to the model in an analogy to the reaction: C_6H_5+C_2H_2=$C_6H_5C_2H$+H [191]. The addition of C_4H_2 on $C_{12}H_8$ is a proposed fluoranthene formation pathway analogous with the addition of C_4H_2 on C_6H_6 to form $C_{10}H_8$ [146].

4.3.3.7 Radical-radical recombination and radical-molecule reactions

The cycloaddition/fragmentation mechanism between o-C_6H_4 and C_6H_6 through the intermediate of benzobicyclo [2, 2, 2] octatriene (BICYCLO) proposed by Comandini and Brezinsky [24] to account for the formation of $C_{10}H_8$ is adopted in the current model. C_5+C_5 reaction is another important pathway to the formation of naphthalene. Its reaction pathway (R54-R58) described by Matsugi and Miyoshi [66] is used in the current model. Furthermore, da Silva and Bozzelli [208] proposed that C_7H_5 can react with C_3H_3 to produce $C_{10}H_8$ which is also taken into consideration in the current model. The consumption of $C_{10}H_8$ occurs mainly via H-atom abstraction reactions to form 1-naphthyl and 2-naphthyl radicals. The hydrogen abstraction rate coefficient of $C_{10}H_8$ by H is updated based on the value recommended by Liu et al. [200]. The $C_{10}H_7$_1 can be converted to $C_{10}H_7$_2 through isomerization reaction. This pressure-dependent pathway was considered with rate constants taken from the work of Chu et al.[201]. Rate coefficients for the decomposition of the $C_{10}H_7$ radicals are from [209]

$C_5H_5+C_5H_5=>C_5H_5C_5H_5$ (R54)

$C_5H_5C_5H_5=C_5H_5C_5H_4+H$ (R55)

$C_5H_5C_5H_5+H=C_5H_5C_5H_4+H_2$ (R56)

$C_5H_5C_5H_5+CH_3=C_5H_5C_5H_4+CH_4$ (R57)

$C_5H_5C_5H_4=C_{10}H_8+H$ (R58)

The formation reactions of biphenyl ($C_{12}H_{10}$) include the self-combination of C_6H_5 and the reaction between C_6H_6 and C_6H_5. The rate constants of these reactions are expropriated from the experimental and theoretical work of Tranter et al. [55].The reaction between C_7H_5+C_5H_5 can also contribute to the formation of biphenyl as proposed by Yuan et al. [70].

The o-C_6H_4 self-recombination and the recombination with C_6H_5 lead to biphenylene ($C_6H_4C_6H_4$) and biphenyl radical ($C_{12}H_9$), respectively. Both $C_{12}H_9$ and $C_6H_4C_6H_4$ lead to different $C_{12}H_8$ isomers, as theoretically illustrated by Shukla et al. [25]. Reactions starting from biphenyl radical ($C_{12}H_9$) that accounts for acenaphthalene production are also proposed by Comandini et al. [26]. All these reaction pathways are integrated in the current model.

The formation reactions of $C_{13}H_{12}$ (diphenylmethane) and $C_{14}H_{14}$ (bibenzyl) include the recombination reaction of C_7H_7 + C_6H_5 and the self-recombination reaction of C_7H_7. C_7H_7 + C_6H_5 is included in the model through analogy with $_{6\ 5} + _{6\ 5} \rightarrow _{6\ 5\ 6\ 5}$, for which the theoretical pressure-dependent rate coefficients were reported by Tranter et al. [55]. The successive dehydrogenation reactions of bibenzyl leading to cis-stilbene formation, taken from [58], are considered in the present model. The

decomposition of $C_{13}H_{12}$ can produce diphenylmethyl radical ($C_{13}H_{11}$). The subsequent decomposition of $C_{13}H_{11}$ forms fluorene ($C_{13}H_{10}$). Matsugi and Miyoshi [68] studied these reactions theoretically and their calculated rate constants are used here. $C_{13}H_{10}$ can loss H-atom to produce fluorenyl radical ($C_{13}H_9$) [68] as a main decomposition route. And it can also decompose to o-C_6H_4 and C_7H_7 [68].

Lumped in the original CRECK model [146], the $C_{14}H_{10}$ isomers, phenanthrene ($PC_{14}H_{10}$) and anthracene ($AC_{14}H_{10}$), are separated. Two lumped reactions, $C_7H_7+CH_3C_6H_4 = C_{14}H_{10}+2H+H_2$ and $CH_3C_6H_4 + CH_3C_6H_4 = C_{14}H_{10}+2H+H_2$, are included in the mechanism to interpret the formation of the lumped $C_{14}H_{10}$ species. As shown in **Scheme 4.11**, the recombination steps result in two different $C_{14}H_{14}$ molecules, 2-methyldiphenylmethane and 2,2-dimethylbiphenyl. $AC_{14}H_{10}$ and $PC_{14}H_{10}$ are assigned as the products of the overall reactions starting from $CH_3C_6H_4+C_7H_7$ and $CH_3C_6H_4+ CH_3C_6H_4$, respectively. Such an assumption is based on the structural features of the corresponding $C_{14}H_{14}$ molecules, as can be noted in **Scheme 4.11**. Phenanthrene can also be produced from the reaction sequence $C_{14}H_{14} \rightarrow C_{14}H_{13} \rightarrow C_{14}H_{12} \rightarrow C_{14}H_{11} \rightarrow C_{14}H_{10}$. In this model, the rate constants of this reaction pathway are taken from the theoretical investigation of Sinha and Raj [58]. The isomerization of hydro-methylenefluorene ($C_{13}H_9CH_2$) also contribute to the formation of $C_{14}H_{10}$. $C_{13}H_9CH_2$ can be produced either from fluorenyl radical ($C_{13}H_9$) + CH_3 [66] or from the reaction of C_7H_7 and C_7H_5 [70]. Moreover, phenanthrene can isomerize to anthracene through the reaction step proposed by Colket and Seery [36].

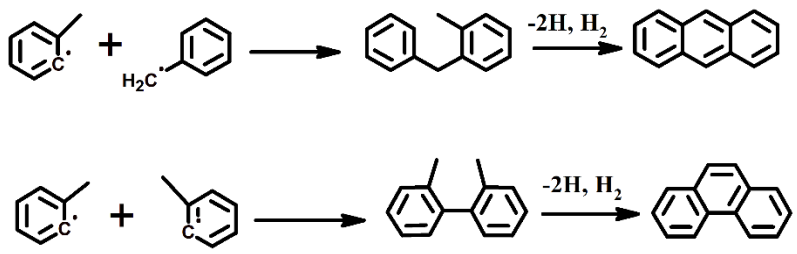

Scheme 4.11: Reaction pathways starting from toluene radicals leading to $C_{14}H_{10}$ isomers

The reactions of indenyl with benzyl leading to $C_{16}H_{10}$ and $FC_{16}H_{10}$ are added in the present model, which are adopted from the quantum chemical calculation of Sinha et al. [210]. The addition reactions of C_6H_5/C_6H_6 and o-C_6H_4 to $C_{10}H_7$ radical and $C_{10}H_6$ respectively, taken from [70], are also considered as potential fluoranthene ($FC_{16}H_{10}$) formation pathways.

5 Results and discussion

All the experimental data presented in this discussion are available online in our published articles [138], [140], [141], [193], [211]–[213] and the results are simulated by the last version of the current model [212].

5.1 Propylene and propyne pyrolysis

5.1.1 Motivation

Propylene (C_3H_6) and propyne (C_3H_4-P) are major intermediate species in the combustion of practical and surrogate fuels. Their further dissociation yields to resonantly stabilized radicals (RSRs) namely, allyl and propargyl. These radicals participate in important reaction pathways leading to the production of the first aromatic ring [166], [168], [214]–[217], which plays a vital role in the formation of PAHs and soot. On the other hand, the formed aromatics can also react with the C_3 species leading to larger PAHs [17], [41], [42], [204], [207]. In this context, it has significant importance to accurately characterize the consumption of propylene and propyne and the subsequent molecular weight growth processes. The earlier investigations done on the pyrolysis of propylene and propyne focused only on the C_3 fuel decomposition reactivity and the formation of small hydrocarbons [169], [218]–[231]. Few studies [173], [232] reported PAH speciation measurements. However, their experiments are limited to sub-atmospheric pressure conditions and narrow temperature ranges (< 1400 K). Therefore, it is essential to extend the PAH measurements to larger temperature ranges and higher pressure conditions that are more relevant to the practical operation conditions in combustion devices. Hence, high-pressure (~20 bar) shock tube pyrolysis experiments of propylene and propyne are carried out over a temperature range of 1050–1650 K. Two argon-diluted experimental mixtures separately contain 518 ppm propylene and 509 ppm propyne are used to obtain the quantitative speciation measurements that provide crucial evidence in proposing the corresponding pyrolytic reaction schemes. The fuels contain impurities which are 2 ppm propane in propylene pyrolysis and 4.5 ppm 2-butene and 3.5 ppm iso-butane in propyne pyrolysis. It is important to underline that these impurities are considered in the simulation of the experimental profiles.

5.1.2 Fuels decomposition and the formation of small hydrocarbons

Figure 5.1 shows the fuel mole fraction profiles as a function of T_5. **Figures 5.2 and 5.3** present the results for small hydrocarbon species in propylene and propyne pyrolysis, respectively. As seen in **Figures 5.1-5.3**, the simulations with the present model using two different methods (constant P_5 – 1st method; measured pressure profile up to 10 ms – 2nd method) can well reproduce the fuel consumption and the formation and the decomposition of most SHCs. Recent kinetic models, including the

NUIMech1.0 updated by Nagaraja et al. [230] and Planography et al. [231] for the combustion of propylene and propyne, respectively, and the LLNL PAH model reported by Shao et al. [123] , are also used to simulate the current experiments for comparison purpose.

Propylene decay follows a smooth curve, while propyne decomposition exhibits two consumption stages at distinct rates. To reveal the major fuel consumption pathways, ROP analyses for propylene and propyne decomposition are performed at 1300 K and 1400 K (see **Figure 5.4**). The chemically activated reaction H + C_3H_6 = CH_3 + C_2H_4 accounts about 40% of propylene consumption, while the contribution of the other three channels varies in the range of 10-20%, at both analyzed temperatures. Because of the high production of CH_3, the H-abstraction reaction by CH_3 is the second important channel responsible for C_3H_6 consumption at 1300 K. The contribution of C-H bond fission and H-abstraction by H reactions forming ally radical (C_3H_5-A) increases at 1400 K. For propyne, its decomposition scheme is more sensitive to temperature. At low temperatures, propyne decomposition is dominantly initiated by its isomerization to allene (C_3H_4-A), which corresponds to the first stage. At high temperatures (i.e. second stage), the unimolecular decomposition reaction C_3H_4-P = C_3H_3 + H releases hydrogen atoms, so that the addition-elimination reaction H + C_3H_4-P = CH_3 +C_2H_2 governs C_3H_4-P consumption, and its contribution exceeds the isomerization reaction (C_3H_4-P = C_3H_4-A) above 1430 K.

Small hydrocarbons are either formed directly through the fuel consumption pathways or through subsequent reactions. The remarkable mole fractions of methane (CH_4) and ethane (C_2H_6) in propylene pyrolysis (**Figure 5.2 a, d**) arise from the abundant CH_3 production via H + C_3H_6 = CH_3 + C_2H_4 reaction, which also accounts for the significant amount of ethylene (C_2H_4) (**Figure 5.2 c**). Likewise, CH_4 and C_2H_6 in propyne pyrolysis (**Figure 5.3 a, d**) derive from the significant CH_3 production via H + C_3H_4-P= CH_3 + C_2H_2, which also accounts for the abundance of acetylene (C_2H_2) (**Figure 5.3 b**). Approximately 40% of C_3H_6 is converted to allyl radicals through various abstraction and unimolecular initiation reactions, which primarily decompose to allene. This subsequently isomerizes to propyne or undergoes H-atom abstraction reactions to produce propargyl radicals. Since propyne is observed to be an important intermediate in propylene pyrolysis (**Figure 5.2 e**), all small species detected in propyne are also seen in the species pool of propylene pyrolysis. In propyne pyrolysis, C_3H_4-A formation (**Figure 5.3 e**) synchronizes with the first stage (1100-1300 K) of C_3H_4-P consumption. This shows that the isomerization is faster than the decomposition, and that it is predominant at the low temperatures. Acetylene is formed by the decomposition of vinyl radicals, the reaction of H atoms with allene and propyne, and β-scission of propen-1-yl radical in propylene pyrolysis. The butene isomers and cyclopentadiene (CY-C_5H_6) are only observed in propylene pyrolysis. 1-butene (1-C_4H_8) (**Figure 5.2 m**) is mainly formed via C_3H_5-A + CH_3 recombination reaction and the reverse reaction of 1-C_4H_8 + H =

$C_3H_6 + CH_3$. The latter channel ($C_3H_6 + CH_3$) also leads to the formation of 2-butene (2-C_4H_8) (**Figure 5.2 n**) and iso-butene (i-C_4H_8) (**Figure 5.2 o**). 15% of 1-C_4H_8 is formed during the quenching period, while the formation of the two other isomers (2-C_4H_8 and i-C_4H_8) is completed during the reaction time of 4ms. This is because the C_3H_5-A + CH_3 recombination reaction continues even after the arrival of the rarefaction wave. CY-C_5H_6 (**Figure 5.2 p**) is mainly produced through the dehydrogenation of cyclopentene (CYC_5H_8). 3-pentadiene (LC_5H_8), formed via $LC_5H_8 + H = C_3H_6 + C_2H_3$ reaction, isomerizes to CYC_5H_8. Four C_4H_6 isomers, including 1-butyne (1-C_4H_6), 2-butyne (2-C_4H_6), 1,2-butadiene (1,2-C_4H_6) and 1,3-butadiene (1,3-C_4H_6) are observed in both propylene and propyne pyrolysis. Quantitative mole fraction profiles for C_4H_6 isomers are scarcely reported in previous studies concerning propylene and propyne pyrolysis. 1,3-C_4H_6 has the highest peak mole fraction among the other three isomers (**Figure 5.2 i and Figure 5.3 i**). The current model can well capture 1,3-C_4H_6 profiles; however, discrepancies exist between the experimental and simulated speciation profiles for the three other minor isomers. **Scheme 5.1** displays the formation pathways of the C_4H_6 isomers based on ROP analyses performed at 1400 K. Reactions between CH_3 and C_3 molecules/radicals (C_3H_4-P, C_3H_4-A and C_3H_3) govern the formation of C_4H_6 isomers. 1,2-C_4H_6 is mainly formed through $CH_3 + C_3H_3$ reaction, which explains the higher simulated mole fraction profile using the pressure profiles as reactions involving resonantly stabilized radicals can potentially proceed during the post-shock quenching process. 1,3-C_4H_6 largely relies on the isomerization reactions of 1,2-C_4H_6. In propylene pyrolysis, the consumption of 1-C_4H_8 through dehydrogenation and H-atom abstraction by H atoms and CH_3 radicals leads to the formation of 1,3-C_4H_6 and 1-buten-3-yl ($C_4H_7$1–3) radicals, respectively. $C_4H_7$1–3 radicals in turn produce 1,3- butadiene via β-scission. Though 1-C_4H_8 is absent from the products pool of propyne pyrolysis, 6% of 1,3-C_4H_6 is produced through $C_4H_7$1–3 decomposition, which alternatively comes from the 2-C_4H_8 impurity. The formation of 1-C_4H_6 and 2-C_4H_6 largely depends on the isomerization reaction of 1,2-C_4H_6 and C_3H_4-P + CH_3 recombination reaction in propylene and propyne pyrolysis, respectively. Vinylacetylene (C_4H_4) and diacetylene (C_4H_2) are formed from C_3H_4-P and C_3H_4-A, via the sequence 1,2-C_4H_6 →1,3-C_4H_6 → i-C_4H_5 →C_4H_4 →C_4H_3 →C_4H_2.

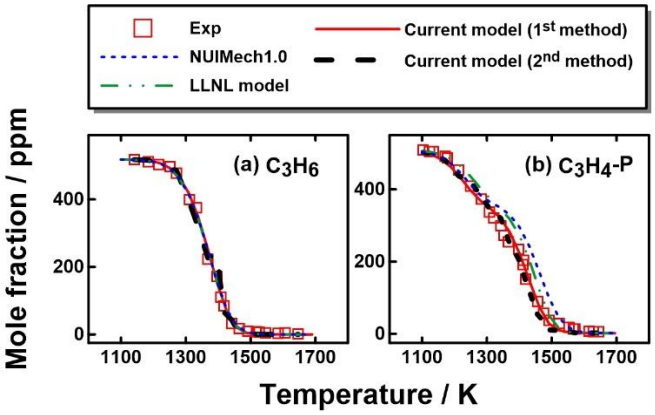

Figure 5.1: Measured (symbols) and simulated (lines) fuel mole fraction profiles as a function of T_5 in (a) propylene pyrolysis and (b) propyne pyrolysis. Thick solid red lines: simulations using the current kinetic model with the constant p_5 of 20 bar and the nominal reaction time of 4 ms; thick dashed black lines: simulations using the current model with measured pressure profiles up to 10 ms; thin dashed blue lines: simulations using the NUIMech1.0 (for propylene *[230]* and for propyne *[231]*) with the constant p_5 of 20 bar and the nominal reaction time of 4 ms; thin dot dashed green lines: simulations using the LLNL PAH model *[123]* with constant p_5 of 20 bar and the nominal reaction time of 4 ms.

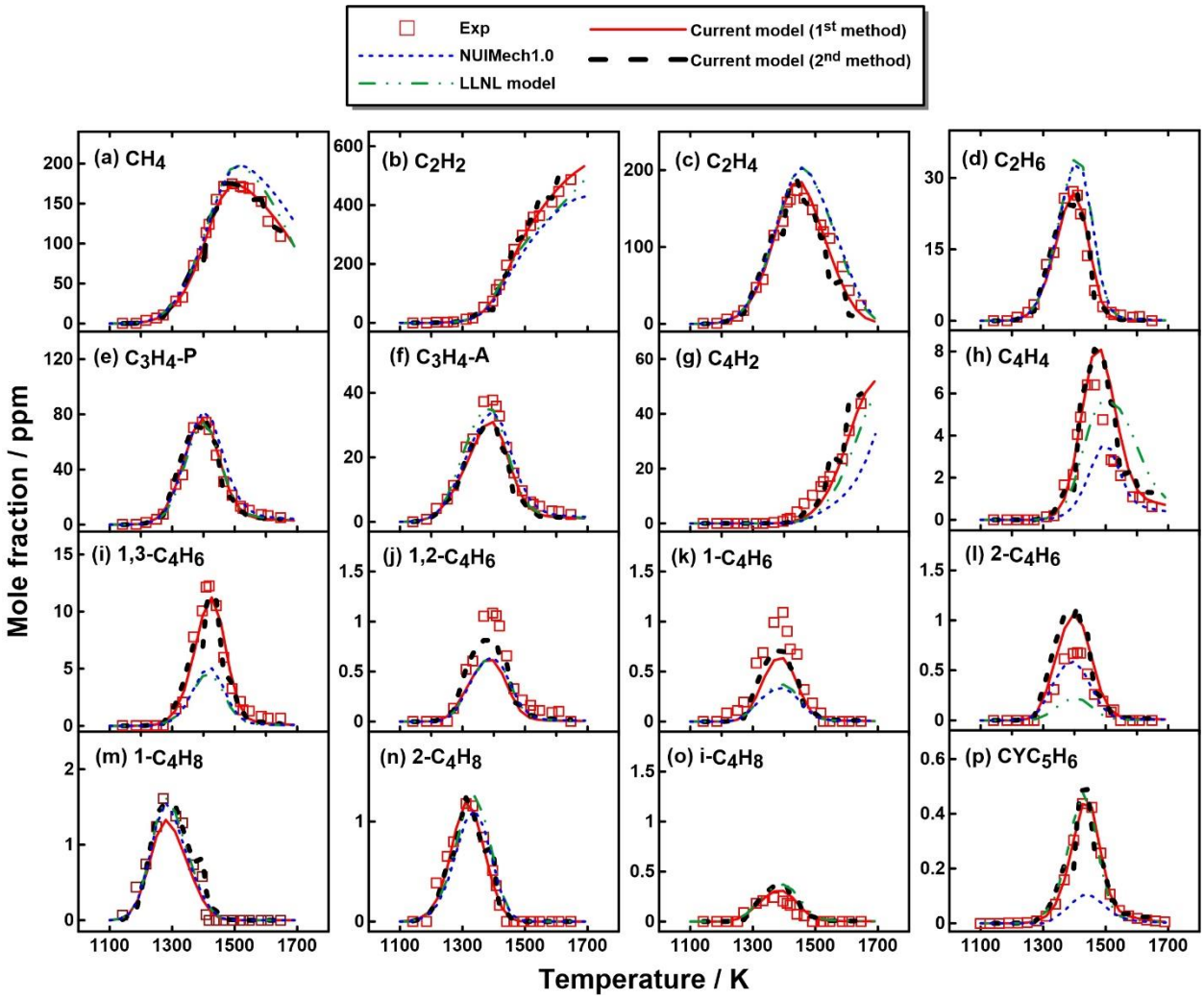

Figure 5.2: Measured (symbols) and simulated (lines) small intermediates mole fraction profiles as a function of T_5 in propylene pyrolysis. Thick solid red lines: simulations using the current kinetic model with the constant p_5 of 20 bar and the nominal reaction time of 4 ms; thick dashed black lines: simulations using the current model with measured pressure profiles up to 10 ms; thin dashed blue lines: simulations using the NUIMech1.0 *[230]* with the constant p_5 of 20 bar and the nominal reaction time of 4 ms; thin dot dashed green lines: simulations using the LLNL PAH model *[123]* with constant p_5 of 20 bar and the nominal reaction time of 4 ms.

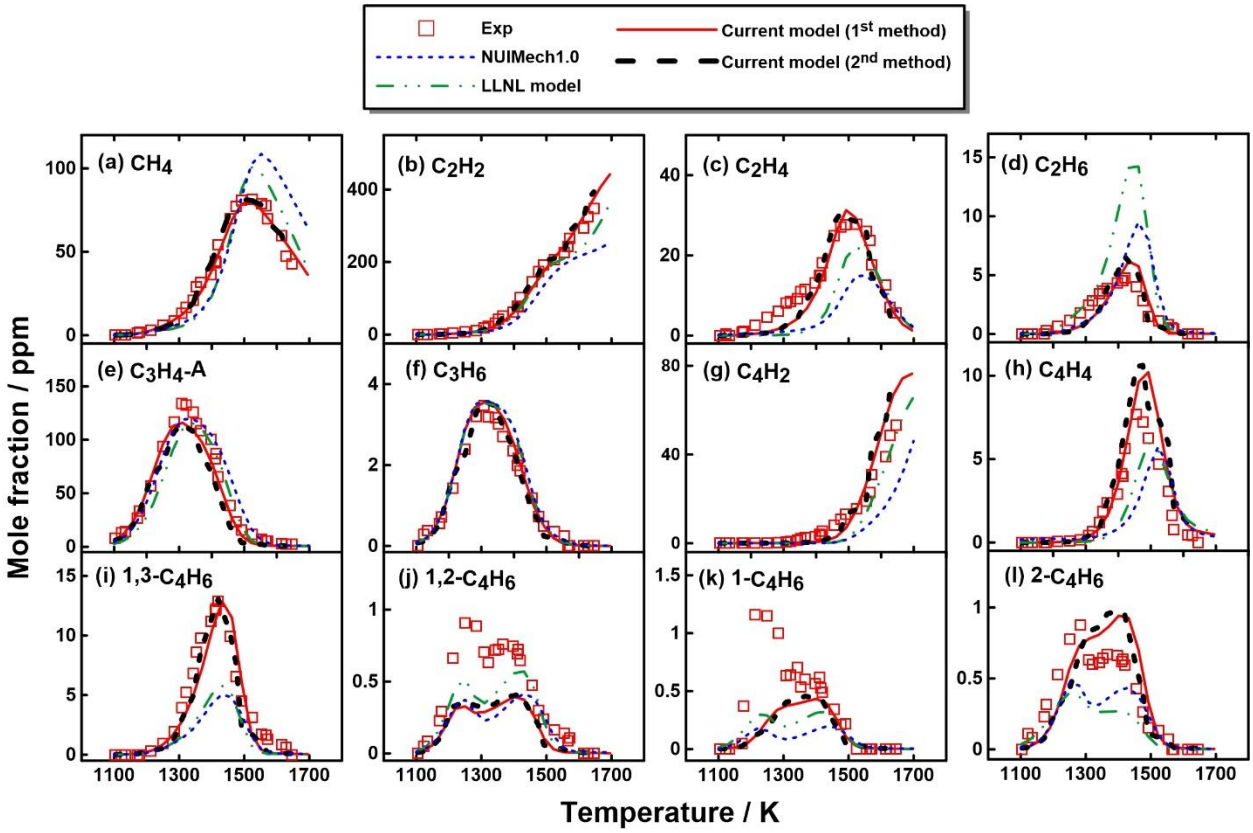

Figure 5.3: Measured (symbols) and simulated (lines) small intermediates mole fraction profiles as a function of T_5 in propyne pyrolysis. Thick solid red lines: simulations using the current kinetic model with the constant p_5 of 20 bar and the nominal reaction time of 4 ms; thick dashed black lines: simulations using the current model with measured pressure profiles up to 10 ms; thin dashed blue lines: simulations using the NUIMech1.0 *[231]* with the constant p_5 of 20 bar and the nominal reaction time of 4 ms; thin dot dashed green lines: simulations using the LLNL PAH model *[123]* with constant p_5 of 20 bar and the nominal reaction time of 4 ms.

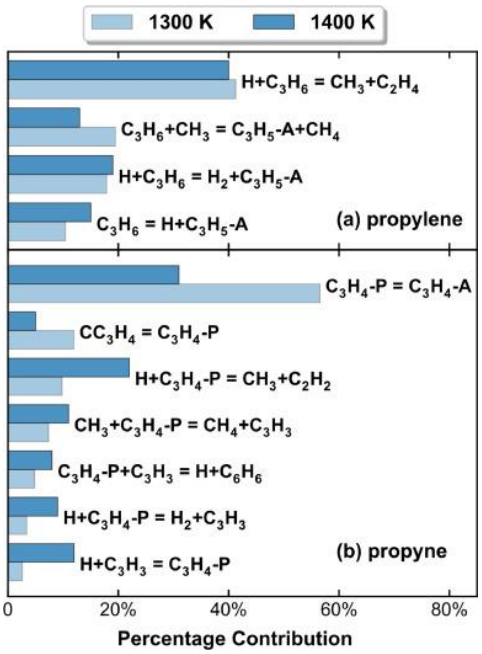

Figure 5.4: Major fuel consumption pathways at T_5 of 1300 K and 1400 K based on integrated ROP analyses results.

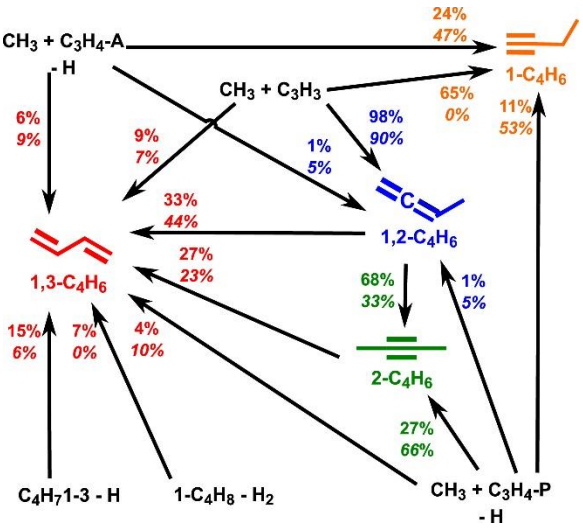

Scheme 5.1. Formation pathways of C_4H_6 isomers at T_5 = 1400 K. The percentage numbers (normal font: in propylene pyrolysis; italic font: in propyne pyrolysis) represent the contributions of corresponding reactions to the formation of C_4H_6 isomers.

5.1.3 Formation of the first aromatic ring

Particular attention has been devoted to the formation of the single-ring aromatics from small aliphatic fuels. In particular, much work has been done to determine the reaction pathways leading to benzene formation. **Figure 5.5** presents the mole fraction profiles of benzene and its isomer fulvene in propylene

and propyne pyrolysis. The experimentally measured species are well predicted by the current model. The measured pressure profiles has no obvious influence on the peak values of the predicted benzene and fulvene mole fractions. Fulvene is formed at lower temperatures compared to benzene, which suggests its role as a precursor of benzene. The ratios between fulvene and benzene peak mole fractions are 0.031 and 0.035 in propylene and propyne pyrolysis, respectively. Hansen et al. [233] referred to the strong linear correlation between the mole fractions of these two isomers in low-pressure premixed flames, which is also valid in this study.

In both analyzed cases, C_3H_3 self-recombination is the major source of fulvene. Another minor pathway through C_3H_5-A + C_3H_3 = FULVENE + 2H leads to fulvene production in propylene pyrolysis. Fulvene consumption can reproduce benzene, through fulvene ↔ C_6H_6 and fulvene + H ↔ C_6H_6 + H reactions. However, the C_3H_3 self-recombination is one of the key sources leading directly to benzene formation for both studied cases. Besides, the C_3H_4-A+C_3H_3 reaction, and the fragmentation/isomerization of $C_5H_5CH_2$-1 and $C_5H_5CH_2$-2 also contribute to benzene formation. The higher-temperature formation window and the three-fold peak difference between fulvene and benzene in propylene and propyne pyrolysis follow two major reasons:

(i) The belatedly C_3 molecules/radicals (C_3H_4-P, C_3H_4-A and C_3H_3) production from propylene as it requires step-wise dehydrogenation.

(ii) The addition-elimination reaction H + C_3H_6 = CH_3 + C_2H_4 competes with the hydrogen abstraction channel leading to C_3.

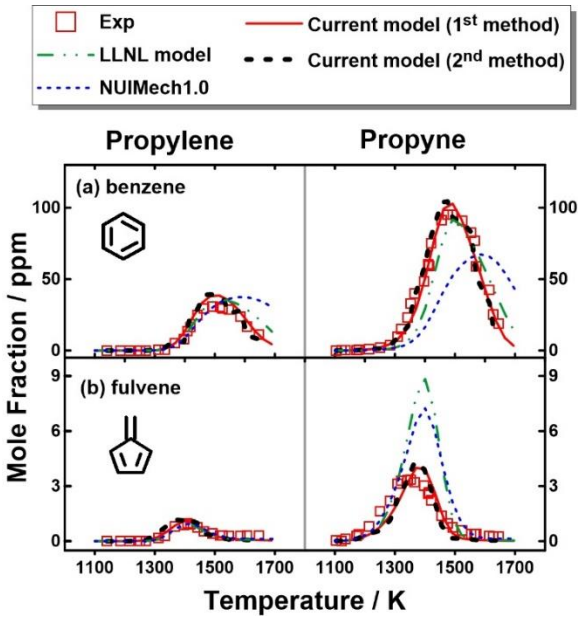

Figure 5.5: Measured (symbols) and simulated (lines) benzene and fulvene mole fraction profiles as a function of T_5 in propylene pyrolysis and propyne pyrolysis. Thick solid red lines: simulations using the current kinetic model with the constant p_5 of 20 bar and the nominal reaction time of 4 ms; thick dashed black lines: simulations using the current model with measured pressure profiles up to 10 ms; thin dashed blue lines: simulations using the NUIMech1.0 (for propylene *[230]* and for propyne *[231]*) with the constant p_5 of 20 bar and the nominal reaction time of 4 ms; thin dot dashed green lines: simulations using the LLNL PAH model *[123]* with constant p_5 of 20 bar and the nominal reaction time of 4 ms.

Figure 5.6 shows the major monocyclic aromatic hydrocarbons (MAHs) detected in propylene and propyne pyrolysis including toluene (C_7H_8), phenylacetylene ($C_6H_5C_2H$) and styrene ($C_6H_5C_2H_3$). The measured mole fractions for these species, as well as simulations with two different methods and different models are also presented. C_7H_8 and $C_6H_5C_2H$ are more abundant in propyne pyrolysis, while $C_6H_5C_2H_3$ has relatively similar mole fractions in the two investigated cases. The reactions that account for the formation of the MAHs are similar in both propylene and propyne pyrolysis. C_7H_8 has two major sources: the recombination of C_3H_3 with but-2-yn-1-yl radical ($\dot{C}H_2CCCH_3$) and the reactions between benzene/phenyl and CH_3 ($H+C_7H_8 = CH_3+C_6H_6$, $C_7H_8 (+M) = CH_3+C_6H_5 (+M)$). The latter pathway is more significant at high temperatures. The formation of $C_6H_5C_2H$ and $C_6H_5C_2H_3$ mostly relies on the $C_6H_5 + C_2H_2$ and $C_6H_5 + C_2H_4$ reactions, respectively. The higher production of benzene, and thus phenyl, accounts for the higher mole fractions of C_7H_8 and $C_6H_5C_2H$ in propyne pyrolysis. However, the limited quantity of C_2H_4 in propyne pyrolysis compared to propylene limits the $C_6H_5C_2H_3$ formation, as can be noted in **Figures 5.2 c and 5.3 c**.

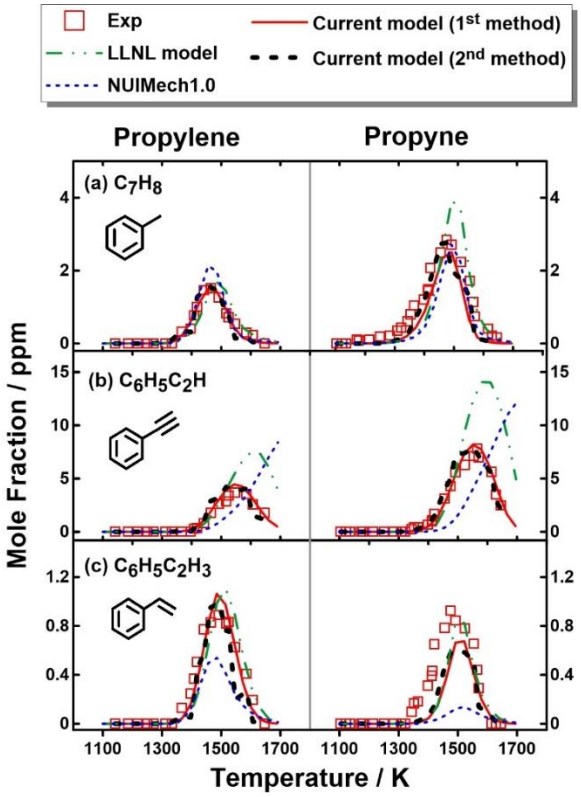

Figure 5.6: Measured (symbols) and simulated (lines) MAHs mole fraction profiles as a function of T_5 in propylene pyrolysis and propyne pyrolysis. Thick solid red lines: simulations using the current kinetic model with the constant p_5 of 20 bar and the nominal reaction time of 4 ms; thick dashed black lines: simulations using the current model with measured pressure profiles up to 10 ms; thin dashed blue lines: simulations using the NUIMech1.0 (for propylene *[230]* and for propyne *[231]*) with the constant p_5 of 20 bar and the nominal reaction time of 4 ms; thin dot dashed green lines: simulations using the LLNL PAH model *[123]* with constant p_5 of 20 bar and the nominal reaction time of 4 ms.

5.1.4 PAH speciation

C_3 fuels are major intermediate species in the pyrolysis of heavier hydrocarbon fuels, and they can decompose to propargyl radicals which can re-combine to form benzene and subsequently larger poly-aromatic hydrocarbons and soot. Thus, providing a deeper insight into the growth of PAHs from the species pools of propylene and propyne pyrolysis is imperative. Quantitative measurements on PAH speciation are scarcely available in the prior studies in the literature on C_3 fuels. However, in this work, a large number of two- to four- ring PAHs are identified and quantified in both propylene and propyne pyrolysis. **Figure 5.7** shows the carbon recovery for the two experimental sets with and without considering the PAHs. Integrating the PAHs helps in achieving a better carbon recovery, in particular, at high temperatures above 1400 K. It is important to note that the PAHs considered here refer to those identified and quantified in the current experiments. There are several PAH peaks that are detected, but either their structure couldn't be distinguished or their calibration factor couldn't be obtained in an

accurate way (species larger than four-ring). The carbon balance would be further improved if all the gas-phase species could be taken into consideration. A much better carbon recovery (with a minimum of 90%) is encountered in propylene pyrolysis in comparison with propyne pyrolysis for similar conditions. This suggests the propensity of propyne to form larger PAHs and eventually soot.

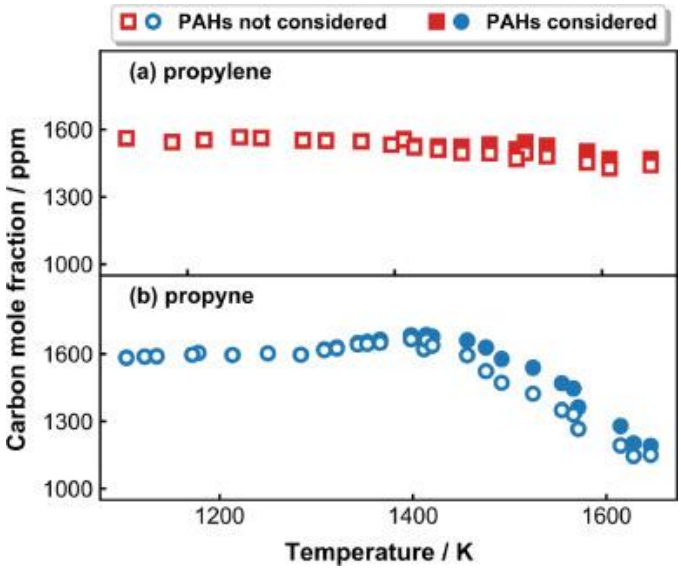

Figure 5.7: Carbon recovery with and without considering the PAH species in the current experiments of (a) propylene pyrolysis and (b) propyne pyrolysis.

Scheme 5.2 shows the major reactions identified based on ROP analyses at 1550 K for the major PAH species measured in this work and the relative contribution of each reaction. The relevant details will be discussed later in this section.

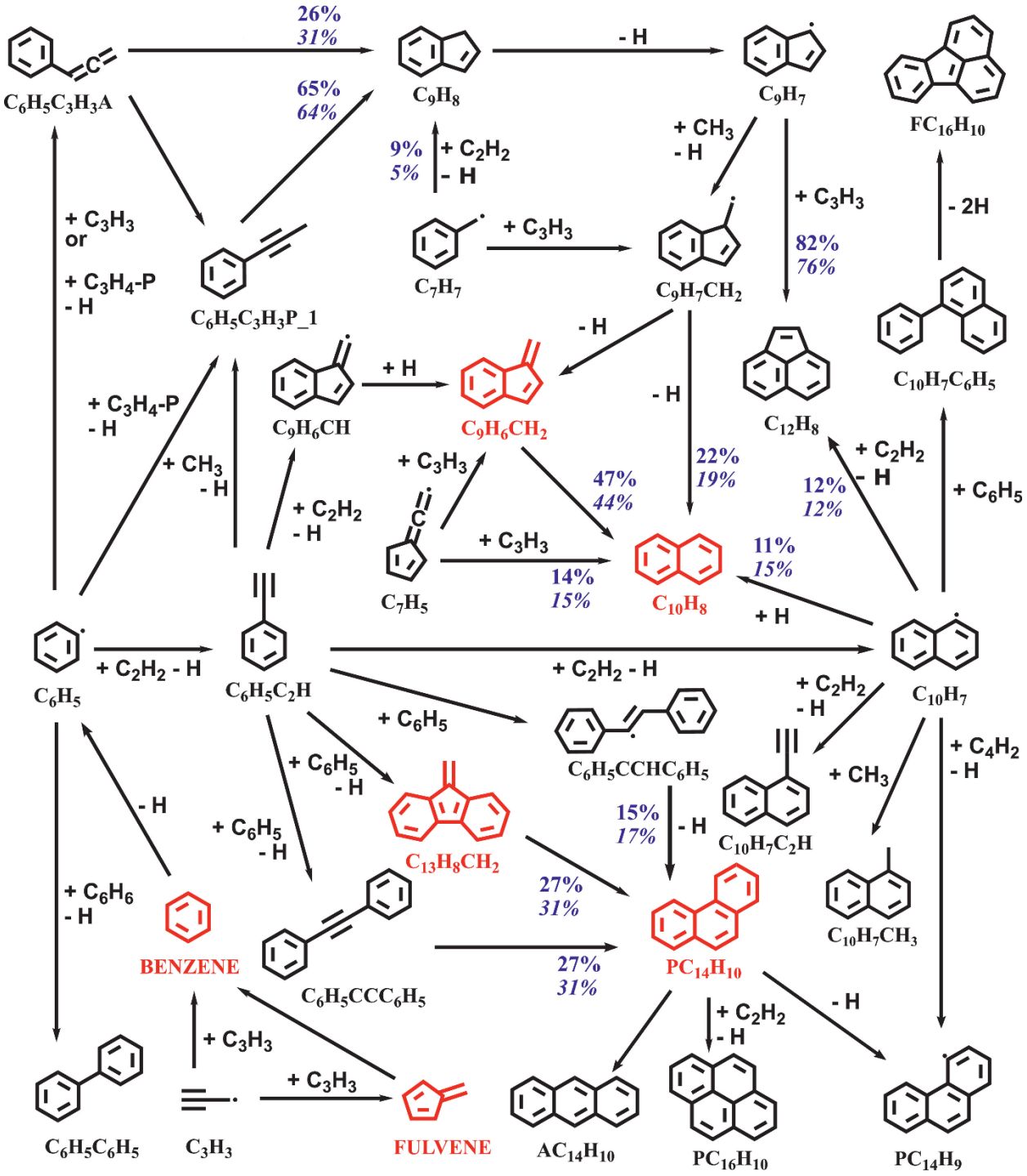

Scheme 5.2: Major PAH formation pathways in propylene and propyne pyrolysis based on ROP analyses at 1550 K. The percentage numbers (normal font: in propylene pyrolysis; italic font: in propyne pyrolysis) represent the contribution of corresponding reactions to the formation of important PAHs.

Formed through the C_6+C_3 reactions, indene is expected to be one of the most abundant PAH species following the production of benzene. **Figure 5.8** shows the comparison of experimental and simulated

mole fraction profiles of indene (C_9H_8) as well as its non-PAH isomers for the temperature range investigated in the present experiments. 1-phenyl-propyne ($C_6H_5CCCH_3$, $C_6H_5C_3H_3P\_1$) is detected in both sets, whereas phenyl-allene ($C_6H_5CHCCH_2$, $C_6H_5C_3H_3A$) is only detected in propyne pyrolysis. The current kinetic model can successfully capture the measured mole fraction distributions of the C_9H_8 isomers. This is due to the inclusion of the theoretical rate coefficients reported in a series of works of Mebel and coworkers [42], [204], [207] on C_9H_9 PES. Although Mebel et al. [41] calculations predicted that 1-phenyl-propyne and phenyl allene are the major C_6+C_3 reaction products, C_9H_8 is much more abundant than $C_6H_5C_3H_3P\_1$ and $C_6H_5C_3H_3A$. $C_6H_5C_3H_3P\_1$ is mainly formed through C_3H_4-P+C_6H_5 and $C_6H_5C_2H$+CH_3 molecule+radical reactions. $C_6H_5C_2H$+CH_3 channel is predominant at high temperatures. $C_6H_5C_3H_3A$ is mainly produced from the recombination reaction of phenyl radical with propargyl radical. The reaction C_3H_4-P+C_6H_5 = $C_6H_5C_3H_3A$+H also contributes to $C_6H_5C_3H_3A$ in propyne pyrolysis at moderate temperatures (1300–1400 K). Regarding indene formation, it is mainly produced from the unimolecular isomerization of both $C_6H_5C_3H_3P\_1$ and $C_6H_5C_3H_3A$ as seen in **scheme 5.2**. Small amounts of indene are formed through C_7H_7 + C_2H_2 channel. As can be seen in **Figure 5.8**, indene formation sustains during the post-shock quenching. This is due to two reasons: (i) $C_6H_5C_3H_3A$ isomerization to indene (the simulated mole fractions decrease when using the pressure profile up to 10 ms); (ii) isomerization of $C_6H_5C_3H_3P\_1$ to indene. 3-phenyl-propyne ($C_6H_5CH_2CCH$, $C_6H_5C_3H_3P\_3$) is not detected in the current experiments, though it is considered to be a major bimolecular product of C_6H_5+C_3H_4-A reactions [41]. The simulated peak mole fractions of $C_6H_5C_3H_3P\_3$ are 0.01 ppm and 0.05 ppm in propylene and propyne pyrolysis, respectively, which are lower than those of $C_6H_5C_3H_3P\_1$ and $C_6H_5C_3H_3A$.

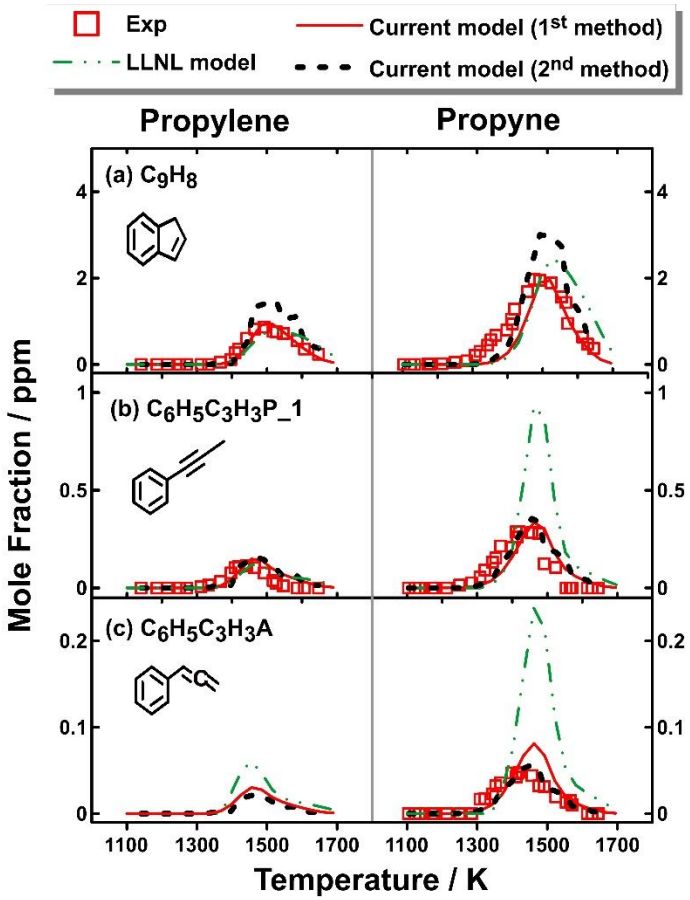

Figure 5.8: Measured (symbols) and simulated (lines) mole fraction profiles for C_9H_8 isomers as a function of T_5 in propylene and propyne pyrolysis. Thick solid red lines: simulations using the current kinetic model with the constant p_5 of 20 bar and the nominal reaction time of 4 ms; thick dashed black lines: simulations using the current model with measured pressure profiles up to 10 ms; thin dot dashed green lines: simulations using the LLNL PAH model *[123]* with constant p_5 of 20 bar and the nominal reaction time of 4 ms.

The consumption of C_9H_8 mainly produces indenyl radical (C_9H_7) through H-abstraction and unimolecular decomposition. The resulting C_9H_7 plays an important role in PAH growth in both propylene and propyne pyrolysis. The reactions of C_9H_7 with CH_3 and C_3H_3 are vital pathways to naphthalene and acenaphthylene formation, respectively (see **Scheme 5.2**). The mole fraction profiles of naphthalene ($C_{10}H_8$) and its isomer benzofulvene ($C_9H_6CH_2$) are shown in **Figure 5.9**. Overall, the current model can well predict the $C_{10}H_8$ isomers with the two different methods. Benzofulvene is formed at lower temperatures compared to naphthalene, which suggests its role as naphthalene precursor. The main formation pathways of both $C_{10}H_8$ and $C_9H_6CH_2$ are:

(i) The decomposition of methyl-indene radical ($C_9H_7CH_2$) following the production of methyl-indene ($C_9H_7CH_3$) that comes from C_9H_7+CH_3 recombination.

(ii) The recombination between fulvenallyl (C_7H_5) and C_3H_3, where C_7H_5 mainly comes from benzyl (C_7H_7) decomposition and the C_3H_3+C_4H_2 recombination reaction.

(iii) The HACA route through phenylacetylene radical ($C_6H_4C_2H$) leading to benzofulvenyl (C_9H_6CH) and naphthyl ($C_{10}H_7$) radicals which reacts with H to form benzofulvene and naphthalene, respectively.

The relative importance of the above-mentioned channels varies with the temperature, and the last one (iii) has relatively high significance at elevated temperatures. Other minor reaction pathways like C_6H_6 + C_4H_2 and o-C_6H_4 + C_4H_4 recombination reactions contribute to naphthalene and benzofulvene formation, respectively.

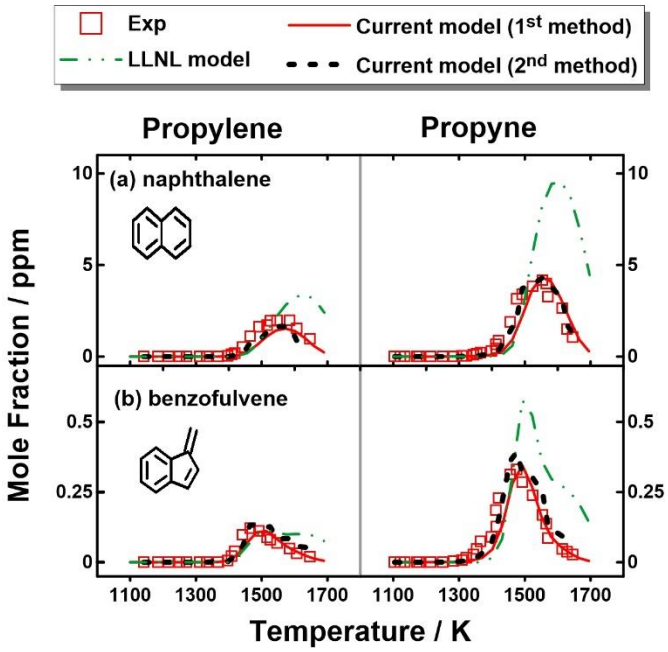

Figure 5.9: Measured (symbols) and simulated (lines) mole fraction profiles for $C_{10}H_8$ isomers as a function of T_5 in propylene and propyne pyrolysis. Thick solid red lines: simulations using the current kinetic model with the constant p_5 of 20 bar and the nominal reaction time of 4 ms; thick dashed black lines: simulations using the current model with measured pressure profiles up to 10 ms; thin dot dashed green lines: simulations using the LLNL PAH model *[123]* with constant p_5 of 20 bar and the nominal reaction time of 4 ms.

Different C_{10}-C_{13} PAHs including 1-methyl-indene ($C_9H_7CH_3$-1), 1-methyl naphthalene ($C_{10}H_7CH_3$_1), biphenyl ($C_6H_5C_6H_5$), 1-ethynyl-naphthalene ($C_{10}H_7C_2H$_1), acenaphthylene ($C_{12}H_8$) and fluorene ($C_{13}H_{10}$) are detected in propylene and propyne pyrolysis. Their mole fraction profiles as well as their simulated results are demonstrated in **Figure 5.10**. All shown PAHs have higher peak concentration in propyne pyrolysis due to the different benzene/phenyl mole fractions in propylene and propyne pyrolysis.

C_9H_7 + CH_3 recombination reaction is the predominant source of $C_9H_7CH_3$-1, benzofulvene-naphthalene precursor. The majority of $C_9H_7CH_3$-1formation takes place during the post-shock quenching. C_6H_6+C_6H_5 = $C_6H_5C_6H_5$+H controls the formation of $C_6H_5C_6H_5$. In addition, the reaction between phenyl-propargyl radical ($C_6H_5C_3H_2$, $C_6H_5CC\dot{C}H_2$) and C_3H_3 contributes 2% in biphenyl production in both experimental sets. $C_{10}H_7CH_3$_1 and $C_{10}H_7C_2H$_1 are mainly produced by the reaction of the naphthyl radical ($C_{10}H_7$_1) radical with CH_3 and C_2H_2, respectively. The $C_{10}H_7$_1 + C_3H_4-P reaction also accounts for a small part of $C_{10}H_7C_2H$_1 production (3% in propyne pyrolysis and 1 % in propylene pyrolysis at 1500 K); not shown in **scheme 5.2**. Acenaphthylene is an abundant PAH in both studied cases (see **Figure 5.10** (e)). Three pathways contribute to its formation: i) the recombination of C_9H_7 and C_3H_3 which eventually lead to the formation of acenaphthylene as proposed recently by Jin et al. [198]; ii) the isomerization of biphenyl radical ($C_{12}H_9$) through BENZO intermediate [25], [26]; iii) the C_2H_2 addition to $C_{10}H_7$_1 (HACA). The former channel is the governing pathway, while the second one and the last one have a limited contribution of 5% and 12% at 1550 K, respectively (see **scheme 5.2**). Acenaphthylene peak increases by 20% when the results are simulated using pressure profiles up to 10 ms. This mainly originates from the recombination reaction between the resonantly stabilized radicals C_9H_7 and C_3H_3. The dominant formation pathways for $C_{13}H_{10}$ in these two investigated sets are the addition reactions of C_3H_4-P on $C_{10}H_7$_2 and C_4H_4 on C_9H_7. The reaction sequence $C_{13}H_{12} \rightarrow C_{13}H_{11} \rightarrow C_{13}H_{10}$ has a slight contribution to the production of $C_{13}H_{10}$. The mechanism underpredicts the concentrations of $C_{13}H_{10}$. This could be attributed to the need of visiting the kinetics of $C_{10}H_7$ + C_3H_4-P reactions, or to missing reaction pathways leading to $C_{13}H_{10}$.

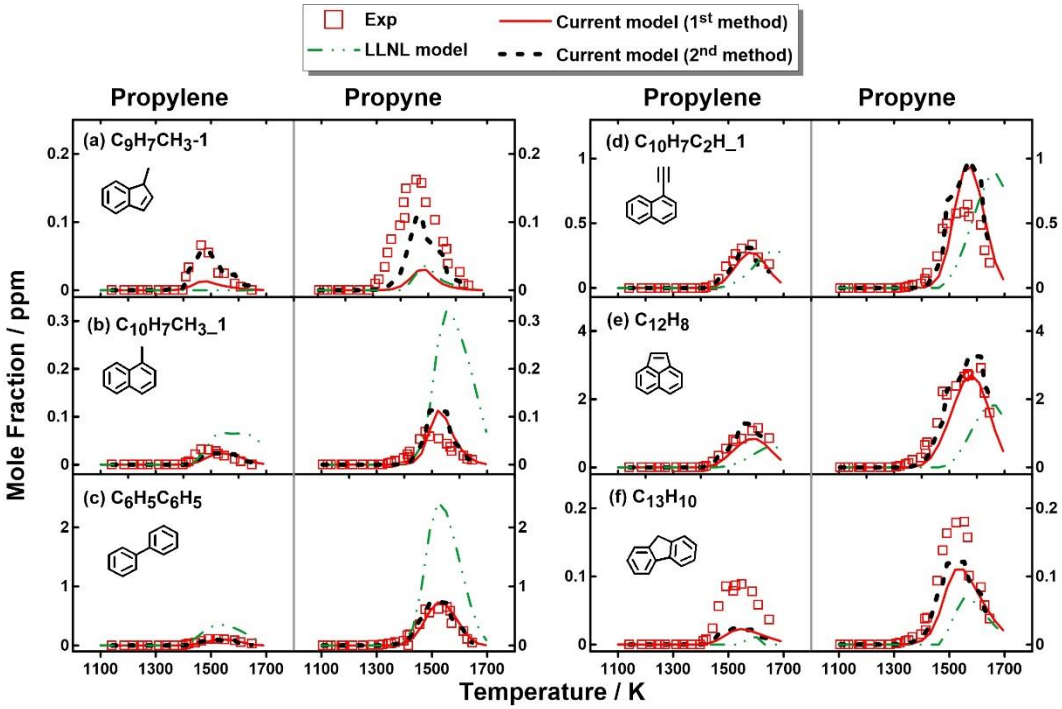

Figure 5.10: Measured (symbols) and simulated (lines) mole fraction profiles for C_{10}–C_{13} PAH species as a function of T_5 in propylene and propyne pyrolysis. Thick solid red lines: simulations using the current kinetic model with the constant p_5 of 20 bar and the nominal reaction time of 4 ms; thick dashed black lines: simulations using the current model with measured pressure profiles up to 10 ms; thin dot dashed green lines: simulations using the LLNL PAH model *[123]* with constant p_5 of 20 bar and the nominal reaction time of 4 ms.

Four different $C_{14}H_{10}$ species are determined in both propylene and propyne pyrolysis, including diphenylacetylene ($C_6H_5CCC_6H_5$), 9-methylene-fluorene ($C_{13}H_8CH_2$), the dominant phenanthrene ($PC_{14}H_{10}$), and anthracene ($AC_{14}H_{10}$). The corresponding simulated and measured mole fraction profiles are shown in **Figure 5.11**. In general, the current mechanism can well predict the different $C_{14}H_{10}$ isomers even compared to LLNL model. The C_6H_5+$C_6H_5C_2H$ addition-elimination reactions are the major pathways leading to $C_{13}H_8CH_2$ and $C_6H_5CCC_6H_5$ production, which further isomerize to $PC_{14}H_{10}$ (see **scheme 5.2**). The more abundant C_6H_5 and $C_6H_5C_2H$ account for the much higher peak mole fractions of $C_{13}H_8CH_2$ and $C_6H_5CCC_6H_5$ in propyne pyrolysis compared to the case of propylene pyrolysis (around 5 times more). However, the $PC_{14}H_{10}$ peak mole fraction in propylene pyrolysis is about half of that in propyne pyrolysis. This is because the isomerization of $C_{13}H_8CH_2$ and $C_6H_5CCC_6H_5$ to $PC_{14}H_{10}$ ($C_{13}H_8CH_2$/$C_6H_5CCC_6H_5$+H = $PC_{14}H_{10}$+H) requires the participation of H atoms, and sufficient amount of H atoms exists in the propylene reaction system. The $PC_{14}H_{10}$ prediction in LLNL model mainly relies on the HACA route through $C_{12}H_9$+C_2H_2 and the dehydrogenation of a $C_{14}H_{11}$ radical formed from C_6H_5 addition to $C_6H_5C_2H$. The $C_{13}H_8CH_2$ and $C_6H_5CCC_6H_5$ isomers are absent in their kinetic mechanism. The inclusion of $C_{13}H_8CH_2$ and $C_6H_5CCC_6H_5$ pathways [66], [194] results in a better

prediction for the relevant $C_{14}H_{10}$ PAHs using the current model. The formation of $AC_{14}H_{10}$ mainly depends on the H-assisted isomerization of $PC_{14}H_{10}$. The C_7H_5 self-recombination have minor contribution to $AC_{14}H_{10}$ formation (not shown in **scheme 5.2**).

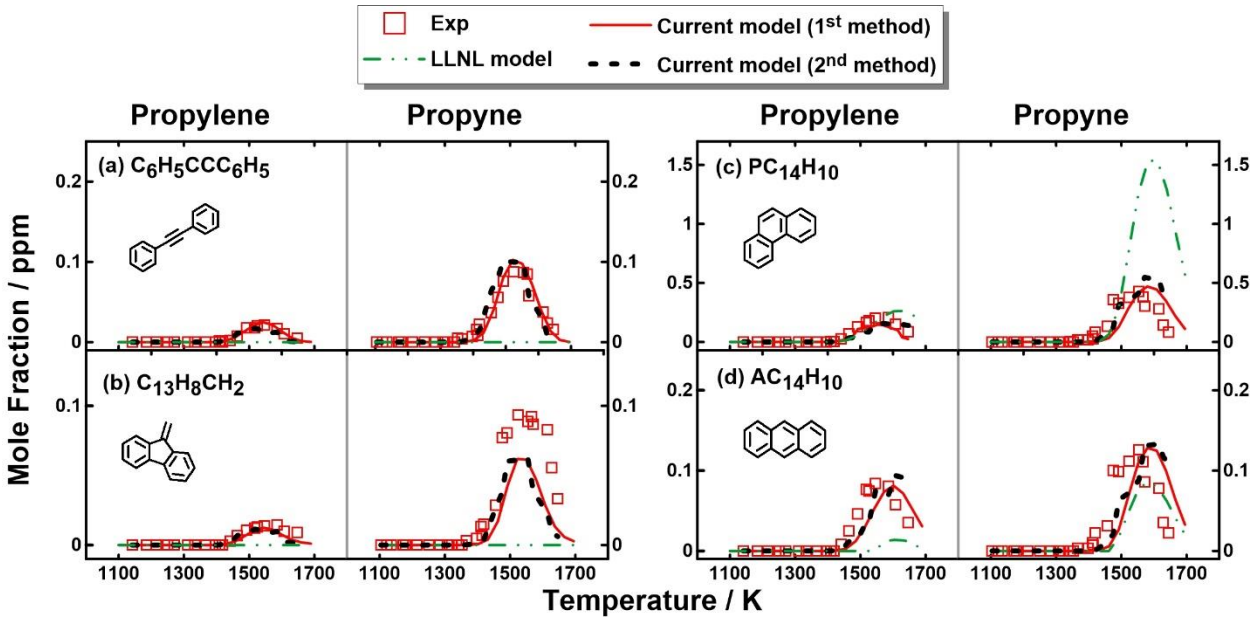

Figure 5.11: Measured (symbols) and simulated (lines) mole fraction profiles for $C_{14}H_{10}$ isomers as a function of T_5 in propylene and propyne pyrolysis. Thick solid red lines: simulations using the current kinetic model with the constant p_5 of 20 bar and the nominal reaction time of 4 ms; thick dashed black lines: simulations using the current model with measured pressure profiles up to 10 ms; thin dot dashed green lines: simulations using the LLNL PAH model *[123]* with constant p_5 of 20 bar and the nominal reaction time of 4 ms.

Three different C_{16} PAH species are identified and quantified in both propylene and propyne pyrolysis, including 1-phenyl-naphthalene ($C_{10}H_7C_6H_5$), fluoranthene ($FC_{16}H_{10}$), and pyrene ($PC_{16}H_{10}$). All C_{16} PAH species are present in trace amounts (below 0.05 ppm), as shown in **Figure 5.12**. The reaction between $C_{10}H_7$ and C_6H_6 mainly yields to $C_{10}H_7C_6H_5$ formation. $C_{10}H_7C_6H_5$ dehydrogenation leads to $FC_{16}H_{10}$ production. $PC_{16}H_{10}$ formation relies on the HACA mechanism of phenanthryl radical ($PC_{14}H_9$) with C_2H_2.

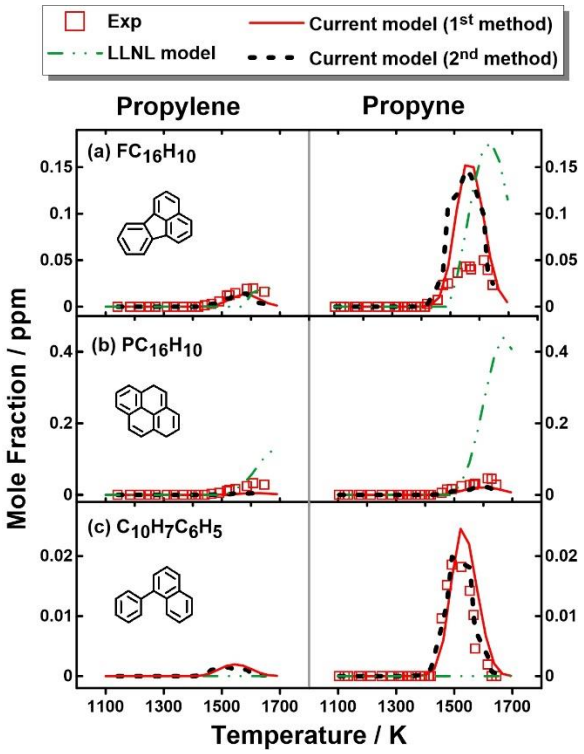

Figure 5.12: Measured (symbols) and simulated (lines) mole fraction profiles for C_{16} PAH species as a function of T_5 in propylene and propyne pyrolysis. Thick solid red lines: simulations using the current kinetic model with the constant p_5 of 20 bar and the nominal reaction time of 4 ms; thick dashed black lines: simulations using the current model with measured pressure profiles up to 10 ms; thin dot dashed green lines: simulations using the LLNL PAH model *[123]* with constant p_5 of 20 bar and the nominal reaction time of 4 ms.

In conclusion, the methylene substituted cyclopenta-ring species are considered important precursors leading to aromatic ring growth in the current investigated study. The aromatic ring formation through the isomerization of its cyclopenta-ring counterpart is seen in fulvene→C_6H_6, $C_9H_6CH_2$→$C_{10}H_8$ and $C_{13}H_8CH_2$→$PC_{14}H_{10}$. This confirms the importance of MAC mechanism in PAH growth under combustion-like conditions. In addition, the aromatic-aromatic reactions dominate the formation of the larger PAH products (C_{14}-C_{16}).

5.1.5 Model validation against experimental data of propylene pyrolysis in literature

Burcat et al. [228] investigated the shock tube pyrolysis of 0.4% and 1.6% C_3H_6 in Ar in the temperature range 1160–1700 K. The experiments were performed at pressures of 1.3-2.9 atm and 5.5-8.8 atm for dwell times ranging between 690 and 910 μs. Mole fraction profiles of small stable hydrocarbon products were measured using gas chromatography, as shown in **Figures 5.13-5.15** along with the simulated results using the current model. Each data point is simulated with homogeneous reactor by inputting the

measured T_5, p_5 and reaction time. It can be seen that this model can well reproduce the decomposition of C_3H_6 and the formation of major products within the experimental uncertainties.

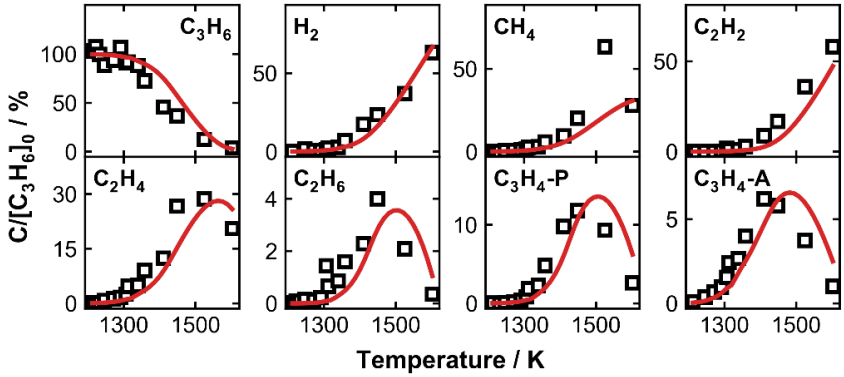

Figure 5.13: Predictions (lines) by the current model for the measured (symbols) species mole fractions in propylene pyrolysis experiments reported by Burcat et al. *[228]* (Shock tube, Set A: 0.4 % C_3H_6 diluted in Ar; post-shock pressure p_5 = 6.2–8.8 atm; reaction time τ = 700–900 µs)

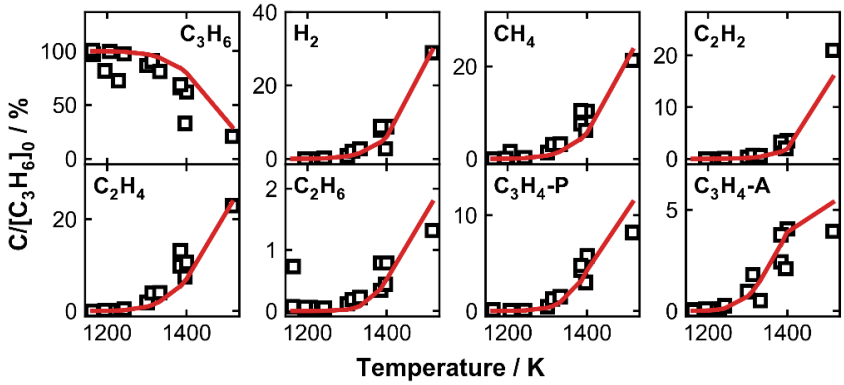

Figure 5.14: Predictions (lines) by the current model for the measured (symbols) species mole fractions in propylene pyrolysis experiments reported by Burcat et al. [228] (Shock tube, Set B: 1.6 % C_3H_6 diluted in Ar; post-shock pressure p_5 = 5.5–8.6 atm; reaction time τ = 690–890 µs)

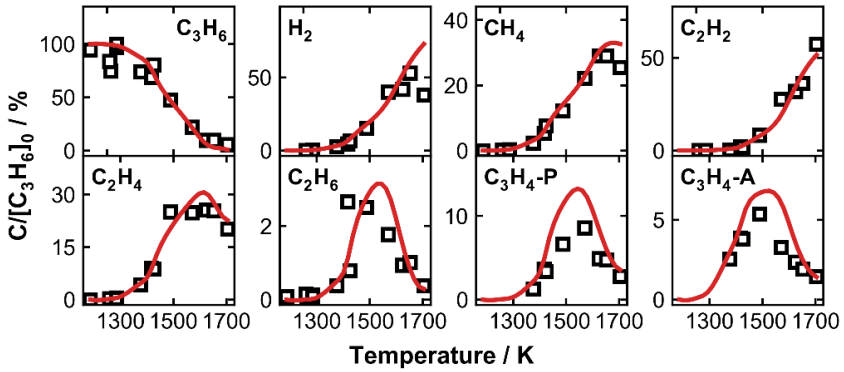

Figure 5.15: Predictions (lines) by the current model for the measured (symbols) species mole fractions in propylene pyrolysis experiments reported by Burcat et al. *[228]* (Shock tube, Set C: 1.6 % C_3H_6 diluted in Ar; post-shock pressure p_5 = 1.3–2.9 atm; reaction time τ = 700–910 μs)

Hidaka et al. [169] have also investigated the shock tube pyrolysis of 2.5% and 5% C_3H_6 in Ar at the pressure of ~2 atm in the temperature range 1200-1800 K with reaction time of 800-2500 μs. Infrared emission spectroscopy technique was used to analyze the chemical compositions of the gas-mixtures behind reflected shock waves. **Figures 5.16 and 5.17** present the experimental and simulated results with the current kinetic model for the two data sets of propylene pyrolysis. The agreements between the experimental and simulated results are satisfactory for all the species.

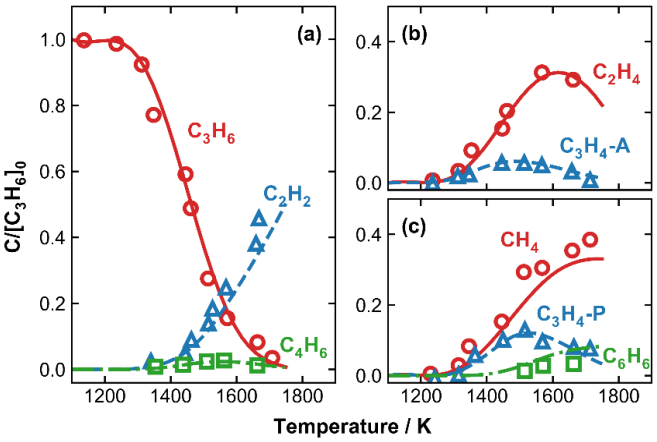

Figure 5.16: Predictions (lines) by the current model for the measured (symbols) species mole fractions in propylene pyrolysis experiments reported by Hidaka et al. *[169]* (Shock tube, Set 1: 2.5 % C_3H_6 diluted in Ar; nominal post-shock pressure p_5 = 2 atm; reaction time τ = 860–1880 μs)

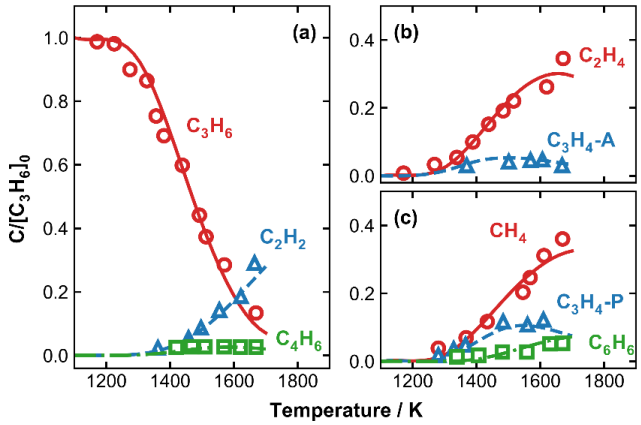

Figure 5.17: Predictions (lines) by the current model for the measured (symbols) species mole fractions in propylene pyrolysis experiments reported by Hidaka et al. *[169]* (Shock tube, Set 2: 5.0 % C_3H_6 diluted in Ar; nominal post-shock pressure p_5 = 2 atm; reaction time τ = 800–2500 µs)

Furthermore, Davis et al. [226] studied the pyrolysis of 0.288% C_3H_6 in N_2 at 1210 K in an atmospheric flow reactor. Small hydrocarbons were detected and their mole fraction profiles were measured as the function of reaction time in order to determine the rate constants of some specific reactions. The calculated rate coefficients for specific reactions are nowadays integrated in the widely used USCMech II. An isobaric and adiabatic zero-dimensional reactor is used to simulate their experimental data by setting the initial temperature, pressure and chemical compositions in order to simulate the species mole fraction time histories. The results are presented in **Figure 5.18**. The fuel reactivity and the formation of the main products (CH_4, C_2H_4, C_4H_6 and C_6H_6) are well captured by the model although a slight under prediction of C_2H_2, C_3H_4-P, C_3H_4-A and C_2H_6 is observed.

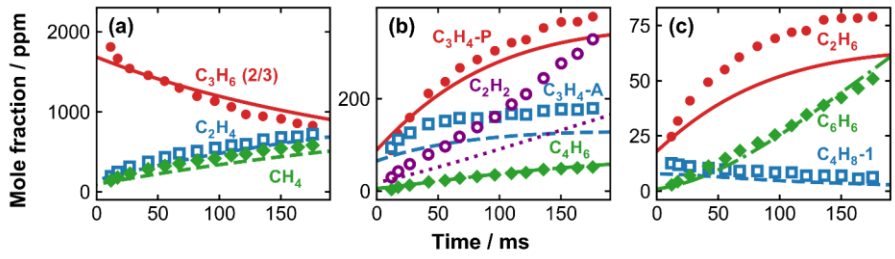

Figure 5.18: Predictions (lines) by the current model for the measured (symbols) species mole fractions in propylene pyrolysis experiments reported by Davis et al. *[226]* (flow reactor, 0.288 % C_3H_6 diluted in N_2; T = 1210 K; p = 1 atm; reaction time τ shifted by 40 ms in the simulation)

Moreover, Wang et al. [173] studied propene pyrolysis in a plug-flow reactor and provided speciation measurements as a function of temperature. Propylene pyrolysis experiments were carried out at 848–

1148 °C with nominal residence times of 2.4, 1.2 and 0.5 s at 0.83 atm. The “plug-flow” model is employed to simulate the speciation of propylene pyrolysis in a laminar flow tube pyrolysis. The measured temperature profiles are used for individual conditions. The species mole fractions at the exit of the reactor are extracted and plotted against the reactor temperatures (the approximately constant temperatures in the central region of the reactor). Generally, the simulated results agree reasonably well with the experimental data, which demonstrates the good performance of the current model, as shown in **Figure 5.19**.

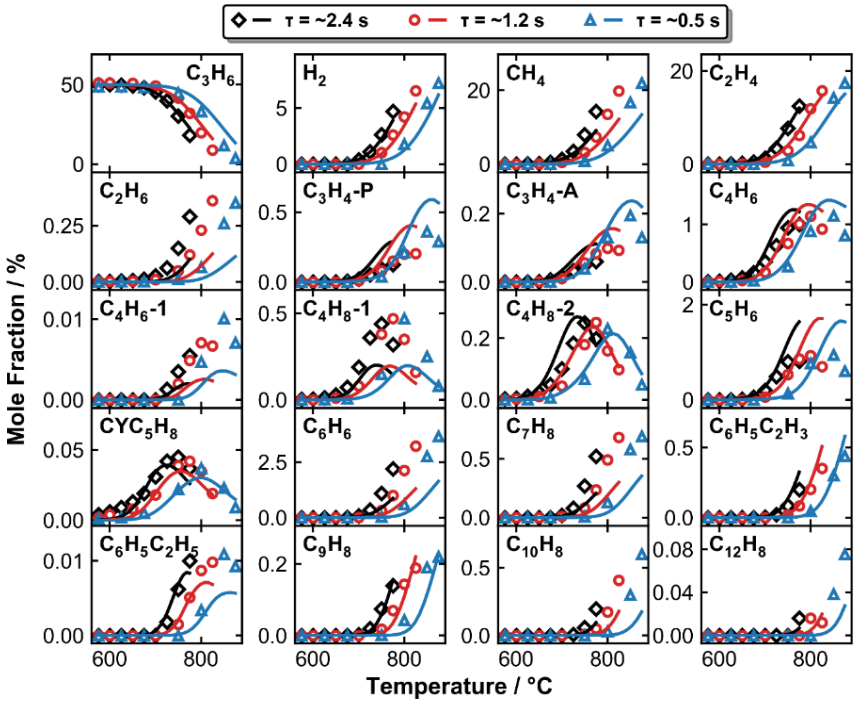

Figure 5.19: Predictions (lines) by the current model for the measured (symbols) species mole fractions in propylene pyrolysis experiments reported by Wang et al. *[173]* (Flow reactor, 50% C_3H_6 diluted in N_2, p = ~0.8 atm; residence time τ = ~2.4, ~1.2 and ~0.5 s)

Lately, Nagaraja et al. [230] performed pyrolytic experiments on 2% C_3H_6 in Ar at 2 bar in the temperature range 900–1800 K using a single-pulse shock tube. Product species are obtained and quantified using gas chromatography-mass spectrometry (GC–MS) technique. **Figure 5.20** shows the experimental and simulated mole fraction profiles of the detected species. The current model can well capture the decomposition of the fuel and the formation of products except for benzene, where the model over-predicts the C_6H_6 peak concentration.

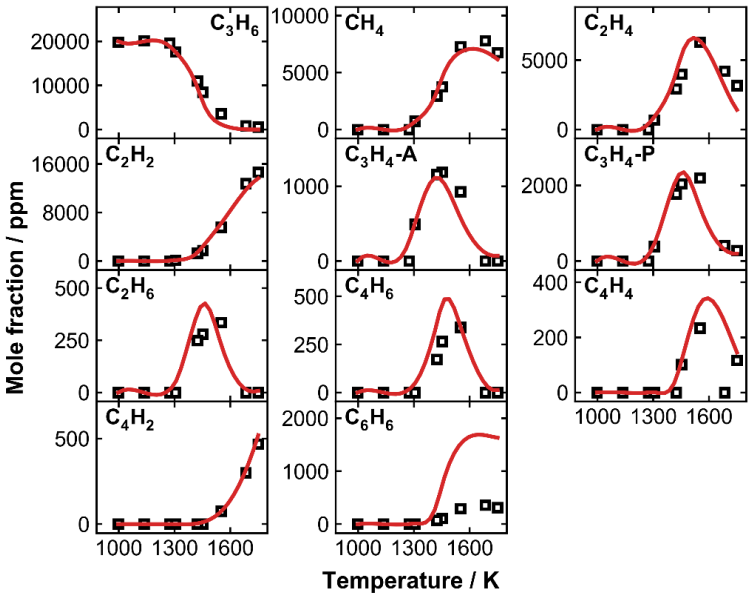

Figure 5.20: Predictions (lines) by the current model for the measured (symbols) species mole fractions in propylene pyrolysis experiments reported by Nagaraja et al. *[230]* (Shock tube, 2% C_3H_6 + 0.5% Kr diluted in Ar, post-shock pressure p_5 = ~2 bar; reaction time τ = 2.8–4.4 ms)

5.1.6 Model validation against experimental data of propyne pyrolysis in literature

In this section, the mechanism is validated against the literature data available on propyne pyrolysis. Hidaka et al. *[169]* investigated the pyrolysis of 4% C_3H_4-P in Ar in the temperature range 1200-1570 K at the pressures of 1.7-2.6 atm for reaction time of 1800-2400 µs behind the reflected shock waves. Infrared emission spectroscopy and gas chromotography techniques were combined together to analyze the chemical compositions of the gas mixtures. **Figures 5.21** presents the experimental and the simulated

results with the current kinetic model. The simulated results are in good agreement with the experimental data.

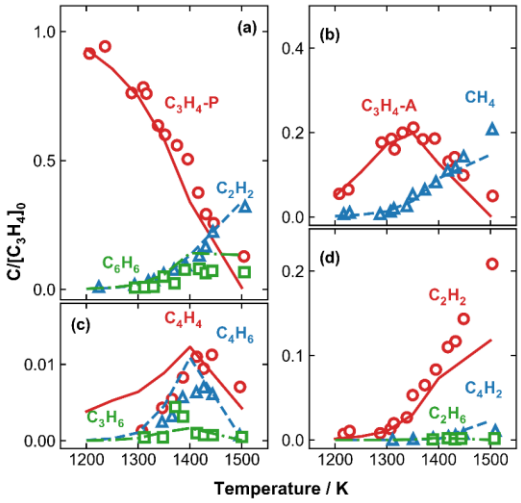

Figure 5.21: Predictions (lines) by the current model for the measured (symbols) species mole fractions in propyne pyrolysis experiments reported by Hidaka et al. *[169]* (Shock tube, 4% C_3H_4-P diluted in Ar, post-shock pressure p_5 = ~2 atm; reaction time τ = 1.8–2.4 ms)

Later, Davis et al. [225] studied the pyrolysis of 0.297% C_3H_4-P in N_2 at 1210 K in an atmospheric flow reactor. Small hydrocarbons were detected and their mole fraction profiles were measured as the function of reaction time. The current kinetic model can well predict the experimental data despite an over prediction of the benzene concentration as shown in **Figure 5.22**.

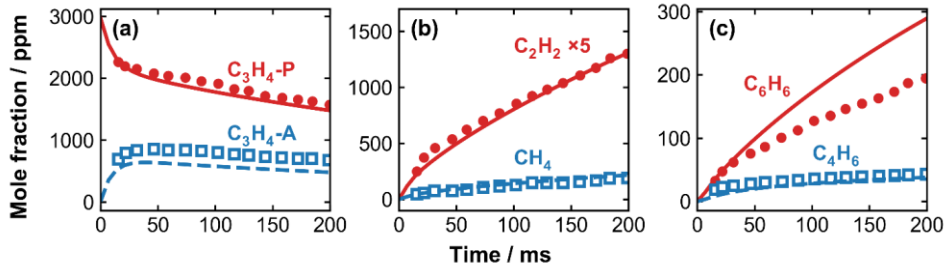

Figure 5.22: Predictions (lines) by the current model for the measured (symbols) species mole fractions in propyne pyrolysis experiments reported by Davis et al. *[225]* (flow reactor, 0.297 % C_3H_6 diluted in N_2; T = 1210 K; p = 1 atm)

Recently, Panigrahy *et al*. [231] utilized a single-pulse shock tube to study 2% C_3H_4-P diluted in Ar at 2 bar pressure in the temperature range 1000–1600 K. Mole fraction profiles of small HCs were measured, as shown in **Figure 5.23** along with the simulated results. It can be seen that once again the current model can get a reasonable prediction of the experimental data with over prediction for benzene.

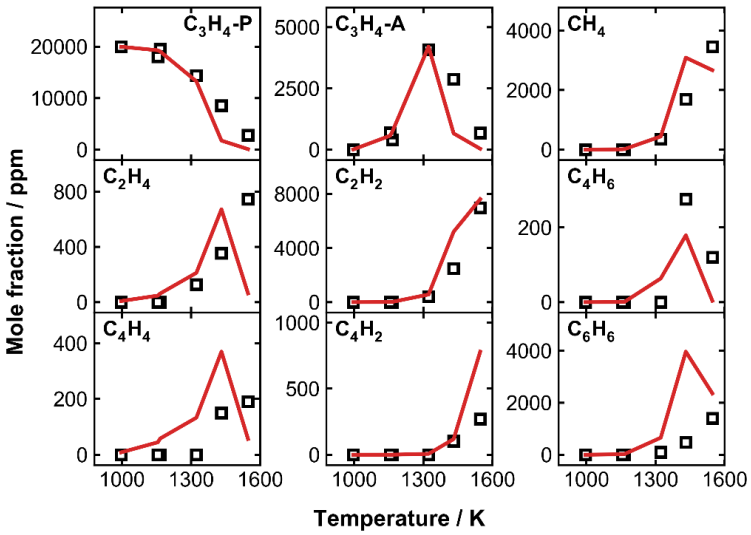

Figure 5.23: Predictions (lines) by the current model for the measured (symbols) species mole fractions in propyne pyrolysis experiments reported by Panigrahy *et al*. [231] (Shock tube, 2% C_3H_4-P + 0.5% Kr diluted in Ar, post-shock pressure p_5 = ~2 bar; reaction time τ = 2.8–4.1 ms)

5.2 Benzene pyrolysis & addition of C_2/C_3 fuels

5.2.1 Motivation

Benzene has been an area of intense research in the chemical kinetics because of its abundance in commercial fuels as well as its importance as combustion intermediate. Many experimental studies on the pyrolysis of benzene has been performed, as described in section 2.2.1. It is recognized that its systematic investigation at high pressures is still insufficient, and a kinetic model that well explore its related PAH formation is still lacking. Further experimental and modeling efforts are needed to thoroughly understand the PAH formation chemistry in benzene pyrolysis.

C_2-C_3 unsaturated hydrocarbons are abundant in combustion environments. Their interaction with benzene and its radical form, C_6H_5, can potentially lead to aromatic growth. C_6H_6/C_6H_5 + C_2H_x reactions have been a search topic for several years, as they constitute the base of HACA and HAVA mechanisms. However, most of the available literature data are theoretically oriented [186], [191], [196], [234], [235], and the experimental ones [22], [26] are confined either to sub-atmospheric pressures or halogenated phenyl precursors. Thus, it is still necessary to analyze the PAH formation pathways through direct benzene-C_2H_x blends. Likewise, C_6H_6/C_6H_5 + C_3H_x reactions are exclusively investigated theoretically [41], [42], [202], [204], [207], [236]–[238], though they are considered potential indene formation pathways. Hence, benzene + C_3H_x pyrolysis experiments are required to scrutinize these reaction channels.

Consequently, one goal of this section is to provide reliable speciation datasets conducted using a single pulsed shock tube coupled with GC-MS techniques at a nominal pressure (P_5) of 20 bar for a reaction time around 4 ± 0.3 ms. Six argon-diluted reagent mixtures are used for these experimental data sets, and their respective detailed compositions are listed in **Table 5.1**. The binary blends contain impurities, which have been measured to be methane (1.7 ppm) in the benzene-acetylene mixture, propane (1.6 ppm) in the benzene-propylene mixture, and 1-butyne (1.5 ppm), 1-butene (0.158 ppm), 2-butene (3.31 ppm), isobutene (0.134 ppm), isobutane (3.15 ppm) and ethylbenzene (0.53 ppm) in the benzene-propyne mixture. The simulations performed in this section take into consideration these impurities in the initial mixtures. The second goal is to examine the effect of added C_2/C_3 on the PAH formation pathways in benzene pyrolysis.

Table 5.1: Compositions of the gas mixtures used for experiments.

Gas mixture	Composition				
	Benzene(C_6H_6)	Ethylene (C_2H_4)	Acetylene (C_2H_2)	Propylene (C_3H_6)	Propyne (C_3H_4-P)
B_200	200 ppm	--	--	--	--
B_100	109 ppm	--	--	--	--
BE	108 ppm	532 ppm	--	--	--
BA	108 ppm	--	500 ppm	--	--
BPene	110 ppm	--	--	531 ppm	--
BPyne	108 ppm	--	--	--	508ppm

5.2.2 Benzene thermal decomposition

Figure 5.24 presents the experimental and simulated mole fraction profiles of benzene (210 ppm in argon) and its decomposition products. The present model can well reproduce the shock tube pyrolysis data.

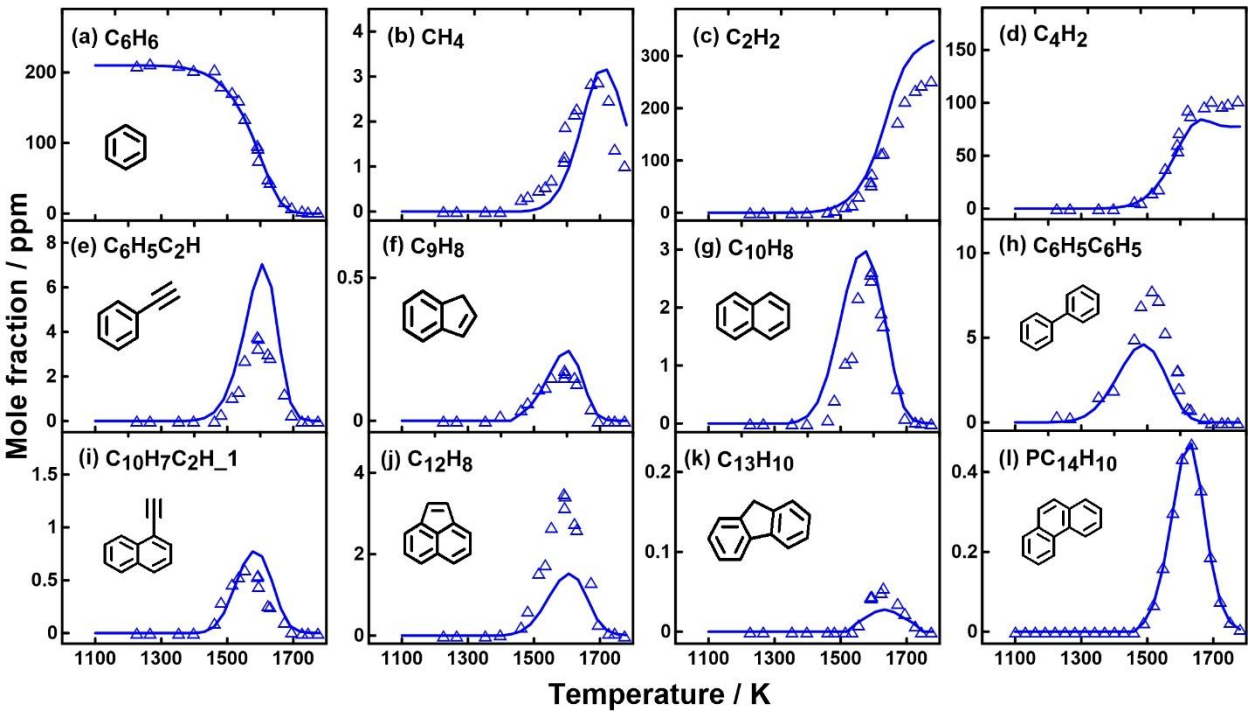

Figure 5.24: Mole fraction profiles (symbols) of fuel and its major products are measured from 210 ppm benzene pyrolysis in a shock tube at 20 bar. Solid lines indicate the model predictions.

The chain-initiation through H-loss from benzene requires high energy. That's why benzene starts decomposing at high temperatures. According to ROP analyses, the consumption of benzene is mainly through H-abstraction reaction by H over the whole temperature range, where it constitutes 80% at 1500 K, 77% at 1610 K and 70% at 1700 K. The unimolecular reaction C_6H_6 (+M) = C_6H_5 + H (+M) has minor contribution in C_6H_6 decay (ranging from 8% at 1500 K to 2% at 1700 K).

C_6H_5 radical is a significant intermediate in the pyrolysis of benzene. At low temperatures (1300-1480 K) C_6H_5 is mainly consumed through C_6H_6+C_6H_5 reaction leading to the formation of biphenyl, the most abundant PAH species as seen in **Figure 5.24**. While at high temperatures (>1600K), C_6H_5 largely breakdown into C_2H_2 and C_4H_2 through the intermediate LC_6H_5. At moderate temperatures, C_6H_5 mainly reacts with other intermediates present in the species pool forming different PAHs. Among these interactions, the HACA route C_6H_5 + C_2H_2 leading to $C_6H_5C_2H$ is the predominant one.

C_9H_8 is one of the simplest PAHs. The ROP analyses reveal that most of indene is produced via the C_6H_6+C_3H_3 reaction. For naphthalene, the pathway o-C_6H_4+C_6H_6 through the intermediate BICYCLO [24] is the dominant source at low temperatures. The HACA route through $C_6H_5C_2H$ leading to naphthyl radical has pronounced effects at high temperatures.

Two $C_{12}H_8$ isomers are detected in benzene pyrolysis acenaphthylene and 1-ethynylnaphthalene. $C_{12}H_8$ is produced through a progressive isomerization process [25], [26] of $C_{12}H_9$, the radical of $C_6H_5C_6H_5$, and this reaction sequence is the principal source of $C_{12}H_8$ formation at low temperatures. The HACA pathway through $C_{10}H_7$+C_2H_2 contributes to around 5% of $C_{12}H_8$ formation at 1500 K, however this value increases to over 30% at higher temperatures (≥1600 K). 1-ethynylnaphthalene, the other $C_{12}H_8$ isomer, is also a competitive product of the HACA route. The model underpredicts acenaphthylene formation and this is mainly due to the incompetency of the model to predict biphenyl. For fluorene, it mainly comes from the recombination reaction of $C_{10}H_7$_1 + C_3H_3. Finally, phenanthrene is produced mainly through the reaction channels of $C_6H_5C_2H$+C_6H_5.

5.2.3 Impacts of added acetylene and ethylene on benzene pyrolysis

5.2.3.1 Fuel consumption and small intermediates

First, the influence of the C_2 fuels on the decomposition reactivity of C_6H_6 is inspected. Mole fraction profiles of C_6H_6 in all the three experimental sets, and those of C_2H_2 and C_2H_4 when they have been added as initial components are shown in **Figure 5.25**. The current model can well capture the C_6H_6 decomposition reactivity throughout the investigated temperature range in all the three separate cases. Both the experimental and the modeling results indicate that the consumption of C_6H_6 is slightly promoted when C_2H_2 and C_2H_4 are added. To reveal the chemical details responsible for the faster benzene consumption in the binary blends, sensitivity analysis for benzene consumption is performed at T_5=1487 K and P_5=20 bar, and the results are shown in **Figure 5.26**. H+C_6H_6=H_2+C_6H_5 plays a dominant role in benzene consumption in all the three cases, and it has more pronounced effect in C_6H_6+C_2H_x pyrolysis due to the increased level of H atoms. According to the ROP analysis, the enhanced level of H atoms derives from the recombination reactions between C_6H_5 + C_2H_2 and C_6H_5 + C_2H_4, which also account to the benzene consumption in BA and BE pyrolysis, respectively.

C_2H_2 and C_2H_4 mole fractions evolve differently with temperature (see **Figure 5.25**). Model-predicted C_2H_2 and C_2H_4 conversion curves when C_6H_6 is replaced with argon are also displayed in **Figure 5.25** for comparison purpose**.** The C_2H_2 decomposition in the temperature range 1400-1500 K indicates a "synergistic effect" in the pyrolysis of C_6H_6+C_2H_2 mixture, which is caused via the reaction C_6H_5+C_2H_2 = $C_6H_5C_2H$ +H producing H atoms. The resulting H atom stimulates the consumption of C_6H_6 and C_2H_2 through the reactions H+C_6H_6=>H_2+C_6H_5 and C_2H_2+H=H_2+C_2H, respectively. In the temperature region of 1500-1600 K, C_2H_2 is produced from C_6H_5 decomposition which compensates its slight consumption. In contrast, the presence of C_6H_6 barely changes the thermal decomposition rate of C_2H_4.

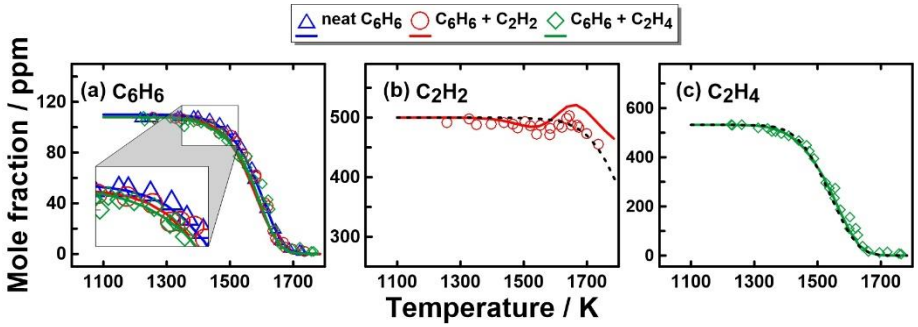

Figure 5.25: Experimental (symbols) and simulated (solid lines) mole fractions of (a) C_6H_6 in the three investigated cases, (b) C_2H_2 in the pyrolysis of 108 ppm C_6H_6 + 500 ppm C_2H_2 mixture and (c) C_2H_4 in the pyrolysis of 108 ppm C_6H_6 + 532 ppm C_2H_4 mixture. The dashed lines in (b) and (c) represent the simulated mole fractions of C_2H_2 and C_2H_4 when C_6H_6 is absent from the corresponding mixtures.

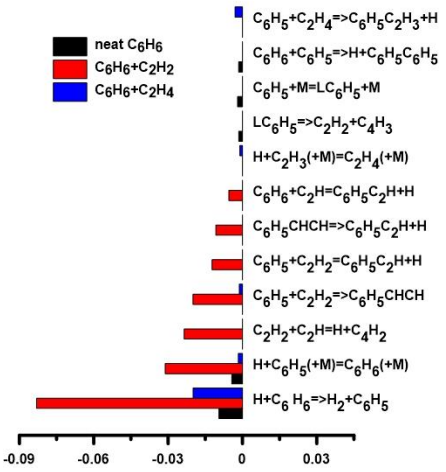

Figure 5.26: Sensitivity analyses for C_6H_6 consumption at T_5=1487 K, P_5=20 bar and reaction time=4 ms in the pyrolysis of neat C_6H_6, C_6H_6+C_2H_2 and C_6H_6+C_2H_4

Figures 5.27 presents the experimental and the simulated mole fraction profiles of C_1-C_4 species and mono-aromatic hydrocarbons in the three sets. CH_4, C_2H_2, C_3H_4-A and C_3H_4-P have the highest mole fractions in C_6H_6 + C_2H_4 co-pyrolysis due to the breakdown of ethylene. The addition of C_2H_2 and C_2H_4 increase the number of carbon atoms in the initial mixture as well as the abundance of C_2H_2, which contribute to the build-up of C_4H_2 mole fraction at elevated temperatures. Concerning MAHs, the formation of $C_6H_5C_2H$ relies on the reactions between C_6H_5 and C_2H_2/C_2H, and the formation of $C_6H_4(C_2H)_2$ further depends on the reactions between $C_6H_4C_2H$ and C_2H_2. In neat benzene pyrolysis, the production of $C_6H_5C_2H$ is limited by the amount of C_2H_2 that is largely formed at elevated temperatures. This explains why the existence of C_2H_2 as fuel or its production from C_2H_4 decomposition shift the

formation of $C_6H_5C_2H$ to lower temperatures and accordingly $C_6H_4(C_2H)_2$. $C_6H_5C_2H_3$ is absent from the species pools of neat benzene and C_6H_6+C_2H_2 pyrolysis, and it mainly originates from the recombination reactions C_6H_6+C_2H_3 and C_6H_5+C_2H_4.

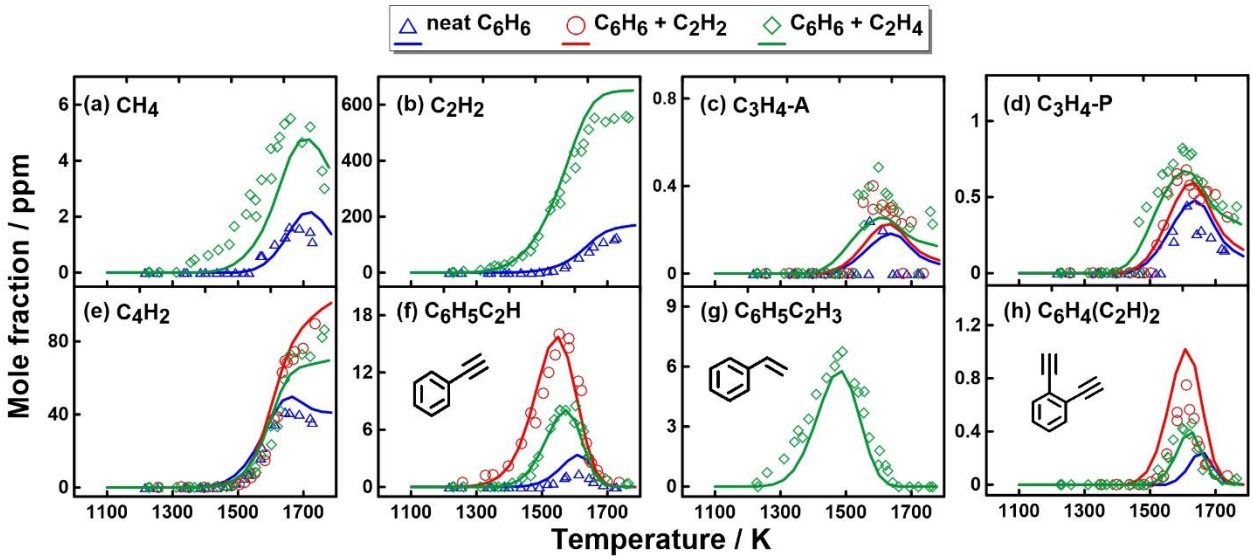

Figure 5.27: Measured (symbols) and simulated (solid lines) mole fractions of small products as a function of T_5 in the pyrolysis of 109 ppm C_6H_6, 108 ppm C_6H_6 + 500 ppm C_2H_2 mixture and 108 ppm C_6H_6 + 532 ppm C_2H_4 mixture at the nominal P_5=20 bar.

5.2.3.2 PAH formation

One main goal of this work is to reveal the influence of the interactions of C_6H_6 with C_2H_2/C_2H_4 on the formation patterns of the PAH species. Experimental and simulated mole fractions of the PAHs species as a function of temperature in the three investigated cases are shown in **Figure 5.28**. Overall, the curent kinetic model can well reproduce the measurements for the PAH species regarding the peak concentration

and the formation temperature window. The formation of PAH species is enhanced when C_2 fuels are added, and this is evident by the higher peak mole fractions realized.

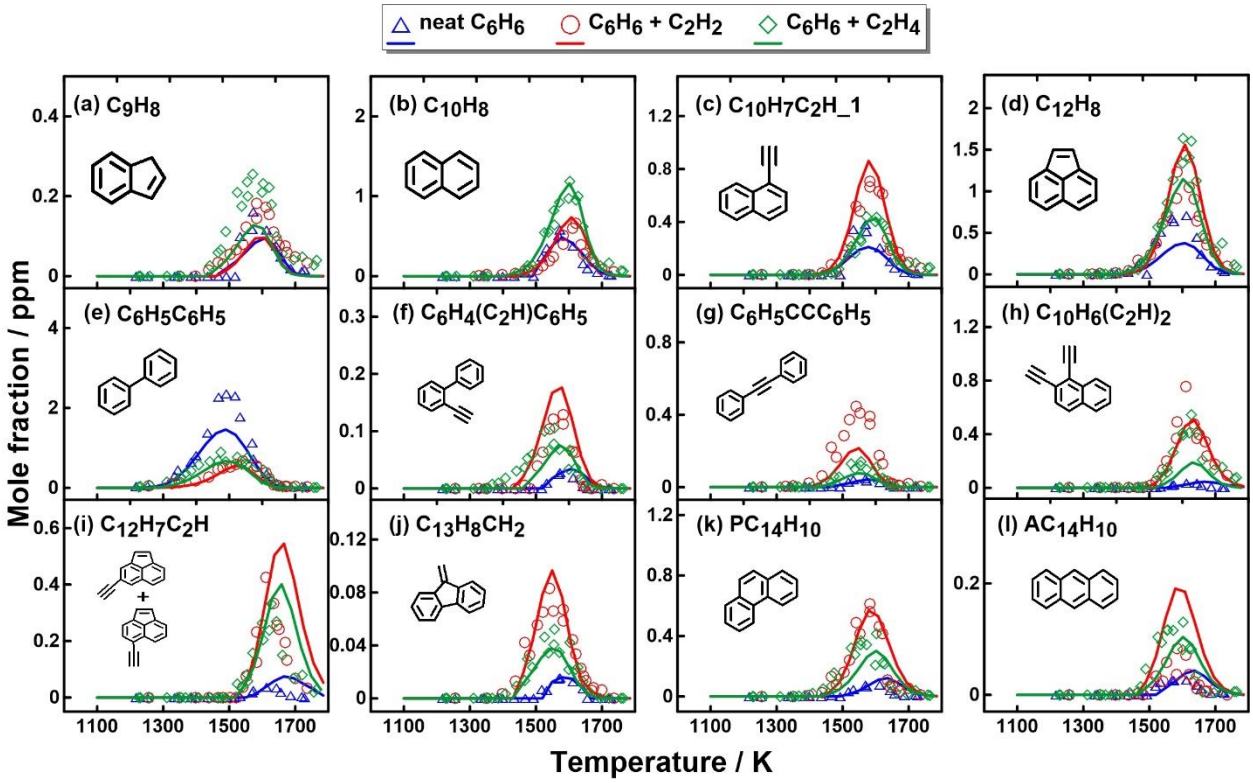

Figure 5.28: Experimental (symbols) and modeling (solid lines) mole fractions of polyaromatic hydrocarbons (PAHs) as a function of the post shock temperature T_5 in neat benzene, benzene+C_2H_2 and benzene+C_2H_4 pyrolysis at a nominal pressure (P_5) of 20 bar.

Biphenyl is the most abundant PAH species in the case of benzene pyrolysis. It is mainly produced through the C_6H_6+C_6H_5 reaction. However, the addition of C_2 fuels shifts the $C_6H_5C_6H_5$ formation temperature window to higher temperatures and lowers its peak concentrations as shown in **Figure 5.28 (e)**. C_6H_5 either decomposes or reacts with other radicals and molecules, including the C_2 fuels. The contributions of reactions involving C_2 fuels increase notably in the C_6H_6+C_2H_2 and C_6H_6+C_2H_4 pyrolysis, and this is evident by the abundant observation of C_8 species, as discussed in the previous section. Thus, the C_6H_6+C_6H_5 pathway is inhibited which leads to a lower $C_6H_5C_6H_5$ formation in benzene/C_2 binary mixtures. The model can well reproduce the biphenyl profiles in the binary mixtures, though it underpredicts $C_6H_5C_6H_5$ formation in benzene pyrolysis, which is probably due the consumption of phenyl radical through thermal decomposition.

The concentration of C_9H_8 is slightly increased by the addition of C_2H_2 and C_2H_4 (see **Figure 5.28** (**a**)). C_6H_6+C_3H_3 is the main formation channel of indene, where C_3H_3 is the limiting reactant. This explains why the addition of the C_2 fuels has slight significance on indene production.

Naphthalene has the highest concentration among the observed fused bicyclic PAHs in the three investigated cases. The addition of C_2H_4 promotes the $C_{10}H_8$ formation at relatively low temperatures, yet the addition of both C_2H_2 and C_2H_4 increases the $C_{10}H_8$ peak concentration (see **Figure 5.28** (**b**)). To obtain detailed kinetic insights onto the remarkable influence of the extra C_2H_2 and C_2H_4 on $C_{10}H_8$, the reaction networks leading to $C_{10}H_8$ formation are shown in **scheme 5.3** based on the ROP analysis at 1530 K in each individual case. The o-C_6H_4+C_6H_6 pathway through the intermediate BICYCLO [24] is a dominant source of $C_{10}H_8$ in the three investigated cases. The HACA pathway through $C_6H_5C_2H$ leading to $C_{10}H_7$_1 depends on the concentration of H-atoms sources (H or H_2, C_6H_6, and C_2H_4 in benzene + ethylene case) in order to convert to $C_{10}H_8$. In benzene + acetylene pyrolysis, the HACA route through $C_6H_5C_2H$ + C_2H_2 leading to $C_9H_6CH_2$ plays a dominant role in the formation of $C_{10}H_8$, where it accounts to 30% of the total integrated ROP. This is related to the fact that $C_6H_5C_2H$ and C_2H_2 are abundant in C_6H_6+C_2H_2 pyrolysis. $C_9H_6CH_2$ can also react with H atom forming $C_9H_6CH_3$, which consequently decomposes to $C_{10}H_8$. In C_6H_6+C_2H_4 pyrolysis, the reaction between $C_6H_4C_2H$ and C_2H_4 produces an adduct $C_6H_4(CHCH_2)(CH\dot{C}H)$ that subsequently undergoes ring closure step forming $C_{10}H_8$ and releasing a hydrogen atom. This channel results in the higher $C_{10}H_8$ mole fraction by skipping $C_{10}H_7$_1 formation at low temperatures. The $C_{10}H_7$_1 + C_2H_4 pathway leads to the production of vinyl naphthalene ($C_{10}H_7C_2H_3$) whose mole fraction profile is shown in **Figure 5.29**. The subsequent unimolecular decomposition of $C_{10}H_7C_2H_3$ also assists the $C_{10}H_8$ formation ($C_{10}H_7C_2H_3$ = H_2CC + $C_{10}H_8$) in C_6H_6+C_2H_4 pyrolysis.

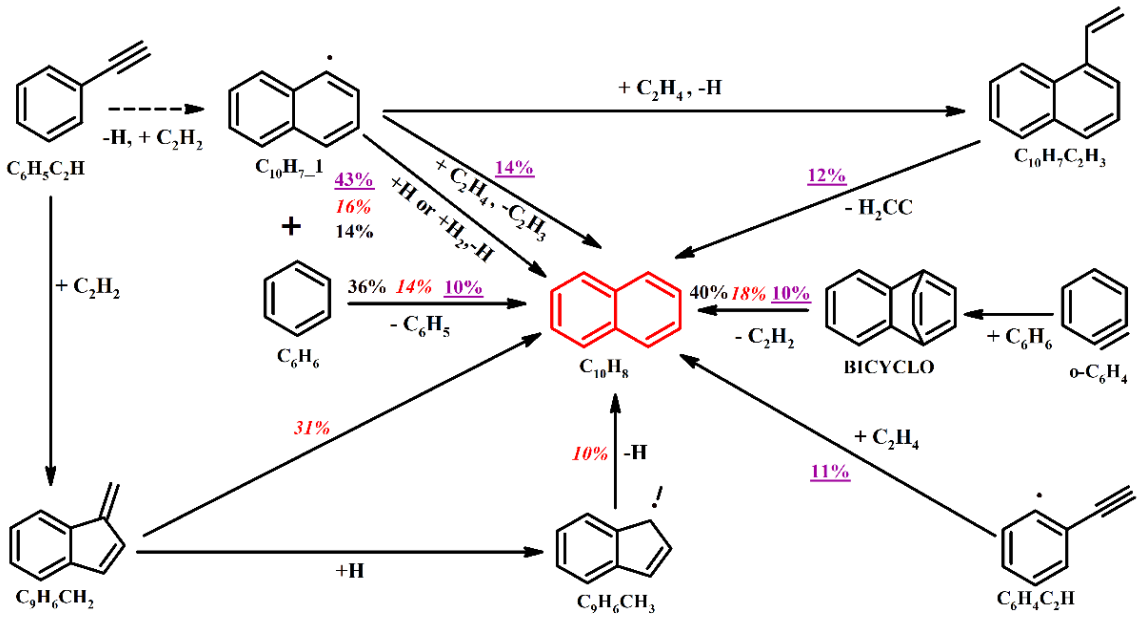

Scheme 5.3: The reaction pathways leading to naphthalene formation at T_5 of 1530 K in the pyrolysis of benzene and benzene/C_2 binary mixtures. The percentage numbers (B: black normal; BA: red italic; BE: purple underlined) represent the contributions of the corresponding reactions in naphthalene formation. The dashed arrows represent multi-step reactions.

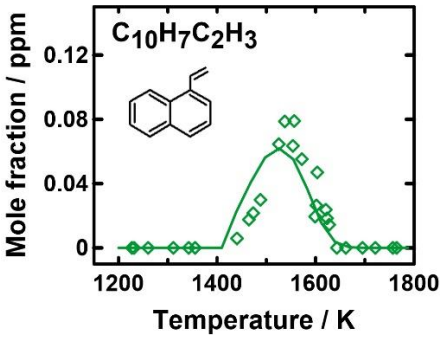

Figure 5.29: Experimental (symbols) and modeling (solid lines) mole fraction of vinyl naphthalene as a function of the post shock temperature T_5 in benzene+C_2H_4 pyrolysis at a nominal P_5=20 bar.

The addition of C_2 fuels to benzene amplifies the peak concentrations of $C_{12}H_8$ isomers (see **Figure 5.28** (c and d)). The formation scheme of acenaphthylene based on the integrated ROP analyses at 1500 K is shown in **Scheme 5.4**. Two main sources are responsible for $C_{12}H_8$ production in the three investigated cases: the isomerization of biphenyl radical ($C_{12}H_9$) through multiple steps and intermediates such as cyclopenta[a]indene (BENZO), and the HACA route through $C_6H_5 \rightarrow C_6H_5C_2H \rightarrow C_{10}H_7\_1 \rightarrow C_{12}H_8$. In $C_6H_6 + C_2H_4$ pyrolysis, the reaction of $C_{10}H_7\_1$ with C_2H_4 leads to acenaphthene ($AC_{12}H_{10}$) production, which further decomposes into $C_{12}H_8$ through the $R5C_{12}H_9$ intermediate. The formation of $C_{10}H_7C_2H\_1$ follows the same HACA pathway as that of $C_{12}H_8$. Besides, the radicals of the $C_{12}H_8$ isomers further react

with C_2H_2 leading to the formation of two $C_{14}H_8$ isomers: ethynyl acenaphthylene ($C_{12}H_7C_2H$) **(Figure 5.28 i)** and diethynyl naphthalene ($C_{10}H_6(C_2H)_2$) **(Figure 5.28 h)**. The higher concentration and the lower formation temperature window of the $C_{14}H_8$ isomers in the binary mixtures are relevant to the abundant C_2H_2 as a fuel or its production from C_2H_4 decomposition. Both $C_{12}H_7C_2H$ and $C_{10}H_6(C_2H)_2$ are identified through their fragmentation spectra in the mass spectrometer.

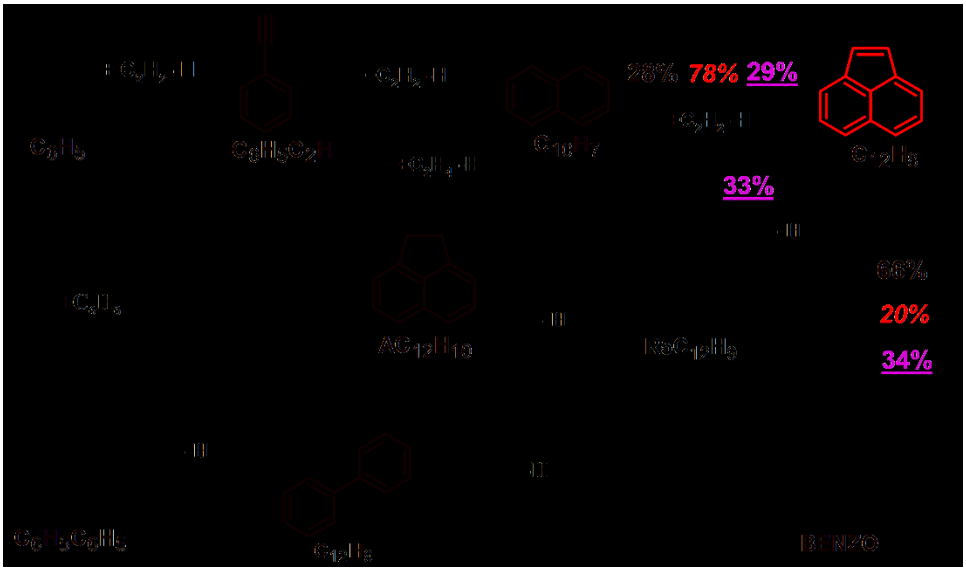

Scheme 5.4: The reaction pathways leading to acenaphthylene formation at T_5 of 1500 K in the pyrolysis of benzene and benzene/C_2 binary mixtures. The percentage numbers (B: black normal; BA: red italic; BE: purple underlined) represent the contributions of the corresponding reactions in naphthalene formation. The dashed arrows represent multi-step reactions.

Figure 5.28 (f, g, j, k and l) displays the mole fraction profiles of the five $C_{14}H_{10}$ isomers, namely, ethynyl biphenyl ($C_6H_4(C_2H)C_6H_5$), $C_6H_5CCC_6H_5$, $C_{13}H_8CH_2$, $PC_{14}H_{10}$, and $AC_{14}H_{10}$. The addition of the C_2 compounds enhances the peak concentration of all the five isomers and tends to their early formation. **Scheme 5.5** presents the reaction pathways leading to the $C_{14}H_{10}$ isomers formation at 1530 K. $C_6H_4(C_2H)C_6H_5$, $C_6H_5CCC_6H_5$, and $C_{13}H_8CH_2$ are mainly produced through $C_6H_5C_2H+C_6H_5$ reactions. $C_6H_4(C_2H)C_6H_5$ is also trivially formed through the reaction channel $C_6H_5C_6H_5+C_2H= C_6H_4 (C_2H) C_6H_5 +H$ in all the reaction systems. In $C_6H_6+C_2H_4$ pyrolysis, 1,1-diphenylethylene ($C_6H_5C(CH_2)C_6H_5$) is formed through $C_6H_5C_2H_3+C_6H_5$. Its decomposition contributes to $C_{13}H_8CH_2$ formation. $PC_{14}H_{10}$, the predominant $C_{14}H_{10}$ isomer, mainly originates from the H-assisted isomerization of $C_6H_5CCC_6H_5$ and $C_{13}H_8CH_2$ and the decomposition of $C_6H_5\dot{C}HC_6H_5$ radical that is produced by the addition of an H atom to $C_6H_5CCC_6H_5$. $AC_{14}H_{10}$ is mostly produced through the isomerization of $PC_{14}H_{10}$. The naphthyne ($C_{10}H_6$-23) + C_6H_6 reaction (not shown in **scheme 5.5**) has minor contribution to $AC_{14}H_{10}$ in all the three investigated cases. Thus, the enhanced formation of all the $C_{14}H_{10}$ isomers derives from the increased $C_6H_5C_2H$ concentration, since their formation largely depends on the $C_6H_5C_2H+C_6H_5$ reactions.

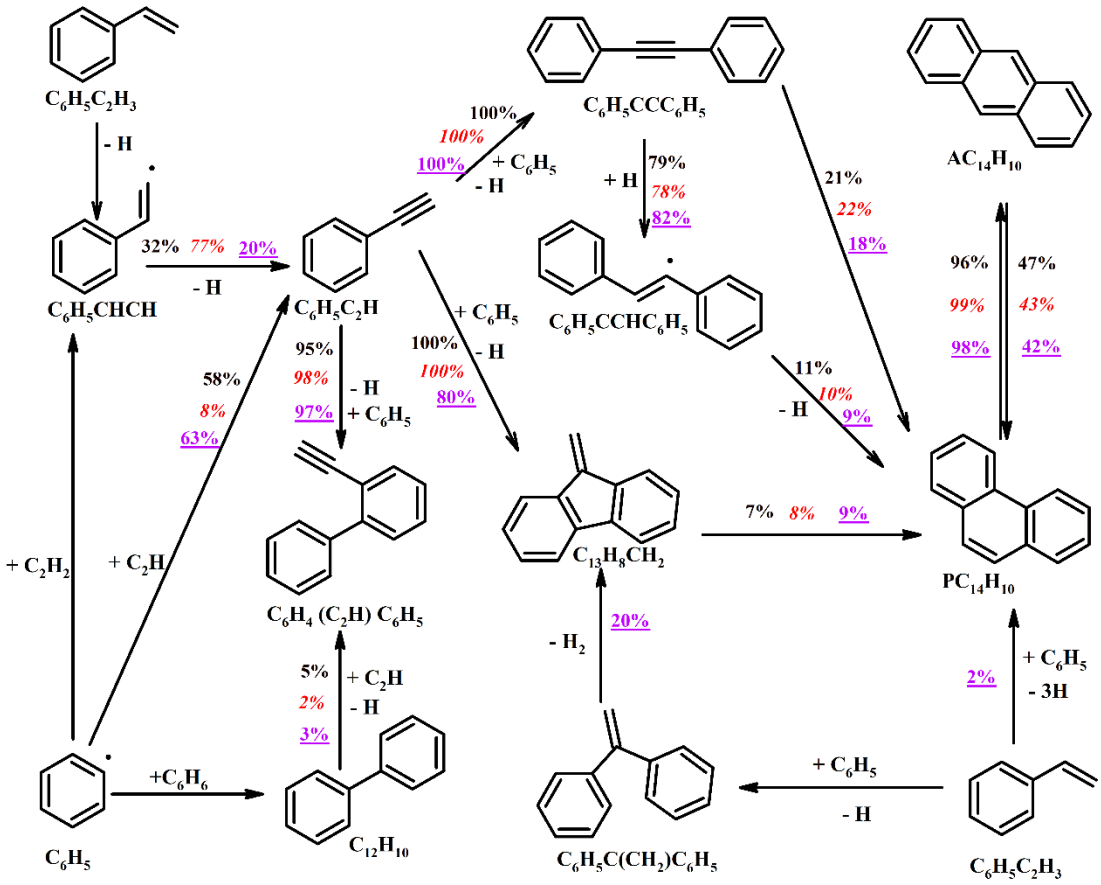

Scheme 5.5: The reaction pathways leading to acenaphthylene formation at T_5 of 1500 K in the pyrolysis of benzene and benzene/C_2 binary mixtures. The percentage numbers (B: black normal; BA: red italic; BE: purple underlined) represent the contributions of the corresponding reactions in naphthalene formation. The dashed arrows represent multi-step reactions.

5.2.3.3 Simulations with pressure profile

Simulations with pressure profiles up to 10 ms are performed for all the three investigated sets. The time dependent mole fraction profiles for the major products and phenyl radical are shown in **Figure 5.30**. The plateaus in the concentration of the major products during the quenching process indicate that products' formation is terminated by the defined reaction time.

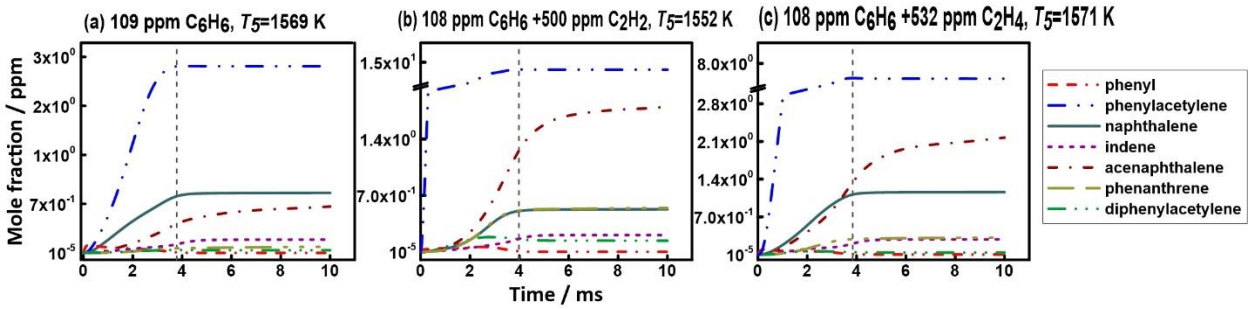

Figure 5.30: Simulated species mole fractions as a function of time with the measured pressure profiles in (a) neat C_6H_6 pyrolysis at T_5=1569 K, P_5= 21.51 bar; (b) C_6H_6/C_2H_2 pyrolysis at T_5=1552 K, P_5=22 bar; (c) C_6H_6/C_2H_4 pyrolysis at T_5=1571 K, P_5= 21.45 bar. The dashed vertical lines indicate the start of quenching.

5.2.4 Impacts of added propylene and propyne on benzene pyrolysis

5.2.4.1 Fuel consumption and small hydrocarbons

In the first place, the impact of added C_3H_6 and C_3H_4-P on C_6H_6 reactivity is investigated. Mole fraction profiles of C_6H_6, C_3H_6 and C_3H_4-P in neat C_6H_6 and C_6H_6 + C_3H_x (x=6, 4) pyrolysis experiments are shown in **Figure 5.31.** The added C_3H_6 and C_3H_4-P have different consequence on C_6H_6 consumption in the temperature range of 1260-1460 K (**Figure 5.31 a**), whereas benzene chemistry has insignificant impact on the decomposition rates of C_3 fuels (see **Figure 5.31 b and c**). The presence of C_3H_6 leads to the C_6H_6 consumption in the temperature range of 1260-1360 K (no decay is observed in benzene pyrolysis case) followed by a slight increase in the C_6H_6 profile (1360-1460 K), while C_3H_4-P induces the C_6H_6 formation in the low temperature range (1260-1460 K). To reveal the reasons behind this difference, ROP analyses for benzene formation are performed at T_5=1387 K for both cases and at T_5=1316 K for the C_6H_6+C_3H_6 mixture as shown in **Figure 5.32**. The C_3H_3 self-recombination is the main source of benzene in C_6H_6+C_3H_4-P pyrolysis, in addition to the C_3H_4-A+ C_3H_3 reaction, the isomerization/fragmentation of $C_5H_5CH_2$-1 and $C_5H_5CH_2$-2, and the isomerization of fulvene. Similar C_6H_6 formation pathways are active in C_6H_6+C_3H_6 case. However, the formation of C_3 precursors from C_3H_6 requires a step-wise dehydrogenation, which make their corresponding reactions incapable to compensate the benzene consumption through hydrogen abstraction reactions by H and CH_3 that are largely formed from C_3H_6 decomposition in the temperature range 1260-1360 K. Therefore, the belatedly C_3H_3 production and the abundance of CH_3 radicals and H atoms resulting from propylene decomposition contribute to the two-step phenomenon seen in C_6H_6+C_3H_6 pyrolysis in the low temperature region (below 1460 K).

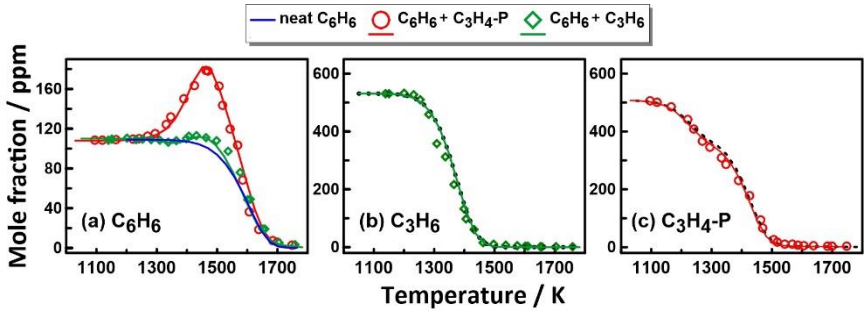

Figure 5.31: Experimental (symbols) and simulated (solid lines) mole fractions of (a) C_6H_6 in the three investigated cases, (b) C_3H_6 in the pyrolysis of 108 ppm C_6H_6 + 532 ppm C_3H_6 mixture and (c) C_3H_4-P in the pyrolysis of 108 ppm C_6H_6 + 500 ppm C_3H_4-P mixture. The dashed lines in (b) and (c) represent the simulated mole fractions of C_3H_6 and C_3H_4-P when C_6H_6 is absent from the corresponding mixtures.

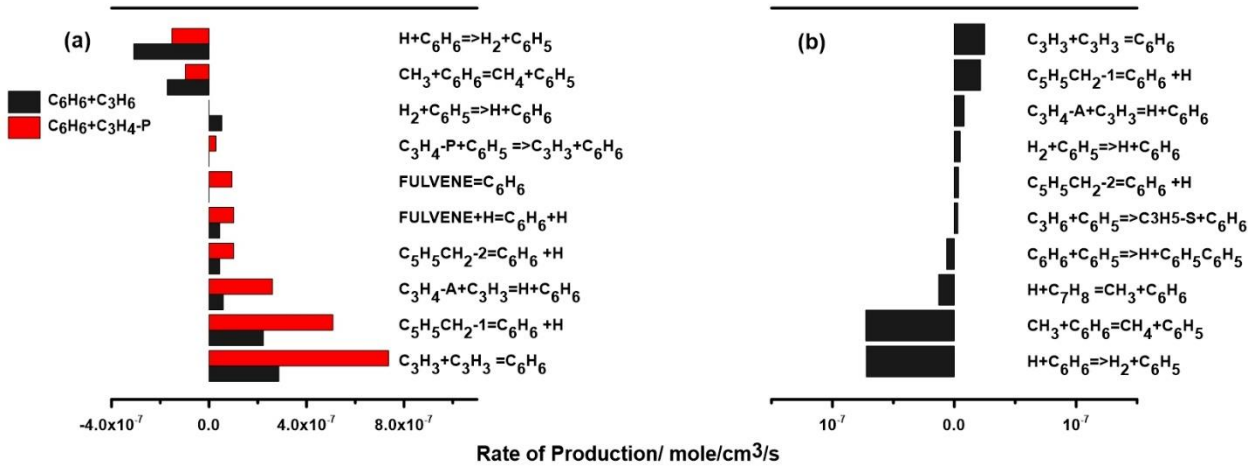

Figure 5.32: Rate of production analyses at reaction time=4ms for benzene in (a) C_6H_6+C_3H_6 and C_6H_6+C_3H_4-P pyrolysis at T_5=1387 K and (b) in C_6H_6+C_3H_6 pyrolysis at T_5=1316 K.

Figure 5.33 presents the experimental and simulated mole fractions of C_1-C_6 non-aromatic hydrocarbons. Only few small hydrocarbons are observed in neat benzene pyrolysis, while the addition of C_3 fuels increases the diversity and abundance of small hydrocarbon intermediates. The types of small intermediates as well as their relevant amounts in benzene-propylene and benzene-propyne co-pyrolysis are the same to those in neat propylene and neat propyne pyrolysis, respectively. Therefore, their related kinetics will not be discussed again here (refer to propylene and propyne pyrolysis section, 5.1).

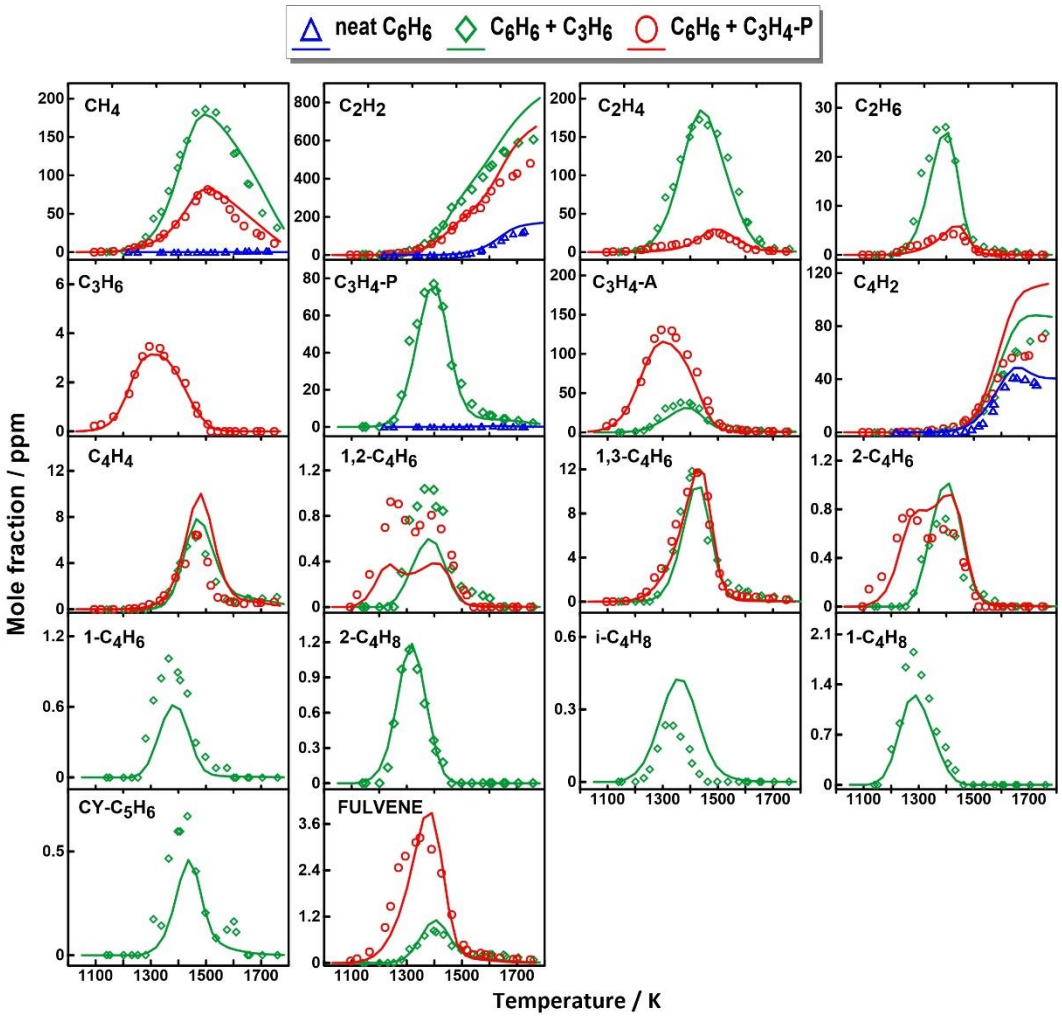

Figure 5.33: Measured (symbols) and simulated (solid lines) mole fraction profiles of small hydrocarbon products as a function of T_5 during the pyrolysis of 109 ppm C_6H_6, 108 ppm C_6H_6+532ppm C_3H_6 and 108ppm C_6H_6+ 500ppm C_3H_4-P mixtures.

5.2.4.2 Mono-aromatic hydrocarbons

Quantitative measurements for MAH products and their corresponding simulations are presented in **Figure 5.34**. The kinetic model can satisfactorily reproduce the measured MAHs mole fraction profiles. The addition of C_3 fuels increases the amounts of the observed MAHs compared to neat benzene pyrolysis and introduces new types of MAHs. The detected MAHs in these experiments mainly include phenylacetylene ($C_6H_5C_2H$), styrene ($C_6H_5C_2H_3$), toluene (C_7H_8), diethynyl benzene ($C_6H_4(C_2H)_2$), 1-phenylpropyne ($C_6H_5C_3H_3$P_1), 4-phenyl-1-butyne ($C_6H_5CH_2CH_2CCH$), allyl benzene ($C_6H_5C_3H_5$-2), 1-phenylpropene ($C_6H_5C_3H_5$-1), methyl styrene ($CH_3C_6H_4C_2H_3$) and ethylbenzene ($C_6H_5C_2H_5$). The formation of $C_6H_5C_2H$ and $C_6H_4(C_2H)_2$ largely depends on C_6H_5+C_2H_2 and $C_6H_5C_2H$+C_2H_2 reactions, respectively. The pyrolysis of C_3 fuels enhances the concentration of C_2H_2 in the reaction system, which boosts the production of $C_6H_5C_2H$ that further facilitates $C_6H_4(C_2H)_2$ formation. All the following MAHs

are absent from the species pools of neat benzene. $C_6H_5C_2H_3$, detected in both binary systems, mainly originates from the combination reactions between C_6H_6+C_2H_3 and C_6H_5+C_2H_4. The late formation of $C_6H_5C_2H_3$ and the lower peak concentration in C_6H_6+C_3H_4-P pyrolysis are due to the limited production of C_2H_4 compared to C_6H_6+C_3H_6 pyrolysis. $C_6H_5C_2H_3$ profile in C_6H_6+C_3H_4-P pyrolysis is identical to that in neat propyne pyrolysis, however the addition of C_6H_6 to C_3H_6 increases the $C_6H_5C_2H_3$ peak mole fraction and lowers its temperature window compared to propylene pyrolysis, where C_6H_6 and its radical C_6H_5 were the limiting factors. C_7H_8 is also a common product measured in the C_6H_6+C_3H_6/C_3H_4-P co-pyrolysis. ROP analysis at 1400 K is performed for both cases to identify the reactions responsible for the higher concentration and early formation of toluene in C_6H_6+C_3H_6 pyrolysis, and the results are shown **Figure 5.35**. C_7H_7+H + (M) =C_7H_8+ (M) is an efficient toluene formation channel in C_6H_6+C_3H_6 pyrolysis, while it has negative sensitivity coefficient in C_6H_6+ C_3H_4-P pyrolysis. This is related to the fact that H-atom level is higher in C_6H_6+C_3H_6 system compared to the highly unsaturated reaction system of C_6H_6+C_3H_4-P. Other reactions also contribute to C_7H_8/C_7H_7 formation, including the reactions of CH_3 with C_6H_6/C_6H_5 and the recombination reactions of C_3H_3 with but-2-yn-1-yl radical ($\dot{C}H_2C \equiv CCH_3$) and 1,3-butadiene. $C_6H_5C_3H_3$P_1 and $C_6H_5C_3H_5$-1/$C_6H_5C_3H_5$-2 are produced from the recombination reactions of C_6H_5 with C_3H_4-P and C_3H_6, respectively. $C_6H_5C_2H$+CH_3 reaction also contributes to $C_6H_5C_3H_3$P_1 formation at elevated temperatures. Since $C_6H_5C_3H_3$P_1 mainly results from the C_6H_5 + C_3H_4-P reactions, it has a wider temperature window and a higher peak mole fraction in C_6H_6+C_3H_4-P co-pyrolysis. The trace quantities of $C_6H_5C_3H_5$-1 and $C_6H_5C_3H_5$-2 show that the interaction between C_6H_5 and C_3H_6 is not as efficient as C_6H_5 + C_3H_4-P. $C_6H_5CH_2CH_2CCH$, which exclusively comes from the $C_6H_5C_3H_3$P_1+CH_3 reaction, is only seen in benzene-propyne pyrolysis. $CH_3C_6H_4C_2H_3$ and $C_6H_5C_2H_5$, detected only in C_6H_6+C_3H_6 pyrolysis, are mainly formed via the isomerization reaction of $C_6H_5C_3H_5$-1through the intermediate indane (C_9H_{10}) and the recombination reaction C_7H_7 + CH_3, respectively.

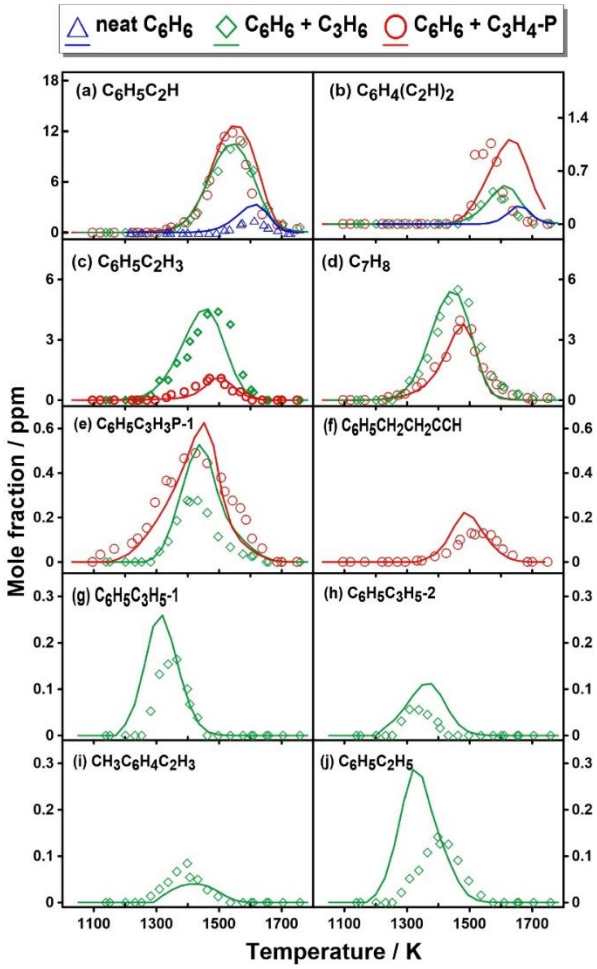

Figure 5.34: Measured (symbols) and simulated (solid lines) mole fractions for MAHs in neat benzene, benzene + C_3H_6 and benzene + C_3H_4-P pyrolysis.

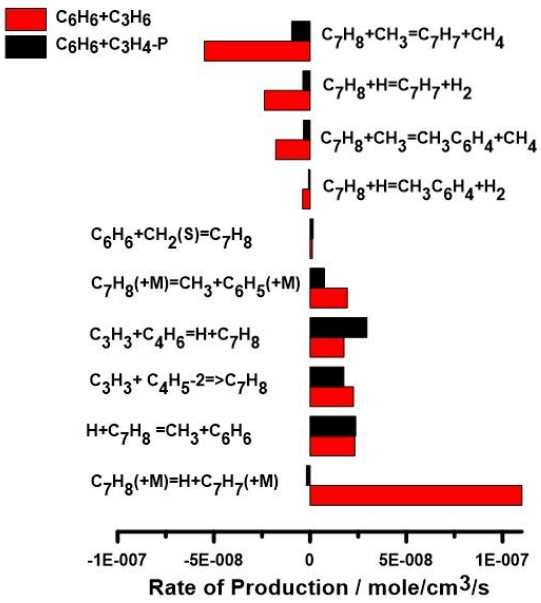

Figure 5.35: Rate of production analysis at reaction time=4ms for toluene in C_6H_6+C_3H_6 and C_6H_6+C_3H_4-P pyrolysis at T_5=1400 K.

5.2.4.3 PAH formation

The interest behind examining the interactions between benzene and C_3 fuels is to validate the formation pathways of indene. In fact, indene is recognized to be the major C_9 product in both C_6H_6+C_3H_6 and C_6H_6+C_3H_4-P co-pyrolysis experiments. **Figure 5.36** shows the experimental and simulated mole fractions of C_9H_8 in these two-investigated cases along with that of benzene pyrolysis. The addition of C_3 fuels not only raises the C_9H_8 peak mole fractions over 3 ppm from less than 0.2 ppm but also shifts the speciation window to much lower temperatures. These observations are accurately reproduced by the kinetic model. According to ROP results, C_9H_8 formation mechanisms mainly include the consumption of $C_6H_5C_3H_3$P_1 and $C_6H_5C_3H_3$A, the reaction of benzyl radical (C_7H_7) with C_2H_2 and the reaction of C_6H_6 with C_3H_3. The unimolecular decomposition of C_9H_{10} originating from $C_6H_5C_3H_5$-1 isomerization and the reaction of C_7H_7 with C_3H_4-P have a minor contribution to C_9H_8 formation in benzene-propylene co-pyrolysis.

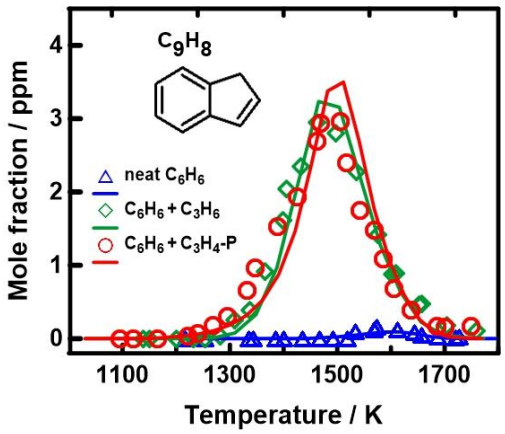

Figure 5.36: Experimental (symbols) and modeling (solid lines) mole fractions of indene (C_9H_8) as a function of the post shock temperature T_5 in neat benzene, benzene+C_3H_4-P and benzene+C_3H_6 pyrolysis

Apart from indene formation, numerous two-to-three ring PAH species are identified and quantified in C_6H_6+C_3H_4-P and C_6H_6+C_3H_6 pyrolysis experiments. **Figure 5.37** displays the measured and the simulated mole fractions profiles for PAHs in both sets against neat benzene pyrolysis. All shown PAHs have higher mole fractions when propylene and propyne are added to benzene. In general, the current kinetic model can well predict the PAH concentrations and the speciation temperature windows; however, it over predicts the peak concentrations for few PAH species in C_6H_6+C_3H_4-P pyrolysis, such as naphthalene, acenaphthylene and phenanthrene. This can be attributed to high formation rate constants, low consumption kinetic rates, or missing consumption pathways. Two points support the last assumption: 1) the kinetic model can well capture the formation temperature window of the species; 2) the carbon recovery in benzene + propyne pyrolysis is the worst among benzene, benzene+ethylene, benzene+acetylene and benzene+propylene pyrolysis, as shown in **Figures 5.38** and **5.39**. At high temperatures, 55% of the carbon is recovered in benzene + propyne pyrolysis, while 75-85% in the other sets. Similar conclusion was obtained by comparing the carbon recovery of propyne pyrolysis to propylene pyrolysis.

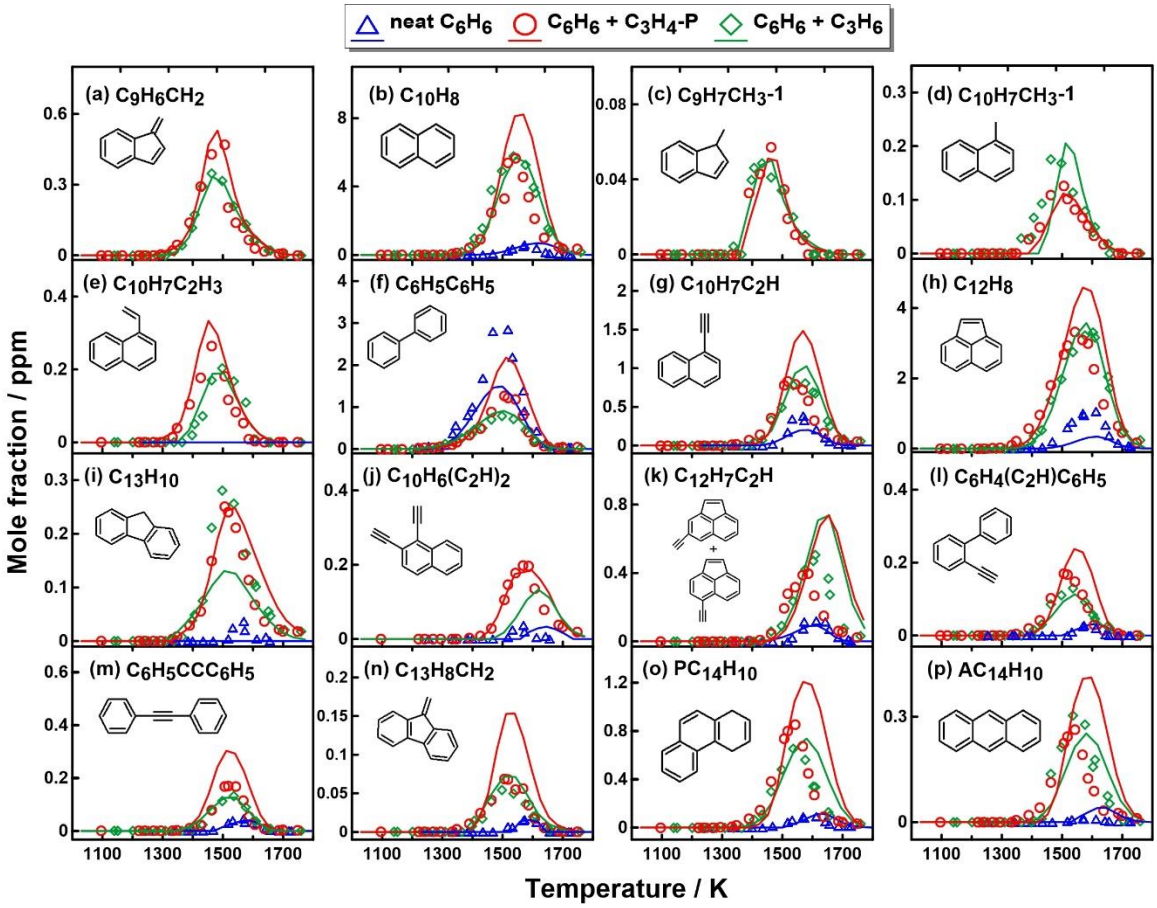

Figure 5.37: Measured (symbols) and simulated (solid lines) mole fractions of polyaromatic hydrocarbons (PAHs) as a function of the post shock temperature T_5 in neat benzene, benzene+C_3H_4-P and benzene+C_3H_6 pyrolysis

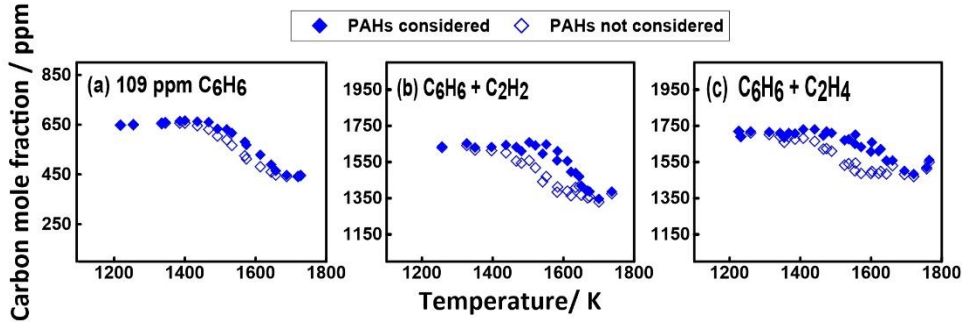

Figure 5.38: Carbon recovery with and without considering the PAH species in (a) benzene pyrolysis (b) benzene + acetylene pyrolysis and (c) benzene + ethylene pyrolysis.

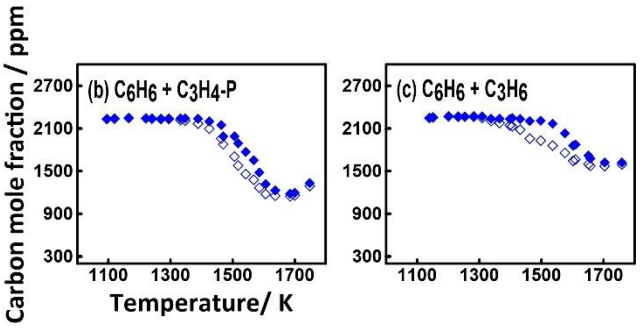

Figure 5.39: Carbon recovery with and without considering the PAH species in (a) benzene + propyne pyrolysis and (b) benzene + propylene pyrolysis.

The consumption of C_9H_8 mainly produces indenyl radical (C_9H_7) through H-abstraction and unimolecular decomposition. The resulting C_9H_7 plays an important role in the growth of PAH in the benzene/C_3 pyrolysis experiments. The reactions of C_9H_7 with CH_3 and C_3H_3 are vital pathways to naphthalene **(Figure 5.37 b)** and acenaphthylene **(Figure 5.37 h)** formation, respectively. The formation mechanism of $C_{10}H_8$ includes several possible reaction pathways that are displayed in **scheme 5.6** based on ROP analysis done at 1530 K. As can be seen in **scheme 5.6**, $C_{10}H_8$ mainly comes from the isomerization of $C_9H_6CH_2$ and the unimolecular decomposition of both $C_9H_6CH_3$-1 and $C_9H_7CH_2$ following the production of 1-methyl indene ($C_9H_7CH_3$-1) through $C_9H_7 + CH_3$. Other important formation pathways of $C_{10}H_8$ include:

i) The HACA pathway through phenylacetylene radical ($C_6H_4C_2H$) and C_2H_2 leading to naphthyl radicals which can convert to naphthalene by recombination with a hydrogen atom.

ii) The recombination reaction between fulvenallyl (C_7H_5) and C_3H_3, where C_7H_5 mainly comes from C_7H_7 decomposition.

iii) The unimolecular decomposition of $C_{10}H_7C_2H_3$ to $H_2CC + C_{10}H_8$ and the bimolecular reaction between $C_{10}H_7C_2H_3$ and H atom leading to $C_{10}H_8 + C_2H_3$; $C_{10}H_7C_2H_3$ mainly originates from the reaction of C_9H_7 with C_3H_3.

iv) The ipso-substitution reaction between 1-methyl naphthalene ($C_{10}H_7CH_3$_1) and H atom forming $C_{10}H_8 + CH_3$ (not shown in **scheme 5.6**); $C_{10}H_7CH_3$_1 is the product of the bimolecular reactions between $C_{10}H_7$_1 and CH_3 and $C_6H_5 + C_5H_5$.

v) The cycloaddition/fragmentation mechanism between o-C_6H_4 and C_6H_6 through the intermediate of benzobicyclo [2, 2, 2] octatriene (BICYCLO) proposed by Comandini and Brezinsky [24] to account for the formation of $C_{10}H_8$.

The relative importance of the above-mentioned channels varies with temperature, and the first one (i) has relatively high significance at elevated temperatures. Although the last channel (v) is considered as an important $C_{10}H_8$ source in benzene/C_2 and neat benzene pyrolysis, it has minor contribution to $C_{10}H_8$ formation throughout the temperature range in benzene/C_3 pyrolysis.

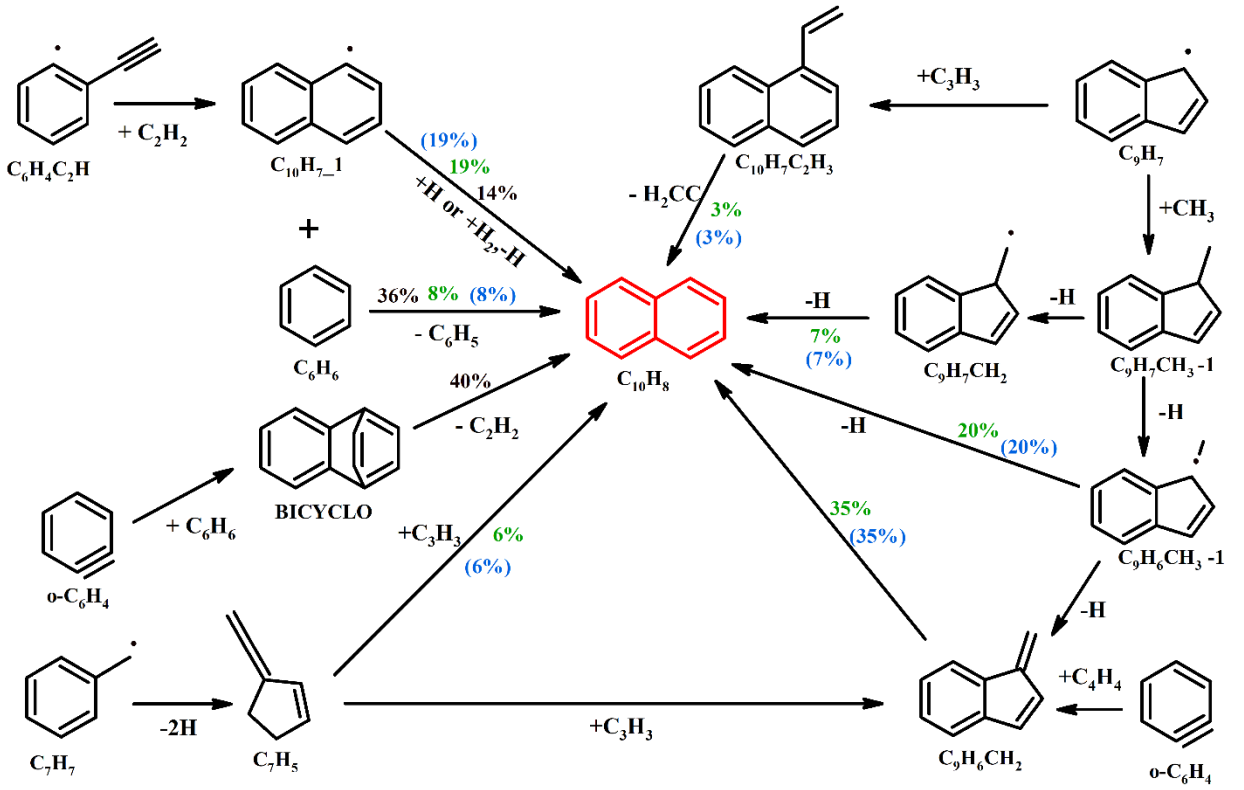

Scheme 5.6: The reaction pathways leading to naphthalene formation at T_5 of 1530 K in the pyrolysis of benzene and benzene/C_3 binary mixtures. The percentage numbers (B: black normal; BPene: green normal; BPyne: blue in brackets) represent the contributions of the corresponding reactions in naphthalene formation.

The formation of $C_9H_6CH_2$ **(Figure 5.37 a)**, naphthalene isomer, relies on four major channels: i) the decomposition of $C_9H_6CH_3$-1; ii) the HACA reaction between $C_6H_4C_2H$ and C_2H_2 leading to benzofulvenyl radical (C_9H_6CH) which further reacts with H atom; iii) the recombination reaction of C_7H_5 with C_3H_3; iv) the bimolecular reaction between o-benzyne (o-C_6H_4) and vinylacetylene (C_4H_4).

Acenaphthylene is an abundant PAH in both BPene and BPyne pyrolysis (see **Figure 5.37** (h)). The added C_3 fuels lower the $C_{12}H_8$ onset temperature and increase its peak concentration from 1 ppm in pure benzene pyrolysis to 3 ppm in benzene + C_3 pyrolysis. **Scheme 5.7** displays a reaction scheme centering on $C_{12}H_8$ formation based on the ROP-analyzed results at T_5 of 1500 K for the studied cases. Three essential pathways contribute to $C_{12}H_8$ formation: i) the recombination of C_9H_7 and C_3H_3 which

eventually lead to the formation of acenaphthylene as proposed recently by Jin et al. [198]; ii) the isomerization of biphenyl radical ($C_{12}H_9$) through BENZO intermediate [26]; iii) the C_2H_2 addition to $C_{10}H_7$-1. The former channel is the governing pathway at low temperatures, while the latter one is more competitive at elevated temperatures.

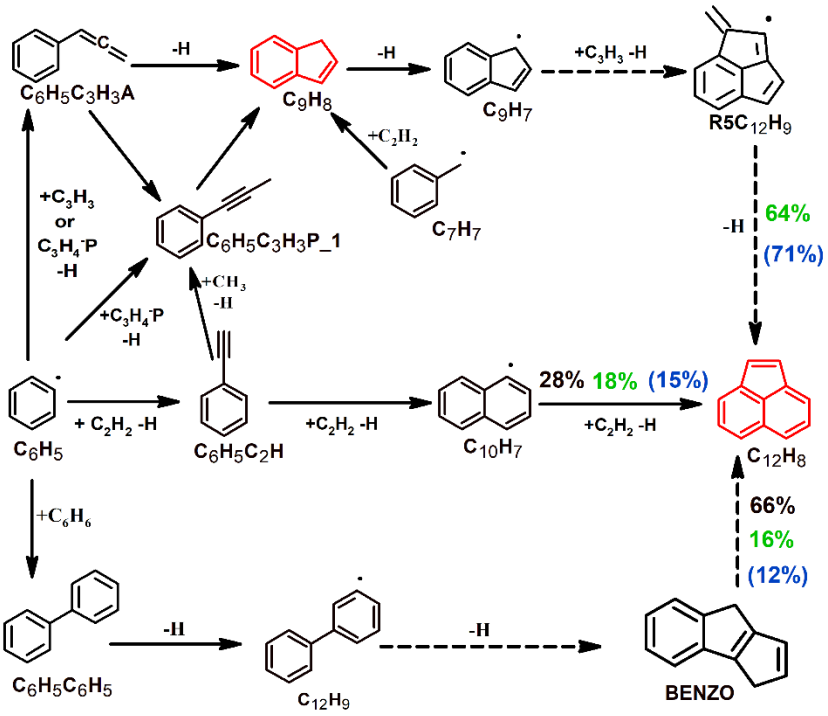

Scheme 5.7: The reaction pathways leading to the formation of acenaphthylene at T_5 of 1500 K in the pyrolysis of benzene and benzene/C_3 binary mixtures. The percentage numbers (B: black normal; BPene: green normal; BPyne: blue in brackets) represent the contributions of the corresponding reactions in acenaphthylene formation. The dashed arrows indicate multi-step processes.

Additional different C_{10}-C_{13} PAHs including $C_9H_7CH_3$, $C_{10}H_7CH_3$_1, $C_{10}H_7C_2H_3$, $C_6H_5C_6H_5$, $C_{10}H_7C_2H$_1 and $C_{13}H_{10}$ are measured in benzene/C_3 pyrolysis. Their mole fraction profiles as well as the simulated results are shown in **Figure 5.37**. $C_9H_7CH_3$ and $C_{10}H_7C_2H_3$ are formed mainly from the reaction of C_9H_7 with CH_3 and C_3H_3, respectively. $C_6H_5C_6H_5$ is mainly produced from the reaction of C_6H_6 + C_6H_5. A minor contribution comes from the reaction between phenyl propargyl radical ($C_6H_5C_2H_3$) and C_3H_3. Similar trend as in benzene/C_2 pyrolysis is expected in benzene/C_3 pyrolysis concerning the peak concentration of $C_6H_5C_6H_5$. This is due the interactions of C_6H_5 with C_3 fuels. The reactions of naphthyl ($C_{10}H_7$_1) radical with CH_3 and C_2H_2 control the formation of $C_{10}H_7CH_3$_1 and $C_{10}H_7C_2H$_1, respectively. The $C_{10}H_7$_1 + C_3H_4-P reaction also accounts for a small part of $C_{10}H_7C_2H$_1 production (3% in BPyne pyrolysis and 1.45% in BPene pyrolysis at 1470 K). $C_{13}H_{10}$ is mainly the result of the addition reactions of C_3H_4-P on $C_{10}H_7$_2 and C_4H_4 on C_9H_7. The reaction sequence diphenylmethane ($C_{13}H_{12}$)→$C_{13}H_{11}$→$C_{13}H_{10}$ has a minor contribution to $C_{13}H_{10}$ production.

The C_{14} PAHs species detected in pure benzene and benzene/C_2 pyrolysis experiments are also present in the species pool of C_6H_6+C_3H_6 and C_6H_6+C_3H_4-P pyrolysis. The ROP analysis shows that the dominant formation pathways of $C_{14}H_8$ isomers: $C_{10}H_6(C_2H)_2$ and $C_{12}H_7C_2H$ strongly depend on $C_{10}H_6C_2H$ + C_2H_2 and $C_{12}H_7$+ C_2H_2 reactions, respectively. **Scheme 5.8** sums up the important reaction pathways leading to the formation of $C_{14}H_{10}$ isomers at 1530K based on the integrated ROP analyses. $C_6H_4(C_2H)C_6H_5$, $C_6H_5CCC_6H_5$ and $C_{13}H_8CH_2$ are mainly produced from the addition-elimination reactions between $C_6H_5C_2H$ and C_6H_5. Newly introduced channels are found to play a minor role in $C_6H_4(C_2H)C_6H_5$ formation, such as the reaction of $C_{12}H_9$ with C_3H_4-P that leads either directly to $C_6H_4(C_2H)C_6H_5$ production or to 1-biphenyl propyne ($C_{12}H_9C_3H_3$P_1) which subsequently decomposes to $C_6H_4(C_2H)C_6H_5$. $C_6H_5C_6H_5$+C_2H= C_6H_4 (C_2H) C_6H_5 +H reaction has also minor contribution to $C_6H_4(C_2H)C_6H_5$ in all the reaction systems. Both $C_6H_5CCC_6H_5$ and $C_{13}H_8CH_2$ are precursors for $PC_{14}H_{10}$. $AC_{14}H_{10}$ is almost totally formed through the isomerization of $PC_{14}H_{10}$. The C_7H_5 self-recombination has minor contribution to $AC_{14}H_{10}$ in benzene+C_3 pyrolysis.

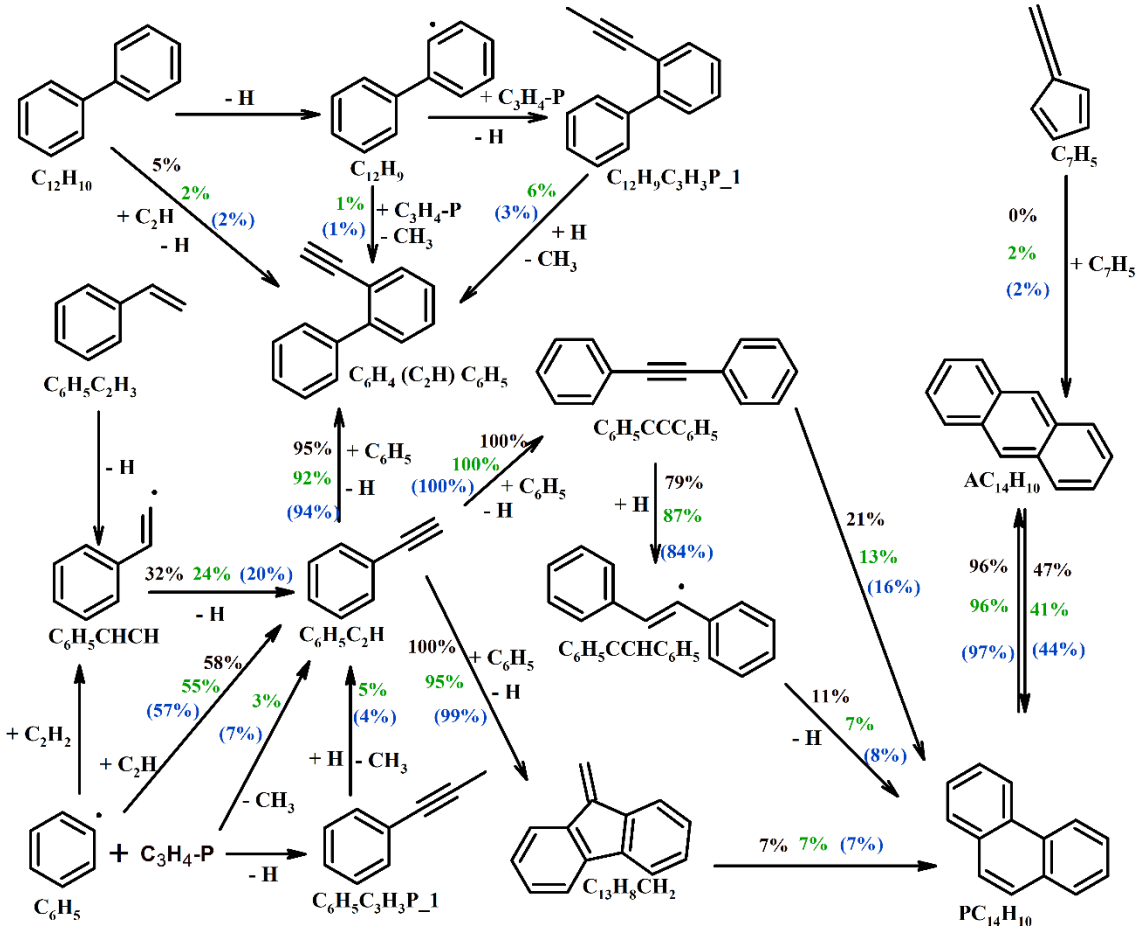

Scheme 5.8: The reaction pathways leading to the formation of $C_{14}H_{10}$ isomers at T_5 of 1530 K in the pyrolysis of benzene and benzene/C_3 binary mixtures. The percentage numbers (B: black normal; BPene: green normal; BPyne: blue in brackets) represent the contributions of the corresponding reactions in $C_{14}H_{10}$ formation.

5.2.4.4 Simulations with pressure profile

Simulations with pressure profiles up to 10 ms are performed for benzene+C_3 pyrolysis. The time dependent mole fraction profiles for the major products and phenyl radical are shown in **Figure 5.40**. The plateaus in the concentration of the major products during the quenching process indicate that products' formation is terminated by the defined reaction time. The error in simulating the present experimental sets with the constant pressure assumption is minimal.

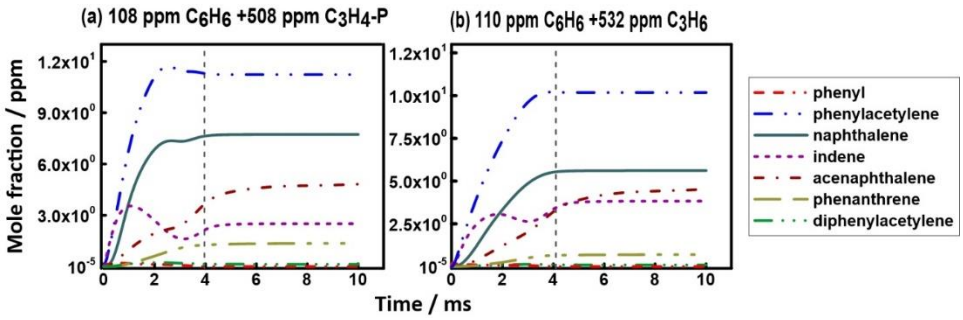

Figure 5.40: Simulated species mole fractions as a function of time with the measured pressure profiles in (a) C_6H_6/C_3H_4-P pyrolysis at T_5=1568 K, P_5=21.57 bar; (c) C_6H_6/C_3H_6 pyrolysis at T_5=1536 K, P_5= 21.4 bar. The dashed vertical lines indicate the start of quenching.

5.3 Toluene pyrolysis and its reactions with C_2/C_3 hydrocarbons

5.3.1 Motivation

Toluene is a major component in gasoline as well as in gasoline surrogate fuels. Consequently, understanding toluene decomposition chemistry is a vital step toward the development of large aromatic hydrocarbons kinetic models. Furthermore, its initial decomposition product the resonantly stabilized, benzyl radical, is an essential intermediate involved in the growth of PAHs. For instance, the reaction of benzyl with acetylene and propargyl is deemed to be an important source of indene and naphthalene, respectively. C_2 and C_3 species are as well abundant decomposition products in combustion systems. Thus, the experimental and kinetic modeling research on toluene and its interactions with C_2 and C_3 species is of extreme value among the aromatic hydrocarbon studies. To this end, shock tube pyrolysis experiments are carried out using eight different argon diluted mixtures, where their detailed compositions are presented in **table 5.2**. The binary blends contain impurities, which have been measured to be methane in toluene-acetylene mixtures, propane (2 ppm) in the toluene-propylene mixture, and 2-butene (4.5 ppm) and isobutane (3.5 ppm) in the toluene-propyne mixture.

Table 5.2: Compositions of the experimental gas mixtures calibrated by the GC

Gas mixture	Composition				
	Toluene (C_7H_8)	Ethylene (C_2H_4)	Acetylene (C_2H_2)	Propylene (C_3H_6)	Propyne (C_3H_4-P)
T_200	216 ppm	--	--	--	--
T_100	105 ppm	--	--	--	--
TE	106 ppm	518 ppm	--	--	--
TA_50	107 ppm	--	50 ppm	--	--

TA_216	106 ppm	--	216 ppm	--	--
TA_459	105 ppm	--	459 ppm	--	--
TPene	106 ppm	--	--	513 ppm	--
TPyne	108 ppm	--	--	--	557ppm

5.3.2 Toluene thermal decomposition

5.3.2.1 Fuel decomposition and formation of small products

Figure 5.41 illustrates the experimental and the simulated mole fraction profiles of C_7H_8, C_0-C_4 species, C_6H_6, $C_6H_5C_2H$, and $C_6H_5C_2H_3$. The fuel molecule, C_7H_8 is consumed through unimolecular decomposition reactions, H-abstraction reactions by H and CH_3, and the ipso-substitution reaction. The two latter pathways are dominant at high temperatures.

Among the small hydrocarbon intermediates, CH_4 is abundantly produced from H-atom abstraction reactions on C_7H_8 by CH_3, while CH_3 is mainly formed from the ipso-substitution reaction H+ C_7H_8= CH_3+ C_6H_6, the decomposition reaction of benzyl (C_7H_7= CH_3+ o-C_6H_4), and it also trivially originates from the unimolecular decomposition of C_7H_8 (C_7H_8 (+M) = CH_3+ C_6H_5 (+M)). C_2H_6 is exclusively produced from the self-recombination of CH_3. The C_2H_6 consumption substaneously contributes to C_2H_4 production. Another important pathway for C_2H_4 formation is through the consumption of styrene (H+$C_6H_5C_2H_3$= C_6H_5+C_2H_4). There are numerous formation pathways for C_2H_2 under the pyrolytic conditions considered here. Most of C_2H_2 is produced via the decomposition of o-C_6H_4 (o-C_6H_4= C_2H_2+ C_4H_2), the H-atom addition fragmentation of C_7H_6 (H+ C_7H_6= C_2H_2+ C_5H_5), C_5H_5 unimolecular decomposition (C_5H_5= C_2H_2+ C_3H_3), and LC_6H_5 unimolecular decomposition (LC_6H_5= C_2H_2+ C_4H_3). Among these intermediates, C_7H_6 is 100% produced from the unimolecular decomposition of benzyl (C_7H_7= H+ C_7H_6). Two C_3 species C_3H_4-A and C_3H_4-P are detected in the experiments. The ROP analysis shows that both C_3H_4-A and C_3H_4-P are predominantly produced by H-atom addition to C_3H_3. C_3H_4-P is also produced from the isomerization of C_3H_4-A. Most of C_3H_3 is produced from the unimolecular decomposition of C_7H_5 through the reaction C_7H_5= C_3H_3+ C_4H_2, and partly from the C_5H_5 unimolecular decomposition; C_7H_5 comes from the C_7H_7 two-step H-elimination reaction sequence. All 1,3-butadiene (C_4H_6) comes from the reaction CH_3+C_3H_3. The subsequent two-step H-elimination reaction sequence leads to the formation of C_4H_4, which has a peak mole fraction of 1.5 ppm (not shown in **Figure 5.41**).

C_4H_2 is mainly formed from the decomposition reactions of C_7H_5 and o-C_6H_4. The decomposition of C_4H_3, which arise from LC_6H_5 unimolecular decomposition, slightly contributes to C_4H_2 formation.

The thermal decomposition of toluene also leads to various single-aromatic structures. C_6H_6 is mainly produced through the ipso-substitution reaction $C_7H_8+H = C_6H_6+CH_3$, which contributes almost 10-15% of the fuel consumption at different temperatures. This was also noticed by Yuan et al. [70] from flow tube reactor pyrolysis experiments under sub-atmospheric pressure conditions. $C_6H_5C_2H_5$, maximum mole fraction of 1.6 ppm (not shown in **Figure 5.41**), is produced from the recombination of C_7H_7 and CH_3 due to the abundantly production of the two radicals in the primary decomposition of toluene. The subsequent decomposition of $C_6H_5C_2H_5$ mainly proceeds through H-atom abstraction and unimolecular decomposition reactions to produce C_8H_9 radicals. Particularly, 1-phenylethyl radical ($C_6H_5CHCH_3$) can quickly decompose to $C_6H_5C_2H_3$ through the β-C-H scission reaction, which is also the most important formation pathway for styrene. The HACA route through $C_6H_5+C_2H_2$ is an important source for $C_6H_5C_2H$, however, the decay of $C_6H_5C_2H_3$ plays a dominant role in the formation of $C_6H_5C_2H$ at lower temperatures.

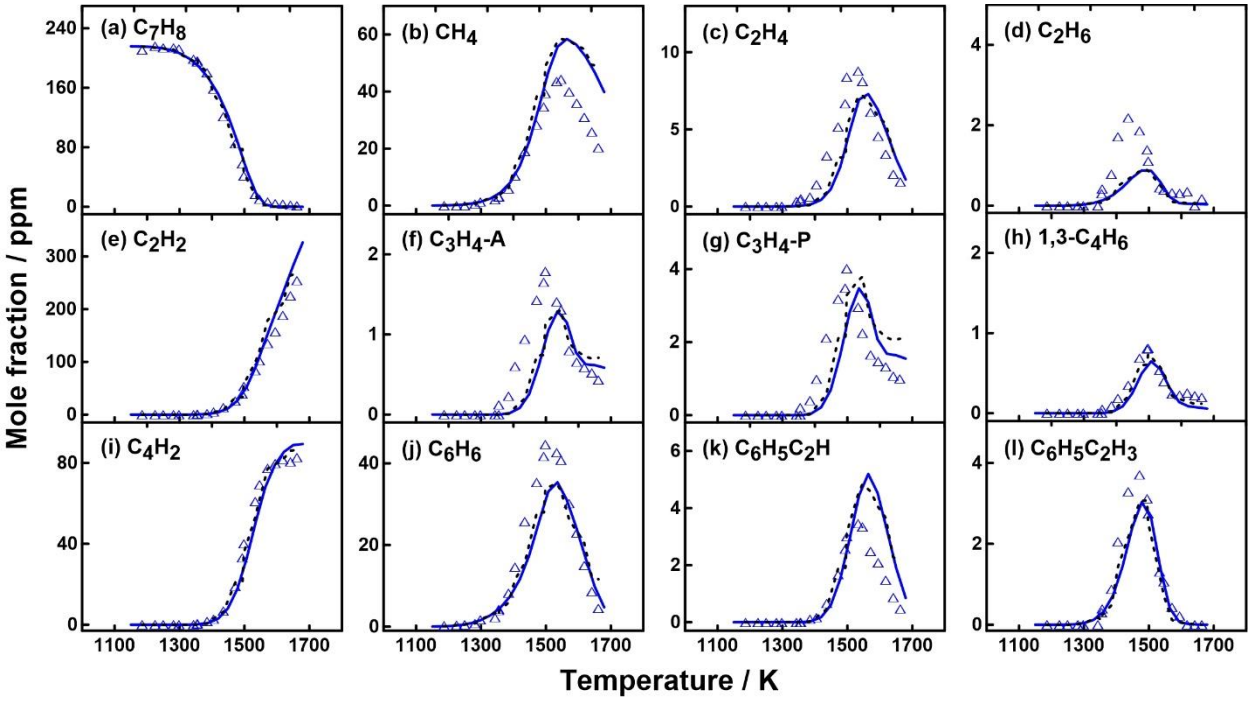

Figure 5.41: Experimental (symbols) and simulated (solid lines) mole fraction profiles of fuel, C_0-C_4 species and MAHs in 216 ppm toluene pyrolysis at P_5=20 bar. Dashed lines indicate the model predictions with the measured pressure-profiles.

5.3.2.2 PAH species formation

The experimental and computed mole fraction profiles of PAHs containing two to four rings are presented in **Figure 5.42**. In this work, two fused-bicyclic PAHs are observed indene and naphthalene. C_9H_8 is formed mainly via C_7H_7+C_2H_2 reaction due to the abundant production of C_7H_7 and C_2H_2 in toluene pyrolysis. The C_6H_5+C_3H_3 reactions also contribute in C_9H_8 through the intermediates $C_6H_5C_3H_3$P_1 and $C_6H_5C_3H_3$A [42] (about 22% at T=1500 K). The consumption of C_9H_8 mainly produces C_9H_7 radical through H-atom abstraction and unimolecular decomposition reactions. The simulation results in both methods (constant pressure and experimental pressure profiles) over-predict C_9H_8 profile. The higher peak mole fraction seen using the second method goes to two reasons: (i) the presence of large amount of C_7H_7 during the quenching period; (ii) the isomerization of both $C_6H_5C_3H_3$P_1 and $C_6H_5C_3H_3$A to indene during the quenching period. $C_{10}H_8$ has the highest experimental peak mole fraction among the observed bicyclic PAHs, and it has a number of possible formation pathways. $C_{10}H_8$ mainly comes from the unimolecular decomposition of $C_9H_6CH_3$-1, which is produced through the reaction of C_9H_7+CH_3. Besides, $C_9H_6CH_3$-1 subsequent decomposition leads to $C_9H_6CH_2$ which isomerizes to $C_{10}H_8$; $C_9H_6CH_2$ is also produced through the combination of C_7H_5+C_3H_3 and o-C_6H_4+C_4H_4. The other important pathway includes the recombination of C_7H_5+C_3H_3. Although the reaction of C_6H_6+o-C_6H_4 through the intermediate BICYCLO [24] is considered an important $C_{10}H_8$ formation channel in benzene pyrolysis, it only contributes about 9% at 1500K according to ROP analysis in toluene pyrolysis.

Besides indene and naphthalene, some non-fused bicyclic PAHs are also observed in the experiments including $C_6H_5C_6H_5$, biphenylmethane ($C_6H_5CH_2C_6H_5$), and bibenzyl ($C_6H_5C_2H_4C_6H_5$). $C_6H_5C_2H_4C_6H_5$ is the most abundant PAH species in toluene pyrolysis and its formation depends on the self-recombination of the resonantly stabilized C_7H_7 radicals. The kinetic model with the first method (constant P_5) underpredicts the formation of $C_6H_5C_2H_4C_6H_5$, while the second method overpredicts its final concentration (see **Figure 5.42 (f)**). This demonstrates that the self-recombination of C_7H_7 carry on during the quenching period, and this is due to the large concentration of C_7H_7 present in the species pool after the arrival of the rarefaction waves. $C_6H_5C_6H_5$ is mainly produced from the bimolecular reaction between C_6H_6 and C_6H_5. The dominant formation pathway of $C_6H_5CH_2C_6H_5$ is the recombination reaction between C_6H_5 and C_7H_7.

Another major PAH intermediate is acenaphthylene (**Figure 5.42 (d)**), the formation mechanism of $C_{12}H_8$ includes: (i) the addition of C_3H_3 to C_9H_7 [198]; (ii) isomerization process [25], [26] of $C_{12}H_9$, the radical of $C_6H_5C_6H_5$; (iii) the HACA route through $C_{10}H_7$_1+C_2H_2. The former pathway is the prevailing one throughout the temperature range, while the latter one is more competitive at high temperatures. Concerning fluorene (**Figure 5.42 (g)**), it directly results from the dehydrogenation sequence ^{13} ^{12} →

$_{13}\ _{11} \rightarrow\ _{13}\ _{10}$ and decomposes mainly to fluorenyl ($C_{13}H_9$). $C_{13}H_9$ recombines with CH_3 forming $C_{13}H_8CH_2$, which also comes from the C_7H_5 self-recombination. The $C_{13}H_8CH_2$ subsequent decomposition is considered to be the prevailing phenanthrene ($C_{14}H_{10}$) pathway in Matsugi and Miyoshi study [66]. On the contrary, the dehydrogenation reaction sequence $_{14}\ _{14} \rightarrow\ _{14}\ _{12} \rightarrow\ _{14}\ _{10}$, which has been theoretically investigated in [58], is analyzed to be the greatest contributor of $C_{14}H_{10}$ formation with the current model due to the high concentration levels of C_{14} bicyclic PAHs in toluene pyrolysis. The C_7H_5 self-recombination is another minor pathway leading to $C_{14}H_{10}$ production (around 4% at T_5=1500 K). $AC_{14}H_{10}$ is almost totally formed from the isomerization of phenanthrene.

The two tetracyclic isomer pair $C_{16}H_{10}$ (**Figure 5.42 (j)**) and $FC_{16}H_{10}$ (**Figure 5.42 (k)**) are well-separated and model-predicted. $FC_{16}H_{10}$ is largely the product of the recombination reaction between $C_{10}H_7$_1 and C_6H_5. The dehydrogenation sequence starting from C_7H_7+C_9H_7 recombination yields to a small part of the total formation of $FC_{16}H_{10}$ (12% at T_5=1500 K). This reaction channel [210] can also end up in $C_{16}H_{10}$, but Sinha et al. [210] pointed out that the pathway leading to $FC_{16}H_{10}$ occurs at short time scales which makes it a more favored route. In the current work, this channel contributes to 8% of the total formation of $C_{16}H_{10}$ at T_5=1500 K. The recombination of methylphenyl ($CH_3C_6H_4$) + $C_{10}H_7$_1, and the HACA route through $C_{14}H_9$+C_2H_2 are the dominant $C_{16}H_{10}$ sources in toluene pyrolysis. Other minor formation pathways include the bimolecular reactions of C_6H_5+$C_{10}H_8$ and xylene radical (RXYLENE) +C_9H_7.

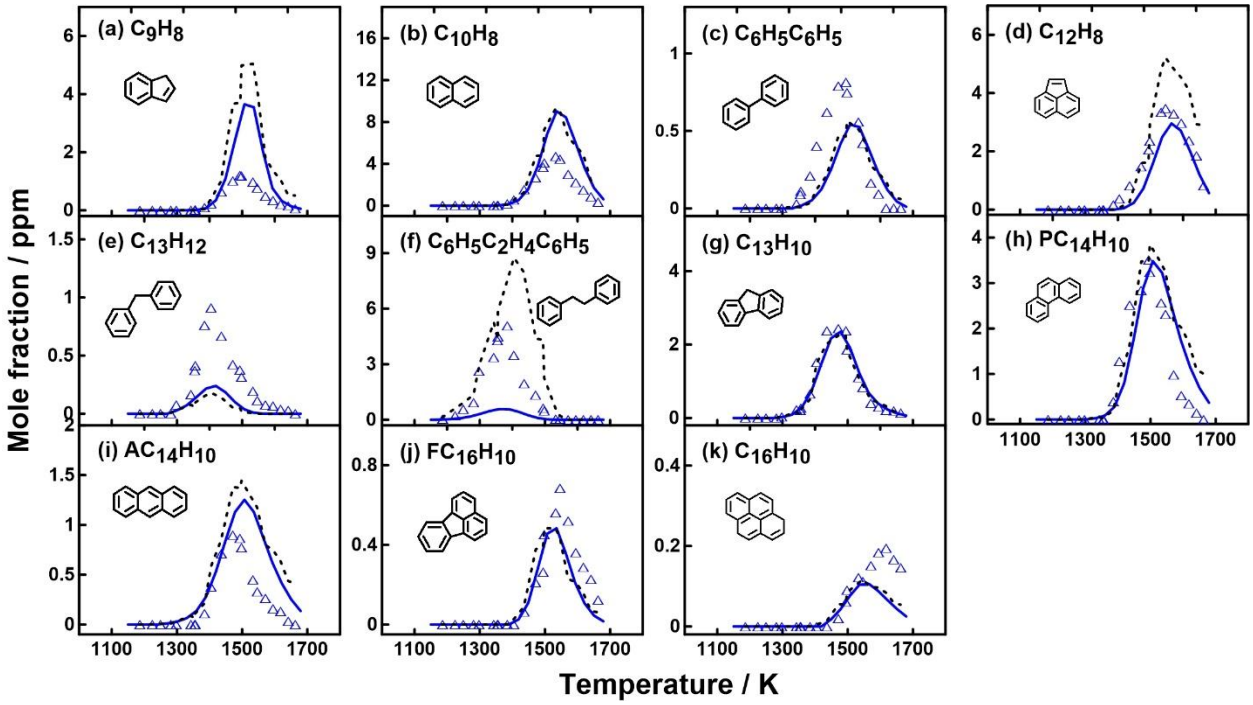

Figure 5.42: Experimental (symbols) and simulated (solid lines) mole fraction profiles of PAHs in 216 ppm toluene pyrolysis at P_5=20 bar. Dashed lines indicate the model predictions with the measured pressure-profiles.

5.3.3 Impacts of added acetylene and ethylene on toluene pyrolysis

Experimental and simulated mole fraction profiles using the two methods (constant pressure and measured pressure profile) for major species in toluene and toluene +C_2 pyrolysis are shown in **Figures 5.43–5.47**. These datasets will be compared among each other and used as a base for more analysis in the next sections. Joint experimental observations and kinetic modeling interpretations will reveal the influences of the added C_2H_4 and C_2H_2 on the speciation from toluene pyrolysis. Moreover, effects brought by the separate addition of C_2H_2 and C_2H_4 will be compared, and the variation trends of specific species concentrations when different amounts of C_2H_2 are present in the fuel mixtures will be illustrated.

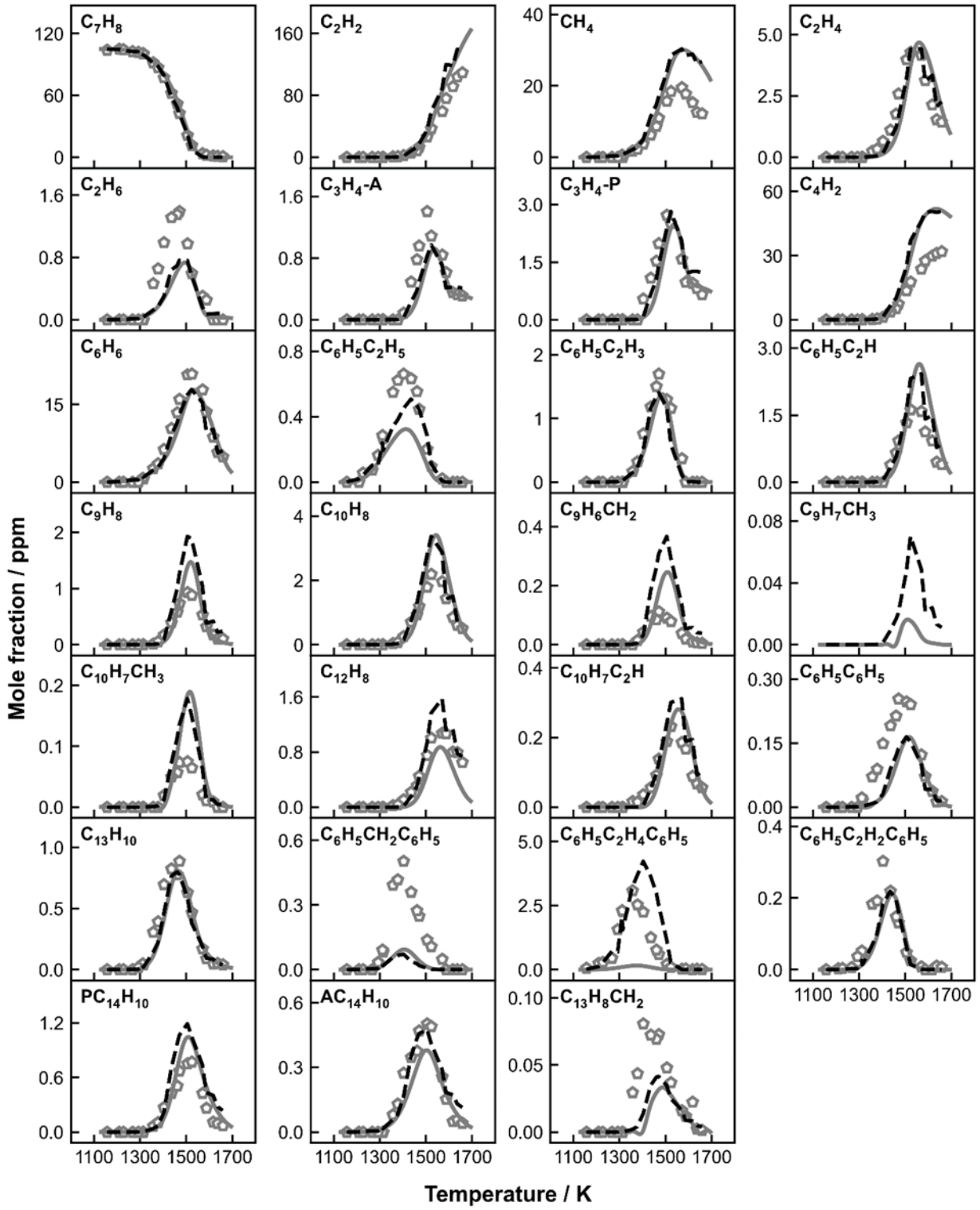

Figure 5.43: Species concentrations as a function of T_5 in neat toluene pyrolysis, including measurements (symbols), modeling results at constant pressure of 20 bar within a fixed reaction time of 4.0 ms (grey solid lines) and simulations with measured pressure profiles up to a time scale of 10 ms (black dashed lines).

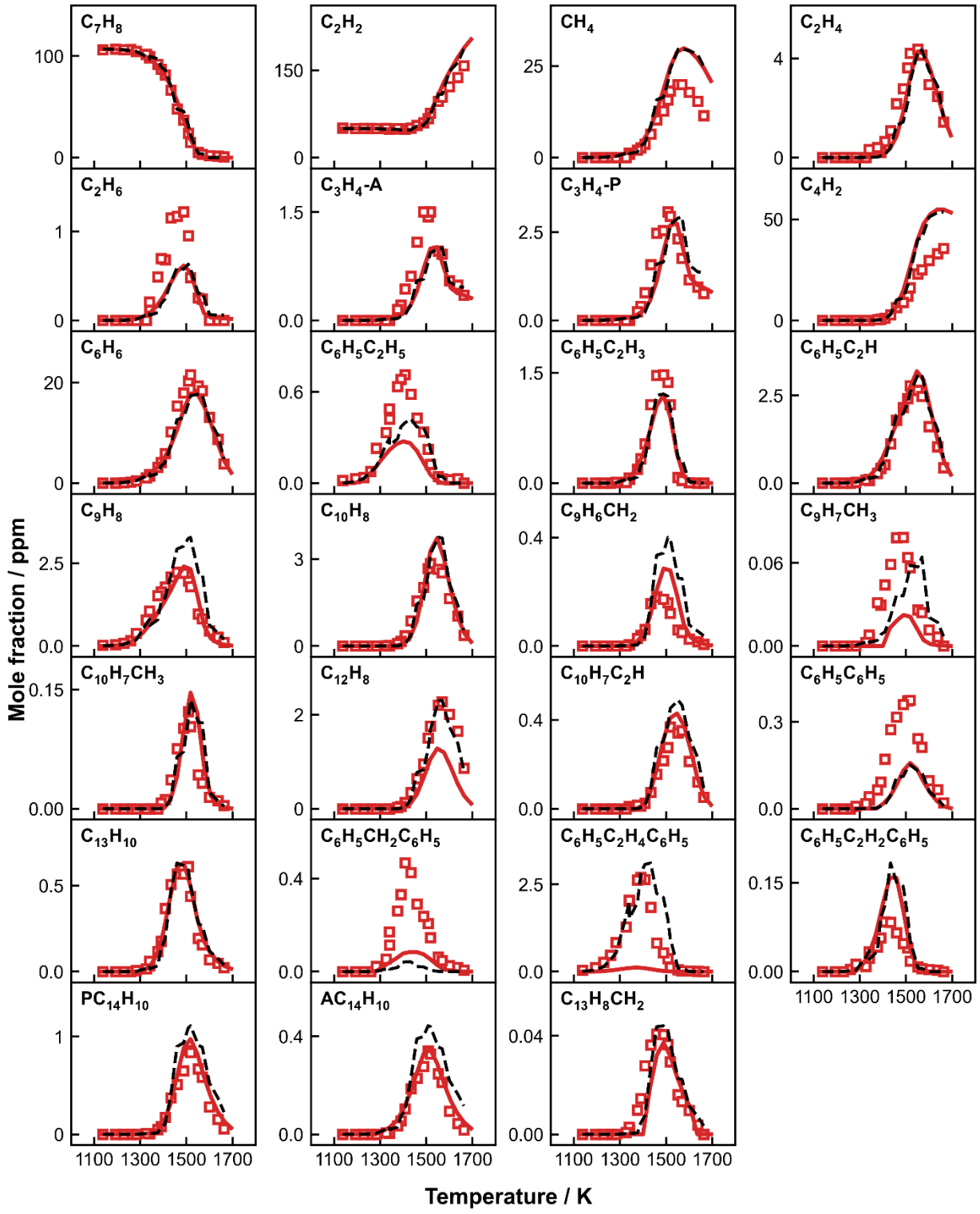

Figure 5.44: Species concentrations as a function of T_5 in TA_50 pyrolysis, including measurements (symbols), modeling results at constant pressure of 20 bar within a fixed reaction time of 4.0 ms (red solid lines) and simulations with measured pressure profiles up to a time scale of 10 ms (black dashed lines).

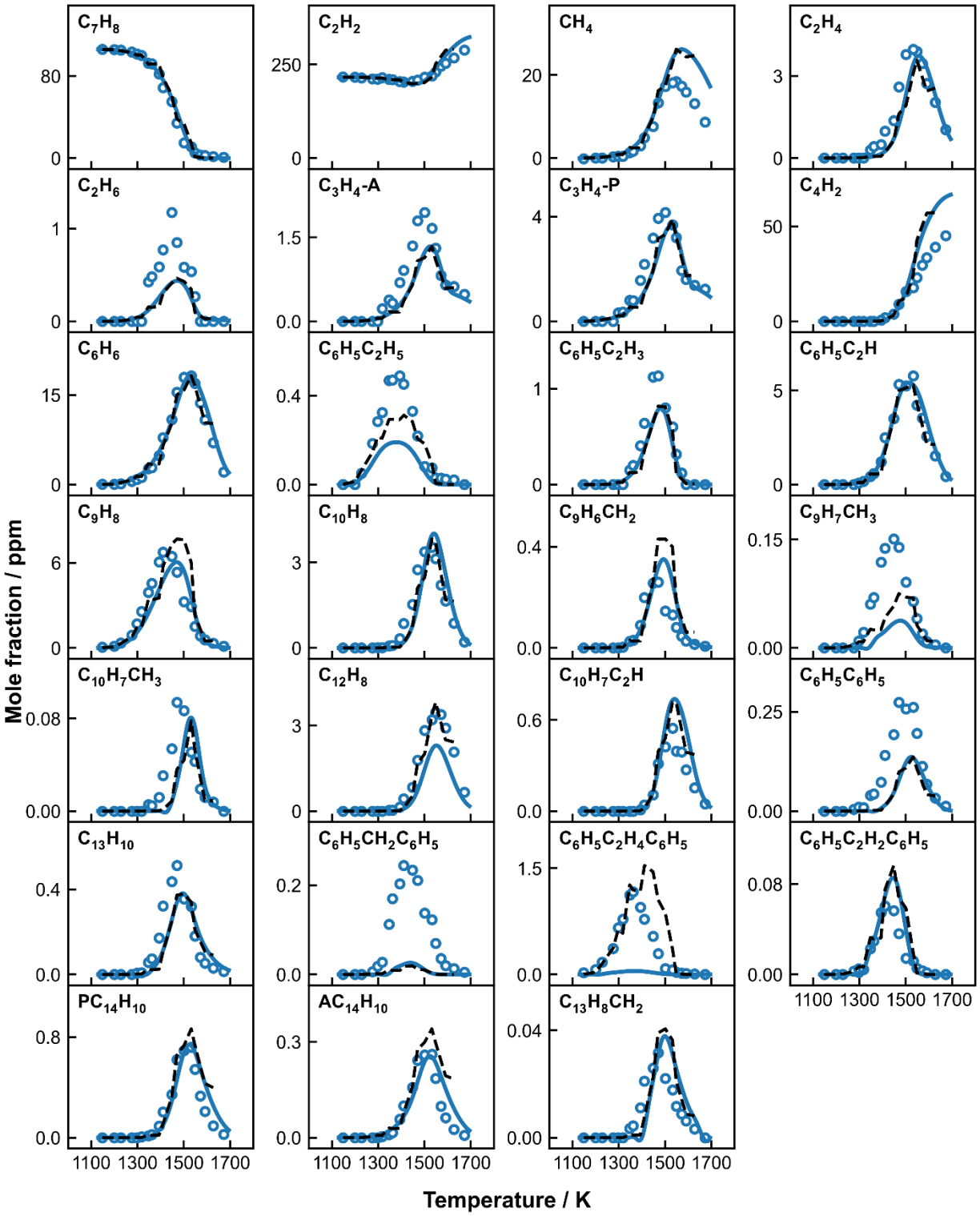

Figure 5.45: Species concentrations as a function of T_5 in TA_216 pyrolysis, including measurements (symbols), modeling results at constant pressure of 20 bar within a fixed reaction time of 4.0 ms (solid lines) and simulations with measured pressure profiles up to a time scale of 10 ms (dashed lines).

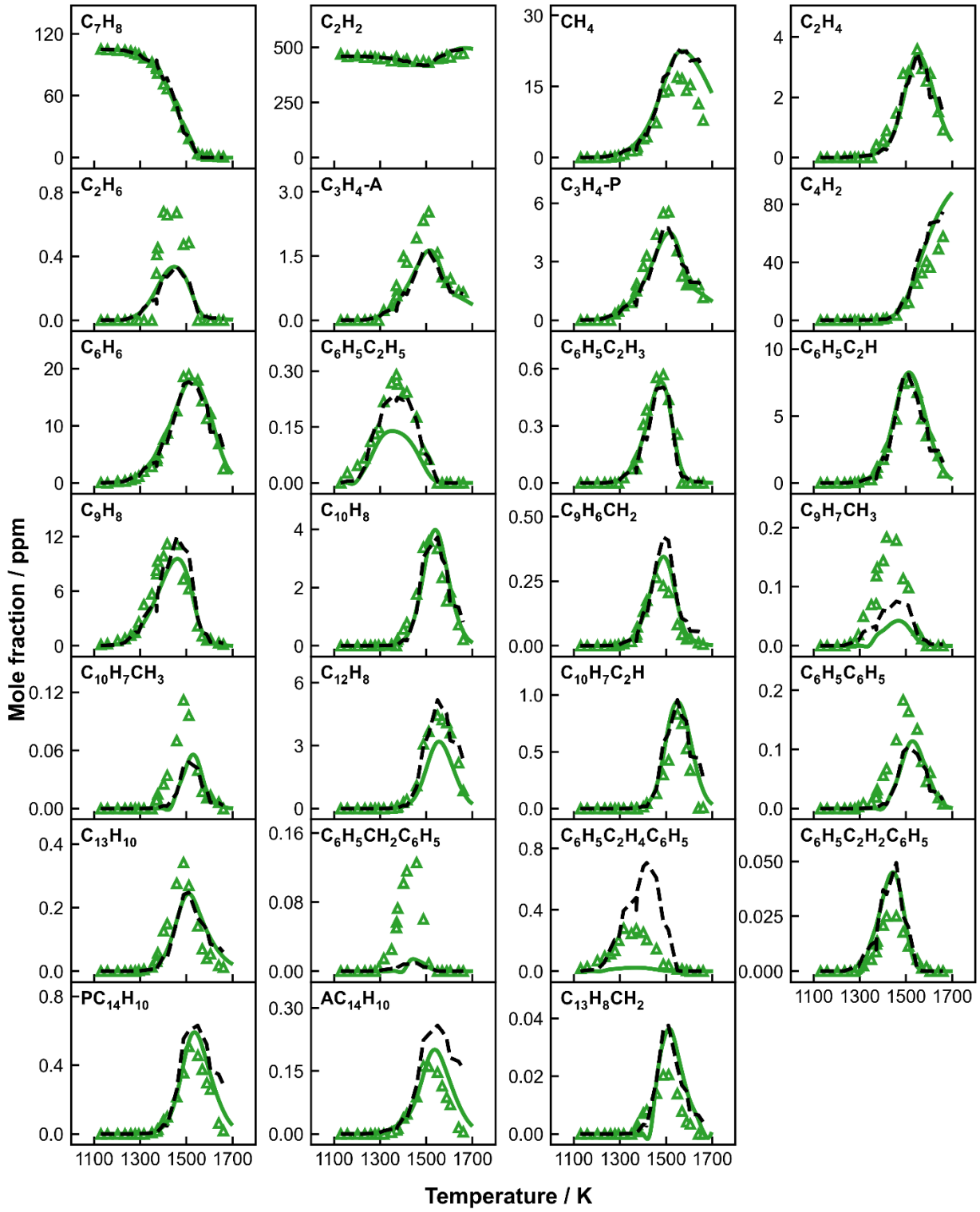

Figure 5.46: Species concentrations as a function of T_5 in TA_459 pyrolysis, including measurements (symbols), modeling results at constant pressure of 20 bar within a fixed reaction time of 4.0 ms (solid lines) and simulations with measured pressure profiles up to a time scale of 10 ms (dashed lines).

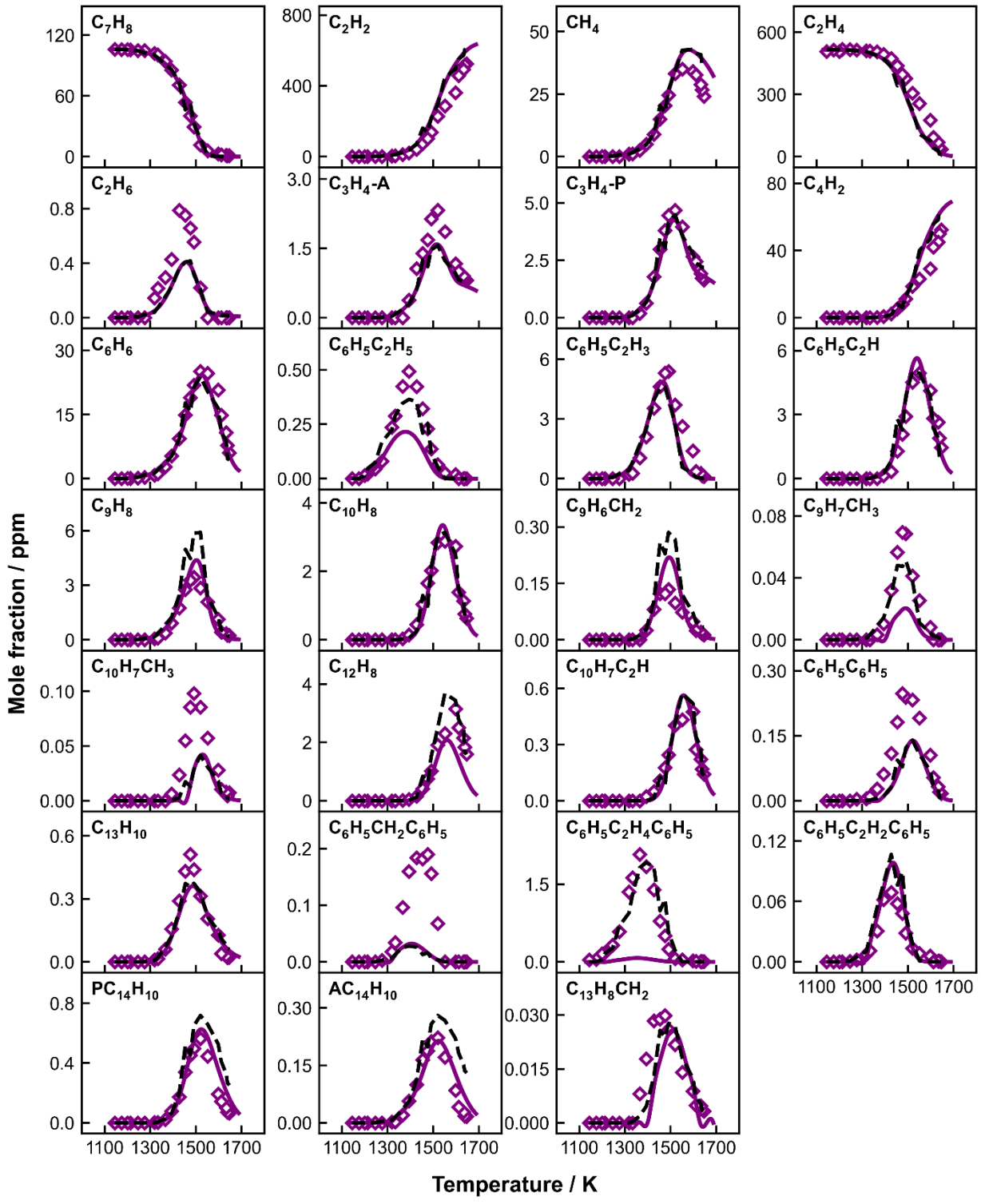

Figure 5.47: Species concentrations as a function of T_5 in TE pyrolysis, including measurements (symbols), modeling results at constant pressure of 20 bar within a fixed reaction time of 4.0 ms (solid lines) and simulations with measured pressure profiles up to a time scale of 10 ms (dashed lines).

5.3.3.1 Fuel decomposition and mono-aromatic ring intermediates

Figure 5.48 displays the experimental and modeling concentration profiles of toluene, acetylene and ethylene as a function of the post-shock temperature T_5 in separate cases of toluene/$C_2H_{x\ (x=2\ or\ 4)}$ pyrolysis. The kinetic model correctly predicts the measured fuel conversion profiles in the individual investigated cases. Simulated fuel decomposition profiles of neat toluene, neat C_2H_2 and neat C_2H_4 are also presented in **Figure 5.48** to effectively visualize the mutual effects between the components of binary fuel mixtures. To better examine the overlapped toluene profiles, the data are enlarged in the temperature range of 1300-1400 K, where the C_7H_8 starts decomposing, and it is shown in the inset of **Figure 5.48 (a).** Both experimental and modeling results indicate that an enhanced C_7H_8 decomposition is obtained with the increase of C_2H_2 initial content in the binary fuel mixtures. On the contrary, the addition of C_2H_4 has no obvious effect on C_7H_8 reactivity. According to ROP analyses, in all the studied cases, C_7H_8 decomposition is dominated by three types of reactions, the unimolecular decomposition reaction, the H-atom abstraction reaction, and the ipso-substitution reaction by H to C_6H_6+CH_3. C_7H_8 is initiated by the unimolecular reaction C_7H_8 (+M) = H+ C_7H_7 (+M) since the bond dissociation energy of methyl C-H bond is the lowest compared to other bonds in C_7H_8 molecule [189]. At high temperatures, C_7H_8 is primarily consumed through the H-abstraction reaction leading to C_7H_7 production and secondarily by the ipso-substitution reaction by H. The extra H-atoms in the toluene+C_2H_2 co-pyrolysis derives from the reaction C_7H_7+C_2H_2=>C_9H_8+H. Compared to neat C_2H_2, C_2H_2 starts to decompose at lower temperatures followed by a subsequent rise at elevated temperatures. The first stage outcome is more evident as the initial quantity of C_2H_2 increases. The kinetic model can well reproduce the C_2H_2 profiles in all the three cases of toluene/ C_2H_2 pyrolysis. ROP analyses show that the slight decline and subsequent growth of C_2H_2 arise from the reactions between toluene radicals (C_7H_7 and $CH_3C_6H_4$) and C_2H_2, and the C_2H_2 formation from the ring-fragmentation, respectively. The synergistic effect between toluene and C_2H_2 is also presented in Li et al. recent study [125], and the authors attributed the enhanced fuel decomposition reactivity to the reaction C_7H_7+C_2H_2 = C_9H_8+H as mentioned above. This reaction consumes C_2H_2 at relatively low temperatures, and produces H atoms which facilitate the H-abstraction reactions from both toluene and C_2H_2. On the other hand, the model suggests a faster consumption of C_2H_4 in toluene/ C_2H_4

pyrolysis compared to neat C_2H_4 pyrolysis, which is not very clear in the experimental profile. Based on the model simulations, the faster C_2H_4 decomposition mainly comes from the reactions between C_7H_7 and C_2H_4. Detailed discussion about the interaction mechanisms between the binary fuel components concerning the formation of small hydrocarbons, mono-aromatics and PAHs will be presented in the next section.

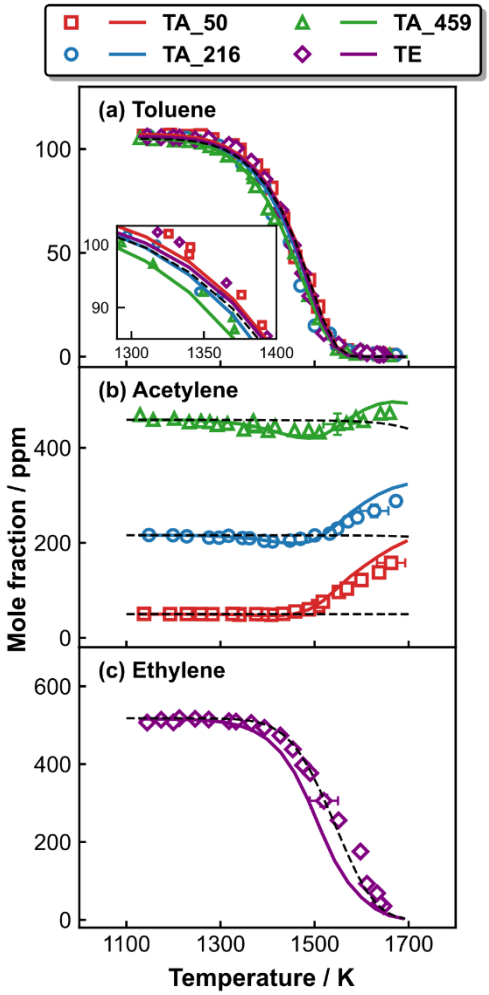

Figure 5.48: Measured (symbols) and simulated (lines) fuel mole fractions as a function of the post-shock temperature T_5 in toluene/acetylene (ethylene) pyrolysis. The dark dashed lines are simulated fuel decomposition profiles of (a) neat toluene (105 ppm in argon), (b) neat acetylene (50, 216 and 459 ppm in argon) and (c) neat ethylene (516 ppm in argon). The inset of (a) shows toluene concentrations over the temperature range of 1300−1400 K.

C_2H_2 and C_2H_4 have distinct decomposition reactivity, and thus different intermediate behavior in the currently investigated cases. Mole fraction profiles of C_2H_4 in toluene/ C_2H_2 pyrolysis and C_2H_2 in toluene/ C_2H_4 pyrolysis are shown in **Figure 5.49**, together with the profiles for neat toluene pyrolysis for comparison purpose. The C_2H_2 addition lowers the C_2H_4 peak mole fraction compared to the peak in neat

toluene case. As stated in the earlier section, the main source of C_2H_4 is the two-step dehydrogenation reactions from C_2H_6, which is formed through the CH_3 recombination. The presence of C_2H_2 in the initial mixture inhibits the CH_3 recombination reaction and favors the recombination reaction between C_2H_2 and CH_3 which leads to a lower production of C_2H_6 and consequently lower C_2H_4, and to a higher C_3H_4-P peak mole fractions (6 ppm in 100ppm C_7H_8+459ppm C_2H_2 reaction system compared to 3 ppm in 105ppm C_7H_8 pyrolysis), respectively. Differently, almost all C_2H_4 is converted to C_2H_2 **(Figure 5.49 (b))**, which results in the fact that the C_7H_8-C_2H_2 reaction chemistry also plays a significant role in toluene/ C_2H_4 pyrolysis.

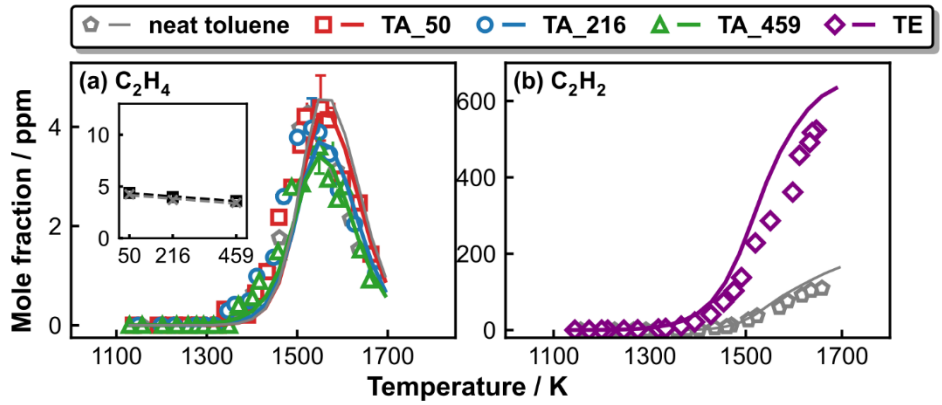

Figure 5.49: Measured (symbols) and simulated (lines) mole fraction profiles of (a) ethylene in toluene/acetylene pyrolysis and (b) acetylene in toluene/ethylene pyrolysis. Simulated and experimental mole fractions in neat toluene (105 ppm in argon) pyrolysis are also shown as a reference. The inset in (a) plots the measured (dark open square) and simulated (gray cross) C_2H_4 peak concentrations against the initial C_2H_2 contents; linear regressions (the dashed lines) of the data points are shown as a visual guide.

C_6H_6 is the most abundant MAH product in toluene/C_2 pyrolysis. The measured and simulated C_6H_6 mole fractions in the binary mixtures as well as in neat toluene are shown in **Figure 5.50.** The current kinetic model can well capture the variation trends of C_6H_6 peak mole fractions in the different binary mixtures. The addition of C_2 fuels has no influence on the C_6H_6 onset temperature. Concerning C_6H_6 peak, C_2H_2 addition tends to lower its peak mole fraction, while C_2H_4 results in an increment in its peak mole fraction. According to ROP analysis, C_7H_8+H = C_6H_6+CH_3 is the main contributor to C_6H_6 formation in all the investigated sets, and it has more pronounced effects in binary mixtures due to the increased level of H-atom (see **Figure 5.51 (a)**). However, the C_7H_7 concentration is lower in binary fuel mixtures (see **Figure 5.51 (b)**) due to its recombination reactions with C_2 fuels. Consequently, C_3H_3 formation from C_7H_5 decomposition (C_7H_7 → C_7H_6 → C_7H_5) is hampered, and therefore the C_3H_3 self-recombination forming C_6H_6 has lower contribution in binary mixtures. This explains the reduced peak mole fractions in toluene/C_2 pyrolysis with increasing the C_2H_2 content. Differently, the styrene

decomposition through $C_6H_5C_2H_3 = C_6H_6+H_2CC$ compensates the C_7H_7 impediment and appears to be an alternative C_6H_6 channel in toluene/C_2H_4 pyrolysis.

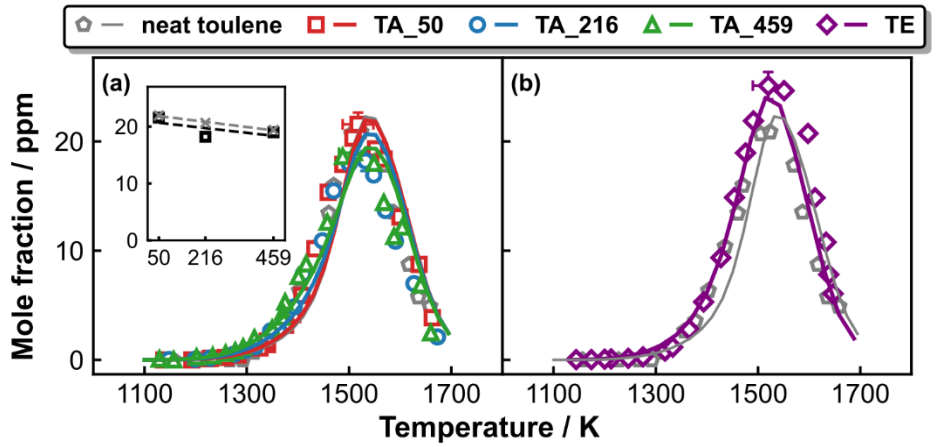

Figure 5.50: Experimental (symbols) and modeling (solid lines) benzene (C_6H_6) mole fractions as a function of the post-shock temperature T_5 in (a) toluene/C_2H_2 pyrolysis and (b) toluene/C_2H_4 pyrolysis. The inset in (a) plots the measured (dark open square) and simulated (gray cross) C_6H_6 peak concentrations against the initial C_2H_2 contents; linear regressions (the dashed lines) of the data points are shown as a visual guide. Simulated and experimental C_6H_6 mole fractions in neat toluene (105 ppm in argon) pyrolysis are also shown as a reference.

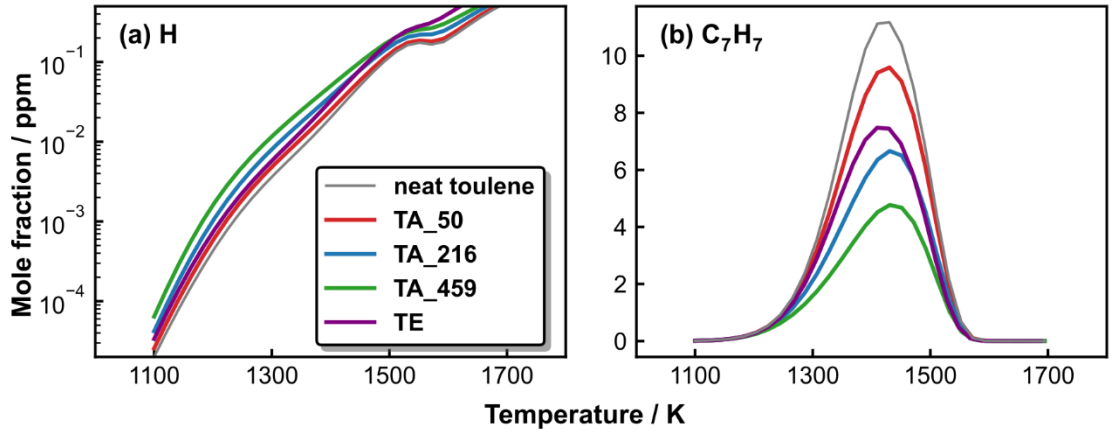

Figure 5.51: Simulated H atom and benzyl radical (C_7H_7) concentrations in the pyrolysis of neat toluene (105 ppm in argon) and toluene/acetylene (ethylene) binary mixtures.

Figure 5.52 shows the experimental and the simulated mole fraction profiles of C_8 MAH species, including ethylbenzene, styrene and phenylacetylene in the pyrolysis of neat toluene and toluene/C_2 binary mixtures. The added C_2 fuels diminish the $C_6H_5C_2H_5$ peak concentration, and C_2H_2 exhibits more conspicuous effects if the same quantity of C_2H_2 and C_2H_4 is added. $C_6H_5C_2H_5$ is mainly formed through $C_7H_7+CH_3$ recombination reaction. The lower C_7H_7 concentration in binary fuels

decreases the carbon flux into $C_6H_5C_2H_5$ through $C_7H_7+CH_3$ recombination. This reaction also proceeds during the quenching period as it involves the resonantly-stabilized benzyl radical and CH_3 radical. Therefore, the measured $C_6H_5C_2H_5$ concentrations can be well predicted by simulations based on measured pressure profiles up to 10ms. Simulations for all measured species are displayed in **Figures 5.43-5.47** using the two different approaches. C_2H_2 and C_2H_4 have distinct effects on $C_6H_5C_2H_3$ production. C_2H_2 presence tends to lower $C_6H_5C_2H_3$ peak concentration, and it demonstrates more pronounced effects as the C_2H_2 initial concentration increases. Differently, C_2H_4 doubles the $C_6H_5C_2H_3$ production compared to that in neat toluene pyrolysis. Such differences arise from the fact that $C_6H_5C_2H_3$ mainly comes from $C_6H_5C_2H_5$ consumption in neat toluene and toluene/C_2H_2 mixture pyrolysis, and from $C_6H_5+C_2H_4 = C_6H_5C_2H_3+H$ reaction in toluene/C_2H_4 mixture pyrolysis. The speciation temperature windows of $C_6H_5C_2H_5$ and $C_6H_5C_2H_3$ are not changed by the addition of C_2 hydrocarbons. On the contrary, $C_6H_5C_2H$ shifts to lower temperature windows only when C_2H_2 is added. Moreover, the extra C_2 fuels enhance the $C_6H_5C_2H$ peak concentration, and C_2H_2 exhibits more pronounced effects if the same amount of C_2H_2 and C_2H_4 is present. Such effects arise from the presence of C_2H_2 in the initial mixture or being produced from C_2H_4 decomposition as $C_6H_5C_2H$ formation relies on the reactions between C_6H_5 and C_2H_2; C_6H_5 originates from toluene unimolecular decomposition ($C_7H_8(+M) = C_6H_5+CH_3(+M)$).

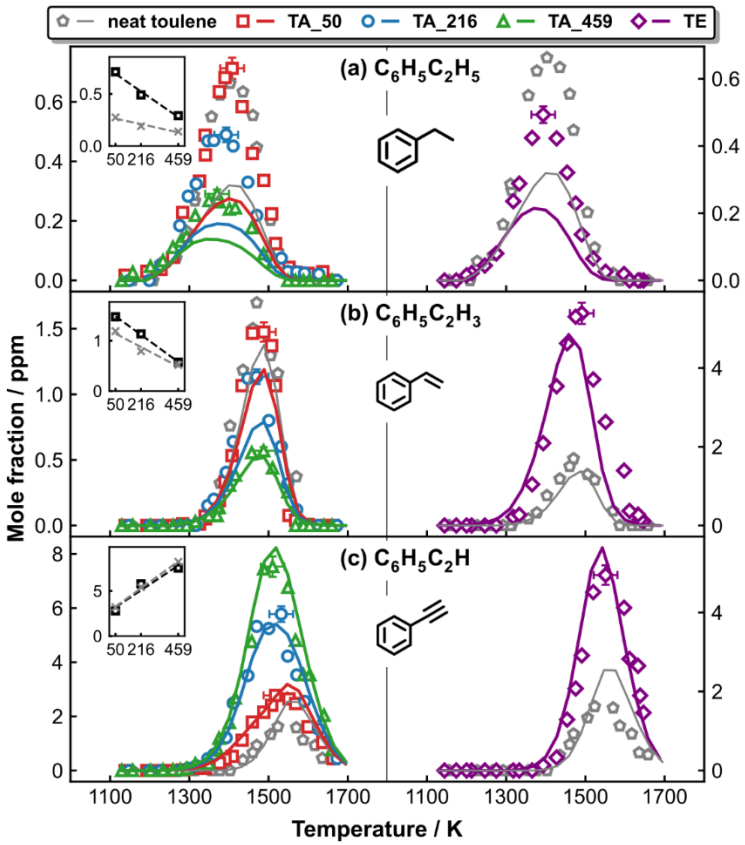

Figure 5.52: Experimental (symbols) and modeling (solid lines) mole fractions of C_8 MAH species as a function of the post-shock temperature T_5. The left panel: toluene/C_2H_2 pyrolysis; the upper left insets plot the measured (dark open square) and simulated (gray cross) peak concentrations of separate species against the initial C_2H_2 contents; linear regressions (the dashed lines) of the data points are shown as a visual guide. The right panel: toluene/C_2H_4 pyrolysis. The experimental and simulated species mole fraction profiles in neat toluene pyrolysis are shown as a reference.

5.3.3.2 Toluene radicals-C_2 interactions

One of the main objectives of this study is to examine the interaction between toluene-related radicals and C_2 fuels. A direct confirmation is the detection of C_9 species in toluene/C_2 pyrolysis experiments. In toluene/C_2H_2 pyrolysis, several C_9H_8 isomers are detected including indene, propynyl-benzene ($C_6H_5C_3H_3$P_3) and ethynyl-toluene ($CH_3C_6H_4C_2H$) species, where indene is the major C_9H_8 product. **Figure 5.53** displays the experimental and simulated mole fraction profiles for indene and the sum of the other C_9H_8 isomers in toluene/C_2H_2 pyrolysis, and the variation trends of the peak concentrations against the initial C_2H_2 concentrations are also reported. The current kinetic model can satisfactorily predict indene concentrations as well as the other C_9H_8 isomers over the entire temperature range in all three toluene/C_2H_2 experimental sets. Indene is predominantly formed through $C_7H_7+C_2H_2 = C_9H_8+H$ reaction, and Mebel et al. [41] rate coefficients are adopted. Indene starts to form at around 1400 K and reaches a peak concentration below 1 ppm at around 1500 K in neat toluene pyrolysis. The addition of C_2H_2 lowers

the onset temperature to about 1200 K and significantly promotes indene formation (over 2 ppm in TA_50 pyrolysis). This indicates that acetylene addition to toluene is more efficient in indene formation compared to the addition of propene and propyne to benzene (around 4 ppm of indene are produced at around 1450 K from the reaction between 108 ppm C_6H_6 and 500 ppm C_3H_4-P/C_3H_6 while more than 10 ppm of indene are produced at around 1450 K from the reaction between 105 ppm C_7H_8 and 459 ppm C_2H_2). The minor C_9H_8 species have same speciation temperature window as indene, and they are mainly formed via the addition of C_7H_7 or $CH_3C_6H_4$ to C_2H_2.

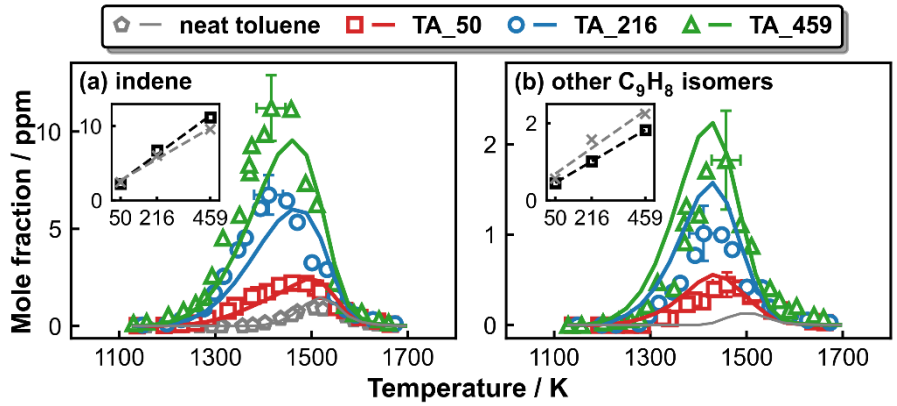

Figure 5.53: Experimental (symbols) and modeling (solid lines) mole fractions of C_9H_8 species as a function of the post-shock temperature T_5 in toluene/acetylene pyrolysis. The upper right insets plot the measured (dark open square) and simulated (gray cross) peak concentrations of separate species against the initial C_2H_2 contents; linear regressions (the dashed lines) of the data points are shown as a visual guide. Simulated and experimental mole fraction profiles in neat toluene pyrolysis are shown as a reference.

In toluene/C_2H_4 pyrolysis, several C_9 species are observed including indene, indane (C_9H_{10}) and other C_9H_{10} isomers, namely, allylbenzene ($C_6H_5C_3H_5$–1), 1-propenyl-benzene ($C_6H_5C_3H_5$–2) and lumped o-, m- and p- vinyl toluene isomers ($CH_3C_6H_4C_2H_3$). **Figure 5.54** presents the experimental and simulated mole fraction profiles for indene, indane and other C_9H_{10} isomers as a function of post-shock temperature T_5. The addition of C_2H_4 also lowers the onset temperature of indene to around 1300 K and increases its peak concentration to about 4 ppm, but to a lower extent compared to a similar amount of C_2H_2. Indane is anticipated to be the major product resulting from the interaction between benzyl and C_2H_4. However, only trace amounts of indane (~0.4 ppm) are measured during toluene/C_2H_4 pyrolysis experiments. This suggests that C_7H_7+C_2H_4 proceeds in a slower rate in comparison to C_7H_7+C_2H_2. As mentioned in the modeling section, the rate coefficients of the reaction C_7H_7+C_2H_4 = indane+H are estimated through an analogy to the reaction C_7H_7+C_2H_2 = indene+H reported in [202]. This procedure most likely introduces uncertainties in the indane speciation kinetics, although the current model can

reasonably capture the measurements of C_9 species in toluene/C_2H_4 pyrolysis. Future theoretical works on the C_7H_7+C_2H_4 reaction system, and how indane decomposes to form indene are highly needed. Indene is mainly formed through indane dehydrogenation at low temperatures, and through C_7H_7+C_2H_2 = C_9H_8+H channel at high temperatures due to the considerable C_2H_2 amounts produced from C_2H_4 decomposition. $C_6H_5C_3H_5$–1 predominantly originates from indane isomerization through ring-opening process. Another minor source of $C_6H_5C_3H_5$–1 is the reaction of C_7H_7 with C_2H_4. $C_6H_5C_3H_5$–2 mainly comes from the bimolecular reaction of C_7H_7 with C_2H_4. $CH_3C_6H_4C_2H_3$ is formed through two main channels: (i) the reaction of $CH_3C_6H_4$ with C_2H_4; (ii) and the isomerization of indane. The model underpredicts the mole fraction of C_9H_{10} isomers in **Figure 5.54 (c)**, suggesting that other pathways maybe possible or that the reaction rate constants implemented in the model may require further considerations.

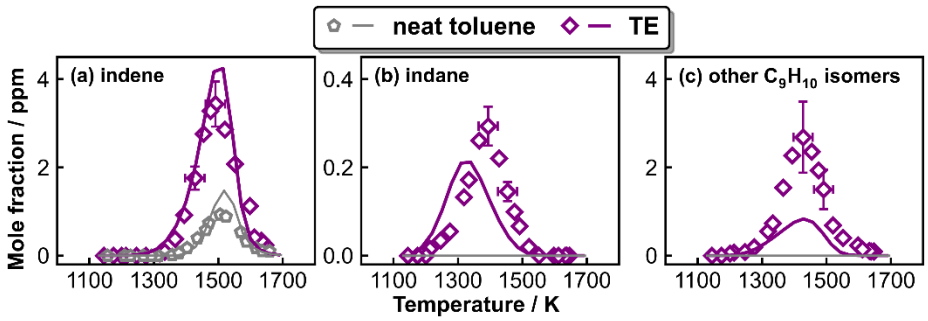

Figure 5.54: Experimental (symbols) and modeling (solid lines) mole fractions of C_9 species as a function of the post-shock temperature T_5 in neat toluene and toluene/ethylene pyrolysis.

It has been seen in the previous section that C_7H_7 plays an important role in PAH formation. To better address the influence of extra C_2 fuels on benzyl radical, ROP analysis is carried out at 1400 K in toluene/ C_2 reaction systems as well as in neat toluene for comparison purpose. According to the **Figure 5.55**, the fate of C_7H_7 is notably influenced by the composition of the initial mixture. In toluene/C_2H_2 pyrolysis, the contribution of the reactions involving C_2H_2 increases significantly with the initial C_2 concentration. Consequently, other reactions including C_7H_7 self-recombination and its reaction with CH_3 are inhibited. Since C_2H_2 is also an important product in toluene/C_2H_4 pyrolysis, similar behavior is also encountered but to a lower extent. Besides, reactions involving C_2H_4 start to be effective when C_2H_4 is introduced to the initial mixture. These results support the analyses performed in the previous paragraphs.

$C_6H_5C_2H_4C_6H_5$ is a major product resulting from C_7H_7 self-recombination, and it is measured to be the most abundant PAH in neat toluene pyrolysis. The addition of C_2 fuels highly stimulates $C_6H_5C_2H_4C_6H_5$ formation where an order of 10^{-1} ppm is measured in TA_459 pyrolysis. **Figure 5.56** displays the experimental $C_6H_5C_2H_4C_6H_5$ mole fractions in toluene/C_2 pyrolysis as well as in neat toluene for comparison purpose. A significant reduction in $C_6H_5C_2H_4C_6H_5$ peak mole fractions is observed when

raising the initial C_2H_2 contents, while a peak drop of 30 % is encountered by adding over 500 ppm C_2H_4, which falls between those in TA_50 and TA_216 pyrolysis. Simulations with two approaches is performed and the measured pressure profile approach satisfactorily predicts the $C_6H_5C_2H_4C_6H_5$ mole fraction profiles. As discussed previously, reactions involving stabilized radicals like C_7H_7, C_9H_7, etc. and CH_3 as pointed out by Manion et al. [153] can carry on during the quenching period. Therefore, the chosen numerical method highly impacts the accuracy of the simulated results. Time-dependent mole fractions of selected species in the studied cases are shown in **Figures 5.57 and 5.58.** As can be seen in the figures, C_7H_7 consumption continues even after the arrival of the rarefaction waves. Accordingly, bibenzyl formation persists during the post-shock cooling (see **Figures 5.57 and 5.58**). Nevertheless, the formation of most species is completed before the arrival of the rarefaction waves, and their mole fractions do not vary with the time. Simulations for all the products are displayed in **Figures 5.48-5.52** for the different investigated cases using the two different approaches**.**

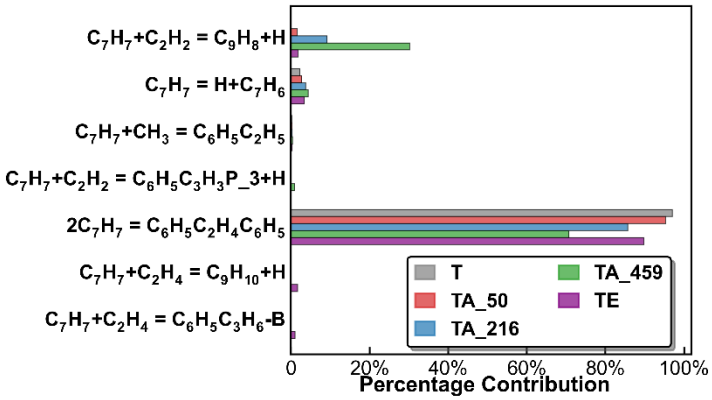

Figure 5.55: ROP-analyzed percentage contributions of benzyl consumption in the pyrolysis of toluene/C_2 binary mixtures at 1400 K. The ROP-analyzed percentage contributions of benzyl consumption in neat toluene pyrolysis (the gray bars) are also shown as a reference.

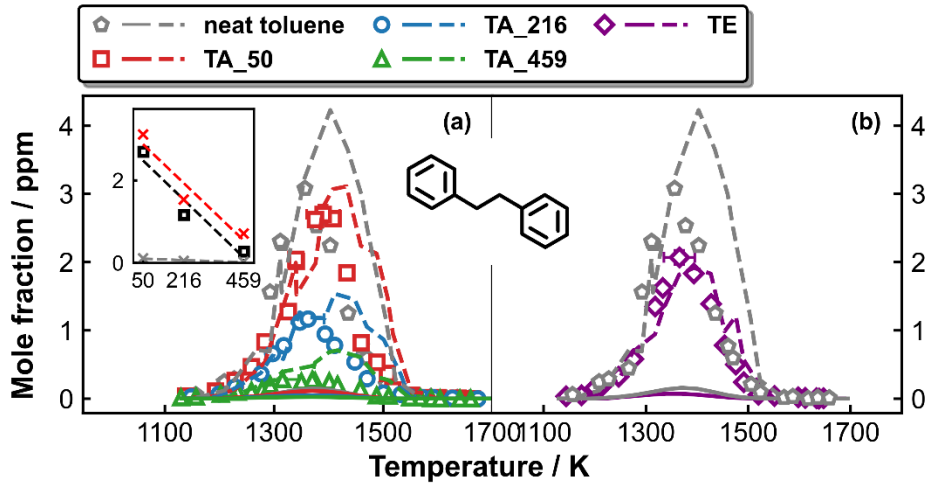

Figure 5.56: Bibenzyl ($C_6H_5C_2H_4C_6H_5$) mole fraction profiles as a function of the post-shock temperature T_5 in (a) toluene/C_2H_2 pyrolysis and (b) toluene/C_2H_4 pyrolysis. Symbols: measurements; solid lines: simulations with a constant pressure of 20 bar within a reaction time of 4.0 ms; dashed lines: simulations with measured pressure histories up to 10 ms. The upper left inset in the left panel plot the measured (dark open square), simulated constant pressure assumption (gray cross) and measured pressure histories (red cross) peak $C_6H_5C_2H_4C_6H_5$ concentrations against the initial C_2H_2 contents; the linear regressions (the dashed lines) of the data points are shown as a visual guide.

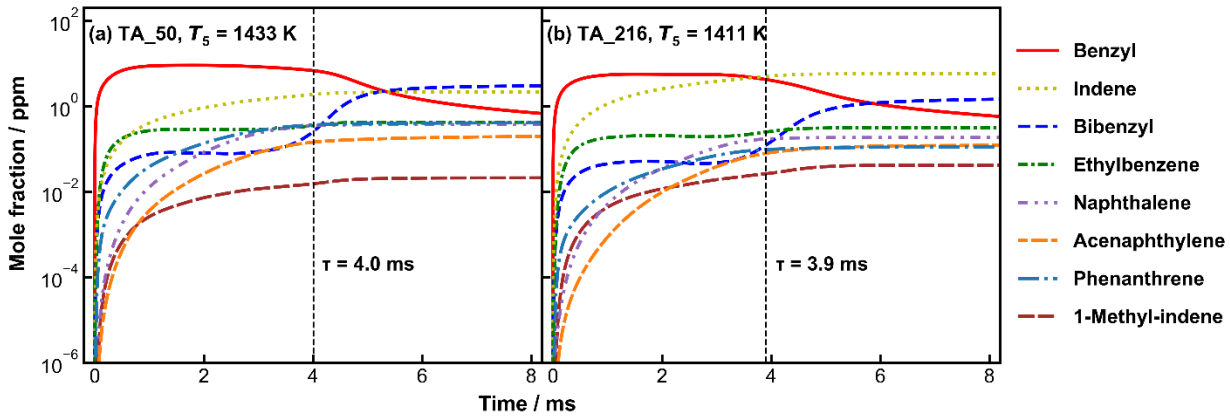

Figure 5.57: Simulated species mole fractions as a function of time with the measured pressure profiles in (a) TA_459 pyrolysis at T_5 =1416 K; (b) TE pyrolysis at T_5 = 1427 K. The dashed vertical lines indicate the start of quenching.

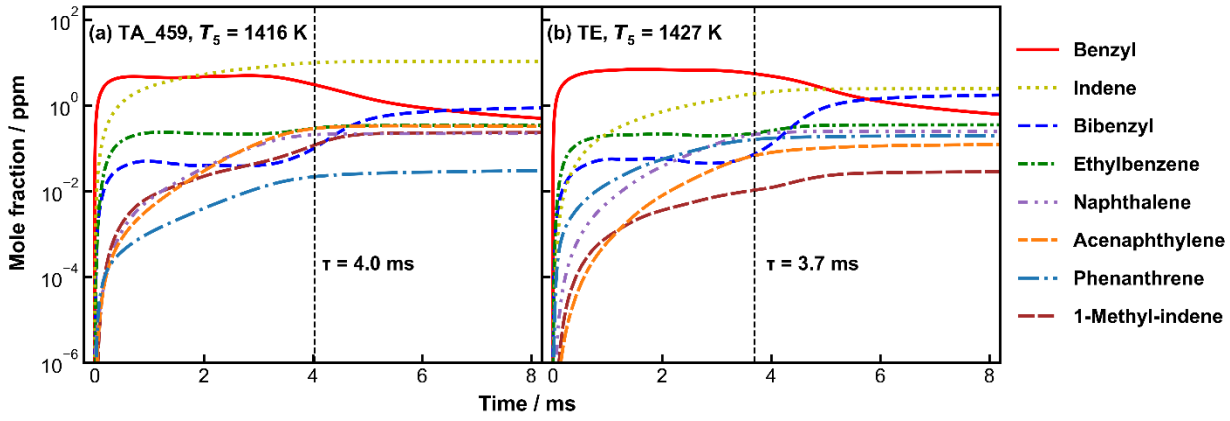

Figure 5.58: Simulated species mole fractions as a function of time with the measured pressure profiles in (a) TA_50 pyrolysis at T_5 =1433 K; (b) TA_216 pyrolysis at T_5 = 1411 K. The dashed vertical lines indicate the start of quenching.

5.3.3.3 Influences of C_2 addition on PAH species

Another major goal of this work is to elucidate the impacts of added C_2 on the PAH speciation in toluene pyrolysis. **Figure 5.59** shows the measured and simulated mole fraction profiles of C_{10} PAH species, including $C_{10}H_8$, $C_9H_6CH_2$ and $C_9H_7CH_3$-1. In general, the C_2 fuels enhance the C_{10} PAH formation. The model slightly over-predicts the peak mole fractions of $C_{10}H_8$ and $C_9H_6CH_2$, while it under-predicts that of $C_9H_7CH_3$-1. This is because a large portion of $C_9H_7CH_3$ is formed during the quenching period. Using the measured pressure profiles, the simulated $C_9H_7CH_3$ mole fractions are greatly improved (see **Figures 5.48-5.52**). $C_{10}H_8$ is the dominant fused bicyclic PAH species present in the pyrolysis of both neat toluene and toluene/C_2 mixtures. As can be seen from **Figure 5.59 (a),** both C_2H_2 and C_2H_4 promote $C_{10}H_8$ formation, but for the same amounts, C_2H_2 is more efficient than C_2H_4. The reaction pathways leading to $C_{10}H_8$ formation are traced in **scheme 5.9** based on the integrated ROP analyses at 1500 K. In neat toluene pyrolysis, $C_{10}H_8$ is dominantly formed through C_7H_5+C_3H_3 recombination reaction and $C_9H_6CH_2$ isomerization. Besides, the $C_9H_7CH_2$ and $C_9H_6CH_3$-1 dehydrogenation and the decomposition of BICYCLO have lower contribution. The relative importance of these mentioned channels varies with the initial fuel compositions. When gradually increasing the C_2H_2 content, the $C_9H_6CH_3$-1 dehydrogenation and $C_9H_6CH_2$ isomerization become the main $C_{10}H_8$ contributors, while the channels through C_7H_5+C_3H_3 recombination and BICYCLO decomposition become less important. This is because C_7H_7 dissociation is suppressed by the C_7H_7+C_2H_2 reaction forming indene, as noted in the previous section. Indene decomposes into C_9H_7, where it reacts with CH_3 forming $C_9H_7CH_3$-1. The one-step and two-step dehydrogenation of $C_9H_7CH_3$-1 lead to $C_9H_6CH_3$-1 and $C_9H_6CH_2$ formation, respectively. In addition, the C_7H_7 decomposition products including C_7H_5, o-C_6H_4 and C_3H_3 are reduced so the $C_{10}H_8$ formation pathways involving these species become negligible. For $C_9H_6CH_2$, the C_2H_2 addition

amplifies the $C_9H_7CH_3$-1 dehydrogenation pathway and reduces $C_7H_5+C_3H_3$ recombination channel. $C_9H_7CH_3$-1 peak mole fractions remarkably increase with the amount C_2H_2 compared to $C_{10}H_8$ and $C_9H_6CH_2$ (see **Figure 5.59)**. This is because $C_9H_7CH_3$-1 exclusively comes from $C_9H_7+CH_3$ recombination. In the case of toluene/C_2H_4 pyrolysis, the growth of the C_{10} PAH species is less attenuated compared to toluene/C_2H_2 pyrolysis. This is due to the lower efficiency of $C_7H_7+C_2H_4$ interaction in producing indene and the indirect C_2H_2 formation that induce lower C_9H_7 mole fractions.

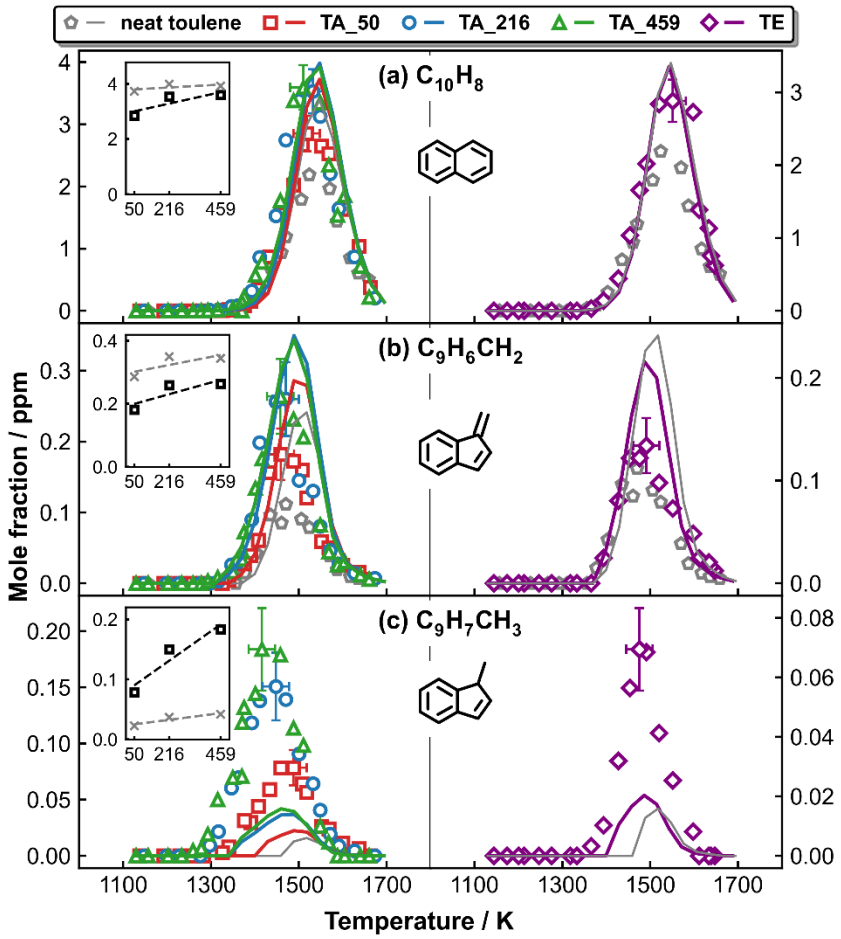

Figure 5.59: Experimental (symbols) and modeling (solid lines) mole fraction of C_{10} PAH species as a function of the post-shock temperature T_5. The left panel: toluene/C_2H_2 pyrolysis; the upper left insets plot the measured (dark open square) and simulated (gray cross) peak concentrations of separate species against the initial C_2H_2 contents; linear regressions (the dashed lines) of the data points are shown as a visual guide. The right panel: toluene/C_2H_4 pyrolysis. The simulated and experimental mole fraction profiles of C_{10} PAH species in neat toluene pyrolysis are shown as a reference.

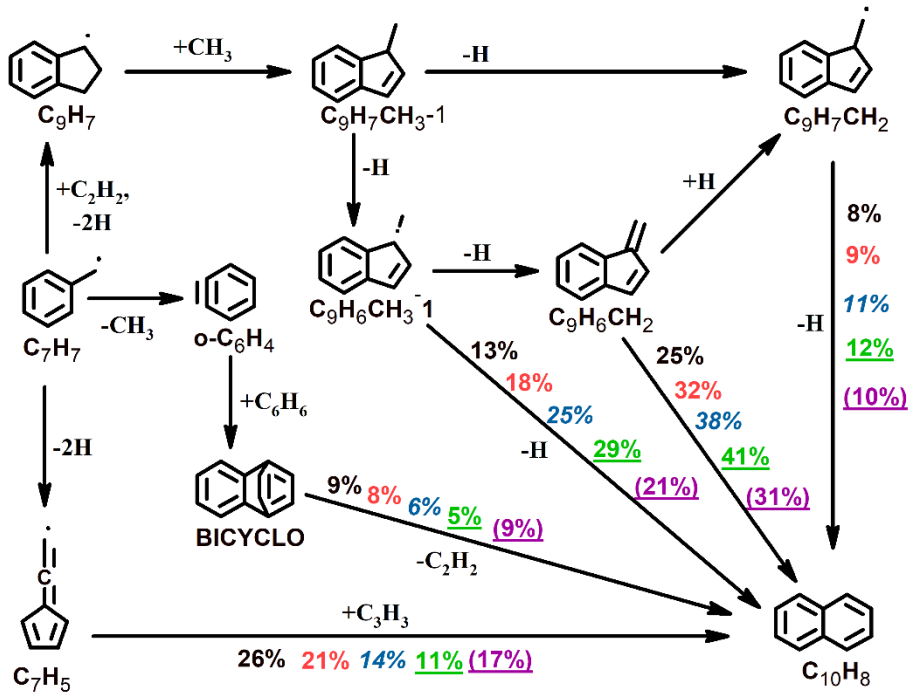

Scheme 5.9: The reaction pathways leading to naphthalene formation at T_5 of 1500 K in the pyrolysis of toluene/C_2 binary mixtures and neat toluene. The percentage numbers (neat toluene: normal black, TA_50: normal red; TA_216: italic; TA_459: underlined; TE: in parenthesis) represent the contributions to naphthalene formation by corresponding reactions.

Mole fraction profiles of C_{11} PAH species, including 1-methylnaphthalene ($C_{10}H_7CH_3$_1) and ethynyl indene ($C_9H_7C_2H$) are shown in **Figure 5.60.** The current model can predict the measurements within experimental uncertainties, but shows limitations in capturing the variation trend of $C_{10}H_7CH_3$_1 peak concentration in the both neat toluene and toluene/C_2 pyrolysis experiments. According to the results of ROP analyses, the $C_9H_7C_2H$ formation largely depends on the HACA route starting from indenyl radical. The abundant C_9H_7 and C_2H_2 precursors in the binary mixtures not only facilitates $C_9H_7C_2H$ formation but also lowers its onset temperature. The limited C_9H_7 mole fractions in toluene/C_2H_4 pyrolysis reduces the production of $C_9H_7C_2H$ compared to toluene/C_2H_2 pyrolysis. $C_{10}H_7CH_3$_1 is the result of $C_{10}H_7$_1 and CH_3 recombination reaction. The main CH_3 source is thermal decomposition of C_7H_7 into o-C_6H_4 and CH_3. Due to the low C_7H_7 content, this pathway is inhibited contributing to lower $C_{10}H_7CH_3$_1 concentrations in binary fuel mixtures. This trend is not observed in the experiments where the $C_{10}H_7CH_3$_1 mole fractions are similar in all the cases. This discrepancy still needs to be addressed in the future model refinements.

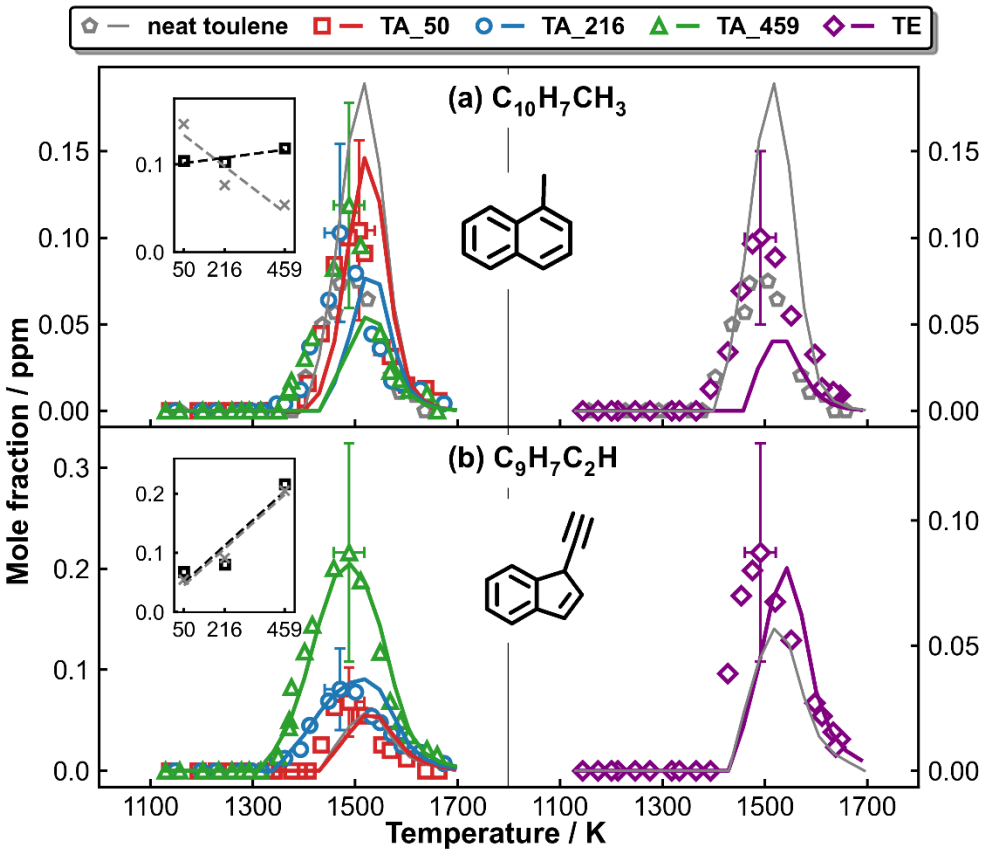

Figure 5.60: Experimental (symbols) and modeling (solid lines) mole fraction of C_{11} PAH species as a function of the post-shock temperature T_5. The left panel: toluene/C_2H_2 pyrolysis; the upper left insets plot the measured (dark open square) and simulated (gray cross) peak concentrations of separate species against the initial C_2H_2 contents; linear regressions (the dashed lines) of the data points are shown as a visual guide. The right panel: toluene/C_2H_4 pyrolysis. The simulated and experimental mole fraction profiles of C_{11} PAH species in neat toluene pyrolysis are shown as a reference.

Mole fraction profiles of major C_{12} PAH species, including $C_{12}H_8$, $C_{10}H_7C_2H\_1$ and $C_6H_5C_6H_5$ are shown in **Figure 5.61.** Overall, the extra C_2 fuels facilitate the formation of the $C_{12}H_8$ isomers and inhibit the $C_6H_5C_6H_5$ formation. The model precisely reproduces $C_{10}H_7C_2H\_1$ profile, while it under-predicts that of $C_{12}H_8$. This is because $C_{12}H_8$ is partly formed during the post-shock cooling process. Using the measured pressure profiles, the simulated $C_{12}H_8$ mole fractions perfectly capture the experimental data (see **Figures 5.43-5.47**). Besides, the model under-estimates $C_6H_5C_6H_5$ concentrations. This has been already shown for benzene decomposition (**chapter 5.2**), and it may depend on the parameters of the reactions responsible for the fragmentation of the ring or for the biphenyl decomposition. It is noteworthy that C_2 fuels generate a steep increase in $C_{12}H_8$ peak mole fractions compared to those of $C_{10}H_8$. The $C_{12}H_8$ formation scheme based on the integrated ROP analyses at T_5=1500 K is shown in **scheme 5.10** for all the investigated cases. Before the addition of the C_2 fuels, $C_{12}H_8$ is predominantly formed by the

isomerization of biphenyl radical ($C_{12}H_9$) through the intermediate cyclopenta[a]indene (BENZO). The other two important pathways include the C_9H_7+C_3H_3 recombination and the subsequent dehydrogenation and ring-rearrangement processes, and the HACA route through $C_{10}H_7$_1+C_2H_2. When adding the C_2 fuels, C_9H_7+C_3H_3 recombination reaction prevails $C_{12}H_8$ formation, while the isomerization of $C_{12}H_9$ through BENZO intermediate becomes less important. This is again due to the fact that C_7H_7 decomposition to C_6H_5 is inhibited by C_7H_7+C_2H_2 reaction which leads to indene. Though C_3H_3 production is also limited as a result of reduced C_7H_7 dissociation, the C_9H_7 level appears to be the limiting factor that influences the efficiency of the C_9H_7+C_3H_3 recombination leading to $C_{12}H_8$ formation. On the other hand, the relative importance of the HACA route is not greatly affected by the different initial fuel compositions. And once again, due to the lower C_9H_7 levels in toluene/C_2H_4 pyrolysis, C_2H_2 has more pronounced effects on $C_{12}H_8$ peak concentration in comparison to the same amount of C_2H_4. Although, the pathway through acenaphthene ($AC_{12}H_{10}$) is only available in the toluene+C_2H_4 co-pyrolysis, but it doesn't compensate the inefficiency of the remaining pathways with respect to the toluene+C_2H_2 case. For $C_{10}H_7C_2H$_1, its major pathway through $C_{10}H_7$_1+C_2H_2 relies on two important precursors $C_6H_5C_2H$ and C_2H_2. The enhanced formation of $C_6H_5C_2H$ in binary mixtures and the presence of C_2H_2 in the initial mixture or being produced from C_2H_4 decomposition significantly increase the $C_6H_5C_2H$ peak concentration in binary reaction systems. Obvious decreasing trends are recognized in the $C_6H_5C_6H_5$ peak concentrations when C_2 fuels are added. The $C_6H_5C_6H_5$ formation mainly comes from the bimolecular reaction between C_6H_6 and C_6H_5. As stated before, C_6H_6 concentrations decrease slightly in the binary fuel mixtures. C_6H_5, which is mostly produced from C_7H_8 unimolecular decomposition (C_7H_8(+M) = C_6H_5+CH_3(+M)), largely reacts with C_2 intermediates. Therefore, less portion of C_6H_5 participates in the C_6H_6+C_6H_5 reaction leading to the sharp decline in $C_6H_5C_6H_5$ peak mole fractions.

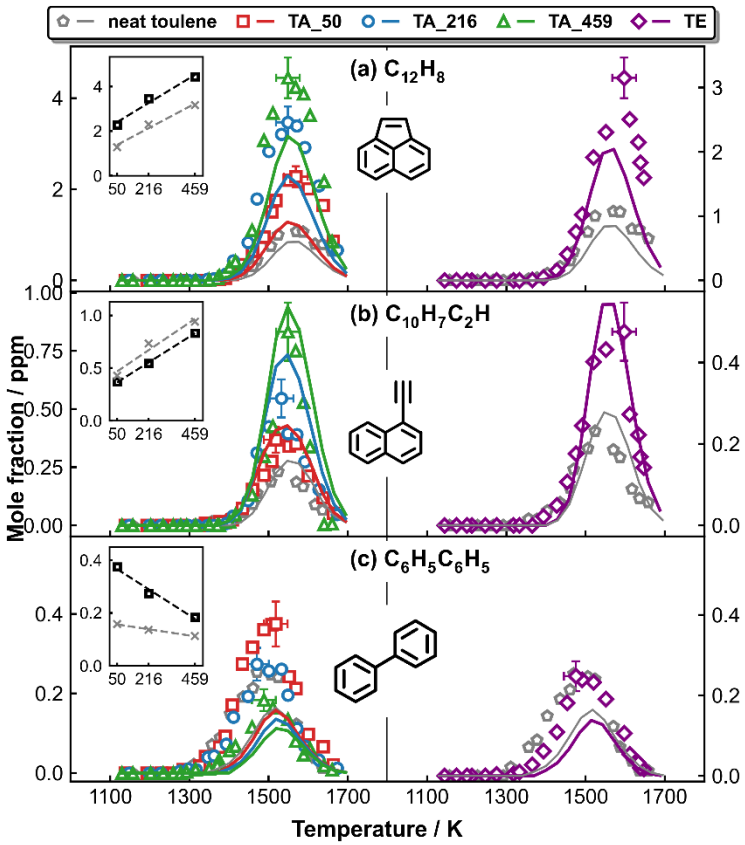

Figure 5.61: Experimental (symbols) and modeling (solid lines) mole fraction of C_{12} PAH species as a function of the post-shock temperature T_5. The left panel: toluene/C_2H_2 pyrolysis; the upper left insets plot the measured (dark open square) and simulated (gray cross) peak concentrations of separate species against the initial C_2H_2 contents; linear regressions (the dashed lines) of the data points are shown as a visual guide. The right panel: toluene/C_2H_4 pyrolysis. The simulated and experimental mole fraction profiles of C_{12} PAH species in neat toluene pyrolysis are shown as a reference.

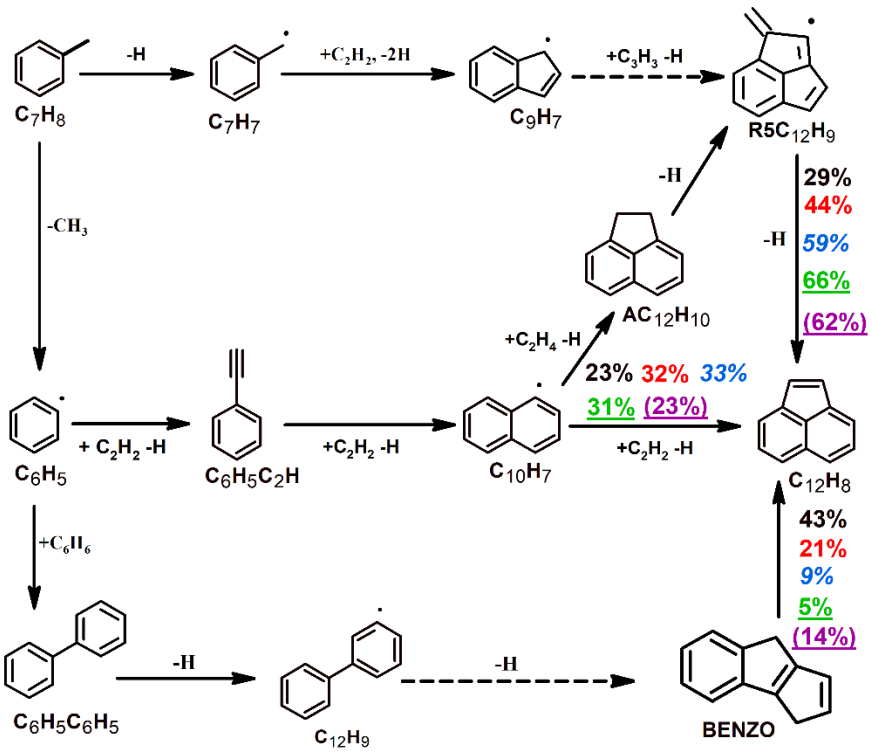

Scheme 5.10: The reaction pathways leading to acenaphthylene formation at T_5 of 1500 K in the pyrolysis of toluene/C_2 binary mixtures and neat toluene. The percentage numbers (neat toluene: normal black, TA_50: normal red; TA_216: italic; TA_459: underlined; TE: in parenthesis) represent the contributions to acenaphthylene formation by corresponding reactions. The dashed arrows represent multi-step reaction.

Different C_{13} PAH species including $C_{13}H_{10}$, $C_6H_5CH_2C_6H_5$, and methyl biphenyl ($C_6H_5C_6H_4CH_3$) are detected in neat toluene and toluene/C_2 pyrolysis. Their experimental and simulated mole fraction profiles are shown in **Figure 5.62.** C_2 molecules impede the formation of the C_{13} PAH species, and the model can satisfactorily capture such trends though it underestimates $C_6H_5CH_2C_6H_5$ peak mole fractions. $C_6H_5CH_2C_6H_5$ is exclusively formed through C_7H_7+C_6H_5 recombination reaction. The reduced C_7H_7 and, in less extent, C_6H_5 mole fractions in binary mixtures **(**see **Figures 5.51 and 5.63)** resulting from their interactions with C_2 hydrocarbons lead to a sharp reduction in $C_6H_5CH_2C_6H_5$ peak concentrations. However, the $C_{13}H_{10}$ peak concentrations, originating from $C_6H_5CH_2C_6H_5$ consumption, drop at a relatively slower rate compared to $C_6H_5CH_2C_6H_5$ when introducing C_2 fuels to toluene pyrolysis. This is principally due to the fact that H atom concentrations are increased by the added C_2 fuels, which promotes the $C_6H_5CH_2C_6H_5$ consumption through hydrogen abstraction reactions. The resulting radical 2-benzylphenyl ($C_{13}H_{11}$) subsequently decomposes to $C_{13}H_{10}$. The formation mechanism of $C_6H_5C_6H_4CH_3$ includes three possible reaction pathways. According to ROP-analyses, it mostly comes from the unimolecular decomposition of dimethyl biphenyl ($CH_3C_6H_4C_6H_4CH_3$), which originates from $CH_3C_6H_4$

self-recombination. The other formation pathways include the bimolecular reactions of C_7H_8+C_6H_5 and $CH_3C_6H_4$+C_6H_6. Likewise, the reduced $CH_3C_6H_4$ and C_6H_5 levels in binary mixtures lowers the $C_6H_5C_6H_4CH_3$ formation efficiency from the mentioned reactions.

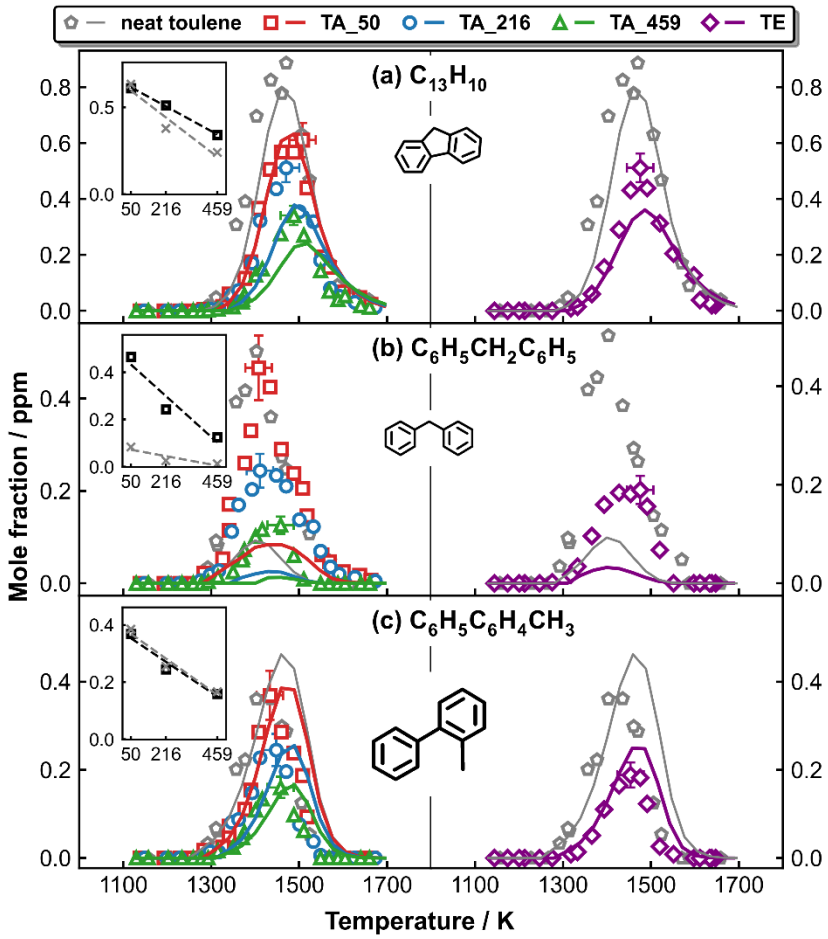

Figure 5.62: Experimental (symbols) and modeling (solid lines) mole fraction of C_{13} PAH species as a function of the post-shock temperature T_5. The left panel: toluene/C_2H_2 pyrolysis; the upper left insets plot the measured (dark open square) and simulated (gray cross) peak concentrations of separate species against the initial C_2H_2 contents; linear regressions (the dashed lines) of the data points are shown as a visual guide. The right panel: toluene/C_2H_4 pyrolysis. The simulated and experimental mole fraction profiles of C_{13} PAH species in neat toluene pyrolysis are shown as a reference.

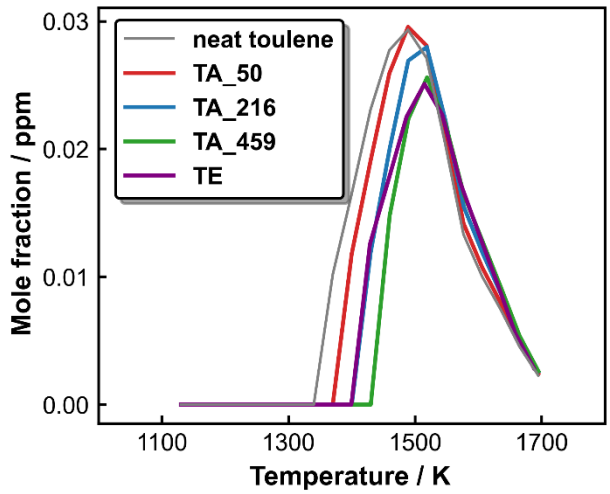

Figure 5.63: Simulated phenyl radical (C_6H_5) concentrations in the pyrolysis of neat toluene (105 ppm in argon) and toluene/C_2H_2 (C_2H_4) binary mixtures.

Figure 5.64 presents the mole fraction profiles for the four $C_{14}H_{10}$ isomers, namely, $PC_{14}H_{10}$, $AC_{14}H_{10}$, $C_{13}H_8CH_2$, and $C_6H_5CCC_6H_5$. $PC_{14}H_{10}$, $AC_{14}H_{10}$ and $C_{13}H_8CH_2$ peak concentrations substantially decrease with the increased C_2 contents, while for $C_6H_5CCC_6H_5$ such decrement is relatively small. The model is capable to simulate with accuracy the major isomers phenanthrene and anthracene, while some discrepancy results in the prediction of the concentrations of minor C_{14} products. The model underpredicts the formation of in $C_{13}H_8CH_2$ toluene pyrolysis, suggesting the possibility of alternative pathways. Concerning diphenylethyne, the model captures the fact that its production is enhanced by the C_2 addition, but it underpredicts the absolute peak mole fractions. Reaction pathways leading to the $C_{14}H_{10}$ isomers formation at 1450 K are presented in **scheme 5.11**. The reduced formation of $PC_{14}H_{10}$, $AC_{14}H_{10}$ and $C_{13}H_8CH_2$ is due to the lower level of C_7 radicals in binary reaction systems, and their formation highly depends on C_7 recombination reactions. $PC_{14}H_{10}$, the major $C_{14}H_{10}$ isomer, results mainly from $AC_{14}H_{10}$ isomerization, bibenzyl dehydrogenation steps and the C_7H_5 self-recombination. Other minor channels also contribute to $PC_{14}H_{10}$ formation: $CH_3C_6H_4$+$CH_3C_6H_4$ reaction, H-assisted isomerization of $C_{13}H_8CH_2$, and the $C_6H_5C_2H$+C_6H_5 addition-elimination reactions. $AC_{14}H_{10}$ predominantly comes from C_7H_7+$CH_3C_6H_4$ recombination. The C_7H_5 self-recombination also slightly contributes in $AC_{14}H_{10}$ formation. The ratio between $PC_{14}H_{10}$ and $AC_{14}H_{10}$ peak concentrations increase with the initial C_2H_2 concentration in the fuel mixtures (2.5 in TA_50 → 2.8 in TA_216 → 3.2 in TA_459). The reason is that $PC_{14}H_{10}$ formation is supported by an alternative $C_6H_5C_2H$+C_6H_5 source, while the production of $AC_{14}H_{10}$ completely depends on C_7 recombination reactions. In neat toluene, $C_{13}H_8CH_2$ predominantly comes the dehydrogenation of hydro-methylene-fluorene radical ($C_{13}H_9CH_2$) that is mainly formed through C_7H_7+C_7H_5 recombination, and slightly through

$C_6H_5C_2H+C_6H_5 = C_{13}H_8CH_2+H$ reaction. However, the addition of C_2 fuels to the initial mixture increases the contribution of $C_6H_5C_2H+C_6H_5$ bimolecular reaction. $C_6H_5CCC_6H_5$ only comes from $C_6H_5C_2H+C_6H_5$ addition-elimination reaction. The enhanced $C_6H_5C_2H$ precursor formation in binary fuel mixtures results in the higher $C_6H_5CCC_6H_5$ peak mole fractions.

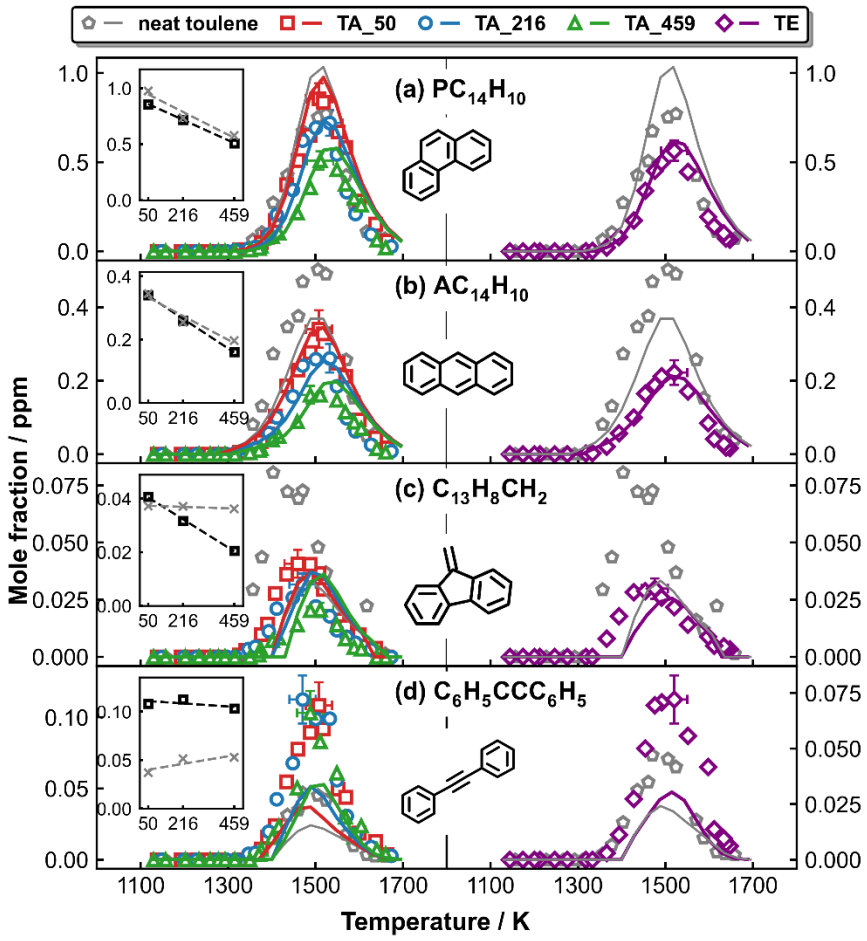

Figure 5.64: Experimental (symbols) and modeling (solid lines) mole fraction of C_{14} PAH species as a function of the post-shock temperature T_5. The left panel: toluene/C_2H_2 pyrolysis; the upper left insets plot the measured (dark open square) and simulated (gray cross) peak concentrations of separate species against the initial C_2H_2 contents; linear regressions (the dashed lines) of the data points are shown as a visual guide. The right panel: toluene/C_2H_4 pyrolysis. The simulated and experimental mole fraction profiles of C_{14} PAH species in neat toluene pyrolysis are shown as a reference.

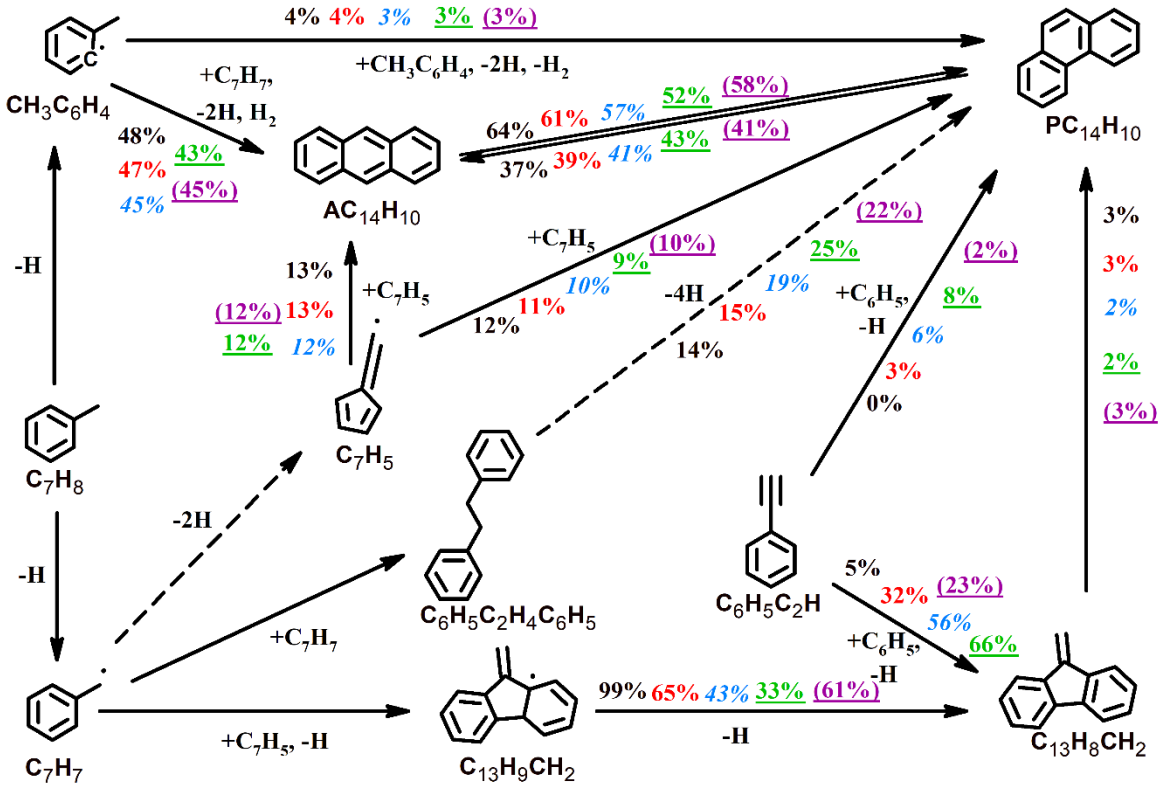

Scheme 5.11: The reaction pathways leading to the formation of $C_{14}H_{10}$ isomers at T_5 of 1450 K in the pyrolysis of toluene/C_2 binary mixtures and in neat toluene. The percentage numbers (neat toluene: normal black; TA_50: normal red; TA_216: italic; TA_459: underlined; TE: in parenthesis) represent the contributions to $C_{14}H_{10}$ PAH formation by corresponding reactions.

5.3.4 Influences of added propyne and propylene on toluene pyrolysis

5.3.4.1 Fuel decomposition reactivity

Figure 5.65 displays the experimental and simulated fuel mole fractions as function of T_5 in neat toluene and toluene-C_3 co-pyrolysis. Simulated mole fraction profiles in neat propylene and propyne pyrolysis are also shown for comparison purpose. The current kinetic model can precisely capture the fuels' measurements in all the three investigated cases. Toluene has higher conversion rates in binary fuel mixtures, while its presence doesn't modify the C_3 fuels' decomposition rates.

To gain insights on the reactions responsible for the faster C_7H_8 consumption in binary fuel mixtures, integrated ROP analyses are performed at T_5=1400 K in all the three studied cases and are shown in **Figure 5.66**. In neat toluene pyrolysis, the C–H bond fission, the H-abstraction by H/CH_3, and the ipso-addition reaction govern C_7H_8 consumption leading to C_7H_7 production. The addition of C_3 fuels extensively enhances the H-abstraction reactions, and in particular the H-abstraction by CH_3 producing C_7H_7 that is recognized to be the prominent toluene decomposition channel. This arise from the fact that

propylene and propyne are mainly consumed through the addition-elimination reaction $C_3H_x+H = C_2H_{x-2}+CH_3$ (x = 4, 6) which results in a large amount of CH_3, as discussed previously in propylene and propyne pyrolysis section. It is noteworthy that the reaction $C_7H_8(+M) = H+C_7H_7(+M)$ turns into a C_7H_8 formation pathway in toluene-propylene pyrolysis as a result of the abundant H-atoms in this reaction system. This compensates the enhanced C_7H_8 consumption through $CH_3+C_7H_8 = CH_4+C_7H_7$ in toluene-propylene co-pyrolysis.

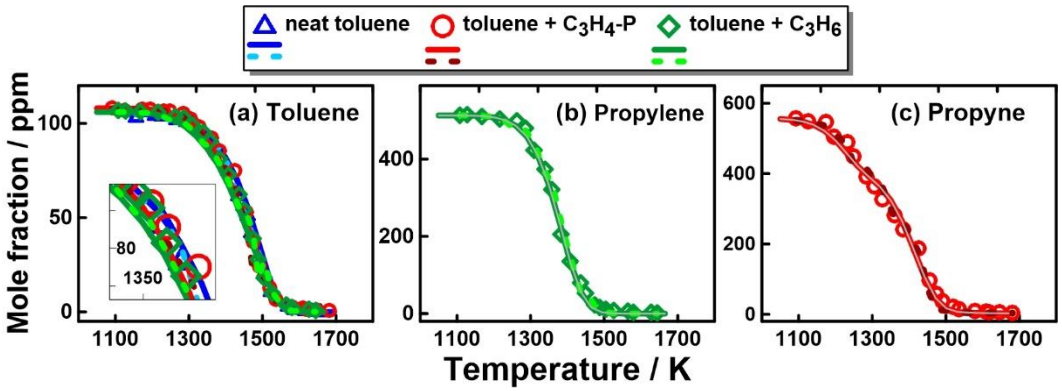

Figure 5.65: Fuel mole fraction profiles as a function of the post-shock temperature T_5 in (a) neat toluene and toluene/C_3 pyrolysis, (b) toluene/C_3H_6 pyrolysis and (c) toluene/C_3H_4-P pyrolysis. Symbols: measurements; solid lines: simulations with a constant pressure of 20 bar within a reaction time of 4.0 ms; dashed lines: simulations with measured pressure histories up to 10 ms. Simulated fuel mole fraction profiles in neat propylene and propyne pyrolysis are given as gray solid lines in (b) and (c).

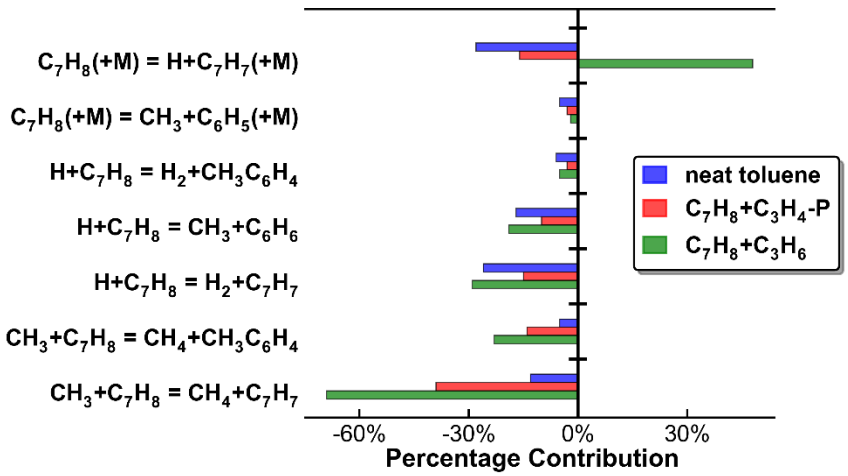

Figure 5.66: Integrated ROP-analyzed percentage contributions of toluene consumption in the pyrolysis of neat toluene toluene/C_3 binary mixtures at 1400 K.

5.3.4.2 Small species and mono-aromatic hydrocarbons

Experimental and simulated mole fraction profiles for C_1–C_6 non-aromatic hydrocarbons are illustrated in **Figure 5.67**. In general, the kinetic model shows satisfactory performance in capturing the formation temperatures and maximum mole fractions for most species. Only a few small species are detected in neat toluene pyrolysis. The addition of C_3 fuels increases the diversity and abundance of small hydrocarbon intermediates. The types of small intermediates as well as their relevant amounts in toluene-propylene and toluene-propyne co-pyrolysis are the same with those in neat propylene and neat propyne pyrolysis, respectively. Therefore, their related kinetics will not be discussed again here (refer to propylene and propyne pyrolysis section).

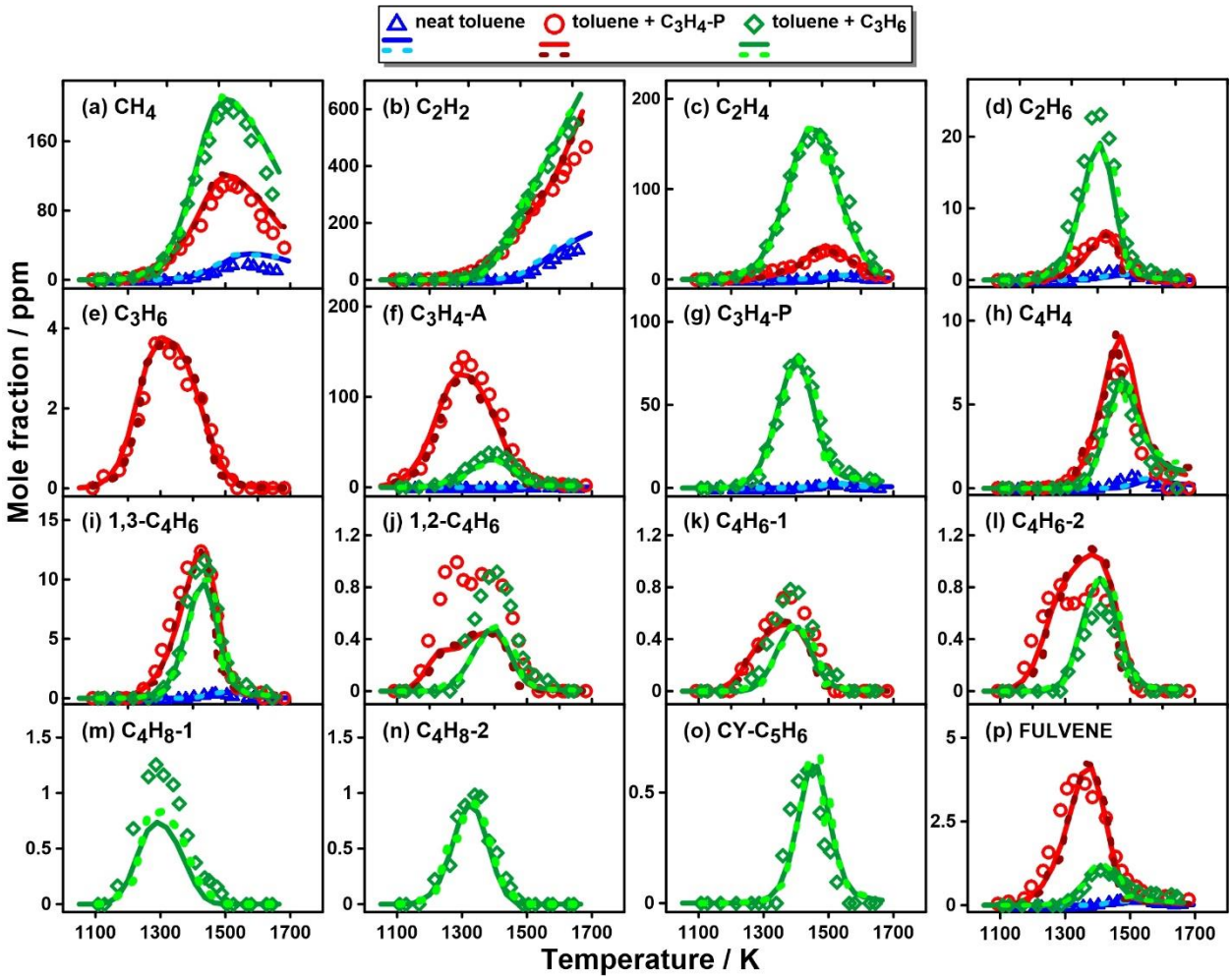

Figure 5.67: Small species mole fraction profiles as a function of the post-shock temperature T_5 in neat toluene, toluene + C_3H_6 and toluene + C_3H_4-P pyrolysis. Symbols: measurements; solid lines: simulations with a constant pressure of 20 bar within a reaction time of 4.0 ms; dashed lines: simulations with measured pressure histories up to 10 ms.

A series of mono-cyclic aromatic hydrocarbons, including benzene, phenylacetylene, styrene, ethylbenzene, xylene, allylbenzene, ethynyl toluene ($CH_3C_6H_4C_2H$), vinyl toluene ($CH_3C_6H_4C_2H_3$), 1-phenylpropyne and phenyl allene are detected and measured. The experimental and simulated mole fraction profiles of these aromatics are shown in **Figure 5.68**. The kinetic model can well predict the experimental measurements. Similar to the case of small hydrocarbons, the C_3 fuels addition enhances the formation of the MAHs present in toluene species pool and introduces new MAHs. C_6H_6 is the major decomposition product in individual cases. The added C_3 fuel intensifies C_6H_6 formation and lowers its temperature formation window. According to ROP analyses, C_6H_6 is entirely produced through the ipso-substitution reaction $H+C_7H_8 = CH_3+C_6H_6$ in neat toluene pyrolysis. The relative importance of this channel decreases in toluene-C_3 co-pyrolysis, where the C_3H_3 self-recombination reaction becomes the predominant C_6H_6 contributor. Additional reactions including the isomerization/fragmentation of

$C_5H_5CH_2$-1 and $C_5H_5CH_2$-2, the isomerization of fulvene, and the C_3H_4-A+ C_3H_3 reaction also contribute to C_6H_6 formation in binary reaction systems. The higher C_3 precursors in toluene-propyne pyrolysis result in the higher C_6H_6 peak mole fraction in comparison with toluene-propylene pyrolysis. $C_6H_5C_2H$ (**Figure 5.68 (b))** and $C_6H_5C_2H_3$ (**Figure 5.68 (c))** formation largely depends on the C_6H_5+C_2H_x (x=2, 4) reactions. The pyrolysis of C_3 fuels increases the concentrations of C_6H_5 and C_2H_x in the reaction system facilitating the production of both $C_6H_5C_2H$ and $C_6H_5C_2H_3$. Besides, $C_6H_5C_2H_5$ decomposition is also the main source of $C_6H_5C_2H_3$. The highest $C_6H_5C_2H_5$ production in toluene-propylene co-pyrolysis accounts for the highest $C_6H_5C_2H_3$ peak concentration. Ethylbenzene and xylene isomers (XYLENE) are produced through C_7H_7+CH_3 and $CH_3C_6H_4$+CH_3 recombination reactions, respectively (**Figure 5.68 (d) and (e))**. In toluene-propylene co-pyrolysis, CH_3 and both C_7H_7 and $CH_3C_6H_4$ precursors are abundant as a consequence of propylene consumption through the addition-elimination reaction C_3H_6+H = C_2H_4+CH_3 and reinforced H-abstraction reactions from toluene, respectively. Therefore, the mole fractions of the C_8H_{10} isomers ($C_6H_5C_2H_5$ and XYLENE) are systematically higher than those in neat toluene and toluene + propyne pyrolysis. $C_6H_5C_3H_5$-1, detected only in toluene-propylene pyrolysis, comes from the C_6H_5 + C_3H_6 and C_6H_5 + C_3H_5-A recombination reactions. $C_6H_5C_3H_3$P_1 (**Figure 5.68 (h))** and $C_6H_5C_3H_3$A (**Figure 5.68 (i))** are only detected in toluene-C_3 co-pyrolysis, and they have the same speciation temperature window as well as the peak mole fraction with those in neat propylene and neat propyne pyrolysis. $C_6H_5C_3H_3$P_1 is mainly formed through C_3H_4-P+C_6H_5 and $C_6H_5C_2H$+CH_3 molecule+radical reactions. $C_6H_5C_2H$+CH_3 channel is predominant at high temperatures. $C_6H_5C_3H_3$A is mainly produced from the recombination reaction of phenyl radical with propargyl radical. The reaction C_3H_4-P+C_6H_5 = $C_6H_5C_3H_3$A+H also contributes to $C_6H_5C_3H_3$A in toluene+propyne pyrolysis at moderate temperatures (1300–1400 K). $C_6H_5C_3H_3$P_1 and $C_6H_5C_3H_3$A have higher peak mole fractions and lower onset temperature in toluene-propyne co-pyrolysis since their production involves C_3H_4-P+C_6H_5 reactions. A relatively large amount of small peaks with C_9H_8 and C_9H_{10} molecular formulas are detected in toluene+C_3 pyrolysis experiments. Mass spectra indicates that they are either ethynyl- or vinyl- toluene structures, however the o-, m- or p- type isomers cannot be explicitly determined. Besides, certain C_9H_8 and C_9H_{10} species have close retention times so their signals are overlapped. Therefore, the total mole fraction measurements of all these small peaks are given in **Figure 5.68 (g)**. The simulated $CH_3C_6H_4C_2H$ and $CH_3C_6H_4C_2H_3$ are summed up to compare with the experimental profile, and a good agreement is realized between the quantified and modeled results. $CH_3C_6H_4C_2H$ and $CH_3C_6H_4C_2H_3$ are mainly formed via $CH_3C_6H_4$+C_2H_2 and $CH_3C_6H_4$+C_2H_4 bimolecular reactions, respectively. Another important channel through $CH_3C_6H_4$+C_3H_4-P= $CH_3C_6H_4C_2H$+CH_3 also contributes to $CH_3C_6H_4C_2H$ formation in toluene/C_3 pyrolysis. A higher peak mole fraction is seen in toluene-propylene pyrolysis attributable to the enhanced toluene fuel radical formation compared to toluene-propyne pyrolysis.

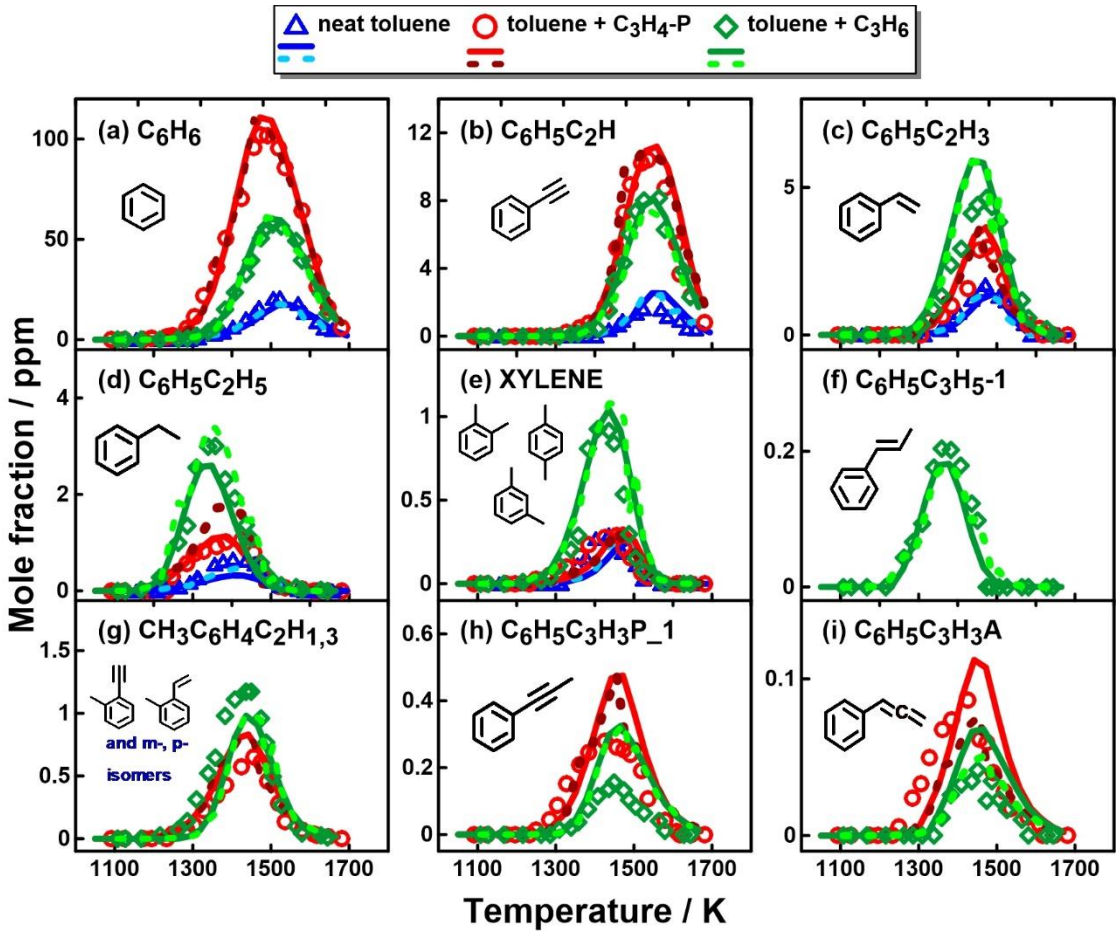

Figure 5.68: MAH mole fraction profiles as a function of the post-shock temperature T_5 in neat toluene, toluene + C_3H_6 and toluene + C_3H_4-P pyrolysis. Symbols: measurements; solid lines: simulations with a constant pressure of 20 bar within a reaction time of 4.0 ms; dashed lines: simulations with measured pressure histories up to 10 ms.

5.3.4.3 PAH species

Several C_9-C_{12} PAH species are observed in the neat toluene and toluene-C_3 experiments. Their measured mole fractions as well as the simulation results using the two different approaches are presented in **Figure 5.69**. In general, the added C_3 fuels tend to enhance the formation of the existing PAHs in neat toluene and bring about new PAHs.

The extra C_3 fuels promote C_9H_8 formation (**Figure 5.69 (a)**), where its onset temperature is shifted to lower temperatures, and its peak concentration is raised from around 1 ppm in neat toluene pyrolysis to over 5 ppm in toluene-C_3 co-pyrolysis. Such observations are accurately reproduced by the kinetic model using the first approach, while the second one slightly overpredicts C_9H_8 peak concentration. In neat toluene, C_9H_8 is almost exclusively formed through C_7H_7+C_2H_2 reaction, where C_2H_2 is the limiting

reactant. However, in binary mixtures, C_9H_8 mainly originates from the bimolecular reaction $C_7H_7+C_3H_4$-P=$C_9H_8+CH_3$ at low temperatures. As the temperature increases, the reaction $C_7H_7+C_2H_2$, and $C_6H_5C_3H_3$P_1 and $C_6H_5C_3H_3$A isomerization become the dominant C_9H_8 formation channels; these reactions channels are supported by the abundant C_2H_2 production from C_3 pyrolysis. In toluene-propylene pyrolysis, an additional pathway through the dehydrogenation of indane also contributes to C_9H_8 formation at high temperatures. Since $C_7H_7+C_3H_4$-P=$C_9H_8+CH_3$ is the dominant reaction at low temperatures, C_9H_8 onset temperature in toluene-propyne pyrolysis is lower than that in toluene-propylene pyrolysis. The higher C_9H_8 prediction using the second method goes to two reasons: (i) $C_6H_5C_3H_3$A isomerization to indene (the simulated mole fraction decrease when using the pressure profile up to 10 ms (**see Figure 5.68 (i)**)); (ii) $C_6H_5C_3H_3$P_1 isomerization. Indane is only observed in toluene-propylene co-pyrolysis. It substantially comes from the $C_7H_7+C_2H_4$ bimolecular reaction. The isomerization of $CH_3C_6H_4C_2H_3$ and $C_6H_5C_3H_5$-1 slightly contributes to C_9H_{10} formation. It is noteworthy that $C_7H_7+C_2H_4$ reaction extends during the quenching period leading to a higher simulated C_9H_{10} peak mole fraction using the measured pressure profiles up to 10 ms (**Figure 5.69 (b)**).

The enhanced indene formation in toluene-C_3 co-pyrolysis gives rise to higher C_9H_7 production. C_9H_7 reacts with the abundant CH_3 radical leading predominantly to the formation of 1-methyl indene ($C_9H_7CH_3$-1). The measured temperature-dependent $C_9H_7CH_3$-1 mole fractions are largely underestimated by the kinetic model regardless the method used (see **Figure 5.69 (f)**). This can be attributed to two reasons: (i) its fast isomerization to 2-methyl indene ($C_9H_7CH_3$-2) that promptly decomposes to C_9H_7 and CH_3; (ii) its rapid decomposition to $C_9H_6CH_3$-1. $C_9H_7CH_3$-2, the other methyl indene isomer, is only formed during the quenching period primarily via 3-methylindene ($C_9H_7CH_3$-3) isomerization, a potential product from $C_7H_7+C_3H_4$-P addition-elimination reactions, and trivially via $C_9H_7+CH_3$ recombination reaction. The model also under-predicts the $C_9H_7CH_3$-2 profile. The conversion of $C_9H_7CH_3$-3 to $C_9H_7CH_3$-2 is perhaps underestimated in the current model, leading to the aforementioned discrepancies between the observations and simulations. Thus, future theoretical works on the $C_7H_7+C_3H_4$-P reactions and the conversion among methyl indene isomers are necessary to better predict methyl indene isomers.

The formation mechanism of $C_9H_6CH_2$ (**Figure 5.69 (c)**) in neat toluene mainly depends on the recombination reaction of C_7H_5 with C_3H_3. Other minor pathways include the decomposition of $C_9H_6CH_3$-1and the bimolecular reaction between o-C_6H_4 and C_4H_4. However, the decomposition of $C_9H_6CH_3$-1 following the production of $C_9H_7CH_3$-1 becomes the prominent reaction pathway leading to $C_9H_6CH_2$ in binary mixtures due to the large concentrations of C_9H_7 and CH_3 radicals in their species pools. The $C_7H_5+C_3H_3$ pathway have minor contribution to $C_9H_6CH_2$ in toluene-C_3 co-pyrolysis though C_3H_3 is abundantly available. This is because C_7H_7 radical mainly reacts with the C_3 and C_2

hydrocarbons, so a lower portion decomposes to C_7H_5. The kinetic model can well reproduce $C_9H_6CH_2$ profiles in all the three cases.

As expected, the supplemental C_3 fuels, in particular propyne, boost $C_{10}H_8$ formation to a large degree and lower its speciation temperature window (**Figure 5.69 (d)**). The $C_{10}H_8$ formation mechanism is depicted in **scheme 5.12** based on the integrated ROP analyses at 1450 K in the three investigated cases. In neat toluene, $C_{10}H_8$ is mainly formed through C_7H_5+C_3H_3 recombination, naphthyl+H recombination and the fragmentation of benzobicyclo [2,2,2] octatriene (BICYCLO) produced from the C_6H_6+o-C_6H_4 reaction. Other minor channels include $C_9H_6CH_2$ isomerization and both $C_9H_6CH_3$-1 and $C_9H_7CH_2$ decomposition; $C_9H_7CH_2$ comes from C_7H_7+C_3H_3 reaction. These minor channels are significantly intensified due to the increased C_3H_3 and C_9H_7 concentrations in toluene/C_3 co-pyrolysis. Besides, the dehydrogenation of dihydronaphthalene ($C_{10}H_{10}$), the newly introduced pathway, plays a crucial role in $C_{10}H_8$ formation at low temperatures in binary reaction systems. $C_{10}H_{10}$ is mainly formed through C_7H_7+C_3H_4-P/C_3H_4-A reactions. It is noteworthy that the major $C_{10}H_8$ formation pathways have comparable relative importance in both binary mixtures, though the absolute $C_{10}H_8$ production in toluene-propylene pyrolysis is much lower than toluene-propyne co-pyrolysis. This is due to the fact that these channels require the participation of propyne and propargyl, which are present in higher mole fractions in toluene-propyne co-pyrolysis.

Different substituted naphthalene PAHs are detected in the current experiments including $C_{10}H_7CH_3$-1 (**Figure 5.69 (h)**), $C_{10}H_7C_2H$-1 (**Figure 5.69 (i)**), and $C_{10}H_7C_2H_3$-1 (**Figure 5.69 (k)**). $C_{10}H_7CH_3$-1 and $C_{10}H_7C_2H$-1 are predominantly formed via $C_{10}H_7$-1+CH_3 and $C_{10}H_7$-1+C_2H_2 bimolecular reactions, respectively. The addition of C_3 fuels enhances the efficiency of these channels due to the enhanced production of $C_{10}H_7$, CH_3, and C_2H_2 molecules. $C_{10}H_7C_2H_3$ is exclusively formed from C_9H_7+C_3H_3 recombination reaction. Both precursors are present in toluene-C_3 co-pyrolysis promoting this recombination reaction. The kinetic model can satisfactorily predict the measurements and the right order of the peak mole fractions among the three cases.

Finally, in all three fuel systems, the $C_6H_5C_6H_5$ formation greatly relies on the reaction C_6H_6+C_6H_5 = $C_6H_5C_6H_5$+H, and the H-abstraction from C_6H_6 is an important C_6H_5 source. Thus, the $C_6H_5C_6H_5$ peak mole fractions follow the same order as those of C_6H_6 among the three cases. Another major PAH intermediate is acenaphthylene (**Figure 5.69 (j)**). The $C_{12}H_8$ peak mole fractions increase remarkably in toluene-C_3 co-pyrolysis. Besides, the $C_{12}H_8$ formation temperature window moves toward lower temperatures in the presence of C_3 fuels and in particular propyne (about 1300 K). According to ROP analyses, $C_{12}H_8$ formation in neat toluene pyrolysis majorly depends on the step-wise isomerization of biphenyl radical ($C_{12}H_9$) through the intermediates biphenylene ($C_6H_4C_6H_4$) and cyclopenta[a]indene

(BENZO) [25], [26]. Other pathways include C_9H_7+C_3H_3 recombination [198] and the HACA route via $C_{10}H_7$-1+C_2H_2. C_9H_7+C_3H_3 recombination becomes the predominant pathway (over 90%) in toluene-C_3 co-pyrolysis throughout the temperature range due to the enhanced production of C_9H_7 and C_3H_3. The HACA route only has a limited contribution (a few percent) at elevated temperatures, while $C_{12}H_9$ isomerization through the BENZO intermediate has almost negligible contribution. In toluene-propylene pyrolysis, the simulations based on the constant pressure assumption over a reaction time of 4 ms underestimates the $C_{12}H_8$ peak mole fraction. This is because the $C_{12}H_8$ formation continues after the arrival of the rarefaction waves through C_9H_7+C_3H_3 reaction, and that's why the simulations with measured pressure histories up to 10 ms can precisely capture the $C_{12}H_8$ profile. However, in toluene-propyne pyrolysis, the model over-predicts the $C_{12}H_8$ peak mole fraction.

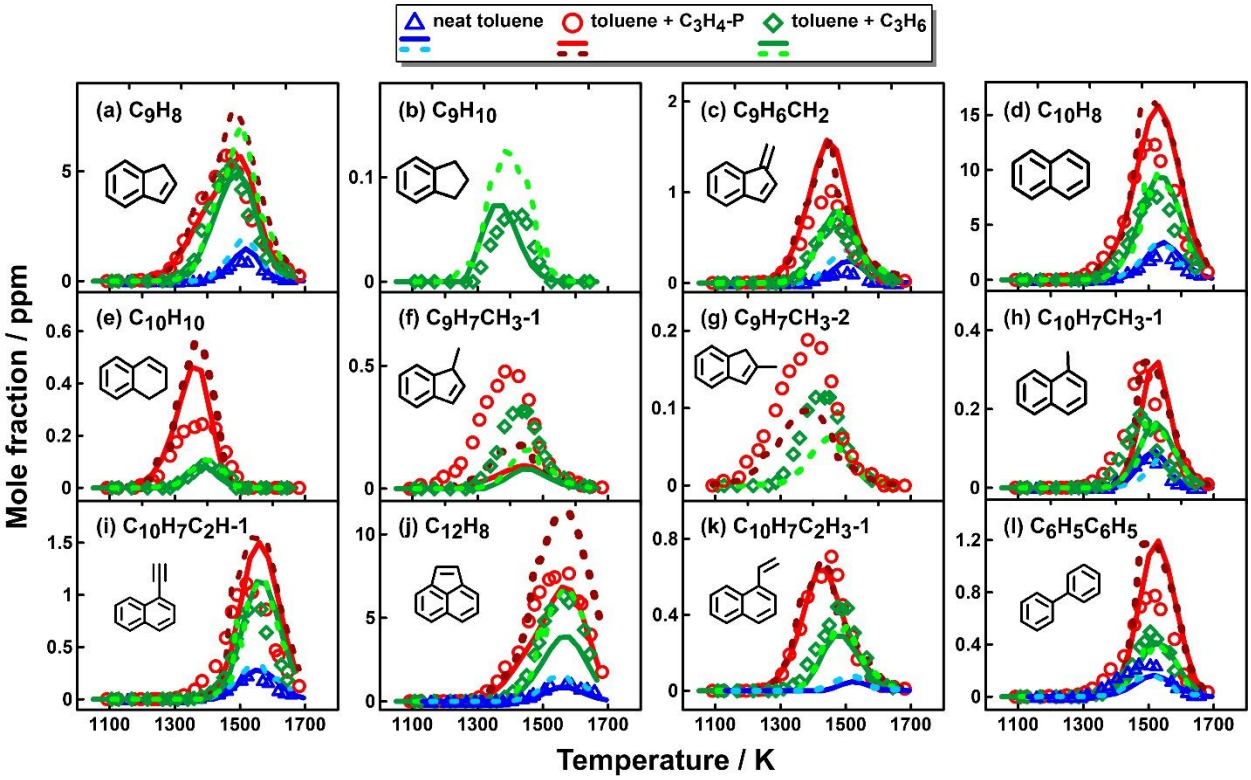

Figure 5.69: C_9-C_{12} PAH mole fraction profiles as a function of the post-shock temperature T_5 in neat toluene, toluene + C_3H_6 and toluene + C_3H_4-P pyrolysis. Symbols: measurements; solid lines: simulations with a constant pressure of 20 bar within a reaction time of 4.0 ms; dashed lines: simulations with measured pressure histories up to 10 ms.

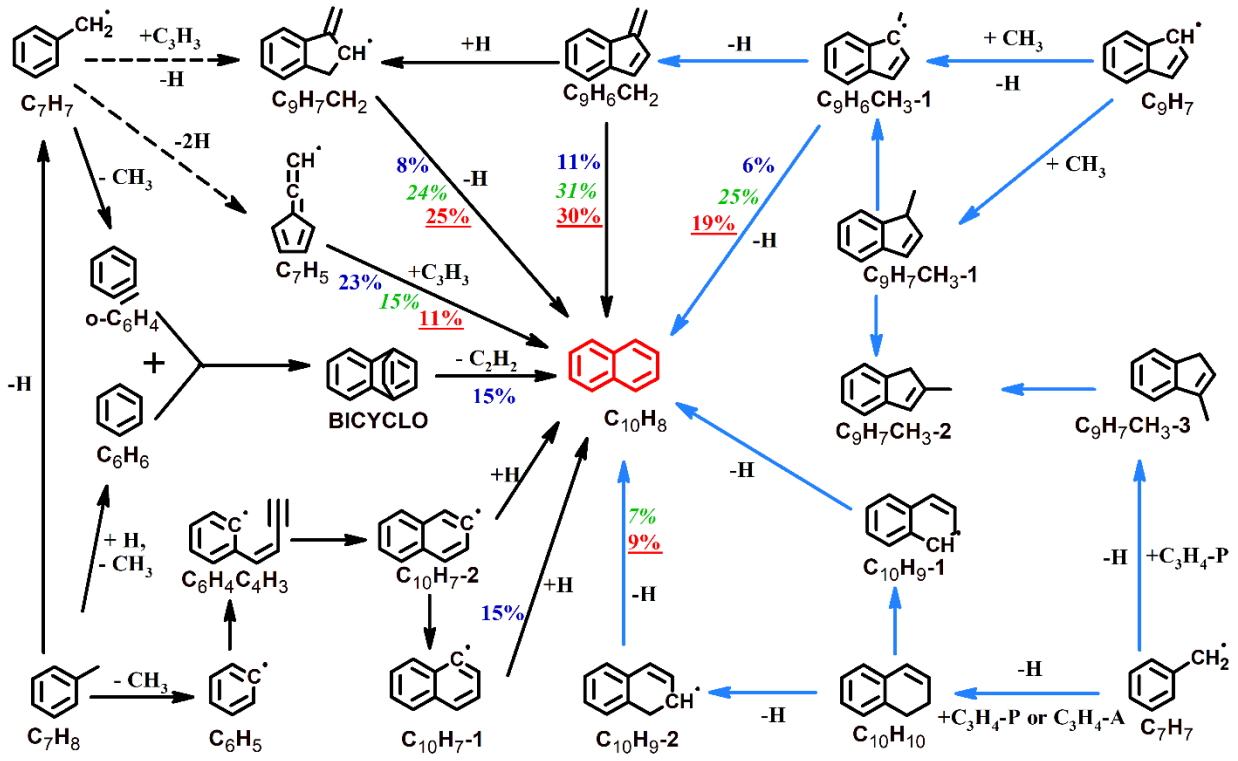

Scheme 5.12: Naphthalene ($C_{10}H_8$) formation pathways in neat toluene and toluene-C_3 pyrolysis. The highlighted pathways are newly introduced by the C_3 fuels. The dashed arrows indicate that the corresponding pathways are multiple step processes. The percentage numbers (neat toluene: normal; toluene+propylene: italic; toluene+propyne: underlined) represent the contributions to $C_{10}H_8$ formation by corresponding reactions.

Similar to the fact that the enhanced indene formation results in a considerable increase in $C_{12}H_8$ formation through C_9+C_3 reactions, it is expected that the enhanced naphthalene formation would result in abundant C_{13} PAHs through C_{10}+C_3 reactions, especially in toluene-propyne co-pyrolysis. Several $C_{13}H_{10}$ peaks are detected in the current experiments, but their exact structures cannot be identified due to the absence of standard mass spectra and the low concentrations of the products. **Figure 5.70** displays the simulated mole fractions of the $C_{13}H_{10}$ isomers that emanate from C_{10}+C_3 reactions (**see Scheme 4.7**). The naphthyl-propyne isomers ($C_{10}H_7CCCH_3$ and $C_{10}H_7CCCH_3$-2), 1H-benz[e]indene ($C_{10}H_7CYC5$) and 1H-benz[f]indene ($C_{10}H_7CYC5$-2) have peak mole fractions in the range of 10^{-7}, while naphthyl-allene isomers ($C_{10}H_7CHCCH_2$ and $C_{10}H_7CHCCH_2$-2) and phenalene ($PC_{13}H_{10}$) have peak mole fractions around 10^{-8}. Thus, $C_{13}H_{10}$ isomers formation through $C_{10}H_7$+C_3 reactions is limited in toluene-propyne pyrolysis, in spite of the largely increased $C_{10}H_8$ formation and the plentiful C_3 species. Such observations result from the relatively low concentration of naphthyl radicals (~10^{-8}) compared to indenyl radical whose concentration is relatively higher (in the order of 10^{-6}). Consequently, $C_{10}H_7$+C_3 reactions are not efficient

pathways leading to PAH growth as the recombination reactions of resonantly-stabilized radicals, such as C_7H_7+C_3H_3 and C_9H_7+C_3H_3 leading to $C_{10}H_8$ and $C_{12}H_8$, respectively.

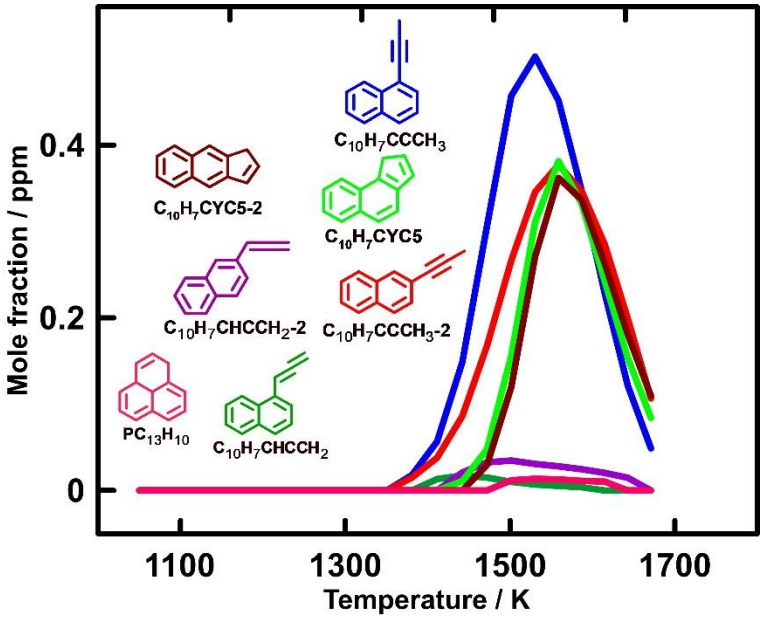

Figure 5.70: Simulated mole fraction profiles of $C_{13}H_{10}$ isomers, which are potential products of $C_{10}H_7$+C_3H_3/C_3H_4 reactions, in toluene-propyne co-pyrolysis. The different colors of the molecules correspond to their relative profile.

Figure 5.71 presents the experimental and simulated mole fraction profiles of C_{13}-C_{14} PAH species. $C_6H_5CH_2C_6H_5$ (**Figure 5.71 (b)**) mole fractions cannot be correctly quantified in toluene-C_3 co-pyrolysis because it is overlapped with that of $C_{10}H_7C_2H_3$, which has much higher mole fractions. The kinetic model can well capture $C_6H_5CH_2C_6H_5$ profile in neat toluene pyrolysis, and it predicts lower $C_6H_5CH_2C_6H_5$ mole fractions in toluene-C_3 co-pyrolysis. $C_6H_5CH_2C_6H_5$ is mainly produced through C_7H_7+C_6H_5 recombination. This pathway is impeded in toluene-C_3 co-pyrolysis as a result of the interactions of C_7H_7 with the abundant C_1–C_3 hydrocarbons. On the other hand, C_6H_5 is more abundant in toluene-propyne pyrolysis compared to toluene-propylene case leading to a slightly higher $C_6H_5CH_2C_6H_5$ peak mole fraction. Fluorene (**Figure 5.71 (a)**) comes largely from $C_6H_5CH_2C_6H_5$ dehydrogenation reactions in neat toluene pyrolysis. As a consequence of the reduced $C_6H_5CH_2C_6H_5$ production in toluene-C_3 co-pyrolysis, $C_{13}H_{10}$ has lower concentrations in binary mixtures compared to neat toluene. Such observations are well captured by the kinetic model. $C_6H_5C_2H_4C_6H_5$ is exclusively formed through C_7H_7 self-recombination, and it is found to be the most abundant PAH species in neat toluene pyrolysis (**Figure 5.71 (c)**). The addition of C_3 fuels reduces C_7H_7 levels, and thus the carbon flux of C_7H_7 self-

recombination reaction is decreased leading to a lower $C_6H_5C_2H_4C_6H_5$ mole fractions. As mentioned before, $C_6H_5C_2H_4C_6H_5$ formation carries on during the quenching period, so simulations using the second approach based on measured pressure profiles are necessary to predict $C_6H_5C_2H_4C_6H_5$ mole fraction distribution. Despite the over-prediction of $C_6H_5C_2H_4C_6H_5$ peak mole fractions, the model can well predict the decreasing trend in peak concentrations of $C_6H_5C_2H_4C_6H_5$ when C_3 fuels are present in the initial mixture. Stilbene ($C_6H_5C_2H_2C_6H_5$) (**Figure 5.71 (d)**) originates from $C_6H_5C_2H_4C_6H_5$ dehydrogenation reactions in all the three cases. Thus, the $C_6H_5C_2H_2C_6H_5$ peak mole fractions follow the same order as those of $C_6H_5C_2H_4C_6H_5$ among the three cases.

Regarding $C_{14}H_{10}$ isomers, the added C_3 fuels enhances the formation of both $C_6H_5CCC_6H_5$ (**Figure 5.71 (e)**) and $C_{13}H_8CH_2$ (**Figure 5.71 (f)**) and reduces that of $PC_{14}H_{10}$ and $AC_{14}H_{10}$ (**Figure 5.71 (g) and (h), respectively**). $C_6H_5CCC_6H_5$ is the product of $C_6H_5C_2H+C_6H_5$ reaction. The formation of both precursors is strengthened by the addition of C_3 fuels. $C_{13}H_8CH_2$ mainly comes from $C_7H_7+C_7H_5$ reaction in neat toluene pyrolysis. This channel is hindered in toluene-C_3 co-pyrolysis accounted to the fact that C_7H_7 radicals are mainly consumed through reactions with C_1-C_3 species. However, $C_{13}H_8CH_2$ in toluene-C_3 co-pyrolysis is formed via an alternative pathway, the $C_6H_5C_2H+C_6H_5$ addition-elimination reaction. It is noteworthy that the $C_{13}H_8CH_2$ peak mole fractions appear at higher temperatures in toluene- C_3 co-pyrolysis. This is due to the fact that $C_6H_5C_2H$ starts forming at relatively high temperatures. $PC_{14}H_{10}$ have almost similar peak mole fractions in all three cases, while $AC_{14}H_{10}$ has higher concentrations in neat toluene pyrolysis. The kinetic model can well predict the $PC_{14}H_{10}$ and $AC_{14}H_{10}$ peak concentrations in neat toluene and toluene-propylene pyrolysis, though it over-predicts them in toluene-propyne pyrolysis. The reason lies in two possibilities: (i) the over-estimation of $C_6H_5CCC_6H_5$ in toluene-propyne which leads to enhanced $PC_{14}H_{10}$ formation and consequently $AC_{14}H_{10}$ through isomerization; (ii) missing of consumption channels. The latter possibility comes from the different observations made in this work: 1) from a modeling point of view, the rate constants have been validated over a vast range of experimental profiles with different fuel components and mixtures [138], [140], [141], [193], [211]–[213], [239]; 2) the early formation of the PAH species is well captured by the model, deviations appear only around the maxima (**Figure 5.71 (e), (g), and (h))**; 3) the carbon recovery is much worst for toluene + propyne case compared to addition of propylene as shown in **Figure 5.72.** Indeed, at high temperatures (T_5=1644 K) only around 55% of the carbon is recovered for the former case, against 72% in both neat toluene and toluene+propylene pyrolysis. It is important to underline the fact that the PAHs considered here only refer to the ones identified and quantified in the current experiments. Several three-to-four ring PAH peaks are detected but their structures could not be determined or the calibration could not be obtained in an accurate way (for the largest 4-ring structures). The carbon balance would be further improved if all the gas-phase products could be taken into consideration. Similar observations are made by comparing

propylene pyrolysis with propyne pyrolysis (**section 5.1.4**). Reaction pathways leading to the formation of $PC_{14}H_{10}$ and $AC_{14}H_{10}$ based on ROP analysis at T_5 of 1500 K are shown in **scheme 5.13**. The importance of C_7+C_7 reactions including C_7H_7+C_7H_7, C_7H_5+C_7H_5, $C_6H_4CH_3$+$C_6H_4CH_3$ and C_7H_7+$C_6H_4CH_3$ is detracted when C_3 fuels are added to toluene pyrolysis. This is related to the fact that the C_7 radicals have lower concentrations after reacting with the C_3 and smaller species, as stated previously. The contribution of $C_6H_5C_2H$+C_6H_5 addition-elimination reactions leading to $PC_{14}H_{10}$ formation increase in the binary fuels. Likewise, the π-bonding process between $C_{10}H_8$+ o-C_6H_4 has enhanced contribution to $AC_{14}H_{10}$ in toluene+C_3 pyrolysis, owing to the higher abundance of $C_{10}H_8$.

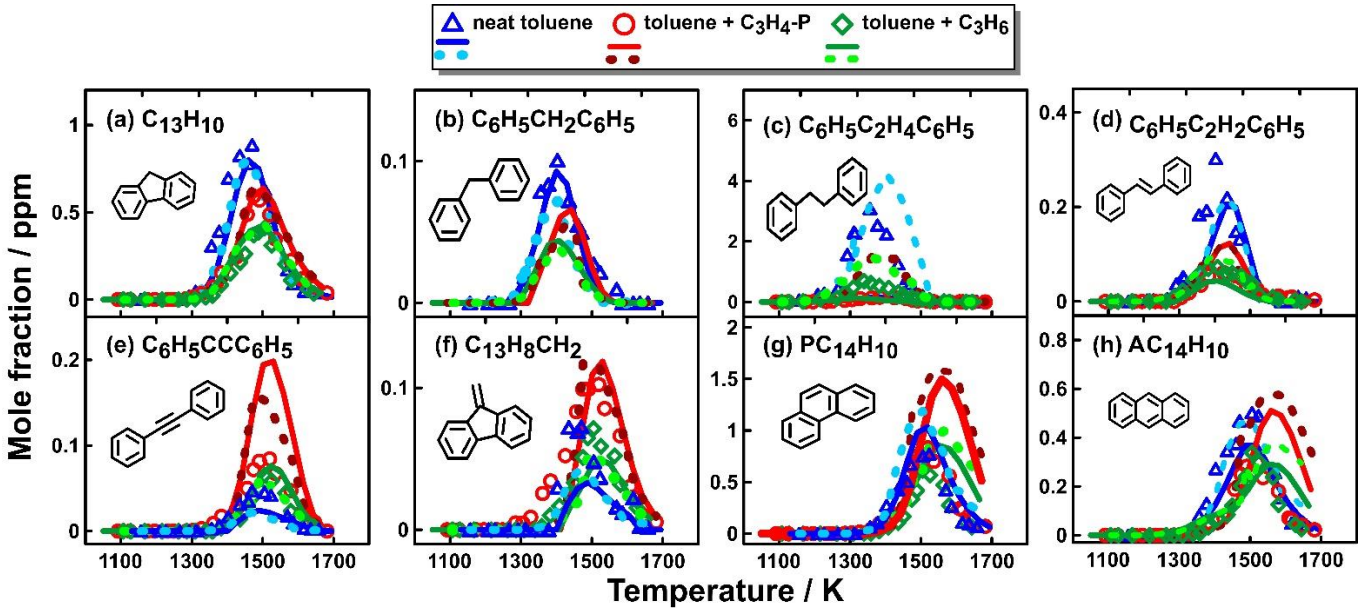

Figure 5.71: C_{13}-C_{14} PAH mole fraction profiles as a function of the post-shock temperature T_5 in neat toluene, toluene + C_3H_6 and toluene + C_3H_4-P pyrolysis. Symbols: measurements; solid lines: simulations with a constant pressure of 20 bar within a reaction time of 4.0 ms; dashed lines: simulations with measured pressure histories up to 10 ms.

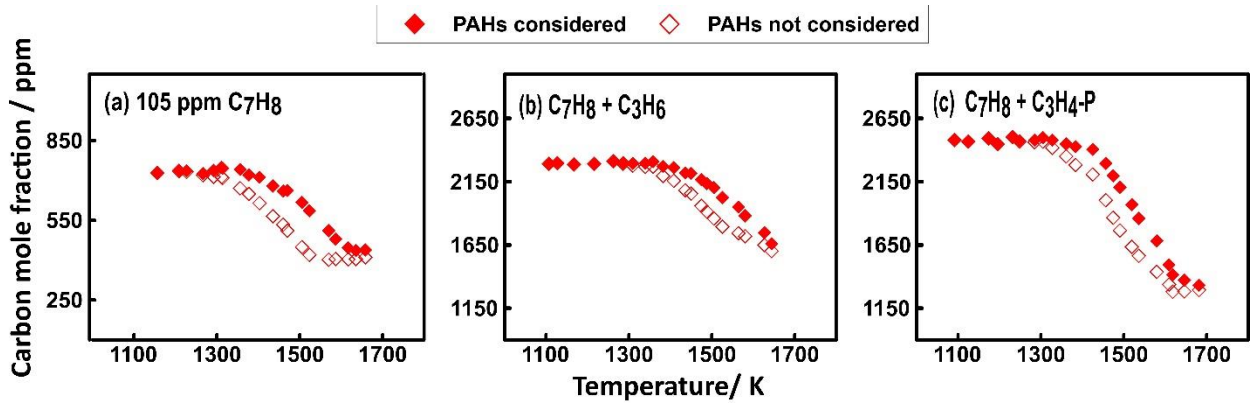

Figure 5.72: Carbon recovery with and without considering the PAH species in (a) toluene pyrolysis (b) toluene + propylene pyrolysis and (c) toluene + propyne pyrolysis.

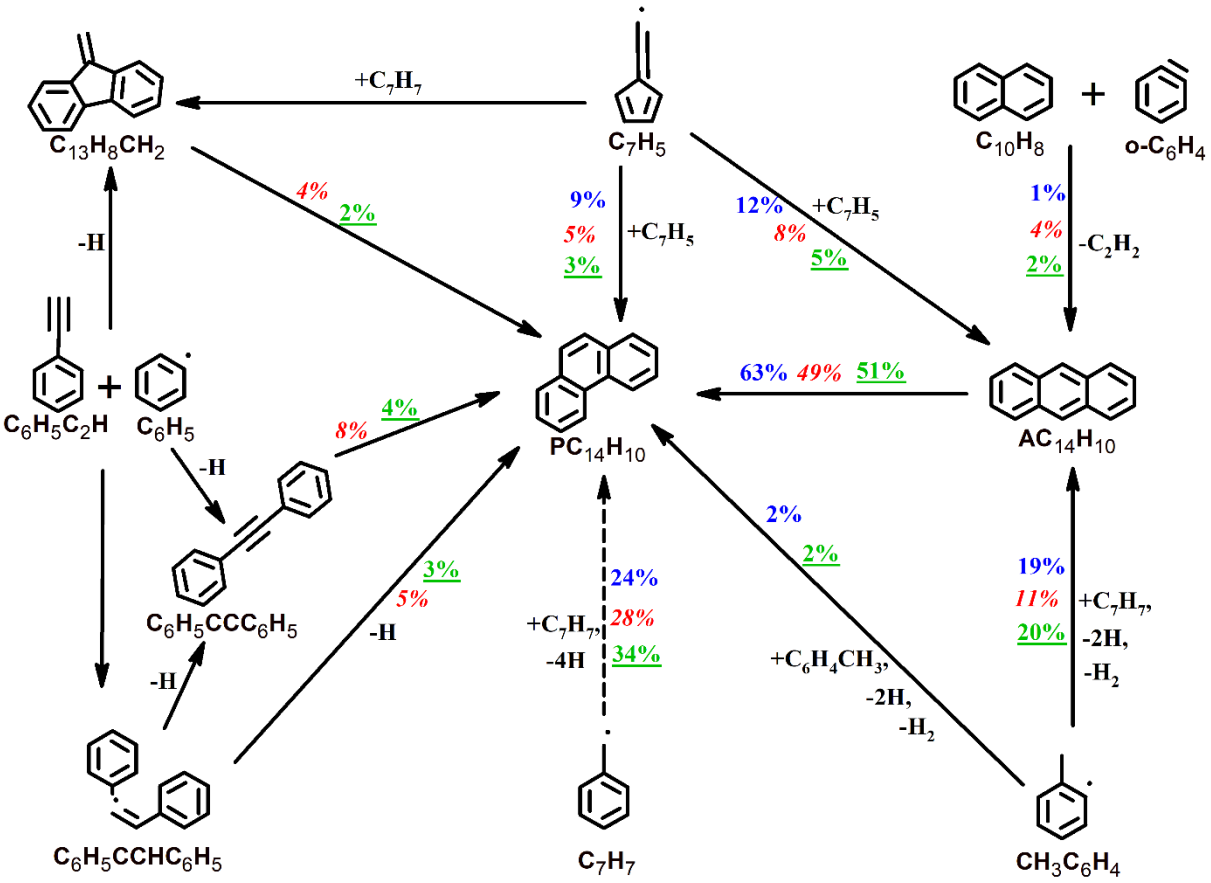

Scheme 5.13: Formation pathways for $PC_{14}H_{10}$ and $AC_{14}H_{10}$ in the pyrolysis of neat toluene and toluene-propylene and toluene-propyne mixtures at T_5 of 1500 K. The percentage numbers (normal: neat toluene; italic: toluene+propylene; underlined: toluene+propyne) represent the contributions of corresponding reactions to the formation of $C_{14}H_{10}$ PAHs. The dashed lines represent multiple step reaction processes

5.4 Phenylacetylene pyrolysis + reactions with acetylene/ethylene

5.4.1 Motivation

Phenylacetylene ($C_6H_5C_2H$) is produced during the oxidation and pyrolysis of hydrocarbons and commercial fuels. Constructed through analogies to other mono-aromatic rings such as benzene, toluene and styrene whose chemical kinetics are better investigated, phenylacetylene sub-mechanisms are embedded in detailed kinetic models. However, its kinetic mechanism describing its consumption scheme and PAH formation is poorly understood due to the lack of the experimental data. Considering the conclusion of recent studies [156], [240], the fuel pyrolysis and oxidation can potentially be decoupled to reduce the complexity. Therefore, phenylacetylene pyrolysis at typical combustion conditions is carried out as a major task to determine its decomposition reactions and to identify the gas-phase reaction products up to PAH including the investigation of their formation mechanisms.

In addition, the reactions of phenylacetylene with acetylene and ethylene are considered. It is extensively well-known that C_2H_x radicals /intermediates such as ethyne/ethynyl (C_2H_2/C_2H) and ethene/ethenyl (C_2H_4/C_2H_3) are produced in significant amounts in the pyrolysis of aliphatic hydrocarbons. Their interaction with aromatic molecules or radicals in the species pools is recognized to be crucial in the build-up of wide variety of products including the PAHs. Among the studies performed to understand the role of C_2H_x species in PAH formation [26], [63], [241]–[245], Shukla and Koshi [19] investigated the formation of naphthalene from benzene through $C_6H_5C_2H$ intermediate via HACA and their proposed HAVA pathways, respectively. Indeed, the $C_6H_5C_2H+C_2H_2$ reaction is the prototype of the HACA step which bring to ring closure through addition of a second acetylene molecule. The HAVA pathway seemed also to be promising for the production of naphthalene in ethylene pyrolysis via C_2H_3 addition at the ortho-position of phenylacetylene. Nonetheless, a direct investigation of C_2H_x addition on $C_6H_5C_2H$ to address their role on PAH formation has never been examined. Hence, introduction of C_2H_2/ C_2H_4 compounds separately with $C_6H_5C_2H$ is carried out not only to clarify the influence of C_2H_x addition on PAH growth and formation but also to assess the relative reactivity of $C_6H_5C_2H$ with respect to C_2H_2 and C_2H_4.

Towards these goals, three argon diluted mixtures respectively containing 103 ppm $C_6H_5C_2H$, 104 ppm $C_6H_5C_2H$+415 ppm C_2H_2 and 105 ppm $C_6H_5C_2H$+504 ppm C_2H_4, are used for the shock tube pyrolysis experiments at the nominal P_5 of 20 bar over the temperature range of 1100-1700 K for a reaction time of 4ms.

5.4.2 Phenylacetylene thermal decomposition

Dozens of pyrolysis products are detected in phenylacetylene pyrolysis experiments, and their mole fraction profiles are plotted as a function of reaction temperature (T_5). The experimental and simulated mole fraction profiles of the major pyrolytic species are shown in **Figure 5.73**. In general, the current model can adequately capture the fuel's reactivity, the peak concentrations, and the formation and the decomposition temperature windows of the observed pyrolysis species. The quantitative agreement between the experiments and the model is quite reasonable. ROP and sensitivity analyses are used to provide insights into the detailed chemistry of phenylacetylene decomposition and aromatic growth.

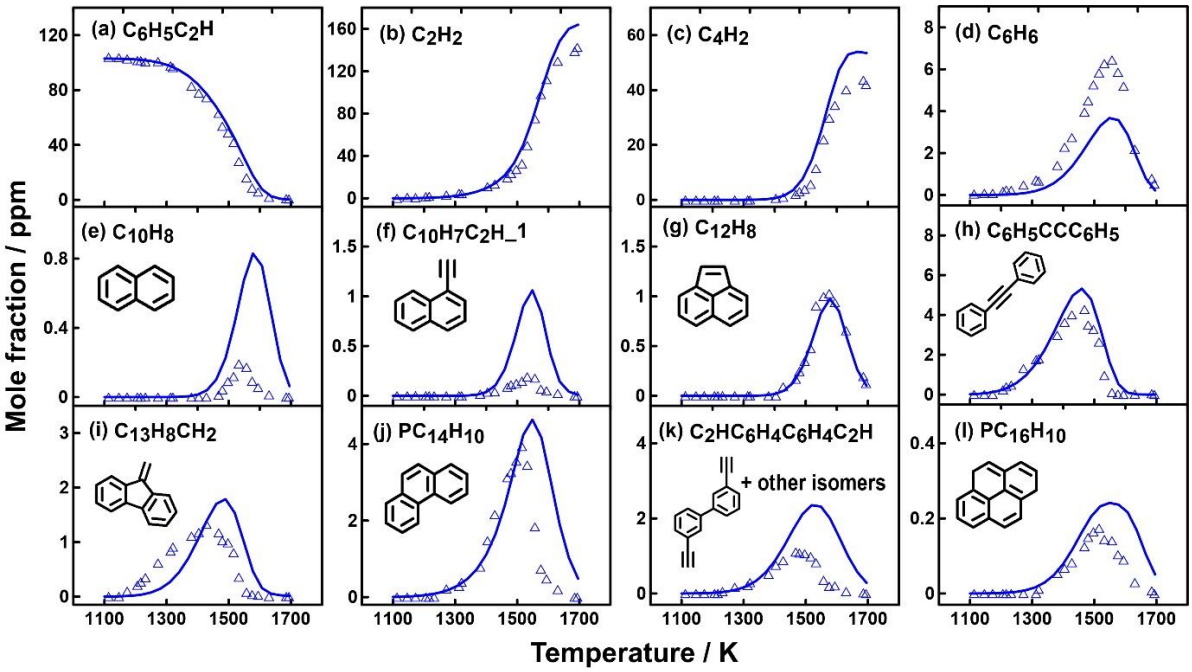

Figure 5.73: Mole fraction profiles (symbols) of fuel and its major products are measured from 103 ppm phenylacetylene pyrolysis in a shock tube at 20 bar. Solid lines indicate the model predictions.

5.4.2.1 Primary decomposition of phenylacetylene

Phenylacetylene consumption profile is presented in **Figure 5.73** (a). Phenylacetylene starts to decompose at temperatures around 1250 K, which is lower than that of benzene (1400K). Sensitivity analyses are performed at three different temperatures (1250 K, 1400 K and 1550 K) to unmask the reactions responsible for this phenomenon, and the results are shown in **Figure 5.74**. The C-H bond energy favors a competitive selectivity of H-elimination reaction compared to C-C bond dissociation reaction in unimolecular consumption channels. This is evident by the preeminence of $C_6H_5C_2H+H = C_6H_5+C_2H_2$ (R8), $C_6H_5C_2H+C_6H_4C_2H = C_2HC_6H_4C_6H_4C_2H+H$ (R24) and the $C_6H_5C_2H+C_6H_5$ reactions at the inspected temperatures. R8 has the highest negative sensitivity coefficient at all the examined

temperatures. The early formation of acetylene (**Figure 5.73** (c)) at low-temperatures confirms the dominance of the R8 reaction in phenylacetylene consumption. Besides C_2H_2 formation, (R8) yields to C_6H_5 radical. The addition-elimination reactions of C_6H_5 with $C_6H_5C_2H$ sustains the fuel reactivity by producing different $C_{14}H_{10}$ isomers ($C_6H_5CCC_6H_5$, $C_6H_4(C_2H)C_6H_5$, $C_{13}H_8CH_2$, and $PC_{14}H_{10}$) and releasing H-atoms. Similarly to the case of early C_2H_2 production, the early formation of $C_2HC_6H_4C_6H_4C_2H$ (**Figure 5.73** (k)) at low-temperatures confirms the importance of $C_6H_5C_2H+C_6H_4C_2H = C_2HC_6H_4C_6H_4C_2H+H$ in the $C_6H_5C_2H$ decay. Finally, the reactions between the phenyl radical and the phenylacetylene fuel lead to numerous C_{14} intermediates as described later in **section 5.4.2.3**. These include early formation of $C_6H_5CCC_6H_5$, $PC_{14}H_{10}$, and $C_{13}H_8CH_2$.

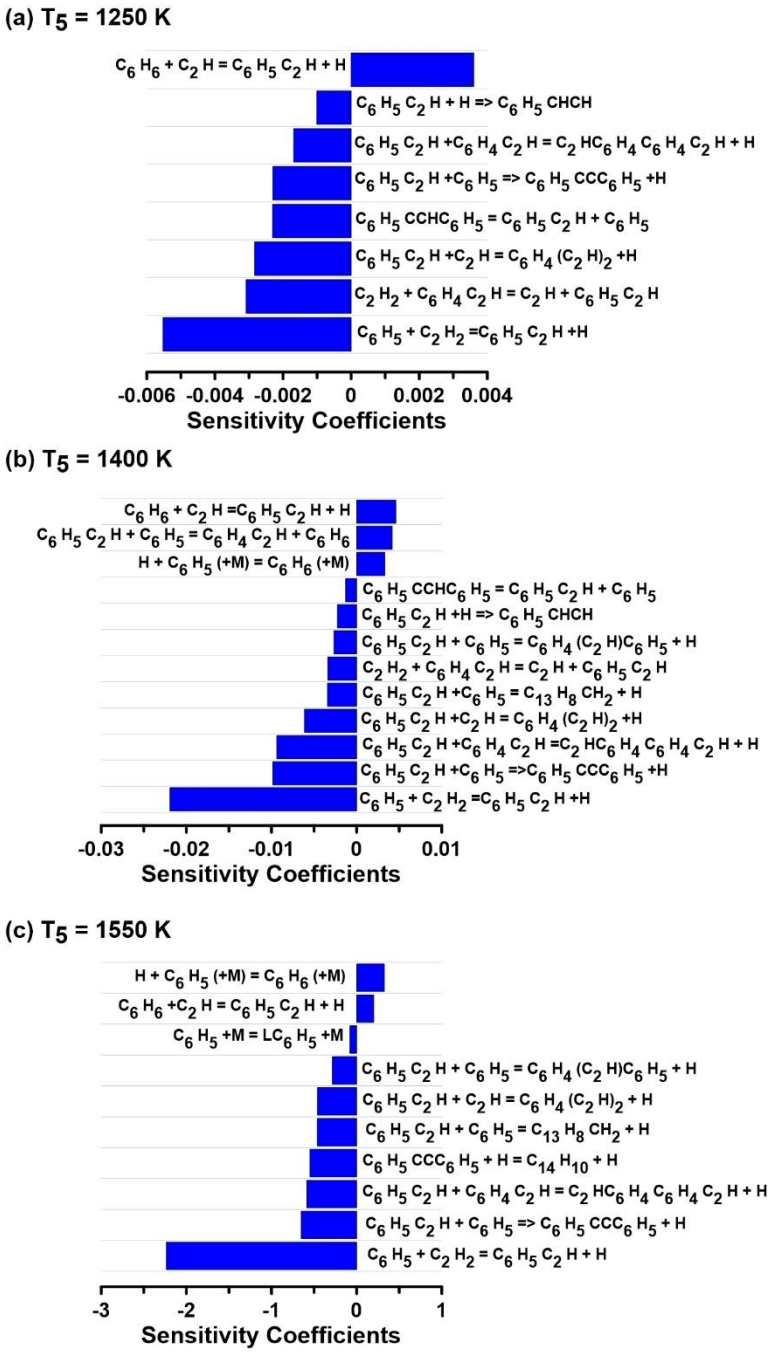

Figure 5.74: Sensitivity analyses for phenylacetylene at different post-shock temperatures (T_5s).

5.4.2.2 Formation of small intermediates

Small intermediates, particularly C_2H_2, C_4H_2, and C_6H_6, are formed through various pathways via multi-elementary reaction steps. C_2H_2 is produced mainly via R8 at low temperatures and via the two-elementary reactions, R8 and the unimolecular decomposition of LC_6H_5 to C_2H_2 and C_4H_3 at high temperatures. The subsequent decomposition of C_4H_3 to C_4H_2 and H is the primary production pathway of

C_4H_2. Benzene is principally formed by the H-abstraction reaction: $C_6H_5C_2H+C_6H_5= C_6H_4C_2H+C_6H_6$. Other reactions such as ipso-substitution reaction of $C_6H_5C_2H$ by H and hydrogen addition to phenyl radical also fairly contribute to benzene production. The H-abstraction reaction of benzene by hydrogen atom constitutes the main decomposition pathway for benzene. Model predictions of these small species are shown in **Figure 5.73** (b), (c) and (d).

5.4.2.3 Formation of PAH intermediates

To gain insights of how $C_6H_5C_2H$ consumption results in PAH formation, ROP analyses are performed at 1450 K, where about half of the fuel is consumed, and the shown PAH species have considerable mole fractions. The reaction networks, based on ROP analyses, are shown in **Scheme 5.14**. Since C_6H_5 radical is abundant in phenylacetylene pyrolysis, it has certain contributions to the PAH formation through its reaction with $C_6H_5C_2H$, leading to the formation of $C_{14}H_{10}$ compounds and the liberation of H atoms through both stepwise and direct pathways as illustrated in **Scheme 5.14**. The phenylethyl ($C_6H_4C_2H$) radical also assist in PAH evolution.

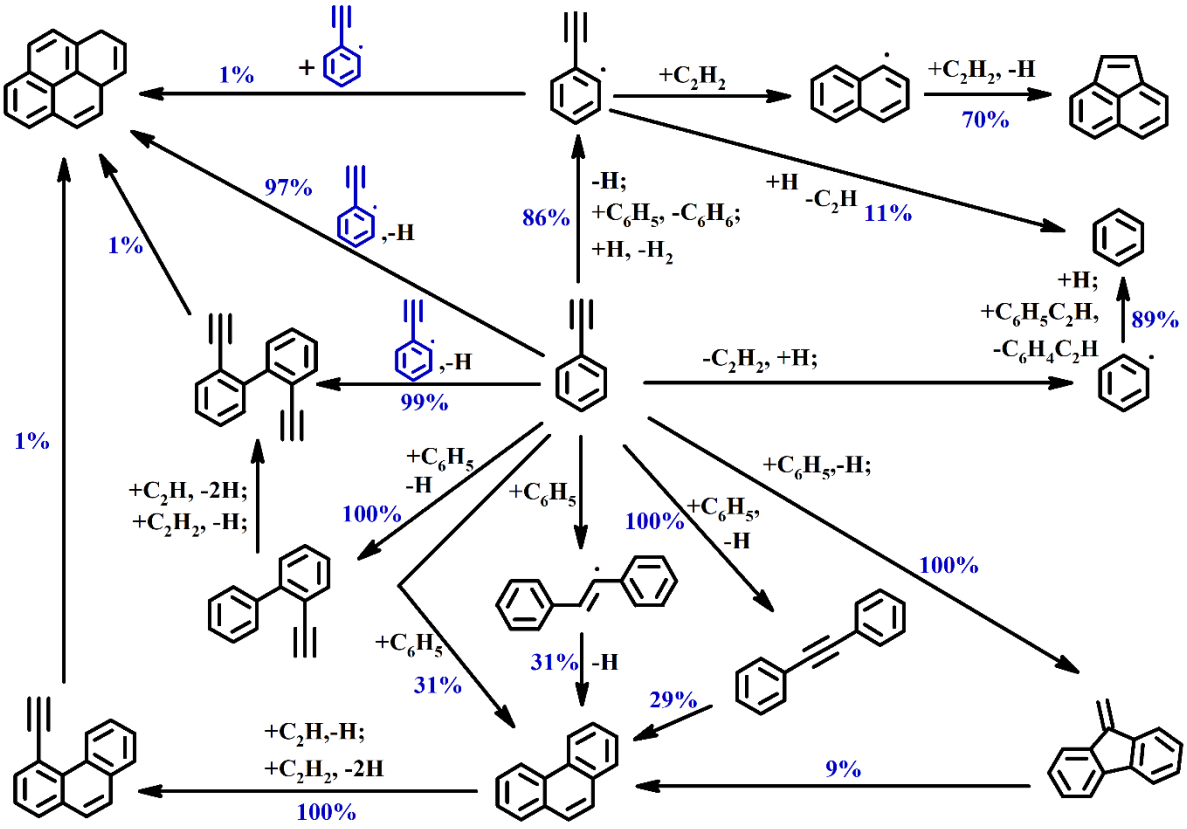

Scheme 5.14: The reaction pathways leading to the PAH formation at T_5 of 1450 K in neat phenylacetylene pyrolysis.. The percentage numbers represent the contributions of the corresponding reactions in the formation of PAH species.

The combination of phenylacetylene with phenyl radical is one of the most favorable reactions. $C_6H_5CCC_6H_5$ is the largest outcome from $C_6H_5C_2H+C_6H_5$ channel. $PC_{14}H_{10}$ and $C_{13}H_8CH_2$ are also produced from this reaction, but the latter one in lower proportions. Both $C_6H_5CCC_6H_5$ and $C_{13}H_8CH_2$ contribute to the formation of $PC_{14}H_{10}$ at higher temperatures through H assisted isomerization reactions in addition to the contributions of $C_6H_5CCHC_6H_5+H$ and $C_6H_5C_2H+C_6H_5$, which are the dominant pathways at low temperatures. The current model can well capture the speciation profiles of $C_6H_5CCC_6H_5$ and $PC_{14}H_{10}$ regarding both the shape and the size (see **Figure 5.73 (h) and (j)**), whereas improvements are still desired to correctly interpret the formation and decomposition temperature windows for $C_{13}H_8CH_2$ (see **Figure 5.73 (i)**). The currently used rate coefficients of R17 ($C_6H_5C_2H+C_6H_5$ = $C_{13}H_8CH_2+H$), R21 ($C_6H_5C(CH)C_6H_5$ = $C_6H_5C(CH_2)C_6H_4$), and R22 ($C_6H_5C(CH_2)C_6H_4$ = $C_{13}H_8CH_2+H$) are chosen in analogy with similar reactions, which may introduce large uncertainties to $C_{13}H_8CH_2$ prediction. Further future detailed calculations on $C_6H_5C_2H+C_6H_5$ scheme are needed to reveal the accurate kinetic parameters.

Concerning the $C_{16}H_{10}$ species, ROP analyses shows that the reaction $C_6H_5C_2H+C_6H_4C_2H$ is the main formation source for both $C_2HC_6H_4C_6H_4C_2H$ and pyrene ($PC_{16}H_{10}$). The self-combination of $C_6H_4C_2H$, the H-assisted isomerization reaction of $C_2HC_6H_4C_6H_4C_2H$ and the HACA route (phenanthrene+C_2H/C_2H_2) have negligible contribution to pyrene formation even at high temperatures. $C_2HC_6H_4C_6H_4C_2H$ mostly decompose to pyrene, ethynyl-biphenyl and ethynyl-phenanthrene.

Two $C_{12}H_8$ species are detected in this study i.e. acenaphthylene and ethynyl-naphthalene. Both are formed by the addition of acetylene on naphthyl radical, which are competing HACA channels. The C_2H_2 addition to $C_6H_4C_2H$ is an essential step in HACA route leading to benzofulvenyl (C_9H_6CH) and naphthyl ($C_{10}H_7$) radicals formation, whose detailed reaction mechanism was investigated by Mebel et al. [186]. Both branching channels continue with subsequent C_2H_2 addition, ending up in C_{12} intermediates, while "skipping" the formation of $C_{10}H_8$ which requires the participation of an H atom. This accounts for the negligible concentration of $C_{10}H_8$ produced in $C_6H_5C_2H$ pyrolysis (see **Figure 5.73** (e)). Besides, BENZO re-arrangement reaction has minor contribution to acenaphthylene formation (not shown in **scheme 5.14**). The model can well reproduce the shape of ethynyl-naphthalene and acenaphthylene, though it over-predicts that of ethynyl-naphthalene.

5.4.3 Influences of added acetylene and ethylene

5.4.3.1 Phenylacetylene consumption and small intermediates formation

First of all, the effect of extra C_2H_2 and C_2H_4 on the fuel decomposition rate is examined. Mole fraction profiles of $C_6H_5C_2H$ in all the three investigated cases are shown in **Figure 5.75**, along with the C_2H_2 and

C_2H_4 profiles in the corresponding mixtures. **Figure 5.75** also presents the simulated C_2H_2 and C_2H_4 mole fractions when $C_6H_5C_2H$ is replaced by Ar. The current model can well capture the fuels' reactivity in the three separate cases. C_2H_2 has almost no influence on the $C_6H_5C_2H$ consumption rate, and C_2H_4 promotes $C_6H_5C_2H$ decomposition, as inferred from the experimental and the modeling results. C_2H_2 is a main product in $C_6H_5C_2H$ pyrolysis. This explains how C_2H_2 consumption is compensated at high temperatures. $C_6H_5C_2H$ has no obvious effect on C_2H_4 thermal decomposition.

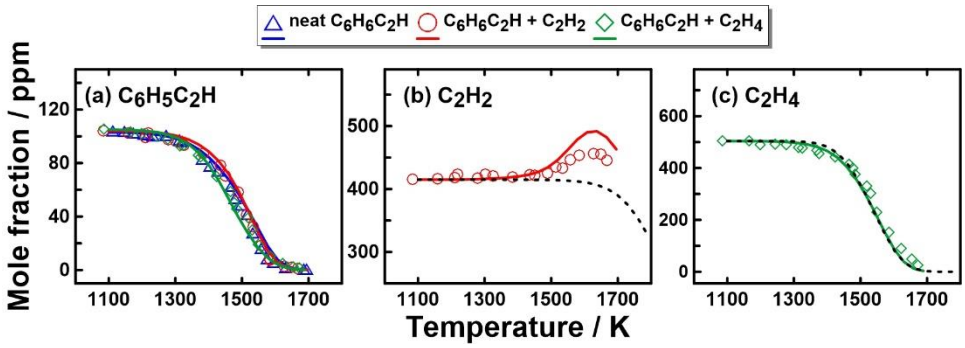

Figure 5.75: Experimental (symbols) and simulated (solid lines) mole fractions of (a) $C_6H_5C_2H$ in the three investigated cases, (b) C_2H_2 in the pyrolysis of 104 ppm $C_6H_5C_2H$ + 415 ppm C_2H_2 mixture and (c) C_2H_4 in the pyrolysis of 105 ppm $C_6H_5C_2H$ + 504 ppm C_2H_4 mixture. The dashed lines in (b) and (c) represent the simulated mole fractions of C_2H_2 and C_2H_4 when $C_6H_5C_2H$ is absent from the corresponding mixtures.

ROP analysis is done at T_5 = 1450 K to better understand the kinetic details responsible for the different $C_6H_5C_2H$ reactivity in the three sets, and the results are shown in **Figure 5.76**. $C_6H_5C_2H+H = C_6H_5+C_2H_2$ (R8) plays a dominant role in $C_6H_5C_2H$ consumption in the three cases, and it has more pronounced effects in binary fuel mixtures as a consequence of the increased level of H atoms, especially in $C_6H_5C_2H+C_2H_4$ pyrolysis. H-addition reactions to $C_6H_5C_2H$ are also more important in binary blends. The C_6H_5CHCH and $C_6H_5CCH_2$ radicals resulted from the $C_6H_5+C_2H_2$ addition reaction contribute to $C_6H_5C_2H$ production. Their high coefficients in $C_6H_5C_2H+C_2H_2$ pyrolysis counterbalance the efficiency of R8 in accelerating $C_6H_5C_2H$ decomposition reactivity. This explains why the reactivity of $C_6H_5C_2H$ is not impacted when C_2H_2 is added. Besides, the role of $C_6H_5C_2H$ + C_6H_5 reactions in assisting H-atom production is not really influenced when C_2H_2 or C_2H_4 is added.

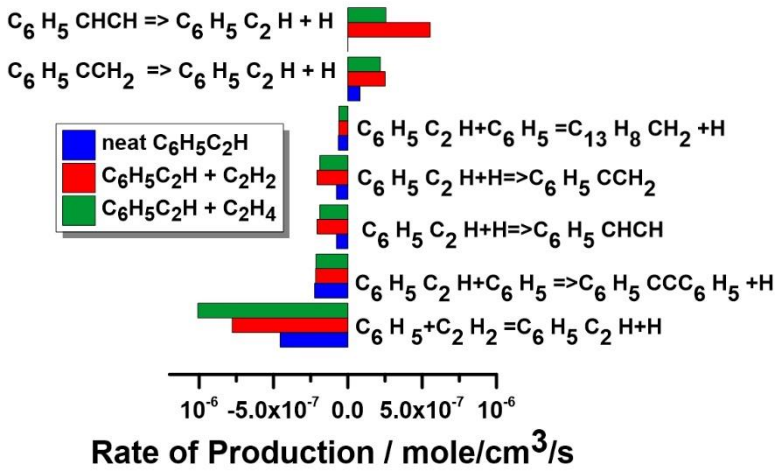

Figure 5.76: ROP-analysis for $C_6H_5C_2H$ consumption at T_5 = 1450 K and P_5 = 20 bar in the pyrolysis of neat $C_6H_5C_2H$, $C_6H_5C_2H+C_2H_2$ and $C_6H_5C_2H+C_2H_4$ mixtures.

Figure 5.77 presents the experimental and simulated mole fraction profiles of small products in the three studied cases. Light hydrocarbons such as CH_4, C_3H_4-A and C_3H_4-P are only observed in $C_6H_5C_2H+C_2H_4$ pyrolysis owed to the thermal decomposition of C_2H_4. C_6H_6 is present in the species pool of the three sets, and it has the highest peak concentration in $C_6H_5C_2H+C_2H_4$ pyrolysis. To determine why the addition of C_2H_4 enhances the C_6H_6 formation, ROP analysis at T_5 = 1550 K is carried out as shown in **Figure 5.78**. The C_6H_5+H recombination reaction, the ipso-addition reaction between $C_6H_5C_2H$ and H, and H-abstraction reaction from $C_6H_5C_2H$ by C_6H_5 play important roles in C_6H_6 production in all the cases. Besides, both added C_2H_x give an H atom to C_6H_5 to form C_6H_6 through $C_2H_2+C_6H_5 = C_2H+C_6H_6$ and $C_2H_4+C_6H_5 = C_2H_3+C_6H_6$ H-abstraction reactions in $C_6H_5C_2H+C_2H_2$ and $C_6H_5C_2H+C_2H_4$ pyrolysis, respectively. $C_2H_4+C_6H_5 = C_2H_3+C_6H_6$ reaction has more notable contribution as hydrogen abstraction from C_2H_4 is remarkably easier compared to the C_2H_2 case. Finally, the consumption reactions of $C_6H_5C_2H_3$, including $C_6H_5C_2H_3 = C_6H_6+H_2CC$ and $C_6H_5C_2H_3+H = C_6H_6+C_2H_3$, are significant contributors to C_6H_6 formation in $C_6H_5C_2H+C_2H_4$ pyrolysis. The former reaction is the predominant one. $C_6H_5C_2H_3$ is absent from the species pool of neat $C_6H_5C_2H$ and $C_6H_5C_2H+C_2H_2$ pyrolysis, and it is mainly formed from the reaction between C_6H_5 and C_2H_4.

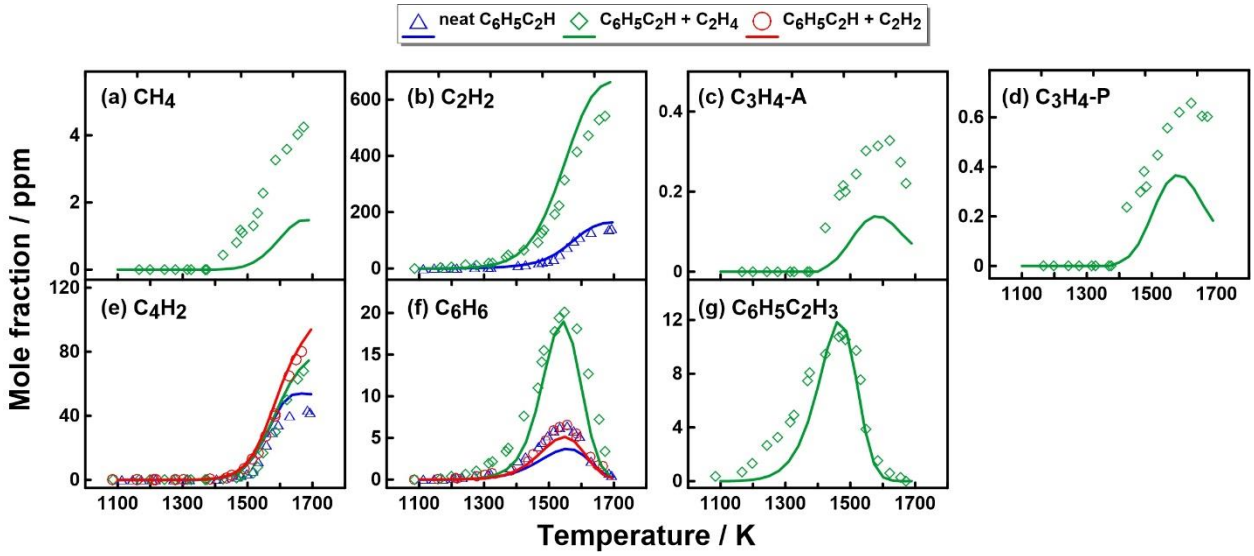

Figure 5.77: Measured (symbols) and simulated (lines) mole fractions of small molecule products as a function of T_5 from the pyrolysis of 104 ppm $C_6H_5C_2H$, 104 ppm $C_6H_5C_2H$ + 415 ppm C_2H_2 and 105 ppm $C_6H_5C_2H$ + 504 ppm C_2H_4 mixtures at the nominal P_5 of 20 bar.

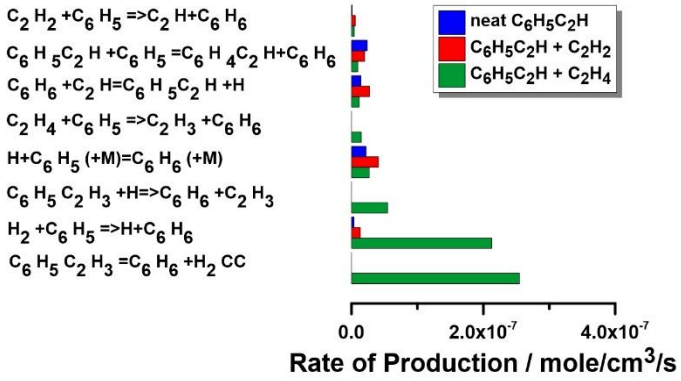

Figure 5.78: ROP analysis for C_6H_6 production at T_5 = 1550 K, P_5 = 20 bar and reaction time = 4ms in the pyrolysis of neat $C_6H_5C_2H$, $C_6H_5C_2H$+C_2H_2 and $C_6H_5C_2H$+C_2H_4.

5.4.3.2 PAH formation

Another objective of this study is to elucidate the impact of extra C_2H_x on the PAH formation pathways from $C_6H_5C_2H$ pyrolysis. The experimental and simulated mole fraction profiles of PAH species as a function of temperature are presented in **Figure 5.79** for the three investigated cases for comparison purpose. Experimental trends for the production of these aromatics are well captured by the present model. $C_{10}H_8$ begins building up at relatively low temperatures when C_2H_x fuels are added, and it has the highest peak concentration in the case of $C_6H_5C_2H$+C_2H_4 pyrolysis. The addition of C_2H_2 enhances the

peak concentration of both $C_{12}H_8$ isomers ($C_{10}H_7C_2H$ and $C_{12}H_8$) and tends to lower their onset temperature, while the addition of C_2H_4 only amplifies their peak concentration but to a lower extent compared to $C_6H_5C_2H+C_2H_2$ case. The formation temperature window for the three $C_{14}H_{10}$ isomers remains the same in the binary mixtures. However, the peak concentration of $C_6H_5CCC_6H_5$ and $C_{13}H_8CH_2$ is higher in neat $C_6H_5C_2H$ pyrolysis based on the kinetic model. Interestingly, the measured mole fractions of $C_{13}H_8CH_2$ are very similar, suggesting that further model refinements are necessary.

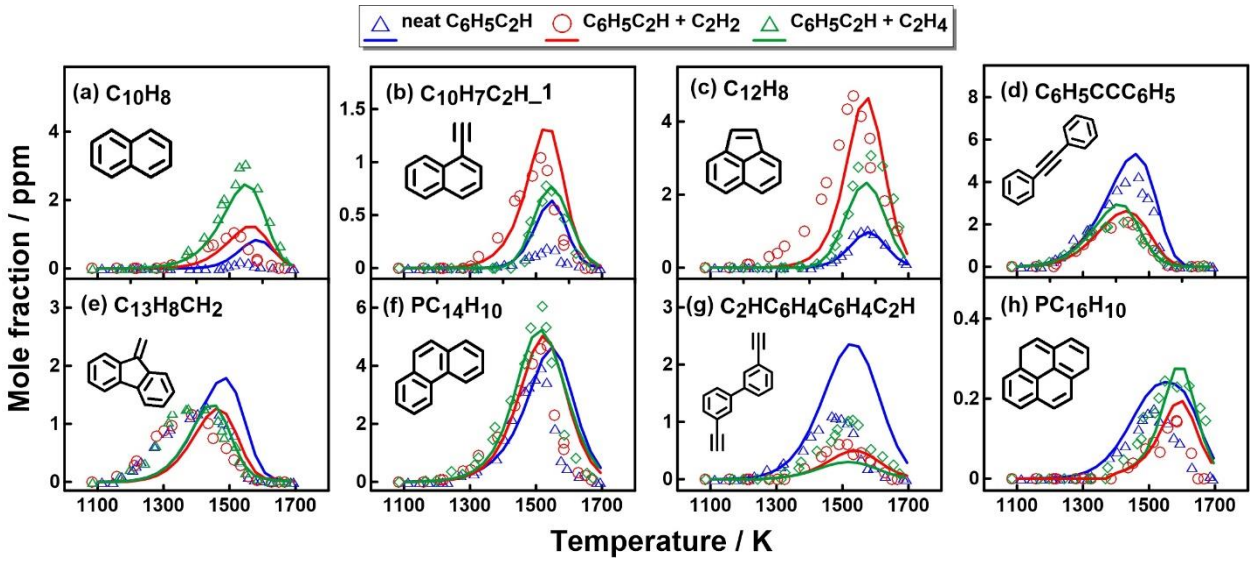

Figure 5.79: Measured (symbols) and simulated (lines) mole fractions of PAHs as a function of T_5 from the pyrolysis of 104 ppm $C_6H_5C_2H$, 104 ppm $C_6H_5C_2H$ + 415 ppm C_2H_2 and 105 ppm $C_6H_5C_2H$ + 504 ppm C_2H_4 mixtures at the nominal P_5 of 20 bar.

To provide insights on the significant influence of added C_2H_2 and C_2H_4 on $C_{10}H_8$ and $C_{12}H_8$ formation, ROP analyses for $C_{10}H_8$ and $C_{12}H_8$ at 1500 K are displayed in **Figures 5.80** and **5.81,** respectively. **Figure 5.80** shows that $C_9H_6CH_2$ isomerization and the thermal decomposition of $C_9H_6CH_3$-1and $C_9H_7CH_2$ promote the $C_{10}H_8$ formation in neat $C_6H_5C_2H$ and $C_6H_5C_2H+C_2H_2$ pyrolysis, while the bimolecular reaction between $C_{10}H_7$ radicals and H atom has less contribution due to the highly unsaturated systems. These reactions have minor contribution to $C_{10}H_8$ formation in $C_6H_5C_2H+C_2H_4$ pyrolysis. Instead in this case, the reaction between $C_6H_4C_2H$ and C_2H_4 governs the $C_{10}H_8$ formation. This pathway produces an adduct $C_6H_4(CHCH_2)(CH\dot{C}H)$ that subsequently undergoes a ring-closure step forming $C_{10}H_8$ and releasing an H atom, as mentioned in the kinetic modeling section. Besides, C_2H_4 donates H-atom to $C_{10}H_7$ to transform into $C_{10}H_8$ through the reaction $C_{10}H_7+C_2H_4$ => $C_{10}H_8+C_2H_3$. Other important reactions in $C_6H_5C_2H+C_2H_4$ system include the reactions between naphthyl radicals and H_2 and the thermal decomposition of $C_{10}H_7C_2H_3$. Two pathways contribute to $C_{12}H_8$ formation in all the three cases as shown in **Figure 5.81**: (i) BENZO re-arrangement; (ii) HACA route $C_6H_4C_2H \rightarrow C_{10}H_7$ (or

$C_9H_6CH) \rightarrow C_{12}H_8$. The former pathway has minor contribution in all the three sets. Though C_6H_6 and C_6H_5 are abundant in these reaction systems, $C_{12}H_8$ formation is prevailed by the HACA route due to the presence of C_2H_2 as a fuel or its early formation from $C_6H_5C_2H$ and C_2H_4 thermal decomposition. The existence of C_2H_2 as a fuel enables the HACA route to occur at low temperatures. This justifies the early formation of $C_{12}H_8$ in $C_6H_5C_2H+C_2H_2$ pyrolysis. $C_{10}H_7C_2H$ follows the same HACA pathway as $C_{12}H_8$ in three investigated cases.

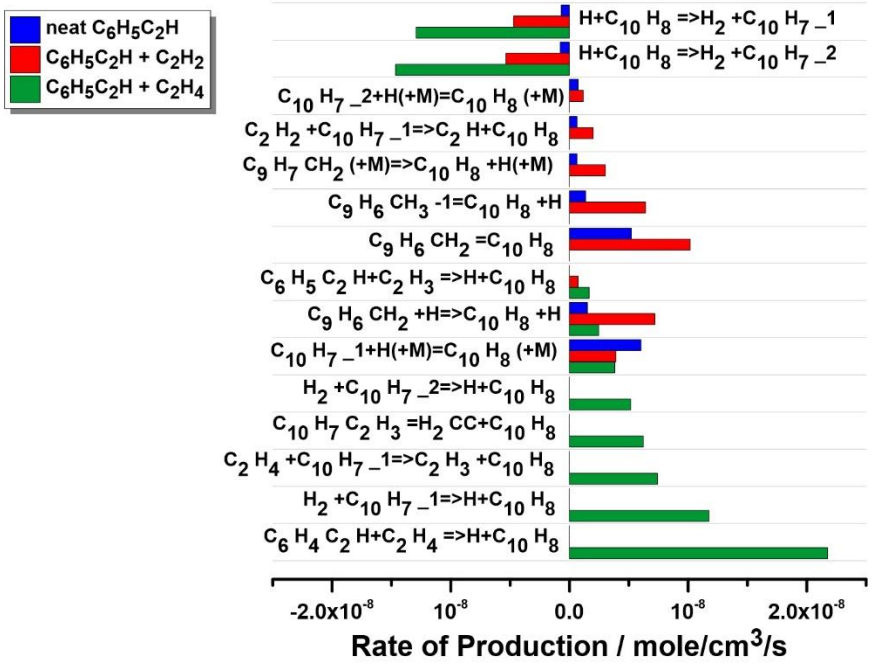

Figure 5.80: ROP analysis for $C_{10}H_8$ production at T_5 = 1500 K, P_5 = 20 bar and reaction time = 4ms in the pyrolysis of neat $C_6H_5C_2H$, $C_6H_5C_2H+C_2H_2$ and $C_6H_5C_2H+C_2H_4$.

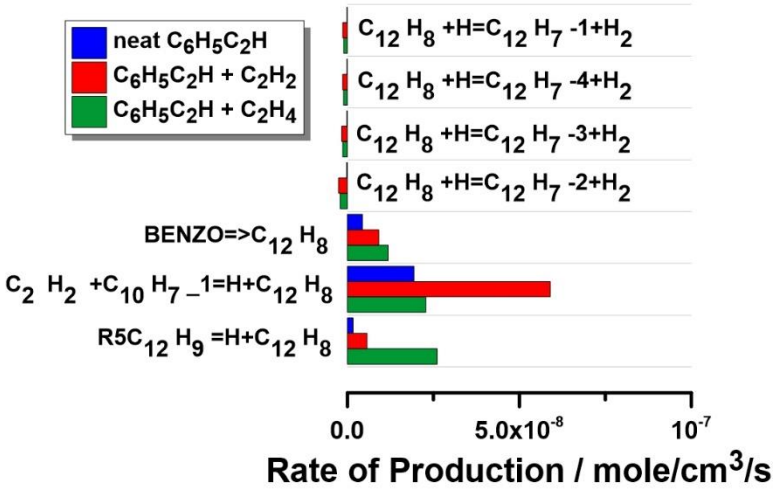

Figure 5.81: ROP analysis for $C_{12}H_8$ production at T_5 = 1500 K, P_5 = 20 bar and reaction time = 4ms in the pyrolysis of neat $C_6H_5C_2H$, $C_6H_5C_2H+C_2H_2$ and $C_6H_5C_2H+C_2H_4$.

Based on the kinetic model, the difference in $C_6H_5CCC_6H_5$ and $C_{13}H_8CH_2$ profiles among the three investigated cases corresponds to the temperature where they reach their peak concentrations in the pyrolysis of $C_6H_5C_2H/C_2H_x$, while they further increase in the case of neat $C_6H_5C_2H$. In the three investigated cases, $C_6H_5C_2H+C_6H_5 = C_6H_5CCC_6H_5+H$ and $C_6H_5C_2H+C_6H_5 = C_{13}H_8CH_2+H$ are the main formation pathways for $C_6H_5CCC_6H_5$ and $C_{13}H_8CH_2$, respectively, as shown in **Figure 5.82**. However, the difference lies in their consumption pathways. The H-assisted isomerization of both $C_6H_5CCC_6H_5$ and $C_{13}H_8CH_2$ leading to phenanthrene and the H-addition reaction to $C_6H_5CCC_6H_5$ have higher negative coefficients compared to neat $C_6H_5C_2H$ pyrolysis because of the high H-atom level in the binary reaction systems. This also partially explains the higher peak concentration of $PC_{14}H_{10}$ in binary mixtures (**Figure 5.79 f)** although the three-ring compound is mainly formed through fuel related pathways ($C_6H_5C_2H+C_6H_5$). $PC_{16}H_{10}$ (**Figure 5.79 h)** is predominantly produced by the HACA route through $C_{14}H_9+C_2H_2$ reaction in binary reaction systems differently to the case of neat $C_6H_5C_2H$ pyrolysis.

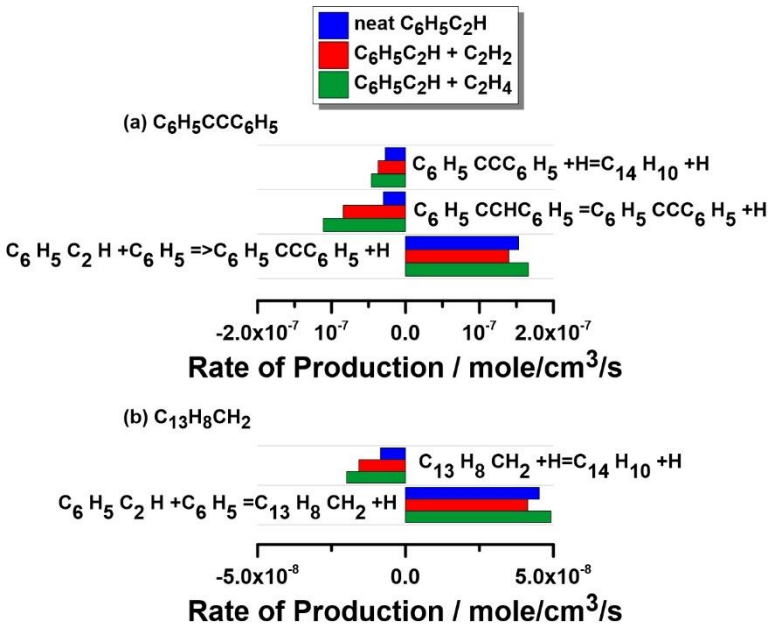

Figure 5.82: ROP analysis for (a) $C_6H_5CCC_6H_5$ and (b) $C_{13}H_8CH_2$ production at T_5 = 1400 K, P_5 = 20 bar and reaction time = 4ms in the pyrolysis of neat $C_6H_5C_2H$, $C_6H_5C_2H+C_2H_2$ and $C_6H_5C_2H+C_2H_4$.

$C_2HC_6H_4C_6H_4C_2H$ profiles show discrepancies between the experimental and the simulation results. This is mainly to the errors related to the reactions added through analogy ($C_6H_5C_2H+C_6H_4C_2H = C_2HC_6H_4C_6H_4C_2H+H$ and $C_6H_4C_2H+C_6H_4C_2H = C_2HC_6H_4C_6H_4C_2H$). Theoretical calculations are highly necessary to derive the rate coefficient for these reactions. Based on the kinetic model, $C_2HC_6H_4C_6H_4C_2H$ has lower peak concentration in the binary mixtures. It is mainly produced through $C_6H_5C_2H+C_6H_4C_2H$ reaction in the case of neat $C_6H_5C_2H$ as mentioned earlier. According to ROP analysis, this reaction is still partly responsible for $C_6H_4C_2H$ consumption in the cases of $C_6H_5C_2H+C_2H_2$ and $C_6H_5C_2H+C_2H_4$ pyrolysis. However, the $C_6H_4C_2H+C_2H_2$ reaction in both binary blends and the $C_6H_4C_2H+C_2H_4$ reaction in $C_6H_5C_2H+C_2H_4$ pyrolysis impedes the efficiency of $C_6H_5C_2H+C_6H_4C_2H$ reaction. This explains the lower concentration profile of $C_2HC_6H_4C_6H_4C_2H$ in binary reaction mixtures.

5.5 Alkylbenzenes pyrolysis

5.5.1 Motivation

Few studies focused on PAH formation from alkylbenzenes as demonstrated in literature overview, though they are indispensable components of surrogates for practical fuels (gasoline, diesel and kerosene). C_8-C_{10} linear alkylbenzenes combustion leads to high concentrations of benzyl and C_1-C_4 alkyl radicals. Thus, the three highly argon-diluted mixtures, separately consisting of 101 ppm ethylbenzene, 103 ppm *n*-propylbenzene and 102 ppm *n*-butylbenzene, provide ideal environments to inspect benzyl

fate and its interaction with small hydrocarbons, which could help significantly in the formation and growth of PAHs. Besides, through comparisons among C_7-C_{10} linear alkylbenzenes, it is possible to investigate the influence of long chain on fuel reactivity and PAH formation under combustion-like conditions.

5.5.2 Fuel decomposition and small hydrocarbon products

Figure 5.83 represents the experimental and simulated mole fraction profiles of the fuel conversion curves in C_8-C_{10} alkylbenzenes pyrolysis as a function of temperature. Good performance is observed in reproducing the fuels' reactivity by the present model. Compared to toluene, alkylbenzenes show higher reactivity and lower decomposition temperature regions. Besides, n-propylbenzene and n-butylbenzene decompose at a faster pace compared to ethylbenzene. The reaction networks of initial fuel consumption pathways in the three cases are illustrated in **schemes 5.16-5.18** based on an integrated ROP analyses, in which approximately 50% of the fuels are consumed. Alkylbenzenes' decomposition proceeds in several pathways, among which the unimolecular C-C bond dissociation and H-atom abstraction are the most favored. The benzylic C-C bond has the weakest bond dissociation energy (BDE). The BDEs of n-propylbenzene and n-butylbenzene have close values ($C_6H_5CH_2$—C_2H_5, 75.3 kcal/mole; $C_6H_5CH_2$—C_3H_7, 74.9 kcal/mole), that are slightly lower than that in ethylbenzene ($C_6H_5CH_2$—CH_3, 76.4 kcal/mole). This supports the observed decomposition trends among the three fuels. The ROP analyses also demonstrates that over 60% of alkylbenzenes decay principally via homolysis reaction producing C_7H_7. Other dissociation reactions including C-H bonds, phenylic C-C bond and alkylic C-C bond have small contributions to the consumption of alkylbenzenes. The rest is mainly consumed by the H-atom abstraction reactions by H and CH_3 and ipso-substitution reactions by H. Among the H-abstractions, those by CH_3 are the dominant ones in ethylbenzene while those by H are the governing ones in n-propylbenzene and n-butylbenzene due to the higher H contents in their species pool.

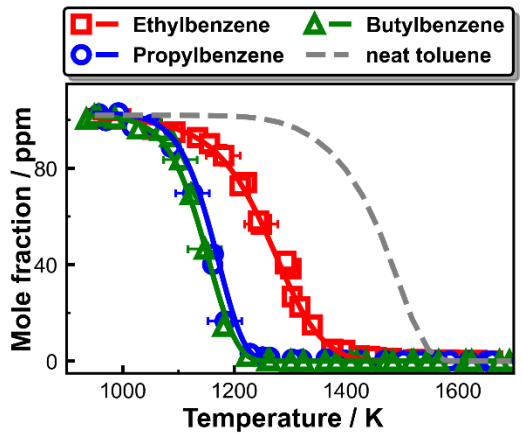

Figure 5.83: Experimental (symbols) and simulated (solid lines) fuel mole fractions as a function of T_5 in C_8–C_{10} linear alkylbenzenes pyrolysis. Simulated fuel conversion profile in 100 ppm toluene pyrolysis is shown as the dashed line for comparison purpose.

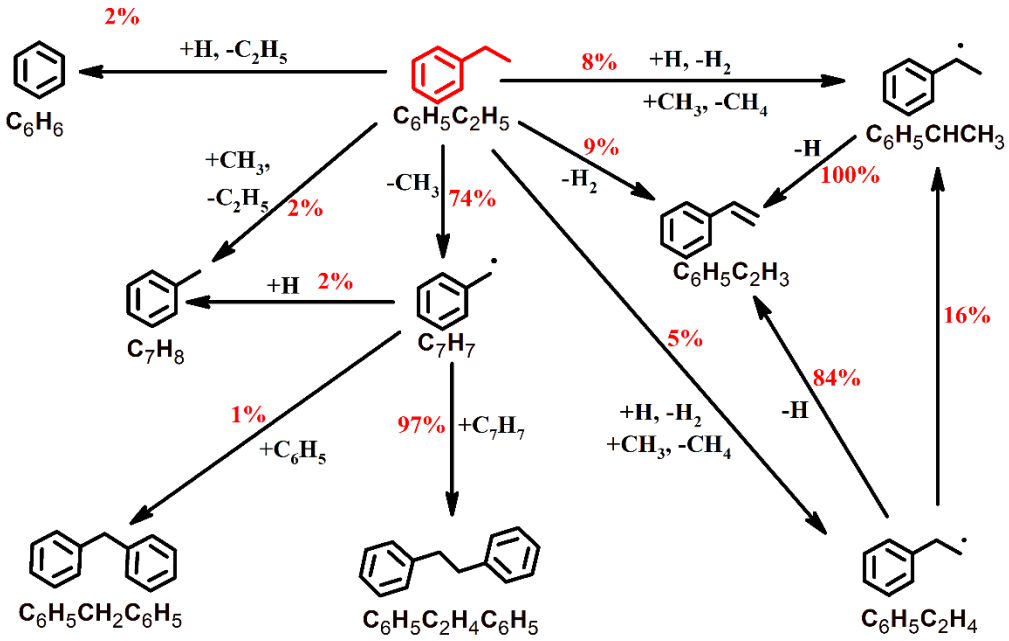

Scheme 5.15: Fuel consumption pathways in ethylbenzene pyrolysis based on integrated ROP analysis at 1250 K. The percentage numbers are the contributions by the corresponding reactions to the consumption of the species on the source side.

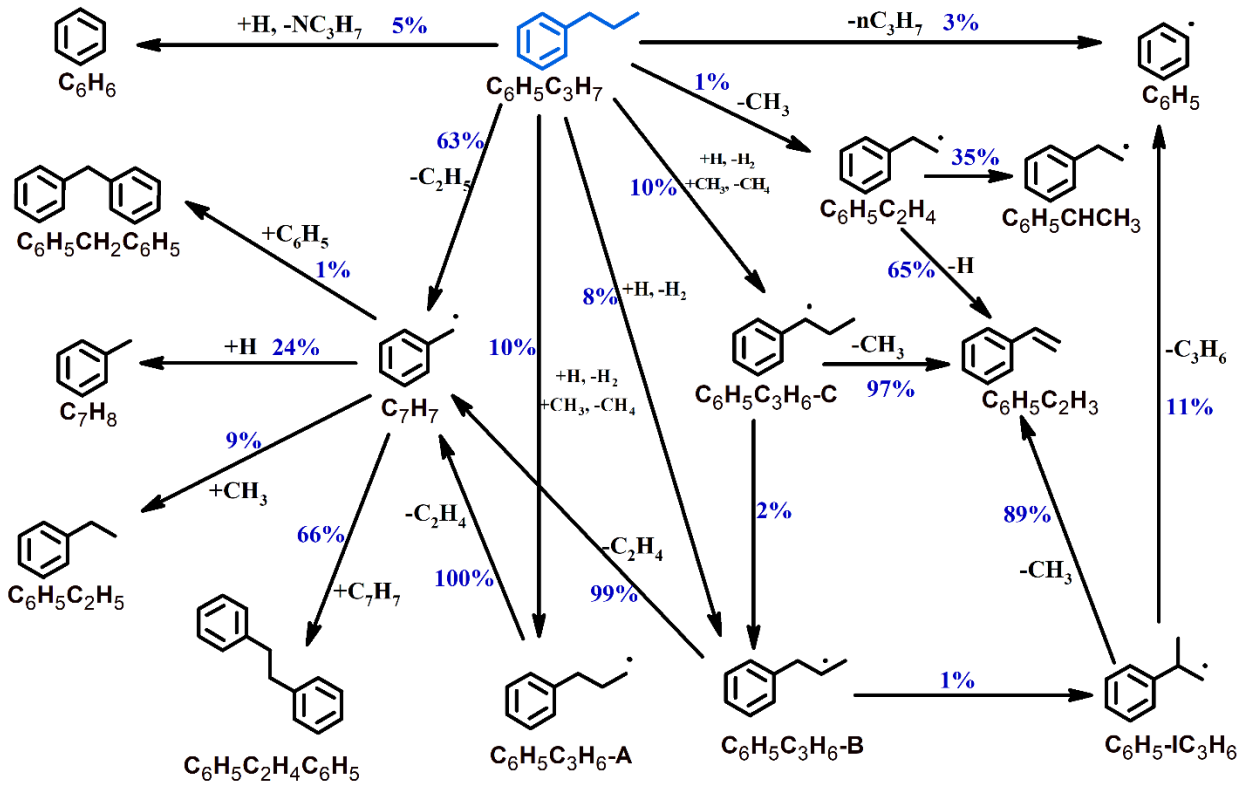

Scheme 5.16: Fuel consumption pathways in n-propylbenzene pyrolysis based on integrated ROP analysis at 1150 K. The percentage numbers are the contributions by the corresponding reactions to the consumption of the species on the source side.

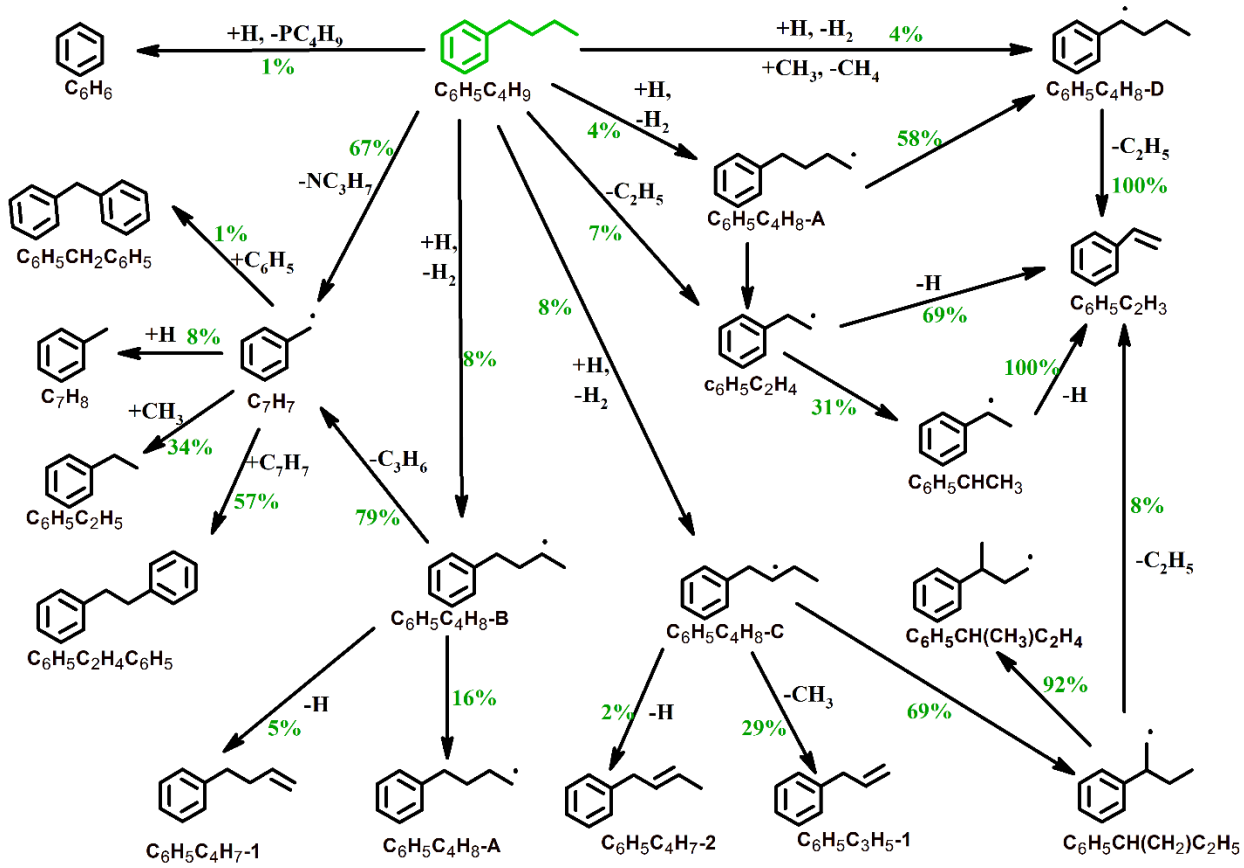

Scheme 5.17: Fuel consumption pathways in n-butylbenzene pyrolysis based on integrated ROP analysis at 1150 K. The percentage numbers are the contributions by the corresponding reactions to the consumption of the species on the source side.

Experimental and simulated mole fraction profiles of C_1–C_4 hydrocarbons during the pyrolysis of ethylbenzene, *n*-propylbenzene and *n*-butylbenzene are shown in **Figures 5.84-5.86**, respectively. The C_1–C_4 products are qualitatively the same but quantitatively different. The kinetic model can reasonably reproduce the experimental results in the separate cases. CH_4 and C_2H_6 peak mole fractions in ethylbenzene pyrolysis are similar to those in *n*-butylbenzene and higher than those in *n*-propylbenzene case. The formation of both CH_4 and C_2H_6 strongly depends on CH_3 concentration. As noted previously, the C-C bond fission leading to C_7H_7 dominates the consumption of the fuels and results in the formation of CH_3, ethyl (C_2H_5), and *n*-propyl (*n*-C_3H_7) in ethylbenzene, *n*-propylbenzene, and *n*-butylbenzene pyrolysis, respectively. C_2H_5 is mainly consumed through $C_2H_5 \rightarrow C_2H_4+H$ reaction and moderately via $C_2H_5+H = 2CH_3$ reaction, which cause the low production of the CH_3 radical. *N*-C_3H_7 easily decomposes to C_2H_4 and CH_3 radical by the C–C *b*-scission reactions, which lead to the large production of the CH_3 radical. C_2H_4 has similar concentration profile in the pyrolysis of *n*-propylbenzene and *n*-butylbenzene, while it has lower peak mole fraction and higher formation temperature window in ethylbenzene pyrolysis. In the pyrolysis of *n*-propylbenzene and *n*-butylbenzene, C_2H_4 is directly produced from the

decomposition of C_2H_5 and *n*-C_3H_7 through $C_2H_5 \rightarrow C_2H_4+H$ and *n*-$C_3H_7 \rightarrow CH_3+C_2H_4$, respectively. In ethylbenzene pyrolysis, C_2H_4 is formed mainly from C_2H_5 unimolecular decomposition; C_2H_5 is the result of the ipso-substitution reaction by H, whose importance is quite minor compared to the dominant C_7H_7 producing channel (see **scheme 5.16**). Other minor pathways contribute to C_2H_4 formation in the three separate cases namely, the consumption of styrene and C_2H_6. C_3H_6 has different formation pathways in the three reaction systems. In ethylbenzene pyrolysis, C_3H_6 is mainly produced from the inefficient addition-elimination channel $C_2H_4+CH_3 \rightarrow C_3H_6+H$. In *n*-propylbenzene pyrolysis, C_3H_6 mainly comes from the consumption of the fuel radical $C_6H_5C_3H_6$-B which has limited carbon flux. In the pyrolysis of *n*-butylbenzene, C_3H_6 is largely formed from the decomposition of the fuel radical $C_6H_5C_4H_8$-B as well as the abundant *n*-C_3H_7. In all the three cases, the consumption of C_3H_6 leads primarily to the formation of C_3H_4-A which further isomerizes to C_3H_4-P. C_2H_2 and C_4H_2 concentrations increase with the fuel molecular sizes, as they related to the carbon content in the reaction system.

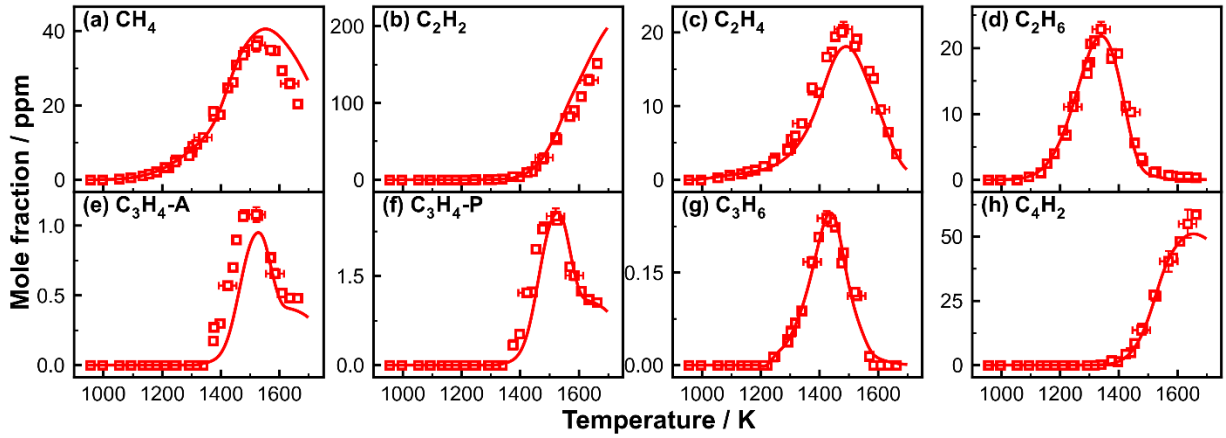

Figure 5.84: Experimental (symbols) and simulated (lines) mole fractions of small hydrocarbon products as a function of T_5 in ethylbenzene pyrolysis.

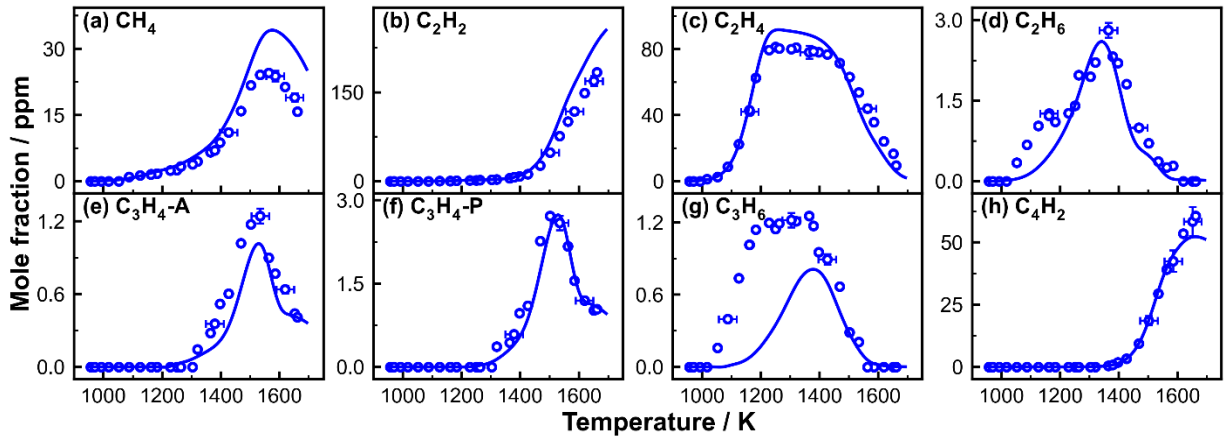

Figure 5.85: Experimental (symbols) and simulated (lines) mole fractions of small hydrocarbon products as a function of T_5 in n-propylbenzene pyrolysis.

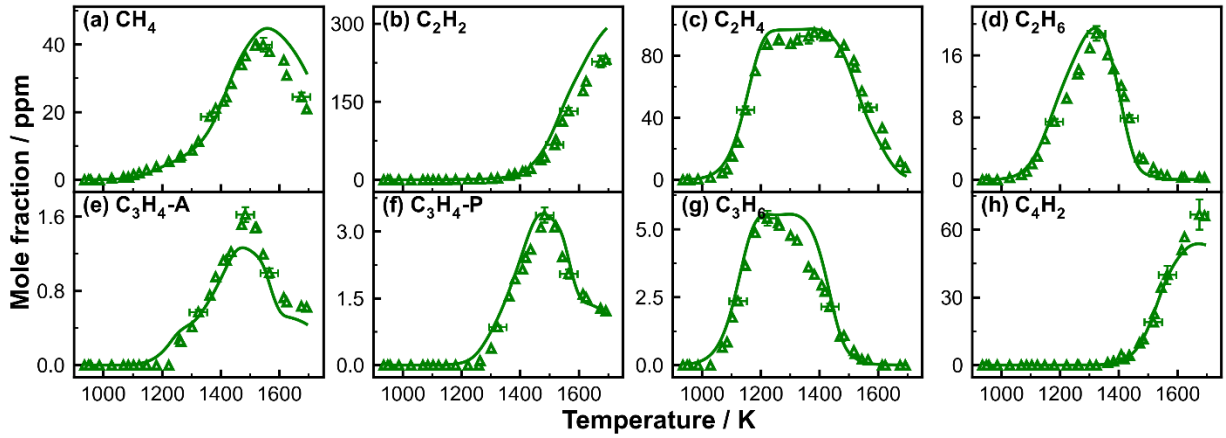

Figure 5.86: Experimental (symbols) and simulated (lines) concentrations of small hydrocarbon products as a function of T_5 in n-butylbenzene pyrolysis.

5.5.3 The formation of MAH species

Figure 5.87 presents the experimental and simulated mole fraction profiles of MAH products in the pyrolysis of C_8-C_{10} linear alkylbenzenes as well as that of neat toluene for comparison purpose. C_6H_6, C_7H_8, $C_6H_5C_2H_3$ and $C_6H_5C_2H$ are common products in the pyrolysis of the three fuels. $C_6H_5C_2H_5$ is present in the species pool of both *n*-propylbenzene and *n*-butylbenzene, while $C_6H_5C_3H_5$-1 is only detected in *n*-butylbenzene pyrolysis.

Benzyl radical is a significant intermediate in the C_8-C_{10} alkylbenzenes pyrolysis according to the ROP analysis (**schemes 5.16-518**). Benzyl radical can easily convert to toluene and ethylbenzene by

recombining with an H atom and a methyl radical, which are also the exclusive formation pathways of toluene and ethylbenzene, respectively. C_7H_8 has the highest mole fractions in n-propylbenzene pyrolysis throughout the temperature range (**Figure 5.87 (b)**), while $C_6H_5C_2H_5$ has the maximum peak mole fraction in n-butylbenzene pyrolysis (**Figure 5.87 (d)**). This derives from the fact that the consumption of *n*-propylbenzene and *n*-butylbenzene result in large quantities of C_2H_5 and *n*-C_3H_7 radicals which subsequently decompose and release H and CH_3 radicals through the reactions $C_2H_5(+M) = C_2H_4+H(+M)$ and *n*-$C_3H_7 \rightarrow CH_3+C_2H_4$, respectively. C_6H_6 mole fractions are the highest in the pyrolysis of *n*-propylbenzene, followed by *n*-butylbenzene, and then ethylbenzene (**Figure 5.87 (a)**). Besides, both the experimental and simulated results show that benzene has a two-stage formation process. To interpret this phenomena, ROP analyses are performed at relatively low and high temperatures. At low temperatures, C_6H_6 formation is governed by the ipso substitution reactions between the fuel and H atom. In *n*-propylbenzene and *n*-butylbenzene pyrolysis, the ipso substitution reactions of smaller alkylbenzenes with H atoms, *i.e.* $H + C_7H_8 = C_6H_6+CH_3$ and $H + C_6H_5C_2H_5 = C_6H_6+C_2H_5$, are also important C_6H_6 sources in low-temperature region, and the relative importance of these two reactions is associated with the concentrations of C_7H_8 and $C_6H_5C_2H_5$. In all the three cases, styrene unimolecular decomposition and the ipso-substitution reactions of toluene and styrene prevail the formation of benzene at high temperatures.

Styrene is observed as an important initial pyrolysis product of C_8–C_{10} linear alkylbenzenes, as its formation initiates at relatively low temperatures compared to other MAH species (**Figure 5.87 (c)**). Styrene exhibits similar peak mole fraction in C_8–C_{10} linear alkylbenzenes pyrolysis, though the temperature-dependent profiles are distinct in the three cases. Styrene profile has two-stage decomposition and formation process in *n*-propylbenzene and *n*-butylbenzene pyrolysis, respectively; however, it shows a continuous profile with a relatively late peak in ethylbenzene pyrolysis. In ethylbenzene pyrolysis, styrene mainly comes from the decomposition of phenylethyl radicals ($C_6H_5\dot{C}HCH_3$ and $C_6H_5CH_2\dot{C}H_2$) throughout the temperature window. In the first stage in *n*-propylbenzene and *n*-butylbenzene pyrolysis, $C_6H_5C_2H_3$ arises from the decomposition of fuel radicals $C_6H_5\dot{C}HCH_2CH_3$ ($C_6H_5C_3H_6$-C) and $C_6H_5\dot{C}HCH_2CH_2CH_3$ ($C_6H_5C_4H_8$-D), respectively, as shown in **schemes 5.17 and 5.18**. In the second stage, the consumption of phenylethyl radicals dominate the formation of styrene which explains the remarkable contrary behavior. Thus, the higher production of phenylethyl radicals in *n*-butylbenzene gives rise to a second concentration increase, and the lower production of phenylethyl radicals in *n*-propylbenzene causes a two-stage decrease. Over-prediction by the model of styrene mole fractions, in particular at temperatures where the 2nd peak is present, suggests the need of a better comprehension of the phenylethyl radicals' formation and decomposition. $C_6H_5C_2H$ has the same mole fraction profile in all the three sets, which implies that its formation is not influenced

by the fuel chemistry. $C_6H_5C_2H$ is mainly formed through C_6H_6/ C_6H_5+ C_2H/C_2H_2 recombination reaction. The consumption of styryl radicals ($C_6H_5\dot{C}CH_2$ and $C_6H_5CH\dot{C}H$) contribute to $C_6H_5C_2H$ formation at relatively low temperatures, which explains the lower formation temperature window in C_8–C_{10} alkylbenzenes pyrolysis compared to that of toluene pyrolysis. $C_6H_5C_3H_5$-1, a secondary decomposition product of *n*-butylbenzene (**Figure 5.87 (f)**), is largely formed through -C-C scission reaction of $C_6H_5C_4H_8$-C radical.

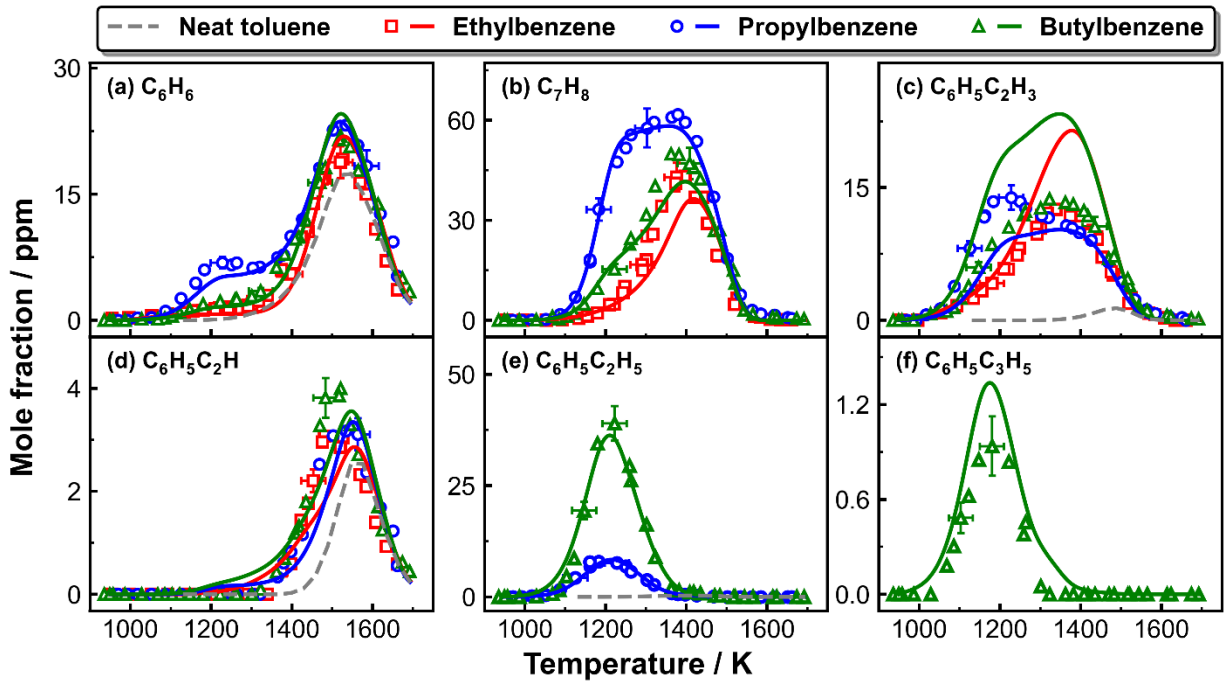

Figure 5.87: Experimental (symbols) and simulated (lines) mole fractions of MAH products as a function of T_5 in C_8–C_{10} linear alkylbenzenes pyrolysis. Simulated speciation profiles in 100 ppm toluene pyrolysis are shown as dashed lines for comparison purpose.

5.5.4 The formation of PAH species

A major goal of this study is to reveal the influence of the fuel molecular structure on PAHs formation pathways through comparison among C_8–C_{10} alkylbenzenes pyrolysis and neat toluene pyrolysis under similar conditions. Experimental and simulated mole fraction profiles of bicyclic and tricyclic PAHs formed during C_8–C_{10} linear alkylbenzenes pyrolysis are presented in **Figure 5.88**. In general, the current model can predict the experimental mole fraction distributions of these large aromatics.

The relatively low pyrolysis temperatures of alkylbenzenes compared to toluene not only reduce C_7H_7 dissociation or reaction with highly unsaturated C_2 and C_3 species but also promote its combination reactions with aromatic radicals. In consequence, bibenzyl is found to be the most abundantly produced

PAH with much higher concentrations compared to neat toluene pyrolysis (see **Figure 5.88 (e)**). It exclusively originates from C_7H_7 self-recombination. The model under-estimates the $C_6H_5C_2H_4C_6H_5$ mole fractions, though it can reproduce its profile. As mentioned previously, reactions involving resonantly stabilized radicals carry on during the quenching period. Hence, simulations with measured profiles represent more the experimental results and can better capture $C_6H_5C_2H_4C_6H_5$ measurements in all the three cases; the results are shown in **Figures 5.89-5.91** as well as for the other pyrolytic products. For other species, the simulation method does not obviously affect the modeling mole fraction profiles, except for a slight increase in C_9H_8 and $C_{12}H_8$ peak mole fractions. This is related to the moderate continuation of C_7+C_2 and C_9+C_3 reactions during the quenching period. In addition to the self-recombination, benzyl radical also undergo the recombination reaction with the phenyl radical, which predominantly leads to diphenylmethane (**Figure 5.88 (d)**). It is noteworthy that the speciation windows of bibenzyl and diphenylmethane overlap with those of the fuel decomposition in each case, which supports the observation that these compounds are formed by reactions involving primary fuel decomposition products. The step-wise H-loss reaction sequence of $C_6H_5CH_2C_6H_5$ controls fluorene formation (**Figure 5.88 (f)**).

Indene (**Figure 5.88 (a)**) starts forming at low temperatures in C_8–C_{10} linear alkylbenzenes pyrolysis compared to neat toluene pyrolysis. At low temperatures, indene is mainly produced from dehydrogenation of indane, which is exclusively formed from $C_7H_7+C_2H_4$ reaction that has more significant contribution in *n*-propylbenzene and *n*-butylbenzene pyrolysis due to the higher abundance of C_2H_4. Cyclization of phenylallyl radical is an additional minor indene formation pathway in *n*-propylbenzene and *n*-butylbenzene pyrolysis. In both cases, phenylallyl radical results from the consumption of allylbenzene ($C_6H_5C_3H_5$–1). $C_6H_5C_3H_5$–1 derives from the decomposition of the fuel radical $C_6H_5C_4H_8$-C in *n*-butylbenzene pyrolysis and is produced from the C-H *ß*-scission reaction of $C_6H_5C_3H_6$-B in *n*-propylbenzene case. Since, the C-H *ß*-scission reaction is less favorable compared to C-C *ß*-scission reaction, the phenylallyl radical cyclization path is more significant in *n*-butylbenzene pyrolysis. However, at high temperatures, indene is dominantly formed through $C_7H_7+C_2H_2$ reaction in all the three cases.

The long side-chain in alkylbenzenes has no influence on the speciation windows and the peak concentrations of naphthalene (**Figure 5.88 (b)**) and acenaphthylene (**Figure 5.88 (c)**), as they are concurrent with neat-toluene results. In all the cases, the formation of naphthalene is governed by $C_7H_5+C_3H_3$ recombination reaction, $C_9H_6CH_2$ isomerization originated from $C_9H_7+CH_3$ pathway, and the ring-arrangement fragmentation of $C_9H_7CH_2$ that is formed through $C_7H_7+C_3H_3$ and $C_9H_7+CH_3$ reactions.

$C_{12}H_8$ is produced primarily through C_9H_7+C_3H_3 reaction and secondarily through $C_{10}H_7$+C_2H_2 HACA route in the pyrolysis of all the fuels.

For $C_{14}H_{10}$ PAHs, $C_{13}H_8CH_2$ (**Figure 5.88 (g)**) predominantly comes from 1,1-diphenylethylene ($C_6H_5C(CH_2)C_6H_5$) decomposition, which is formed through $C_6H_5C_2H_3$+C_6H_5 relative to the abundant styrene production in alkylbenzenes. The other channels, $C_6H_5C_2H$+C_6H_5 and C_7H_5+C_3H_3, minimally contribute to $C_{13}H_8CH_2$ formation. Differently, $PC_{14}H_{10}$ (**Figure 5.88 (h)**) mainly arises from the dehydrogenation of bibenzyl, the conventional pathway in toluene pyrolysis. It is noteworthy that $PC_{14}H_{10}$ profiles follow the same trend as that of bibenzyl in all the three fuels. Other minor pathways include C_7H_7+C_7H_5 bimolecular reaction, H-assisted isomerization of $C_{13}H_8CH_2$ and $C_6H_5CCC_6H_5$, and $C_6H_5C_2H$+C_6H_5 reaction.

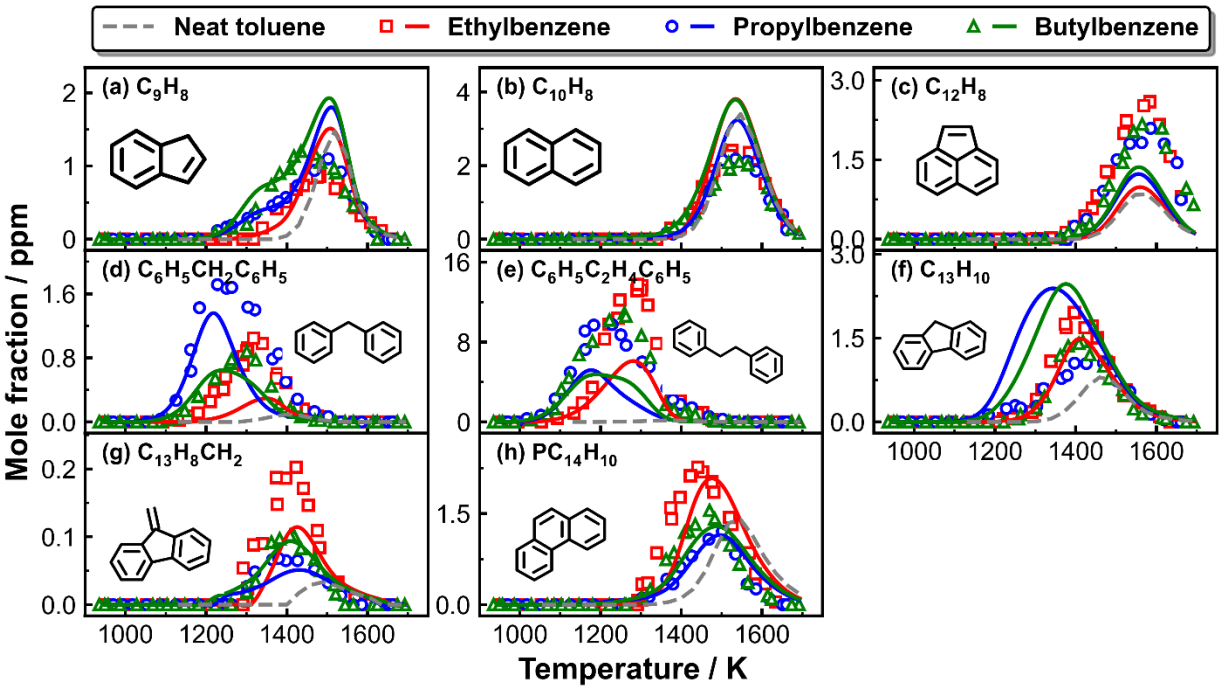

Figure 5.88: Experimental (symbols) and simulated (lines) mole fractions of PAH products as a function of T_5 in C_8–C_{10} linear alkylbenzenes pyrolysis. Simulated speciation profiles in 100 ppm toluene pyrolysis are shown as dashed lines for comparison purpose.

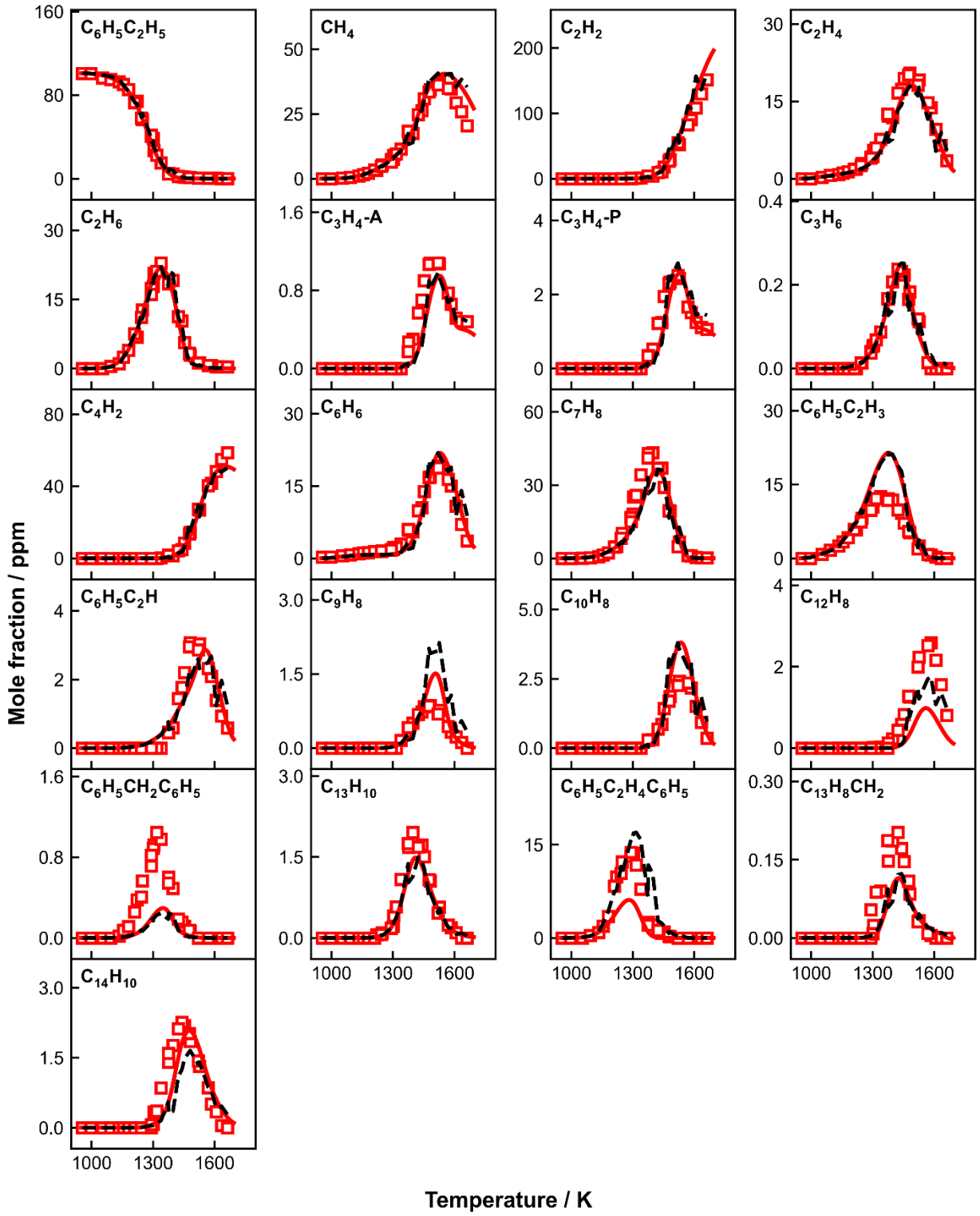

Figure 5.89: Species mole fractions as a function of T_5 in ethylbenzene pyrolysis. Symbols: measurements; solid lines: modeling results at constant 20 bar within a fixed reaction time of 4.0 ms; dashed lines: simulations with measured pressure profiles up to a time scale of 10 ms.

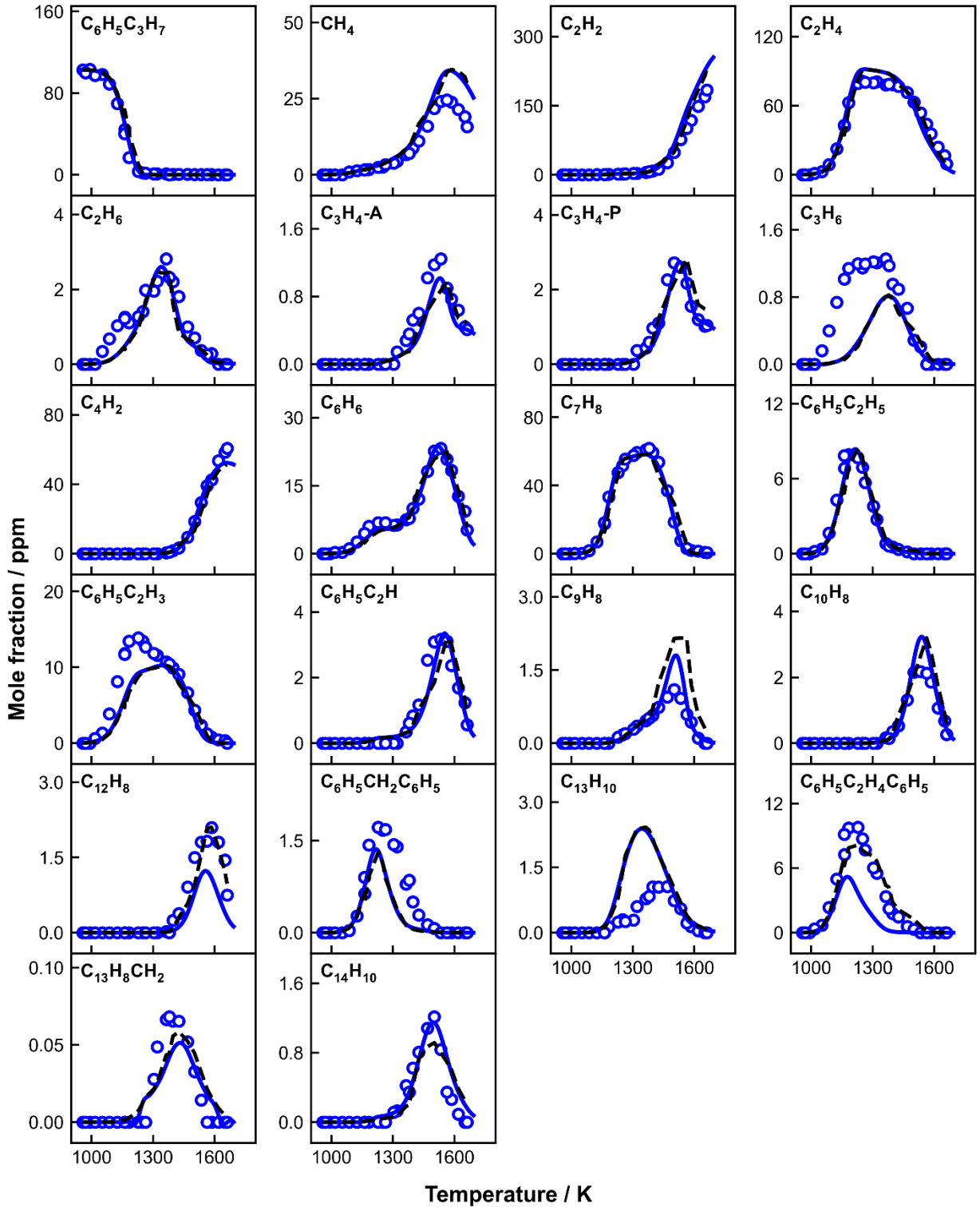

Figure 5.90: Species mole fractions as a function of T_5 in *n*-propylbenzene pyrolysis. Symbols: measurements; solid lines: modeling results at constant 20 bar within a fixed reaction time of 4.0 ms; dashed lines: simulations with measured pressure profiles up to a time scale of 10 ms.

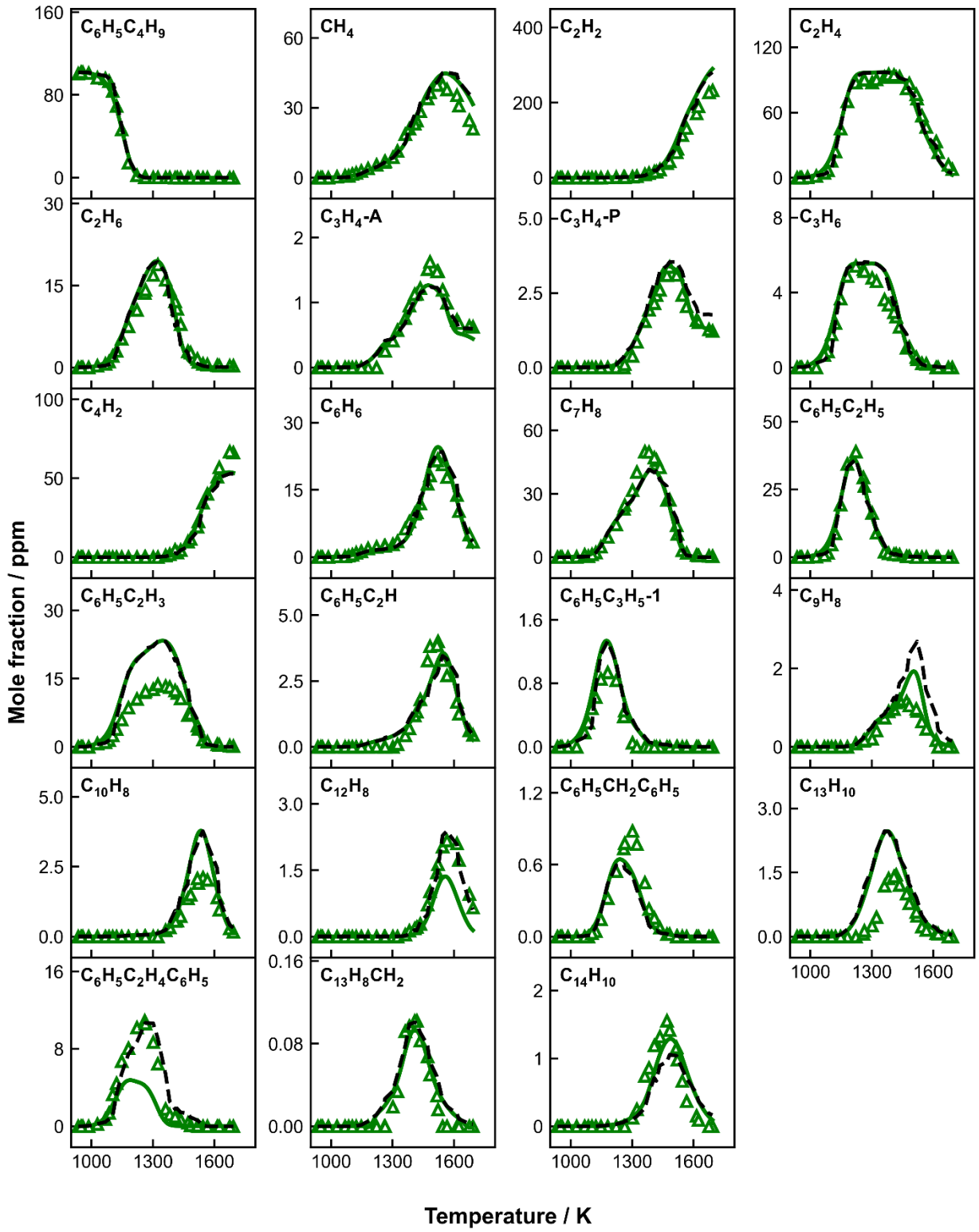

Figure 5.91: Species mole fractions as a function of T_5 in *n*-butylbenzene pyrolysis. Symbols: measurements; solid lines: modeling results at constant 20 bar within a fixed reaction time of 4.0 ms; dashed lines: simulations with measured pressure profiles up to a time scale of 10 ms.

6 Conclusion

PAHs formation has been always an interesting topic for combustion researchers as they are considered the most important precursors of soot, a combustion-generated pollutant known to be harmful to both human health and environment. Understanding PAH formation helps developing predictive kinetic models that are vastly used in designing clean combustion technologies. Therefore, the experimental and modeling investigations on PAH formation kinetics from different hydrocarbon fuel components and mixtures are of great importance for a large number of industrial applications, from transportation and energy conversion to fuel reformulation.

In this work, pyrolysis experiments of different hydrocarbon fuels including propylene, propyne, benzene, toluene, phenylacetylene, C_8–C_{10} linear alkylbenzenes, and fuel mixtures with C_2/C_3 unsaturated hydrocarbons are carried out using a single-pulse shock tube over a temperature range of 950-1800 K for a nominal pressure of 20 bar and a reaction time of around 4 ms. Chemical compositions of the post shock mixtures are sampled and analyzed using the GC/MS techniques. Species mole fraction profiles as a function of T_5 are obtained. First, the experimental method is validated using a well-known fuel like n-heptane, for which chemical kinetic models have been developed for decades now. N-Heptane pyrolysis test experiments are executed and the good agreement between the measurements and the simulations proves the reliability of the current experimental set-up to be employed for the goal of this thesis. The latest CRECK model is used as a starting point to develop a comprehensive kinetic model emphasizing on PAH formation. A number of reactions are updated and added based on recent theoretical studies, and possible formation and decomposition reaction pathways are proposed based on experimental observations. In general, the kinetic model can satisfactorily reproduce the fuel decomposition and the species measurements ranging from acyclic small hydrocarbons to PAHs in all the individual reaction systems. Details about the single fuels are summarized below. Simulations are performed using the homogenous reactor module in COSILAB software. Two different simulation methods are employed: (i) Constant pressure (P_5) of 20 bar and a nominal reaction time of 4 ms; (ii) Measured pressure profiles up to 10 ms together with the measured T_5 and residence time. The latter method is more accurate when reactions involve resonantly stabilized radicals, as these reactions can carry on during the quenching period. By performing ROP and sensitivity analyses, reaction networks for fuel consumption and aromatic growth are highlighted for the investigated cases.

Among the main fuel decomposition products, C_3 unsaturated hydrocarbons appear as major pyrolytic intermediates. The study on C_3 fuels is conducted with around 500 ppm of propylene and propyne in argon as initial reactant. Propylene and propyne have distinct decomposition profile. Propylene follows a

smooth curve, while propyne exhibits two-stage decay profile. Propylene is mainly consumed through the chemically activated reaction $H+C_3H_6=CH_3+C_2H_4$ throughout the temperature range. In the first stage, the isomerization to allene governs propyne consumption, while in second stage, the reaction $H+C_3H_4$-$P=CH_3+C_2H_2$ becomes the predominant decomposition pathway of propyne. Propyne is among the propylene decomposition products, and thus all the pyrolysis products produced by propyne experiments are also present in propylene species pool. On the other hand, propylene pyrolysis results in a variety of small hydrocarbons and lower contents of aromatics compared to propyne pyrolysis. The aromatics contents strongly depend on the formation of the first aromatic ring benzene that accounts largely on propargyl self-recombination reaction. Dissociation of propyne induces more propargyl radicals and thus more benzene. However, modeling analyses show that reaction pathways responsible for PAH formation are similar in propylene and propyne pyrolysis. Indene is formed through C_6+C_3 reactions. The subsequent interactions of indenyl with methyl and propargyl lead to the formation of the most abundant PAH species naphthalene and acenaphthylene, respectively. Naphthyl radicals further participate in the production of larger aromatics including methylnaphthalene, ethynyl-naphthalene, fluorene, and phenyl-naphthalene. Besides, the MAC mechanism plays an important role in PAH growth through direct or H-assisted isomerization reactions as noted in fulvene$\rightarrow C_6H_6$, $C_9H_6CH_2\rightarrow C_{10}H_8$ and $C_{13}H_8CH_2\rightarrow PC_{14}H_{10}$.

Following the thermal fuel breakdown, the path towards the soot particles continues with the formation of the first aromatic ring, benzene. Benzene is here studied as a single fuel (100 and 200 ppm in argon) and with addition of around 500 ppm of the typical C_2/C_3 hydrocarbons available in all combustion environments. Benzene is mainly consumed through $H+C_6H_6=H_2+C_6H_5$ reaction in all the investigated systems constituting benzene in the initial mixture. Strong interactions are noted between phenyl and C_2 fuels, particularly acetylene, through $C_6H_5+ C_2H_x= C_6H_5C_2H_{x-1} +H$ (x=2, 4) reactions. Direct evidences of such interactions include the enhanced decomposition reactivity of both fuel components due to the abundant H atoms resulted from $C_6H_5+C_2H_x$ (x=2, 4) reactions, and the remarkable formation of C_8 MAHs. In benzene-C_3 co-pyrolysis, the levels of C_1-C_3 species are higher compared to neat benzene pyrolysis. This provokes benzene formation through propargyl self-recombination reactions in the low temperature region, and propyne has more pronounced effects. Among the small hydrocarbons added to the initial mixture, only the profile of acetylene is significantly affected by the presence of benzene. Concerning the single-ring aromatic products, the presence of acetylene in the initial mixture or as a product of the thermal decomposition of ethylene or the C_3 fuels results, at different extents, in the formation of large mole fractions of phenylacetylene compared to the pure benzene case through the $C_6H_5+C_2H_2$ reaction. Phenylacetylene has a central role in the formation of large PAHs. For similar reasons, the concentrations of diethynyl benzene are higher in the binary mixtures compared to the benzene case. Styrene is one of the main products in the benzene + ethylene and benzene + propylene

case, through the reactions $C_6H_5+C_2H_4$ and $C_6H_6+C_2H_3$, while it is produced in smaller amounts in the benzene + propyne co-pyrolysis. The presence of the C_3 fuels also promotes the formation of toluene and other alkylated aromatic hydrocarbons. The chemistry of the PAH products is strongly affected by the reactions involving the added unsaturated hydrocarbons. In particular, the central role of the reactions involving C_3 intermediates and the single ring in the formation of indene has been experimentally confirmed and validated for the first time. In the benzene + C_3 co-pyrolysis, the indenyl radical is also important for the formation of methyl indene and benzofulvene, which are fundamental precursors of naphthalene, and acenaphthylene. These pathways complement the conventional HACA routes. Indeed, naphthalene and acenaphthylene formation is highly enhanced when C_3 fuels are considered compared to benzene + ethylene co-pyrolysis and benzene + acetylene co-pyrolysis. In the benzene + C_2 cases, the HACA routes are the main sources of naphthalene although the low H-atom concentrations inhibits the $C_{10}H_7$ + H reaction. Regarding acenaphthylene, in the benzene + acetylene co-pyrolysis the HACA route and the thermal decomposition / isomerization of biphenyl play a major role, while for benzene + ethylene co-pyrolysis, an additional route through the reaction $C_{10}H_7 + C_2H_4$ is accessible. The abundance of C_2H_2 in the reaction system of the binary fuels results in numerous compounds with ethynyl branches such as ethynyl naphthalene, diethynyl naphthalene, ethynyl acenaphthylene, and ethynyl biphenyl. On the other hand, the reactions of $C_{10}H_7$ radicals with CH_3 and C_3 species in benzene-C_3 co-pyrolysis lead to the formation of methyl naphthalene and enhance the production of fluorene, respectively. Finally, the formation pathways to the C_{14} products are similar for all cases, although significantly enhanced by the presence higher phenylacetylene concentrations in the cases of binary mixtures.

Another fundamental intermediate for PAH growth as well as a major component of real fuels and surrogated is toluene. As for the case of benzene, toluene is here studied as a single component (100 and 200 ppm) and in addition with C_2/C_3 hydrocarbons. Toluene is mainly consumed through H-abstraction reaction producing benzyl radical. In all the binary mixtures, improved C_7H_8 decomposition reactivity is attained due to the great quantity of H-atoms produced from $C_7H_7+C_2H_x$ reactions and abundant CH_3 radicals generated from propylene and propyne consumption in toluene-C_2 and toluene-C_3 co-pyrolysis, respectively. Toluene presence enhances C_2H_x consumption rates which demonstrates a synergistic effect between the fuel components. In contrast, C_7H_8 existence has no impact on C_3 fuels' conversion rates. The addition of C_3 fuels promotes benzene formation mainly through propargyl self-recombination reaction, while the addition of C_2 fuels has almost no impact on benzene concentration. C_9 aromatics are largely observed in the species pool of binary mixtures, and indene is the dominant C_9 species. Indeed, the reaction through indenyl + acetylene has been studied in the past as a main route for indene formation, and this route, including the related kinetic parameters, has been confirmed and validated in this study with a concentration-dependent investigation of the toluene (100 ppm) + acetylene (~50 to ~500 ppm)

system. The formation of indene through $C_7H_7+C_2H_2$ reaction is more efficient than the corresponding C_6+C_3 reactions. On the other hand, the trace amounts of indane in the toluene + ethylene co-pyrolysis indicate that the interaction between benzyl and ethylene is weaker than that of benzyl + acetylene. It is worth mentioning that the reaction pathways responsible for PAH formation in neat toluene pyrolysis and toluene-C_2/C_3 co-pyrolysis are the same. PAHs whose formation depends on reactions involving C_1-C_3 species and indenyl radical have higher mole fractions in binary systems, and such PAHs include methylene indene, methyl indene, naphthalene, acenaphthylene, and vinyl naphthalene. In particular, naphthalene and acenaphthylene are the major ones and they will be briefly analyzed here. The addition of C_3 fuels has more pronounced effects on naphthalene formation compared to C_2 fuels. Naphthalene is mainly formed through $C_7H_7+C_3H_3$ and $C_9H_7+CH_3$ reactions in all the toluene-studied cases. The abundant production of all the mentioned precursors and the additional pathway through $C_7H_7+C_3H_4$-P/C_3H_4-A in toluene-C_3 co-pyrolysis result in this sharp increase in naphthalene formation, and especially in toluene-propyne co-pyrolysis. The enhanced formation of C_{10} species is a direct evidence about the efficiency of the interactions between toluene and C_3 fuels. Acenaphthylene formation through $C_9H_7+C_3H_3$ is facilitated in all binary mixtures and mostly in toluene-propyne pyrolysis due to the enhanced production of both precursors. Increasing trends are also observed in the peak concentrations of the PAHs who account on naphthyl radicals and C_1-C_2 species as precursors, including methylnaphthalene and ethynylnaphthalene. The level of C_7 radicals are reduced because of their reactions with C_1−C_3 species. Hence, the PAHs that largely rely on C_7 reactions, namely bibenzyl, diphenylmethane, fluorene, and the three-ring aromatics phenanthrene and anthracene, have lower peak mole fractions in binary mixtures.

One of the main pathways for the appearance and growth of PAHs and particles is the HACA mechanism. Phenylacetylene is the product of the first acetylene addition to the single-ring structure, thus it constitutes the base for the appearance of the second ring. Phenylacetylene is studied as single component (~100 ppm in argon) and with added C2 intermediates (around 500 ppm) in order to investigate the subsequent C_2H_2 additions as for the HACA route. Phenylacetylene decomposition starts by C-H bond fission from the aromatic ring. Subsequently, the bimolecular reaction $C_6H_5C_2H+H = C_6H_5+C_2H_2$ dominates the $C_6H_5C_2H$ consumption throughout the whole temperature range. The addition-elimination reactions between phenylacetylene and phenyl maintain the reactivity of the fuel decay by producing H atoms and directly contribute to the formation of several $C_{14}H_{10}$ PAH isomers including diphenylacetylene, 9-methylene-fluorene, and phenanthrene. Likewise, the combination reaction $C_6H_5C_2H+C_6H_4C_2H$ sustains the fuel reactivity by producing $C_{16}H_{10}$ species ($C_2HC_6H_4C_6H_4C_2H$ and pyrene) and liberating H atoms. Extra C_2H_2 barely influences $C_6H_5C_2H$ consumption rate, and its consumption at high temperatures is compensated by its direct production from $C_6H_5C_2H$ decomposition. However, the added C_2H_4 slightly

enhances $C_6H_5C_2H$ decay due to the increased level of H atoms. Though the addition of both C_2H_2 and C_2H_4 negligibly affects $C_6H_5C_2H$ conversion rate, they considerably modify the PAH speciation behaviors. The added acetylene enables the HACA mechanism starting from phenylacetylene radical to occur at relatively low temperatures. The yielded naphthyl core does not stabilize in naphthalene due to the shortage of H-atoms in the reaction system, and alternatively, it further reacts with another acetylene molecule, ending up in high acenaphthylene concentrations. The added ethylene also intensifies the HACA routes as its consumption produces acetylene. C_2H_4 presence in the reaction system promotes $C_{10}H_8$ formation through $C_6H_4C_2H+C_2H_4$ reaction and provides H-atom to $C_{10}H_7$ to transform into $C_{10}H_8$ through the reaction $C_{10}H_7+C_2H_4 => C_{10}H_8+C_2H_3$. The level of $C_6H_4C_2H$ radicals are reduced because of their reactions with C_2 species in the binary mixtures, which inhibits the formation of $C_6H_5CCC_6H_5$, $C_{13}H_8CH_2$, and $C_2HC_6H_4C_6H_4C_2H$. $PC_{14}H_{10}$ has slightly higher peak mole fractions in binary mixtures due to the increased level of H-atoms, which facilitate the H-assisted isomerization reactions from both $C_6H_5CCC_6H_5$ and $C_{13}H_8CH_2$. $PC_{16}H_{10}$ is predominantly produced by the HACA route through $C_{14}H_9+C_2H_2$ reaction in binary reaction systems differently to the case of neat $C_6H_5C_2H$ pyrolysis, which justifies the displacement of its profile to higher temperatures.

Alkylbenzenes are major components of fuel mixtures. A comparative study is here implemented to compare the pyrolytic behavior of three alkylbenzenes, namely ethylbenzene, *n*-propylbenzene and *n*-butylbenzene. For all the fuels, the initial consumption pathway proceed through benzylic C-C fission forming benzyl and C_1-C_3 alkyl radicals, followed by H-abstraction reactions and ipso-additions. All the three fuels have higher decomposition reactivity compared to toluene, the simplest alkylbenzene. *N*-propylbenzene decomposes at lower temperatures than ethylbenzene and at similar temperatures to *n*-butylbenzene. The reason behinds this difference lies in the *n*-propylbenzene initial decomposition which results in the formation of C_7H_7 and C_2H_5 radicals. C_2H_5 consumption leads to a large amount of H atoms which stimulate *n*-propylbenzene decomposition and enhance benzene and toluene formation compared to the other two alkylbenzenes. Simultaneously the formed C_1-C_3 alkyl radicals remarkably impact the formation of small hydrocarbons and MAHs including ethylbenzene and allylbenzene. Compared to neat toluene pyrolysis, styrene has much higher concentrations in alkylbenzenes pyrolysis and it is directly stemmed from the fuel-related pathways. The PAH formation pathways are merely influenced by the fuel chemistry and are similar to the case of toluene pyrolysis, where C_7H_7 and C_7H_5 radicals play crucial roles in PAH formation. The only notable fuel-specific pathway is the indene formation from 1-phenyl-2-propenyl in *n*-propylbenzene and *n*-butylbenzene pyrolysis at relatively low temperatures. Styrene is an abundant product and its reaction with phenyl plays a key role in the formation of the C_{14} products.

To conclude, the present work presents an exhaustive investigation on PAH formation kinetics obtained implementing advanced experimental techniques (shock tube and gas chromatography) and chemical kinetic modeling. The experimental results constitute a wide database of species profiles, including PAH intermediates up to 4 rings, produced from the pyrolysis of numerous fuels and fuel mixtures, at the high-temperature and high-pressure conditions encountered in modern combustion devices. These profiles are used as a benchmark for the validation of a detailed and comprehensive chemical kinetic model, based on the recent advances in theoretical chemical kinetics. Kinetic analyses coupled to the experimental observations provides new insights on the pyrolytic chemistry of key fuels, their decomposition path, and the formation of the typical PAH soot precursor intermediates. The model can be used as a base for subsequent studies on more complex fuel mixtures, including surrogates and real fuels, and for coupling with soot codes for simulation of particle appearance and growth in combustion applications.

Appendix

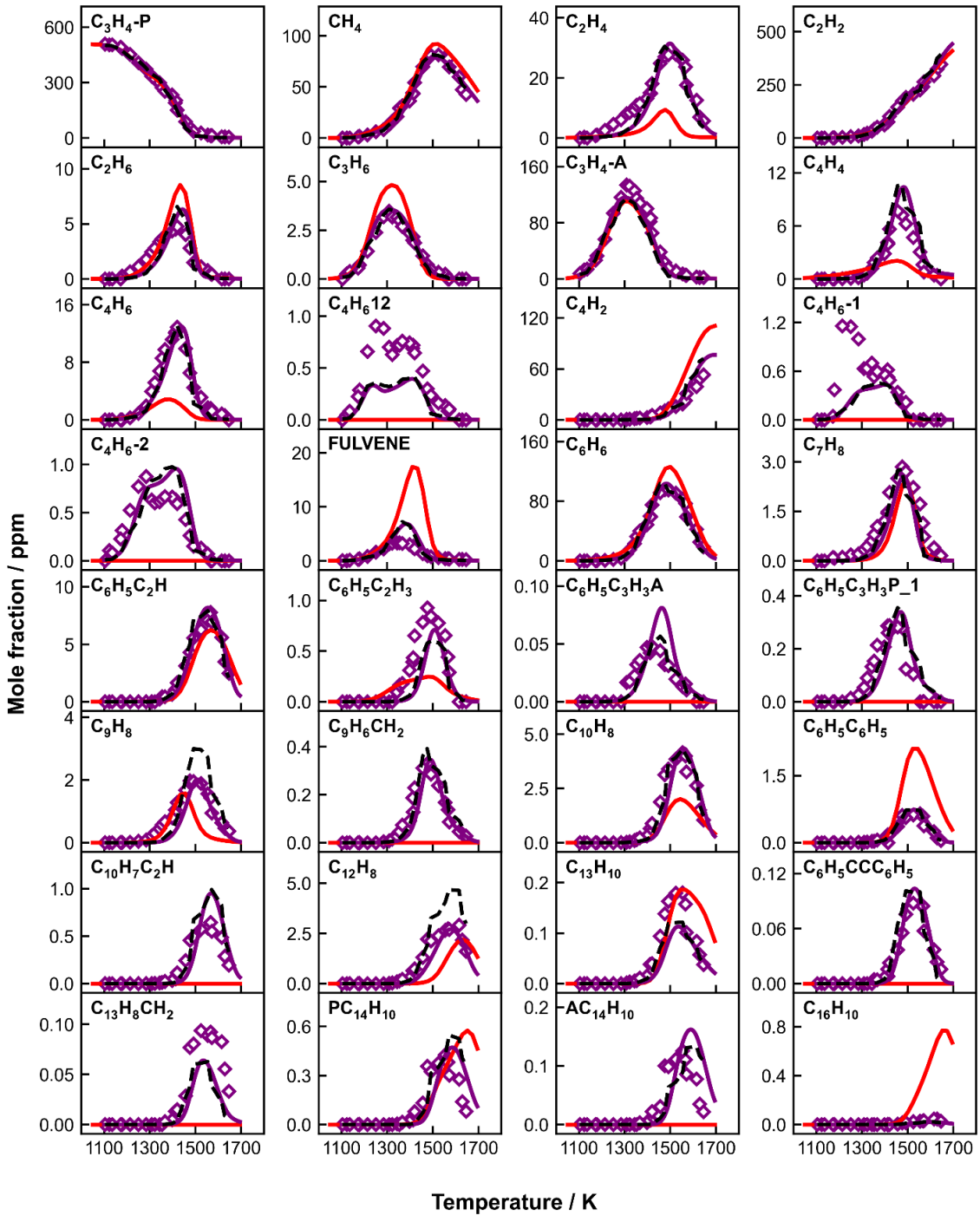

A 1: Measured (symbols) and simulated (lines) species mole fraction profiles as a function of T_5 in propyne pyrolysis. Thick solid purple lines: simulations using the current kinetic model with the constant p_5 of 20 bar and the nominal reaction time of 4

ms; thick dashed black lines: simulations using the current model with measured pressure profiles up to 10 ms; thick solid red line: simulations using CRECK model with the constant p_5 of 20 bar and the nominal reaction time of 4 ms.

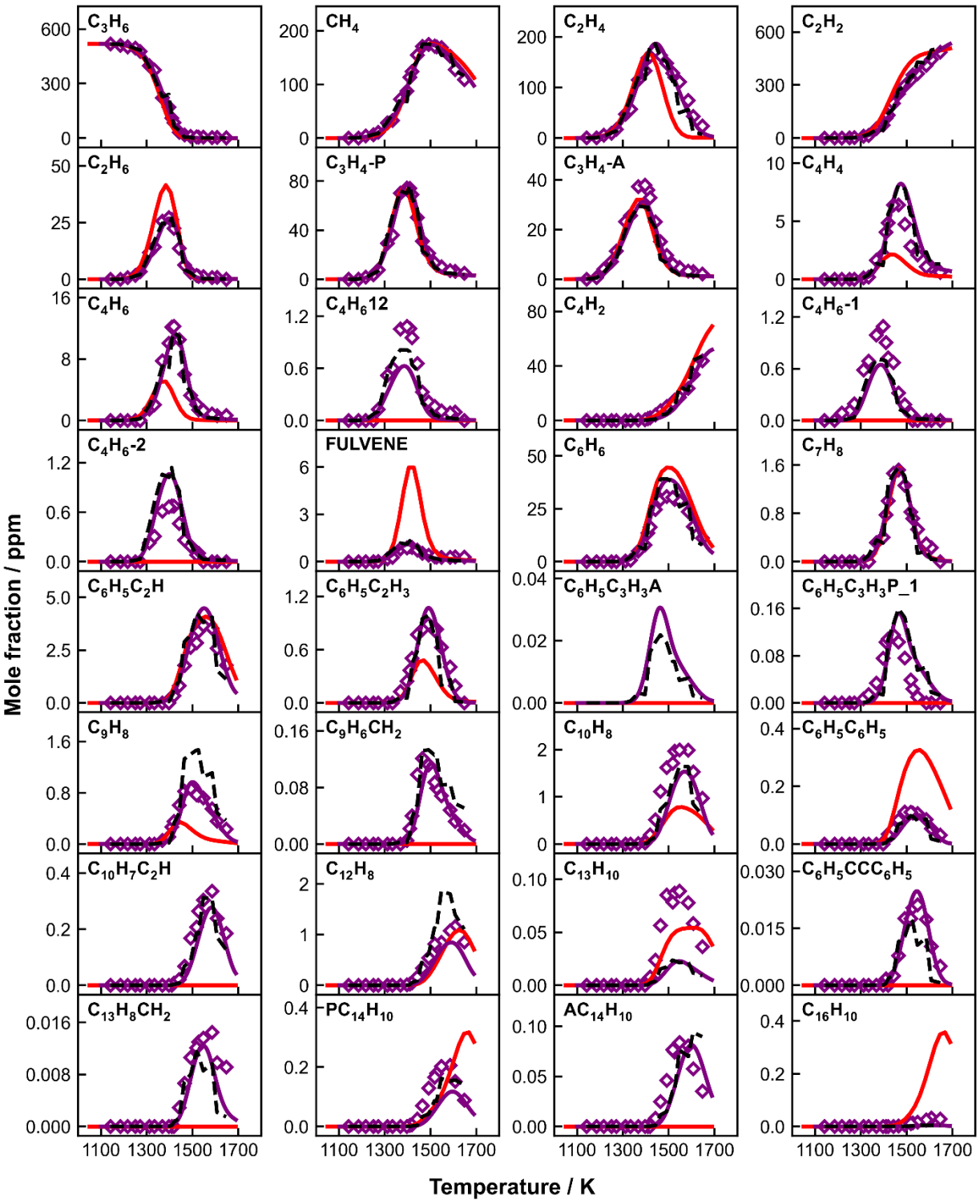

A 2: Measured (symbols) and simulated (lines) species mole fraction profiles as a function of T_5 in propylene pyrolysis. Thick solid purple lines: simulations using the current kinetic model with the constant p_5 of 20 bar and the nominal reaction time of 4

ms; thick dashed black lines: simulations using the current model with measured pressure profiles up to 10 ms; thick solid red line: simulations using CRECK model with the constant p_5 of 20 bar and the nominal reaction time of 4 ms.

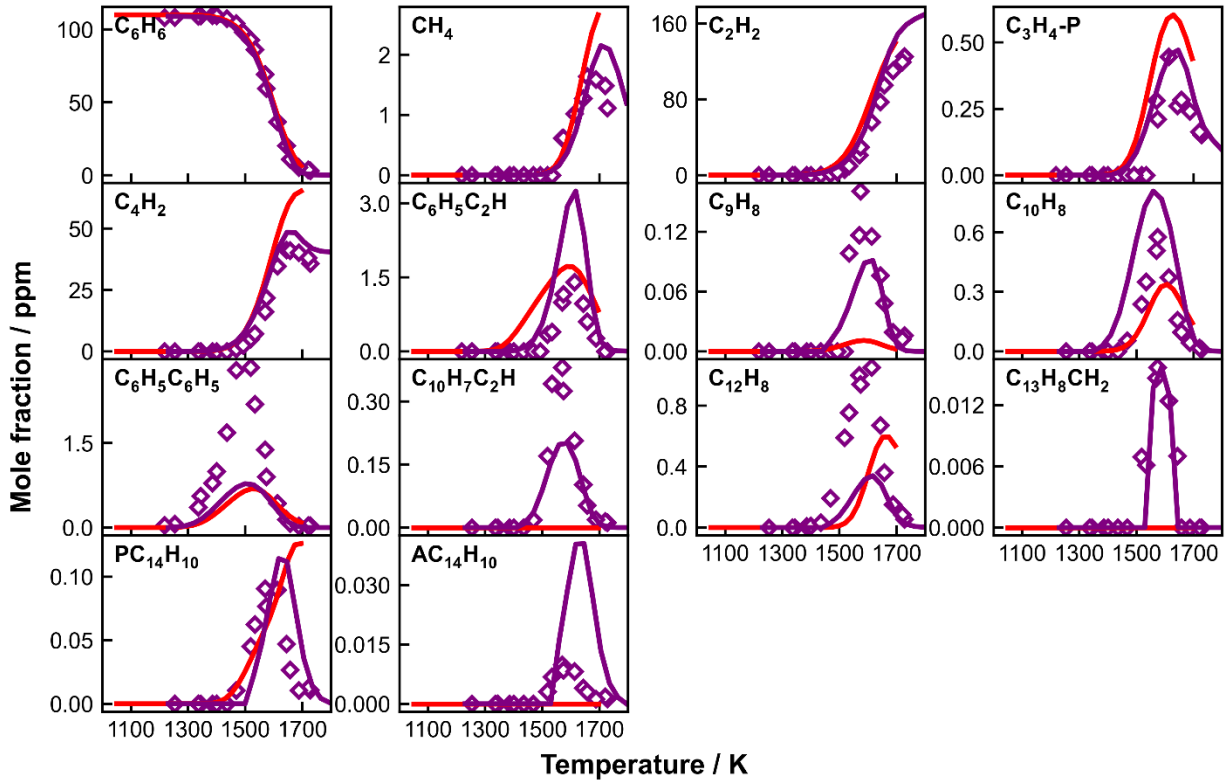

A 3: Measured (symbols) and simulated (lines) species mole fraction profiles as a function of T_5 in 109 ppm benzene pyrolysis. Thick solid purple lines: simulations using the current kinetic model with the constant p_5 of 20 bar and the nominal reaction time of 4 ms; thick solid red line: simulations using CRECK model with the constant p_5 of 20 bar and the nominal reaction time of 4 ms.

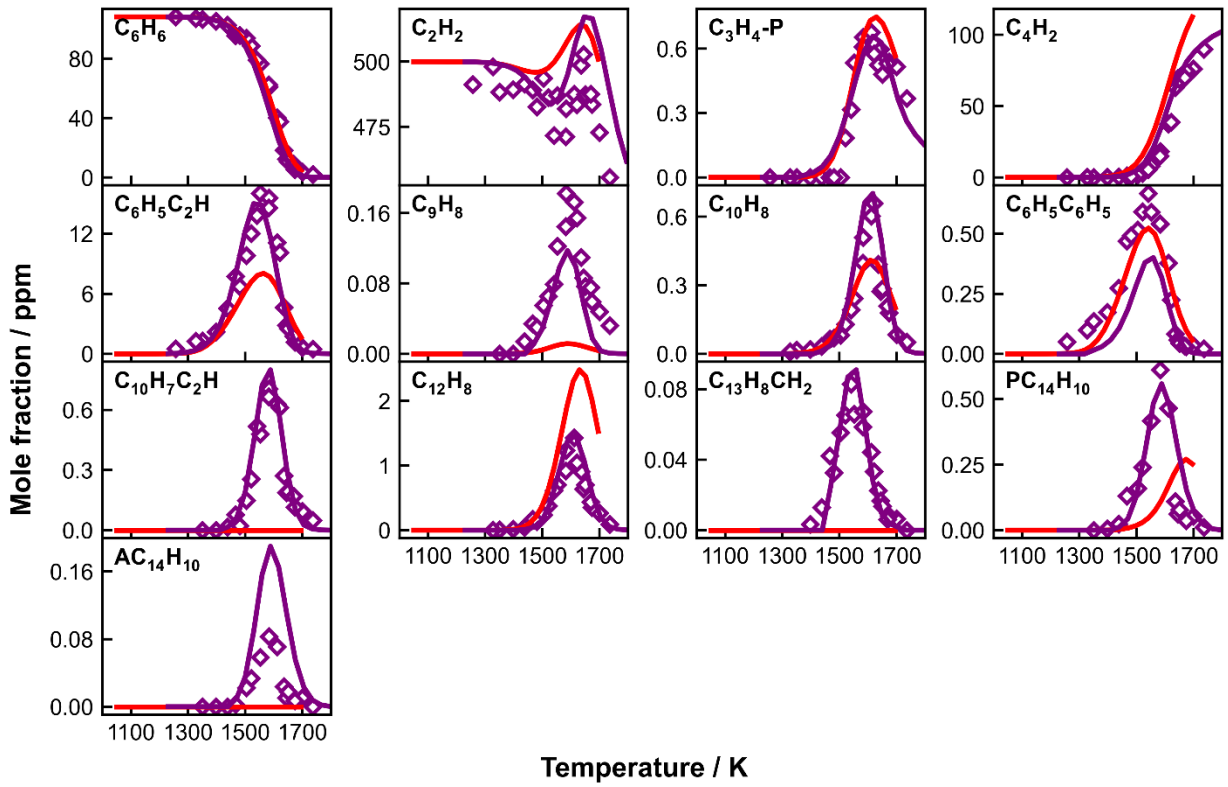

A 4: Measured (symbols) and simulated (lines) species mole fraction profiles as a function of T_5 in 108 ppm benzene+ 500 ppm acetylene co-pyrolysis.. Thick solid purple lines: simulations using the current kinetic model with the constant p_5 of 20 bar and the nominal reaction time of 4 ms; thick solid red line: simulations using CRECK model with the constant p_5 of 20 bar and the nominal reaction time of 4 ms.

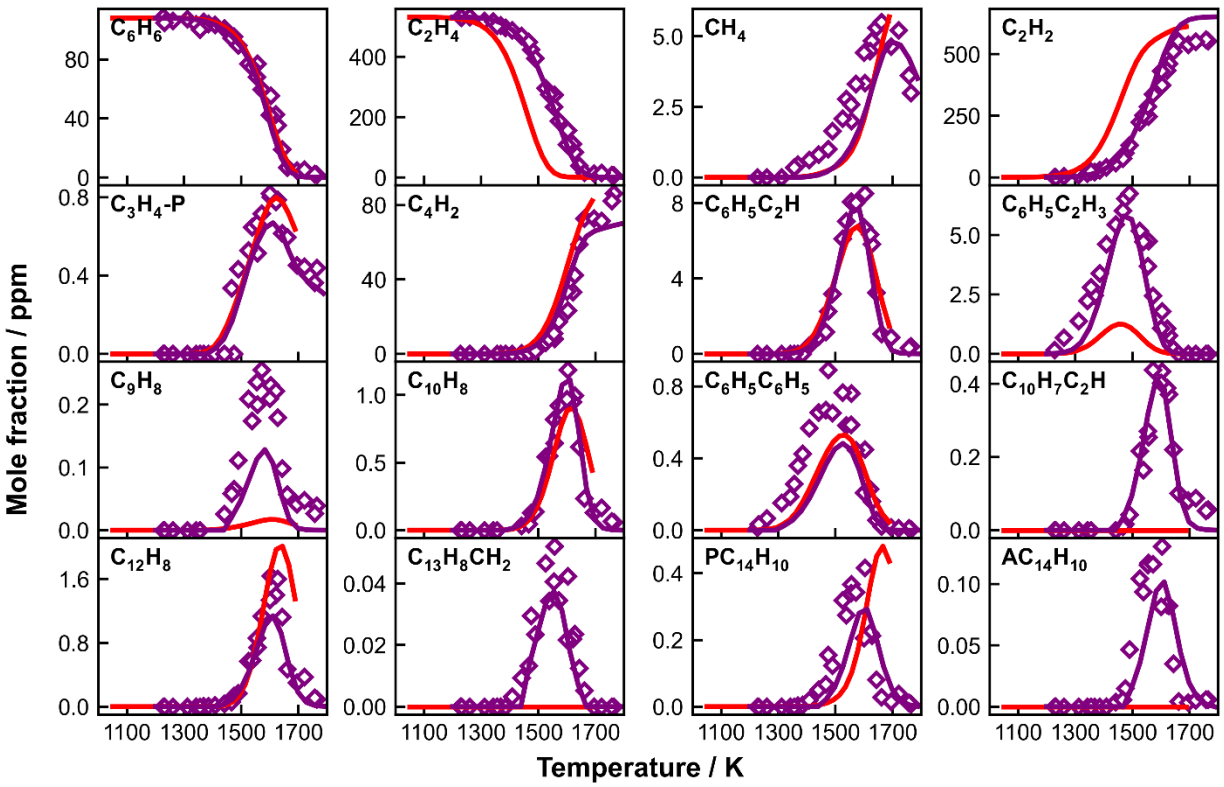

A 5: Measured (symbols) and simulated (lines) species mole fraction profiles as a function of T_5 in 108 ppm benzene+ 532 ppm ethylene co-pyrolysis. Thick solid purple lines: simulations using the current kinetic model with the constant p_5 of 20 bar and the nominal reaction time of 4 ms; thick solid red line: simulations using CRECK model with the constant p_5 of 20 bar and the nominal reaction time of 4 ms.

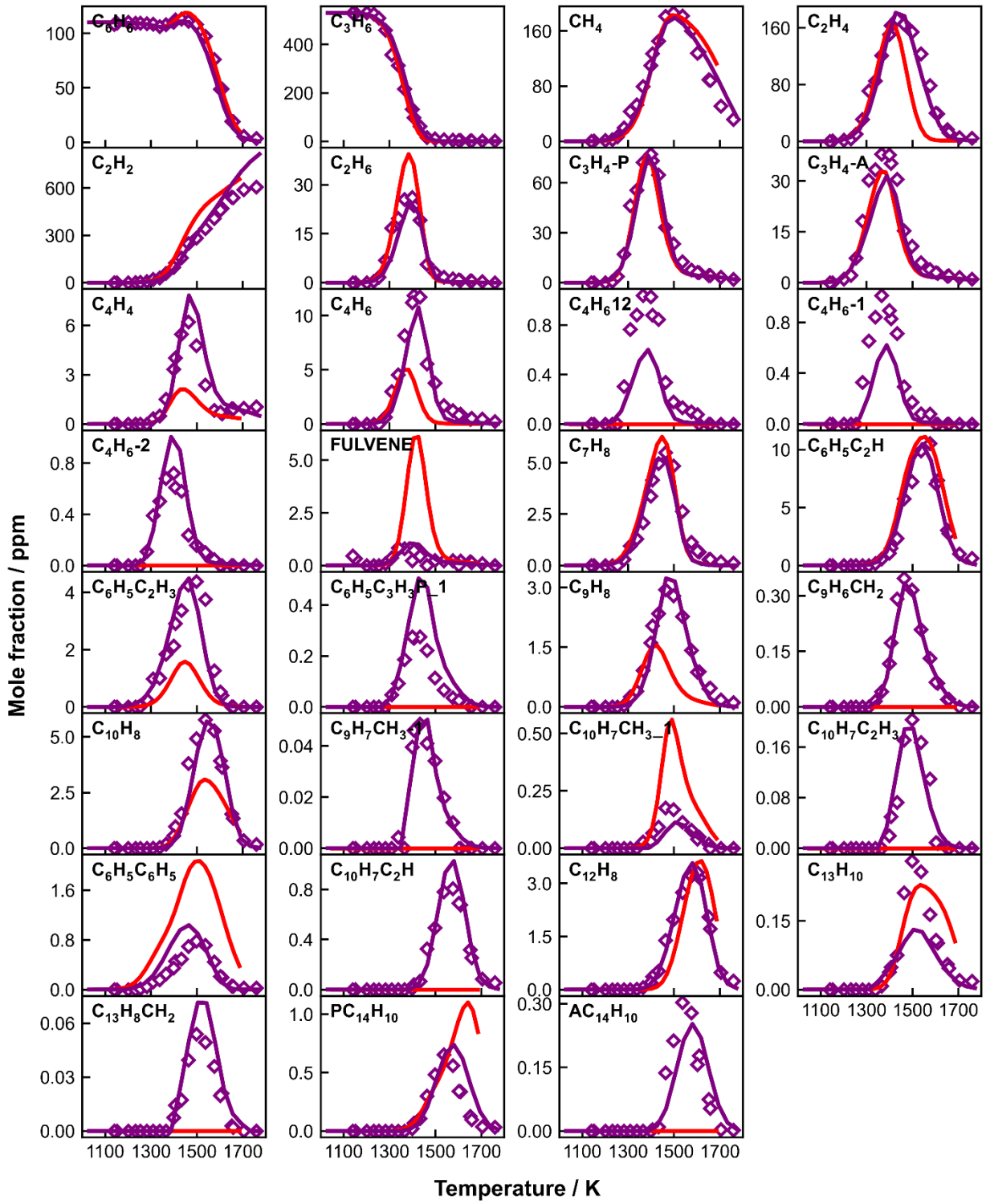

A 6: Measured (symbols) and simulated (lines) species mole fraction profiles as a function of T_5 in 110 benzene+ 531 ppm propylene co-pyrolysis. Thick solid purple lines: simulations using the current kinetic model with the constant p_5 of 20 bar and

the nominal reaction time of 4 ms; thick solid red line: simulations using CRECK model with the constant p_5 of 20 bar and the nominal reaction time of 4 ms.

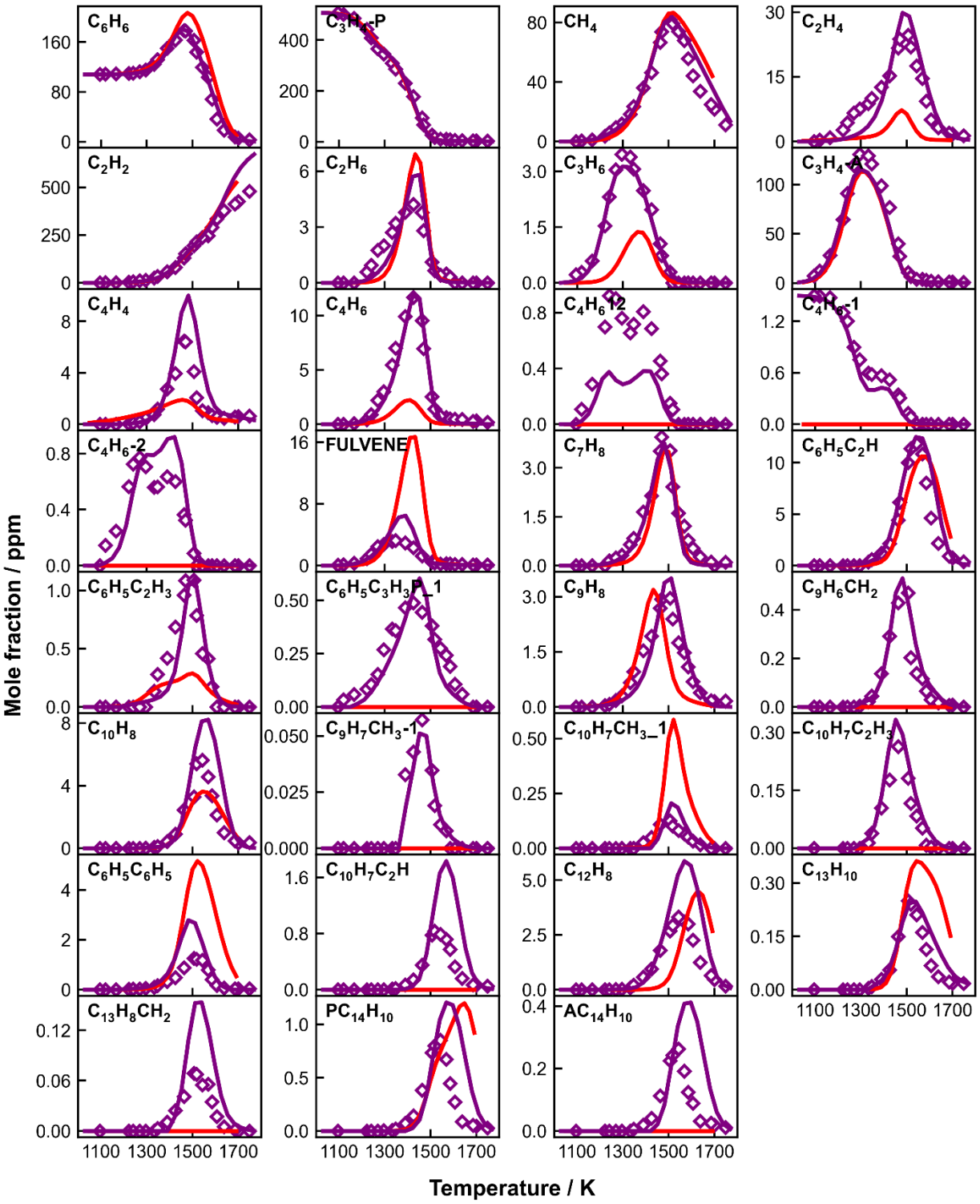

A 7: Measured (symbols) and simulated (lines) species mole fraction profiles as a function of T_5 in 108 benzene+ 508 ppm propyne co-pyrolysis. Thick solid purple lines: simulations using the current kinetic model with the constant p_5 of 20 bar and the

nominal reaction time of 4 ms; thick solid red line: simulations using CRECK model with the constant p_5 of 20 bar and the nominal reaction time of 4 ms.

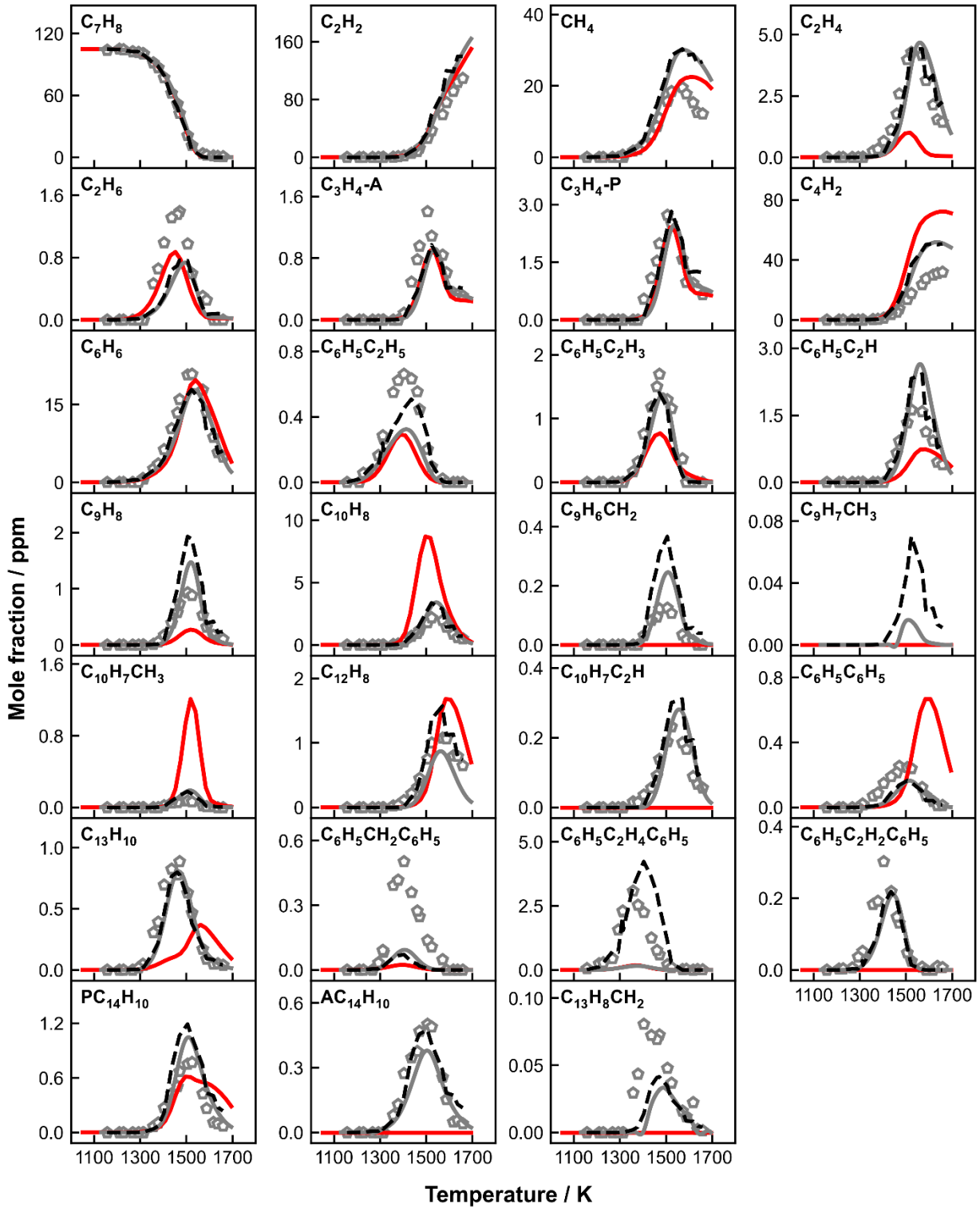

A 8: Measured (symbols) and simulated (lines) species mole fraction profiles as a function of T_5 in 105 ppm toluene pyrolysis. Thick solid grey lines: simulations using the current kinetic model with the constant p_5 of 20 bar and the nominal reaction time of

4 ms; thick dashed black lines: simulations using the current model with measured pressure profiles up to 10 ms; thick solid red line: simulations using CRECK model with the constant p_5 of 20 bar and the nominal reaction time of 4 ms.

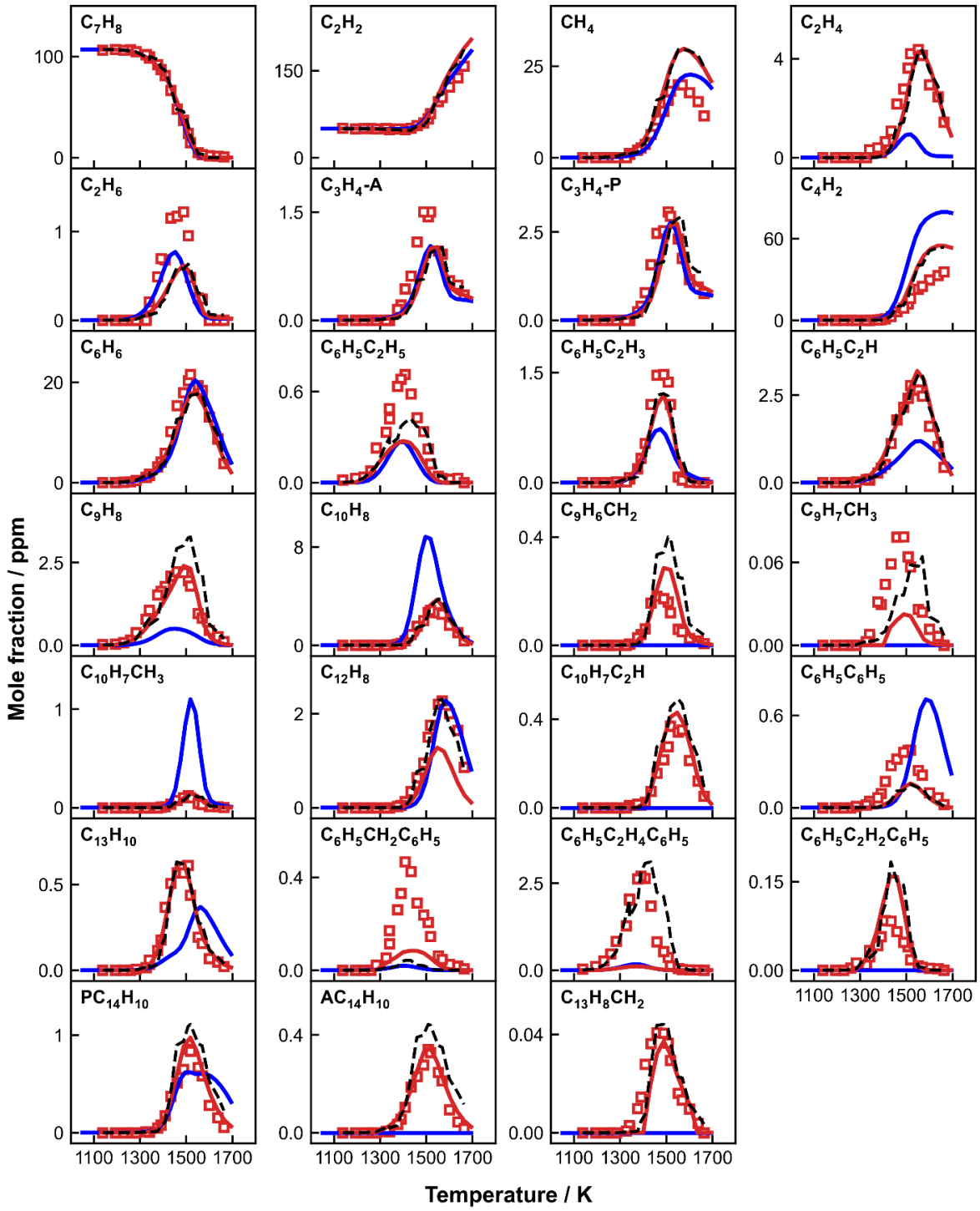

A 9: Measured (symbols) and simulated (lines) species mole fraction profiles as a function of T_5 in 107 toluene+ 50 ppm acetylene co-pyrolysis. Thick solid red lines: simulations using the current kinetic model with the constant p_5 of 20 bar and the nominal reaction time of 4 ms; thick dashed black lines: simulations using the current model with measured pressure profiles up to 10 ms; thick solid blue line: simulations using CRECK model with the constant p_5 of 20 bar and the nominal reaction time of 4 ms.

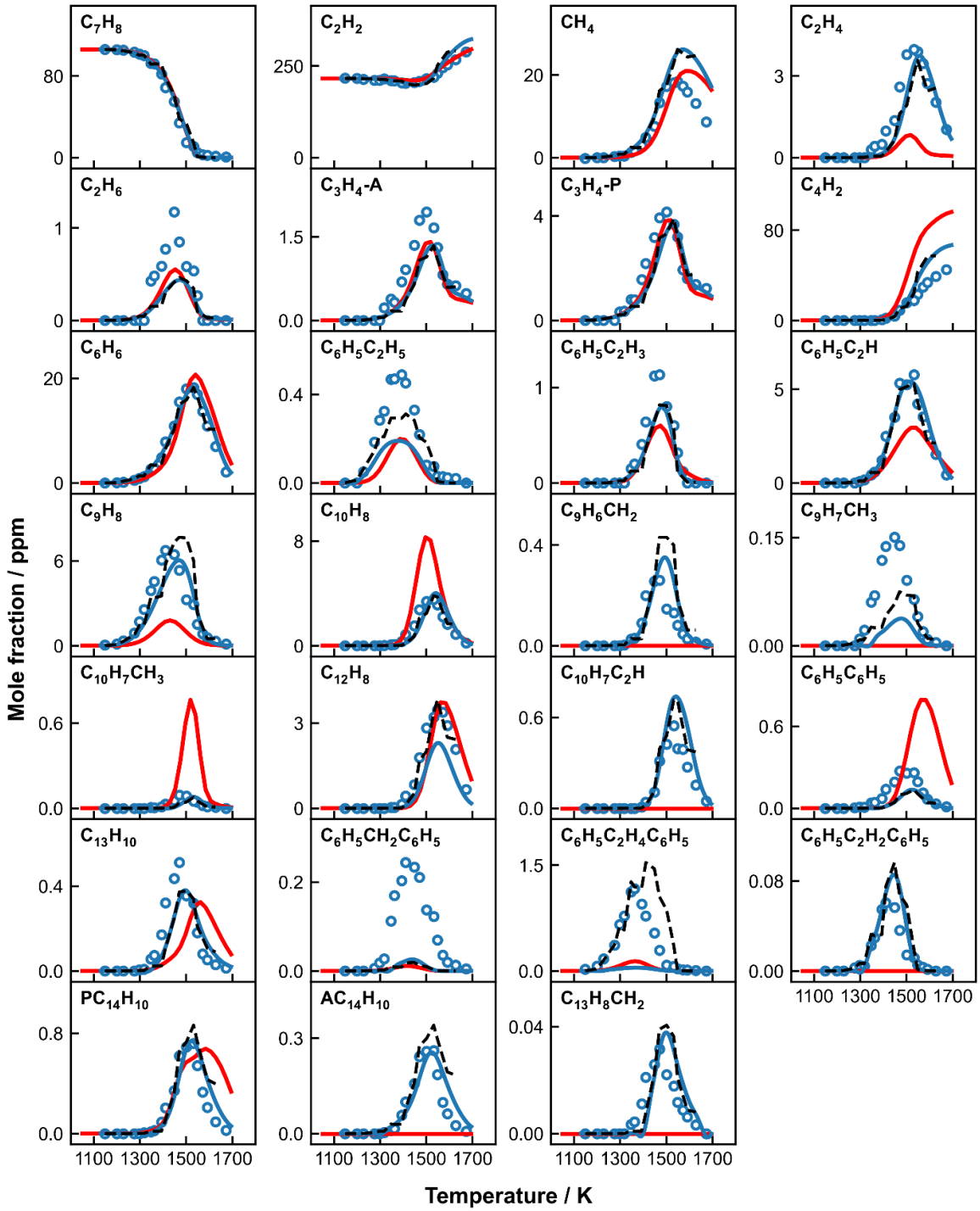

A 10: Measured (symbols) and simulated (lines) species mole fraction profiles as a function of T_5 in 106 toluene+ 216 ppm acetylene co-pyrolysis. Thick solid blue lines: simulations using the current kinetic model with the constant p_5 of 20 bar and the nominal reaction time of 4 ms; thick dashed black lines: simulations using the current model with measured pressure profiles up to 10 ms; thick solid red line: simulations using CRECK model with the constant p_5 of 20 bar and the nominal reaction time of 4 ms.

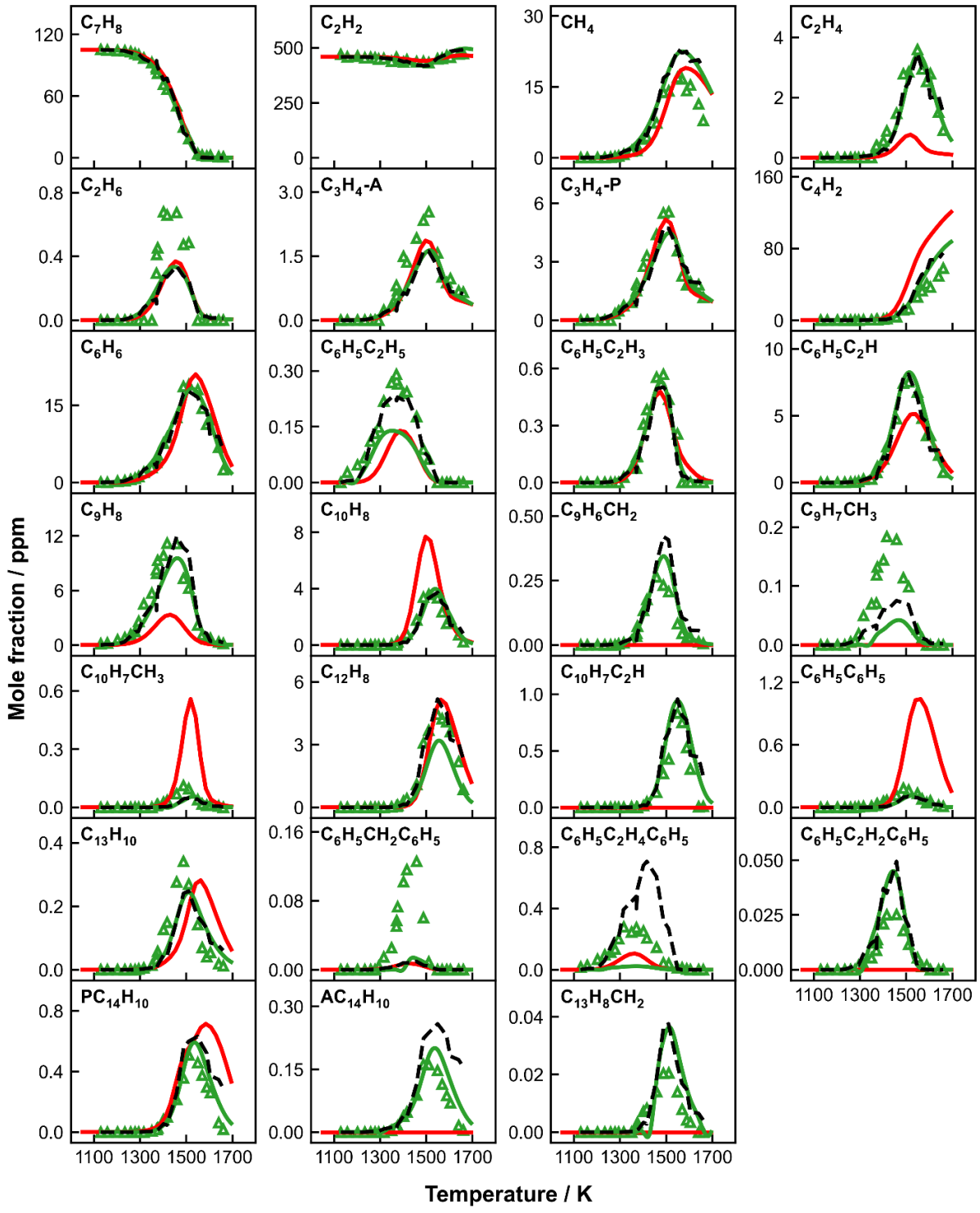

A 11: Measured (symbols) and simulated (lines) species mole fraction profiles as a function of T_5 in 105 toluene+ 459 ppm acetylene co-pyrolysis. Thick solid green lines: simulations using the current kinetic model with the constant p_5 of 20 bar and the nominal reaction time of 4 ms; thick dashed black lines: simulations using the current model with measured pressure profiles up

to 10 ms; thick solid red line: simulations using CRECK model with the constant p_5 of 20 bar and the nominal reaction time of 4 ms.

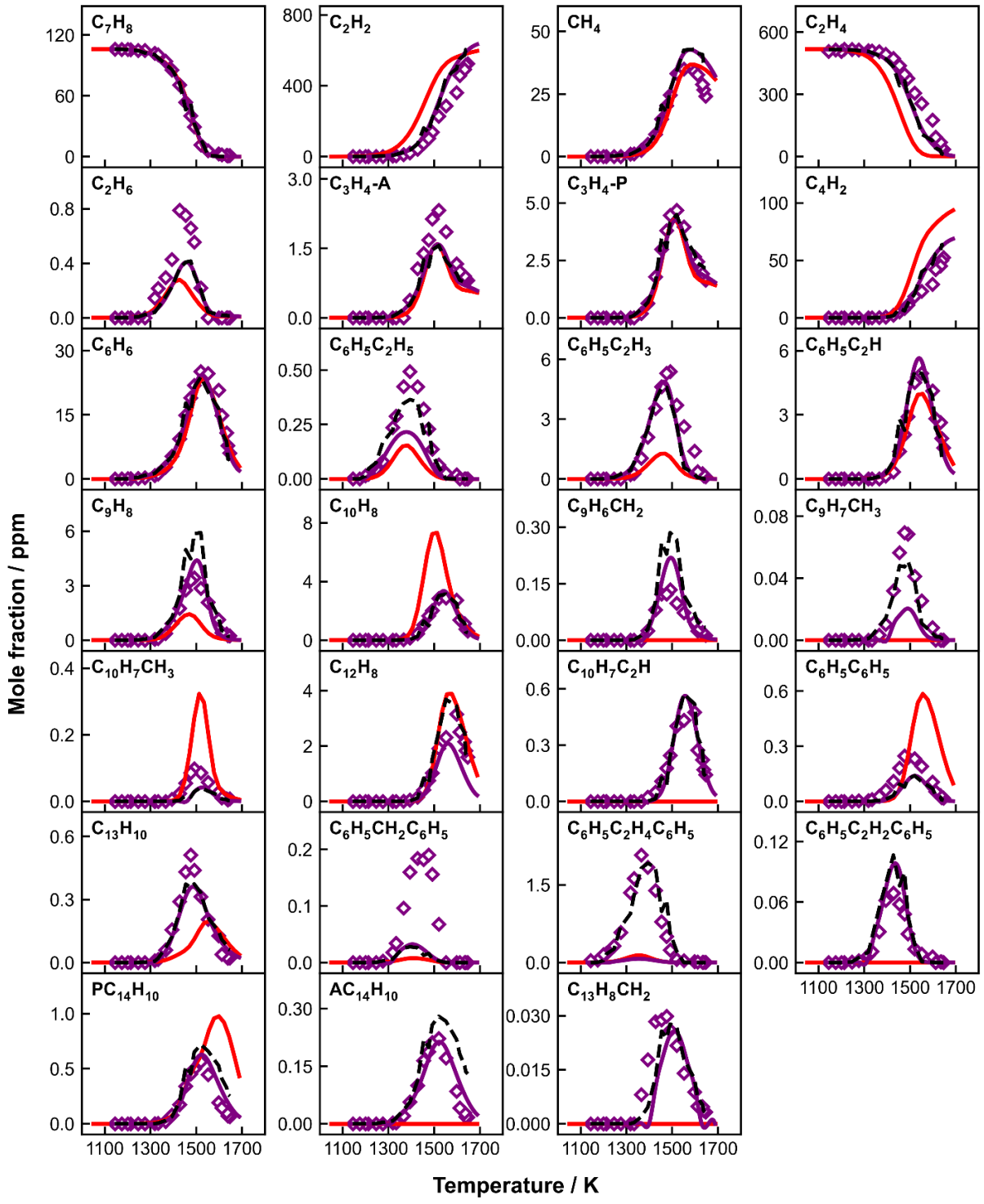

A 12: Measured (symbols) and simulated (lines) species mole fraction profiles as a function of T_5 in 106 toluene+ 518 ppm ethylene co-pyrolysis. Thick solid purple lines: simulations using the current kinetic model with the constant p_5 of 20 bar and the nominal reaction time of 4 ms; thick dashed black lines: simulations using the current model with measured pressure profiles up

to 10 ms; thick solid red line: simulations using CRECK model with the constant p_5 of 20 bar and the nominal reaction time of 4 ms.

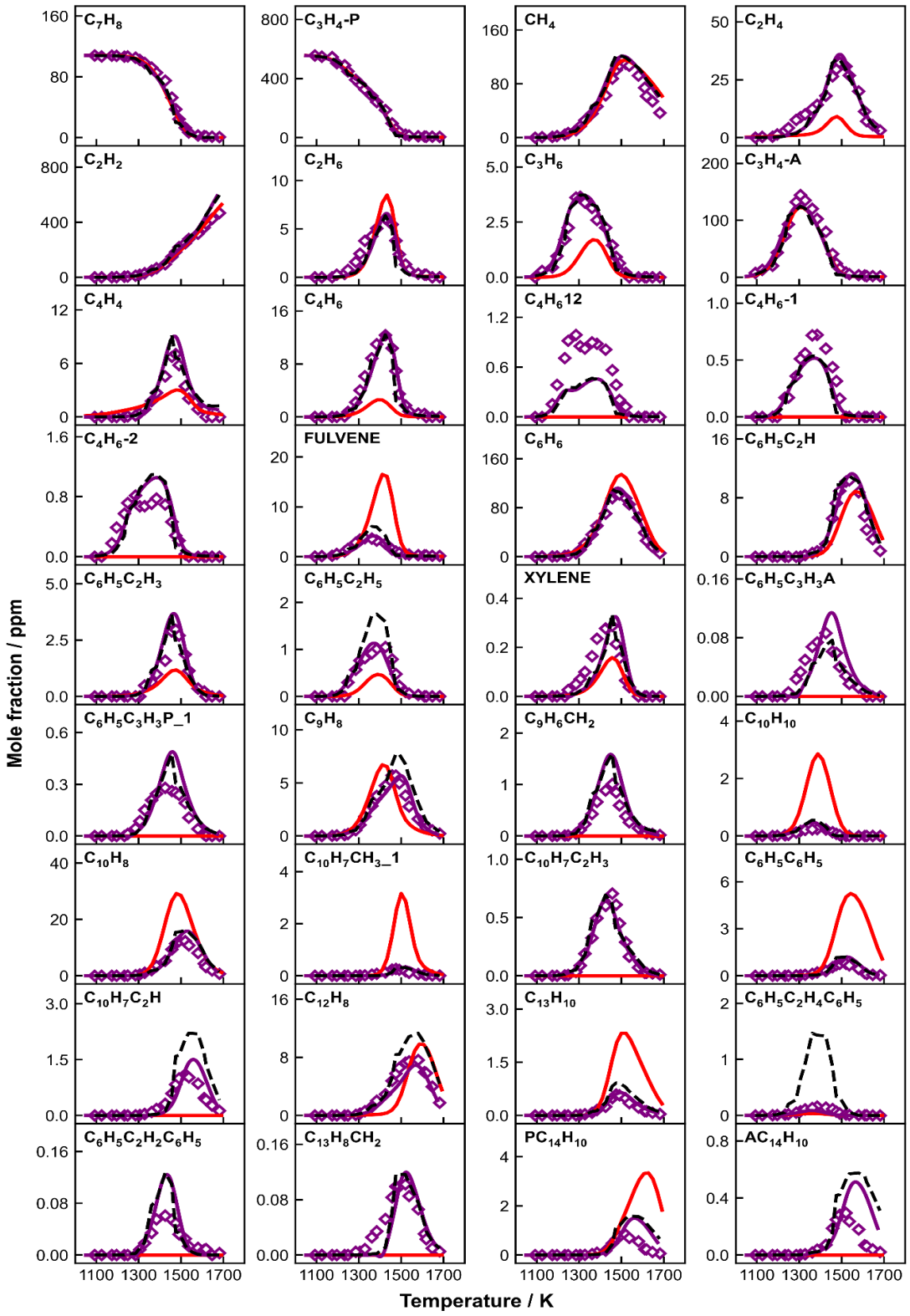

A 13: Measured (symbols) and simulated (lines) species mole fraction profiles as a function of T_5 in 108 toluene+ 557 ppm propyne co-pyrolysis. Thick solid purple lines: simulations using the current kinetic model with the constant p_5 of 20 bar and the

nominal reaction time of 4 ms; thick dashed black lines: simulations using the current model with measured pressure profiles up to 10 ms; thick solid red line: simulations using CRECK model with the constant p_5 of 20 bar and the nominal reaction time of 4 ms.

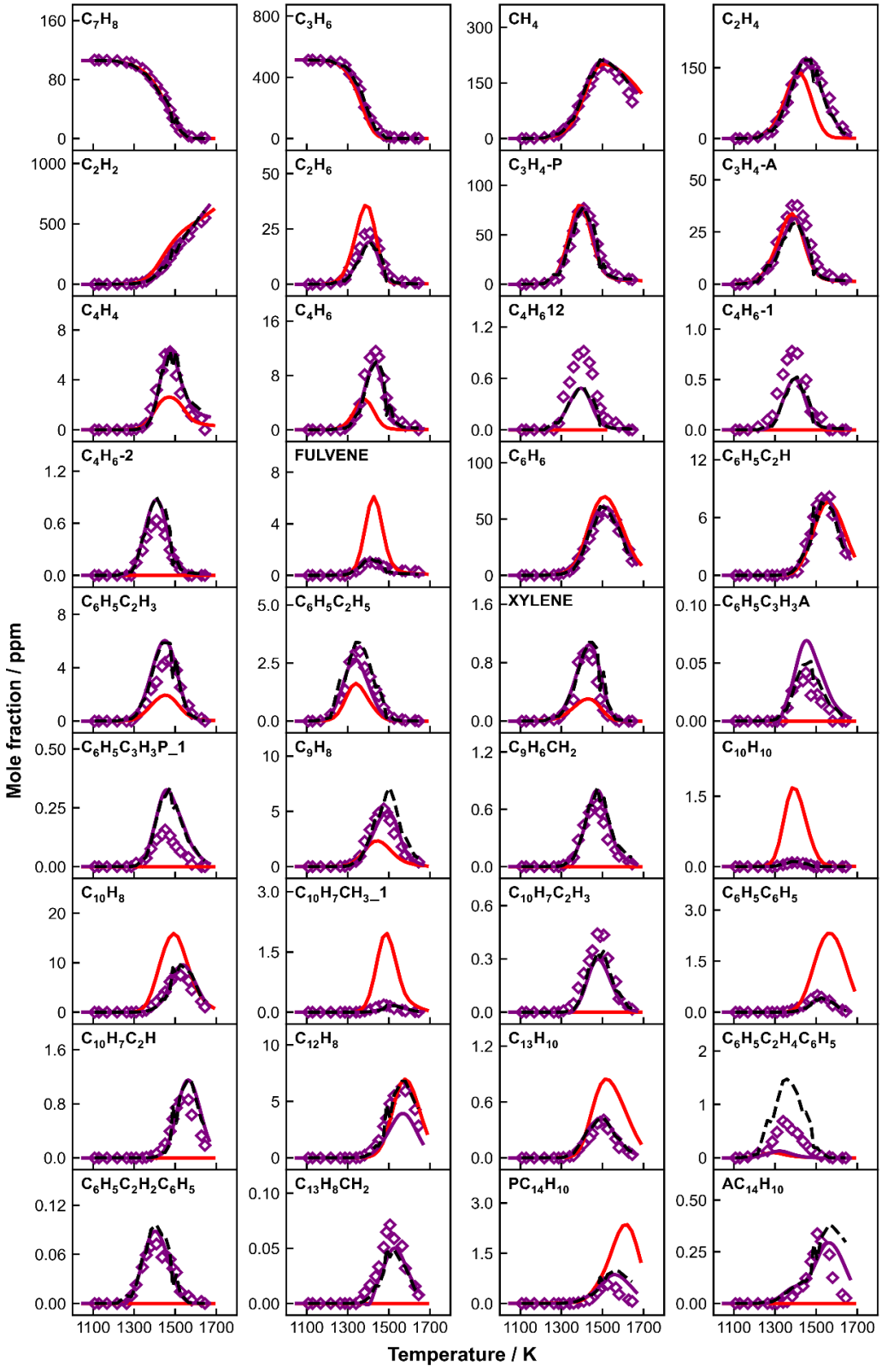
Mole fraction / ppm
Temperature / K
C7H8
C3H6
CH4
C2H4
C2H2
C2H6
C3H4-P
C3H4-A
C4H4
C4H6
C4H612
C4H6-1
C4H6-2
FULVENE
C6H6
C6H5C2H
C6H5C2H3
C6H5C2H5
XYLENE
C6H5C3H3A
C6H5C3H3P_1
C9H8
C9H6CH2
C10H10
C10H8
C10H7CH3_1
C10H7C2H3
C6H5C6H5
C10H7C2H
C12H8
C13H10
C6H5C2H4C6H5
C6H5C2H2C6H5
C13H8CH2
PC14H10
AC14H10

A 14: Measured (symbols) and simulated (lines) species mole fraction profiles as a function of T_5 in 106 toluene+ 513 ppm propylene co-pyrolysis. Thick solid purple lines: simulations using the current kinetic model with the constant p_5 of 20 bar and the nominal reaction time of 4 ms; thick dashed black lines: simulations using the current model with measured pressure profiles up to 10 ms; thick solid red line: simulations using CRECK model with the constant p_5 of 20 bar and the nominal reaction time of 4 ms.

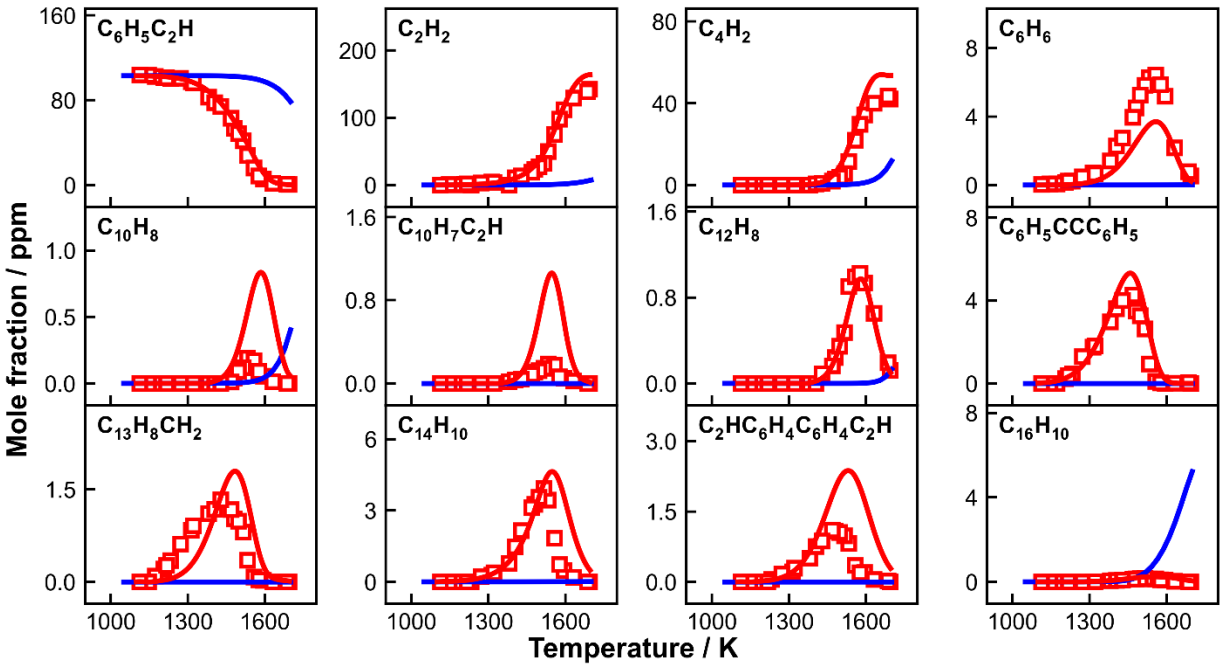

A 15: Measured (symbols) and simulated (lines) species mole fraction profiles as a function of T_5 in 103 ppm phenylacetylene pyrolysis. Thick solid red lines: simulations using the current kinetic model with the constant p_5 of 20 bar and the nominal reaction time of 4 ms; thick solid blue line: simulations using CRECK model with the constant p_5 of 20 bar and the nominal reaction time of 4 ms.

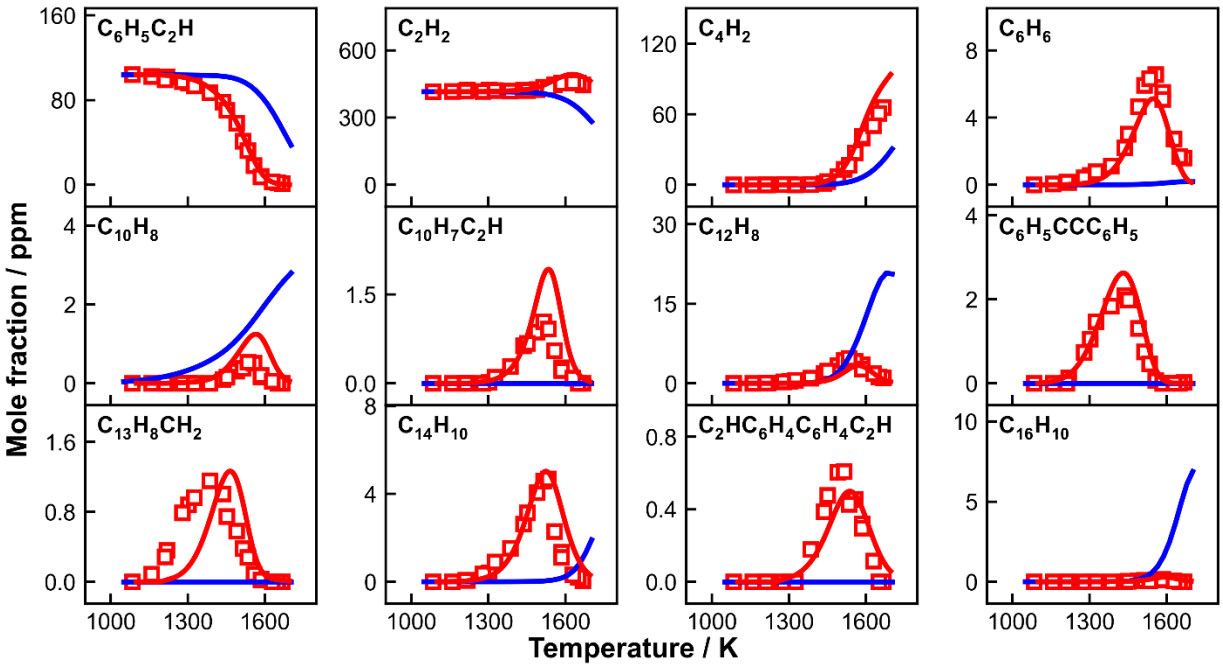

A 16: Measured (symbols) and simulated (lines) species mole fraction profiles as a function of T_5 in 104 ppm phenylacetylene+ 415 ppm acetylene co-pyrolysis. Thick solid red lines: simulations using the current kinetic model with the constant p_5 of 20 bar and the nominal reaction time of 4 ms; thick solid blue line: simulations using CRECK model with the constant p_5 of 20 bar and the nominal reaction time of 4 ms.

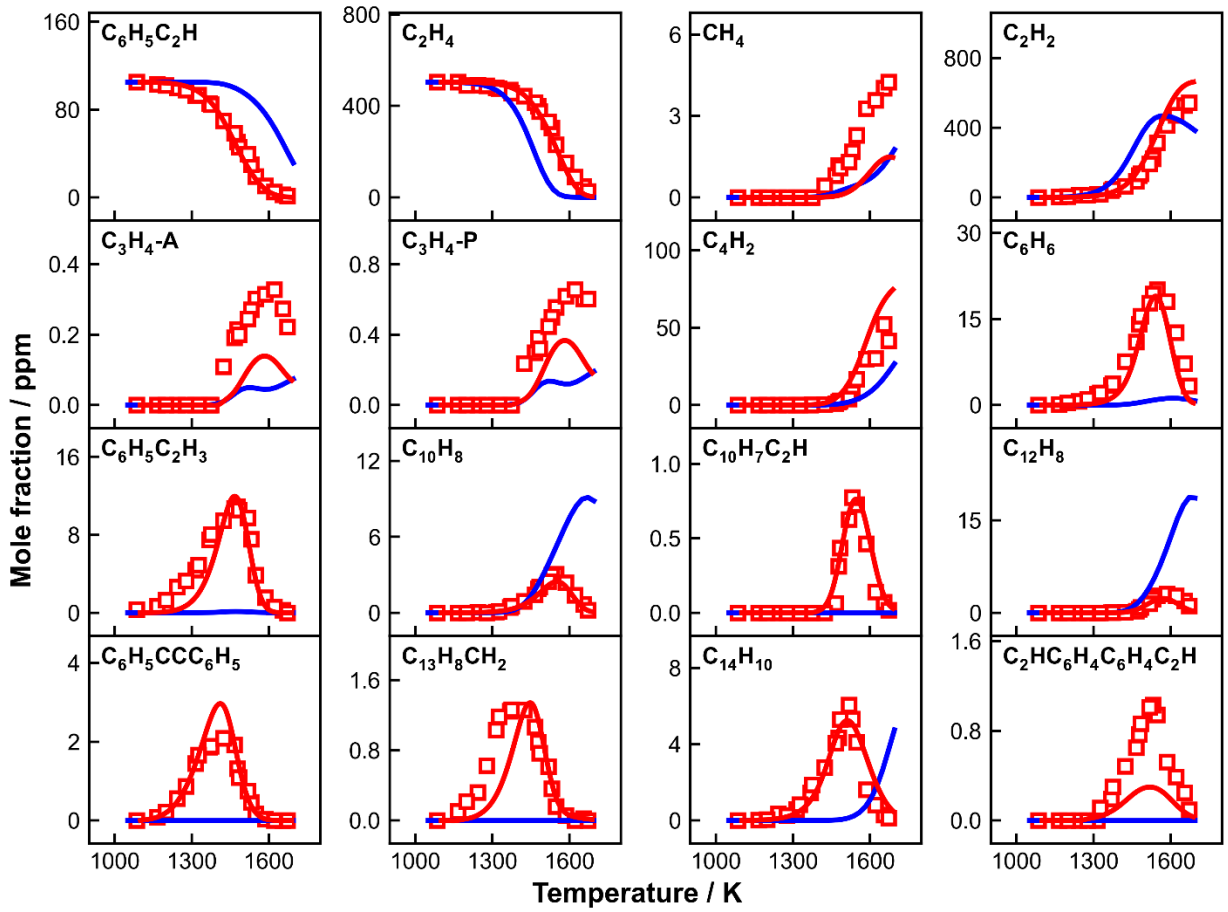

A 17: Measured (symbols) and simulated (lines) species mole fraction profiles as a function of T_5 in 105 ppm phenylacetylene+ 504 ppm ethylene co-pyrolysis. Thick solid red lines: simulations using the current kinetic model with the constant p_5 of 20 bar and the nominal reaction time of 4 ms; thick solid blue line: simulations using CRECK model with the constant p_5 of 20 bar and the nominal reaction time of 4 ms.

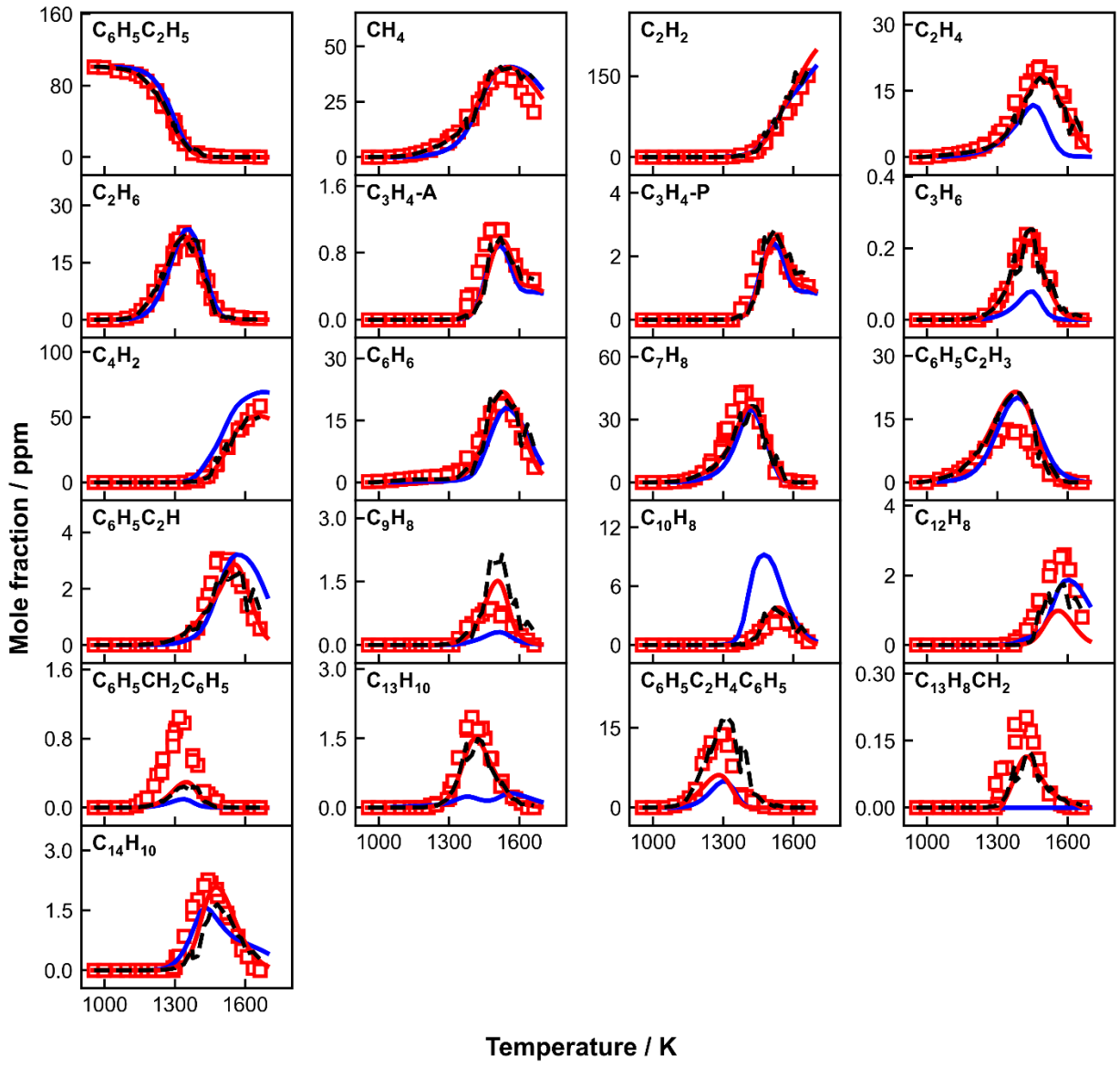

A 18: Measured (symbols) and simulated (lines) species mole fraction profiles as a function of T_5 in 101 ppm ethylbenzene pyrolysis. Thick solid red lines: simulations using the current kinetic model with the constant p_5 of 20 bar and the nominal reaction time of 4 ms; thick dashed black lines: simulations using the current model with measured pressure profiles up to 10 ms; thick solid blue line: simulations using CRECK model with the constant p_5 of 20 bar and the nominal reaction time of 4 ms.

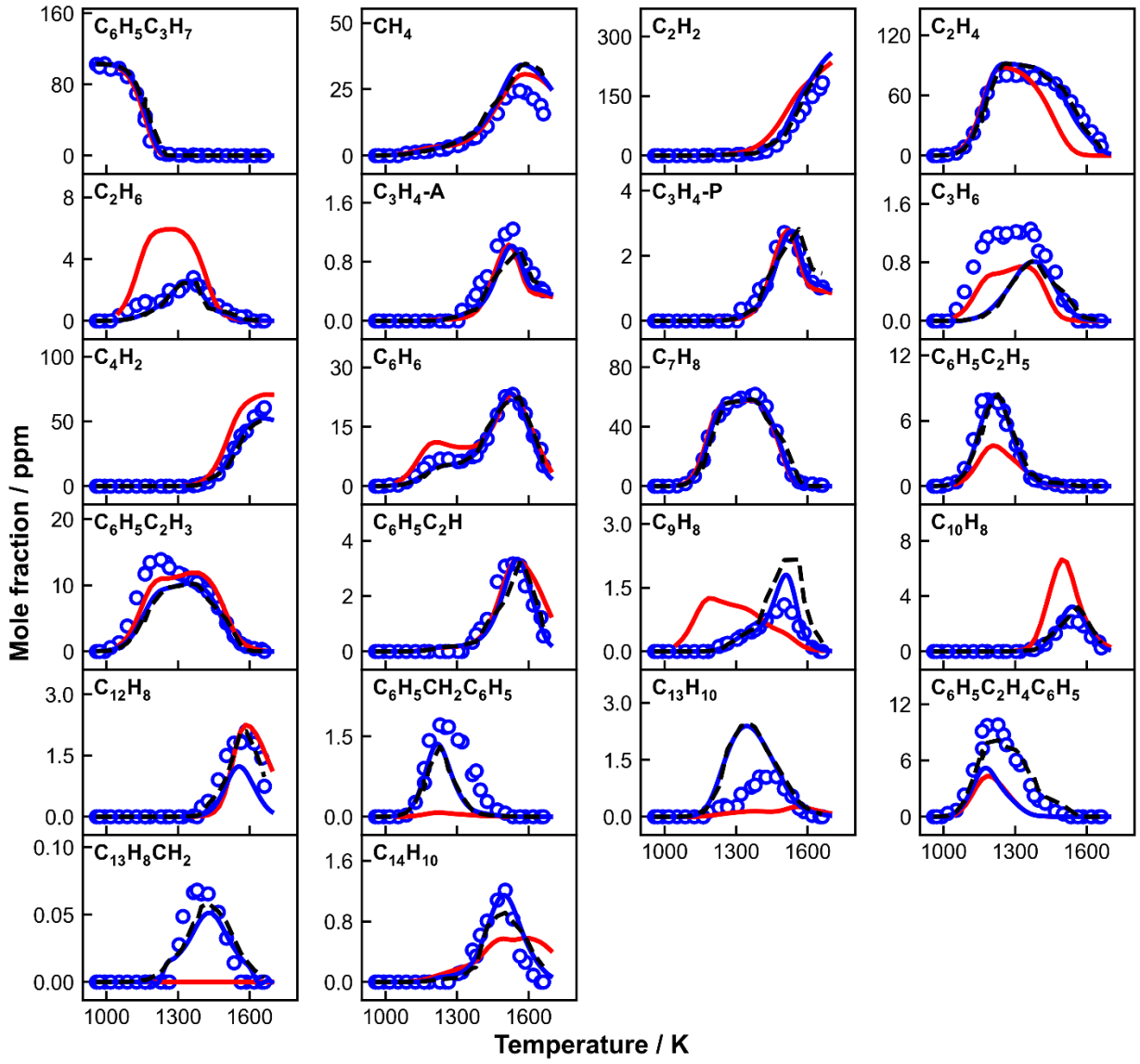

A 19: Measured (symbols) and simulated (lines) species mole fraction profiles as a function of T_5 in 103 ppm propylbenzene pyrolysis. Thick solid blue lines: simulations using the current kinetic model with the constant p_5 of 20 bar and the nominal reaction time of 4 ms; thick dashed black lines: simulations using the current model with measured pressure profiles up to 10 ms; thick solid red line: simulations using CRECK model with the constant p_5 of 20 bar and the nominal reaction time of 4 ms.

Bibliography

[1] "Key World Energy Statistics 2020 – Analysis," *IEA*. https://www.iea.org/reports/key-world-energy-statistics-2020 (accessed May 04, 2021).

[2] T. C. Bond *et al.*, “Bounding the role of black carbon in the climate system: A scientific assessment,” *J. Geophys. Res. Atmospheres*, vol. 118, no. 11, pp. 5380–5552, 2013, doi: 10.1002/jgrd.50171.
[3] K.-H. Kim, E. Kabir, and S. Kabir, “A review on the human health impact of airborne particulate matter,” *Environ. Int.*, vol. 74, pp. 136–143, Jan. 2015, doi: 10.1016/j.envint.2014.10.005.
[4] P. M. Sharif *et al.*, “International regulation of vehicle emissions control rules and its influence on academic engine development experimental study and vehicle manufacturing,” *IOP Conf. Ser. Mater. Sci. Eng.*, vol. 469, p. 012070, Jan. 2019, doi: 10.1088/1757-899X/469/1/012070.
[5] H. Richter and J. B. Howard, “Formation of polycyclic aromatic hydrocarbons and their growth to soot—a review of chemical reaction pathways,” *Prog. Energy Combust. Sci.*, vol. 26, no. 4, pp. 565–608, Aug. 2000, doi: 10.1016/S0360-1285(00)00009-5.
[6] Z. Mansurov, “Soot Formation in Combustion Processes (Review),” *Combust. Explos. Shock Waves*, vol. 41, pp. 727–744, Nov. 2005, doi: 10.1007/s10573-005-0083-2.
[7] M. Frenklach and H. Wang, “Detailed Mechanism and Modeling of Soot Particle Formation,” in *Soot Formation in Combustion: Mechanisms and Models*, H. Bockhorn, Ed. Berlin, Heidelberg: Springer, 1994, pp. 165–192. doi: 10.1007/978-3-642-85167-4_10.
[8] M. Frenklach, “Reaction mechanism of soot formation in flames,” *Phys. Chem. Chem. Phys.*, vol. 4, no. 11, pp. 2028–2037, May 2002, doi: 10.1039/B110045A.
[9] H. Bockhorn, Ed., *Soot Formation in Combustion: Mechanisms and Models*. Berlin Heidelberg: Springer-Verlag, 1994. doi: 10.1007/978-3-642-85167-4.
[10] H. Wang, “Formation of nascent soot and other condensed-phase materials in flames,” *Proc. Combust. Inst.*, vol. 33, no. 1, pp. 41–67, Jan. 2011, doi: 10.1016/j.proci.2010.09.009.
[11] H. Bockhorn, F. Fetting, U. Meyer, R. Reck, and G. Wannemacher, “Measurement of the soot concentration and soot particle sizes in propane oxygen flames,” *Symp. Int. Combust.*, vol. 18, no. 1, pp. 1137–1147, Jan. 1981, doi: 10.1016/S0082-0784(81)80118-X.
[12] M. Frenklach, D. W. Clary, W. C. Gardiner, and S. E. Stein, “Detailed kinetic modeling of soot formation in shock-tube pyrolysis of acetylene,” *Symp. Int. Combust.*, vol. 20, no. 1, pp. 887–901, Jan. 1985, doi: 10.1016/S0082-0784(85)80578-6.
[13] M. Frenklach and H. Wang, “Detailed modeling of soot particle nucleation and growth,” *Symp. Int. Combust.*, vol. 23, no. 1, pp. 1559–1566, Jan. 1991, doi: 10.1016/S0082-0784(06)80426-1.
[14] J. Appel, H. Bockhorn, and M. Frenklach, “Kinetic modeling of soot formation with detailed chemistry and physics: laminar premixed flames of C2 hydrocarbons,” *Combust. Flame*, vol. 121, no. 1, pp. 122–136, Apr. 2000, doi: 10.1016/S0010-2180(99)00135-2.
[15] V. V. Kislov, A. I. Sadovnikov, and A. M. Mebel, “Formation Mechanism of Polycyclic Aromatic Hydrocarbons beyond the Second Aromatic Ring,” *J. Phys. Chem. A*, vol. 117, no. 23, pp. 4794–4816, Jun. 2013, doi: 10.1021/jp402481y.
[16] † Nigel W. Moriarty, ‡ and Nancy J. Brown, and † Michael Frenklach*, “Hydrogen Migration in the Phenylethen-2-yl Radical,” *ACS Publications*, Aug. 18, 1999. https://pubs.acs.org/doi/pdf/10.1021/jp991481f (accessed Sep. 15, 2021).
[17] A. Raj, M. J. Al Rashidi, S. H. Chung, and S. M. Sarathy, “PAH Growth Initiated by Propargyl Addition: Mechanism Development and Computational Kinetics,” *J. Phys. Chem. A*, vol. 118, no. 16, pp. 2865–2885, Apr. 2014, doi: 10.1021/jp410704b.
[18] Y. Wang, A. Raj, and S. H. Chung, “A PAH growth mechanism and synergistic effect on PAH formation in counterflow diffusion flames,” *Combust. Flame*, vol. 160, no. 9, pp. 1667–1676, Sep. 2013, doi: 10.1016/j.combustflame.2013.03.013.
[19] B. Shukla and M. Koshi, “A novel route for PAH growth in HACA based mechanisms,” *Combust. Flame*, vol. 159, pp. 3589–3596, Dec. 2012, doi: 10.1016/j.combustflame.2012.08.007.
[20] J. B. Howard, “Fullerenes formation in flames,” *Symp. Int. Combust.*, vol. 24, no. 1, pp. 933–946, Jan. 1992, doi: 10.1016/S0082-0784(06)80111-6.

[21] H. Richter, W. J. Grieco, and J. B. Howard, “Formation mechanism of polycyclic aromatic hydrocarbons and fullerenes in premixed benzene flames,” *Combust. Flame*, vol. 119, no. 1, pp. 1–22, Oct. 1999, doi: 10.1016/S0010-2180(99)00032-2.
[22] B. Shukla and M. Koshi, “A highly efficient growth mechanism of polycyclic aromatic hydrocarbons,” *Phys. Chem. Chem. Phys.*, vol. 12, no. 10, pp. 2427–2437, Feb. 2010, doi: 10.1039/B919644G.
[23] B. Shukla and M. Koshi, “Comparative study on the growth mechanisms of PAHs,” *Combust. Flame*, vol. 158, no. 2, pp. 369–375, Feb. 2011, doi: 10.1016/j.combustflame.2010.09.012.
[24] A. Comandini and K. Brezinsky, “Theoretical study of the formation of naphthalene from the radical/π-bond addition between single-ring aromatic hydrocarbons,” *J. Phys. Chem. A*, vol. 115, no. 22, pp. 5547–5559, Jun. 2011, doi: 10.1021/jp200201c.
[25] B. Shukla, K. Tsuchiya, and M. Koshi, “Novel Products from C6H5 + C6H6/C6H5 Reactions,” *J. Phys. Chem. A*, vol. 115, no. 21, pp. 5284–5293, Jun. 2011, doi: 10.1021/jp201817n.
[26] A. Comandini, T. Malewicki, and K. Brezinsky, “Chemistry of Polycyclic Aromatic Hydrocarbons Formation from Phenyl Radical Pyrolysis and Reaction of Phenyl and Acetylene,” *J. Phys. Chem. A*, vol. 116, no. 10, pp. 2409–2434, Mar. 2012, doi: 10.1021/jp207461a.
[27] A. Comandini and K. Brezinsky, “Radical/π-Bond Addition between o-Benzyne and Cyclic C5 Hydrocarbons,” *J. Phys. Chem. A*, vol. 116, no. 4, pp. 1183–1190, Feb. 2012, doi: 10.1021/jp208368a.
[28] A. Comandini, S. Abid, and N. Chaumeix, “Polycyclic Aromatic Hydrocarbon Growth by Diradical Cycloaddition/Fragmentation,” *J. Phys. Chem. A*, vol. 121, no. 31, pp. 5921–5931, Aug. 2017, doi: 10.1021/acs.jpca.7b05562.
[29] R. Wellmann, A. Böttcher, M. Kappes, U. Kohl, and H. Niehus, “Growth of graphene layers on HOPG via exposure to methyl radicals,” *Surf. Sci.*, vol. 542, no. 1, pp. 81–93, Sep. 2003, doi: 10.1016/S0039-6028(03)00928-2.
[30] B. Shukla, A. Miyoshi, and M. Koshi, “Role of Methyl Radicals in the Growth of PAHs,” *J. Am. Soc. Mass Spectrom.*, vol. 21, no. 4, pp. 534–544, Apr. 2010, doi: 10.1016/j.jasms.2009.12.019.
[31] C. S. McENALLY and L. D. PFEFFERLE, “An Experimental Study in Non-Premixed Flames of Hydrocarbon Growth Processes that Involve Five-Membered Carbon Rings,” *Combust. Sci. Technol.*, vol. 131, no. 1–6, pp. 323–344, Jan. 1998, doi: 10.1080/00102209808935766.
[32] C. S. McEnally and L. D. Pfefferle, “Improved sooting tendency measurements for aromatic hydrocarbons and their implications for naphthalene formation pathways,” *Combust. Flame*, vol. 148, no. 4, pp. 210–222, Mar. 2007, doi: 10.1016/j.combustflame.2006.11.003.
[33] A. Lifshitz, C. Tamburu, A. Suslensky, and F. Dubnikova, “Decomposition, Isomerization, and Ring Expansion in 2-Methylindene: Single-pulse Shock Tube and Modeling Study,” *J. Phys. Chem. A*, vol. 108, no. 16, pp. 3430–3438, Apr. 2004, doi: 10.1021/jp031160a.
[34] M. J. Castaldi *et al.*, “Experimental and modeling investigation of aromatic and polycyclic aromatic hydrocarbon formation in a premixed ethylene flame,” *Symp. Int. Combust.*, vol. 26, no. 1, pp. 693–702, Jan. 1996, doi: 10.1016/S0082-0784(96)80277-3.
[35] M. Lu and J. A. Mulholland, “Aromatic hydrocarbon growth from indene,” *Chemosphere*, vol. 42, no. 5–7, pp. 625–633, Mar. 2001, doi: 10.1016/s0045-6535(00)00236-8.
[36] M. B. Colket and D. J. Seery, “Reaction mechanisms for toluene pyrolysis,” *Symp. Int. Combust.*, vol. 25, no. 1, pp. 883–891, Jan. 1994, doi: 10.1016/S0082-0784(06)80723-X.
[37] N. M. Marinov, W. J. Pitz, C. K. Westbrook, A. E. Lutz, A. M. Vincitore, and S. M. Senkan, “Chemical kinetic modeling of a methane opposed-flow diffusion flame and comparison to experiments,” *Symp. Int. Combust.*, vol. 27, no. 1, pp. 605–613, Jan. 1998, doi: 10.1016/S0082-0784(98)80452-9.
[38] K. H. Homann and H. Gg. Wagner, “Some new aspects of the mechanism of carbon formation in premixed flames,” *Symp. Int. Combust.*, vol. 11, no. 1, pp. 371–379, Jan. 1967, doi: 10.1016/S0082-0784(67)80161-9.

[39] H. Wang, M. Yao, Z. Yue, M. Jia, and R. D. Reitz, “A reduced toluene reference fuel chemical kinetic mechanism for combustion and polycyclic-aromatic hydrocarbon predictions,” *Combust. Flame*, vol. 162, no. 6, pp. 2390–2404, Jun. 2015, doi: 10.1016/j.combustflame.2015.02.005.
[40] B. V. Unterreiner, M. Sierka, and R. Ahlrichs, “Reaction pathways for growth of polycyclic aromatic hydrocarbons under combustion conditions, a DFT study,” *Phys. Chem. Chem. Phys.*, vol. 6, no. 18, pp. 4377–4384, Sep. 2004, doi: 10.1039/B407279K.
[41] A. M. Mebel, Y. Georgievskii, A. W. Jasper, and S. J. Klippenstein, “Pressure-dependent rate constants for PAH growth: formation of indene and its conversion to naphthalene,” *Faraday Discuss.*, vol. 195, no. 0, pp. 637–670, Jan. 2017, doi: 10.1039/C6FD00111D.
[42] A. N. Morozov and A. M. Mebel, “Theoretical study of the reaction mechanism and kinetics of the phenyl + propargyl association,” *Phys. Chem. Chem. Phys. PCCP*, vol. 22, no. 13, pp. 6868–6880, Apr. 2020, doi: 10.1039/d0cp00306a.
[43] L. Zhao *et al.*, “Molecular mass growth through ring expansion in polycyclic aromatic hydrocarbons via radical–radical reactions,” *Nat. Commun.*, vol. 10, no. 1, Art. no. 1, Aug. 2019, doi: 10.1038/s41467-019-11652-5.
[44] W. G. Lovell, “Knocking Characteristics of Hydrocarbons,” May 01, 2002. https://pubs.acs.org/doi/pdf/10.1021/ie50468a033 (accessed Apr. 04, 2020).
[45] C. S. McEnally, L. D. Pfefferle, B. Atakan, and K. Kohse-Höinghaus, “Studies of aromatic hydrocarbon formation mechanisms in flames: Progress towards closing the fuel gap,” *Prog. Energy Combust. Sci.*, vol. 32, no. 3, pp. 247–294, Jan. 2006, doi: 10.1016/j.pecs.2005.11.003.
[46] H. Richter, T. G. Benish, O. A. Mazyar, W. H. Green, and J. B. Howard, “Formation of polycyclic aromatic hydrocarbons and their radicals in a nearly sooting premixed benzene flame,” *Proc. Combust. Inst.*, vol. 28, no. 2, pp. 2609–2618, Jan. 2000, doi: 10.1016/S0082-0784(00)80679-7.
[47] K. C. Hou and H. B. Palmer, “The Kinetics of Thermal Decomposition of Benzene in a Flow System,” *J. Phys. Chem.*, vol. 69, no. 3, pp. 863–868, Mar. 1965, doi: 10.1021/j100887a027.
[48] R. D. Kern, H. J. Singh, M. A. Esslinger, and P. W. Winkeler, “Product profiles observed during the pyrolyses of toluene, benzene, butadiene, and acetylene,” *Symp. Int. Combust.*, vol. 19, no. 1, pp. 1351–1358, Jan. 1982, doi: 10.1016/S0082-0784(82)80311-1.
[49] H. Böhm, H. Jander, and D. Tanke, “PAH growth and soot formation in the pyrolysis of acetylene and benzene at high temperatures and pressures: Modeling and experiment,” *Symp. Int. Combust.*, vol. 27, no. 1, pp. 1605–1612, Jan. 1998, doi: 10.1016/S0082-0784(98)80570-5.
[50] A. Laskin and A. Lifshit, “Thermal decomposition of benene. Single-pulse shock-tube investigation,” *Symp. Int. Combust.*, vol. 26, no. 1, pp. 669–675, Jan. 1996, doi: 10.1016/S0082-0784(96)80274-8.
[51] R. Sivaramakrishnan, K. Brezinsky, and R. Tranter, “A shock-tube study of the high-pressure thermal decomposition of benzene,” *Combust. Sci. Technol.*, vol. 178, pp. 285–305, Jan. 2006, doi: 10.1080/00102200500292340.
[52] R. Sivaramakrishnan, R. S. Tranter, and K. Brezinsky, “A high pressure model for the oxidation of toluene,” *Proc. Combust. Inst.*, vol. 30, no. 1, pp. 1165–1173, Jan. 2005, doi: 10.1016/j.proci.2004.08.128.
[53] C. Horn, P. Frank, R. S. Tranter, J. Schaugg, H.-H. Grotheer, and T. Just, “Direct measurement of the reaction pair C6H5NO→C6H5+NO by a combined shock tube and flow reactor approach,” *Symp. Int. Combust.*, vol. 26, no. 1, pp. 575–582, Jan. 1996, doi: 10.1016/S0082-0784(96)80262-1.
[54] E. Heckmann, H. Hippler, and J. Troe, “High-temperature reactions and thermodynamic properties of phenyl radicals,” *Symp. Int. Combust.*, vol. 26, no. 1, pp. 543–550, Jan. 1996, doi: 10.1016/S0082-0784(96)80258-X.
[55] R. S. Tranter, S. J. Klippenstein, L. B. Harding, B. R. Giri, X. Yang, and J. H. Kiefer, “Experimental and Theoretical Investigation of the Self-Reaction of Phenyl Radicals,” *J. Phys. Chem. A*, vol. 114, no. 32, pp. 8240–8261, Aug. 2010, doi: 10.1021/jp1031064.

[56] C. Saggese, A. Frassoldati, A. Cuoci, T. Faravelli, and E. Ranzi, “A wide range kinetic modeling study of pyrolysis and oxidation of benzene,” *Combust. Flame*, vol. 160, no. 7, pp. 1168–1190, Jul. 2013, doi: 10.1016/j.combustflame.2013.02.013.
[57] E. Ranzi *et al.*, “Hierarchical and comparative kinetic modeling of laminar flame speeds of hydrocarbon and oxygenated fuels,” *Prog. Energy Combust. Sci.*, vol. 38, no. 4, pp. 468–501, Aug. 2012, doi: 10.1016/j.pecs.2012.03.004.
[58] S. Sinha and A. Raj, “Polycyclic aromatic hydrocarbon (PAH) formation from benzyl radicals: a reaction kinetics study,” *Phys. Chem. Chem. Phys.*, vol. 18, no. 11, pp. 8120–8131, Mar. 2016, doi: 10.1039/C5CP06465A.
[59] R. D. Smith, “A direct mass spectrometric study of the mechanism of toluene pyrolysis at high temperatures,” *J. Phys. Chem.*, vol. 83, no. 12, pp. 1553–1563, Jun. 1979, doi: 10.1021/j100475a001.
[60] K. M. Pamidimukkala, R. D. Kern, M. R. Patel, H. C. Wei, and J. H. Kiefer, “High-temperature pyrolysis of toluene,” *J. Phys. Chem.*, vol. 91, no. 8, pp. 2148–2154, Apr. 1987, doi: 10.1021/j100292a034.
[61] R. Sivaramakrishnan, R. S. Tranter, and K. Brezinsky, “High Pressure Pyrolysis of Toluene. 1. Experiments and Modeling of Toluene Decomposition,” *J. Phys. Chem. A*, vol. 110, no. 30, pp. 9388–9399, Aug. 2006, doi: 10.1021/jp060820j.
[62] R. Sivaramakrishnan, R. S. Tranter, and K. Brezinsky, “High Pressure Pyrolysis of Toluene. 2. Modeling Benzyl Decomposition and Formation of Soot Precursors,” *J. Phys. Chem. A*, vol. 110, no. 30, pp. 9400–9404, Aug. 2006, doi: 10.1021/jp0608224.
[63] B. Shukla, A. Susa, A. Miyoshi, and M. Koshi, “In Situ Direct Sampling Mass Spectrometric Study on Formation of Polycyclic Aromatic Hydrocarbons in Toluene Pyrolysis,” *J. Phys. Chem. A*, vol. 111, no. 34, pp. 8308–8324, Aug. 2007, doi: 10.1021/jp071813d.
[64] T. Zhang *et al.*, “An experimental and theoretical study of toluene pyrolysis with tunable synchrotron VUV photoionization and molecular-beam mass spectrometry,” *Combust. Flame*, vol. 156, no. 11, pp. 2071–2083, Nov. 2009, doi: 10.1016/j.combustflame.2009.06.001.
[65] L. Zhang, J. Cai, T. Zhang, and F. Qi, “Kinetic modeling study of toluene pyrolysis at low pressure,” *Combust. Flame*, vol. 157, pp. 1686–1697, Sep. 2010, doi: 10.1016/j.combustflame.2010.04.002.
[66] A. Matsugi and A. Miyoshi, “Modeling of two- and three-ring aromatics formation in the pyrolysis of toluene,” *Proc. Combust. Inst.*, vol. 34, no. 1, pp. 269–277, Jan. 2013, doi: 10.1016/j.proci.2012.06.032.
[67] A. Matsugi and A. Miyoshi, “Computational study on the recombination reaction between benzyl and propargyl radicals,” *Int. J. Chem. Kinet.*, vol. 44, no. 3, pp. 206–218, 2012, doi: 10.1002/kin.20625.
[68] A. Matsugi and A. Miyoshi, “Reactions of o-benzyne with propargyl and benzyl radicals: potential sources of polycyclic aromatic hydrocarbons in combustion,” *Phys. Chem. Chem. Phys.*, vol. 14, no. 27, pp. 9722–9728, Jun. 2012, doi: 10.1039/C2CP41002H.
[69] B. Shukla, A. Susa, A. Miyoshi, and M. Koshi, “Role of Phenyl Radicals in the Growth of Polycyclic Aromatic Hydrocarbons,” *J. Phys. Chem. A*, vol. 112, no. 11, pp. 2362–2369, Mar. 2008, doi: 10.1021/jp7098398.
[70] W. Yuan, Y. Li, P. Dagaut, J. Yang, and F. Qi, “Investigation on the pyrolysis and oxidation of toluene over a wide range conditions. I. Flow reactor pyrolysis and jet stirred reactor oxidation,” *Combust. Flame*, vol. 162, no. 1, pp. 3–21, Jan. 2015, doi: 10.1016/j.combustflame.2014.07.009.
[71] W. Yuan, Y. Li, P. Dagaut, J. Yang, and F. Qi, “Investigation on the pyrolysis and oxidation of toluene over a wide range conditions. II. A comprehensive kinetic modeling study,” *Combust. Flame*, vol. 162, no. 1, pp. 22–40, Jan. 2015, doi: 10.1016/j.combustflame.2014.07.011.
[72] T. A. Litzinger, K. Brezinsky, and I. Glassman, “The oxidation of ethylbenzene near 1060K,” *Combust. Flame*, vol. 63, no. 1, pp. 251–267, Jan. 1986, doi: 10.1016/0010-2180(86)90125-2.

[73] W. Yuan, Y. Li, G. Pengloan, C. Togbé, P. Dagaut, and F. Qi, “A comprehensive experimental and kinetic modeling study of ethylbenzene combustion,” *Combust. Flame*, vol. 166, pp. 255–265, Apr. 2016, doi: 10.1016/j.combustflame.2016.01.026.
[74] W. Yuan, Y. Li, P. Dagaut, Y. Wang, Z. Wang, and F. Qi, “A comprehensive experimental and kinetic modeling study of n-propylbenzene combustion,” *Combust. Flame*, vol. 186, pp. 178–192, Dec. 2017, doi: 10.1016/j.combustflame.2017.08.010.
[75] W. Yuan *et al.*, “Experimental and kinetic modeling study of premixed n-butylbenzene flames,” *Proc. Combust. Inst.*, vol. 36, no. 1, pp. 815–823, Jan. 2017, doi: 10.1016/j.proci.2016.06.049.
[76] W. Mueller-Markgraf and J. Troe, “Thermal decomposition of ethylbenzene, styrene, and bromophenylethane: UV absorption study in shock waves,” *J. Phys. Chem.*, vol. 92, no. 17, pp. 4914–4922, Aug. 1988, doi: 10.1021/j100328a022.
[77] M. A. Grela, V. T. Amorebieta, and A. J. Colussi, “Pyrolysis of styrene: kinetics and mechanism of the equilibrium styrene .tautm. benzene + acetylene,” *J. Phys. Chem.*, vol. 96, no. 24, pp. 9861–9865, Nov. 1992, doi: 10.1021/j100203a052.
[78] W. Yuan, Y. Li, P. Dagaut, J. Yang, and F. Qi, “Experimental and kinetic modeling study of styrene combustion,” *Combust. Flame*, vol. 162, no. 5, pp. 1868–1883, May 2015, doi: 10.1016/j.combustflame.2014.12.008.
[79] A. Comandini, G. Pengloan, S. Abid, and N. Chaumeix, “Experimental and modeling study of styrene oxidation in spherical reactor and shock tube,” *Combust. Flame*, vol. 173, pp. 425–440, Nov. 2016, doi: 10.1016/j.combustflame.2016.08.026.
[80] W. K. Metcalfe, S. Dooley, and F. L. Dryer, “Comprehensive Detailed Chemical Kinetic Modeling Study of Toluene Oxidation,” *Energy Fuels*, vol. 25, no. 11, pp. 4915–4936, Nov. 2011, doi: 10.1021/ef200900q.
[81] J. Herzler and P. Frank, “High Temperature Reactions of Phenylacetylene,” *Berichte Bunsenges. Für Phys. Chem.*, vol. 96, no. 10, pp. 1333–1338, 1992, doi: 10.1002/bbpc.19920961003.
[82] Z. Li, P. Liu, P. Zhang, H. He, S. H. Chung, and W. L. Roberts, “Theoretical Study of PAH Growth by Phenylacetylene Addition,” *J. Phys. Chem. A*, vol. 123, no. 47, pp. 10323–10332, Nov. 2019, doi: 10.1021/acs.jpca.9b09450.
[83] M. Szwarc, “The C–C Bond Energy in Ethylbenzene,” *J. Chem. Phys.*, vol. 17, no. 5, pp. 431–435, May 1949, doi: 10.1063/1.1747283.
[84] E. H. Lee and G. D. Oliver, “Calculating Homogeneous Reaction Rates and Orders in a Flowing Gas Reactor. Thermal Decomposition of Ethylbenzene,” Nov. 01, 1959. https://pubs.acs.org/doi/pdf/10.1021/ie50599a024 (accessed Apr. 09, 2020).
[85] G. L. Esteban, J. A. Kerr, and A. F. Trotman-Dickenson, “719. Pyrolysis of ethyl-, n-propyl-, and n-butyl-benzene and the heats of formation of the benzyl and n-propyl radicals,” *J. Chem. Soc. Resumed*, no. 0, pp. 3873–3879, Jan. 1963, doi: 10.1039/JR9630003873.
[86] E. D. Hausmann and C. J. King, “Pyrolysis of Ethylbenzene with and without Oxygen Initiation,” *Ind. Eng. Chem. Fundam.*, vol. 5, no. 3, pp. 295–301, Aug. 1966, doi: 10.1021/i160019a002.
[87] C. W. P. Crowne, V. J. Grigulis, and J. J. Throssell, “Pyrolysis of ethylbenzene by the toluene carrier method,” *Trans. Faraday Soc.*, vol. 65, no. 0, pp. 1051–1058, Jan. 1969, doi: 10.1039/TF9696501051.
[88] W. D. Clark and S. J. Price, “Free-radical and molecular processes in the pyrolysis of ethylbenzene,” *Can. J. Chem.*, vol. 48, no. 7, pp. 1059–1064, Apr. 1970, doi: 10.1139/v70-176.
[89] D. A. Robaugh and S. E. Stein, “Very-low-pressure pyrolysis of ethylbenzene, isopropylbenzene, and tert-butylbenzene,” *Int. J. Chem. Kinet.*, vol. 13, no. 5, pp. 445–462, 1981, doi: 10.1002/kin.550130503.
[90] H. G. Davis, “Rate of formation of toluene from ethylbenzene,” *Int. J. Chem. Kinet.*, vol. 15, no. 5, pp. 469–474, 1983, doi: 10.1002/kin.550150507.
[91] L. Brouwer, W. Müller-Markgraf, and J. Troe, “Thermal Decomposition of Ethylbenzene in Shock Waves,” *Berichte Bunsenges. Für Phys. Chem.*, vol. 87, no. 11, pp. 1031–1036, 1983, doi: 10.1002/bbpc.19830871114.

[92] V. S. Rao and G. B. Skinner, “Formation of hydrogen atoms in pyrolysis of ethylbenzene behind shock waves. Rate constants for the thermal dissociation of the benzyl radical,” *Symp. Int. Combust.*, vol. 21, no. 1, pp. 809–814, Jan. 1988, doi: 10.1016/S0082-0784(88)80312-6.
[93] L. J. Mizerka and J. H. Kiefer, “The high temperature pyrolysis of ethylbenzene: Evidence for dissociation to benzyl and methyl radicals,” *Int. J. Chem. Kinet.*, vol. 18, no. 3, pp. 363–378, 1986, doi: 10.1002/kin.550180309.
[94] C. T. Brooks, S. J. Peacock, and B. G. Reuben, “Pyrolysis of ethylbenzene,” *J. Chem. Soc. Faraday Trans. 1 Phys. Chem. Condens. Phases*, vol. 78, no. 11, pp. 3187–3202, Jan. 1982, doi: 10.1039/F19827803187.
[95] K. M. Pamidimukkala and R. D. Kern, “The high temperature pyrolysis of ethylbenzene,” *Int. J. Chem. Kinet.*, vol. 18, no. 12, pp. 1341–1353, 1986, doi: 10.1002/kin.550181206.
[96] O. S. L. Bruinsma and J. A. Moulijn, “The pyrolytic formation of polycyclic aromatic hydrocarbons from benzene, toluene, ethylbenze,e, styrene, phenylacetylene and n-decane in relation to fossil fuels utilization,” *Fuel Process. Technol.*, vol. 18, no. 3, pp. 213–236, May 1988, doi: 10.1016/0378-3820(88)90048-3.
[97] S. Dooley *et al.*, “A jet fuel surrogate formulated by real fuel properties,” *Combust. Flame*, vol. 157, no. 12, pp. 2333–2339, Dec. 2010, doi: 10.1016/j.combustflame.2010.07.001.
[98] C. H. Leigh and M. Szwarc, “The Pyrolysis of n-Propyl-Benzene and the Heat of Formation of Ethyl Radical,” *J. Chem. Phys.*, vol. 20, no. 3, pp. 403–406, Mar. 1952, doi: 10.1063/1.1700433.
[99] D. A. Robaugh, B. D. Barton, and S. E. Stein, “Thermal decomposition of propyl-, isobutyl-, and neopentylbenzene,” *J. Phys. Chem.*, vol. 85, no. 16, pp. 2378–2383, Aug. 1981, doi: 10.1021/j150616a017.
[100] Q. Chen and G. F. Froment, “Thermal cracking of substituted aromatic hydrocarbons. II. Kinetic study of the thermal cracking of n-propylbenzene and ethylbenzene,” *J. Anal. Appl. Pyrolysis*, vol. 21, no. 1, pp. 51–77, Sep. 1991, doi: 10.1016/0165-2370(91)80015-Z.
[101] S. Gudiyella and K. Brezinsky, “The high pressure study of n-propylbenzene pyrolysis,” *Proc. Combust. Inst.*, vol. 34, no. 1, pp. 1767–1774, Jan. 2013, doi: 10.1016/j.proci.2012.05.007.
[102] S. Gudiyella and K. Brezinsky, “High pressure study of n-propylbenzene oxidation,” *Combust. Flame*, vol. 159, no. 3, pp. 940–958, Mar. 2012, doi: 10.1016/j.combustflame.2011.09.013.
[103] M. Colket *et al.*, “Development of an Experimental Database and Kinetic Models for Surrogate Jet Fuels,” *AIAA*, vol. 14, Jan. 2007, doi: 10.2514/6.2007-770.
[104] W. J. Pitz and C. J. Mueller, “Recent progress in the development of diesel surrogate fuels,” *Prog. Energy Combust. Sci.*, vol. 37, no. 3, pp. 330–350, Jun. 2011, doi: 10.1016/j.pecs.2010.06.004.
[105] H. Nakamura *et al.*, “An experimental and modeling study of shock tube and rapid compression machine ignition of n-butylbenzene/air mixtures,” *Combust. Flame*, vol. 161, no. 1, pp. 49–64, Jan. 2014, doi: 10.1016/j.combustflame.2013.08.002.
[106] M. Ribaucour, A. Roubaud, R. Minetti, and L. R. Sochet, “The low-temperature autoignition of alkylaromatics: Experimental study and modeling of the oxidation of n-butylbenzene,” *Proc. Combust. Inst.*, vol. 28, no. 2, pp. 1701–1707, Jan. 2000, doi: 10.1016/S0082-0784(00)80570-6.
[107] A. Roubaud, O. Lemaire, R. Minetti, and L. R. Sochet, “High pressure auto-ignition and oxidation mechanisms of o-xylene, o-ethyltoluene, and n-butylbenzene between 600 and 900 K,” *Combust. Flame*, vol. 123, no. 4, pp. 561–571, Dec. 2000, doi: 10.1016/S0010-2180(00)00174-7.
[108] D. Darcy *et al.*, “A high pressure shock tube study of n-propylbenzene oxidation and its comparison with n-butylbenzene,” *Combust. Flame*, vol. 159, no. 7, pp. 2219–2232, Jul. 2012, doi: 10.1016/j.combustflame.2012.02.009.
[109] A. Comandini, T. Dubois, and N. Chaumeix, “Autoignition of n-Decane/n-Butylbenzene/n-Propylcyclohexane Mixtures and the Effects of the Exhaust Gas Recirculation,” *Combust. Sci. Technol.*, vol. 186, no. 10–11, pp. 1536–1551, Nov. 2014, doi: 10.1080/00102202.2014.935222.
[110] M. Mehl *et al.*, “Experimental and modeling study of burning velocities for alkyl aromatic components relevant to diesel fuels,” *Proc. Combust. Inst.*, vol. 35, no. 1, pp. 341–348, Jan. 2015, doi: 10.1016/j.proci.2014.06.064.

[111] A. Comandini, T. Dubois, and N. Chaumeix, “Laminar flame speeds of n-decane, n-butylbenzene, and n-propylcyclohexane mixtures,” *Proc. Combust. Inst.*, vol. 35, no. 1, pp. 671–678, Jan. 2015, doi: 10.1016/j.proci.2014.05.125.
[112] K. Brezinsky, G. T. Linteris, T. A. Litzinger, and I. Glassman, “High temperature oxidation of n-alkyl benzenes,” *Symp. Int. Combust.*, vol. 21, no. 1, pp. 833–840, Jan. 1988, doi: 10.1016/S0082-0784(88)80315-1.
[113] P. Diévart and P. Dagaut, “The oxidation of n-butylbenzene: Experimental study in a JSR at 10atm and detailed chemical kinetic modeling,” *Proc. Combust. Inst.*, vol. 33, no. 1, pp. 209–216, Jan. 2011, doi: 10.1016/j.proci.2010.05.013.
[114] B. Husson *et al.*, “Experimental and modeling study of the oxidation of n-butylbenzene,” *Combust. Flame*, vol. 159, no. 4, pp. 1399–1416, Apr. 2012, doi: 10.1016/j.combustflame.2011.12.006.
[115] J. Yu and S. Eser, “Thermal Decomposition of Jet Fuel Model Compounds under Near-Critical and Supercritical Conditions. 1. n-Butylbenzene and n-Butylcyclohexane,” *Ind. Eng. Chem. Res.*, vol. 37, no. 12, pp. 4591–4600, Dec. 1998, doi: 10.1021/ie980303q.
[116] D. Belisario-Lara, A. M. Mebel, and R. I. Kaiser, “Computational Study on the Unimolecular Decomposition of JP-8 Jet Fuel Surrogates III: Butylbenzene Isomers (n-, s-, and t-C14H10),” *J. Phys. Chem. A*, vol. 122, no. 16, pp. 3980–4001, Apr. 2018, doi: 10.1021/acs.jpca.8b01836.
[117] H. Freund and W. N. Olmstead, “Detailed chemical kinetic modeling of butylbenzene pyrolysis,” *Int. J. Chem. Kinet.*, vol. 21, no. 7, pp. 561–574, 1989, doi: 10.1002/kin.550210707.
[118] Y. Zhang *et al.*, “Pyrolysis of n-Butylbenzene at Various Pressures: Influence of Long Side-Chain Structure on Alkylbenzene Pyrolysis,” *Energy Fuels*, vol. 31, no. 12, pp. 14270–14279, Dec. 2017, doi: 10.1021/acs.energyfuels.7b02855.
[119] S. M. Lee, S. S. Yoon, and S. H. Chung, “Synergistic effect on soot formation in counterflow diffusion flames of ethylene–propane mixtures with benzene addition,” *Combust. Flame*, vol. 136, no. 4, pp. 493–500, Mar. 2004, doi: 10.1016/j.combustflame.2003.12.005.
[120] J. Y. Hwang, W. Lee, H. G. Kang, and S. H. Chung, “Synergistic Effect of Ethylene–Propane Mixture on Soot Formation in Laminar Diffusion Flames,” *Combust. Flame*, vol. 114, no. 3, pp. 370–380, Aug. 1998, doi: 10.1016/S0010-2180(97)00295-2.
[121] S. S. Yoon, S. M. Lee, and S. H. Chung, “Effect of mixing methane, ethane, propane, and propene on the synergistic effect of PAH and soot formation in ethylene-base counterflow diffusion flames,” *Proc. Combust. Inst.*, vol. 30, no. 1, pp. 1417–1424, Jan. 2005, doi: 10.1016/j.proci.2004.08.038.
[122] N. B. Poddar, S. Thomas, and M. J. Wornat, “Polycyclic aromatic hydrocarbons from the co-pyrolysis of 1,3-butadiene and propyne,” *Proc. Combust. Inst.*, vol. 34, no. 1, pp. 1775–1783, Jan. 2013, doi: 10.1016/j.proci.2012.05.013.
[123] C. Shao, G. Kukkadapu, S. W. Wagnon, W. J. Pitz, and S. M. Sarathy, “PAH formation from jet stirred reactor pyrolysis of gasoline surrogates,” *Combust. Flame*, vol. 219, pp. 312–326, Sep. 2020, doi: 10.1016/j.combustflame.2020.06.001.
[124] V. G. Knorre, D. Tanke, Th. Thienel, and H. Gg. Wagner, “Soot formation in the pyrolysis of bezene/acetylene and acetylene/hydrogen mixtures at high carbon concentrations,” *Symp. Int. Combust.*, vol. 26, no. 2, pp. 2303–2310, Jan. 1996, doi: 10.1016/S0082-0784(96)80058-0.
[125] T. Li *et al.*, “Unraveling synergistic effects on pyrolysis reactivity and indene formation in co-pyrolysis of toluene and acetylene,” *Proc. Combust. Inst.*, vol. 38, no. 1, pp. 1413–1421, Jan. 2021, doi: 10.1016/j.proci.2020.06.176.
[126] A. G. Gaydon and I. R. Hurle, *The Shock Tube in High-Temperature Chemical Physics*. Springer US, 1963. Accessed: Mar. 26, 2020. [Online]. Available: https://www.springer.com/gp/book/9781504121712
[127] G. Ben-Dor, O. Igra, and T. Elperin, *Handbook of Shock Waves, Three Volume Set*, 1st ed. Academic Press, 2000.

[128] K. A. Bhaskaran and P. Roth, “The shock tube as wave reactor for kinetic studies and material systems,” *Prog. Energy Combust. Sci.*, vol. 28, pp. 151–192, Mar. 2002, doi: 10.1016/S0360-1285(01)00011-9.
[129] W. J. M. Rankine, “XV. On the thermodynamic theory of waves of finite longitudinal disturbance,” *Philos. Trans. R. Soc. Lond.*, vol. 160, pp. 277–288, Jan. 1870, doi: 10.1098/rstl.1870.0015.
[130] P. H. Hugoniot, “Sur la Propagation du Mouvement dans les Corps et Spécialement dans les Gaz Parfaits (première partie),” *J. Ecole Polytech.*, vol. 57, pp. 3–97, 1887.
[131] P. H. Hugoniot, “Sur la Propagation du Mouvement dans les Corps et Spécialement dans les Gaz Parfaits (deuxième partie),” *J. Ecole Polytech*, vol. 58, pp. 1–125, 1889.
[132] A. Lifshitz, S. H. Bauer, and E. L. Resler, “Studies with a Single-Pulse Shock Tube. I. The Cis—Trans Isomerization of Butene-2,” *J. Chem. Phys.*, vol. 38, no. 9, pp. 2056–2063, May 1963, doi: 10.1063/1.1733933.
[133] F. Battin-Leclerc, J. M. Simmie, and E. Blurock, Eds., *Cleaner Combustion: Developing Detailed Chemical Kinetic Models*. London: Springer-Verlag, 2013. doi: 10.1007/978-1-4471-5307-8.
[134] R. S. Tranter, K. Brezinsky, and D. Fulle, “Design of a high-pressure single pulse shock tube for chemical kinetic investigations,” *Rev. Sci. Instrum.*, vol. 72, no. 7, pp. 3046–3054, Jun. 2001, doi: 10.1063/1.1379963.
[135] A. Lifshitz, “The single pulse shock tube: its Odyssey in chemical kinetics,” in *Shock Waves*, Berlin, Heidelberg, 2005, pp. 57–64. doi: 10.1007/978-3-540-27009-6_6.
[136] Y. Hidaka, S. Shiba, H. Takuma, and M. Suga, “Thermal decomposition of ethane in shock waves,” *Int. J. Chem. Kinet.*, vol. 17, no. 4, pp. 441–453, 1985, doi: 10.1002/kin.550170410.
[137] W. Tang and K. Brezinsky, “Chemical kinetic simulations behind reflected shock waves,” *Int. J. Chem. Kinet.*, vol. 38, no. 2, pp. 75–97, 2006, doi: 10.1002/kin.20134.
[138] W. Sun, A. Hamadi, S. Abid, N. Chaumeix, and A. Comandini, “Probing PAH formation chemical kinetics from benzene and toluene pyrolysis in a single-pulse shock tube,” *Proc. Combust. Inst.*, vol. 38, no. 1, pp. 891–900, Jan. 2021, doi: 10.1016/j.proci.2020.06.077.
[139] J. N. Bradley and G. B. Kistiakowsky, “Shock Wave Studies by Mass Spectrometry. I. Thermal Decomposition of Nitrous Oxide,” *J. Chem. Phys.*, vol. 35, no. 1, pp. 256–263, Jul. 1961, doi: 10.1063/1.1731897.
[140] W. Sun, A. Hamadi, S. Abid, N. Chaumeix, and A. Comandini, “A comprehensive kinetic study on the speciation from propylene and propyne pyrolysis in a single-pulse shock tube,” *Combust. Flame*, vol. 231, p. 111485, Sep. 2021, doi: 10.1016/j.combustflame.2021.111485.
[141] W. Sun, A. Hamadi, S. Abid, N. Chaumeix, and A. Comandini, “Influences of propylene/propyne addition on toluene pyrolysis in a single-pulse shock tube,” *Combust. Flame*, vol. 236, p. 111799, Feb. 2022, doi: 10.1016/j.combustflame.2021.111799.
[142] A. Comandini, T. Malewicki, and K. Brezinsky, “Online and offline experimental techniques for polycyclic aromatic hydrocarbons recovery and measurement,” *Rev. Sci. Instrum.*, vol. 83, no. 3, p. 034101, Mar. 2012, doi: 10.1063/1.3692748.
[143] W. Sun, A. Hamadi, S. Abid, N. Chaumeix, and A. Comandini, “A comprehensive kinetic study on the speciation from propylene and propyne pyrolysis in a single-pulse shock tube.”
[144] H. J. Curran, P. Gaffuri, W. J. Pitz, and C. K. Westbrook, “A Comprehensive Modeling Study of n-Heptane Oxidation,” *Combust. Flame*, vol. 114, no. 1, pp. 149–177, Jul. 1998, doi: 10.1016/S0010-2180(97)00282-4.
[145] H Wang, E Dames, B Sirjean, DA Sheen, R Tangko, A Violi, JYW Lai, FN Egolfopoulos, DF Davidson, RK Hanson, CT Bowman, CK Law, W Tsang, NP Cernansky, DL Miller, RP Lindstedt, “A hightemperature chemical kinetic model of n-alkane (up to n-dodecane), cyclohexane, and methyl-, ethyl-, n-propyl and n-butyl-cyclohexane oxidation at high temperatures,” *JetSurF version*, vol. 2, p. 19, Oct. 2010.

[146] W. Pejpichestakul *et al.*, “Examination of a soot model in premixed laminar flames at fuel-rich conditions,” *Proc. Combust. Inst.*, vol. 37, no. 1, pp. 1013–1021, Jan. 2019, doi: 10.1016/j.proci.2018.06.104.
[147] R. J. Kee, F. M. Rupley, and J. A. Miller, “The Chemkin Thermodynamic Data Base,” *Unknown*, Mar. 1990, Accessed: May 20, 2021. [Online]. Available: http://adsabs.harvard.edu/abs/1990ctdb.rept.....K
[148] M. W. Chase, “NIST-JANAF Thermochemical Tables, 4th Edition,” Aug. 1998, Accessed: May 20, 2021. [Online]. Available: https://www.nist.gov/publications/nist-janaf-thermochemical-tables-4th-edition
[149] “Burcat’s Thermodynamic Data.” http://garfield.chem.elte.hu/Burcat/burcat.html (accessed May 20, 2021).
[150] E. R. Ritter and J. W. Bozzelli, “THERM: Thermodynamic property estimation for gas phase radicals and molecules,” *Int. J. Chem. Kinet.*, vol. 23, no. 9, pp. 767–778, 1991, doi: https://doi.org/10.1002/kin.550230903.
[151] “SoftPredict - Provider of Cosilab Software and Related Services for Chemically Reactive Flow,” Aug. 20, 2006. https://web.archive.org/web/20060820105242/http://www.softpredict.com/?page=5 (accessed Apr. 23, 2020).
[152] X. Han, J. M. Mehta, and K. Brezinsky, “Temperature approximations in chemical kinetics studies using single pulse shock tubes,” 2019, doi: 10.1016/J.COMBUSTFLAME.2019.07.022.
[153] J. A. Manion, D. A. Sheen, and I. A. Awan, “Evaluated Kinetics of the Reactions of H and CH3 with n-Alkanes: Experiments with n-Butane and a Combustion Model Reaction Network Analysis,” *J. Phys. Chem. A*, vol. 119, no. 28, pp. 7637–7658, Jul. 2015, doi: 10.1021/acs.jpca.5b01004.
[154] L. A. Mertens, I. A. Awan, D. A. Sheen, and J. A. Manion, “Evaluated Site-Specific Rate Constants for Reaction of Isobutane with H and CH3: Shock Tube Experiments Combined with Bayesian Model Optimization,” *J. Phys. Chem. A*, vol. 122, no. 49, pp. 9518–9541, Dec. 2018, doi: 10.1021/acs.jpca.8b08781.
[155] T. Malewicki and K. Brezinsky, “Experimental and modeling study on the pyrolysis and oxidation of n-decane and n-dodecane,” *Proc. Combust. Inst.*, vol. 34, no. 1, pp. 361–368, Jan. 2013, doi: 10.1016/j.proci.2012.06.156.
[156] H. Wang *et al.*, “A physics-based approach to modeling real-fuel combustion chemistry - I. Evidence from experiments, and thermodynamic, chemical kinetic and statistical considerations,” *Combust. Flame*, vol. 193, pp. 502–519, Jul. 2018, doi: 10.1016/j.combustflame.2018.03.019.
[157] H. Wang, X. You, A.V. Joshi, S.G. Davis, A. Laskin, F. Egolfopoulos, C.K. Law, “High-temperature combustion reaction model of H2. Reaction Model of H2/CO/C1-C4 Compounds, Version II, USC Mech,” May 2007, [Online]. Available: http://ignis.usc.edu/USC_Mech_II.htm
[158] K. Raghavachari, M. J. Frisch, J. A. Pople, and P. von R. Schleyer, “The ground-state singlet potential surface for C2H4,” *Chem. Phys. Lett.*, vol. 85, no. 2, pp. 145–149, Jan. 1982, doi: 10.1016/0009-2614(82)80319-9.
[159] J. H. Jensen, K. Morokuma, and M. S. Gordon, “Pathways for H2 elimination from ethylene: A theoretical study,” *J. Chem. Phys.*, vol. 100, no. 3, pp. 1981–1987, Feb. 1994, doi: 10.1063/1.466550.
[160] D. L. Baulch *et al.*, “Evaluated kinetic data for combustion modelling. Supplement 1,” *J. Phys. Chem. Ref. Data*, vol. 23, no. 6, Nov. 1994, doi: 10.1063/1.555953.
[161] S. J. Klippenstein and J. A. Miller, “From the Time-Dependent, Multiple-Well Master Equation to Phenomenological Rate Coefficients,” *J. Phys. Chem. A*, vol. 106, no. 40, pp. 9267–9277, Oct. 2002, doi: 10.1021/jp021175t.
[162] J. A. Miller, J. P. Senosiain, S. J. Klippenstein, and Y. Georgievskii, “Reactions over Multiple, Interconnected Potential Wells: Unimolecular and Bimolecular Reactions on a C3H5 Potential,” *J. Phys. Chem. A*, vol. 112, no. 39, pp. 9429–9438, Oct. 2008, doi: 10.1021/jp804510k.

[163] J. A. Miller and S. J. Klippenstein, “Dissociation of Propyl Radicals and Other Reactions on a C3H7 Potential,” *J. Phys. Chem. A*, vol. 117, no. 13, pp. 2718–2727, Apr. 2013, doi: 10.1021/jp312712p.
[164] L. Ye, Y. Georgievskii, and S. J. Klippenstein, “Pressure-dependent branching in the reaction of 1CH2 with C2H4 and other reactions on the C3H6 potential energy surface,” *Proc. Combust. Inst.*, vol. 35, no. 1, pp. 223–230, Jan. 2015, doi: 10.1016/j.proci.2014.05.097.
[165] D. Polino, S. J. Klippenstein, L. B. Harding, and Y. Georgievskii, “Predictive theory for the addition and insertion kinetics of 1CH2 reacting with unsaturated hydrocarbons,” *J. Phys. Chem. A*, vol. 117, no. 48, pp. 12677–12692, Dec. 2013, doi: 10.1021/jp406246y.
[166] J. A. Miller and S. J. Klippenstein, “The Recombination of Propargyl Radicals and Other Reactions on a C6H6 Potential,” *J. Phys. Chem. A*, vol. 107, no. 39, pp. 7783–7799, Oct. 2003, doi: 10.1021/jp030375h.
[167] A. W. Jasper and N. Hansen, “Hydrogen-assisted isomerizations of fulvene to benzene and of larger cyclic aromatic hydrocarbons,” *Proc. Combust. Inst.*, vol. 34, no. 1, pp. 279–287, Jan. 2013, doi: 10.1016/j.proci.2012.06.165.
[168] N. Hansen *et al.*, “Isomer-specific combustion chemistry in allene and propyne flames,” *Combust. Flame*, vol. 156, no. 11, pp. 2153–2164, Nov. 2009, doi: 10.1016/j.combustflame.2009.07.014.
[169] Y. Hidaka, T. Nakamura, A. Miyauchi, T. Shiraishi, and H. Kawano, “Thermal decomposition of propyne and allene in shock waves,” *Int. J. Chem. Kinet.*, vol. 21, no. 8, pp. 643–666, 1989, doi: 10.1002/kin.550210805.
[170] P. T. Lynch, C. J. Annesley, C. J. Aul, X. Yang, and R. S. Tranter, “Recombination of Allyl Radicals in the High Temperature Fall-Off Regime,” *J. Phys. Chem. A*, vol. 117, no. 23, pp. 4750–4761, Jun. 2013, doi: 10.1021/jp402484v.
[171] A. Fridlyand, P. T. Lynch, R. S. Tranter, and K. Brezinsky, “Single Pulse Shock Tube Study of Allyl Radical Recombination,” *J. Phys. Chem. A*, vol. 117, no. 23, pp. 4762–4776, Jun. 2013, doi: 10.1021/jp402391n.
[172] K. Wang, S. M. Villano, and A. M. Dean, “Reactions of allylic radicals that impact molecular weight growth kinetics,” *Phys. Chem. Chem. Phys.*, vol. 17, no. 9, pp. 6255–6273, Feb. 2015, doi: 10.1039/C4CP05308G.
[173] K. Wang, S. M. Villano, and A. M. Dean, “Fundamentally-based kinetic model for propene pyrolysis,” *Combust. Flame*, vol. 162, no. 12, pp. 4456–4470, Dec. 2015, doi: 10.1016/j.combustflame.2015.08.012.
[174] S. Sharma and W. H. Green, “Computed rate coefficients and product yields for c-C5H5 + CH3 --> products,” *J. Phys. Chem. A*, vol. 113, no. 31, pp. 8871–8882, Aug. 2009, doi: 10.1021/jp900679t.
[175] V. S. Krasnoukhov, D. P. Porfiriev, I. P. Zavershinskiy, V. N. Azyazov, and A. M. Mebel, “Kinetics of the CH3 + C5H5 Reaction: A Theoretical Study,” *J. Phys. Chem. A*, vol. 121, no. 48, pp. 9191–9200, Dec. 2017, doi: 10.1021/acs.jpca.7b09873.
[176] G. da Silva, J. A. Cole, and J. W. Bozzelli, “Kinetics of the cyclopentadienyl + acetylene, fulvenallene + H, and 1-ethynylcyclopentadiene + H reactions,” *J. Phys. Chem. A*, vol. 114, no. 6, pp. 2275–2283, Feb. 2010, doi: 10.1021/jp906835w.
[177] C. Huang, B. Yang, and F. Zhang, “Initiation mechanism of 1,3-butadiene combustion and its effect on soot precursors,” *Combust. Flame*, vol. 184, pp. 167–175, Oct. 2017, doi: 10.1016/j.combustflame.2017.06.003.
[178] J. P. A. Lockhart, C. F. Goldsmith, J. B. Randazzo, B. Ruscic, and R. S. Tranter, “An Experimental and Theoretical Study of the Thermal Decomposition of C4H6 Isomers,” *J. Phys. Chem. A*, vol. 121, no. 20, pp. 3827–3850, May 2017, doi: 10.1021/acs.jpca.7b01186.
[179] T. V. Pham, H. T. Tue Trang, C. Tuan Ngo, and H. Minh Thi Nguyen, “A quantum chemical study of the mechanisms and kinetics of the reaction between propargyl (C3H3) and methyl (CH3) radicals,” *Chem. Phys. Lett.*, vol. 762, p. 138126, Jan. 2021, doi: 10.1016/j.cplett.2020.138126.

[180] J. Zádor, M. D. Fellows, and J. A. Miller, “Initiation Reactions in Acetylene Pyrolysis,” *J. Phys. Chem. A*, vol. 121, no. 22, pp. 4203–4217, Jun. 2017, doi: 10.1021/acs.jpca.7b03040.
[181] D. Trogolo, A. Maranzana, G. Ghigo, and G. Tonachini, “First Ring Formation by Radical Addition of Propargyl to But-1-ene-3-yne in Combustion. Theoretical Study of the C7H7 Radical System,” *J. Phys. Chem. A*, vol. 118, no. 2, pp. 427–440, Jan. 2014, doi: 10.1021/jp4082905.
[182] G. Ghigo, A. Maranzana, and G. Tonachini, “o-Benzyne fragmentation and isomerization pathways: a CASPT2 study,” *Phys. Chem. Chem. Phys.*, vol. 16, no. 43, pp. 23944–23951, Oct. 2014, doi: 10.1039/C4CP02582B.
[183] H. Wang and M. Frenklach, “Calculations of Rate Coefficients for the Chemically Activated Reactions of Acetylene with Vinylic and Aromatic Radicals,” *J. Phys. Chem.*, vol. 98, no. 44, pp. 11465–11489, Nov. 1994, doi: 10.1021/j100095a033.
[184] J. D. Bittner and J. B. Howard, “Composition profiles and reaction mechanisms in a near-sooting premixed benzene/oxygen/argon flame,” *Symp. Int. Combust.*, vol. 18, no. 1, pp. 1105–1116, Jan. 1981, doi: 10.1016/S0082-0784(81)80115-4.
[185] M. Frenklach, N. W. Moriarty, and N. J. Brown, “Hydrogen migration in polyaromatic growth,” *Symp. Int. Combust.*, vol. 27, no. 2, pp. 1655–1661, Jan. 1998, doi: 10.1016/S0082-0784(98)80004-0.
[186] A. M. Mebel, Y. Georgievskii, A. W. Jasper, and S. J. Klippenstein, “Temperature- and pressure-dependent rate coefficients for the HACA pathways from benzene to naphthalene,” *Proc. Combust. Inst.*, vol. 36, no. 1, pp. 919–926, Jan. 2017, doi: 10.1016/j.proci.2016.07.013.
[187] G. P. F. Wood, L. Radom, G. A. Petersson, E. C. Barnes, M. J. Frisch, and J. A. Montgomery, “A restricted-open-shell complete-basis-set model chemistry,” *J. Chem. Phys.*, vol. 125, no. 9, p. 094106, Sep. 2006, doi: 10.1063/1.2335438.
[188] J. A. Montgomery, M. J. Frisch, J. W. Ochterski, and G. A. Petersson, “A complete basis set model chemistry. VI. Use of density functional geometries and frequencies,” *J. Chem. Phys.*, vol. 110, no. 6, pp. 2822–2827, Jan. 1999, doi: 10.1063/1.477924.
[189] Y.-R. Luo, *Handbook of Bond Dissociation Energies in Organic Compounds*. CRC Press, 2002. doi: 10.1201/9781420039863.
[190] A. Fahr and S. E. Stein, “Reactions of vinyl and phenyl radicals with ethyne, ethene and benzene,” *Symp. Int. Combust.*, vol. 22, no. 1, pp. 1023–1029, Jan. 1989, doi: 10.1016/S0082-0784(89)80112-2.
[191] I. V. Tokmakov and M. C. Lin, “Reaction of Phenyl Radicals with Acetylene: Quantum Chemical Investigation of the Mechanism and Master Equation Analysis of the Kinetics,” *J. Am. Chem. Soc.*, vol. 125, no. 37, pp. 11397–11408, Sep. 2003, doi: 10.1021/ja0301121.
[192] H. Wang and M. Frenklach, “A detailed kinetic modeling study of aromatics formation in laminar premixed acetylene and ethylene flames,” *Combust. Flame*, vol. 110, no. 1, pp. 173–221, Jul. 1997, doi: 10.1016/S0010-2180(97)00068-0.
[193] W. Sun, A. Hamadi, S. Abid, N. Chaumeix, and A. Comandini, “An experimental and kinetic modeling study of phenylacetylene decomposition and the reactions with acetylene/ethylene under shock tube pyrolysis conditions,” *Combust. Flame*, vol. 220, pp. 257–271, Oct. 2020, doi: 10.1016/j.combustflame.2020.06.044.
[194] L. B. Tuli and A. M. Mebel, “Formation of phenanthrene via H-assisted isomerization of 2-ethynylbiphenyl produced in the reaction of phenyl with phenylacetylene,” *Int. J. Chem. Kinet.*, vol. 52, no. 12, pp. 875–883, 2020, doi: https://doi.org/10.1002/kin.21406.
[195] J. Park, S. Burova, A. S. Rodgers, and M. C. Lin, “Experimental and Theoretical Studies of the C6H5 + C6H6 Reaction,” *J. Phys. Chem. A*, vol. 103, no. 45, pp. 9036–9041, Nov. 1999, doi: 10.1021/jp9920592.
[196] I. V. Tokmakov and M. C. Lin, “Combined Quantum Chemical/RRKM-ME Computational Study of the Phenyl + Ethylene, Vinyl + Benzene, and H + Styrene Reactions,” *J. Phys. Chem. A*, vol. 108, no. 45, pp. 9697–9714, Nov. 2004, doi: 10.1021/jp049950n.

[197] R. K. Robinson and R. P. Lindstedt, “A comparative ab initio study of hydrogen abstraction from n-propyl benzene,” *Combust. Flame*, vol. 160, no. 12, pp. 2642–2653, Dec. 2013, doi: 10.1016/j.combustflame.2013.07.005.
[198] H. Jin *et al.*, “A chemical kinetic modeling study of indene pyrolysis,” *Combust. Flame*, vol. 206, pp. 1–20, Aug. 2019, doi: 10.1016/j.combustflame.2019.04.040.
[199] D. P. Porfiriev, V. N. Azyazov, and A. M. Mebel, “Conversion of acenaphthalene to phenalene via methylation: A theoretical study,” *Combust. Flame*, vol. 213, pp. 302–313, Mar. 2020, doi: 10.1016/j.combustflame.2019.11.038.
[200] P. Liu, Z. Li, A. Bennett, H. Lin, S. M. Sarathy, and W. L. Roberts, “The site effect on PAHs formation in HACA-based mass growth process,” *Combust. Flame*, vol. 199, pp. 54–68, Jan. 2019, doi: 10.1016/j.combustflame.2018.10.010.
[201] T.-C. Chu, M. C. Smith, J. Yang, M. Liu, and W. H. Green, “Theoretical study on the HACA chemistry of naphthalenyl radicals and acetylene: The formation of C12H8, C14H8, and C14H10 species,” *Int. J. Chem. Kinet.*, vol. 52, no. 11, pp. 752–768, 2020, doi: https://doi.org/10.1002/kin.21397.
[202] L. Vereecken and J. Peeters, “Reactions of chemically activated C9H9 species II: The reaction of phenyl radicals with allene and cyclopropene, and of benzyl radicals with acetylene,” *Phys Chem Chem Phys*, vol. 5, pp. 2807–2817, Jun. 2003, doi: 10.1039/B303908K.
[203] J. A. Manion and I. A. Awan, “A Shock Tube Study of H Atom Addition to Cyclopentene,” *Int. J. Chem. Kinet.*, vol. 50, no. 4, pp. 225–242, 2018, doi: 10.1002/kin.21150.
[204] A. N. Morozov and A. M. (ORCID:0000000272333133) Mebel, “Theoretical Study of the Reaction Mechanism and Kinetics of the Phenyl + Allyl and Related Benzyl + Vinyl Associations,” *J. Phys. Chem. Mol. Spectrosc. Kinet. Environ. Gen. Theory*, vol. 123, no. 9, Feb. 2019, doi: 10.1021/acs.jpca.9b00345.
[205] L. Zhao *et al.*, “Gas phase formation of phenalene via 10π-aromatic, resonantly stabilized free radical intermediates,” *Phys. Chem. Chem. Phys.*, vol. 22, no. 27, pp. 15381–15388, Jul. 2020, doi: 10.1039/D0CP02216K.
[206] A. Oleinikov, A. Mebel, and V. Azyazov, “Kinetics of Reactions of 1- and 2-Naphthyl with Propyne and Allene,” *Bull. Lebedev Phys. Inst.*, vol. 47, pp. 97–100, Mar. 2020, doi: 10.3103/S1068335620030057.
[207] A. M. Mebel, A. Landera, and R. I. Kaiser, “Formation Mechanisms of Naphthalene and Indene: From the Interstellar Medium to Combustion Flames,” *J. Phys. Chem. A*, vol. 121, no. 5, pp. 901–926, Feb. 2017, doi: 10.1021/acs.jpca.6b09735.
[208] G. da Silva and J. W. Bozzelli, “The C7H5 fulvenallenyl radical as a combustion intermediate: potential new pathways to two- and three-ring PAHs,” *J. Phys. Chem. A*, vol. 113, no. 44, pp. 12045–12048, Nov. 2009, doi: 10.1021/jp907230b.
[209] A. Laskin, C. Tamburu, F. Dubnikova, and A. Lifshitz, “Production of major reaction products in the initial steps of the thermal decomposition of naphthalene. Experimental shock-tube results and computer simulation,” *Proc. Combust. Inst.*, vol. 35, no. 1, pp. 299–307, Jan. 2015, doi: 10.1016/j.proci.2014.06.019.
[210] S. Sinha, R. K. Rahman, and A. Raj, “On the role of resonantly stabilized radicals in polycyclic aromatic hydrocarbon (PAH) formation: pyrene and fluoranthene formation from benzyl–indenyl addition,” *Phys. Chem. Chem. Phys.*, vol. 19, no. 29, pp. 19262–19278, Jul. 2017, doi: 10.1039/C7CP02539D.
[211] W. Sun, A. Hamadi, S. Abid, N. Chaumeix, and A. Comandini, “A comparative kinetic study of C8–C10 linear alkylbenzenes pyrolysis in a single-pulse shock tube,” *Combust. Flame*, vol. 221, pp. 136–149, Nov. 2020, doi: 10.1016/j.combustflame.2020.07.031.
[212] A. Hamadi, W. Sun, S. Abid, N. Chaumeix, and A. Comandini, “An experimental and kinetic modeling study of benzene pyrolysis with C2−C3 unsaturated hydrocarbons,” *Combust. Flame*, vol. 237, p. 111858, Mar. 2022, doi: 10.1016/j.combustflame.2021.111858.

[213] W. Sun, A. Hamadi, S. Abid, N. Chaumeix, and A. Comandini, “Detailed experimental and kinetic modeling study of toluene/C2 pyrolysis in a single-pulse shock tube,” *Combust. Flame*, vol. 226, pp. 129–142, Apr. 2021, doi: 10.1016/j.combustflame.2020.11.044.
[214] J. A. Miller and C. F. Melius, “Kinetic and thermodynamic issues in the formation of aromatic compounds in flames of aliphatic fuels,” *Combust. Flame*, vol. 91, no. 1, pp. 21–39, Oct. 1992, doi: 10.1016/0010-2180(92)90124-8.
[215] C. J. Pope and J. A. Miller, “Exploring old and new benzene formation pathways in low-pressure premixed flames of aliphatic fuels,” *Proc. Combust. Inst.*, vol. 28, no. 2, pp. 1519–1527, Jan. 2000, doi: 10.1016/S0082-0784(00)80549-4.
[216] J. A. Miller and S. J. Klippenstein, “The Recombination of Propargyl Radicals: Solving the Master Equation,” *J. Phys. Chem. A*, vol. 105, no. 30, pp. 7254–7266, Aug. 2001, doi: 10.1021/jp0102973.
[217] N. Hansen *et al.*, “Photoionization mass spectrometric studies and modeling of fuel-rich allene and propyne flames,” *Proc. Combust. Inst.*, vol. 31, no. 1, pp. 1157–1164, Jan. 2007, doi: 10.1016/j.proci.2006.07.045.
[218] I. Weber, L. Golka, and M. Olzmann, “Thermal decomposition of propene: A shock-tube/H-ARAS and modeling study,” *Proc. Combust. Inst.*, vol. 1, no. 36, pp. 299–306, 2017, doi: 10.1016/j.proci.2016.06.091.
[219] A. S. Kallend, J. H. Purnell, B. C. Shurlock, and R. G. W. Norrish, “The pyrolysis of propylene,” *Proc. R. Soc. Lond. Ser. Math. Phys. Sci.*, vol. 300, no. 1460, pp. 120–139, Aug. 1967, doi: 10.1098/rspa.1967.0161.
[220] V. S. Rao and G. B. Skinner, “Study of the high-temperature pyrolysis of propene by determination of H and D atoms formed from partially deuterated propenes heated behind shock waves,” *J. Phys. Chem.*, vol. 93, no. 5, pp. 1869–1876, Mar. 1989, doi: 10.1021/j100342a034.
[221] A. Lifshitz, M. Frenklach, and A. Burcat, “Structural isomerization allene .dblarw. propyne. Studies with a single pulse shock tube,” *J. Phys. Chem.*, vol. 79, no. 12, pp. 1148–1152, Jun. 1975, doi: 10.1021/j100579a002.
[222] J. N. Bradley and K. O. West, “Single-pulse shock tube studies of hydrocarbon pyrolysis. Part 4.—Isomerization of allene to methylacetylene,” *J. Chem. Soc. Faraday Trans. 1 Phys. Chem. Condens. Phases*, vol. 71, no. 0, pp. 967–971, Jan. 1975, doi: 10.1039/F19757100967.
[223] Y. Hidaka, T. Nakamura, H. Tanaka, A. Jinno, H. Kawano, and T. Higashihara, “Shock tube and modeling study of propene pyrolysis,” *Int. J. Chem. Kinet.*, vol. 24, no. 9, pp. 761–780, 1992, doi: 10.1002/kin.550240902.
[224] T. Bentz, B. R. Giri, H. Hippler, M. Olzmann, F. Striebel, and M. Szöri, “Reaction of Hydrogen Atoms with Propyne at High Temperatures: An Experimental and Theoretical Study,” *J. Phys. Chem. A*, vol. 111, no. 19, pp. 3812–3818, May 2007, doi: 10.1021/jp070833c.
[225] S. G. Davis, C. K. Law, and H. Wang, “Propyne Pyrolysis in a Flow Reactor: An Experimental, RRKM, and Detailed Kinetic Modeling Study,” *J. Phys. Chem. A*, vol. 103, no. 30, pp. 5889–5899, Jul. 1999, doi: 10.1021/jp982762a.
[226] S. G. Davis, C. K. Law, and H. Wang, “Propene pyrolysis and oxidation kinetics in a flow reactor and laminar flames,” *Combust. Flame*, vol. 119, no. 4, pp. 375–399, Dec. 1999, doi: 10.1016/S0010-2180(99)00070-X.
[227] Terumitsu. Kakumoto, Toshiaki. Ushirogouchi, Ko. Saito, and Akira. Imamura, “Isomerization of allene .dblarw. propyne in shock waves and ab initio calculations,” *J. Phys. Chem.*, vol. 91, no. 1, pp. 183–189, Jan. 1987, doi: 10.1021/j100285a040.
[228] A. Burcat, “Cracking of propylene in a shock tube,” *Fuel*, vol. 54, no. 2, pp. 87–93, Apr. 1975, doi: 10.1016/0016-2361(75)90062-9.
[229] J. H. Kiefer, M. Z. Al-Alami, and K. A. Budach, “A shock tube, laser-schlieren study of propene pyrolysis at high temperatures,” *J. Phys. Chem.*, vol. 86, no. 5, pp. 808–813, Mar. 1982, doi: 10.1021/j100394a043.

[230] S. S. Nagaraja *et al.*, “A hierarchical single-pulse shock tube pyrolysis study of C2–C6 1-alkenes,” *Combust. Flame*, vol. 219, pp. 456–466, Sep. 2020, doi: 10.1016/j.combustflame.2020.06.021.
[231] S. Panigrahy *et al.*, “A comprehensive experimental and improved kinetic modeling study on the pyrolysis and oxidation of propyne,” *Proc. Combust. Inst.*, vol. 38, no. 1, pp. 479–488, Jan. 2021, doi: 10.1016/j.proci.2020.06.320.
[232] K. Norinaga, V. M. Janardhanan, and O. Deutschmann, “Detailed chemical kinetic modeling of pyrolysis of ethylene, acetylene, and propylene at 1073–1373 K with a plug-flow reactor model,” *Int. J. Chem. Kinet.*, vol. 40, no. 4, pp. 199–208, 2008, doi: 10.1002/kin.20302.
[233] N. Hansen, X. He, R. Griggs, and K. Moshammer, “Knowledge generation through data research: New validation targets for the refinement of kinetic mechanisms,” *Proc. Combust. Inst.*, vol. 37, no. 1, pp. 743–750, Jan. 2019, doi: 10.1016/j.proci.2018.07.023.
[234] T. Yu and M. C. Lin, “Kinetics of the phenyl radical reaction with ethylene: An RRKM theoretical analysis of low and high temperature data,” *Combust. Flame*, vol. 100, no. 1, pp. 169–176, Jan. 1995, doi: 10.1016/0010-2180(94)00085-7.
[235] T.-C. Chu, Z. J. Buras, B. Eyob, M. C. Smith, M. Liu, and W. H. Green, “Direct Kinetics and Product Measurement of Phenyl Radical + Ethylene,” *J. Phys. Chem. A*, vol. 124, no. 12, pp. 2352–2365, Mar. 2020, doi: 10.1021/acs.jpca.9b11543.
[236] L. Vereecken, H. F. Bettinger, and J. Peeters, “Reactions of chemically activated C9H9 species.,” *Phys. Chem. Chem. Phys.*, vol. 4, no. 11, pp. 2019–2027, May 2002, doi: 10.1039/B109452A.
[237] L. Vereecken, J. Peeters, H. F. Bettinger, R. I. Kaiser, P. v. R. Schleyer, and H. F. Schaefer, “Reaction of Phenyl Radicals with Propyne,” *J. Am. Chem. Soc.*, vol. 124, no. 11, pp. 2781–2789, Mar. 2002, doi: 10.1021/ja017018+.
[238] V. V. Kislov and A. M. Mebel, “Ab initio G3-type/statistical theory study of the formation of indene in combustion flames. I. Pathways involving benzene and phenyl radical,” *J. Phys. Chem. A*, vol. 111, no. 19, pp. 3922–3931, May 2007, doi: 10.1021/jp067135x.
[239] W. Sun, A. Hamadi, S. Abid, N. Chaumeix, and A. Comandini, “Insights into the pyrolysis kinetics of xylene isomers behind reflected shock waves,” *Combustion and Flame*, vol. Submitted, 2021.
[240] R. Xu *et al.*, “A physics-based approach to modeling real-fuel combustion chemistry – II. Reaction kinetic models of jet and rocket fuels,” *Combust. Flame*, vol. 193, pp. 520–537, Jul. 2018, doi: 10.1016/j.combustflame.2018.03.021.
[241] R. A. Tesner and S. v. Shurupov, “Soot Formation from Acetylene-Benzene Mixture,” *Combust. Sci. Technol.*, vol. 92, no. 1–3, pp. 61–67, Jul. 1993, doi: 10.1080/00102209308907661.
[242] H. Böhm and H. Jander, “PAH formation in acetylene–benzene pyrolysis,” *Phys. Chem. Chem. Phys.*, vol. 1, no. 16, pp. 3775–3781, Jan. 1999, doi: 10.1039/A903306H.
[243] A. D. Abid, E. D. Tolmachoff, D. J. Phares, H. Wang, Y. Liu, and A. Laskin, “Size distribution and morphology of nascent soot in premixed ethylene flames with and without benzene doping,” *Proc. Combust. Inst.*, vol. 32, no. 1, pp. 681–688, Jan. 2009, doi: 10.1016/j.proci.2008.07.023.
[244] C. A. Echavarria, A. F. Sarofim, J. S. Lighty, and A. D’Anna, “Evolution of soot size distribution in premixed ethylene/air and ethylene/benzene/air flames: Experimental and modeling study,” *Combust. Flame*, vol. 158, no. 1, pp. 98–104, Jan. 2011, doi: 10.1016/j.combustflame.2010.07.021.
[245] S. J. Harris and A. M. Weiner, “Soot Particle Growth in Premixed Toluene/Ethylene Flames,” *Combust. Sci. Technol.*, vol. 38, no. 1–2, pp. 75–87, Jun. 1984, doi: 10.1080/00102208408923764.